Semi-transparent perovskite solar cells for large area 4-terminal silicon-based tandem devices

Émilie Raoult

Émilie Raoult. Semi-transparent perovskite solar cells for large area 4-terminal silicon-based tandem devices. Optics [physics.optics]. Université Paris-Saclay, 2022. English. NNT : 2022UPAST078 . tel-03700456

HAL Id: tel-03700456
https://theses.hal.science/tel-03700456v1

Submitted on 21 Jun 2022

Semi-transparent perovskite solar cells for large area 4-terminal silicon-based tandem devices

Cellules solaires semi-transparentes en pérovskite pour des dispositifs tandem de grande surface à 4 terminaux à base de silicium

Thèse de doctorat de l'université Paris-Saclay

École doctorale n°575 : electrical, optical, bio : physics and engineering (EOBE)
Spécialité de doctorat : Electronique et Optoélectronique, Nano- et Microtechnologies
Graduate School : Sciences de l'ingénierie et des systèmes
Référent : Faculté des sciences d'Orsay

Thèse préparée dans l'unité de recherche C2N (Université Paris-Saclay, CNRS), sous la direction de Stéphane COLLIN, directeur de thèse et Romain BODEUX, encadrant industriel

Thèse soutenue à Paris-Saclay, le 18 mai 2022, par

Emilie RAOULT

Composition du jury

Emmanuelle Deleporte Professeur, ENS Paris-Saclay (LuMIn)	Président
Emilie Planès Maître de conférence, Université Savoie Mont-Blanc (LEPMI)	Rapporteur & Examinateur
Gilles Lérondel Professeur, Université de Technologie de Troyes (L2n)	Rapporteur & Examinateur
Jacky Even Professeur, INSA Rennes (FOTON)	Examinateur
Peter Reiss Directeur de recherche, CEA (SyMMES)	Examinateur
Stéphane Collin Directeur de recherche, Université Paris-Saclay (C2N)	Directeur de thèse

THESE DE DOCTORAT

NNT : 2022UPAST078

Remerciments

La rédaction de ces remerciements symbolise aujourd’hui la fin de ces 3 années de doctorat. Cette thèse, et les résultats qu’elle contient, n’auraient pas pu voir le jour sans l’appui d’un grand nombre de personnes que je tiens à remercier ici.

Tout d’abord, je souhaite remercier Romain BODEUX (encadrant EDF) et Stéphane COLLIN (directeur de thèse, C2N) qui m’ont suivie tout au long de ce parcours avec beaucoup de bienveillance. Romain, je te remercie notamment pour ton soutien sans faille lors de ces 3 années. Tu m’as laissé toute l’autonomie dont j’avais besoin tout en te rendant toujours disponible lorsque que cela était nécessaire. Tes conseils, toujours délivrés avec beaucoup de gentillesse, m’auront motivée à donner le meilleur de moi-même. Stéphane, je te remercie aussi, tu m’auras permis de progresser énormément que cela soit au niveau de mes présentations ou de la rédaction. Je sais que les pérovskites resteront toujours un peu de la magie noire à tes yeux, mais ton expertise et ton regard extérieur m’ont beaucoup aidée sur différents points bloquants. Merci du fond du cœur à vous deux.

Je remercie aussi l’entité qui m’a accueillie et m’a permis de réaliser mes travaux de thèse dans ses locaux à savoir l’Institut Photovoltaïque d’Ile de France (IPVF). De même, mes remerciements vont aussi à EDF pour le financement de cette thèse et notamment à Cédric GUERARD et Matthieu VERSAVEL (Chefs du groupe R17), qui ont veillé à ce que je travaille dans les meilleures conditions possibles. J’adresse également mes remerciments aux membres de mon jury de thèse qui ont accepté d’évaluer mon travail et avec qui j’ai pu avoir de riches discussions pendant la soutenance. Merci donc à mes rapporteurs Gilles LERONDEL et Emilie PLANES, ainsi qu’à mes examinateurs Emmanuelle DELEPORTE, Jacky EVEN et Peter REISS pour leurs commentaires constructifs et leurs félicitations.

Durant ces 3 ans, vous avez été nombreux à m’épauler. Pour commencer, un merci tout particulier à Armelle pour toutes les cellules que tu m’as aidée synthétiser, rien n’aurait été possible sans toi. Merci aussi à Marion, qui grâce à son travail sur le développement des couches extractrices, a permis à mon travail de thèse de prendre une toute autre dimension. Iwan et Sophie, je vous remercie aussi pour le travail que nous avons mené ensemble sur les cellules semi-transparentes par Slot die. Merci aussi à vous, Frédérique et Andre, votre aide a été cruciale lors du développement de l’IO:H par ALD, j’ai énormément appris à votre contact sur cette technique que je ne connaissais pas bien. Merci à Alexandre, Alexandra, Daniel et Marie pour votre expertise sur différentes techniques de caractérisations fines, et pour votre disponibilité à m’expliquer tous les tenants et aboutissants des résultats obtenus. Merci aussi Thomas, pour ton aide sur ces derniers mois de manips, ainsi que ta motivation et ton dynamisme à toute épreuve qui nous auront permis de fabriquer ces si jolis prototypes. Un grand merci aussi à Sam pour ton aide quotidienne sur les bâtis de sputtering, parfois bien capricieux, ainsi qu’à Valérie et Mélanie, j’espère avoir pu vous transmettre ce petit savoir-faire sur l’ITO. Enfin, un merci tout particulier à Sébastien et Jean, pour leur encadrement sur ce grand projet pérovskite à l’IPVF. J’ai toujours trouvé avec vous une oreille attentive lors de mes questionnements et vous avez toujours réussi à me pousser à aller plus loin dans mes recherches. Je n’oublie pas Marc, Cécilia, Damien, Nathanaëlle, Clotaire, Karim, Aurélien, Phillip, Julie, Katherine, avec qui j’ai aussi pu échanger et travailler sur différents sujets. Merci aussi à tous mes autres collègues Jorge, Jean, Capucine, Bérangère, Géraud, Guillaume, Andy, Vincent, Thomas avec qui j’ai pu rire et échanger pendant les pauses déjeuner ou autour d’un verre. Enfin, merci à mes collègues de bureau : Amelle, Stéphanie, Javid, Amadéo, l’ambiance et la paisibilité de cet open-space étaient aussi de votre fait.

Parce qu'on a tous traversé la même chose et qu'il était agréable et rassurant de partager les meilleurs comme les moins bons moments, je remercie aussi les doctorants qui ont gravité autour de moi ces 3 dernières années : Sophie, Anatole, Margot, Olivier, Salim, Célia, Linh, Arpit, Elisa, Thomas . Dédicace spéciale à mes Tuches, qui sont aussi devenus de véritables amis avec le temps. J'espère que nos soirées cinés mélangeant nos goûts plus ou moins douteux se poursuivront encore longtemps.

Je vais maintenant passer aux remerciements un peu plus personnels, pour mes amis tout d'abord : Manon, Loic, Cyril, Camille, Emilie, Pauline, Rémi, Neil, Amandine, Maikane. Vous m'avez apporté votre soutien chacun à votre manière et les moments passés avec vous étaient (et sont) toujours si chers à mes yeux. Merci également à Clément, pour ton soutien sans faille pendant cette dernière année de thèse, chaque moment passé avec toi semblait hors du temps et je te suis très reconnaissante d'avoir été là pour moi. Merci à toi aussi Talya, mon gros chat, qui est à la fois la meilleure des peluches et des boules anti-stress. Un grand merci aussi à ma famille, pour avoir toujours cru en moi et m'avoir permis de mener à terme ces longues études. La fierté que je vois dans vos yeux représente un immense bonheur pour moi et m'a donnée la force nécessaire à chaque étape pour en arriver là aujourd'hui.

Table of contents

List of figures

List of tables

Acronyms

Al-BSF	Aluminium Back-Surface Field
ALD	Atomic Layer Deposition
ARC	Anti-Refection Coating
AZO	Aluminium-doped Zinc Oxide
CBD	Chemical Bath Deposition
CIGS	Copper Indium Gallium Selenide
CLTE	Coefficient of Linear Thermal Expansion
DA	Dead Area
DMF	N, N-dimethylformamide
DOE	Design Of Experiment
EQE	External Quantum Efficiency
ETL	Electron Transport Layer
FA	Formamidinium
FF	Fill Factor
FTO	Fluor doped Tin Oxide
FW	Forward scan (IV measurement)
F4TCNQ	I2,3,5,6-tetrafluoro-7,7,8,8-tetracyanoquinodimethane
GDOES	Glow-Discharge Optical Emission spectroscopy
GFF	Geometrical Fill Factor
GXRD	Grazing X-Ray Diffraction
HCl	Chloridic acid
HTL	Hole Transport Layer
IBC	Interdigitated Back Contact
IO:H	Hydrogenated Indium Oxide
IQE	Internal Quantum Efficiency
IR/NIR	Infrared/Near-Infrared Region
ITO	Indium Tin Oxide
ITO PGO	ITO/Glass commercial substrate
IZO	Indium Zinc Oxide

IZTO	Indium Zinc Tin Oxide
Li-TFSI	Bis(trifluoromethane)sulfonimide lithium salt
MA	Methylammonium
MAE	Mean Absolute Error
MPP	Maximum Power Point
NAM	New Amorphous Model
PCE	Photo-Conversion Efficiency
PDMS	Polydimethylsiloxane
PEALD	Plasma Enhanced Atomic Layer Deposition
PEN	Polyethylene naphthalate
PERT	Passivated Emitter and Rear Cells
PET	Polyethylene terephthalate
PL	Pholuminescence
PLA	Polylactic Acid
PO	Polyolefin
PTAA	Polytriarylamine
QCM	Quartz Crystal Microbalance
RF	Radio Frequency
RMS	Root Mean Square value
RV	Reverse scan (IV measurement)
Sa	Average roughness value of peaks and valleys
SEM	Scanning Electron Microscopy
SHJ	Silicon Heterojunction
SPT	Series-Parallel Tandem
STPC	Semi-Transparent Perovskite solar Cell
STPM	Semi-Transparent Module solar Cell
t-BP	4-tert-butylpyridine
TCO	Transparent Conductive Oxide
TEC-7	FTO/Glass commercial substrate
TLM	Transfer Length Method
TMI	Trimethyindium
TMM	Transfer Matrix Method
TRA	Transmission-Reflection-Absorption spectra
XPS	X-ray Photoelectron Spectrometry
XRD	X-ray Diffraction
XRF	X-ray Fluorescence
2/3/4T	2/3/4 Terminals

General introduction

Global energy context

We live in a modern society where energy is central in our live. The energy demand is strong and continues to grow due to the both developed and emerging countries and the growth of the world population, which is expected to reach 9.7 billion by 2050 [1]. In particular, demand for fossil fuels continued to grow significantly in 2021, despite the global coronavirus pandemic which had severely curbed global energy consumption in 2020 [2]. Indeed today, 80% of the world's primary energy consumption comes from fossil resources (gas, coal, oil) as shown in Fig. 1a. The general trend shows a increase of almost 5% per year over the last decades [3]. This is a major issue today because the burning of fossil fuels is responsible for most of the world's greenhouse gas emissions and air pollution, which have continued to increase since the 1970s, see Fig. 1b. Moreover, these resources are also very unevenly distributed, which is a source of geopolitical pressure in critical areas [2]. Finally, extraction difficulties are increasingly common due to the depletion of reserves and thus increase the operational cost and investment required. Awareness of global warming is becoming an unavoidable societal issue. The scientific community expresses his concern since the 1950s. During the recent international climate negotiations, most of the players committed themselves to limit global warming to 1.5°C by reducing their carbon footprint [4]. To reach this commitment, a rebalancing of primary energy resources by renewable resources is essential and has been launched these last years. This is particularly evident in the demand for renewable energies, which increased by 3% in 2020 [5].

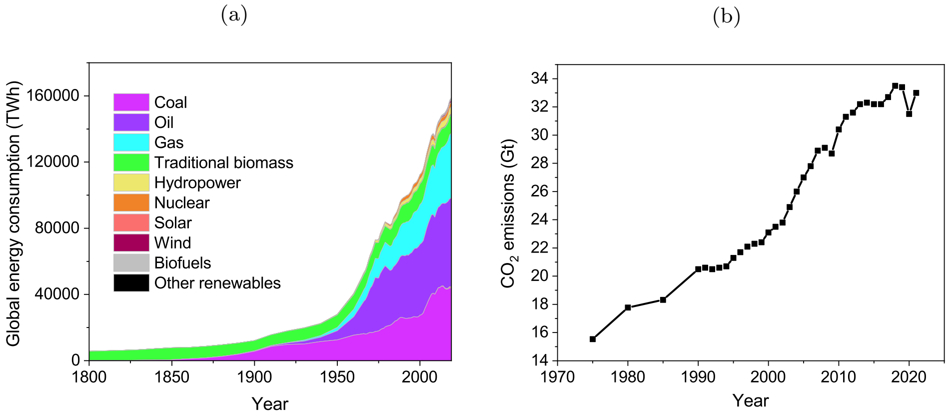
(a) (b)

Figure 1: (a) World Primary energy consumption by resource [6]. (b) Global energy-related CO$_2$ emission [3].

Solar energy is today an serious alternative to fossil fuels. In the last 15 years, the worldwide number of photovoltaic installations has exploded, while the cost of systems has considerably dropped, as shown in Fig. 2a. This is associated with the introduction of silicon-based solar cells that allow a low-cost energy production and today, the market for solar technologies is dominated by silicon-based solar cells (95%). Between 2010 and 2020, the price of crystalline silicon modules was divided by 9.5 to reach an average price of 0.18 €/Wp. This decrease is due to various factors such as offshoring, a dedicated wafer industry and an increase in the number of PV modules and their efficiency. As a result, the cost of electricity produced by solar PV on an industrial scale has decreased by 13% per year, reaching 1.3 US cents per kWh for a large scale PV project in Portugal in 2019. In parallel, the global PV production capacity has increased by an average of 20% per year since 2000, see Fig. 2b. This new capacity is the highest among all renewable energy technologies. Indeed, total installed capacity has reached 713 GWp at the end of 2020 (3% of the global power generation mix), in which China accounts for almost a third of this capacity (i.e. 260 GWp) [7].

However, the power conversion efficiencies of silicon cells are approaching their theoretical limit, set by the Shockley-Queisser limit, at 29.4% [8]. In this context, tandem cells, which are composed of a stack of two single-junction cells, are currently investigated because their efficiency limit is much higher (up to 45%). This is possible because each cell absorbs in a specific spectral range. The advantage of the tandem technology is that the silicon cell can be used as the bottom cell. Concerning the top cell, different candidates are suitable.

Recently, a new class of material called perovskite has become popular as a promising top solar cell in tandem configuration with a silicon bottom cell. First synthesized in 2009 by Kojima et al [9], the development of perovskite solar cells has been extremely rapid and it has now achieved an efficiency of 25.5% for a single junction solar cell [10]. Perovskite cells are also a promising option for low-cost tandems thanks to the materials that are used. Today, the state-of-the-art efficiencies of perovskite-based tandems have reached 29.2% and exceeded the theoretical limit of silicon cells but remain well below their theoretical limit of more than 40% [11]. Indeed, in an ideal and perfect cell, all photons with an energy higher than the bandgap of the first and second cell would be absorbed. In practice, part of the light is lost through parasitic absorption in the other layers of the cell and various electrical losses reduce the actual efficiency. This means that there is still a lot of work to be done to improve these cells.

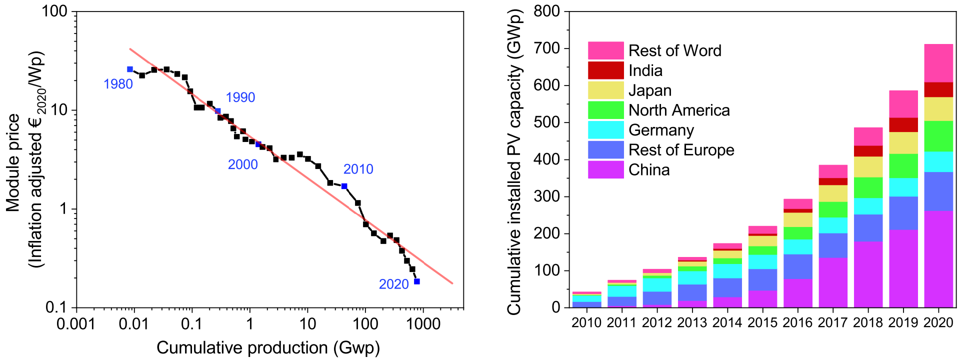
(a) (b)

Figure 2: (a) Price learning curve includes all commercially available PV Technologies [7]. (b) Global cumulative PV installation from 2010 to 2020 [7].

Goal of this work

In this thesis, we develop perovskite cells specifically for tandem applications. Starting from opaque cells, this work aims to make them transparent in the infrared spectral range while maintaining optimal electrical properties to offer high-performance to the silicon bottom cell and consequently to the tandem solar cells. A summary of the current state-of-the-art on this topic will be presented in Chapter 1 and the different equipment's used to synthesize and characterize the solar cells are detailed in Chapter 2.

The first study of this thesis consists in improving the reproducibility of the semi-transparent perovskite cell, with a particular attention to the sputtered Indium Tin Oxide (ITO) electrode. This aspect will be mainly discussed in Chapter 3. It is essential to optimize the synthesis of the cells while maintaining high performance. In particularly, the study of the influence of passivation layers inside the structure and the impact of the temperature will be studied. The tandem performance obtained with the current structure once stabilized will be presented.

Beyond the expectations concerning reproducibility, which also concern the opaque perovskite cell, the transmission of the semi-transparent perovskite cell in the near IR have to be maximized as much as possible to allow the silicon cell underneath to operate at its full potential. In Chapter 4, we will model an experimental semi-transparent perovskite cell and we will precisely identify the layers and interfaces responsible for absorption and parasitic reflection. This will allow us to propose different materials and designs that will be implemented later.

For example, a first step will be to implement the developments realized for the replacement of TiO_2 and Spiro-OMeTAD in the opaque cell by SnO_2 and PTAA, respectively, within the semi-transparent perovskite cell. Indeed Spiro-OMeTAD has an optimal band alignment with the perovskite compound but it has a poor stability in time, and a parasitic absorption in the IR. On the other hand, TiO_2 requires a high temperature of synthesis, superior to 500°C which limits the use of different substrates, flexible for example. These results are presented in Chapter 5.

The replacement of the front and back electrodes will be a key to improve optically our cells since ITO and Fluorine doped Tin Oxide (FTO) currently used have significant parasitic absorption in the infrared. Chapter 6 of this thesis will be dedicated to the development of two Transparent Conductive Oxides (TCO) more adapted to our applications: Indium Zinc Oxide (IZO) and Indium Oxide doped by Hydrogen (IO:H). These materials are more transparent in the infrared than ITO and FTO for similar electrical properties.

These chapters are based on semi-transparent perovskite cells of 0.09 cm^2 area. However, industrial applications require to increase the size of these devices. Large scale tandem cells will be achieved by two complementary approaches discussed in Chapter 7: the development of perovskite mini-modules with several cells arranged in series via a P1P2P3 structuring architecture, and the use of a new process of deposition by slot die coating, which contrary to the spin coating conventionally used, allows the synthesis of solar cells on surfaces larger than 16 cm^2.

Contributions

This thesis was realized within the IPVF lab in the team dedicated to perovskite cells and mini-modules, and benefited from the contributions of several people. My work was focused on the development of the electrodes, and more particularly for semi-transparent cells. Within this team, Armelle YAICHE was in charge of the TiO_2, perovskite and Spiro-OMeTAD depositions on the conventional (baseline) architecture, Marion PROVOST developed the SnO_2 and PTAA layers for opaque cells and Sophie BERNARD developed the perovskite deposition by slot die coating. In addition to the deposition of the electrodes, I carried out the complete opto-electrical characterization of the cells presented in this manuscript (IV dark and under illumination, and monitoring over time for the investigation of the stability, optical spectroscopy,...). I also used various methods for characterizing the physical and chemical properties of materials, including SEM, confocal microscopy, XRF, XRD and GDOES. Regarding the simulations presented in this manuscript, I carried out all the work presented, from the optical characterization of the individual and stacked layers to the determination of the indices by ellipsometry, the development of specific ellipsometric models, of electrical models, and the comparison with cell measurements (EQE, TRA spectra...). Advanced characterizations such as XPS measurements have been performed and analyzed by the Institut Lavoisier de Versailles (ILV), AFM images were made by Alexandre BLAIZOT and Hyperspectral Photoluminescence Imaging were measured by Alexandra LEVTCHENKO. The development of the IZO layer was done in collaboration with Cécilia TEL and the development of IO:H with the help of Frédérique DONSANTI and Andre GRISHIN. The various encapsulation processes were carried out with Thomas GUILLEMOT. Finally, Sébastien JUTTEAU, Salim MEJAOURI and Marc ALATEM developed the process to fabricate mini-modules on opaque structures.

Chapter 1

Context and background

Introduction

The photovoltaic effect, or photo-galvanic effect, was discovered by Edmond Becquerel in 1839 when he observed the appearance of an electrical voltage across a semiconductor material exposed to light [12]. 45 years later, Charles Fritts exploited this effect for the first time by installing the world's first prototype photovoltaic solar panel, based on selenium cells [13]. It was much later, during the Cold War, that the photovoltaic technology really took off, especially for use in various space program. Solar panels still equip the vast majority of satellites today. Thanks to access to constant radiation, independent of the seasons and weather conditions, solar energy was as reliable as nuclear energy in space, with less risk. Between the 1973 oil embargo and the subsequent energy crisis, and the oil and gas supply problems in the 90's, PV technologies came into consideration in energy policy reorganisations around the world. For example, at the turn of the century, the European Union contributed to a high level of investment and a large PV deployment in Europe.

Today, the market for solar technologies is dominated by silicon-based solar cells (95%), mainly represented by the monocrystalline technology [7]. However, thin-film technologies based on alternative materials such as Cadmium Telluride (CdTe), Copper Indium Gallium Selenide (CIGS), and other materials (dye-sensitized, concentrated PV, organic PV) have gradually emerged since the 2000s when the price of silicon was still high, as shown in Fig. 1.1. Among the recent technologies, perovskite solar cells have become one of the most promising avenues with the idea of combining them with the silicon technology in tandem architectures.

In this first chapter we will review the operation of single junction solar cells and discuss why it is now important to look at other types of devices such as tandem configurations. In the context of a double junction, we will discuss the advantages and disadvantages of the different possible architectures and why we have chosen to focus on 4 Terminals perovskite/silicon tandem devices. Finally, we will detail the particularities of each of these cells, and in the case of perovskite cells, we will focus on the conditions required for their industrialization.

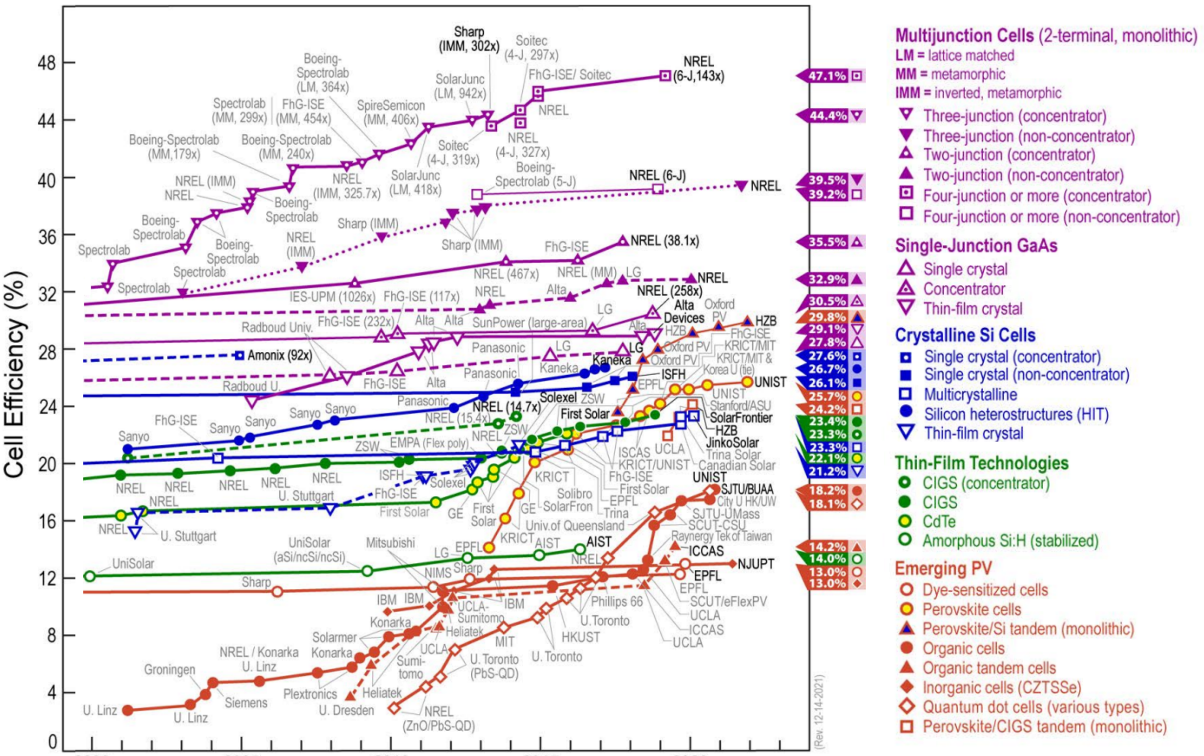

Figure 1.1: Evolution of photovoltaic efficiency by sector from 2000 to 2021 by the National laboratory Renewable Energy Laboratory (NREL) [10].

1.1 Working principles of a solar cell with a p-n junction

1.1.1 Example of the homojunction

A solar cell is an electronic device that converts sunlight directly into electricity, the current created is called photocurrent. The generation of photocurrent in a cell involves two key processes:

1. An incident photon is absorbed and creates an electron-hole pair in the absorber material. This absorption is only possible if the incident photon has an energy greater than the bandgap Eg of the semi-conductor.

2. It is necessary to prevent the immediate recombination of this e-h pair by spatially separating the electron and the hole.

To enable both of these processes to work, a p-n junction is located within the solar cell. A p-n junction is the connection of a p-doped region (holes are the majority carriers) and an n-doped region (electrons are the majority carriers). A homojunction is a semiconductor interface that occurs between layers of similar semiconductor material, these materials have equal band gaps but typically have different doping. Since the n-type region has a high electron concentration and the p-type a high hole concentration, electrons diffuse from the n-type side to the p-type side, and inversely. When the electrons and holes move to the other side of the junction, they leave behind exposed charges on dopant atom sites, which are fixed in the crystal lattice and are unable to move. An electric field E forms between the positive ion cores in the n-type material and negative ion cores in the p-type material, as illustrated in Fig. 1.2a. This region is called the "depletion region" since the electric field quickly sweeps free carriers out, hence the region is depleted of free carriers.

When a junction is exposed to light, there is an additional source of mobile charge carriers, namely the energy provided by incoming photons. If a photon generates an electron-hole pair in or near the depletion region, the electric field in the depletion region can push the mobile charge carriers through the junction. This is called photocurrent: the current resulting from the light-induced movement of charge carriers. Fig. 1.2b shows this process via the movement of charges within the solar cell.

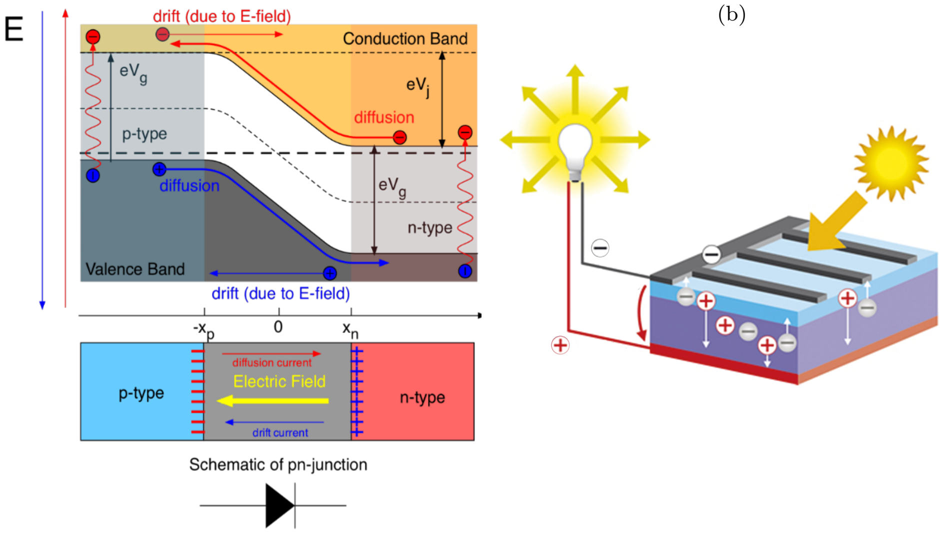
(a)
(b)

Figure 1.2: (a) Diagram of the operation of a p-n junction with the band structure and the different currents involved [14]. (b) Charge displacement in a solar cell with a p-n junction [15].

1.1.2 Limit of a single-junction cell

The power conversion efficiency of solar cells is a crucial factor in reducing the cost per area of photovoltaic electricity. However, single p-n junction cells as commercial silicon cells have a theoretical maximum efficiency that depends on their gap and is fixed by the Shockley-Queisser detailed balanced limit. This theoretical limit is due to various phenomena: a large part of the radiation is transformed into heat, photons with energies below Eg are not absorbed and some electron-hole pairs recombine too quickly, see Fig. 1.3a [8].

Despite rapid improvements in solar cell efficiency over the last twenty years, the best technologies are now approaching the limit, see Fig. 1.3b. For example, the efficiencies of silicon cells are getting closer and closer to their Shockley-Queisser limit at 32%. Furthermore, this limit is considered unattainable because there are other limitations intrinsic to the cell: the real theoretical limit is considered to be

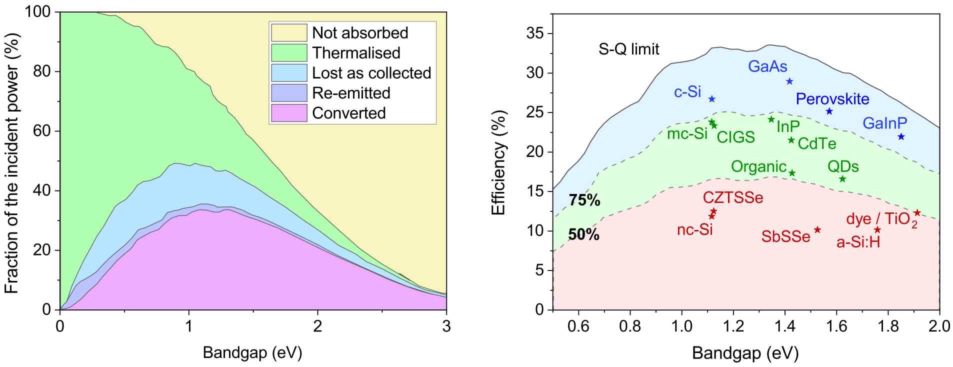
(a)
(b)

Figure 1.3: (a) Fraction of the incident power as a function of the gap of the cell considered, the Shockley-Queisser limit in turquoise depends on the gap of the absorber material. (b) Record efficiency of solar cells of different materials against their bandgap compared to the associated Shockley-Queisser limit (top solid line) [16].

29.4% [8]. Today, the efficiency of silicon cells already reaches 26.7% [10]. The same can be observed with perovskite cells: efficiencies already reach 25.5 % in the laboratory, whereas their Shockley-Queisser limit is 33% [10, 17].

1.2 The tandem cell: interest and configuration

Several approaches have been proposed to overcome the Shockley-Queisser limit. Some of them consist of increasing the number of extracted charges (i.e. increasing the device current), for example by using several sub band gap energy photons to generate one photon above the gap (up-conversion) or to use one high energy photon to generate several charge carriers (multiple exciton generation, singlet exciton fission) [18, 19]. On the other hand, reducing the losses due to carrier relaxation (thus increasing the device voltage) could be achieved through by extracting charge carriers before relaxation, a concept called hot carrier solar cell, although experimental demonstration remains a major challenge today [20, 21]. This can also be achieved through the use of multiple junctions with existing solar cells to form tandem solar cells, and it appears to be a promising strategy to improve photovoltaic performances.

The appearance of multi-junction cells dates back to the 1980s. Thus, III-V multi-junction tandem cells have been around for a long time and are now used commercially because of their higher efficiency compared to conventional cells. Multi-junction configurations are intended to combine several photovoltaic cells, each of which will absorb in a specific spectral range. For this reason, cells of this type are no longer affected by the single junction limit but by higher theoretical limits. This limit evolves with the number of junctions to reach, with an infinite number of junctions, 66% maximum efficiency under 1 sun illumination, which corresponds to standard illumination at AM1.5 (global annual average for mid-latitudes) [11, 22]. The most efficient PV device ever manufactured is based on very expensive multi-junction configurations whose application is mainly related to self-powered systems installed in space and reaches 39.2% (conventional) and 47.1% (concentrator), see Fig. 1.1 [23].

1.2.1 Operation of multi-junctions and tandems

In the case of a simple junction with a bandgap of 1.1 eV, as illustrated in Fig. 1.4a, the most energetic radiation is not converted efficiently due to the small gap of the cell. However, in the case of a 2-junction tandem as in Fig. 1.4b, the top cell absorbs the short wavelengths (blue area) and the bottom cell absorbs the infrared light (green area). This type of device limits losses by thermalization.

In the context of this thesis, we limit ourselves to 2-junction tandem cells because the goal is to manufacture low cost tandem junctions unlike multi-junctions for space which are very expensive. Their theoretical limit is around 47% and the actual record is 32.9% [10], see Fig. 1.1.

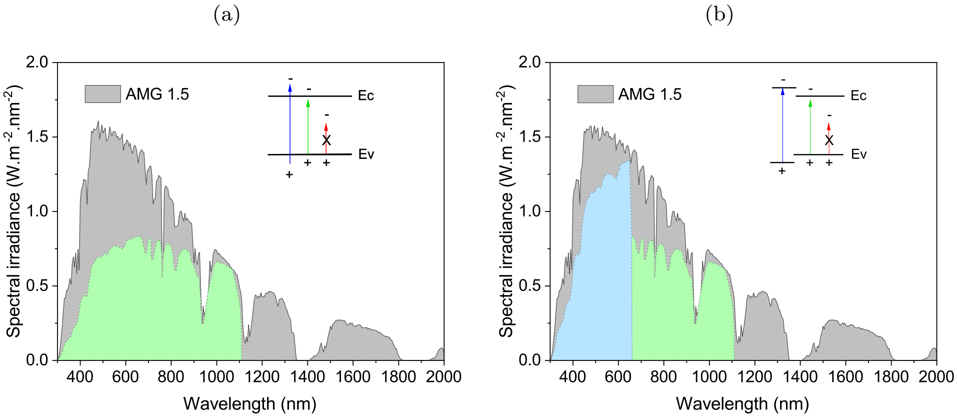
(a) (b)

Figure 1.4: Spectral absorption coverage of (a) a single junction cell in green and (b) a double junction tandem cell, in blue the top cell and in green the bottom cell [24].

1.2.2 Configurations

There are two main types of tandem configurations: 2 Terminals or 4 Terminals (classic, spectrally split and reflective), each shown in Fig. 1.5. There are also hybrid configurations such as 3 Terminals [25] or Series-Parallel Tandem (SPT) [26]. Their structure and operation are quite different, each having its own advantages and disadvantages.

1.2.2.1 4 terminals configuration (4T)

From a manufacturing point of view, the 4T tandem is the simplest configuration. The two cells are manufactured independently of each other before being stacked, see Fig. 1.5a. Each requires a complete electrical connection (e.g. front and rear electrodes) and they are only connected to each other externally. This allows the best manufacturing process to be used for each cell while respecting their constraints related to temperature, substrate roughness, the solvent used and the polarity chosen (n-i-p or p-i-n type). In addition, when operating the tandem, each cell can maintain its own maximum power value as the electrical systems are completely separated [27–29].

In the most typical configuration and considering electrodes that cover the entire surface of the cells, some need to be transparent at certain wavelengths so that the bottom cell can absorbs the longer wavelengths, as shown in Fig. 1.5a. Thus, the first electrode encountered by light needs to have transparency over the entire solar spectrum, while the second and third only need to be transparent in the near infrared. Finally, the back electrode can be reflective as in a single junction cell. However, a bifacial tandem with a transparent back electrode can takes advantage of the albedo, which is important on certain surfaces such as ice or limestone, to increase the amount of light entering the cell [26, 30]. The challenge today with this type of configuration is to minimise the parasitic absorption due to the presence of two intermediate electrodes and the manufacturing costs associated with the multiple electrodes and electrical connections. Indeed, the inverter associated with these solar cells needs have one sub-circuits for each cell to operate at its maximum power, instead of just one as in the standard case. In practice, this doubles the associated costs for a commercial module.

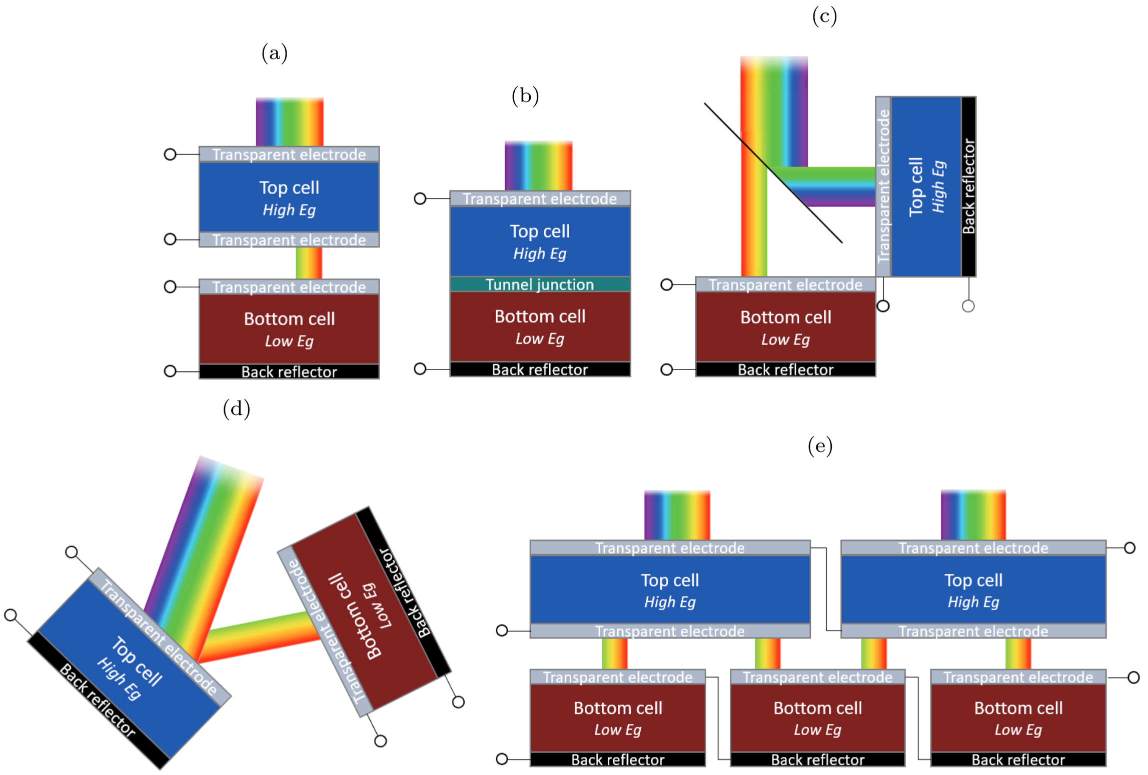

Figure 1.5: (a) Classical 4T configuration [31]. (b) 2T configuration [31]. (c) Spectral split 4T configuration [31]. (d) Reflective 4T configuration [31]. (e) SPT configuration [26].

There are two more special types of 4T configurations: spectrally split and reflective, see Fig. 1.5c and d. In the case of a spectral split 4T tandem, a dichroic mirror separates the light between a large gap cell and a smaller gap cell. With this system, it is possible to use standard single junction cells without the need to add transparent intermediate electrodes. In addition, there is less parasitic absorption loss as the photons only pass through the cell corresponding to their energy. However, the optical components are expensive, which raises doubts about the economic viability of such an arrangement for conventional photovoltaic panels [28, 29, 32]. The reflective 4T system works on a similar principle, but the spectral separation occurs at the surface of one of the two cells. The latter reflects part of the radiation onto the second [33].

1.2.2.2 2 terminals configuration (2T)

In the 2T configuration, the two cells are electrically connected in series via a tunnel junction or a recombination layer, see Fig. 1.5b. Unlike the previous configuration, they are not independent. This structure eliminates the need for back and front electrodes for the top and bottom cells respectively, which results in lower costs [26].

However, there are some technical difficulties with this type of configuration, although different from those of the 4T. The two cells must be fabricated in such a way as to generate a similar electrical current during tandem operation, as the overall current produced will be determined by the lower of the two currents generated by the two cells. This electrical match requires a top cell bandgap between 1.7 and 1.8 eV when the bottom cell gap is 1.1 eV (as silicon cells) in order to distribute the photons efficiently, see Fig. 1.6. Therefore it makes the 2T tandem cell more sensitive than a 4T to spectral variations. Thus, the cell must be designed to operate in an identified geographical area [28].

The bottom cell acts as a substrate for the top cell, so it is important to have a surface with a suitable texture for the deposition of subsequent layers [34]. In parallel, it is also important not to damage the bottom cell during the manufacture of the top cell. This requires a bottom cell that is robust enough to withstand the manufacturing process of the second cell, or to adapt the fabrication of the top cell to these constraints.

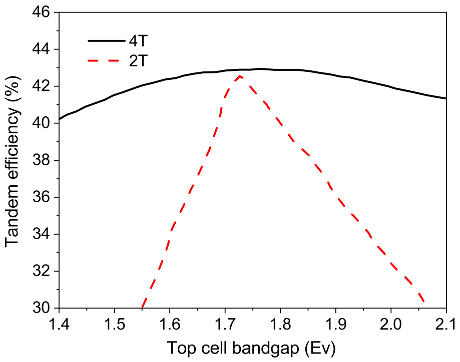

Figure 1.6: Maximum theoretical efficiency of 4T or 2T tandem as a function of the top cell bandgap when the bottom cell bandgap is 1.1 eV [35].

1.2.2.3 Series-Parallel Tandem configuration

In the classic 4T configuration, the cells in each line are independent. The SPT configuration is a hybrid configuration between 2T and 4T, based on a very similar model. It consists of connecting cells of similar type together in series, and then the ”lines” of cells are connected together in parallel, as shown in Fig. 1.5e. This approach requires a current matching as in the 2T, but between two lines of cells rather than just a top and bottom cell as in a 2T. Since this ratio can be easily adjusted, greater freedom in the choice of cell gap is possible compared to a 2T configuration. The advantages over the classic 4T configuration are that the material costs for the connections are lower because there are fewer of them.

In addition, for laboratory use, having top and bottom cells of different sizes is no longer a problem here. Indeed, ensuring that the top and bottom cells are the same size so as not to lose space is an additional constraint for 2T and 4T tandems, which is not the case in the SPT configuration [31, 36, 37].

The advantages of 4T and more particularly of SPT in terms of the manufacturing process make it a very interesting choice of configuration. The development of SPT cells would solve the cost problems associated with 4T. For these reasons, in the following we will focus on 4T cell configurations. As the manufacturing techniques for 4T and SPT are similar, the topics discussed below are also valid for this configuration.

1.2.3 4T perovskite/silicon tandem solar cell

A good choice of cells for a 4T tandem configuration still depends on the gap values of the two cells, although this is less important than in the 2T configuration. Fig. 1.7a shows the theoretical maximum efficiency for 4T tandems as a function of the gap of each cell [26]. An area of maximum efficiency at 46% stands out with gaps of 1.62 and 0.95 eV [38]. It is nevertheless possible to find very close efficiencies with gaps of ±0.1 eV on each side of the peak in both directions. The choice of 4T appears here to be a very interesting solution because for a tandem with, for example, a 1.1 eV absorber in the bottom cell, the choice of top cells remains vast.

Silicon cells appear at first sight to be the ideal candidates for use as bottom cells. They have a sufficiently low gap of 1.1 eV, a competitive manufacturing cost, proven efficiency, and are reliable. As the technology is already mature, these cells are very interesting for a 4T configuration where the cell manufacturing remains independent. Other bottom cell types may be of interest such as small gap perovskite, CIGS and Copper Zinc Tin Sulfide (CZTS) solar cells but their development is still ongoing, which represents an additional cost [17, 41, 42]. For this reason, we will concentrate on 4T tandem cells with a silicon bottom cell.

Similarly, there are several choices for the top cell if silicon is chosen as the bottom cell. Indeed, according to Fig. 1.7a, the gap of the top cell should be between 1.65 and 1.85 eV. Large gap CIGS, III-V semiconductors and perovskite cells are relatively suitable absorbers as they have a bandgap in this range. III-V semiconductors are now achieving very high efficiencies. Thus, the 2 junction record efficiency (32.9%) was achieved with a top cell of III-V and a silicon bottom cell, see Fig. 1.1 [43]. However, their manufacturing costs are very high, even if there are now several serious possibilities for cost reductions, such as the reuse of the substrate [44]. For terrestrial applications, these tandem cells will only become economically viable if they can be manufactured at a similar cost to silicon. This has not yet been achieved and this prevents their large-scale deployment [45]. On the other hand, the efficiency of large gap CIGS cells is still too low to consider a tandem configuration (15% at 1.6 eV [46]), and more research is needed to improve the performance of these thin films [17]. In view of the current know-how of the lab, we will only use perovskite cells as top-cell.

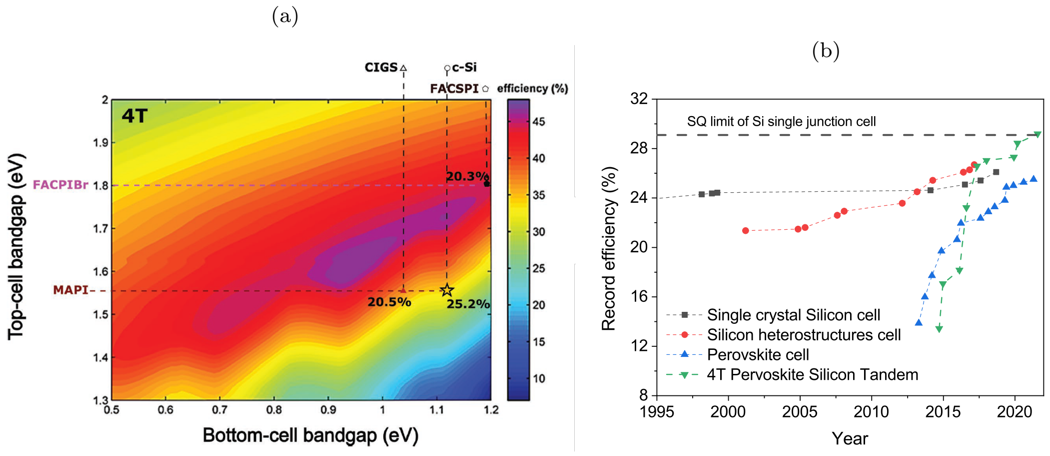

Figure 1.7: (a) Maximum theoretical efficiency for a 4T tandem as a function of the bandgap of the bottom and top cells [26]. (b) Certified world record efficiency evolution of various PV technologies including single crystal silicon cell (26.1%), heterostructure silicon cell (26.7%), perovskite single cell (25.5%), and 4T perovskite/silicon tandem solar cell (29.2%) [39, 40].

The first reports of a 4T perovskite/silicon tandem solar cell were published at the end of 2014 by Löper et al. [47] and by Bailie et al. [48] showing efficiencies of 13.4% and 17%, respectively. The Appendix A summarises the different tandems that have appeared in recent years, with the different types of perovskite and silicon cells used. This type of tandem shows a rapid improvement in efficiency increasing by more than a factor of two in 5 years, see Fig. 1.7b [10, 49, 50]. They exceeded the efficiency of single-junction silicon solar cells for the first time in 2018 by researchers at Oxford PV and IMEC. Today, the efficiency record is 29.2%, achieved by the European Solliance Solar Research consortium. This tandem is very close to the theoretical limit for a silicon single junction cell, and to the record obtained on 2T configuration at 29.8% [10]. However, the efficiency limit of the perovskite/silicon tandem is above 40%, indicating that there is still possible to increase the efficiency of the tandem solar cell device [36].

In the following sections we will detail the particularities of silicon and perovskite cells, as single junction and when they are used in a 4T tandem configuration.

1.3 The bottom cell: silicon solar cell

Today, the photovoltaic industry relies most heavily on the use of silicon as a semiconductor material. This type of solar panel accounted for up to 95% of the total photovoltaic market in 2018 and is based on the use of crystalline silicon wafers [7]. The majority of current solar cells are based on monocrystalline silicon wafers which provide good device performance and rely on energy-intensive manufacturing processes. The efficiency of conventional silicon cells in industrial production is around 22% for a monocrystalline substrate, and 18% for a multicrystalline substrate [3]. In the laboratory, much higher efficiencies are achieved, usually through the use of more advanced technologies. Several innovations are common to many types of silicon cells, such as surface texturing and anti-reflection coatings that maximize the amount of light entering the cell. After presenting the different technologies available today, we will give a quick overview of the specific silicon cells used in the 4T tandem configuration with perovskite solar cells.

1.3.1 Different silicon cell technologies

1.3.1.1 Aluminium Back-Surface Field solar cell

Standard silicon cells are based on a silicon substrate with a p-type and n-type regions. This homojunction can be combined with an Anti-Reflection Coating (ARC), a surface texturing or a back surface field (BSF) [51–53]. The BSF consists of creating a potential barrier on the back side of the cell. By doping the back of the cell more strongly, an electric field is created which confines the minority carriers in the absorber. This limits the recombination of carriers at the back surface which otherwise reduces the electrical current. This form of doping is achieved by ion implantation, which allows very good control of the dopant profiles.

The historical architecture of industrial solar cells is the Aluminium Back-Surface Field (Al-BSF) structure (see Fig. 1.8), due to its simple manufacturing process and low manufacturing cost [54]. It was the dominant technology in silicon cells until 2018. However, despite the simplicity of the process, this structure has some disadvantages: it has a poor red response due to the high absorption of light by free carriers at the Al-Silicon interface, and the large metallic surface area leads to high recombination losses. Maximum efficiencies of 20% have been achieved with such a structure [55].

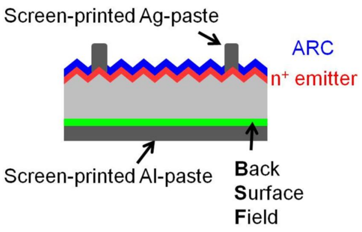

Figure 1.8: Architecture of Al-BSF solar cell [56].

1.3.1.2 Passivated Emitter and Rear solar Cell

Passivated Emitter and Rear Cells (PERCs) use two different features not found in conventional cells. They have a film on their back surface and sometimes on the emitter layer, which acts as a passivation surface [57]. The passivation layers on the emitter and on the back surface, such as SiO_2, will reduce carrier recombination at the interface of the absorber and the emitter, which is responsible for a decrease in the electrical current generated by the cell. These architectures also combine other technological innovations, such as a contact grid with a reduced surface area and localised BSF, see Fig. 1.9a. This type of structure is therefore very interesting, but it involves many different layers, which implies complex manufacturing and uses of microelectronic technologies, which for a long time seemed incompatible with manufacturing at a reasonable cost [58]. Nevertheless, PERC has become the dominant technology on the market since 2019.

Under the acronym PERC are also found technologies called PERL (Passivated Emitter, Rear Locally diffused cell), PERT (Passivated Emitter, Rear Totally diffused cell) or PERF (Passivated Emitter, Rear Floating junction cell), which have many points in common with the PERC structure, in particular the selective doping on the front side, and the passivation of the rear side. In the PERT structure for example, the BSF is no longer localised as in PERC cell, but the back surface is "totally diffused" with boron (p-type) or phosphorus (n-type).

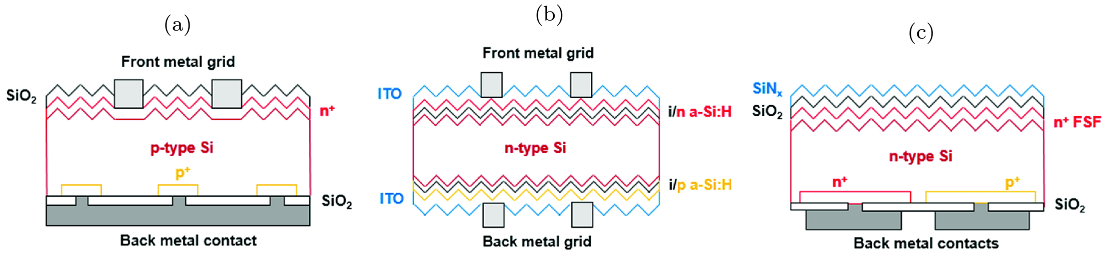

Figure 1.9: Architecture of (a) PERC, (b) SHJ and (b) IBC silicon cells [59].

1.3.1.3 Heterojunction and rear Contact Cells

The heterojunction (SHJ) combines two different semiconductor materials, whereas the homojunction like Al-BSF or PERC combines layers of the same material, see Fig. 1.9b. In the case of heterojunction cells, two semiconductors that do not have the same bandgap are used (for example, a undoped hydrogenated amorphous silicon (a-Si:H) p-doped and a crystalline silicon absorber layer (c-Si) n-doped.

As with homojunction cells, heterojunction cells can be enhanced with the use of ARC on a textured surface and a BSF. In addition, Rear Contact Cells (RCCs) place, as the name suggests, the emitter areas on the rear side. This avoids the shadowing caused by contacts and metallization on the front side and increases the absorption. It also facilitates the interconnection of the cells in the modules. The high-efficiency RCCs developed so far have an Interdigitated Back Contact (IBC) technology [60]. In IBC structures, the p-n junction and the BSF, and their metallizations, are located on the back side as interdigitated combs as shown in Fig. 1.9c. The trade-off in standard cells between shading ratio (need for thin metallizations) and resistive losses of the contacts (need for wide metallizations) is then not necessary. This structure also has an aesthetic advantage since its front side is free of any metallization. Other structures, such as EWT (Emitter Wrap Through) [61], MWT (Metallization Wrap Through) [62], and MWA (Metallization Wrap Around) [63] retain an emitter on the front side, but use collection points on the back side. This allows the use of poorer quality substrates as compared to IBC. Recently, Kaneka Corporation achieved an efficiency 26.7% for 79 cm^2 IBC-SHJ solar cell, which is the current world-record silicon solar cell [10], see Fig. 1.1.

1.3.2 Silicon cells in 4T tandem architecture

As we have seen previously, there are several types of silicon cell technologies. SHJ cells are currently the most efficient silicon cells and are therefore the ones most often used in tandem cells with perovskites to achieve record efficiency. The 4T tandem which sets the current efficiency record at 29.2% [10], used IBC-SHJ cell developed by the Japanese electronics manufacturer Panasonic. This is also the case for the previous record like the tandem cell at 27% of Wang et al. [64] or the 4T tandem cells from the University Park at 28.3% of efficiency [65]. However, IBC technologies are much more expensive than PERC type silicon cells. The commercial interest of the tandem exists only if it allows a significant gain in efficiency for a reasonable cost.

In the vast majority of cases 4T perovskite/silicon tandem, already efficient single-junction cells are used in tandem without further modification. However, these silicon cells can be adapted to the particular context of tandem and also undergo special treatment to achieve better performance in this configuration. For example, with an additional layer of MgF_2 or LiF as an anti-reflection coating on the front surface, reflection losses can be reduced to less than 2%, see Fig. 1.10a [66–68]. Another optical loss results from the escape of long wavelength photons from the backside (due to back reflection). An efficient light trapping system can effectively increase the absorption of long wavelength photons in tandem solar cells [69]. Razzaq et al. have thus proposed a particular texturing of the silicon cell specifically for tandem applications. Unlike the conventional random pyramidal texture found on silicon cells, the gratings can be designed to target specific wavelength ranges by selecting the pitch of the grating. This results in periodic nanostructures that are carefully tailored to efficiently trap weakly absorbing infrared photons as shown in Fig. 1.10b [70]. Bush et al. also demonstrated that the SiNP layer on the backside could improve the collection of infrared light [68]. Finally, the bottom silicon cell experiences higher long-wave optical loss (as a percentage of total incident light) than in conventional single-junction cells. Therefore, the optimal wafer thickness should be thicker for tandem devices than for conventional cells [71].

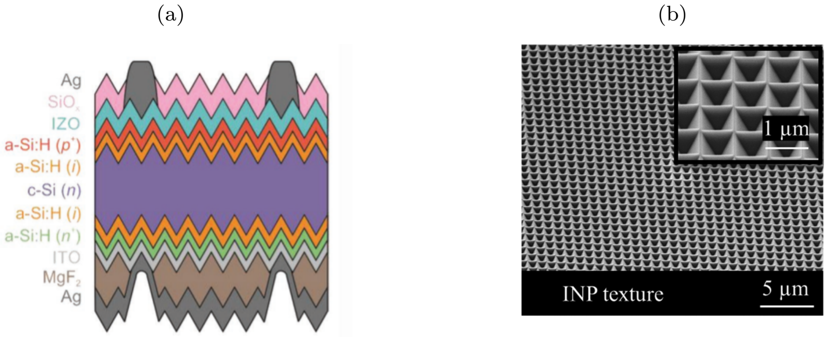
(a) (b)

Figure 1.10: (a) Schematic of the infrared-enhanced SHJ cell [66]. (b) Periodic INP gratings of 800 nm pitch were fabricated by NIL [70].

1.4 The top cell: perovskite solar cell

Scientific interest in photovoltaic technologies has grown exponentially as evidenced by the evolution of the number of scientific papers devoted to photovoltaics since 1980 [27], see Fig. 1.11. In this context, metal halide perovskite solar cells have emerged over the last decade as a new technology that is both efficient and inexpensive. This type of cell is causing a revolution in the field of photovoltaics and holds great promise for large-scale green energy production. Indeed, perovskite solar cells already account for 21% of published papers in the field of photovoltaics in 2021 [72].

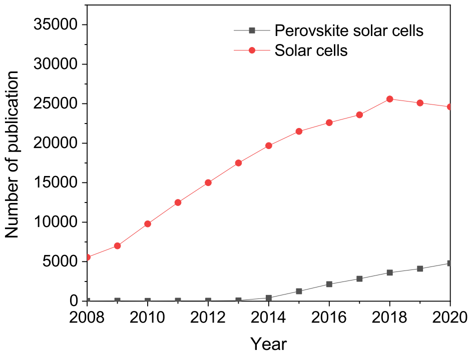

Figure 1.11: Results of the searches “photovoltaic and solar cell” and “perovskite solar cell” in Web of Science.

In this section, we will first present a quick overview of the historical background and the rapid development of these cells over the last 10 years. We will discuss the physical characteristics of this material and the n-i-p junction that characterises them in the context of solar cells. Then, still considering single junction cells in a first step, we will review the progress made recently on performance, stability, upscale and the key points hindering the industrialization today. Finally, a last part will be devoted to the specificities of semi-transparent perovskite cells for tandem applications.

1.4.1 History and context

Perovskite originally referred to calcium titanate, a mineral with the formula $CaTiO_3$ first described in 1839 by the German mineralogist Gustav Rose and named after the Russian mineralogist Lev Alexeyevich Perovski, see Fig. 1.12a. Today, it refers to a particular crystallographic structure shown in Fig. 1.12b, common to many oxides of formula ABX_3. The first incorporation of perovskite material into a solar cell was done by Kojima in 2009 and it generated only 3.8% efficiency. The cell was stable for only a few minutes because a liquid corrosive electrolyte was used [9]. A major breakthrough was achieved in 2012 when Henry Snaith and Mike Lee of Oxford University showed that perovskite was stable if brought into contact with a solid hole transport material such as Spiro-OMeTAD. This was followed by evidence that perovskite itself could also transport holes as well as electrons. As a result, a thin film perovskite solar cell, with an efficiency of more than 10% was obtained [73]. In 2013, Tan et al. succeeded in showing that it was possible to fabricate perovskite solar cells in the typical "organic solar cell" architecture, i.e. an n-i-p type configuration with the hole transport layer underneath and the electron transport layer on top of the perovskite absorber layer [74]. Snaith's group reported a planar perovskite cell with a efficiency of 12.3% [75]. In 2014, the efficiency increased to a certified 17.9% and then 20.1% [76, 77]. From 2015 to 2019, the efficiency increased rather slowly but continuously and eventually reached 25.2% thanks to composition and interface engineering [78]. Finally, an efficiency of 25.7% has been achieved in 2022 for a perovskite solar cell by Ulsan National Institute of Science and Technology (UNIST) and the Swiss Federal Institute of Technology Lausanne (EPFL) [10], see Fig. 1.1.

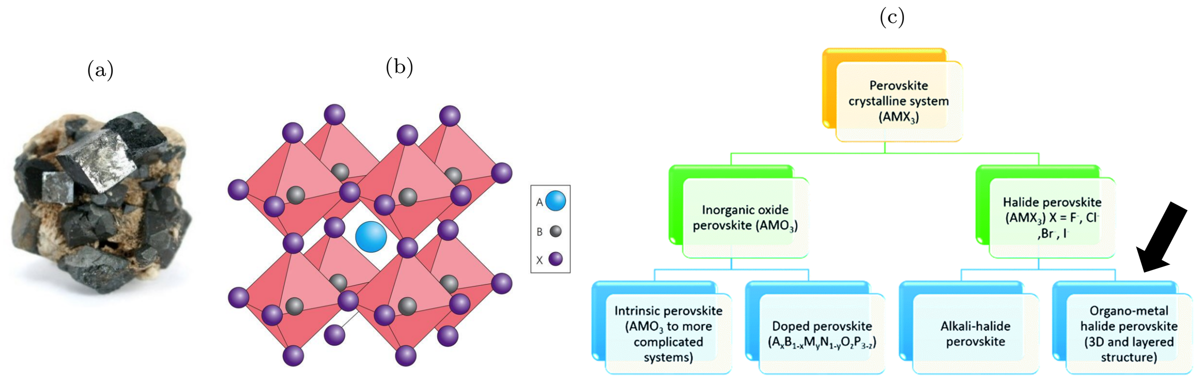

Figure 1.12: (a) Perovskite crystals on matrix, American Museum of Natural History. (b) Schematic of the perovskite-type crystal structure [79]. (c) Classification of perovskite families [80].

1.4.2 Chemical composition and opto-electronic properties of the perovskite layer

In its most simplified description, ABX_3 perovskites consist of a hexacoordinate metal cation (B) occupying the centres of octahedra whose corners are halide (X). A cation (A) fills the void left in the centre of eight of octahedra located at the corners of a classical cubic cell [27], see Fig. 1.12b. The possibilities are thus multiple and in our case, it is the organic-inorganic hybrid perovskites that are mostly used in the field of photovoltaics, see Fig. 1.12c. The most common compounds found are [26, 79, 81, 82] :

- In A, we find methylammonium (CH_3NH_3 or MA, an ammonium ion with an alkyl substitution group), rubidium (Rb), caesium (Cs), formamidinium (FA, specific amidine ions) or 5-aminovaleric acid (5-AVA)
- In B, it is usually lead (Pb), tin (Sn) or sometimes germanium (Ge)

- In X, various halogens such as chlorine (Cl), bromine (Br), or iodine (I) are used

The modification of certain elements in A, B or X causes a change in the gap of the cell under study (between 1.2 and 2.2 eV) as shown in Fig. 1.13a. The most common substitution is to replace the halogen at the X-site. When the larger, iodine, is substituted by a smaller one (I $>$ Br $>$ Cl), the onset of absorption is gradually shifted towards the blue. For the $MAPbX_3$ family, Eg is equal to 1.6 eV for $MAPbI_3$, then Eg = 2.3 eV for $MAPbBr_3$, and finally Eg = 3.1 eV for $MAPbCl_3$. In addition, it is possible to vary the stoichiometric ratio of halogens in the lattice, which allows a very fine tuning of the material gap as for the $FAPb(I_xBr_{1-x})_3$ composition which contains a mixture of bromine and iodine [83, 84]. An increase in the size of the cation A results in a decrease in Eg (Cs $<$ MA $<$ FA), as with Eg at 1.6 eV for $MAPbI_3$ and 1.45 eV for $FAPbI_3$ [41, 81].

Most devices in the literature have been made with perovskites with a bandgap of about 1.55-1.65 eV, as shown on Fig. 1.13b, which corresponds to the historical composition of $MAPbI_3$. However, this composition is nowadays less and less used. Fig. 1.13c allow to visualise how the popularity of certain perovskite compositions, $MAPbI_3$, $FA_xMA_{1-x}PbBr_yI_{3-y}$ and $Cs_zFA_xMA_{1-x-z}PbBr_yI_{3-y}$, has evolved over time. The $MAPbI_3$ is now replaced by double, triple or even quadruple cation compositions, with at least 2 different halogens. These structures are indeed more stable and have higher UV and heat resistance [68, 83, 85, 86]. Thus all the latest record single-junction perovskite cells since 2016 use a composition with at least two cations, most often MA/FA, see Table A.1 in Appendix A. Nevertheless, there are many other compositions, with now more than 400 different families of perovskites in the photovoltaic field. Concerning deposition process, perovskite is historically deposited by spin-coating on small surfaces. Other techniques exist such as evaporation, spray or slot die coating, which will be detailed in Section 1.4.4.2.

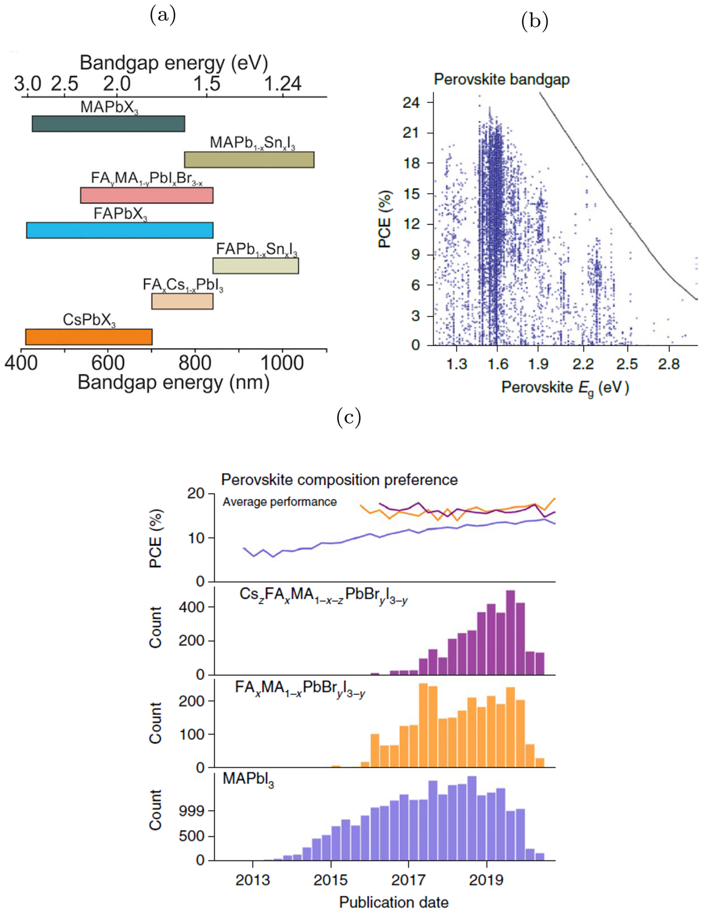
(a)

(b)

(c)

Figure 1.13: (a) Achievable gap value for different combination of elements in the perovskite structure [27]. (b) Efficiency versus bandgap Eg for perovskite solar cells in the literature, the solid line is the Shockley–Queisser limit [87]. (c) Average performance and popularity of a $MAPbI_3$, $FA_xMA_{1-x}PbBr_yI_{3-y}$ and $Cs_zFA_xMA_{1-x-z}PbBr_yI_{3-y}$ perovskite compositions in the literature as a function of time [87].

In addition, perovskite has excellent opto-electronic properties, such as a high absorption coefficient over a wide spectrum with a steep absorption edge and no sub-bandgap parasitic absorption. It should also be noted that perovskites have a direct gap unlike silicon, which makes them more efficient absorbers [29, 88]. Furthermore, electrons and holes in hybrid perovskites have a low effective mass. As a result, charges have a high mobility at room temperature. These properties are important because the charges can then diffuse over several hundred nanometers before recombining, which facilitates their collection [81, 89]. It is also a material that has a high degree of tolerance to crystal defects unlike most semiconductors.

1.4.3 Working principles of a perovskite solar cell and architectures

The operation of the perovskite cell differs from the p-n junction shown in Fig. 1.2a because it is a p-i-n junction. The perovskite layer is sandwiched between two other materials called "Electron Transport Layer" (ETL) and "Hole Transport Layer" (HTL), whose band diagram is shown in Fig. 1.14.

When an electron-hole pair is created within the perovskite, the charges diffuse to the ETL or HTL, where they are separated. The ETL has a conduction band of lower energy than the conduction band of the absorber. The electrons then move from a higher energy level to a lower energy level, which holes cannot do. Inversely, holes are collected by the HTL because it has a higher energy valence band than the absorber [81]. A perovskite cell can have two different structures, namely n-i-p or p-i-n, depending on the order of the layers encountered by light, as illustrated in Fig. 1.15a and b.

A distinction is also made between superstrate and substrate configurations in Fig. 1.15c depending on how the cell was manufactured. The superstrate configuration is most often found as it allows the deposition of the transparent top electrode (often a Transparent Conductive Oxide called TCO) before the perovskite. The latter can then be annealed without damaging the perovskite layer.

The interest of perovskite based cell and which can partly explain its popularity, is also its great flexibility in the construction of the architecture. We have already seen that there are many possibilities for the composition of the perovskite layer, but this also applies to other layers of the structure. Of the 42,400 devices found in the Jacobsson's database [87], there are more than 5,500 unique device stacks (i.e. different combinations of contact materials) and more than 1,000 of these stacks have achieved efficiencies greater than 18%. It is therefore complicated, given the multitude of existing architecture and materials used, to draw up an exhaustive list.

However, some options are more common than others. For example, there are 1,957 stacks with a specific HTL, but the ten most common HTL are used in 85% of cases, and Spiro-OMeTAD is even used in half of them. Focusing on the n-i-p superstrate architecture, the popular HTL also include some small molecules [90–94], metal-phthalocyanines (metal complexes containing tetrapyrrolic cyclic organic ligands) [95–97], organic polymers (PEDOT:PSS, P3HT, PTAA ...) [98–100] and p-type inorganic semiconductors (CuO, MoO_3 and NiO_x) [101–103]. The use of mesoporous and/or compact TiO_2 as an ETL is often found in early manufactured structures. Recently, the use of SnO_2, which is synthesized at lower temperatures, has emerged, as well as numerous n-type metal oxides such as ZnO [104], WO_3 [105], $SrTiO_3$ [106], Nb_2O_5 [107] and $BaSnO_3$ [108]. Finally, as far as electrodes are concerned, FTO is one of the few TCO that can withstand the annealing of TiO_2. When TiO_2 is not used, ITO is frequently used, which has both good conductivity and high transparency. The back electrode is usually a thin metallic layer of gold or silver.

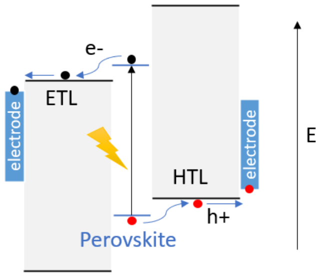

Figure 1.14: Band diagram of a perovskite cell.

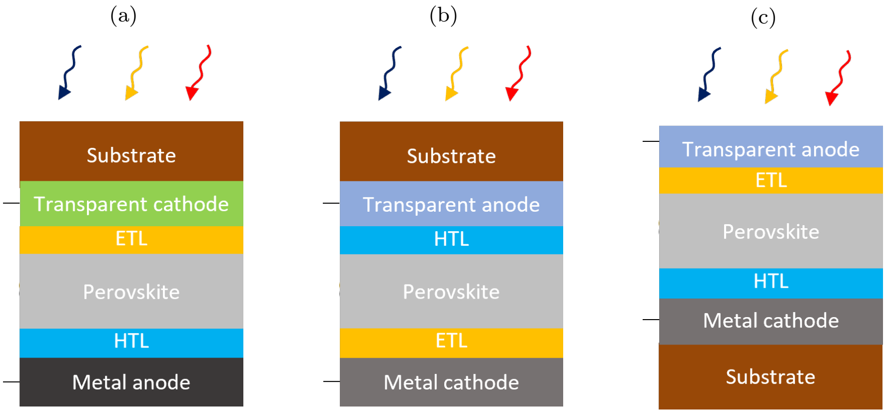

Figure 1.15: (a) n-i-p superstrate configuration. (b) p-i-n superstrate configuration. (c) p-i-n substrate configuration.

1.4.4 Development axis for industrialisation

Advances in device architecture and manufacturing processes have led to increased device performance and also to an impressive trend toward the commercialisation of perovskite cells. There are three decisive factors for the commercialisation of a solar cell: stability, large area device performance and cost. We will address these three points in this section, in addition to a focus on the toxicity concerns encountered.

1.4.4.1 Stability

The stability of perovskite cells depends on various environmental factors, including temperature, light, oxygen, humidity, preparation methods and material precursors [109, 110]. In particular, irreversible decomposition of organic species and migration of ions readily occurs in the presence of oxygen and humidity due to the hygroscopic amine component of the compound [111]. Therefore, in order to obtain a high performance solar cell, the perovskite material is usually fabricated in a glove box filled with an inert gas. It has also been found that storage of photovoltaic devices under ambient conditions leads to moisture degradation of perovskite materials. These stability issues are the main bottleneck for the commercialisation of perovskites.

As seen previously, multiple cation compositions are more stable to moisture than the classical $MAPbI_3$. Substitution or doping of the A and X positions, consisting mainly of Cs+, FA+, Rb+, Ag+, Ni2+, Cl-, and Br-, are widely used to enhance the structural stability of a perovskite film by improving the tolerance factor of the material. The introduction of additive molecules that could form additional chemical interactions with the volatile components is another effective way to suppress ion migration and irreversible decomposition of perovskite films [112]. Lead chloride, organic dye molecules, phosphorus-based Lewis acid and cyano derivatives have been reported to suppress ion migration and passivate surface ionic defects, thereby improving long-term stability [113–115].

The interfaces formed between the perovskite and the charge transport layers also play an important role in the long-term stability of the overall device by extending the path of moisture penetration, passivation of interfacial defects and formation of hydrophobic layers to isolate water. The materials used for interfacial modification are numerous, including inorganic molecules, organic molecules and polymers, indicating that new potential modification materials and technical methods still need to be explored [116, 117].

Finally, the encapsulation of perovskite cell is a direct and effective method to isolate it from the external environment. If properly designed, encapsulating films or coatings can act as barrier layers limiting oxygen and moisture diffusion, preventing UV light penetration, reducing sensitivity to strong thermal fluctuations and also preventing the irreversible escape of volatile decomposition products [118]. One of the most common approaches is based on glass-to-glass encapsulation, where the cell device is sandwiched between two sheets of glass using thermosetting sealants as ethylene vinyl acetate (EVA) [68], Surlyn [119], polyisobutylene (PIB) [120] or UV curable sealants [121, 122]. Similarly, edge sealants (PIB [120] or UV epoxy adhesives [122]) should be applied to prevent, or at least delay, the entry of moisture and oxygen through the side perimeter, thus extending the life of the perovskite cell [123]. This technique is very affordable, relatively simple and extremely effective since glass has the best water and oxygen blocking properties as a transparent material. Other encapsulation approaches for flexible applications use polymeric laminates and polymeric tapes coated with a thin film barrier [124, 125].

The most stable devices managed to show a retention of more than 80% of their initial efficiency over durations between 1000 and 2500 hours under 1 sun illumination [66, 123, 126, 127]. The exception is the device of Grancini et al. using Surlyn sealants, which has the longest duration of operation without loss of efficiency after 10,000 hours of follow-up under illumination [128].

1.4.4.2 Large area and upscale

The development of perovskite solar cells is illustrated in Fig. 1.16 by ranking the performance of all available devices and plotting them against the date of publication. This study was carried out by collecting data from over 42,400 photovoltaic devices [87]. It demonstrates the expected trend towards more efficient devices, while giving an idea of the underlying variability by showing the distribution of performance, and thus providing an overview of the progress of the field. Thus today, the majority of devices have an efficiency between 16 and 19%, but there is a significant proportion of devices that do not exceed 10%.

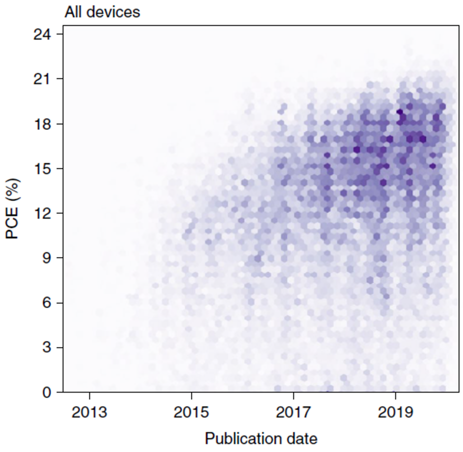

Figure 1.16: Efficiency measured under standard conditions as a function of the publication date for all devices in the database [87].

Record efficiency of 25.7% has been achieved with an active area as small as about 0.1 cm^2. To be commercialized, such efficiency must be achieved with large surface area modules. The spin coating method usually used for small area substrates (2.5*2.5 cm^2) is however not suitable for scaling up the perovskite technology to larger areas (> 25 cm^2). This process also induces a significant fraction (> 90%) of material waste during rotation, and this manual procedure is highly human dependent, which partly explains the often large differences found in the literature between different works using the same preparation method. Thus, materials and methods need to be further developed. Solution and vapor-phase deposition methods are studied in parallel.

For solution deposition techniques, perovskite precursors are first dissolved in organic solvents and deposited on large substrates. Among these techniques, blade-coating [129], spray-coating [130], screen-printing [131], or slot-die coating [132, 133], are interesting candidates for the fabrication of large area perovskite solar cells. Fig. 1.17 shows schematic representations of these deposition techniques and Fig. 1.18 shows the best performances obtained depending on the size of the devices and the deposition technique used.. Recently, perovskite solar cells fabricated using these techniques have begun to compete with spin-coated devices. For example, in 2021, Xu et al. achieved an efficiency of 21.35% using the slot-die technique [134]. This result equals the previous record set by the blade coating technique, which reached an efficiency of 21.9% using a cadmium iodide surface treatment [135].

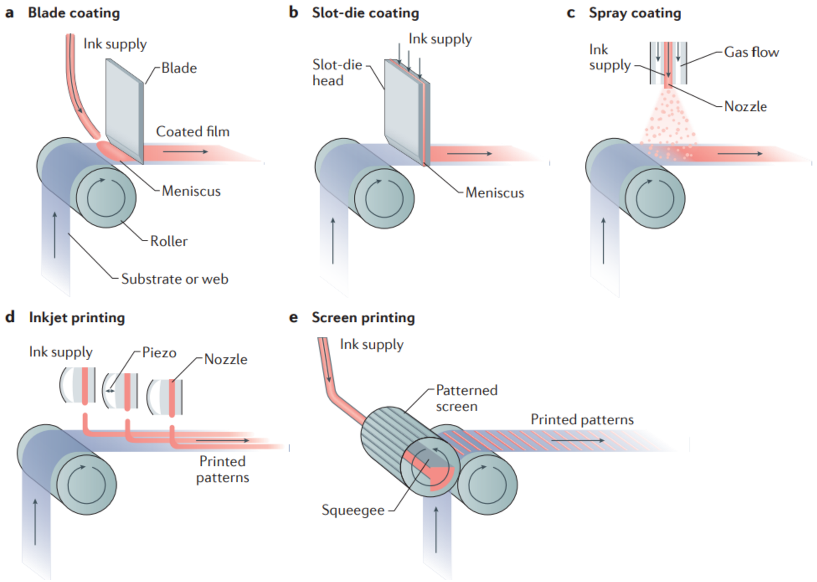

Figure 1.17: Solution-based scalable solution deposition methods for large-scale fabrication of perovskite solar cells, including (a) blade coating, (b) slot-die coating, (c) spray coating, (d) inkjet printing, and (e) screen printing [87] [136].

Similarly, several variants of perovskite layer deposition by evaporation have also been demonstrated. These include single source evaporation [137], sequential evaporation [138] and multi-source co-evaporation [139]. The most common approach is based on multi-source evaporation, in which each precursor is loaded into a separate crucible and co-evaporated with all other precursors to form the perovskite layer. However, these processes are still less used in the literature than those based on the solution deposition method. Considering this disproportionality, it is remarkable that evaporated devices have reached a efficiency of 20.8% in 2018 [140]. There are many other methods for depositing perovskite films, as spray coating [141] or flash evaporation [142]. However, these methods are less common in the literature and generally have lower performances than the methods described above.

At the same time, surface areas continue to target large-scale modules (> 800 cm^2) at high efficiency. In practice, the serial interconnection of several cells on a module is based on three successive etching steps, called P1, P2 and P3. Notably, by combining slot die coating with high-pressure nitrogen blowing, Du et al. achieved an efficiency of over 22% for a 16 cm^2 module [143]. These very encouraging results have triggered industry interest in larger perovskite modules. In 2019, the Chinese company MicroQuanta claimed the first large perovskite-based module of 200*800 cm^2, giving an efficiency of 14.24% [144]. Since then, another Chinese company, Utmolight Corp, has achieved a efficiency of 20.5% for a mini-module with an active area of 63.98 cm^2 [145]. Finally in 2020, Japan's Panasonic Corp. announced the world's

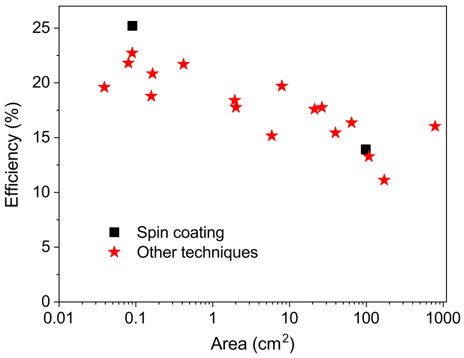

Figure 1.18: Certified efficiency records for champion perovskite solar cells and modules as a function of the area [10].

highest efficiency of 17.9% for a larger perovskite module (> 800 cm^2) [10, 146]. Although significant progress has been made, the efficiency of perovskite modules still lags behind small area (0.1 cm^2) state-of-the-art cells. The loss of efficiency is mainly due to non-uniform deposition/crystallisation of all functional layers.

1.4.4.3 Cost and toxicity

In order to achieve excellent efficiency, the cost is not considered for the synthesis of perovskite cells in laboratory. The glass/ITO substrates used today or the most popular HTL such as Spiro-OMeTAD represent a significant cost of the perovskite cell and the use of other materials could bring down the final price of the tandem. The increasing demand for indium for other uses of ITO as well as the techniques for obtaining indium (a by-product of the energy-intensive and environmentally damaging extraction of zinc) have led to significant price increases in recent years and may suggest a difficult supply in the future. In addition, a life cycle analysis of several types of 2T tandem cells (perovskite/silicon, perovskite/perovskite, perovskite/CIGS and perovskite/CZTS) also showed that ITO was the material with the greatest environmental impact after silicon and CIGS. It alone contributes in perovskite/perovskite cells to 70% of the environmental impact of these tandem types, which is due to the considerable energy needed to sputter the layer and the conditions needed to extract indium. The use of indium-free TCO, such as FTO, is however possible but requires a compromise on transmission in the IR. [147, 148]. Finally, other organic layers that make up perovskite cells are synthesised often using rather expensive materials. The price associated with the preparation of Spiro-OMeTAD, one of the best known HTL is estimated to be about 92 US$/g, which makes it one of the most expensive components of a perovskite cell [149]. Research is currently being carried out on HTL to reach a good balance between device cost and efficiency [150]. For example, diphenyl imidazole substituents have been introduced as a very promising hole transport material for the large-scale fabrication of cost-effective perovskite solar cells [151].

Finally, the presence of lead in their composition could be an obstacle to their widespread dissemination. It is well known that lead toxicity can cause serious health risks and also has a deplorable impact on our ecosystem. This is one of the factors that creates a negative impact on users and prevents the acceptance of the final product by the market. Several attempts have been made to solve the toxicity problem by replacing lead with another low toxic metal such as tin or copper [152], but an efficiency comparable to that of lead halide-based perovskite has still not been achieved [153]. However, perovskite cells are not the only solar cells that contain the incorporation of toxic elements. Other toxic compounds and alloys widely used in PV panels are copper indium selenide, cadmium telluride, copper gallium (di)selenide and cadmium gallium (di)selenide. Furthermore, the amount of lead used in perovskites is very low (0.4 $g.m^{-2}$) compared to the lead used in the solder of commercial Silicon PV panels [154].

1.4.5 Semi-transparent perovskite cell for tandem application

In the 4T configuration, the conventional perovskite cell must undergo an architectural change: it must become transparent to infrared radiation so that this radiation reaches the bottom silicon cell. This is achieved by replacing the metal electrode with a transparent electrode, usually a TCO. This creates the following problems: there is a drop in performance between opaque and semi-transparent cells and there is always a trade-off between transparency and efficiency.

In semi-transparent perovskite top cells with n-i-p superstrate structure, the ETL materials commonly used are similar to those used in opaque structures: compact TiO_2, followed by mesoporous TiO_2 or SnO_2 [155–158]. The same applies to the classical HTL materials such as PTAA, Spiro-OMeTAD and CuSCN [158–160]. In the following, we will see the different types of back electrode used, as well as the different optical optimisations needed to obtain a high transparency in the IR.

Finally, calculations indicate that the top cell with a band gap between 1.6 and 1.8 eV is optimal for the lower crystalline silicon cell (1.1 eV) to build a tandem. In comparison, the best performance obtained is between 1.55-1.65 eV so far. As the 4T configuration has a good gap tolerance, it is preferable to use a higher performing cell even if the gap is not perfectly optimal. The usual $MAPbI_3$ type compositions and associated variations are therefore adequate.

1.4.5.1 Transparent back electrode

In order to convert an opaque device into a semi-transparent one, the metallic back electrode of conventional opaque solar cells is replaced by a transparent electrode. Several properties are required for the material used in this process:

- High transmission over in the near infrared (750-1200 nm).
- A minimum of electrical losses. The metals used on opaque cells have a resistivity of a 10 µΩ.cm. Conductive and transparent materials are highly doped semiconductors with a resistivity of few mΩ.cm, and this should be minimised as much as possible to not generate high series resistance.
- Chemical, mechanical and thermal stability for a material that does not degrade in contact with other layers.
- Deposition methods compatible with the chosen tandem configuration and the adjacent HTL/ETL.

Sputtered ITO is the current industry standard commercial TCO in opto-electronic devices and has been the most reported top TCO in semi-transparent perovskite cells [161]. Despite its high transparency in the visible region, the optical transparency of ITO drops in the long wavelength region (above 800 nm), due to its high parasitic absorption when not annealed. In addition to ITO, studies have reported various sputtered TCO: IZO [148, 162, 163], Aluminium-doped Zinc Oxide (AZO) [164–166], IO:H [167, 168] and Zirconium-doped Indium Oxide (ZrIO) [169]. A majority of the tandem cells registered since 2014 have sputtered indium-doped oxides as the top electrode. Most optimised sputtering conditions involve post annealing or sputtering at high substrate temperatures, around 200 °C, to achieve high conductivity. However, processes at such high temperatures are mainly limited for back electrodes due to the low thermal stress resistance of the underlying organic layers. In addition, the sputtering can damage the underlying organic HTL due to the high kinetic energy of the sprayed particles. Thus, a protective layer is often required to protect it. The conventional protective layer used in n-i-p structures is molybdenum oxide (MoO_x) deposited by thermal evaporation, but this material is known to have poor long-term stability and causes optical and electrical losses in the device [170–172].

Ultra-thin metal layers (less than 10 nm) obtained by thermal evaporation are also alternative electrodes. However, they suffer from reduced transparency from 550 nm despite their high conductivity, see Fig. 1.19 [47, 173, 174]. Semi-transparent electrodes with 1 nm Cu followed by 7 nm Au have allowed a semi-transparent devices with an efficiency of 16.5%, but a transmittance of about 60% in the IR region [66]. In parallel, Cui et al. used ink-jet printing of Ag on top of a thin polyethylenimine (PEI) protecting layer, which also serves as a work function modifier and reached a efficiency of 13.27% [175].

Multilayer stacks consisting of two dielectric layers sandwiched between an ultra-thin metal of about 10 nm also exist. Several reports on transparent MoO_x-metal-MoO_x electrodes have successfully demonstrated their incorporation into semi-transparent perovskite cells. The top MoO_x dielectric layer is indeed

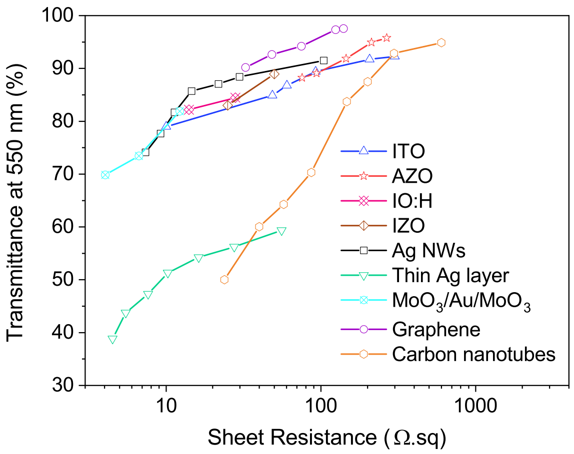

Figure 1.19: Transmittance at 550 nm and sheet resistance for ITO, AZO, IO:H, IZO, silver nanowires (Ag NWs), ultra-thin silver layer, multilayer stacks MoO_x-Au-MoO_x, graphene and carbon nanotubes [176–178].

used to create optical interference and can be considered as an anti-reflection layer. The advantage of the multilayer architecture is that it offers better transparency in the visible range compared to pure metal films, but still retains low transparency in the near infrared range due to high parasitic absorption [42, 179, 180]. For example, 1–5 nm of MoO_x followed by 10 nm of Au and another MoO_x layer for anti-refection resulted in semi-transparent perovskite cell with 13.6% efficiency and an average IR transmittance of 50%. [173]. SnO_x-Ag-SnO_x transparent electrodes have also been incorporated into semi-transparent perovskite devices, and demonstrated self-encapsulation abilities as well [181].

The interest of metal nanowires as Ag lies in their high transparency and high mechanical flexibility with conductivities below 20 Ω.sq, see Fig. 1.19. The fact that the manufacturing processes are mainly based on soft chemistry methods is also very interesting. On the other hand, they tend to have a high surface roughness after deposition and oxidation phenomena lead to an increase in their electrical resistivity through the formation of insulating phases that weaken the contacts between the nanowires [48, 138, 182]. Incorporating silver nanowires into semi-transparent perovskite and applying antirefective lithium fuoride films on both top and bottom sides of the device resulted in 12.7% efficiency with an average NIR transmittance of 70% [183]. More recently, Yoon et al reported double-walled carbon nanotubes (DWNT) and an efficiency of 17.% without hysteresis [184].

Due to their opto-electronic properties, good chemical and mechanical stability, transparent carbon-based electrodes such as graphene [185, 186] and carbon nanotubes [187, 188] have been also incorporated into semi-transparent perovskites. However, they are not easy to produce in large quantities with good efficiency, as graphene is reluctant to remain in individual sheets [189–191]. Furthermore, graphene is produced by chemical vapour deposition at high temperatures (> 1000 C°), which is not compatible with direct application to perovskite. However, a mechanical transfer process from a flexible plastic sheet is possible but the success rates per test are low, as for nanowires [189, 192]. Recently, Tran et al reported a monolayer graphene-based flexible and transparent bottom electrode. The graphene was directly synthesized at 150°C without transfer process via plasma-assisted thermal chemical vapor deposition on polymer substrate. AZO/Ag/AZO was utilized as the top electrode and the semi-transparent perovskite showed about 14.2% efficiency with 26% transmittance at wavelength of 700 nm [193]. Consequently, optimizing between conductivity and IR transparency still remains an issue.

1.4.5.2 Other optical losses

In addition to the infrared transparency of the back electrode, it must be ensured that none of the other layers of the semi-transparent cell causes optical loss in this range. This can be due to both parasitic absorption in the infrared or refractive index contrast between multiple layers. Today, the most optimised semi-transparent perovskite cells reach 90% transparency in the IR.

Concerning parasitic absorption problems, in order to identify their origin, numerical simulations based on the propagation of optical waves in planar layers have been performed by several groups [194–197]. TCO, substrate and HTL as spiro-OMeTAD have already been identified as IR absorbers. However, use of optical simulations is often hindered by the lack of accurate data for the complex refractive indices of each constitutive layer of the device. Indeed, the optical indices of such thin layer depend on the deposition and post-treatment conditions such as annealing. A reliable determination of the refractive index of perovskite layers is still highly needed to be implemented in the optical simulation of complete solar cells.

The refractive index mismatch of the multiple layers in the semi-transparent device results in power loss in the tandem device. To reduce reflection, ARC as MgF_2 [85, 198], SiO_2 [76] or LiF [67, 68, 199] are often used on both sides of the device to reduce photocurrent loss due to surface reflection. More complex optical strategies such as photonic crystals [200–202], metamaterials [203], surface texturing [204, 205], light scatterers [206], or metallic nanostructures with plasmonic resonances [207] can be used to allow for better light guidance in the device.

Finally, there is little information on the intermediate zone between the two cells. Most of the research teams only mention mechanically stacked cells without any further details. This zone must limit optical losses at the interfaces of the two cells, which implies a refractive index close to that of the electrodes, and must also be insulating and transparent. In order to remain within the scope of a marketable cell, it must also serve as an adhesive at a reasonable price [157, 167, 208, 209]. Duong et al., in his 4T record cell, proposed the use of a silicone-based gel to improve the optical coupling between a perovskite cell and a silicon cell [85]. A transparent and insulating adhesive, LOCTITE ECCOBOND 931-1, manufactured by HENKEL, was also used to bond the three cells in a triple-junction tandem [43]. In some cases, this area is just optimised for measurements, as in the case of the EPFL record cell, where the author mentions an optical coupling liquid, e.g. ethanol, to optically connect the two sub-cells and reduce reflection losses [167].

Conclusion

In this chapter, we have reviewed the development of 4T perovskite/silicon tandem cells in order to extend the Shockley-Queisser limit of single junctions. We have shown that this architecture has many advantages over a 2T configuration: it allows the total separation of the two cells synthesis, is not very sensitive to spectral variations and allows a wide choice in the gap of each cell. In particular, it allows the use of a lower silicon cell, which today represents 95% of the total photovoltaic market and which, due to the 4T configuration, does not require fundamental modification of its structure to be used in a tandem. Today there are different types of silicon cells using more or less complex stacks. The best current devices and therefore the ones that could achieve the highest efficiencies in tandem configuration are the IBC-SHJ cells.

Futhermore, we observed that perovskite cells are today very interesting candidates to fill the role of top cell in tandem configuration. They have benefited from a real craze in the scientific community and in ten years, reached very high efficiency (25.7%). The possibility of modifying their gap according to their composition over a wide range with common elements, as well as their direct gap, their very good absorption over a wide spectrum and their high degree of tolerance to crystal defects, make them an ideal material to imagine the development of new low-cost cells.

However, there are still a number of issues to be overcome before their use at an industrial scale can be imagined. First of all, perovskite cells have a stability problem when in contact with the atmosphere and more particularly with humidity. Encapsulation processes are currently an important area of research in order to effectively isolate them from the outside environment. Moreover, the most efficient cells are currently small (< 0.1 cm^2) and experience a significant drop in performance as soon as the size exceeds 10 cm^2. This is notably constrained by the most commonly used deposition method: spin coating. New techniques such as slot die coating are currently being studied to significantly increase the size of the devices. Finally, even if perovskites could eventually allow for the manufacture of safe and low-cost solar cells, lead is currently used in their composition as well as expensive materials such as electrodes using indium oxides or HTL/ETL based on organic compounds such as Spiro-OMeTAD.

Finally, these existing issues for single junction perovskite cells are transferable to semi-transparent cells for tandem application due to the trade-off between transparency in the IR and efficiency. By replacing the usual metallic back electrode with a transparent one, additional electrical losses are occur and a decrease in performance is observed compared to conventional cells. The majority of research teams today use indium oxides deposited by sputtering, but thin metallic layers, nanotubes and even graphene are also investigated. However, the replacement of the back electrode alone is generally not sufficient to achieve a very high transparency in the IR, and to obtain an efficient tandem. Reflection phenomena at the interface of the two cells and parasitic absorption caused by the different layers of the top cell must be studied and removed to improve the transmission of the semi-transparent perovskite cell.

Taking into account the different points mentioned in this chapter, the different steps necessary for the realisation of this thesis appear. A first one must be to improve the reproducibility and stability of the semi-transparent perovskite cell. In particular, the use of Spiro-OMeTAD as HTL makes the perovskite cell particularly sensitive when depositing the transparent ITO electrode by sputtering. The tandem performance obtained with the current structure once stabilized will then allow us to evaluate the presence of parasitic absorption and reflection in our structure. By optically modelling our experimental semi-transparent perovskite cell, we will precisely identify the layers and interfaces responsible for absorption and parasitic reflection and will be able to propose new materials and designs. For example, a first step will be to work on the replacement of TiO_2 and Spiro-OMeTAD. The replacement of Spiro-OMeTAD could allow us to gain more stability, while the use of low-temperature SnO_2 instead of TiO_2 would allow us to consider the use of another TCO on the front side. This is indeed a key to improve optically our cells since ITO and FTO used in the reference structure have significant parasitic absorption in the infrared. The development of other TCO more adapted to our applications (like IZO, IZTO or IO:H) could be conducted in parallel. Finally, the size of these devices could be increased to consider large scale tandem cells, either by the use of a new process of deposition or the development of perovskite mini-modules with several cells arranged in series via a P1P2P3 structuring architecture.

Chapter 2

Experimental method and synthesis of perovskite solar cells

Introduction

This chapter will detail the different methods and experimental procedures used during this study for the elaboration of semi-transparent perovskite solar cells for tandem applications on silicon. First, we will describe in detail the synthesis process of small perovskite cells in the laboratory, by spin-coating or slot die coating. We will describe the different layers, their method of synthesis and deposition as well as the architecture of the cell and the different steps of etching.

Particular attention will be paid to the deposition methods used for the different electrodes (metal evaporation, sputtering and Atomic Layer Deposition - ALD). Concerning the sputtering, the characteristics and properties of the ITO used as top electrode will be described, but optimization of the deposition having already been identified in the laboratory, we will not revisit them in this manuscript. The principle of Plasma Enhanced Atomic Layer Deposition (PEALD) for IO:H will also be a key process, since it is a deposition method with additional constraints compared to a classical ALD.

Finally, we will discuss the different methods of electrical characterization mentioned along this study. The IV (light and dark) and External Quantum Efficiency (EQE) measurements will be detailed, as well as the sheet resistance measurements and hyperspectral photoluminescence imaging. Others experimental details, concerning the different optical, morphological, as well as the crystallographic and compositional characterization techniques will also be detailed. More advanced and fine characterization methods also used in this study will be described such as X-ray Photoelectron Spectrometry (XPS) and Glow-Discharge Optical Emission spectroscopy (GDOES).

2.1 Synthesis of perovskite solar cells at IPVF

In this first part, we detail the two processes used at the IPVF to fabricate perovskite solar cells. The original spin coating process, also called baseline, is the reference process. The second, currently under development, is based on the synthesis of the perovskite layer by the slot die coating method.

2.1.1 Reference spin coating process (Baseline)

The process described hereafter allows to obtain reproducible opaque or semi-transparent perovskite cells (STPC) with an average efficiency of about 17-18%. The architecture is detailed in Fig. 2.1a. Perovskite cells are prepared in batches of 16 or 20 samples, each on 2.25 cm^2 substrate.

A commercial sample from Solems called TEC-7 is used as a substrate. It is composed by FTO of 450 nm coated on a soda-lime glass of 3 mm. On similar substrates, different groups report the presence of SiO_2 and SnO_2 between glass and FTO layers [195, 210]. Cell and batch numbers are written down on the glass side (AY28-03 for example). By protecting almost the substrate with Kapton tape, a first chemical etching is performed on the FTO on top side with zinc powder and diluted hydrochloric acid solution (30% in water), as shown in Fig. 2.1a. This etching is symbolized by the red line. The substrates are then cleaned by ultrasonic washing in RBS (2%) for 45 min, in acetone for 20 min and finally in ethanol during 20 minutes too. Once cleaned, the sample was introduced in UV-ozone cleaner for 15 minutes.

Then, the sample is placed on a hot plate which will gradually rise to 450°C during 30 min. A glass plate were deposited on the top of the substrate to protect a part of the FTO from the spray-coating of the compact TiO_2 layer, see Fig. 2.1a. For a total volume of 40 mL, the solution was composed of 2.4 mL of titanium diisopropoxide bis(acetylacetonate) (TAA), 1.6 mL of acetylacetone and 36 mL of IPA. After 20 deposition steps, the compact TiO_2 thickness is around 20 nm. The sample was kept at 450°C for 15 minutes and then cooled down to room temperature.

Kapton tape is again used to protect the top and bottom of the substrate from the deposition of mesoporous TiO_2 by spin-coating as shown in Fig. 2.1a, and create the active part of the perovskite cell. The top tape is slightly below the FTO area while the bottom tape is at the level of the etched strip. The colloidal solution of TiO_2 nanoparticles (Greatcell Solar Materials, 30 NR-D, titania paste diluted in absolute ethanol) was used. The solution concentration was an ethanol:TiO_2 mass ratio of 7:1. 35-50 µL of the TiO_2 solution is deposited on the immobile substrate and the spin coating is then started according to the following parameters: a rotation of 4000 rpm with an acceleration of 2000 rpm.s^{-1}, for a duration of 35 s. The substrate is then annealed on a hot plate following the process displayed in Table 2.1. The mesoporous TiO_2 thickness is around 120 nm.

$Cs_{0.05}(MA_{0.166}FA_{0.833})_{0.95}Pb(Br_{0.166}I_{0.833})_3$ triple cation perovskite of 650 nm is used for the absorber. 1 mL of solution is obtained by the combination of 652.79 mg of $PbBr_2$, 171.97 mg of FAI, 507.11 mg of PbI_2, 22.39 mg of MABr, 800 µL of N, N-dimethylformamide (DMF) and 200 µL of Dimethylsulfoxide (DMSO); and 194.86 mg of CsI and 500 µL of DMSO. This solution (35 µL) is deposited on the sample by spin coating in a glove box (2000 rpm for 9 s then 6000 rpm for 20 s) and followed by a 100 µL chlorobenzene wash while the spin-coater continues to rotate (6000 rpm for 10 s). The samples are then annealed at 100 °C for 20 min.

Finally 300 nm of Spiro-OMeTAD is also deposited by spin-coating in a glove box. The solution is composed of Spiro-OMeTAD powder at C = 11.14 M. It is doped by including 3 oxydizing additives, namely lithium bistrifluoromethanesulfonimidate (LiTFSI) at C = 0.045 mol.L^{-1}, tris[2-(1H-pyrazol-1-

Steps	**1**	**2**	**3**	**4**	**5**
Time (min)	5	15	5	5	5
Temperature (°C)	125	325	375	450	500
Ramp (°C/min)	25	13.3	10	15	10
Dwell time (min)	5	5	5	15	15

Table 2.1: Parameters of annealing of the TiO_2 mesoporous layer.

yl)-4-tert-butylpyridine cobalt(III) tris bis(trifluoromethylsulfonyl)imide)] (FK209) at 5.10-3 mol.L^{-1} and a commercial solution of 4-tertbutylpyridine (t-BP) at C = 0.31 mol.L^{-1}. The layer was deposited with a volume of 30 µL on each sample by dynamic spin-coating (3000 rpm for 30 s). The samples are then etched one last time with DMF and acetonitrile on the top and bottom edges to revealed the FTO.

The electrode synthesis will be detailed in the next section, but in the case of opaque cells, 100 nm of gold was thermally evaporated under high vacuum, see Fig. 2.1c. For semi-transparent devices, ITO has been deposited by RF magnetron sputtering. Over ITO cathodes, a U-shape pattern of gold (100 nm thick) was thermally evaporated over the edges of ITO area in order to minimize the series resistance, as shown on Fig. 2.1d. The realized perovskite cells have a n-i-p superstrate structure, i.e. the cell is illuminated by the substrate, see Fig. 2.1b.

(a)

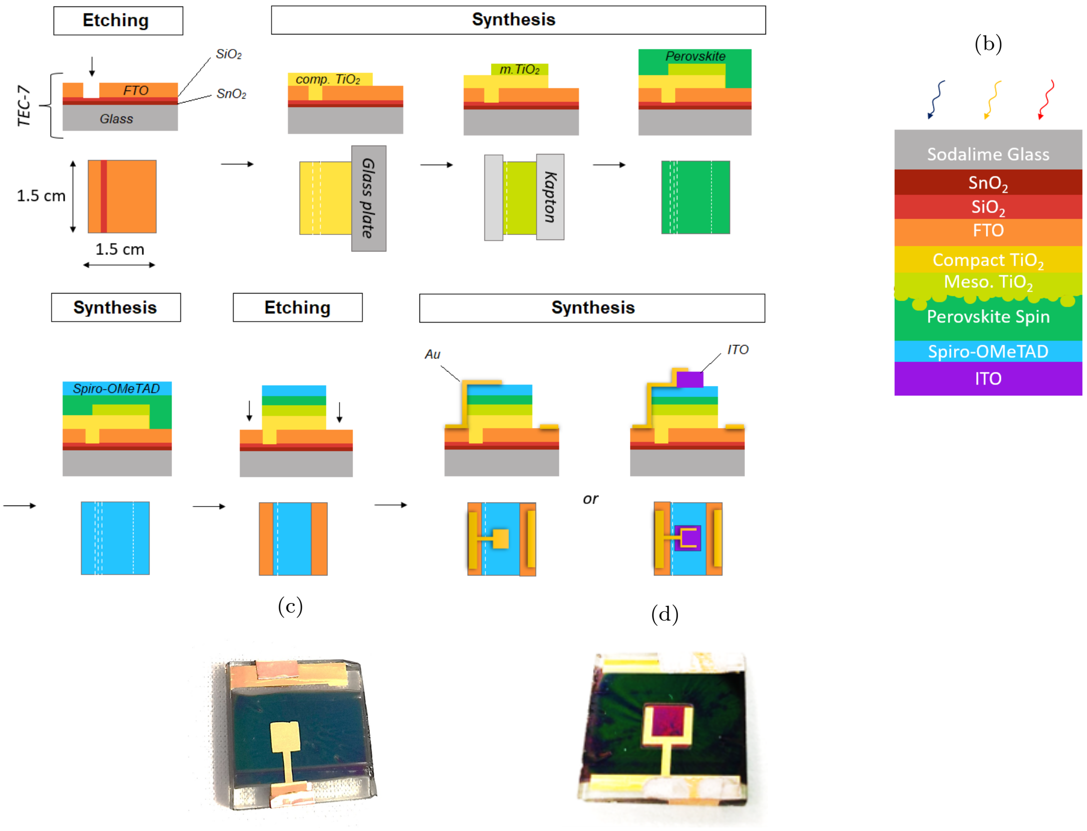

(b)

(c)

(d)

Figure 2.1: (a) Schematic description of the main steps for the fabrication of a perovskite solar cell in superstrate configuration when the perovskite layer is deposited by spin-coating. (b) Complete stack of semi-transparent perovskite cells. Photograph of a (c) opaque perovskite cell and (d) STPC, the pink square corresponds to the cell covered by an ITO layer (0.16 cm^2).

2.1.2 Slot die process

The spin coating process is not applicable for samples larger than 25 cm^2 because it generates an irregular spreading of the layer and limited efficiencies. Moreover, it induces an important fraction (> 90%) of material waste during rotation, which is an important obstacle to the transfer of the process to industrial manufacturing. In addition, in the case of perovskite deposition, this procedure is highly dependent on the manipulator, which partly explains the often large differences found in the literature between different works using the same preparation method. As an alternative, several compatible large-scale fabrication techniques have been investigated and slot die coating is the preferred technique at IPVF. The most crucial and complex step concerns the perovskite layer, which is why work began on this layer first, while the other layers continued to be deposited using the baseline process described above.

Concerning the fabrication of a 0.09 cm^2 cell by this technique, TEC-7 substrates identical to those of the baseline are used, but they measure 10*5 cm^2 to allow a sufficiently large deposition area. The etching of the FTO consists of two lines etched by a process identical to the baseline, at 1 cm from the edges along the length of the substrate, see Fig. 2.2a. Then, glass slides are deposited in the middle of the substrate to protect part of the FTO from the compact TiO_2 spray. Finally, mesoporous TiO_2 is deposited by spin coating in a similar way to the baseline on the whole substrate without any particular etching because this layer is removed during the subsequent perovskite etching.

An nTact® nRad slot-die coater is used to deposit the wet perovskite film. The slot die is enclosed in a specially adapted MBraun glove box. The maximum coating size possible with this instrument is 20*20 cm^2. The chuck is made of marble with vacuum suction to ensure perfect flatness and immobility of the substrate during coating. The slot-die head mold can move over the substrate placed on the marble along the X and Y axes. After an optimization of the process in the laboratory, a double cation perovskite of composition $Cs_{0.17}FA_{0.83}Pb(I_{0.83}Br_{0.17})_3$ was chosen as the absorber, with the use of the surfactant 3DPS at a concentration of 2.3 mM and the addition of the additive methylammonium chloride (MACl) in the perovskite's precursors solution (ratio MACl:FAI 0.3:1). This composition was first developed for slot-die deposition at IMEC (Interuniversity Microelectronics Centre) and transferred to EnergyVille center (Leuven, Belgium). The height of the deposition head with respect to the sample is fixed at 30 µm at the beginning of the deposition to allow the formation of the meniscus. It then rises to a height of 60 µm to accumulate a volume of solution inside the meniscus to form the coating bed for 2 seconds. The deposition is then made at a speed of 14 mm.s^{-1} for a head height of 50 µm. The realized deposition is homogeneous on 9 cm of coating. On the last centimeter, a significant decrease in the thickness of the perovskite layer is observed, and therefore, the first and last 1 cm of the substrate will be considered as a sacrificial area and never used.

After the deposition, a wet perovskite layer is obtained, see Fig. 2.2c. To trigger nucleation and growth of the crystalline phase, it is essential to extract the solvent. With spin-coating, the solvent is removed by dripping an anti-solvent onto the substrate (chlorobenzene in our case). However, this technique is unsuitable for large-area deposition and contributes to excessive chemical waste in the development process. Thus, the wet film is placed in the vacuum chamber, and the solvent was removed by vacuum extraction (0.7 mbar after 5 minutes). Finally, the film is converted to a perovskite structure by post

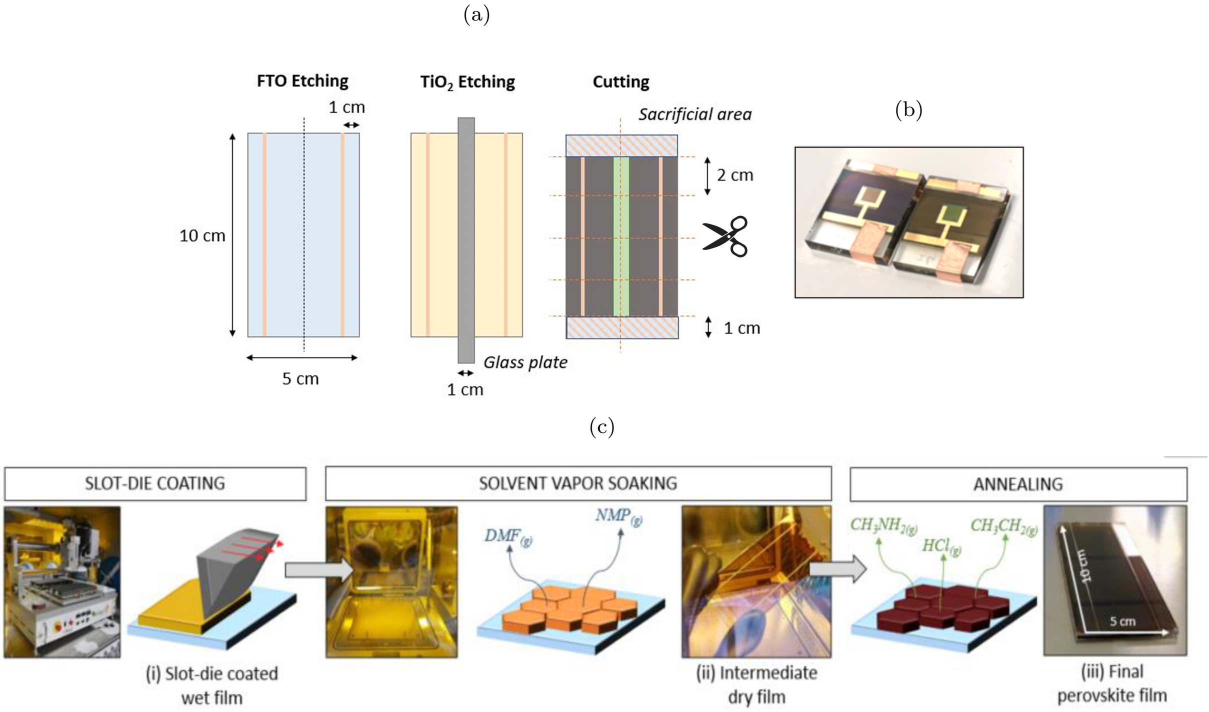
(a)

(b)

(c)

Figure 2.2: (a) Schematic description of the main steps of etching and cutting of 8 perovskite solar cells when the perovskite layer is deposited by slot-die coating. (b) Photograph of two slot-die STPC with different HTL. (c) Schematic deposition route and associated perovskite crystallization step using a slot-die technique.

annealing at 140°C for 30 minutes. The substrate is then cut into 8 samples of 5 cm^2 on which the last synthesis steps (HTL deposition and electrode) are performed in the same way as the baseline process as shown on the picture Fig. 2.2b.

2.2 Method of electrode synthesis

2.2.1 Metal e-beam evaporation

The evaporation of gold as an electrode on both opaque perovskite cells and STPC is carried out in a Plassys MEB550SL. The equipment is composed of a deposition chamber put under vacuum (10^{-7} mbar) by a CT8 cryogenic pump, a sample introduction lock connected to an ADIXEN 2033SD primary pump, as shown on the diagram in Fig. 2.3a. It also has 6 metallic crucibles that can accommodate different metals which include: gold, germanium, nickel, silver, tin, titanium and chromium. The crucibles are bombarded by an electron gun which generates an evaporation of the metal contained inside. The evaporated species are transported ballistically due to the vacuum, reaches the sample holder located 60 cm above and recondense in the solid state on the samples.

The upper electrode of the perovskite cells is composed of 100 nm Au. The first 10 nm of Au are deposited with a reduced deposition speed (0.01 nm.s^{-1}) determined by the microbalance, in order to protect the lower layers (notably the Spiro-OMeTAD and the perovskite) while the remaining 90 nm are deposited at a more sustained speed (0.1 nm.s^{-1}). We obtain a conform coverage of the underlayer as seen by Scanning Electron Microscopy (SEM), see Fig. 2.3b. The details of this technique are discussed later in this chapter.

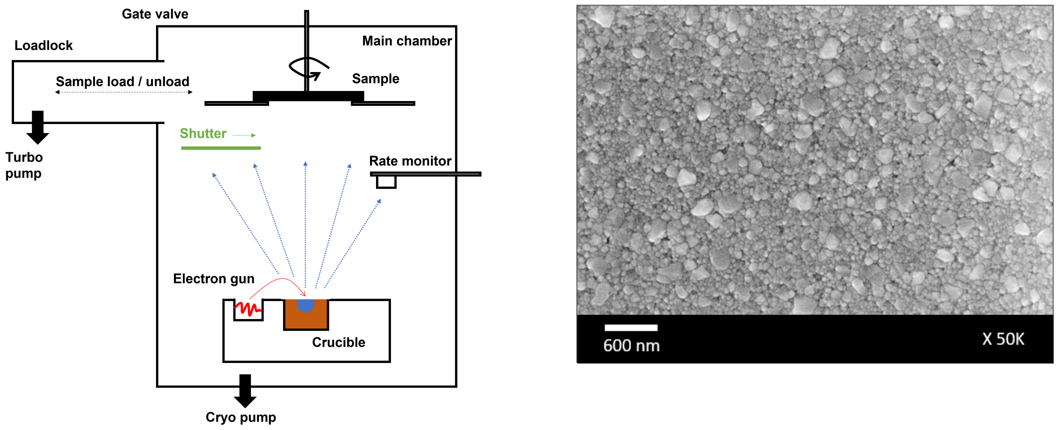
(a)

(b)

Figure 2.3: (a) Schematic of e-beam evaporator Plassys MEB550S. (b) SEM images of Au surface on perovskite cell, with a thickness of 100 nm.

2.2.2 Radio Frequency Magnetron sputtering

2.2.2.1 Principle

It is a technique used for the synthesis of materials from a solid source (also called target) on a substrate, see Fig. 2.4. The chamber is first evacuated to 10^{-7} mbar and then a cold plasma is created by ionising a pure gas (in our case argon or oxygen) by a potential difference. The plasma is composed of negatively and positively charged particles that are attracted to the target and strike it. This allow to eject particles from the target material which be deposited everywhere in the chamber. In addition, magnetron sputtering uses magnets behind the cathode to produce field lines around the target. The magnetic field focuses and intensifies the plasma in the space immediately above the target to improve ion bombardment and sputtering speed. Finally, Radio Frequency (RF) sputtering is used for sputtering insulators. It involves alternating the electrical potential of the current in the vacuum environment at radio frequencies to avoid charge build-up on sputtering target materials. This technique is widely used to manufacture commercial thin films because it allows to deposit on large surfaces, uniform and consistent layers regardless of the surface texture. The main drawback is the high energy released when the particles ejected from the target hit the substrate surface.

The main parameters of the deposition are the following:

- The pressure in the chamber : it fixes the number of ionised species, and therefore the mean free path of the particles.
- The power: it is the product of the voltage and the current, the voltage is related to the electric field and thus to the energy of the species, the current is related to the number of species connected.

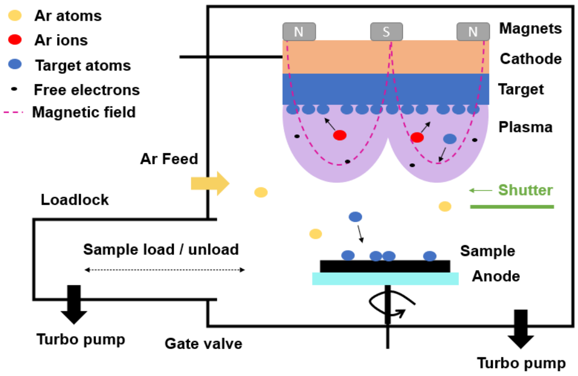

Figure 2.4: Schematic representation of principle of the RF magnetron sputtering.

2.2.2.2 Equipment and deposition parameters on STPC

The equipment Plassis MP500 can accommodate up to three 3-inch diameter targets, as it shown on Fig. 2.5a. This machine is manually operated. In the main chamber, the vacuum is 10^{-7} mbar and the samples first go through a transfer airlock that reaches 10^{-2} mbar. The sample holder measures 6*6 cm^2. On STPC, ITO is deposited on 4 samples of 2.5*2.5 cm^2 simultaneously. Fig. 2.5b, c and d shows the mask used and the positioning of the STPC to obtain a 4*4 mm^2 ITO layer centered on the samples.

The ITO target used is composed of 90% In_2O_3 and 10% SnO_2 (99.99% purity). The ITO deposition is homogeneous on a surface of 6*6 cm^2 as shown by the X-Ray Fluorescence (XRF) mapping in Fig. 2.6a. The details of this technique are discussed later in this chapter. The characteristic lines of indium and tin are found with the same instrument, see Fig. 2.6b. The details of this technique are discussed later in this chapter. A mass spectrometer is connected to the deposition chamber. It allows to notice during the 100 min classical ITO deposition that the H_2O rate is more important at the beginning than at the end while the nitrogen and oxygen flux remain stable as shown on Fig. 2.6c. As for the species detected, see Table 2.2, we find three isotopes of argon 36N/38N/40N in an expected ratio of 0.34/0.06/99.60%, as well as oxygen, nitrogen, water, hydrogen and helium. We also note the presence of an artifact at 20.1°, see Fig. 2.6d, which follows exactly the evolution of the main argon peak at 40.2 m/z.

The characteristics of ITO deposition as a function of chamber pressure, power, and deposition time having already been identified in the laboratory, we will not revisit them in this manuscript. We consider at this point a standard optimal deposition performed at 50 W, during 100 min at 2 mTorr pressure with a pure argon plasma which allows to obtain an ITO of about 280 nm thickness for a sheet resistance of 16 Ω.sq. The optimisation of the IZO deposition will be discussed in the Chapter 6.

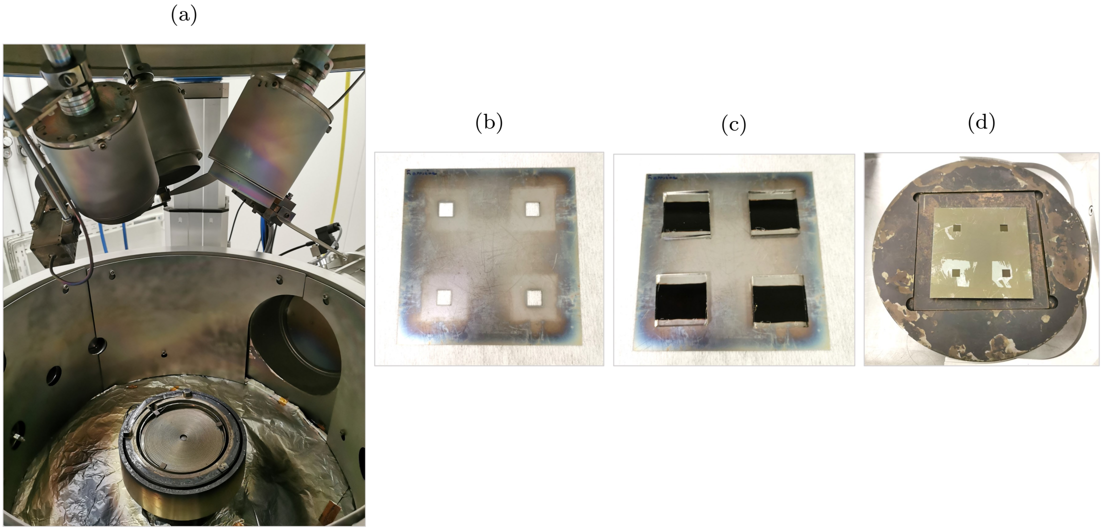

Figure 2.5: (a) MP500 deposition chamber with the 3 targets and their shutter. (b) Mask used for the deposition of the ITO electrodes on the STPC. (c) Position of the STPC on the back of the mask. (d) Positioning of the mask with the STPC on the substrate holder before the ITO deposition.

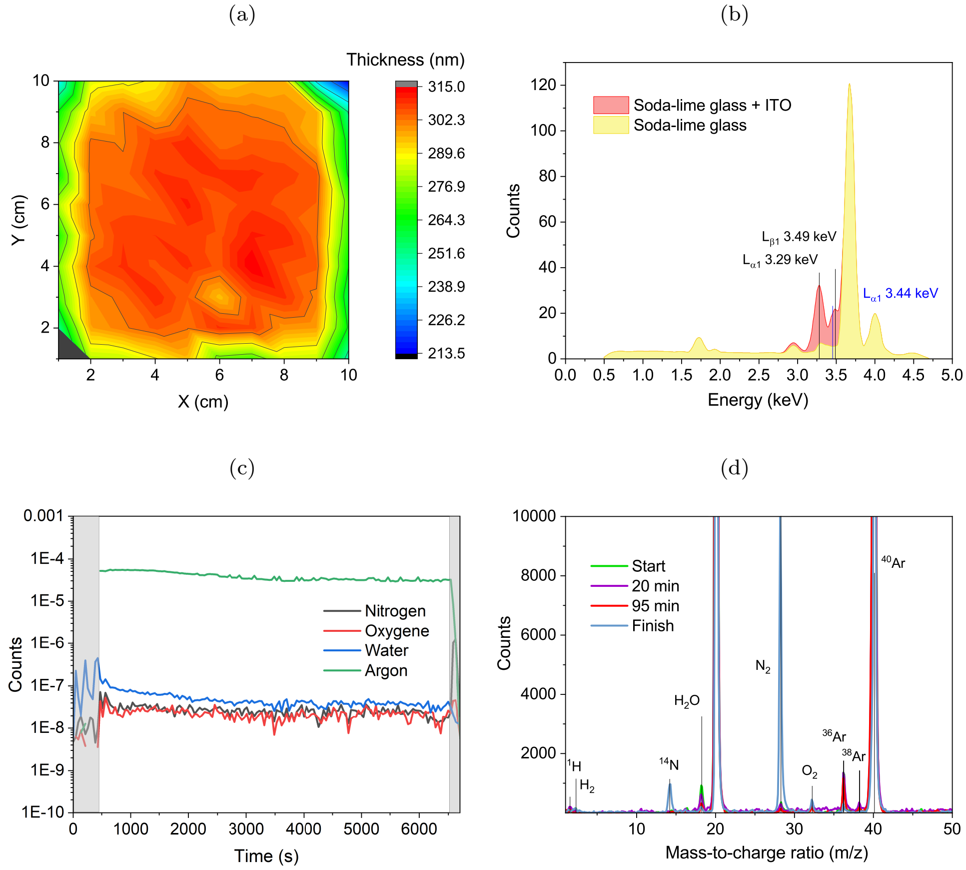

Figure 2.6: (a) Thickness mapping of a 10*10 cm^2 ITO sample on soda-lime glass made with XRF. (b) XRF emission spectra of a 230 nm ITO sample on soda-lime glass and a soda-lime glass alone. The contribution of indium emission lines are shown in black and tin one in blue. (c) Mass spectroscopy of Ar, O, Zn and H_2O in time during ITO sputtering. (d) Detailed mass spectroscopy at different times of ITO deposition.

Species	**Mass-to-charge ratio (m/z)**
^{1}H	1.57
H_2	2.32
^{14}N	14.2
H_2O	18.26
Artifact	20.1
N_2	28.32
O_2	32.28
^{36}Ar	36.24
^{38}Ar	38.22
^{40}Ar	40.2

Table 2.2: Species identified on the Fig. 2.6d with the mass spectrometer and their associated mass-to-charge ratio (m/z).

2.2.3 Atomic Layer Deposition (ALD)

2.2.3.1 Principle of thermal ALD

ALD allows the growth of thin films by exposing a surface to two or more precursors, sequentially and repeatedly, in order to form a material by reaction between the following precursors and the monolayer formed during the exposure of the first precursor. It is a technique used today in the realization of passivation layers like AlO_x in PERC silicon cells. For perovskite cell, this deposition technique is commonly used for the synthesis of HTL and ETL (TiO_2, SnO_2).

An ALD cycle consists of at least 4 steps as shown in Fig. 2.7a :

1. Introduction of a first precursor which adsorbs to the surface and establishes chemical bonds with the sites available on it.
2. Purging of the gas phase with an inert gas, nitrogen in our case, in order to evacuate the excess of precursor and to avoid the superposition of the molecules of several precursor pulses.
3. Another reactant react with the precursor previously deposited and form a material on the surface of the substrate.
4. A new purge to evacuate the surplus of reactant and the undesirable compounds which were formed the vapor phase.

Growth control is based on surface saturation reactions for each of the reactants. This saturation mechanism of the monoatomic layers is a necessary condition for a process to be called ALD. In addition, there is an operating window known as the ”ALD window” in which the growth rate is constant as a function of temperature, see Fig. 2.7b. At low temperatures, the increase in growth rate at L1 indicates the condensation of one or more precursors or the presence of exchange reactions. In contrast, the decrease in growth per cycle in L2 indicates that the process is limited by activation energy. In other words, this indicates too low reactivity of the precursor at the chosen deposition temperature. At intermediate temperature, the formation of a monolayer per growth cycle in W1 indicates that each saturation reaction is complete. This part generally refers to the ALD window and the growth rate is assumed to be constant there and linearly dependent of the number of cycles. However, when there is less than one monolayer as in W2, it means that there is surface reconstruction for at least one of the monolayers formed. At high temperatures, an increase in growth per cycle in H1 indicates the formation of nonvolatile products from precursors or ligands located on the surface. Finally, when there is a decrease in the growth rate per cycle as in H2, it means that there has been desorption of the monolayer formed or desorption/dissociation of the ligands on the surface, essential for its activation.

(a)

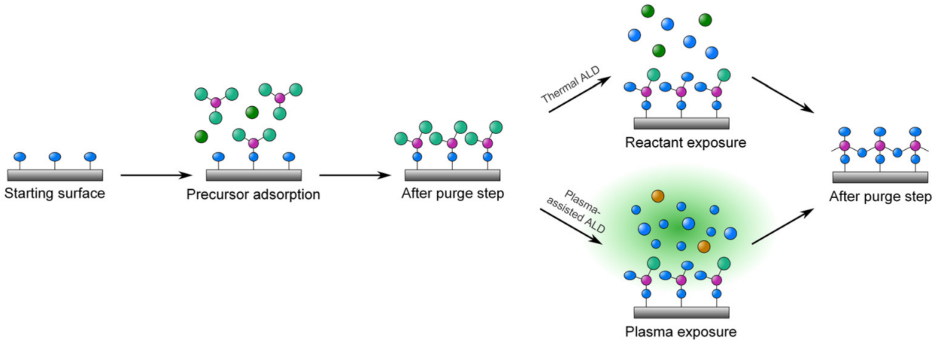

(b)

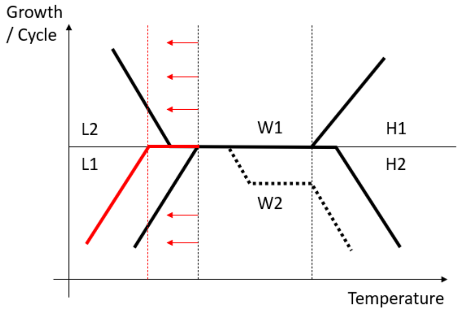

Figure 2.7: (a) Schematic representation of thermal ALD and plasma enhanced ALD. During the co-reactant step of the cycle, the surface is exposed to a reactant gas or vapor, or to species generated by a plasma [211]. (b) Comparison of the temperature windows of the PEALD and ALD processes. The red dotted line indicates the lower limit of the PEALD window, and the solid black lines the ALD window. [212].

2.2.3.2 Plasma Enhanced Atomic Layer Deposition (PEALD)

Plasma Enhanced Atomic Layer Deposition (PEALD) has been developed to address the need to decrease thin film growth temperatures and increase deposition rates. The presence of plasma completely modifies the reaction mechanisms that occur in the vapor phase, see Fig. 2.7a. Thanks to electronic collisions, ionization and dissociation reactions can occur and create new and more reactive species, essentially radicals and ions. The latter give access to new reactivities and deeply modify the growth and properties of thin films. The PEALD process allows the synthesis of materials whose growth is not possible or is complex by ALD (e.g. tantalum, a metal hydride $TaCl_5$, synthesized with a very reactive hydrogen plasma) [213]. The most common plasma for oxide synthesis today are Argon/O_2 plasma.

In PEALD, the growth temperature, at which saturation is still possible, is generally lower than in thermal ALD processes, see Fig. 2.7b. This is mainly due to the reactivity of the radicals. Thus, the ALD window is generally wider in PEALD processes than in thermal ALD. However, when these mechanisms are not controlled and the ions acquire too much energy, an ion bombardment phenomenon occurs. The surface of the substrate can be damaged or implantation phenomena due to Ar+ ions can occur, altering the properties of the layers.

2.2.3.3 Equipment and deposition parameters

The studies carried out during this thesis were performed on two similar experimental setups (A and B) presented in Fig. 2.8. The main elements of these devices are an ALD reactor R200 Basic Sunale (Picosun Oy) and a plasma module Litmas RPS (Advanced Energy). The inner chamber or reaction chamber is maintained at a vacuum of around 5 hPa and a temperature of 100°C. The substrate holder located in the reaction chamber is 15*15 cm^2. In our process, nitrogen is used as a carrier gas, as it is inert even at high temperatures. Each precursor is connected to the nitrogen line by a pneumatic valve allowing to realize pulses of a minimum duration of 0.1 s. In addition to the precursors, a plasma source is located

25 cm above the reaction chamber. It is a frequency inductive plasma module supplied by Avanced Energy. It has its own power source which allows to vary the frequency of the plasma between 1.9 and 3.2 MHz and its power between 100 and 3000 W. However, only the power of the plasma is adjustable by the user, since it is the power source itself which ensures the regulation of the RF frequency. It is connected to an oxygen line and the O_2 flux is fixed at 500 hPa and 200 sccm. The species created in the module can diffuse to the reactor through an argon flow during the plasma pulse. It is not possible to ignite the plasma continuously since the cooling system is not adapted to the heating produced in such a situation. Depositions were performed on 3 types of substrates each time: Soda-lime and borosilicate glass and silicon (100) wafer cut. The glass substrates were cleaned by ultrasonic bath with acetone and then with isopropanol for 10 min each time.

The first setup (A) was used for the deposition of IO:H with the precursor Indium (III) acetylacetonate ($In(acac)_3$ - 98%, Strem Chemicals). 10 g of the $In(acac)_3$ precursor (in powder form) is placed in a canister and maintained at room temperature between deposition processes. It is heated during deposition to obtain a vapor pressure suitable for ALD deposition. All deposition parameters are controlled by a computer.

For the deposition of IO:H with the Trimethyindium (TMI) precursor, a second ALD chamber (B) is used. This one has an loadlock to avoid venting the chamber at each sample change. An ozone generator is associated with the reactor and allows to send a mixture of 14% O_3, 85% O_2 and 1% N_2. It is also equipped with a Quartz Crystal Microbalance (QCM), whose crystal is located under the substrate holder. The QCM is controlled by a computer independent of the one controlling the deposition parameters. TMI is placed inside a containment cylinder provided by the supplier because it is pyrophoric.

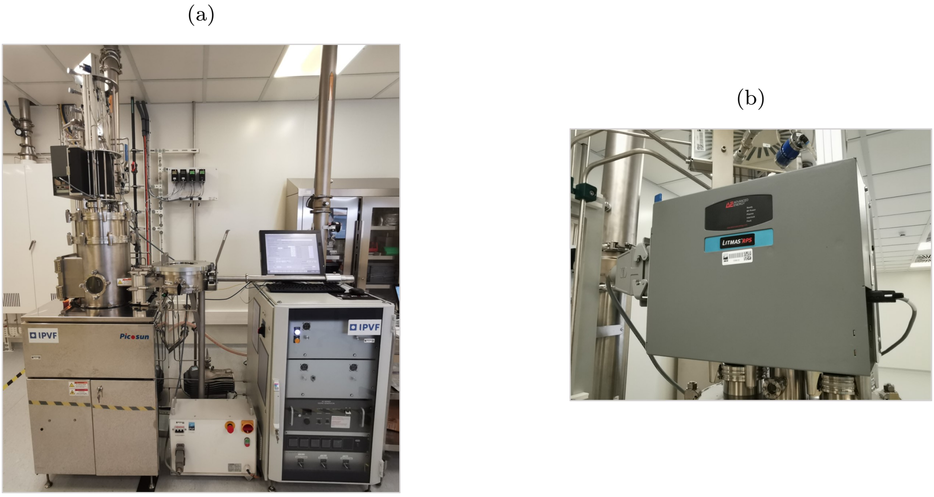
(a)

(b)

Figure 2.8: (a) ALD R200 Basic Sunale reactor (Picosun Oy) - Setup B - and (b) the associated Litmas RPS (Advanced Energy) plasma module.

2.3 Electrical characterizations

2.3.1 IV measurements

In this section, we discuss IV measurements ans the characteristic parameters of photovoltaic cells such as the efficiency, the short-circuit current, the open circuit voltage and the Fill Factor (FF). As a preamble, we define these values:

- PCE is the Photo-Conversion Efficiency, defined by

$$PCE = \frac{P_m}{P_{inc}} = \frac{V_{mpp}J_{mpp}}{P_{inc}} = \frac{FF * Voc * Jsc}{P_{inc}} \tag{2.1}$$

- P_{inc} is the incident power on the device (1 sun).
- MPP is the Maximum Power Point, which corresponds to the maximum power P_m that the cell can provide. V_{mpp} and J_{mpp} are the voltage and current associated with this point, see Fig. 2.9a.

- Jsc is the short-circuit current.
- Voc is the open circuit voltage.
- FF is the Fill Factor, which corresponds to the ratio between the real characteristic of the cell and its ideal characteristic shape.

Without illumination, the IV curve has the characteristic of a diode as shown on Fig. 2.9b. The curves obtained are then fitted with a single diode model as follow:

$$I = I_0 \left[exp\left(\frac{V + IR_s}{nV_T} \right) - 1 \right] - \frac{V + IR_s}{R_{sh}} \tag{2.2}$$

with :

- m is the diode ideality factor (unitless, usually between 1 and 2 for a single junction cell).
- I_0 is diode reverse saturation current.
- V_T is the thermal voltage given by kT_c/q where k is Boltzmann's constant and q the elementary charge.
- R_{sh} is the parallel or shunt resistance which is related to defects in the structure.
- R_s is the series resistance.

Concerning our samples, perovskite solar cells are measured in superstrate configuration, cells are illuminated through the glass. IV characteristics are measured using a digital source meter (Keithley 2400) for bias voltages between -0.2 V and 1.2 V with a sweeping rate of 20 mV.s^{-1}. An AM1.5G solar illumination is obtained with an AAA sun simulator (Oriel Sol3A). They are also performed with a potential sweep in both directions to highlight the measurement hysteresis (forward FW and reverse RV scan), see Fig. 2.9a. The dark IV are measured under the same equipment but this time without light. The cell and its connections are hidden under a box, itself covered with a thick black sheet to limit the influence of ambient light. Tracking of the MPP over time can also be achieved over periods of several months in an ARKEOS Illuminator dedicated to aging samples in ambient air under constant illumination. Reference perovskite cells have an active area of 0.16 cm^2 (corresponding to the pink square visible on the cell image Fig. 2.1d) and a black metallic mask is used to illuminate only 0.09 cm^2 in order to avoid the gold finger shading.

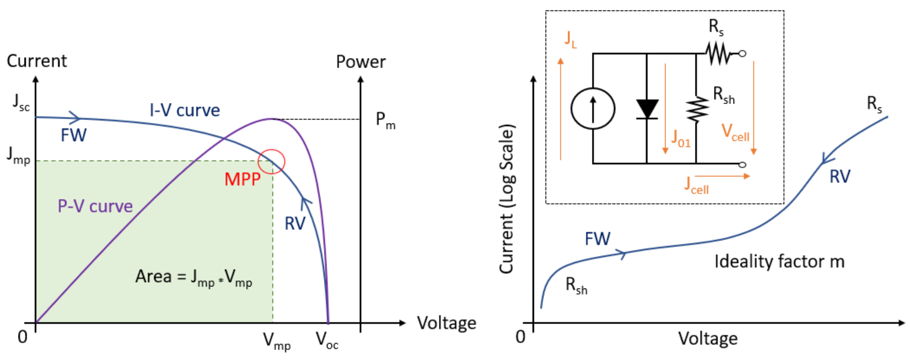
(a) (b)

Figure 2.9: (a) Light and (b) dark IV measurements, with the principal values (Jsc, Voc, MPP, Rs and Rsh), the FW/RV scan and the equivalent circuit for dark IV fitting with a one-diode model.

2.3.2 External Quantum Efficiency (EQE)

The External Quantum Efficiency (EQE) is the ratio of the number of charge carriers collected by the solar cell to the number of photons of a given energy incident on the solar cell. If all photons of a certain wavelength are absorbed and the resulting minority carriers are collected, then the EQE at that particular wavelength is equal to 100%. Although the quantum efficiency is ideally 100% over the entire spectrum, it is reduced on most solar cells, see Fig. 2.10. Firstly, the quantum efficiency for photons with energy below the band gap is zero. In addition, defects in the front surface affect the carriers generated near the surface, and since blue light is absorbed very close to the surface, strong recombination of the front surface will affect the "blue" part of the quantum efficiency.

The integration of the EQE spectrum multiplied by the spectral density of incident photons $\phi(\lambda)$ can be used to determine Jsc via the following equation:

$$J_{sc} = -q \int_0^\infty EQE(\lambda)\phi(\lambda)d\lambda \tag{2.3}$$

The Internal Quantum Efficiency (IQE), on the other hand, is the ratio of the number of electronic charges collected to the number of photons absorbed.

At IPVF, EQE is measured between 300 and 850 nm for perovskite cells, and between 300 and 1200 nm for silicon cells using an Oriel IQE200 system connected with a source meter (Keithley 2400) and a 300W xenon lamp. The sample is illuminated via a monochromator at a power lower than a AM1.5G solar illumination. For this reason, there may be differences between the Jsc calculated by integration of the EQE and the direct measurement made at IV. Indeed, this may be due to a photocurrent barrier which is large under low light intensity or monochromatic illumination but becomes smaller by photodoping at AM1.5 illumination. By measuring the reflection and transmission of a device, or simulating it as we will show in Chapter 4, we can deduce the IQE of a cell.

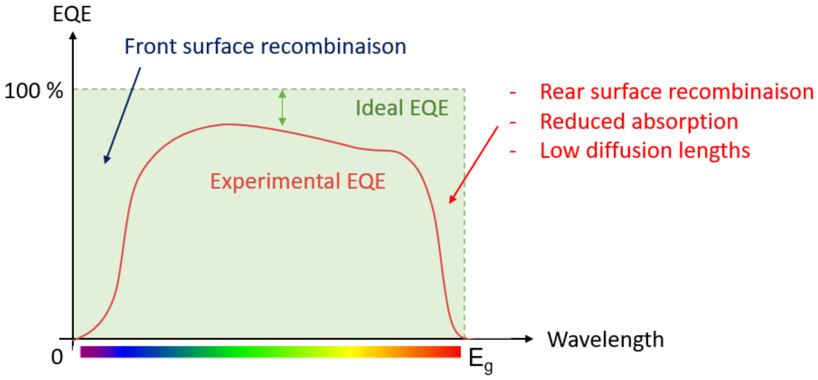

Figure 2.10: Schematic representation of EQE measurement on a solar cell.

2.3.3 4-point probes and Hall effect method

The difference in efficiency observed between opaque perovskite cells and STPC is essentially due to resistive losses caused by the replacement of the highly conductive metal electrode by a more resistive ITO electrode. It is therefore important to evaluate the resistivity or sheet resistance of this layer to characterise its impact on the series resistance and therefore the FF observed in IV measurements.

The 4-point probes method is used to measure the sheet resistances of the different conducting oxides mentioned in this manuscript. Current is supplied by a current generator between probes 1 and 4, while the voltage is measured between probes 2 and 3. The ratio of the measured voltage to the current flowing through the sample gives the resistance between probes 2 and 3. By entering the thickness of the sample, previously determined by profilometer for example, it is possible to determine the resistivity and the sheet resistance of the thin layer. This measurement is realized at IPVF with the software Ad Hoc connected to a source meter (Keithley 2400) and a 4 point head, each 1 mm apart, with a manual raising and lowering system.

The Hall effect measurement allows to measure the sheet resistance too but also the doping and the mobilities of the thin films. When a magnetic field perpendicular to the current is applied to a conductive material through which a current is flowing, an electric field appears perpendicular to the direction of transport and the magnetic field. The measurement of the potential difference (Hall voltage) corresponding to this electric field makes it possible to determine the concentration of charge carriers and their nature (electrons or holes). By combining this measurement with the resistivity measurement, their mobility can also be determined. The Hall voltage is measured on an AMP55T device with the ECOPIA software in the presence of a fixed magnetic field of about 0.5T at room temperature.

2.3.4 Hyperspectral photoluminescence imaging

Pholuminescence (PL) spectroscopy is a contact-less method that is often used to probe the opto-electronic properties of solar cells. Samples are illuminated with a light source whose energy is larger than the bandgap so as photons can be absorbed. The light-matter interaction called photoelectric effect allows then to create an excess of electron-hole pairs in the semi-conductor. The excess energy is lost as heat, and radiative photoluminescence occur at energies close to the bandgap. However, as materials have defects, this process is balanced with non-radiative recombination (corresponding to the recombination of electrons or holes with defects in the bulk of the material or at the interfaces without photon emission). If the defects are located close to the bandgap, there can be PL emission from these states, and the more there are, the more intense is the high energy part of the PL spectrum. However, if the defects are deep (located closer to the middle of the band gap, or far enough from the conduction or valence band), they are usually as non-radiative recombination centers, thus their increase leads to a decrease of the PL intensity.

The experimental setup consists in an hyperspectral imager (Grand-EOS from Photon) coupled with an CMOS camera (Orca-Flash 4.0 from Hamamatsu) that allows acquiring large-size images (160*160 mm^2) with a resolution of 133 µm/pixel, and for different wavelengths (400-900 nm) with a spectral resolution of 2 nm. This detection system is placed above the samples, which are illuminated simultaneously with two LED based devices (UCUBE 100 LEDs from UWAVE) situated at opposite each other and oriented towards the sample, allowing a relatively homogeneous illumination. The experimental data is acquired with the dedicated software (PHySpecV2 from Photon etc.) and then post-treated with Matlab.

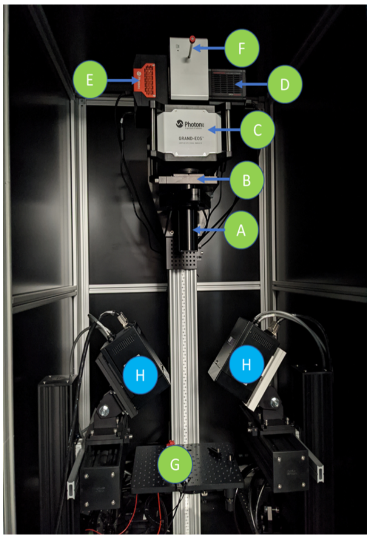

Figure 2.11: Wide-field hyperspectral measurement equipement (A) wide-field objective, (B) filter wheel, (C) hyperspectral imaging filter, (D) sCMOS camera, (E) InGaAs camera, (F) pull tab, (G) sample holder, (H) wide-field illumination system.

2.4 Optical characterizations

The transformation of a perovskite solar cell design from opaque to semi-transparent in the IR implies a fine optical characterisation of the different layers composing the device. This was achieved by two methods: the use of a UV/visible/IR spectrophotometer and an ellipsometer.

2.4.1 Spectrophotometer

The ability of a material to reflect, absorb or be transparent to certain radiation can be assessed by transmission, reflection and absorption spectra as a function of the wavelength. A beam of light from an optical source is directed toward a sample, and from the intensity of incident light and the measurement of the transmitted (or reflected) intensity, the transmission (or reflection) of the sample ca be deduced.

In our case, a spectrophotometer (Agilent Cary 5000) has been used to measure the transmission T and the reflection R between 200 and 1300 nm. It uses two different light sources: a deuterium arc UV source up to 300 nm and a tungsten halogen source above. It also has two detectors, one for UV-Visible (R928 PMT) and one for IR (Cooled PbS). The samples are presented with the substrate side towards the light source. The absorption A is obtained by the following equation:

$$A(\lambda) = 100 - R(\lambda) - T(\lambda) \tag{2.4}$$

2.4.2 Ellipsometer

Spectroscopic Ellipsometry is a characterisation method that allows to extract the optical properties of a material, as well as the thickness of the layer studied. A light beam collimated at a given incidence and linearly polarized at 45° is sent onto the surface of a sample. The reflection of the beam on the sample changes the polarization state and the intensity of the beam is measured as a function of the angle of a second polarizer (the analyzer). The parameters ψ and Δ describe the output elliptical polarisation state. However, ellipsometers do not measure ψ and Δ directly but rather functions of ψ and Δ. In the case of phase-modulated ellipsometers like the one we use, the three measurable elements are: Is, Ic, and Ic', which are functions of ψ and Δ according to Is = $\sin 2\psi.\sin\Delta$, Ic = $\sin 2\psi.\cos\Delta$, and Ic' = $\cos 2\psi$.

A spectroscopic model is then used to assess the optical properties of the stack of materials that is being investigated. The acquired data are then fitted with this model, in particular by matching the experimental values of Is and Ic with the values predicted by the chosen model. Once the model is correct and in agreement with the experimental values, it can give information on the optical properties (n, k) of the films, their thickness, their roughness...

An Uvisel 2 ellipsometer from Horiba is used to measure the optical parameters of the different layers of the perovskite cell. The measurement is made for photon energies between 0.68 and 5.4 eV with an integration time of 300 ms and a step of 0.02 eV. The spot size is 2030*705 μm^2 with an angle of 70°. The software DeltaPsi2 developed by Horiba is used to analyze the data.

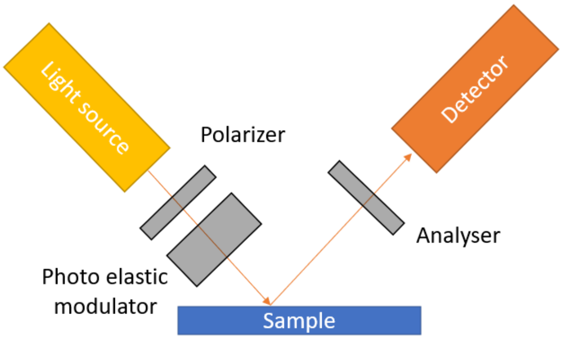

Figure 2.12: Schematic representation of the Spectroscopic Ellipsometry optical system.

2.5 Physico-chemical characterizations

2.5.1 Scanning Electron Microscopy (SEM)

SEM an electron microscopy technique capable of producing high resolution images of the surface or slice of a sample. The interaction between an electron beam and the sample generates low energy secondary electrons which are accelerated towards a detector which amplifies the signal. Each point of impact is associated with an electrical signal and its intensity depends both on the nature and the topography of the sample at the impact point. However, this requires a conductive sample, which is not the case for the perovskite cells seen in cross-section with their 3 mm glass substrate. Primary vacuum metallization allows the deposition of a thin metallic layer a few nanometers thick on the sample. The metalized samples are thus made conductive under the electron beam of the SEM.

At IPVF, a SEM ZEISS Merlin VP compact 35 field emission gun (FEG) with 15 kV voltage is used with a resolution of a few nanometers and the metalization by spraying carbon fibre strands is realised with a Denton Vaccum Desk V Evaporator.

2.5.2 Confocal microscope

The confocal microscope is an optical microscope that has the property of making images with a very small depth of field (about 400 nm). The surface is not illuminated by a beam of white light produced by a lamp, but by a laser beam, concentrated by a lens which scans the surface by positioning a pinhole in front of the detector, in a focal plane conjugate to the focal plane of the objective. In this way, only the photons coming from the focal plane pass the pinhole and participate in the formation of the image. By positioning the focal plane of the lens at different depths in the sample, it is possible to obtain a three-dimensional representation of the object.

The confocal microscope images were acquired with a Olympus LEXT OLS5100 and the Sa value, calculated as the average roughness value of peaks and valleys, was extracted by 3D acquisition of the sample surface (129*129 mm^2 area).

2.5.3 Atomic Force Microscope (AFM) and Profilometer

AFM is a type of local probe microscope for visualising the surface topography of a sample. It exploits the interaction between the atoms of a very fine tip positioned at the free end of a flexible micro-lever and the surface atoms of a sample. The tapping mode, by far the most widely used, consists of vibrating the lever at its natural resonance frequency (typically around 100 kHz), with a certain amplitude. When the tip interacts with the surface, the amplitude decreases (ecause the resonance frequency changes. The deflection of the lever in either direction is measured by a laser reflection.

AFM used in this manuscript is a Agilent Picosun 300 with a probe ACT from Appnano in tapping mode. The surface roughness is then characterised by the Root Mean Square (RMS) value. This is another representation of surface roughness than the Sa used by the confocal microscope presented above. For example, a slightly broad peak or an anomaly in the microscopic texture will have a greater effect (increase in measurement sensitivity) on the RMS than on the arithmetic mean Sa. Based on a similar principle, a Dektak profilometer has also been used to determine the thickness of single layers on glass substrates.

2.5.4 X-Ray Diffraction (XRD) and Grazing X-Ray Diffraction (GXRD)

When an X-ray beam encounters a crystal, it is reflected in specific directions determined by the X-ray wavelength and by the dimensions and orientation of the crystal lattice. This is called elastic scattering, because the photons do not lose energy (unchanged wavelengths). This results in interference that is as pronounced as the material is ordered. By measuring the angles and intensity of the diffracted rays, it is possible to identify the crystalline compounds present in a material as well as to obtain information on the dimensions of the crystal lattice and the symmetries of the crystal structure.

GXRD is based on a similar principle but uses small angles of incidence for the X-ray beam. It is used to study very thin surfaces and layers because the penetration of the waves is limited. The distances are in the nanometer range.

The Panalytical XRD analyzer was used to characterize the crystal structure of the sample (Cu Ka_1 and Ka_2 radiations) and HighScore software to analyze the obtained spectra.

2.5.5 X-Ray Fluorescence (XRF)

When a material is subjected to X-rays, the atoms may undergo ionisation, i.e. one or more electrons may be ejected from the electronic layers. The atom is then in an excited state but the loss of an electron has rendered the electronic structure of the atom unstable. The de-excitation is done by an electronic transition that releases the energy corresponding to the energy difference of the levels involved. This occurs either by emitting a photon (X-ray fluorescence) or by transmitting the energy to one of the atomic electrons (Auger emission). The energy of the emitted photon during X-ray fluorescence is equal to the difference in energy of the two orbitals involved which is characteristic of the atom where the emission was generated. Indeed, each chemical element is characterised by electronic orbitals of a certain energy. Since the electronic layers are called K, L, M, N, the L→K transition is traditionally called Kα, the M→K transition is called Kβ, the M→L transition is called Lα and so on (Siegbahn notation).

The measurements presented are made with a Fluo X Fishier Instrument (Fisherscope XDV50) between 0.5 and 10 eV in order to characterise the different TCO studied in this thesis.

2.5.6 Glow-Discharge Optical Emission spectroscopy (GDOES)

This technique combines a Glow-Discharge (GD) and an Optical Emission Spectrometer (OES). It provides both the surface/depth profile and the overall elemental composition of solid materials and layers, rapidly and with high sensitivity for all elements. Only available for conductive samples in our case with the GDOES instrument supplied by Horiba (GD Profiler 2), the latter are used as a cathode in a direct current plasma. From the surface, the sample is removed in layers by sputtering with argon ions. The sputtered atoms pass into the plasma by diffusion. Photons are emitted with excited waves and have characteristic wavelengths which are recorded by a spectrometer and subsequently quantified.

2.5.7 X-ray Photoelectron Spectrometry (XPS)

A way to probe the chemical composition of the surface of a film is the use of X-ray-Photoelectron Spectroscopy (XPS). During an XPS measurement, a sample is bombarded with X-rays of a certain wavelength, which emits a photoelectron that is then detected. The photoelectrons have specific kinetic energy and this allows to extract the binding energy of the electron E_B. This energy corresponds to the energy position of the electron below the Fermi level. Consequently, this technique allows to probe the occupied states in the matter. The photopeaks that are seen in XPS spectra correspond to dedicated chemical bonds that allow to identify the nature of the atom, as well as the chemical environment of the bond. Since X-rays are mostly absorbed near the surface, and that the photoelectrons emitted below the surface can be reabsorbed by the material, the detected photoelectrons mostly come from a region that is situated less than 10 nm under the surface of the sample.

XPS analyses were carried out with a Thermo Electron K-Alpha+ spectrometer using a monochromatic Al Kα X-ray source (1486.6 eV). The Thermo Electron K-Alpha spectrometer procedure was used to calibrate the spectrometer and verified using Cu and Au samples following the ASTM-E-90294 standard procedure. The X-ray spot size was 400 µm. High-energy-resolution spectra were acquired using a constant analyzer energy (CAE) mode of 20 and 0.1 eV as the energy step size, without charge compensation. The energy scale was calibrated with respect to the C 1s peak settled at 284.6 eV to facilitate comparison of chemical shifts between the various samples investigated.

Conclusion

We have seen in this chapter how opaque perovskite cells and STPC have been synthesised. The different techniques such as spin-coating, spray-coating, or slot die coating, as well as the etching schemes have been described. We have detailled the Baseline process, which will often be referred to throughout this manuscript, as the one allowing the fabrication of the following device: TEC-7 / TiO_2 bilayer/ triple cation perovskite / Spiro-OMeTAD / Au.

We then chose to focus particularly on the synthesis techniques used for the electrode deposition. The Au electrode deposited on the surface of opaque cells is achieved by metal e-beam evaporation. The process transfer to semi-transparent cells is done by replacing a part of the Au electrode with an ITO electrode by sputtering. We have detailed the operation of this technique and the specific characteristics of ITO deposition. We have also detailed the principle of thin film deposition by ALD and PEALD, which will be used in Chapter 6 for the deposition of IO:H.

The fabricated cells are then optically and electrically characterised to determine the performance of the tandems. We first described the two main electrical characterisations of our cells, namely the IV and EQE measurements, and how we proceed. These measurements are crucial and absolutely necessary to understand how our cells work. They allow us to compare our results with each other and are essential for building better devices. Complementary sheet resistance measurements using the 4-point probe method and Hall effect allow us to evaluate the influence of the higher resistivity of a TCO electrode compared to a metal electrode. Finally, the hyperspectral photoluminescence imaging technique was detailed.

For the optical characterisation of the semi-transparent devices, the UV/Visible/IR spectrophotometer was used to evaluate the transmission, reflection and absorption properties of the different layers. Ellipsometry was then used to determine the optical indices n and k of the thin films used in our architecture for optical simulation.

Other equipments are used to determine the physical and chemical properties of materials. These include SEM, which combined with confocal microscopy and AFM measurements allow us to characterise the morphology of our different layers. The various techniques based on the use of X-rays (XRF, XRD and XPS) as well as GDOES have enabled us to analyse the composition and structure of our materials.

Chapter 3

A reproducible process for efficient semi-transparent perovskite cell based on Spiro-OMeTAD

Introduction

The tandem vision requires adapting the "classic" opaque perovskite cell by replacing the metallic back contact with an IR-transparent conductive material (such as ITO) in order to let part of the solar spectrum pass toward the bottom cell. This requires a profound modification of the existing perovskite cell because the different layers are interdependent. Our main objective is to fabricate a semi-transparent cell with electrical performances similar to the opaque cell, a good stability and reproductibility, and which should be transparent as possible in the IR. We started by replacing the Au electrode of the opaque perovskite cells by an ITO electrode deposited by sputtering, as described in the previous chapter. Firstly, we will discuss the electrical properties of our semi-transparent perovskite cells (STPC) compared to opaque perovskite cells, their evolution and stability in time, as well as the important dispersion of the results observed. These first types of STPC will be our main working tool for the rest of this manuscript and will serve as a reference for our subsequent work. This is why we will also proceed with a quick description of their optical and morphological properties.

It is therefore crucial to be able to have a robust and reproducible reference cell to increment new materials, via the establishment of a STPC baseline. In order to stabilize our process, a first study will be presented on the origin of the non-functional cells as well as on the impact of the temperature on the electrical performances, during or after the deposition of the last electrode. Then, we will focus on the Spiro-OMeTAD and ITO interface to evaluate its role in the electrical properties of STPC compared to opaque reference cells. The use of different buffer layers between the HTL and the ITO electrode will be discussed as a potential solution to improve performance and reduce dispersion. Finally, a first 4T tandem at 22.3% of efficiency, composed of one of our best STPC and an Al-BSF silicon cell will be presented. We will highlight the key points on which optical and material optimizations will be necessary for further development.

3.1 The reference semi-transparent perovskite cell

In this section, we present the electrical, optical and morphological characteristics of the reference STPC that will be discussed and used throughout this manuscript. The Chapter 2 section 2.1 describes in detail the synthesis process of perovskite cells fabricated in the laboratory.

3.1.1 Structure and Morphology

The reference STPC is represented in Fig. 3.1a. This figure shows the different layers of the cell on a SEM cross-section. In brief, it is composed, first of all, of a compact/mesoporous TiO_2 bilayer of 150 nm, deposited on a commercial substrate TEC-7 from Solems. This substrate is composed by a FTO layer of 450 nm on a soda-lime glass of 3 mm. Two thin layers of SiO_2 and SnO_2 are located at the interface. $Cs_{0.05}(MA_{0.166}FA_{0.833})_{0.95}Pb(Br_{0.166}I_{0.833})_3$ triple cation perovskite layer of 650 nm is used as the absorber. HTL is made of Spiro-OMeTAD (250 nm). The ITO electrode has been deposited by RF magnetron sputtering, and over it, a U-shape pattern of gold (100 nm thick) is deposited in order to minimize the series resistance, see Chapter 2 Section 2.2.2 for more experimental details. Fig. 3.1b is a SEM surface image and shows that the top layer of ITO on STPC is composed on its surface of grains of sizes from 20 to 50 nm. These grains grow perpendicularly to the surface of Spiro-OMeTAD. Their origin is detailed later in this chapter, Section 3.2.3.

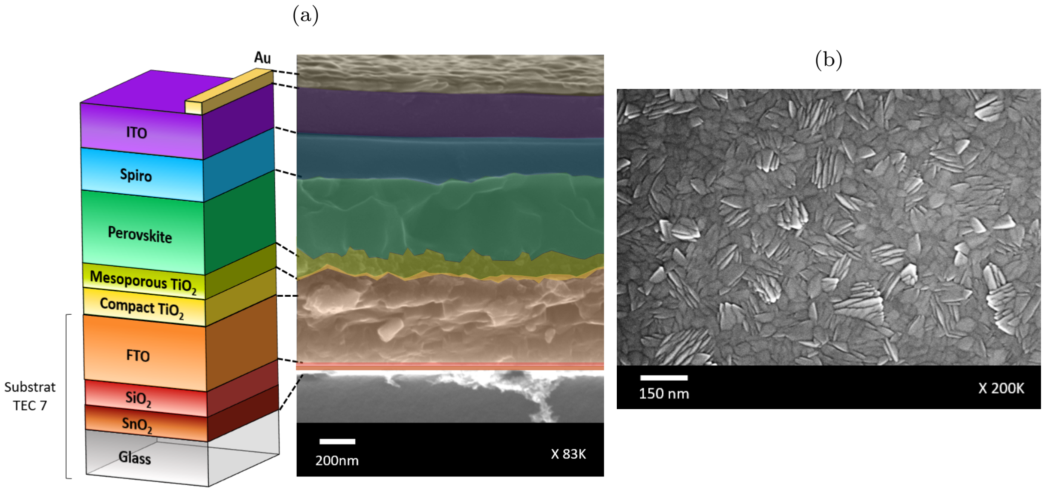
(a)

(b)

Figure 3.1: (a) Sketch and SEM cross-section image of a classical STPC. (b) SEM image of the ITO surface of the STPC.

XRD diagram of a complete STPC is presented in Fig. 3.2a. The diffraction patterns of the triple cation perovskite, PbI_2, ITO, FTO and gold electrode were identified. The diffraction peaks around 2ϑ seen at 19.92°, 24.49°, 28.34°, 31.78°, 34.98°, 40.59°and 43.23°can be assigned to the (100), (110), (111), (200), (210), (211), (220), and (221) planes of the ideal cubic perovskite structure (space group Pm3m), corresponding to a 6.29 Å in d-spacing [214, 215]. PbI_2 diffraction peak can be observed at 12.64°. Excess PbI_2 content in perovskite is known as an important factor of film properties and device storage stability degradation [216, 217]. However, Y. Chen et al. have shown that a little excess of PbI_2 can reduce the trap density and suppress non radiative recombination, and consequently improve the efficiency (I/Pb ratio of 2.57:1) [218]. In our case, we were not able to link the better or worse performance of our cells to the presence or absence of this diffraction peak. Finally, the presence of the ITO diffraction peak at 30.40° is directly related to the presence or absence of grain at the surface of the layer, see Section 3.2.3.

3.1.2 Optical properties

Absorption, transmission and reflection spectra of STPC are shown in Fig. 3.2b. Above the bandgap, transmission reaches quickly 72% at 820 nm and slowly decreases in the IR. Due to the absorption of the perovskite layer, transmission starts only at 500 nm. It increases slowly up to the perovskite band gap of 750 nm. This sub-gap transmission is caused by a too thin perovskite layer. The reflection spectra is constant at 6.5% between 400 and 750 nm, which corresponds at the perovskite absorption range.

Interference patterns are visible in the IR but also between 300 and 400 nm. Finally, absorption in IR is important with 30% at 1000 nm. It reaches 93% between 300 and 500 nm, and causes no transmission in this region.

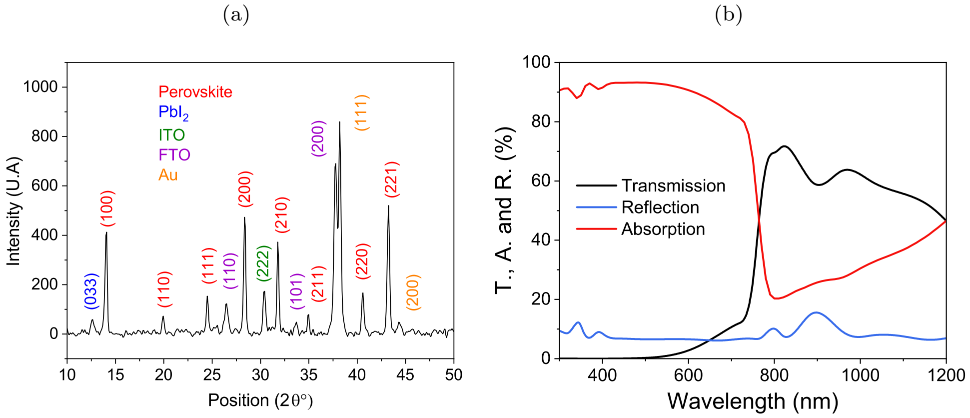
(a) (b)

Figure 3.2: (a) XRD diagram and (b) experimental data of the transmission, absorption and reflection of a classical STPC.

3.1.3 Electrical properties

As described in Chapter 2 Section 2.3.1, IV of perovskite cells are measured in superstrate configuration as shown in Fig. 2.1a and a metal mask is placed on the glass to define an opening of 0.09 cm^2, which defines the size of our cell.

The current-voltage characteristic (IV) curves under dark and illumination are measured for each cell the first day after synthesis. These measurements are then repeated regularly over time, on the order of once a week until the loss of performance is too important. EQE is measured at the same frequency.

As shown in the energy band diagram in Fig. 3.3, the ITO is suitable to play the role of back contact as its work function is correctly aligned with the valence band of the Spiro-OMeTAD.

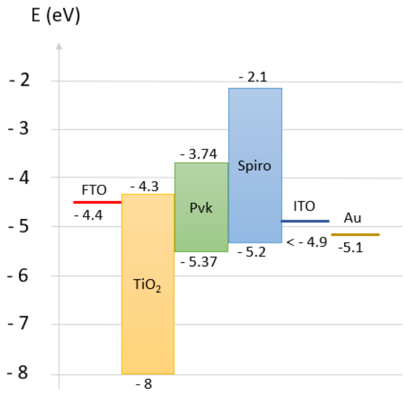

Figure 3.3: Energy band diagram of reference STPC with an ITO electrode on the back side [219–221].

3.1.3.1 Comparison between Au and ITO electrodes

A classical IV curve of a stabilized high performance opaque perovskite cell obtained in batch AY04 are presented in Fig. 3.4a (orange curve). An opaque cell (AY04-16) is representative of the performance achievable with the structure used and has an efficiency of 16.5%, characterized by a high FF of 75%. However, it shows a significant hysteresis with a higher efficiency in forward (FW) measurement (-2.1% in reverse (RV) measurement). Perovskite cells are known to suffer from hysteresis effects more severely than inorganic solar cells. It is attributed to an extremely high charge carrier mobility and an excessive defect concentrations in these materials and interfaces within device structures, since it is still under debate. Many theories have been proposed to elucidate the underlying causes, but the origin of this hysteresis is still a very controversial subject today (ferroelectric polarization, charge trapping, capacitive effects or ion migration) [222, 223]. The replacement of the gold electrode on the backside by an ITO electrode is responsible in the bast a case (AY04-12, blue curve on Fig. 3.4a), of a smaller FF (68%) due to the electrical resistances generated. Nevertheless, the hysteresis is less marked in the case of STPC, here for example (-1.7% in RV measurement). This higher instability of the opaque cells also appears when the MPP tracking position is measured for 90 seconds at constant voltage: at the end of this time, the efficiency of the opaque cell drops until it reaches the efficiency of the STPC, about of 15.5%.

Concerning the dark IV curves, see Fig. 3.4b, the values of the shunt resistance Rsh, series resistance Rs and the ideality factor m are obtained after fitting the curves with a single diode model, which is described in detail in Section 2.3.1. Rsh is higher in the case of the opaque cell (1600 vs. 771 kΩ.cm^{-2}) and Rs is slightly lower (20 vs. 30 Ω.cm^2). m is evaluated at 1.8 for the opaque cell, which means that the cell is mainly limited by non radiative recombination losses contrary to the ideal case where m = 1 [224]. On the other hand for the STPC, m is equal to 2.2. The presence of defects in the absorber material, an inefficient charge extraction or current leakage through shunts can already cause a m value superior to 2. A high ideality factor affects and limit the achievable FF below the maximum value, even in the absence of resistance effects in the electrodes or other layers [225, 226]. Nerveless, even with m = 3, the maximum reachable FF is superior to 75% [227] which makes it possible to propose STPC with more than 16% efficiency.

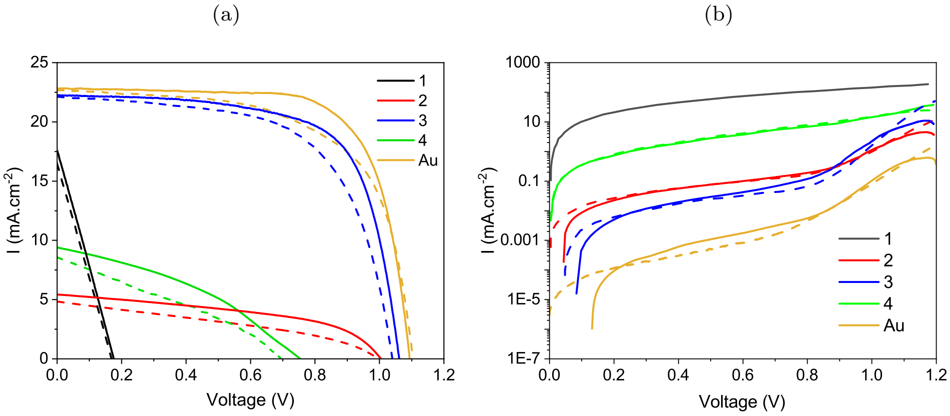
(a) (b)

Figure 3.4: (a) IV curves under illumination and (b) in dark of 4 STPC and one opaque reference cell representing the different issues of performance. The dotted curves represent the RV measurement and the solid curves the FW measurement.

3.1.3.2 Dispersion and repeatability

After studying classical IV curves of stabilized high performance opaque and semi-transparent perovskite cells, we are interested in the set of cells produced in a batch and the dispersion of the results obtained. Fig. 3.5a, b, c and d shows the dispersion of the electrical properties measured by IV for STPC, grouped by batch and manufactured each time under the same conditions. The grey stars show the average value obtained for the opaque reference cells at each time. Similar scatter plots for the opaque cells can be found in Appendix B, as well as a summary of all the batches discussed throughout this thesis. Concerning the opaque cells, we notice that some batches have a very high reproducibility like AY04 and AY15 with a standard deviation σ lower than 1 (0.39 and 0.65 respectively) and average efficiencies higher than 16%. On the other hand, the batches AY12 and AY13 show a higher dispersion (σ = 3.52 and 6.83 respectively) with lower efficiencies on average (11.96% and 9.74%) which seems to be caused by variations of the FF and the Jsc. Therefore, there are already some parameters that can affect the reproducibility of the opaque cells and these are multiple: solvent contamination, preparation problems, humidity level, glove box atmosphere... However, it is noted that triple cation (Cs/MA/FA) perovskite results in highly monolithic grains of MA/FA compositions which are more sensitive to pro-

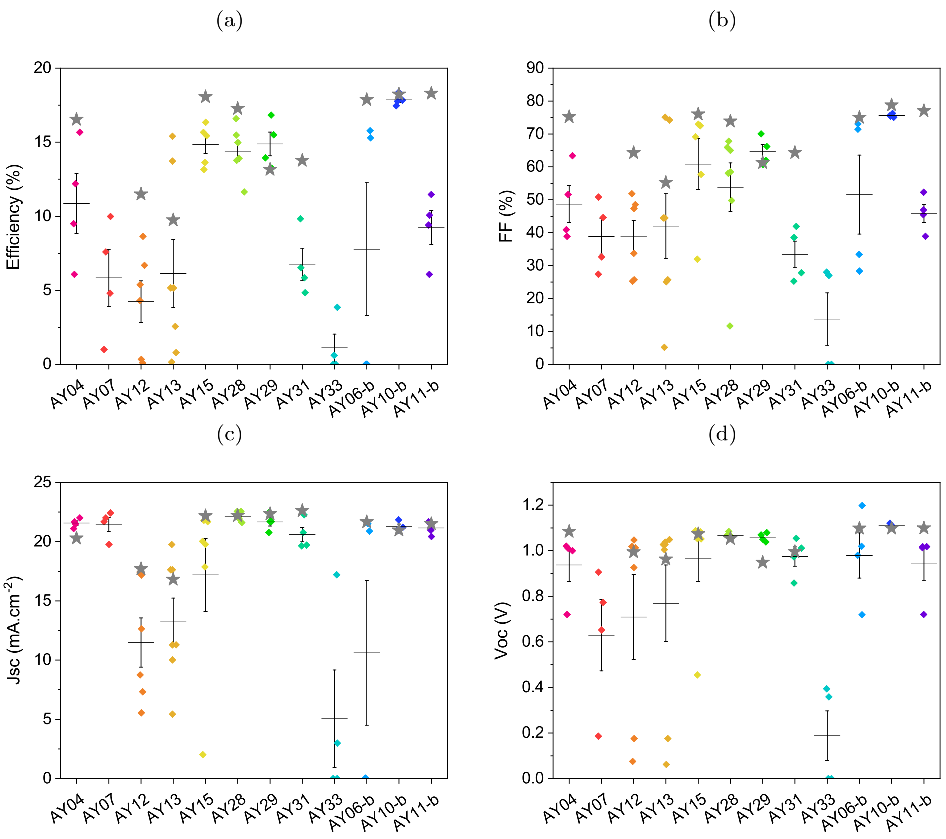
(a) (b) (c) (d)

Figure 3.5: Dispersion of the electrical properties (a) efficiency, (b) FF, (c) Jsc and (d) Voc of STPC from different batch. Grey star represents the average of opaque perovskite cell values for the same batch.

cessing conditions because of their intrinsic structural and thermal instability [228–231]. Triple cation films are intrinsically more robust to subtle variations during the fabrication process, which explains the global good reproducibility observed here [232, 233].

As far as the STPC are concerned, the dispersion is important even in the batch where the reproducibility of the opaque cells was correct (σ at 3.85 against 0.35) and this is caused by variations in the set of electrical properties. In Fig. 3.5, grey stars allow to realize that the performances of the STPC are systematically lower and seem to follow, in spite of the dispersion, the same tendency (average difference between the efficiencies of 5.57%). These lower performances are directly caused by a lower FF and Jsc (less reflection at the ITO-air interface compared to Au-air). As mentioned in the previous section, the STPC with the blue IV curve in Fig. 3.4a is representative only of the best STPC obtained in a batch. We note the presence of several cells with efficiencies lower than 1% which lower the overall average. The reasons for their failure are multiple.

In order to understand the origins of this large dispersion, we can classify the IV of dysfunctional STPC into 4 categories. Only a low Jsc as the red curve on Fig. 3.4a can be caused by a bad quality of the perovskite film, or a high recombination of photogenerated minority carriers/barrier for the photo current at an interface. This effect is not directly visible on the dark IV curves, see Fig. 3.4b. When a low FF ($\leq$ 30%) is associated to a low Jsc as the green curve, performances can be the result of a high serial resistance Rs issue, caused by an ITO/Spiro-OMeTAD or ITO/Au bad contacts or a bad quality of ITO film. On the other hand, a low FF associated with a low Voc as the black curve will be indicative of a drop in shunt resistance Rsh and the presence of a short circuit within the cell: the cell is shunted. At this point, the cell looses its photodiode behavior with an almost linear dark IV curve. In the case of STPC, the deposition of Au electrodes on top of the ITO electrode and the degradation/scratches of the electrodes has been identified as one of the main reasons for the fabrication of shunted cells. Finally, some STPC are not even measurable with IV and appear completely insulating.

3.1.3.3 Evolution in time, S-shape and stability

The performances presented so far were the highest performances reached by the cells during their aging. Regarding the opaque perovskite cells, they reach their best performances in the few days following the synthesis with an improvement of the FF of a few percentages. Then, their performance declines rapidly over time. The stability of opaque cell was found to greatly depend on device architecture [234–238]. This was explained partly by interfacial degradation [235, 239] and also by degradation of the charge transporting layers [240, 241]. Humidity was identified as the main degradation trigger [242, 243].

The behavior of STPC is different. Just after synthesis, the IV has a very characteristic shape, with a low FF ($\leq$ 50%) and lower than normal Voc (0.9 vs. 1.1 V), see Fig. 3.6a for the cell AY28-16. This particular shape, called S-shape, is synonymous of a nonlinear ohmic contact in the structure, and the interface effect is generally considered to be the main cause [244, 245]. From this point of view, the interfaces with the ITO electrode are suspected to be the cause of this behavior, this point will be further developed in Chapter 5. By keeping the cell under vacuum, the curve IV rectifies itself over time and it finds a normal shape here after 66 days, see Fig. 3.6c. We also notice that the hysteresis decreases. This evolution is also visible on the black IV curve, where the serial resistance decreases up to a factor 10 as shown on Fig. 3.6b.

While the Jsc does not seem to evolve over time, the EQE spectra (Fig. 3.6d) show an important evolution while keeping a similar shape, so that the integrated Jsc of the EQE spectrum does not match the Jsc obtained on the IV measurement. This seems to show that at the first day, a barrier for the photo current is large under low light intensity or monochromatic illumination but becomes lower by photodoping at AM1.5 illumination.

The duration of the evolution of the electrical performance is variable from one batch to another. On average, it takes from 2 to 3 weeks. Once the maximum performance is reached, the STPC stabilize and are then able to maintain such properties for several months as long as they are kept under vacuum between measurements. This difference with opaque cells can be explained by the ability of ITO to preserve the lower layers from moisture and the diffusion of the gold electrode. Nevertheless annealing the cell after ITO deposition, even at low temperature, generates an instability that causes a drop in performance over time, see Appendix C for more details.

In summary, STPC transparency reaches 70% in the IR, which shows the presence of parasitic absorption in the structure. From the electrical point of view, STPC have a higher stability over time than opaque cells even if they require a longer aging time to reach their best performance due to the presence of a S-shape just after the synthesis. Nevertheless, they suffer from a higher dispersion of performances within and between batches than the reference cells. We have been able to distinguish several cases of dysfunctional cells, and in the rest of this chapter we propose explanations for each of them.

3.2 Shunted and non-functional STPC

As we have seen in the section 3.1.3.2, STPC suffer from dispersion problems in terms of electrical results not visible on the opaque perovskite cells. In order to improve their reproducibility, we present in this section a first batch of studies aiming at reducing the number of shunted and non-functional STPC in the batch, with efficiencies lower than 1%.

3.2.1 Origin of shunt effect

Some of the STPC in each batch are shunted and do not work. This is due to a difficulty in aligning the gold and ITO electrodes without creating a short circuit at the anode, as shown in Fig. 3.7a.

We have tried firstly to invert the ITO and the gold layers in the STPC architecture (batch AY09) in order to better arrange the ITO with respect to the gold grid, as shown in Fig. 3.7c and d. This effectively allowed a better alignment of the electrodes and thus to avoid shunting cells. However, the cells do not age as usual STPC and do not show a progressive improvement. 11 days after the synthesis, the efficiency dropped with a decrease of the FF of 10% and the Jsc of 1.20 mA.cm^{-2} as it is the case on the classic opaque cells. It has been shown that at temperatures above 30°C, gold atoms start to migrate directly to the perovskite layer through the pinholes in the organic Spiro-OMeTAD layer and degrade cell performance [246, 247]. It would be possible that after the Au deposition, the deposition of ITO at relatively high power would generate a temperature increase in the Au/Spiro-OMeTAD interface and

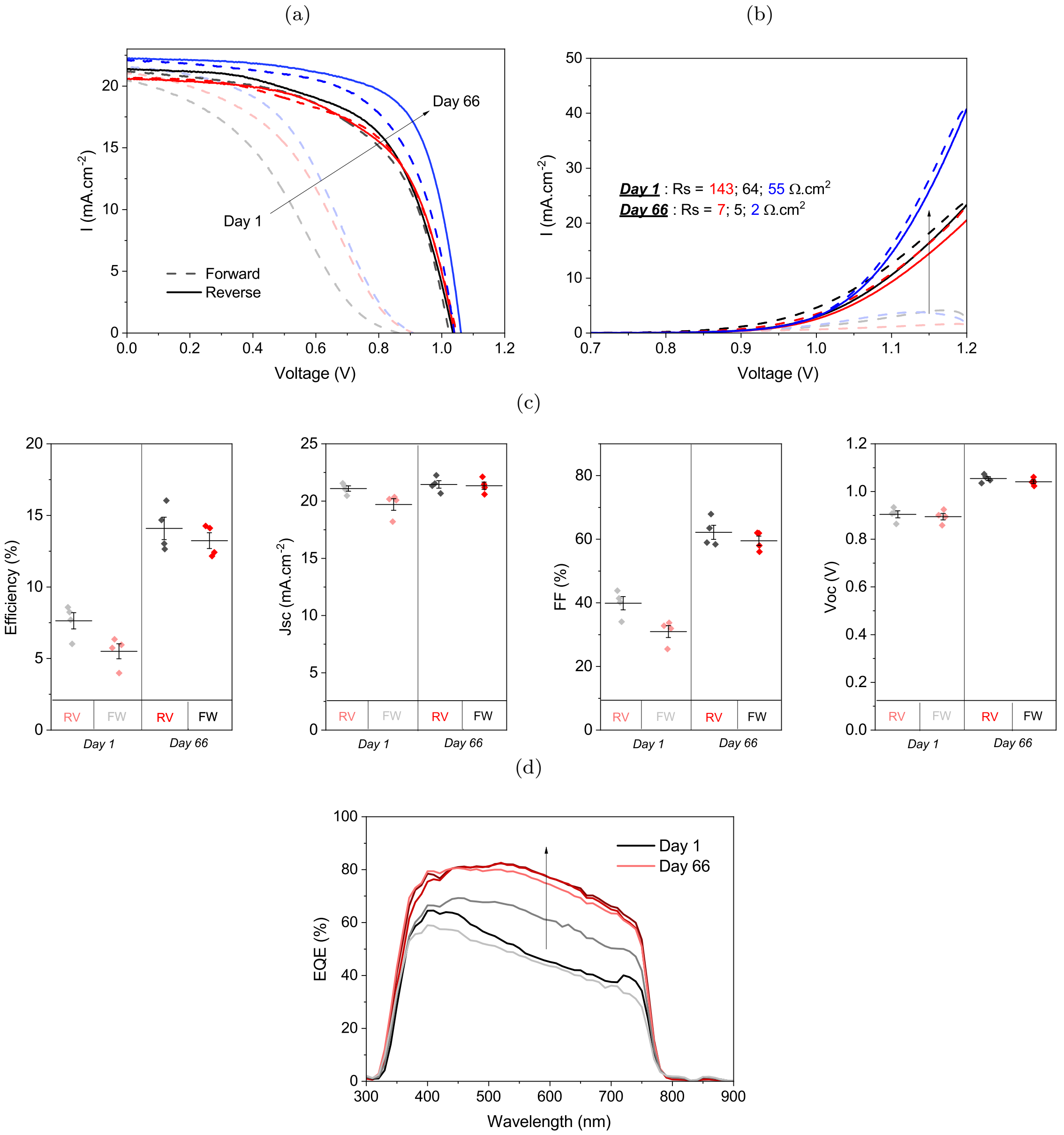

Figure 3.6: (a) IV curves under illumination and (b) in dark of three STPC, first day after the synthesis and 66 days later. (c) Evolution of the dispersion of the electrical properties of four STPC, first day after the synthesis and 66 days later. (d) Evolution of the EQE spectra of three STPC, first day after the synthesis and 66 days later.

that the migration of Au atoms towards the perovskite layer would take place. The phenomenon does not occur when the ITO layer is placed between the Spiro-OMeTAD and the gold, because this TCO is also a good barrier to diffusion. For example, only 60 nm thick ITO thin film is enough to avoid the diffusion of Ag and Au on p-type GaN [248]. Therefore, this architecture should be avoided in the future.

A better solution to avoid shunt is to avoid the use of a gold anode and to use a contact directly on FTO, as shown on pictures presented in Fig. 3.7b. This has been done on the AY15 batch presented Fig. 3.5, and we can actually see that no cell has a very low efficiency due to a low Voc and a low FF, contrary to the batch AY07, AY12 and AY13. Therefore, the following batches after AY15 have this new configuration.

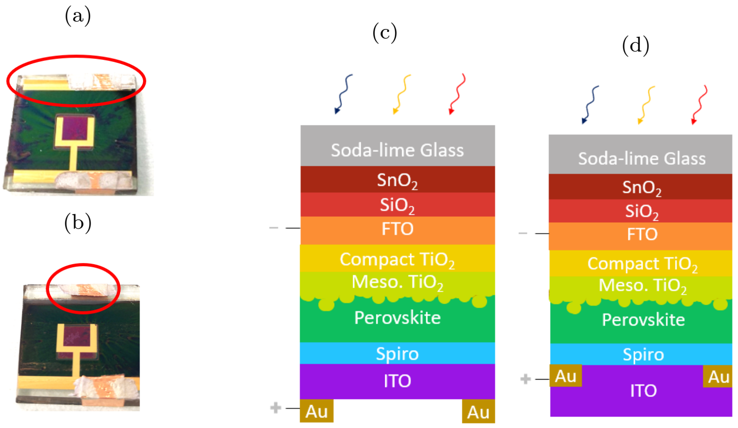

Figure 3.7: Pictures of STPC with an anode contact recovery via copper tape on (a) the Au electrode which generates here a shunt and (b) directly on the FTO layer. (c) Classic STPC structure where the gold electrodes are above the ITO and (d) a modified structure where the gold electrodes are deposited before the ITO.

3.2.2 Impact of temperature during ITO sputtering

Composed in part of organic layers, STPC are more sensitive to temperature than other types of solar cells. Thus, the perovskite layer for example cannot be heated to more than 110°C without suffering irreparable consequences [242]. However, sputtering is a more energetic deposition technique than metal evaporation and generates more heat. For this reason, a cooling system of the sample holder by ice water is necessary at all times. The higher the power on target or the longer the deposition time, the higher the heating will be and the more visible it will be via an increase of the cooling water temperature. After a standard ITO deposition on STPC (described in Chapter 2 Section 2.1 - 100 min at 50 W), the cooling water is increased from 21 to 26°C and sample holder was measured by thermal probe at 42°C after deposition.

When the cooling time between two deposition processes is not respected and that the substrate holder and the cooling water do not have time to cool down (AY13), or the cooling system stops (AY33), or the power is too high (AY31), the cells undergo a heating which results in a modification of their aspect and a decrease in electrical performances. Without heating, the surface of the gold and ITO appears relatively flat (Fig. 3.8a), with nevertheless the presence of pinholes. These pinholes come from the lower layers, they are also visible on the surface of the Spiro-OMeTAD (Fig. 3.8b). If the ITO deposition occurs at a too high temperature, the ITO electrode appears much pinker and very brittle at the surface of the cell, either partially or entirely, see the purple square in Fig. 3.8e and f. Seen under the confocal microscope, the surface of the ITO (Fig. 3.8c) is covered with venules that spread even under the gold electrode. These venules modify the reflection of the layer and generate this very brilliant aspect of the electrode. The Spiro-OMeTAD changes color under the microscope, indicating a change in its properties/thickness (Fig. 3.8d) but the venules are not present. This phenomenon could also be observed on Glass/ITO/Spiro-OMeTAD/ITO stacks, where the formation of venules does not happen instantly but can be observed with the naked eye for a few minutes.

If we look at the mechanical properties of Spiro-OMeTAD and ITO, see Table 3.1 , we realize that Spiro-OMeTAD has a Coefficient of Linear Thermal Expansion (CLTE) of more than 300.10^{-6} K^{-1}, which is 50 times higher than ITO and 6 times higher than gold.

Layer	**Young modulus E (GPa)**	**CLTE (10^{6} K^{-1})**
Perovskite (350 nm)	15-60	30-84
Spiro-OMeTAD (200 nm)	15	300-450
Au (100 nm)	6-12	50
ITO (215 nm)	116	5-6.3

Table 3.1: Young Modulus E and CLTE of perovskite, Spiro-OMeTAD, Au and ITO thin films.

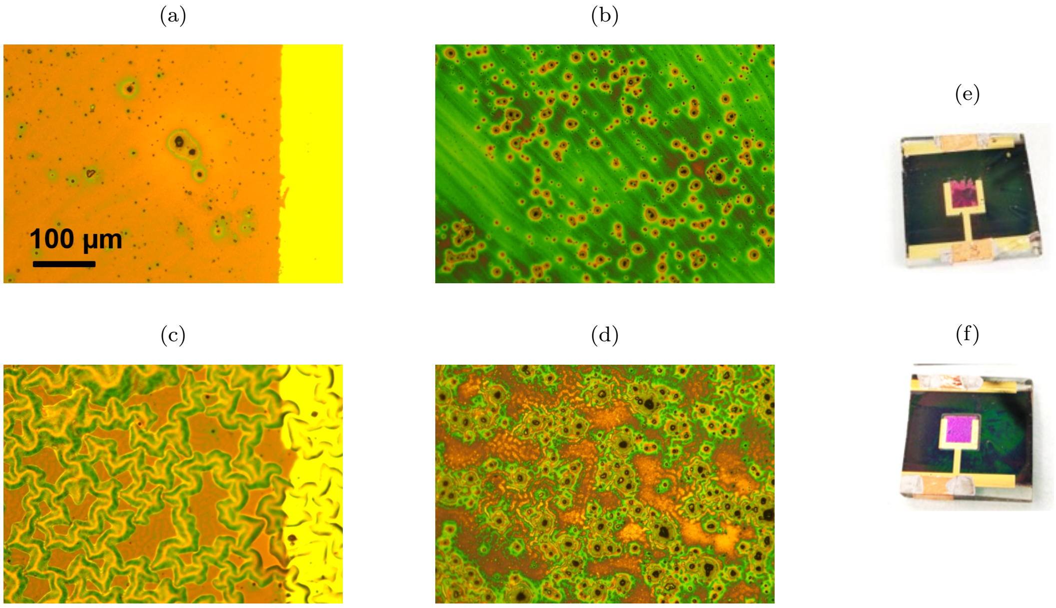
(a) (b) (e) (c) (d) (f)

Figure 3.8: Confocal Microscopy image of ITO and Spiro-OMeTAD surface of a STPC before (respectively (a) and (c)) and after annealing (respectively (b) and (d)). Photo of a STPC after an annealing with (e) partial and (f) total detachment of ITO electrode.

CLTE describes the length change of a material as a function of the temperature. The Spiro-OMeTAD will therefore expand during the ITO deposition by sputtering and then retract.

In addition, ITO is also a so-called rigid material with a high Young's modulus (116 GPa, i.e. 7 times higher than the Spiro-OMeTAD which is more elastic). The Young's modulus is the mechanical stress that would cause a 100% elongation of the initial length of a material (i.e. it would double in length), if it could be applied in reality: in fact, the material deforms permanently, or breaks, well before this value is reached. A material with a high Young's modulus will not handle the deformation imposed by tension/compression well and will break or deform permanently. This is probably what is happening here with ITO, which is deposited on a heat-expanded Spiro-OMeTAD and does not withstand the compression imposed by the Spiro-OMeTAD shrinkage. The ITO does not break, but will partially detach by forming these venules on the surface. These variations in the thickness of these venules, characterized by confocal microscopy (Fig. 3.9a), are of the order of 4-6 µm, i.e. 4 to 6 times the thickness of the complete STPC. SEM cross-section of heated STPC confirms that the ITO layer lifts while the other layers of the cell remain attached to each other, see Fig. 3.9b.

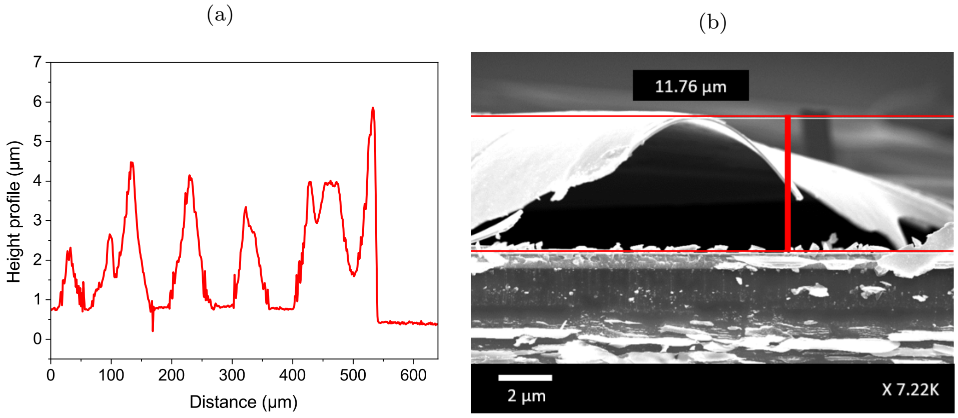
(a) (b)

Figure 3.9: (a) Confocal Microscopy measurement of roughness at the ITO surface of STPC after annealing. (b) SEM cross-section of a STPC after annealing.

The cells with these venules everywhere on the surface as for the batch AY33 do not work and are not electrically measurable, see Fig. 3.5. Indeed, beyond the fact that the ITO electrode is friable and extremely fragile, the contact with the Spiro-OMeTAD is only partial or non-existent. When only part of the surface is affected, as in the case of batch AY31, cells work in the best case as the green IV curve on Fig. 3.4a, with a low FF (inferior at 30%) associated to a Jsc and a Voc two times lower than usual. The high serial resistance observed can be caused by the ITO/Spiro-OMeTAD bad and partial contacts. The temperature in the sputtering machine plays a big role in the process of semi-transparent cells. It is therefore necessary to make short depositions, with moderate power and to respect the cooling time of the substrate holder and the cooling water between the depositions.

3.2.3 Effect of ITO thickness on the cristallinity

It is known that polycrystalline ITO films can be obtained even when the substrate temperature was lower than the theoretical crystallization temperature of amorphous ITO (180°C) [249, 250] and the thickness exceeds a critical value around 230 nm [251–253]. At this point, the growth becomes columnar, see Fig. 3.10c. The structure is no longer homogeneous in thickness: amorphous near the substrate [254, 255], and polycrystalline towards the surface. By default, ITO films deposited on our STPC with the above classical process have a thickness of 280 nm and are poly crystalline, see orange curve on XRD pattern on Fig. 3.11a. A surface roughness is apparent by SEM observation, see Fig. 3.10a.

By performing a thickness study of ITO on glass by varying the deposition time from 40 to 150 min, it seems that the crystalline phase appears after 250 nm thickness, see Fig. 3.11a. Below this value, the sample is amorphous and no roughness is visible on the SEM images as shown on Fig. 3.10b. From the electrical point of view, the sheet resistance reaches a minimum, see Fig. 3.11b, because the presence of crystallites in the upper part of the layer degrades the conductance [256]. In extreme cases, there is no longer an electrical contact between the top of the columns, as show in Fig. 3.10c. In order to obtain the best possible contact between the gold and ITO electrodes on our cells, it seems important to limit this surface inhomogeneity to a minimum. Thus, in our case it is necessary to reduce the thickness of our layer to about 210 nm because the layer is perfectly amorphous in this case, see Fig. 3.11a. This can be done either by reducing the deposition time or the power used, and we have chosen the second option by using 40W power from now on.

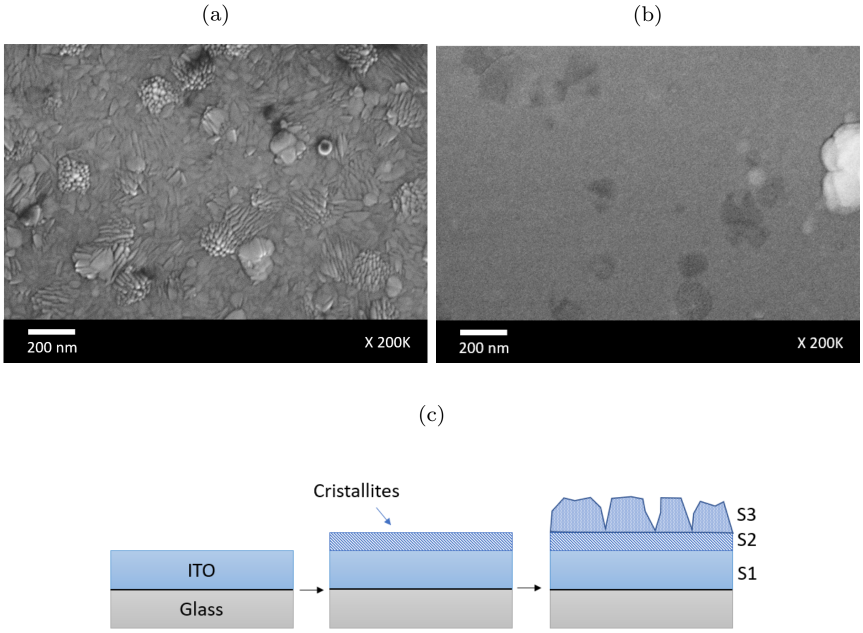

Figure 3.10: SEM images of ITO surface on glass, with a thickness of (a) 275 nm and (b) 150 nm respectively. (c) Scheme describing the columnar growth that occurs beyond a certain thickness on amorphous ITO deposition and form crystallites (S2). If the deposition continues, the columns eventually separate from each other (S3).

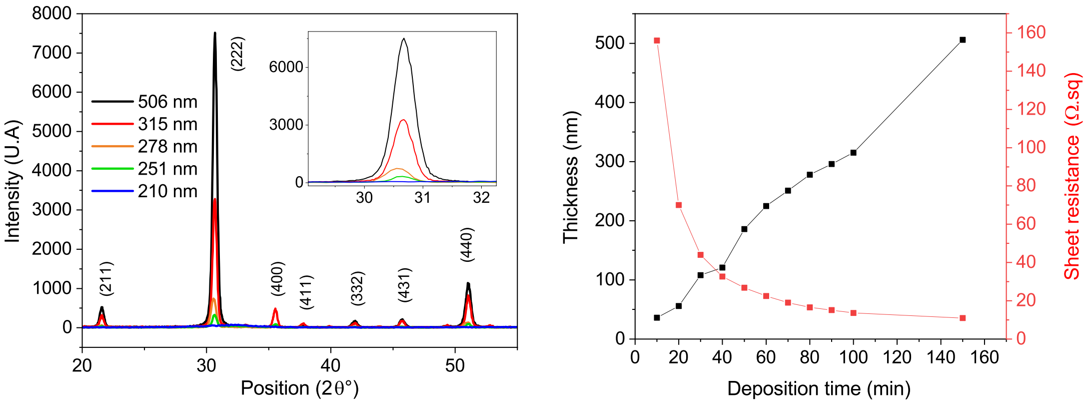

(a)

(b)

Figure 3.11: (a) XRD spectra of ITO samples with thicknesses between 210 (dark blue) and 506 nm (black). The 251 nm sample in green is the first to show a crystalline character. (b) Evolution of the thickness of the sheet resistance of standard ITO deposited on glass as a function of the deposition time.

We have seen that the reproducibility of STPC was lower than that of opaque cells, but can be improved by taking care not to expose the cells to high temperatures and by adjusting the position of the electrodes. In addition, the formation of crystallite on the surface of the ITO must be avoided to ensure optimal contact with the gold electrode. Nevertheless, we still notice dispersion in the AY15 batch for example (Fig. 3.5), and the best STPC suffer from a lower efficiency than the opaque perovskite cells (mainly due to a smaller FF).

3.3 Study of the Spiro-OMeTAD/ITO interface

A hypothesis for the origin of this persistent difference is a degradation of the Spiro-OMeTAD layer during the first minutes of ITO deposition, even if the cell does not show signs of heating as in Section 3.2.2. In order to study this interface, we first evaluate the impact of the ITO lateral resistivity and the interface resistance between the Spiro-OMeTAD and the ITO.

3.3.1 Determination of ITO lateral resistivity

To know if the lower FF observed on the STPC comes only from Spiro-OMeTAD/ITO/Au interfaces or can be caused by the lateral resistivity of ITO, we tried to add an ITO layer between the full gold electrode and the Spiro-OMeTAD in opaque perovskite cells in batch AY13, see Fig. 3.12a for the structure. This could maintain a very good lateral conductivity, as well as highlight the origin of the particle transport of STPC. The IV curves on Fig. 3.12b show a behavior similar to the classical STPC cells, with a poor reproducibility (Fig. 3.12c) and the appearance of the S shape after the synthesis.

Thus, the differences observed between opaque and STPC cells do not come from the lower lateral conduction of ITO as compared to gold, here absent in this study. Rather, the atypical behavior of STPC comes from the interfaces with Spiro-OMeTAD or gold or from the quality of the ITO layer.

3.3.2 Determination of interface resistances

To evaluate the different interface resistances around our ITO electrode, we used the Transfer Length Method (TLM). Let's consider a simple resistor geometry with two contacts located at each end, see Fig. 3.13a.A. The measured terminal resistance will then be :

$$R_t = 2R_m + 2R_c + R_{sheet} \tag{3.1}$$

with R_m the resistance of the metal contact, R_c the resistance of the metal/semiconductor interface and R_{sheet} the sheet resistance of the semiconductor. The total resistance has a linear dependency to the length of the resistor which means if we construct several of them with different lengths L, the total

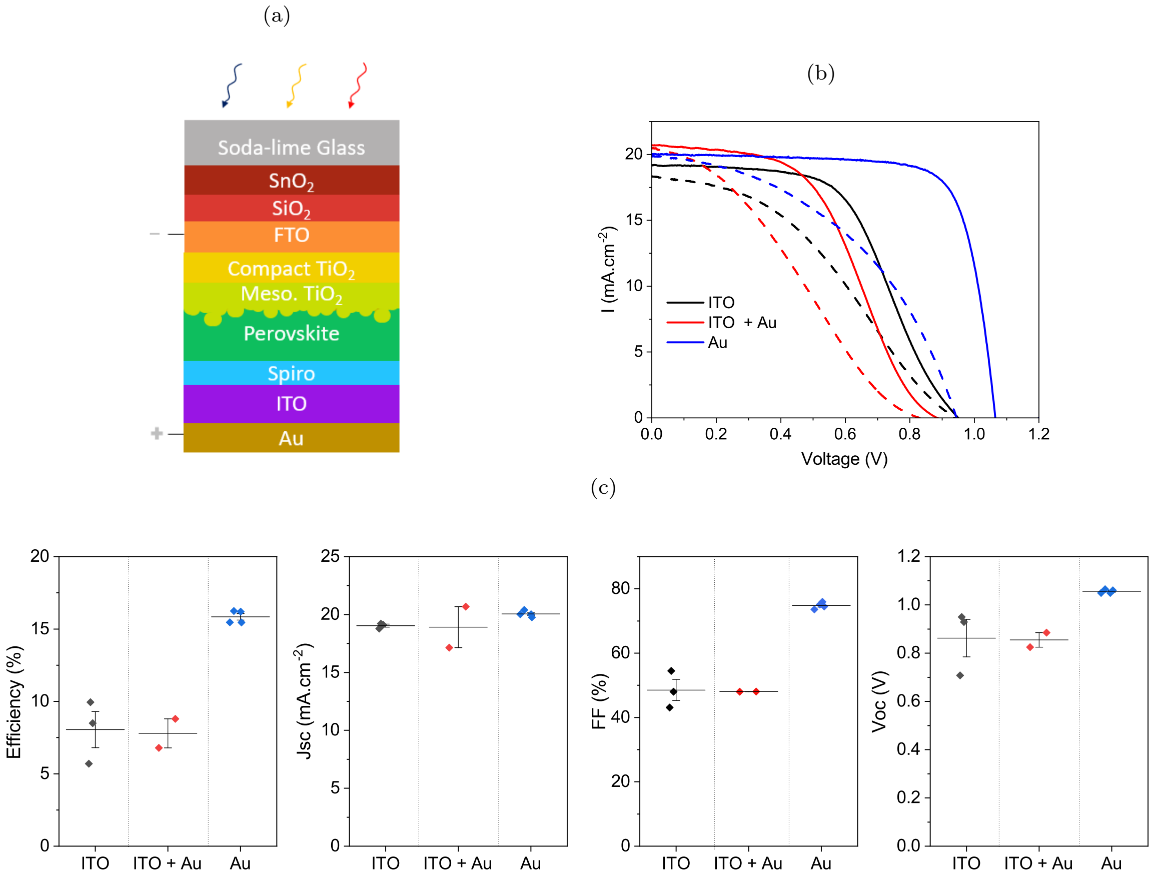

Figure 3.12: (a) Opaque perovskite cell modified structure where ITO layer is placed between the Au electrode and the Spiro-OMeTAD layer. (b) IV curves under illumination of an classical STPC, an opaque perovskite cell with a Au electrode and another opaque cell with ITO interlayer between Au electrode and Spiro-OMeTAD. (c) Dispersion of the electrical properties of 3 STPC, 4 classical opaque perovskite cells and 2 opaque cells with an ITO interlayer between the Au electrode and the Spiro-OMeTAD layer.

resistance can be measured and plotted. By extrapolating the results to L = 0, the residual resistance would be just twice the contact resistance R_c and R_m. The sheet resistance R_{sh} of the semiconductor can be found from the slope of the line as well.

In order to determine the R_c between ITO and Spiro-OMeTAD, we will study 4 different architectures, see Fig. 3.13a. The contacts are taken on the gold buses arranged according to the architecture in Fig. 3.13b. 7 measurements will be made with different distances, ranging from 0.7 cm to 4.7 cm, and repeated 3 times at the center, left and right of the contacts. The results will then be averaged. Before the measurements, we have checked the coverage of the different layers, thanks to SEM cross section like for the sample D on Fig. 3.13c.

The sample A, see Fig. 3.13a, allows to measure R_m, the resistance between the measuring pins and the gold electrodes and the equation become :

$$R_t = 2R_m + R_{sheet-Au} \tag{3.2}$$

Subsequently, Sample B allows us to deduce the $R_{c-ITO/Au}$ using the equation :

$$R_t = 2R_m + 2R_{c-ITO/Au} + R_{sheet-ITO} \tag{3.3}$$

Assuming that the current flows preferentially in the gold rather than the Spiro-OMeTAD, the following equation allows to determine the $R_{c-Spiro-OMeTAD-/Au}$:

$$R_t = 2R_m + 4R_{c-Spiro-OMeTAD/Au} + R_{sheet-Au} \tag{3.4}$$

Finally, the equation for structure D can be defined as follows and allows to deduce the $R_{c-Spiro-OMeTAD/ITO}$:

$$R_t = 2 * R_m + 2 * R_{c-Spiro-OMeTAD/Au} + 2 * R_{c-Spiro-OMeTAD/ITO} + R_{sheet-Au} \tag{3.5}$$

Results of the measurements are presented in Fig. 3.13d, which shows for each sample the resistance obtained as a function of the measuring distance. The slope appears null for the samples because the gold R_{sh} can be considered as negligible, except for the sample B. The resistance of each interface can be deduced and thus, the pins/Au interface has a small resistance R_m (0.12 Ω) as does the ITO/Au R_c (0.23 Ω). The Spiro-OMeTAD/Au interface does not show any significant resistance (R_c 0.01 Ω), unlike the Spiro-OMeTAD/ITO interface which has the highest R_c (0.32 Ω). We thus confirm that the addition of simple ITO layer at the Spiro-OMeTAD-Au interface adds small electrical resistance, both on the Spiro-OMeTAD and Au sides. Nevertheless, the ohmic contact ITO/Spiro-OMeTAD seems to be good because the resistance is much lower than what we observe on dark IV of STPC (1 kΩ).

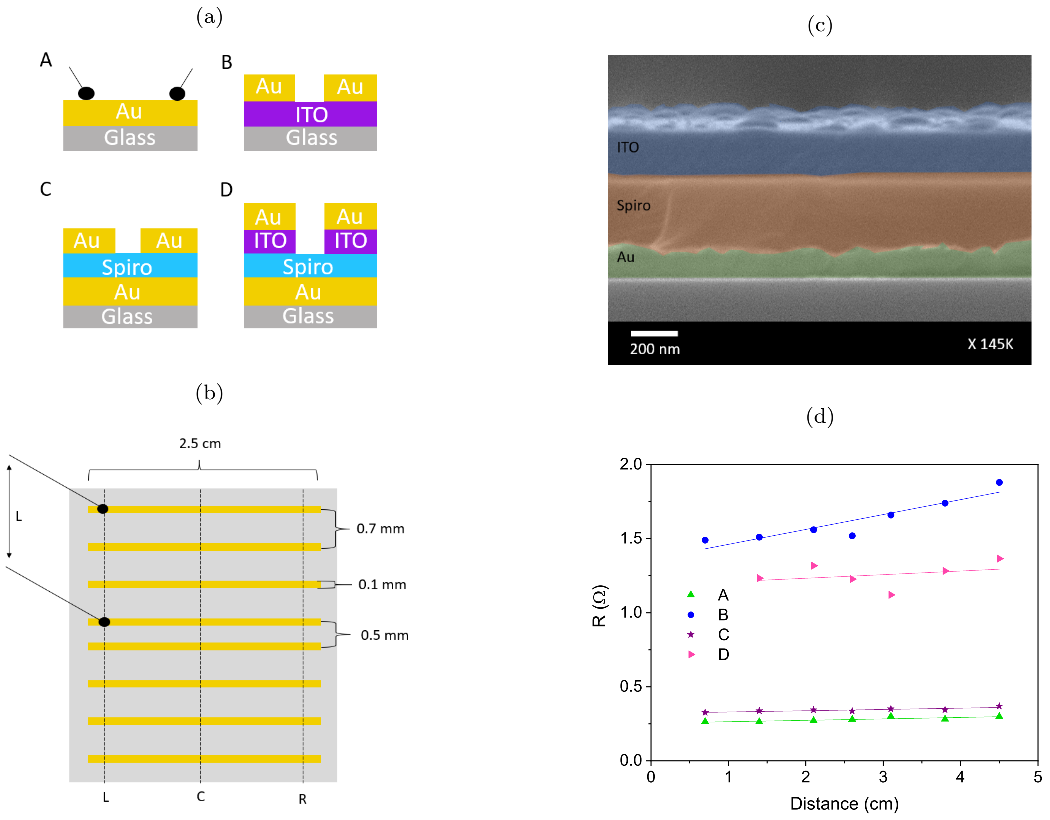
(a)
(b)
(c)
(d)

Figure 3.13: (a) 4 structures measured with TLM. (b) Architecture of Au electrodes for TLM measurement. (c) Colored SEM cross-section of the sample D. (d) TLM curves (resistance as a function of the distance) for the 4 structures presented on Fig. 3.13a.

Structure	**A**	**B**	**C**	**D**
Intercept (Ω)	0.25	1.19	0.32	1.18
Slope (Ω.cm^{-1})	0.01	0.14	0.01	0.02

Table 3.2: Slopes and intersections with the y axis of the TLM curves presented in Fig. 3.13d.

There is no obvious electrical degradation of the interface in terms of conductivity, the ITO sputtering process on Spiro-OMeTAD does not significantly increase the resistance of the Spiro-OMeTAD and its interface for electron transport. Nevertheless, these measurements do not allow to know how the holes behave and their extraction, and thus do not exclude a chemical degradation. Moreover the TLM measurement is not done on a complete cell stack and excludes perhaps interactions with other layers.

3.3.3 Metal buffer layer

The use of a buffer layer on the Spiro-OMeTAD can help protect this fragile organic layer. For p-type contacts, these are most often oxides such as Molybdenum oxide (MoO_x) [27–29], Tungsten oxide (WoO_x) [208] or Vanadium oxide (VoO_x) [257, 258] that are currently described as possible solutions in the literature. These materials show good band alignment with ITO, can be deposited at low temperature via an evaporation process and do not require annealing afterwards. However, their deposition impact FF and decrease the efficiency of STPC. It has also been shown that they can react with perovskite that have an increased sensitivity to metal oxides, decreasing the lifetime of STPC. For this reason, we will test here other alternatives such as thin pure metal layers. In order not to modify the performance of the tandem, this layer must be energetically well aligned with the two layers surrounding it, in order to act as a selective barrier for the carriers. It must also prevent diffusion into the lower layers in addition to overcoming the thermal instability of the Spiro-OMeTAD.

As consequence, we try the deposition of different metal buffers of 2 nm (gold, silver, nickel and titanium) between the ITO electrode and the Spiro-OMeTAD layers. These buffers were evaporated at low speed (0.01 nm.s^{-1}) in order to avoid damage of Spiro-OMeTAD.

3.3.3.1 Optical and morphological properties

Before being tested on cell, these buffers were deposited on glass to check their optical compatibility with STPC. Fig. 3.14a shows the transparency of these 4 ultra thin layers on glass compared to a glass sample. Only the Au layer shows a significant absorption over the entire spectra, and the Ag buffer only shows a parasitic absorption between 350 and 600 nm. This is not a problem because the radiation in this range is absorbed by the perovskite before reaching this part of the STPC.

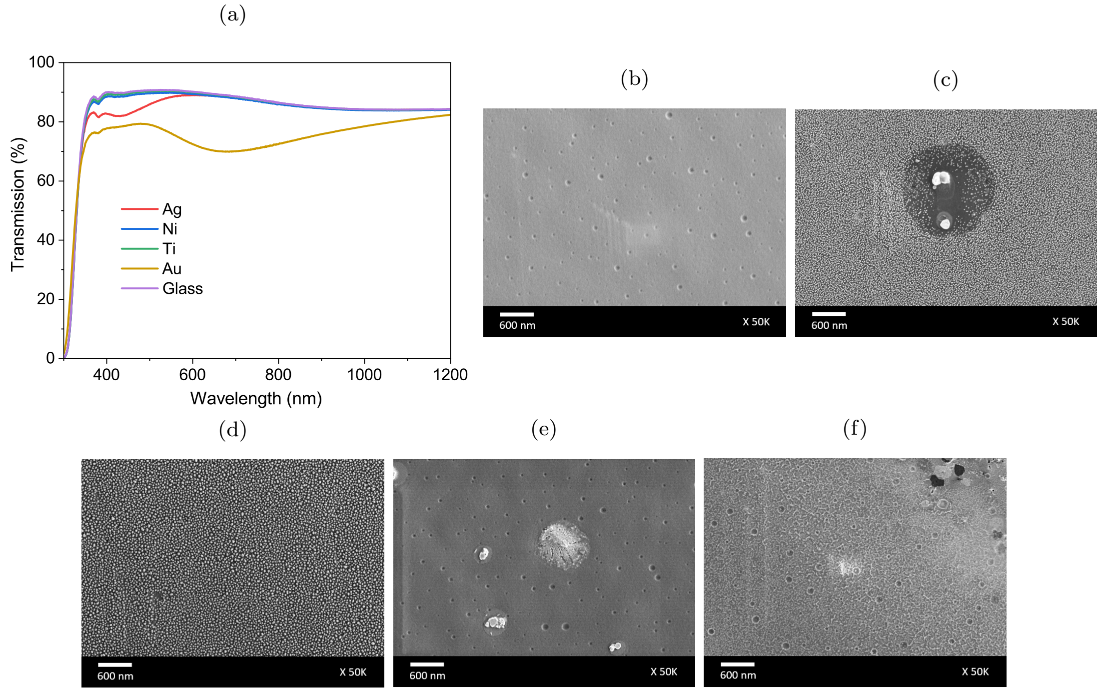

Figure 3.14: (a) Transmission spectra of buffer layer (Au, Ag, Ni or Ti) on soda-lime glass. SEM surface of (b) Spiro-OMeTAD on a STPC and after the deposition of (c) Au, (d) Ag, (e) Ti and (f) Ni buffer layer of 2 nm.

Regarding the coverage of these ultra-thin layers, the SEM images presented in Fig. 3.14b, c, d, e and f show that the Ag and Au buffers are not covering and form small aggregates of about 30 and 15 nm respectively on the surface. Concerning the Ti buffer, no aggregate appears on the surface although the deposition is visible to the naked eye and at the level of the defects as in Fig. 3.14e there is a different surface aspect. Finally, the Ni buffer has a particular surface state and different from other buffers while being covered as shown the Fig. 3.14f and forms venules on the surface of the Spiro-OMeTAD.

3.3.3.2 Gold buffer layer

In order to study the interest of using a buffer, we first used a Au buffer layer because we are sure of its compatibility with our structure as it is used on opaque cells. However, its diffusion in the lower layers and its consequences on the stability over time prevent us from considering it as a real solution in our case. We have placed a 2, 10 and 20 nm gold layer between the ITO electrode and the Spiro-OMeTAD layer in the batch AY11-b.

In Fig. 3.15a, we notice that as soon as 2 nm of Au is used, the dispersion decreases (σ = 0.91 vs. 2.29) and the average efficiency increases (12.4% vs. 9.3%). This is mainly due to an improvement in FF (48% vs. 55%). Fig. 3.15b and c represent respectively the IV curve and the EQE of the best cells for each condition. The IV curve is straightened, the S-shape is less marked in the presence of the Au buffer and at the level of the EQE, we note a clear improvement on the whole spectrum (+ 8% at 500 nm) while the Jsc measured on the IV did not evolve. This is in line with the observations made in Section 3.1.3.3, which noted an inconsistency between EQE and Jsc for STPC during their aging.

By using a thicker buffer (10 then 20 nm), the average efficiency continues to increase until it exceeds the average efficiency of the opaque reference cells (18.6% vs. 18.4%). This is directly caused by a higher Jsc (22.3 vs. 21.53 mA.cm^{-2}) which can be explained by a reflection phenomenon at the Spiro-OMeTAD/Au/ITO interfaces particularly well adapted. This is consistent with the EQE measurements

(a)

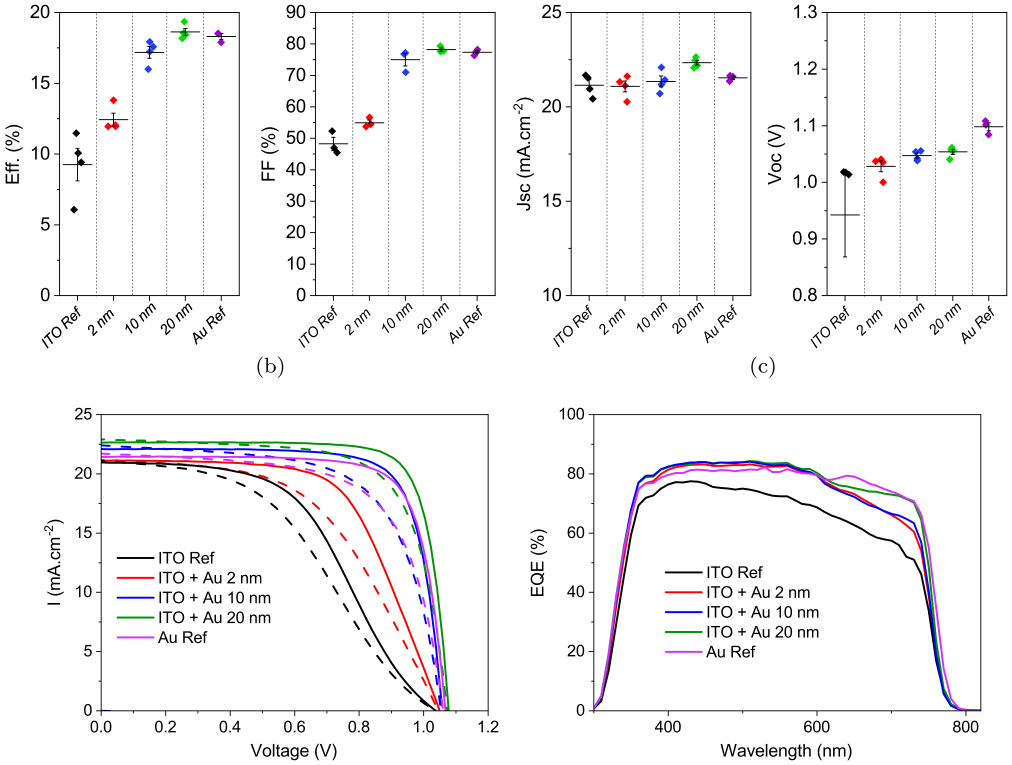

(b)

(c)

Figure 3.15: (a) Dispersion of the electrical properties of opaque perovskite cell and STPC (reference ones and with different thicknesses of Au buffer) from batch AY11-b, 1st day after the synthesis. (b) IV curves under illumination and (c) EQE of best cells of each type presented on Fig. 3.15a

which show that in the presence of a 20 nm Au layer, the EQE of the STPC is higher between 600 and 750 nm and follows that of the opaque references, whose behavior was detailed in Section 3.1.3.1. In the same way, the thicker the Au buffer, the more marked the hysteresis and the closer the behavior with the opaque cells. It should be noted here that the presence of 20 nm of Au makes the STPC opaque and is not a viable solution for a tandem setting.

Thus the S-shape and the particular aging of the STPC seem to be directly caused by the sputtering of ITO on the Spiro-OMeTAD layer when the latter is not protected. Moreover, the important hysteresis observed on the opaque cells seems to come from the Au layer. The use of a buffer, other than Au, seems to be an interesting solution to reduce both the dispersion and the recovery time of the STPC while maintaining the superior stability of the STPC compared to the opaque references.

3.3.3.3 Silver buffer layer

Lee et al. showed that an Ag buffer on a similar structure acts as a seed layer for ITO crystalline growth along one direction of (222). The incorporation of the thin Ag layer helps to improve the mechanical flexibility and decrease the sheet resistance of ITO electrode [259].

The electrical properties of cells with a 2 nm Ag buffer compared to conventional STPC and opaque cells in batch AY07 are presented in Fig. 3.16a. The best IV obtained for each type of cell can be found in Fig. 3.16b. We can see that the Ag buffer does not give satisfactory results on STPC. The efficiencies do not exceed 2% with a very low Voc. The shape of the IV is similar to that of shunted cells of Section 3.2.1.

Other studies have been performed on the degradation of perovskite cells due to the addition of Ag. Katol et al. demonstrated that when a silver electrode is used instead of gold $MAPbI_3$, perovskite decomposes into PbI_2 and MAI. They migrate through the pinholes of the Spiro-OMeTAD layer and forms AgI in the silver electrode, degrading the cell performance [238]. On the other hand, Liang et

(a)

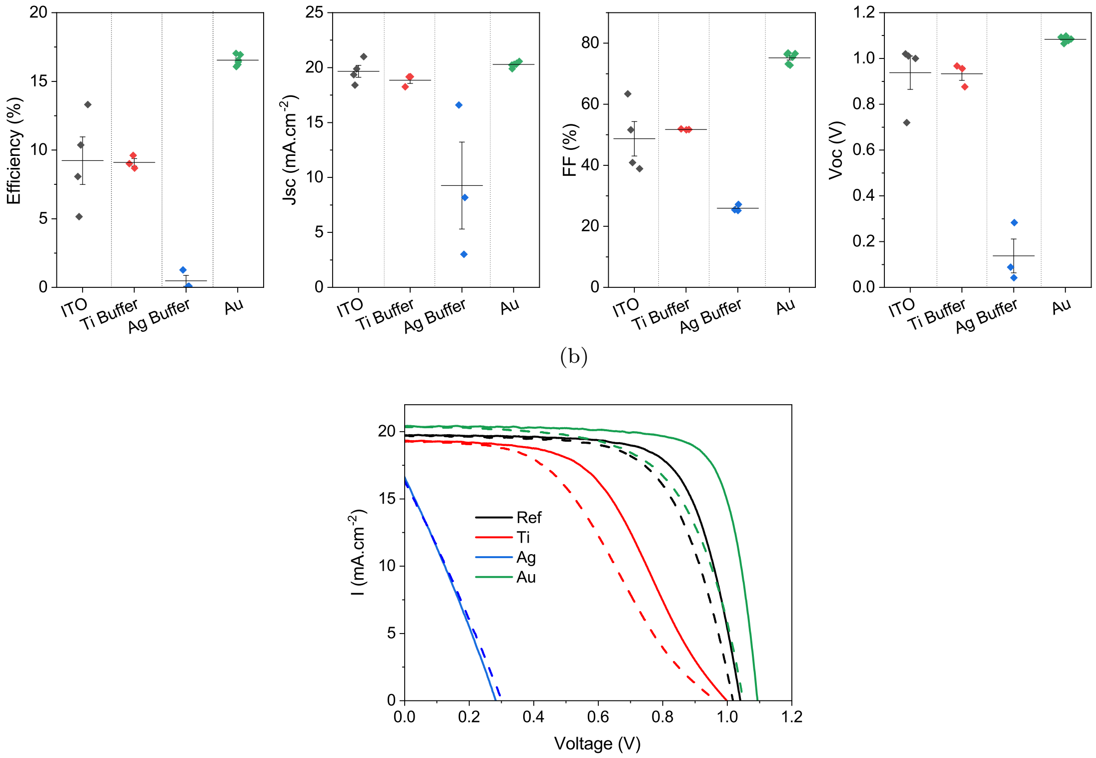

(b)

Figure 3.16: (a) Dispersion of the electrical properties of 12 STPC (without and with a Ti or Ag buffer layer of 2 nm between ITO and Spiro-OMeTAD) and 4 opaque perovskite cells. (b) IV curves of best cells of each type presented in Fig. 3.16a once stabilized.

al. artificially doped the Spiro-OMeTAD layer with silver. They found that more defects appear in the Spiro-OMeTAD and the electrical properties decrease as compared to undoped cells and degrade faster over time [260]. Therefore, migration of PbI_2 and MAI ions and formation of AgI in the perovskite can be suspected. In conclusion, even in very thin layers, silver cannot be a good buffer if it is in contact with the Spiro-OMeTAD.

3.3.3.4 Titanium buffer layer

As titanium is a very reactive metal and oxidizes spontaneously in air, it is likely that a buffer of 2 nm is composed of TiO_2 rather than pure Ti. Even if TiO_2 is usually used as ETL, as in our structure, Seo et al. showed that it was possible to use amorphous TiO_2 deposited by ALD on the surface of Spiro-OMeTAD in order to prevent ion migration of LiTFSI additives in the perovskite. This layer even improved the performance of opaque cells and enhanced their stability because of the presence of hole traps in the gap [261].

The performances obtained are shown in the same figure as for the cells with silver buffer for the batch AY07 (Fig. 3.16a and b). We can see that the average efficiency obtained is similar to that of the classical STPC this time (9.11 vs. 9.25%). However, the reproducibility is greatly improved with σ which decreases from 3.46 to 0.46, which is essentially due to a lower dispersion of the FF. Titanium therefore plays an effective role in protecting against the power of ITO deposition, which reduces the usual dispersion of STPC. However, if we look at the IV, we realize that the best cell with titanium suffers from an S-shape curve which, contrary to the classical STPC, does not resolve itself with time. The efficiency is then limited to 9.61% at best, where the best reference STPC reaches the 13.31%. It seems that our titanium buffer, although having a good reproducibility, well covering and reducing the dispersion, generates additional resistances and prevents the positive evolution of the STPC via the disappearance of the S-shape in time.

3.3.3.5 Nickel buffer layer

Jiang et al. completely replaced the 80 nm gold electrode with the 300 nm Ni electrode and achieved the comparable performance with classic structure [262]. It is therefore possible that Ni can play an adequate role as a buffer, without diffusing or becoming blocking. In batch AY06-b, we deposited 2 nm of Ni between the Spiro-OMeTAD and ITO. This deposition was done twice on 3 cells each time (these groups are called Ni n°1 and Ni n°2) and the results are compared to 4 reference STPC.

We found that the performance of cells with Ni buffer n°1 was comparable to the best cells without buffer (16.7% vs. 15.8%), see Fig. 3.17a for dispersion of the electrical properties 15 days after the synthesis. In addition, the presence of the buffer significantly reduces the dispersion (σ = 0.4 vs. 8.9). However, this observation was only valid for cells with the first Ni deposition. The cells with the Ni n°2 all suffered from electrical connection problems that generate large current variations during IV measurements, see Fig. 3.16b. However, their average efficiency appears close to STPC with the Ni n°1 (14.5% vs. 16.2%). This batch was reproduced with this time a first buffer of 4 nm of Ni on 4 STPC, and a second of 2 nm on 4 others. The same results could be observed.

Our hypothesis concerning these results is that the first Ni buffer deposited on the STPC results from the evaporation of a oxidized surface of the crucible in the evaporation chamber (NiO_x instead of Ni) which is also known to be a HTL. In addition, it is known that NiO_x is a very good substitute for Spiro-OMeTAD. Guo et al. deposited a HTL of NiO_x at low temperature by sputtering and doped it carefully with an oxygen flux inferior at 10%. An efficiency of 11.6% was obtained [263].

In order to verify this hypothesis, XPS measurements were performed. Two Ni depositions were done on silicon substrates, a first deposition of 4 nm and then a second of 2 nm. The substrates were first washed with Hydrofluoric Acid (HF) to be deoxidized on the surface.

Firstly, fluctuations of the background level are observed at different binding energies of the spectra at the location of the $Ni2p_{3/2}$ and O1s photopeaks, see Fig. 3.18a and b. Once the spectra are normalized (Fig. 3.18c and d), we observe a larger Full Width at Half Maximum (FWHM) for the O1s photopeak at 531.6 eV for the 4 nm sample, which indicates the presence of a new contribution. We also observe the appearance of an additional peak at 855.7 eV, related to different Ni levels. This proves that the chemical state of the layer is changing.

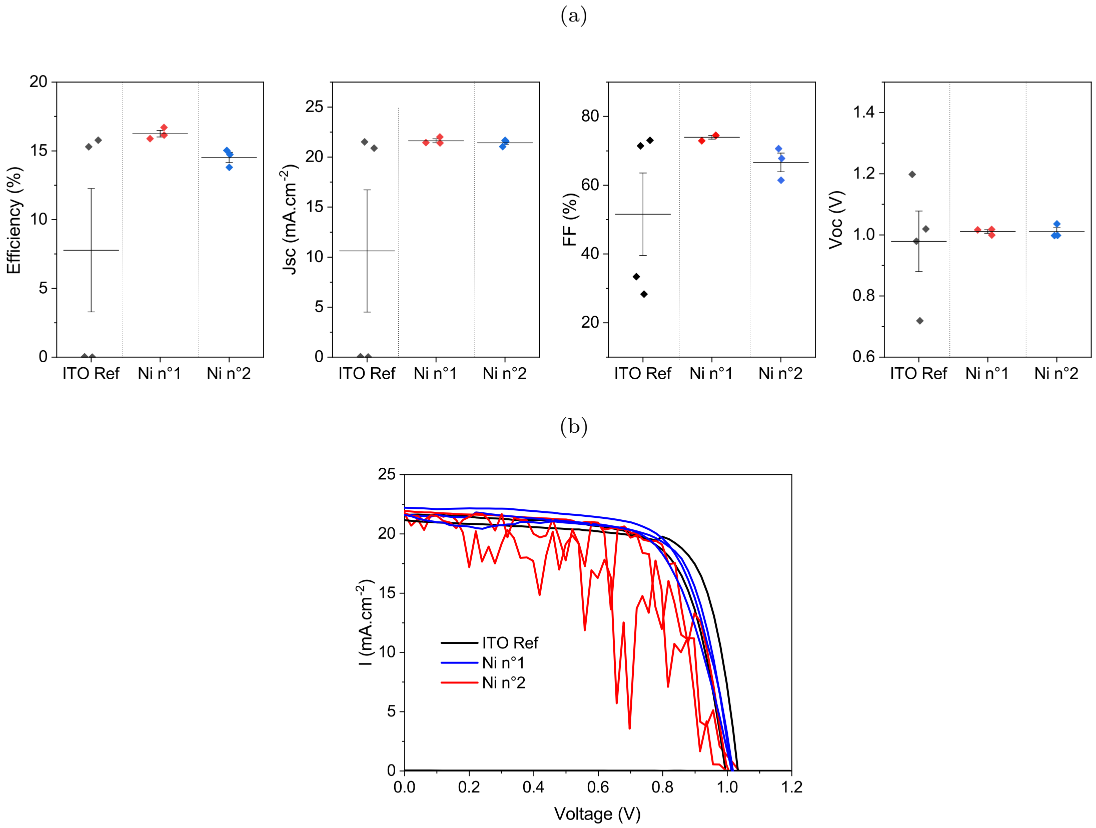

Figure 3.17: (a) Dispersion of the electrical properties of 10 STPC in batch AY06-b (4 with a classical ITO and 6 with an additional Ni buffer layer of 2 nm deposited in 2 different processes). (b) IV curves of STPC without and with a Ni buffer layer of 2 nm between ITO and Spiro-OMeTAD.

After peak deconvolution, the envelope matches the measurements for the 2 nm sample when O1s and Ni2p$_{3/2}$ photopeaks were plotted using only two and a single contributions, respectively, see Fig. 3.18e and f. Oxygen detected related to both a carbonaceous contamination (C-O, C=O, COOH) and silicon (SiO$_x$). In contrast, for the 4 nm sample, a third contribution is related to Ni (NiO$_x$). This contribution is below the detection limit for the 2 nm sample. Similarly for the Ni2p$_{3/2}$ photopeaks, the contribution of oxidized Ni (NiO,Ni(OH)$_2$) must be added to have a good fit. This contribution represents then 7.8% of the atomic percentage while the native Ni represents always the same percentage (9.8% vs. 10.6%).

As show in Table 3.3, the amount of Ni2p is greater in the case of the 4 nm sample (17.6% vs 10.6%), which confirms that the sample is indeed thicker.

We can conclude that the Ni buffer evaporated first, is partly oxidized contrary to the second, evaporated later, which is completely metallic. New measurements could allow to obtain more information like the oxidation degrees, unknown today. To conclude, Ni is an interesting buffer provided that its degree of oxidation is controlled, which is not possible in our current setup. A solution to deposit NiO$_x$ on Spiro-OMeTAD would be to use spin coating via the use of nickel formate dihydrate and ethylenediamine solutions [264], or by the dissolution of NiO$_x$ nanocrytals in chlorobenzene [265].

Thus, we were able to show in this section that buffer layers can play an important role in the performance of STPC. The use of a gold buffer, although not viable because of its diffusion in the lower layers and its strong parasitic absorption, can improves the reproducibility of STPC by reducing the dispersion of the results. On the other hand, Ag buffer just degraded the electrical properties while the oxidized Ni could be an interesting solution if its oxidation is controlled. Finally, the Ti buffer allows to decrease the dispersion of STPC performances in a reproducible way but induces a slight decrease in FF. Another approach to solve this dispersion problem is to replace the Spiro-OMeTAD by another HTL, this time inorganic and less sensitive. This approach will be investigated in Chapter 5.

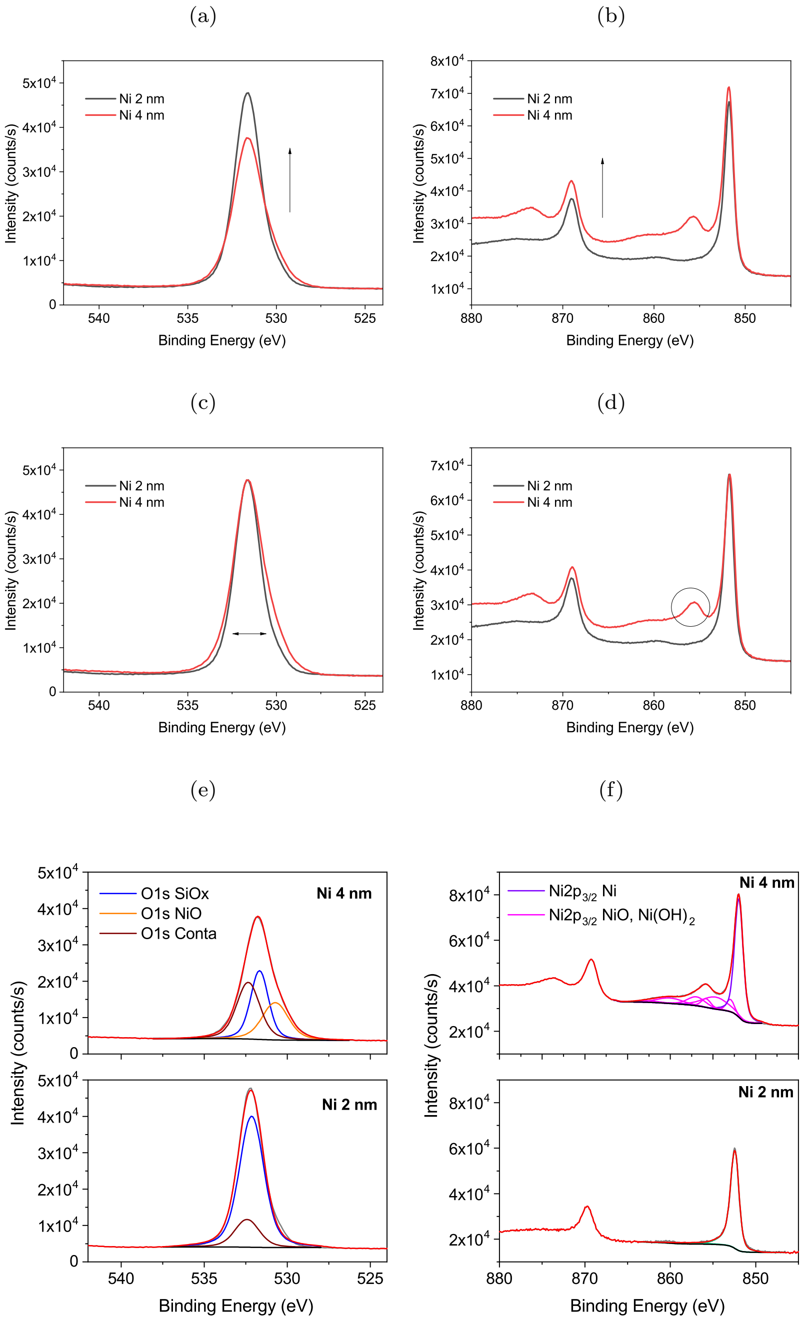
(a) (b) (c) (d) (e) (f)

Figure 3.18: Raw and normalized XPS spectra of O1s, (a) and (c), and Ni2p , (b) and (d), respectively, for 2 and 4 nm of Ni. De-convolution of (e) the O1s and (f) Ni2p normalized XPS spectra for 2 or 4 nm of Ni.

	Ni 2 nm	**Ni 4 nm**
C1s C-C SiO_x	3.9	6.7
C1s C-O	1.7	2.5
C1s C=O	1.5	0.6
C1s RCOOH	1	3.7
Σ O1s	8.1	13.2
Si2p SiO_2	18.7	10.4
Si2p $SiO_{x¡2}$	18.7	11.4
Σ Si2p	37.4	21.8
O1s SiO_x	36.3	13.7
O1s consta (C-O, C=O, COOH)	7.7	14.7
O1s NiO_x	-	10.9
Σ O1s	44.0	39.3
Ni2p Ni	10.6	9.8
Ni2p (NiO, $Ni(OH)_2$)	-	7.8
Σ Ni2p	10.5	17.6

Table 3.3: Atomic percentage of the element according to the XPS analysis for 2 or 4 nm of Ni. Peak characteristics and atomic percentages extracted from the high energy resolution photopeaks deconvolution displayed in Fig. 3.18e and f.

3.4 First prototype of 4T perovskite/silicon tandem

Finally, even in the absence of a buffer and thanks to the improvement of the process via temperature control and electrode deposition, the maximum efficiency obtained on a STPC was increased up to 18.4% with the cell AY10-b-09, see Fig. 3.19. This cell stands out from the others by a very high FF up to a 78%. As shown on the dispersion graphs in Fig. 3.5, all the STPC of this batch present a even lower dispersion than the batch AY15, AY28 and AY29. Other AY10-b cells also have very high efficiencies, which is allowed by the high performances of the opaque cells of this batch (average efficiency at 18.2%). Only 0.4% separates the average efficiency of opaque cells from STPC in this batch, showing that it is possible to synthesize STPC with performances equivalent to high efficiency opaque cells. However, the mechanisms responsible for this very low dispersion compared to the previous batches and for these very good performances are not yet fully identified.

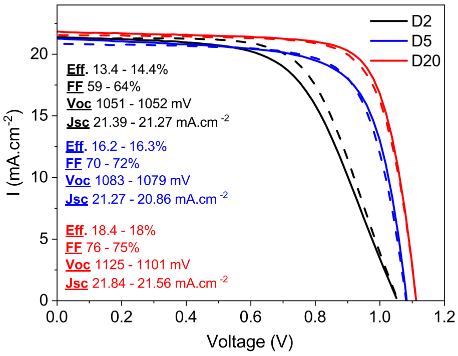

Figure 3.19: Evolution of the 20-day IV of STPC AY10-b-09, which achieves the highest efficiency at 18.48% at IPVF using Spiro-OMeTAD as HTL.

In parallel, a first tandem was assembled with another high efficiency STPC because it was not possible for material reasons with our record cell. We used the STPC AY15-16 as a top cell and the silicon cell used as bottom cell is an Al-BSF device supplied by the cell and module producer Photowatt. The original cell of 156*156 mm^2 was downsized by creating smaller pieces with 1 cm^2 active area (including 6 metallic fingers). Then, two electrical wires were soldered on the front and back of the smaller silicon cell to keep bottom cell contacts when the top cell was stacked over.

IV curves are shown in Fig. 3.20a for both STPC and silicon devices, which exhibit 16.6% and 18.5%, respectively, without hysteresis. EQE measurements are shown in Fig. 3.20b for STPC and unfiltered/filtered silicon devices. The EQE spectra exhibit a maximum of 80% and 70% for the STPC and filtered silicon cell, respectively. This indicates that optical losses reduce the absorption of the perovskite layer below the band gap at 750 nm and the transmission through the STPC above 750 nm. In addition, an interference pattern is clearly visible on the silicon EQE, and decreases its efficiency.

Cell	**Jsc (mA.cm^2)**	**Voc (mV)**	**FF (%)**	**Efficiency (%)**
Perovskite	21.1	1075	73	16.6
Silicon	38.9	619	77	18.5
Filtered Silicon	11.5	590	76	5.1
Tandem	-	-	-	21.7

Table 3.4: Electrical characteristics of the STPC, silicon and filtered silicon reference cell.

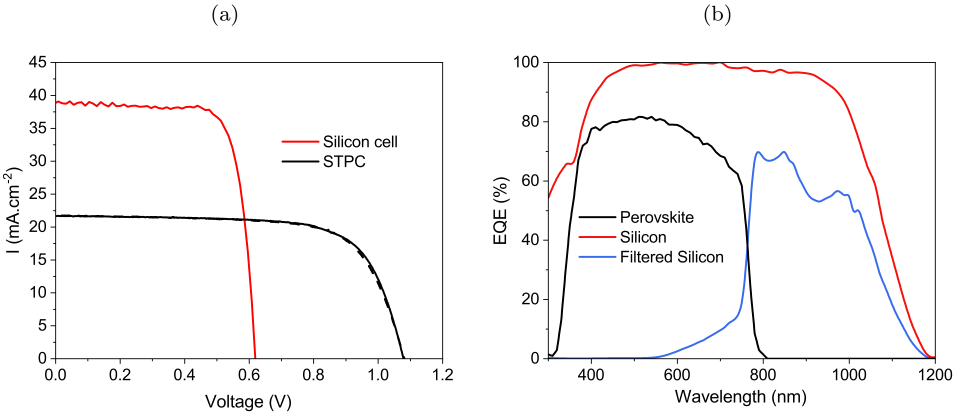

Figure 3.20: (a) IV curves of the STPC and the unfiltered silicon cell. (b) Experimental EQE of the STPC, the unfiltered and the filtered silicon cell by the perovskite.

The performance of the filtered silicon cell cannot be measured with an IV due to the size difference observed with the top cell (0.09 vs. 1 cm^2) and the need to use a mask on the STPC to collimate the light only on this surface. On the other hand, the light beam used for the EQE measurements is smaller than the size of the STPC and therefore makes it possible to measure the EQE of the filtered silicon cell. The theoretical efficiency η_{filt} of the filtered silicon cell is obtained with its EQE spectrum and the IV measurement of the unfiltered cell. Assuming the FF is unchanged, the efficiency can be derived from the following equations:

$$J_{sc-filt} = -q \int_{\lambda_1}^{\lambda_2} EQE_{Si-filt}(\lambda)\phi(\lambda)d\lambda \tag{3.6}$$

$$V_{oc-filt} = ln(\frac{J_{sc-filt}}{J_{sc-unfilt}}) * \frac{mk_bT}{q} + V_{oc-unfilt} \tag{3.7}$$

$$\eta_{filt} = \frac{J_{sc-filt}V_{oc-filt}FF}{P_{in}} \tag{3.8}$$

The filtered silicon cell shows a final overall efficiency of 5.1%. Finally, 4T tandem efficiency of 21.7% is obtained when combining the STPC and the filtered silicon cell.

Conclusion

In this chapter, we focused on describing and understanding the performance of our STPC compared to opaque perovskite cells. First, we showed that the STPC could reach high efficiencies as well as opaque cells but that the dispersion of the results within the same batch was much more important. The origins of this dispersion appear manifold and the IV curves allow us to classify the dysfunctional cells in several categories: short circuit, insulating, fabrication issues, degraded interface ... On the other hand, STPC have a stability in time that opaque cells do not have. They require a variable time of 1 to 3 weeks to reach their full potential, which they can then maintain for several months as long as they are kept under vacuum.

The study of the non-functional cells allowed us to identify a shunt problem caused by the placement of the electrodes as well as the important sensitivity of the Spiro-OMeTAD / ITO interface to heat and damage during sputtering. Simple solutions could be implemented such as using a contact directly on the FTO for the anode and for ITO sputtering, making short depositions with moderate power while respecting the cooling time between depositions.

Nevertheless, despite the elimination of the non-functional cells from the process, the dispersion of the results remained more important than for the opaque cells. We have also shown that the ITO interfaces (Au and Spiro-OMeTAD) have no significant electrical resistance and are not sufficient to explain a lower average FF. Similarly we also showed that the lateral resistance of the ITO is too low to be the cause. The use of 2 nm Au buffer nevertheless showed a significant effect on reproducibility by strongly decreasing the dispersion. On the other hand, the use of gold was also responsible for the disappearance of the S-shape and its possible diffusion in the lower layers is a risk for the excellent stability of STPC. Other tests with metallic buffers like Ni or Ti have shown the interest of protecting the Spiro-OMeTAD layer. However, even if Ni buffer allows to reduce the dispersion without consequence on the electrical performances, it does not have the reproducibility offered by the Ti buffer which generates an additional resistance at the Spiro-OMeTAD / ITO interface. To further reduce the dispersion, another solution would be to replace the Spiro-OMeTAD with another less sensitive HTL. This will be discussed in Chapter 5.

We finally fabricated a first prototype of tandem at 21.7%. In spite of this good efficiency, the transmission and EQE spectra reveal the presence of absorption and parasitic reflection within the perovskite cell. The identification of their origin and the proposal of a new optically optimized structure will be the focus of the next chapter.

Chapter 4

Optical modeling of perovskite-based tandem solar cells

Introduction

As seen in the previous chapter, a 4T tandem has been built in our lab combining semi-transparent $Cs_{0.05}(MA_{0.166}FA_{0.833})_{0.95}Pb(Br_{0.166}I_{0.833})_3$ triple cations perovskite solar cell with a commercially available Al-BSF silicon solar cell. The efficiency of the tandem reaches 21.7%, with a perovskite cell at 16.6% and a filtered silicon cell at 5.1%. The spectral response of the silicon cell as well as the infrared transmission of the semi-transparent perovskite cell shows significant optical losses that limit the efficiency of the device. In order to identify their origin, numerical simulations based on the propagation of optical waves in planar layers have been performed by several groups [29, 138, 194, 195, 197, 266, 267]. One of the most used models for optical modeling is the Transfer Matrix Method (TMM) which is based on the path light simulation [268]. However, their use is often hindered by the lack of accurate data for the complex refractive indices of each layer constitutive of the device, i.e. the triple cation perovskite, the Spiro-OMeTAD extraction layer or the unannealed and amorphous ITO. Indeed, the optical indices of a thin layer can depend on the deposition and post-treatment conditions such as annealing. A reliable determination of the refractive index of perovskite layers is still highly needed, to be implemented in the optical simulation of complete solar cells.

In this chapter, we present firstly a comprehensive iterative method to model the optical properties of a complete STPC. It is based on the experimental characterization of the optical properties of the PV devices (EQE, reflection and transmission, absorption, and reflection spectra) and of each layer separately using various spectroscopic techniques. As a result, we provide accurate values for the complex refractive indices of each layer, and we identify and quantify the main sources of optical losses in the STPC. Then, the optical model is coupled to a simple electrical model to predict these effects and the performances of 4T perovskite/silicon tandem solar cells. In a second step, this opto-electrical model is used to try to target a viable structure at 30% and more. Different technical solutions for the STPC, such as the implementation of new dielectric layers or rethinking the design of the electrodes, are proposed to achieve this objective, while remaining compatible with the rest of the process. Finally, the use of silicon cells based on other technologies allows to further increase the achievable efficiency and to propose a very high performance 4T perovskite/silicon tandem.

4.1 Development of the semi-empirical iterative method

An iterating process sketched in Fig. 4.1 was used to build an optical model that corresponds to our actual STPC. The first step A focuses on the complex optical index (real part n(λ) and extinction coefficient k(λ)) of each layer of the structure, represented on Fig. 4.2a. Each layer of the structure was deposited on glass and its thickness is characterized by a profilometer and cross-section SEM measurements. The roughness of FTO, ITO and mesoporous TiO_2 are also characterized by AFM or confocal microscopy.

Then ellipsometry measurements are performed and analyzed to create a model of the complex optical indices. Different dispersion models are chosen according to the material (dielectric, wide-bandgap material, TCO or semiconductor absorber), they are given in Table 4.1. The value of the least square error coefficient X^2 obtained after an iterative procedure indicates the good agreement between the model and the experimental data. In principle, there is no target value for X^2, which would depend on materials, stack complexity and morphology. The value of X^2 must be evaluated on a case by case basis. However, we consider here that X^2 lower than 15 for complex stacks or materials is acceptable, and lower than 5 for simple layers. The thickness can be measured experimentally with a profilometer and can be bounded quite finely in the ellipsometric model. Ellipsometric simulation of roughness is based on effective medium and not on experimental values i.e. RMS or Sa which can be obtained by AFM or confocal microscope respectively. Thus, roughness has to be adjusted using the iterative process as the optical indices.

The optical indices are subsequently used in a MATLAB code developed by the McGehee group at Sandford University [268] and based on the TMM to model the transmission, reflection and absorption spectra of the structure. The details of how the TMM works are described in Appendix D. The simulated spectra are compared with spectrophotometry experiments.

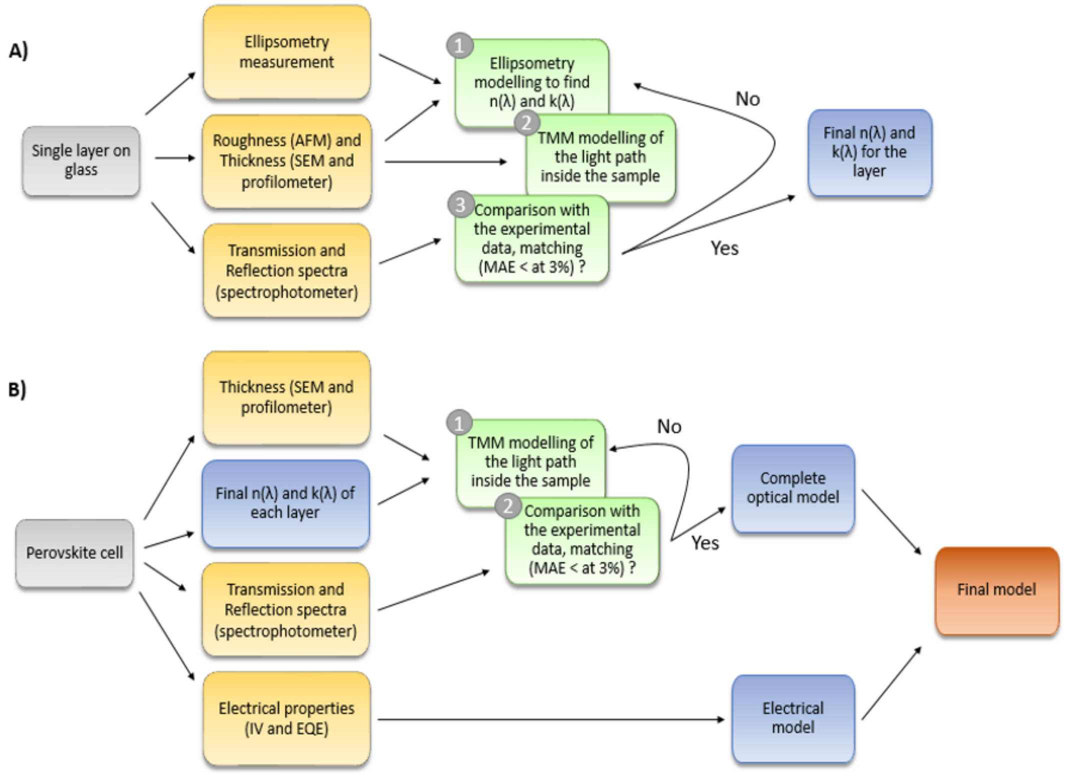

Figure 4.1: Process with two steps used to find the correct optical indices with the iteration cycle and the final model.

The Mean Absolute Error (MAE) of the simulated data in comparison with the experimental data, is obtained by the following equations:

$$MAE_T(\%) = \frac{\sum_{i=300}^{1200} |T_{simu}(i) - T_{exp}(i)|}{901} \tag{4.1}$$

$$MAE_R(\%) = \frac{\sum_{i=300}^{1200} |R_{simu}(i) - R_{exp}(i)|}{901} \tag{4.2}$$

$$MAE_A(\%) = \frac{\sum_{i=300}^{1200} |A_{simu}(i) - A_{exp}(i)|}{901} \tag{4.3}$$

where the sum is done on the series of wavelengths from 300 nm to 1200 nm every nm. The result is considered as acceptable if the MAE is smaller than 3%, see the final results in Table 4.2. If the MAE is above 3%, the values of indices, thickness and roughness in the optical model used to fit ellipsometry measurements are modified until reaching a new minimum for X^2, and the TMM simulations are repeated until a good match is obtained. There is no number of iterations to perform to reach a MAE above 3%, it is just a matter of finding the right set of values (indices/thickness/roughness). It should be noted that the ellipsometry analysis only guarantees that the values obtained for indices, thickness and roughness allow to reach a local minimum for X^2. As an example, Fig. 4.2b shows a diagram of the evolution of X^2 and MAE as a function of the number of iterations with the perovskite layer on glass. The optical indices for the perovskite layer are those obtained in iteration 10 because they allow a MAE value below 3%, although it is not the iteration with the lowest X^2 or the last one performed.

Once the results are satisfactory for every layer, the optical indices can be used to model the complete perovskite solar cell, see Fig. 4.1b, with a similar method as described above. The optical indices of the different layers are considered similar to those deposited on glass. Thus, the iteration is done only on the TMM simulation by modifying slightly the thicknesses of the layer according to the SEM cross-section measurements, and the roughness of interfaces. Once the final optical model is obtained, it is then coupled to an electrical model that we will detailed in Section 4.1.2.2.

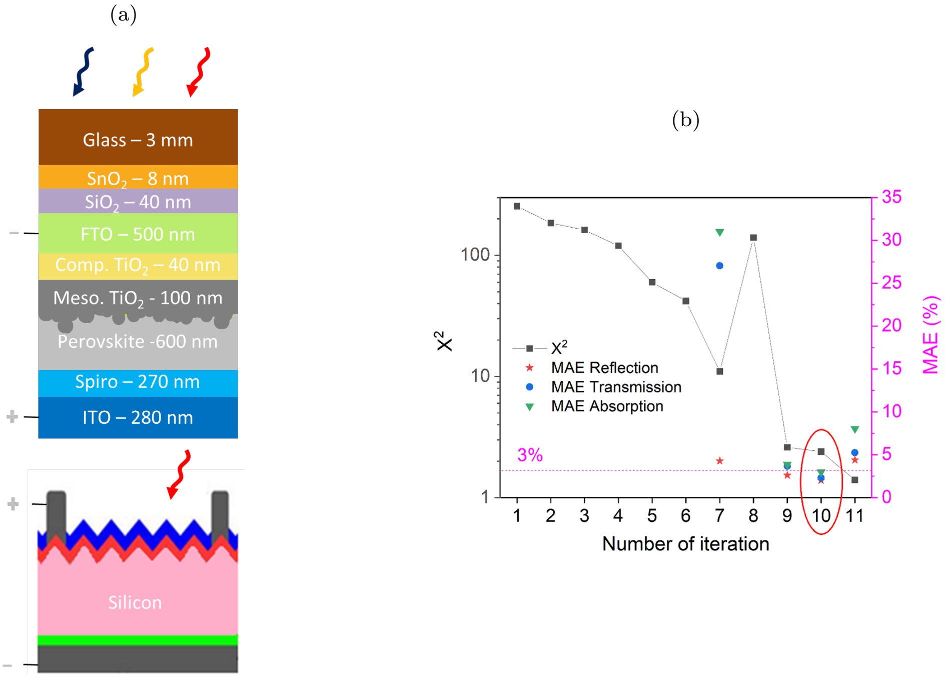
(a)

(b)

Figure 4.2: (a) Stack of the 4T perovskite/silicon tandem and the thickness of each layer of the perovskite cell. (b) Simplified diagram of the evolution of X^2 and MAE as a function of the number of iterations for the perovskite layer on glass. The optical indices retained for the perovskite layer are those obtained in iteration 10, enabling MAE values below 3%.

Layer	**Models of dispersion**	X^2
Glass (TEC-7)	Rubin-Herzberger	0.1
SnO_2 (TEC-7)	Lorentz Oscillator	1.4
SiO_2 (TEC-7)	Lorentz Oscillator	1.4
FTO (TEC-7)	New Amorphous + Drude	3.9
Compact TiO_2	Lorentz Oscillator	4.4
Mesoporous TiO_2	Lorentz Oscillator	2.3
Perovskite	5x Tauc Lorentz + Lorentz Oscillator	1.4
Spiro-OMeTAD	4x Tauc Lorentz + Lorentz Oscillator	1.7
ITO	New amorphous + Drude	13.1

Table 4.1: Dispersion models used to fit the refractive indices in ellipsometry measurements for each material, and value of the least square error coefficient X^2.

Sample	**T(%)**	**R(%)**	**A(%)**
Glass	0.99	1.08	1.50
TEC-7 without FTO	1.87	2.02	1.96
TEC-7 with FTO	2.33	1.58	2.43
Compact TiO_2	1.35	2.42	1.89
Mesoporous TiO_2	2.74	1.28	0.99
Perovskite	1.60	1.82	1.19
Spiro-OMeTAD	2.14	2.44	1.61
ITO	2.31	2.01	2.06

Table 4.2: MAE between the fitted model and the experimental data for transmission (T), reflection (R) and absorption (A), for layer on glass.

4.1.1 Determination of the optical indices of the different layers

4.1.1.1 Soda-lime glass substrate modeled as an incoherent layer

As described in Chapter 2, the TEC-7 substrate we use for our STPC is a commercial substrate from Solems, composed of FTO deposited on a 3 mm soda-lime glass. Different groups have already reported the presence of a SiO_2 and SnO_2 bilayer between glass and the FTO layer [194, 195].

In order to model the TEC-7 substrate, the analysis is performed in three steps: the glass alone, the etched TEC-7 (without FTO) and the complete TEC-7 substrate. For the soda-lime glass alone, the most used method to determine refractive index of glass is the Cauchy formulation [269, 270] :

$$n(\lambda) = A + \frac{10^4 B}{\lambda^2} + \frac{10^9 C}{\lambda^2} \tag{4.4}$$

$$k(\lambda) = 10^{-5} D + \frac{10^4 E}{\lambda^2} + \frac{10^9 F}{\lambda^2} \tag{4.5}$$

with A, B, C, D, E and F are positive coefficients characteristic of each environment.

Cauchy formula is not Kramers-Kronig consistent and only based on experimental measurements (the parameter A, B, C, D, E and F do not have any physical meaning). Moreover, the first trials with some optical indices found in the literature show that is necessary to have an accuracy for k of the order of 10^{-6}

at 1200 nm to obtain a good fit between our model and the experimental data. The software Deltapsi has a accuracy at 10^{-5} for the value of the k coefficient, so it is not possible to define precisely the value of this coefficient with this software.

However, the optical indices for soda-lime glass were also proposed by Rubin [271], based on the work of Herzberger [272] with a simplified form of the dispersion equations. He determined the indices n and k with the following equations:

$$n(\lambda) = 1.5130 - 0.003169\lambda^2 + \frac{0.003962}{\lambda^2} \tag{4.6}$$

$$k(\lambda) = \frac{\lambda}{2\pi d} * ln\left(\frac{\sqrt{(1-\rho_\lambda)^4 + 4\rho_\lambda^4\tau_0^4} - (1-\rho_\lambda)^2}{2\rho_\lambda^2\tau_0}\right) \tag{4.7}$$

with τ_0 the normal transmittance of the sample, ρ the spectral reflectivity, and d the thickness of the glass.

With this formula, Rubin was able to provide the optical indices for a classic soda-lime glass, with a high precision. The comparison between simulated and experimental ellipsometric data for the glass substrate alone shows a very good matching with X^2 at 0.1. We therefore choose to use the optical indices calculated by Rubin for soda-lime glass, since we are not able to determine them accurately.

However, even with correct indices, the simulation of transmission, reflection and absorption (TRA) spectra still does not match the experimental measurements. Conventional TMM simulation of thick transparent substrates results in interferences originating from reflections at both planar interfaces, see the black curve on Fig. 4.3a. In contrast, the bottom and top surfaces of glass substrates are not perfectly flat and parallel and such oscillations are not visible in their experimental optical response. In addition, the coherence length of the light is much shorter than the thickness of the glass, which causes a complete disappearance of the interference patterns.

To account for this behavior, thick glass layers can be modeled as incoherent layers in the TMM code by following Troparevsky et al. [273]. The propagation matrix L_j of an incoherent layer j placed anywhere in the stack is calculated by adding a random phase ξ:

$$L_j = \begin{bmatrix} e^{-i(\frac{2\pi\tilde{n}_j d_j}{\lambda}+\beta.\xi)} & 0 \\ 0 & e^{i(\frac{2\pi\tilde{n}_j d_j}{\lambda}+\beta.\xi)} \end{bmatrix} \tag{4.8}$$

with d_j the thickness of the layer j, $\tilde{n}_j$ the complex refractive index of the layer j, λ the wavelength and ξ a random number between -1 and 1. If $\beta = 0$, the phase is not randomized, the layer simulated is coherent. In the following, we choose $\beta = \pi$ to simulate a completely random phase in the incoherent glass substrate. With this solution, it is now necessary to run several times the TMM code with different

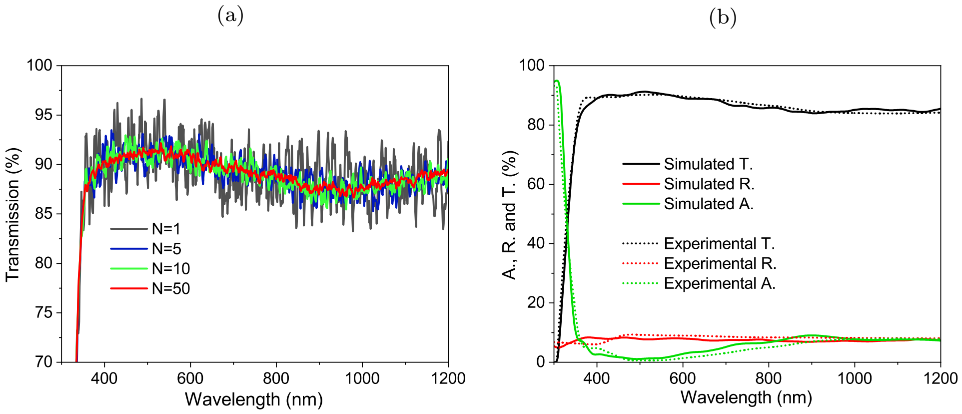

Figure 4.3: (a) Transmission spectra simulations of soda-lime glass using random phases to smooth interference effects, as function of the number of iterations N. (b) Simulated and experimental spectra of transmission, reflection and absorption of Soda-lime glass.

ξ values, and then average the results to eliminate the random variation of the phase and interference effects, as shown in Fig. 4.3a. 50 simulations are sufficient to smooth the optical response and obtain a MAE of 0.99, 1.08 and 1.5 for the transmission, reflection and absorption spectra respectively as shown in Fig. 4.3b. We already notice that the glass alone is already responsible for a parasitic absorption in the IR of 8%. The incoherent layer model will now be used in all the following structures based on a thick glass substrate.

4.1.1.2 Etched TEC-7 substrate

The SiO_2 and SnO_2 bilayer between glass and the FTO layer must be taken into account in the optical modeling even if they have no electrical role in the structure, just like the glass substrate. The thin film of SnO_2 is used to increase the hardness of the glass and facilitates the adhesion of SiO_2. Then the SiO_2layer acts as diffusion barrier of alkali oxides from the glass into the upper layers. To model these two materials, we use a TEC-7 substrate etched with diluted hydrochloric acid (HCl) (30% in water) and zinc powder, in order to remove completely the FTO layer. According to the paper by Chung [274], HCl performs a very small etching on SiO_2 only at sufficiently high temperatures (525 °C). The presence of hydrogen limits the reaction because the formation of HCl is preferred to the formation of $SiCl_4$.

Indices of SnO_2 and SiO_2 can be modeled with a single Lorentz oscillator, which is one of the simplest dispersion models with the least number of parameters. This model derives the equation of an electron motion driven by an oscillating electric field. The displacement of the electrons influences the polarization and generates harmonic oscillation. This relation is adapted to model an insulator, like SiO_2, and a semiconductor below its band gap, like SnO_2 with its band gap superior to 4.1 eV [275]. The optical indices n and k are obtained by the derivation of the complex electric permittivity $\tilde{\varepsilon}$ of each layer:

$$\tilde{\varepsilon} = \varepsilon_r + i\varepsilon_i = \varepsilon_\infty + \frac{(\varepsilon_s - \varepsilon_\infty) * \omega_t^2}{\omega_t^2 - \omega^2 + i\varGamma_0\omega} + \sum_{j=1}^{2} \frac{f_j\omega_{0j}^2}{\omega_{0j}^2 + i\gamma_j\omega} \tag{4.9}$$

$$n = \sqrt{\frac{|\tilde{\varepsilon}| + \varepsilon_r}{2}} \tag{4.10}$$

$$k = \sqrt{\frac{|\tilde{\varepsilon}| - \varepsilon_r}{2}} \tag{4.11}$$

with ε_r the real and ε_i the imaginary part of the electric permittivity, ε_∞ the high frequency dielectric constant, ε_s the static dielectric function at a zero frequency, ω_t the resonant frequency of the oscillator and $\varGamma_0$ the broadening of the oscillator. Table 4.3 shows the values for each parameter used in our model.

The “etched TEC-7” substrate was successfully modeled considering 9 nm of SnO_2 and 30 nm of SiO_2, leading to a X^2 at 1.4 for this stack with 3 layers. Fig. 4.4a show the matching between the simulated and experimental data for the ellipsometry measurement. Only a part of the Ic values in the IR does not fit perfectly. Concerning Fig. 4.4b, the very good agreement observed between the simulated and optical TRA spectra for this structure is confirmed by a MAE inferior to 2.1 for each spectrum. There is a small difference in the IR between the experimental and simulated spectra for transmission and reflection, but with no impact on the total absorption. The latter is slightly higher than in the case of glass substrate alone (+ 2%).

Materials	**Lorentz oscillator**			
	$\varepsilon(\infty)$	ε_r	ω_t	$\varGamma_0$
SnO_2	3.15	3.99	4.78	1.23
SiO_2	1	2.12	12	0

Table 4.3: Values of variables of Lorentz Oscillator model used for SnO_2 and SiO_2.

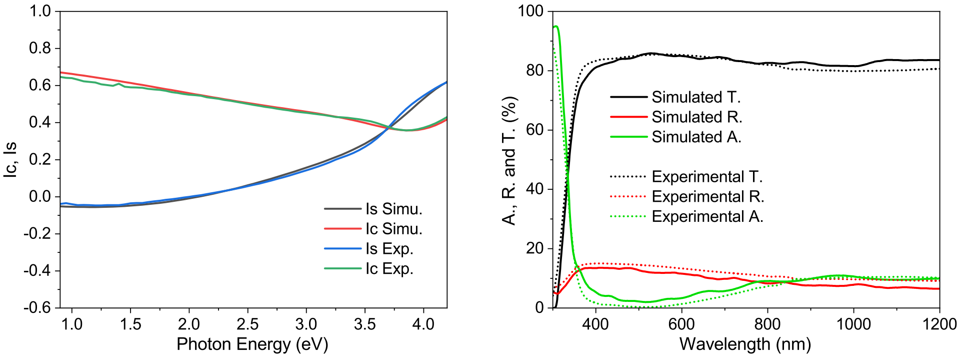
(a)

(b)

Figure 4.4: (a) Simulated and experimental ellipsometry measurements for TEC-7 etched. (b) Simulated and experimental spectra of transmission, reflection and absorption of TEC-7 without FTO.

4.1.1.3 TEC-7 substrate

For modelling the FTO electrode, the top layer of the TEC-7 substrate, another dispersion model is used. Due to its bandgap of 3.8 eV, Lorentz oscillators are not the most suitable for tuning the bandgap and energies in the near UV region [276, 277]. In addition, its free-carriers absorb in the infrared region. Consequently, the New Amorphous Model (NAM) is used for the absorption in the UV range and the Drude model for the absorption in the IR region.

The NAM, develop by Horiba, is based on the Forouhi-bloomer formulation and can be used for amorphous semiconductor and dielectric materials. It derives n and k as a function of the photon energy, and assumes that the conduction band and valence band are parabolic and separated by an energy gap. Moreover, there are no allowed electronic states in this region and, it is possible with this model to simulate the impact of the inter-band transition of electrons on optical properties [278, 279]. However, the model does not allow absorption below the bandgap (a residual absorption called Urbach tail) existing for certain materials of this type as undoped ZnO [280–282]. The difference between the NAM and Forouhi-bloomer formulation resides in the fact that here, the optical indices n and k have a Lorentzian shape. The equation for the indices are for X oscillators:

$$n(\omega) = n_\infty + \sum_{j=1}^{X} \frac{B_j(\omega-\omega_j)+C_j}{(\omega-\omega_j)^2+\Gamma_j^2} \tag{4.12}$$

$$k(\omega) = \begin{cases} \sum_{j=1}^{X} \frac{f_j(\omega-\omega_g)^2}{(\omega-\omega_j)^2+\Gamma_j^2}\; for\ \omega > \omega_g \\ 0\; for\ \omega \leq \omega_g \end{cases} \tag{4.13}$$

$$with\ B_j = \frac{f_j}{\Gamma_j} * (\Gamma_j^2 - (\omega_j-\omega_g)^2) \tag{4.14}$$

$$and\ C_j = 2 f_j \Gamma_j (\omega_j - \omega_g) \tag{4.15}$$

with X the number of oscillators considered, n_∞ the value of n when ω tend to infinity, Γ_j the broadening of the oscillator j, f_j is the oscillator strength and linked to the amplitude of k, ω_j the photon energy when the k reaches a maximum for the oscillator j, and ω_g the energy band gap.

For the infrared absorption, we used the Drude model. It is an extension of Lorentz oscillator model without restoration force, so the free electrons are not bound to a particular nucleus but subject to external electric fields. It is adapted to describe the transport properties of electrons in conductive material, with the hypothesis that there are a non-interacting electron gas and motionless positive ion. The indices n and k are also obtained by the derivation of the electric permittivity:

$$\tilde{\varepsilon}(\omega) = \frac{\omega_p^2}{-\omega^2 + i\tau_d\omega} \tag{4.16}$$

with τ_d is the collision frequency between electrons and phonons and ω_p is the plasma frequency. The values used for each parameter for NAM et Drude models are summarized in Table. 4.4.

The fit of the complete TEC-7 substrate with FTO is slightly degraded compared to the TEC-7 etched, but remains correct with a coefficient $X^2 = 3.9$. The higher value of X^2 compared to the TEC-7 etched stack originates from the presence of the additional FTO layer and can be attributed to it roughness (RMS = 15.78 nm, see Fig. 4.5c), that is not considered in our models. On Fig. 4.5a, We notice that some interferences of Is and Ic between 0.9 and 3.5 eV are not perfectly fit by the model. This is confirmed by the comparison between experimental and simulated TRA spectra plotted on Fig. 4.5b, where the small fringes at short wavelengths are smoothed in experimental spectra. For the sake of simplicity, we stay with a model with no roughness effect, and we obtain a good overall agreement (MAE of less than 2.5%).

Materials	**New Amorphous**						**Drude**	
	X	$\boldsymbol{\omega_g}$	$\boldsymbol{n_\infty}$	$\boldsymbol{f_1}$	$\boldsymbol{\omega_1}$	$\boldsymbol{\Gamma_1}$	$\boldsymbol{\omega_p}$	$\boldsymbol{\tau_d}$
FTO	1	3.07	1.74	0.03	5.16	0.47	1.26	0.08
ITO	1	2.24	1.47	0.34	5.04	2.15	0.95	0.52

Table 4.4: Values of variables of NAM and Drude models used for FTO and ITO.

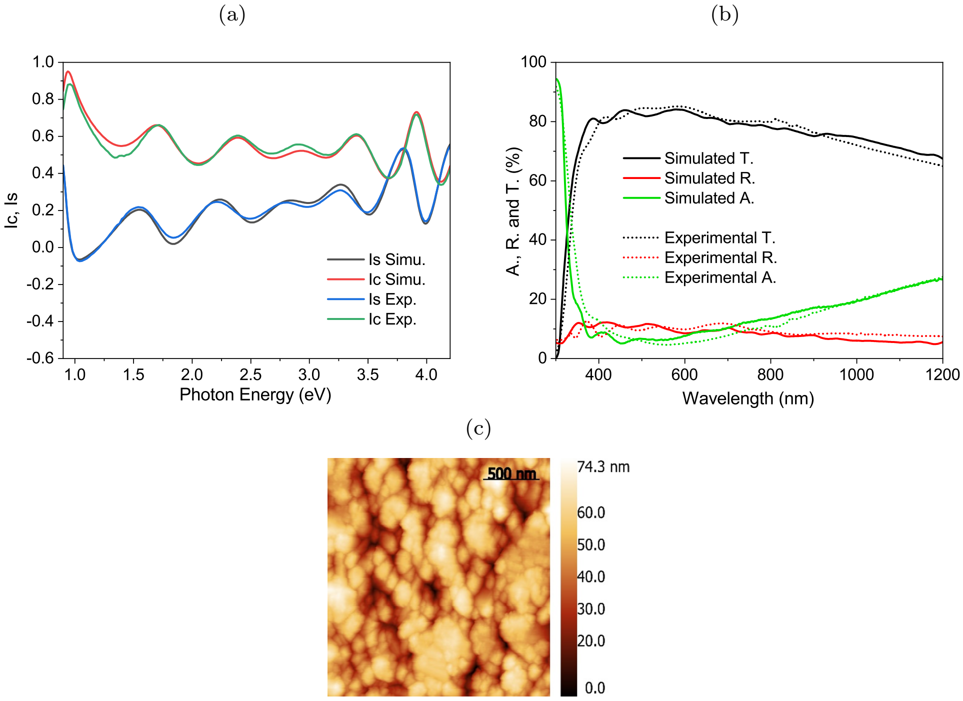
(a)

(b)

(c)

Figure 4.5: (a) Simulated and experimental ellipsometry measurements for TEC-7 substrate. (b) Simulated and experimental spectra of transmission, reflection and absorption of TEC-7. (c) AFM measurement of the FTO surface.

4.1.1.4 ITO

The same dispersion models are used for ITO as FTO (NAM and Drude) because it is also a TCO. The values of the parameters used are shown in Table. 4.4 and can be compared with those of the FTO.

X^2 for the ITO film (13.1) is higher than that of other films. In the simulated and experimental ellipsometric measurements, see Fig. 4.6a, we observe an inaccurate fit in the amplitudes of the oscillations between 1.25 and 3 eV, i.e. under the ITO band gap. The optical indices obtained allow nevertheless to obtain a MAE lower than 3% with the TMM (2.31, 2.01 and 2.06% for the TRA spectra respectively).

However, we observe a difference in the intensities of the interference patterns between 400 and 800 nm for the simulated and experimental transmission and reflection spectra, see Fig. 4.6b. On the other hand, the simulated and experimental absorption spectra are in very good agreement. The refractive index n is probably responsible for this shift rather than the extinction coefficient k.

As seen in the previous Chapter, ITO is deposited at room temperature in order to avoid damage of the Spiro-OMeTAD layer. However, it has been shown in Chapter 3 Section 3.2.3 that at room temperature, ITO layers change from amorphous to polycrystalline for layers thicker than about 200 nm. Thus, with a thickness of 270 nm and a sheet resistance of 17.5 Ω.sq, the film may be no longer homogeneous in depth, with a material potentially amorphous near the substrate and polycrystalline close to the surface. Since the degree of crystallization of a material impact its optical properties, the refractive indices average the contributions of the different crystalline states present in the actual layer. Fig. 4.6c and b shows the optical indices n and k of different ITO layers deposited in the same conditions but with different deposition times in order to vary the thickness. The sheet resistance decreases from 29 Ω.sq for a thickness of 180 nm to 17 Ω.sq for a thickness of 270 nm, and then is constant for thicknesses up to 470 nm (16 Ω.sq). In parallel the extinction coefficient k continues to increase in the infrared when the thickness of the ITO layer increases.

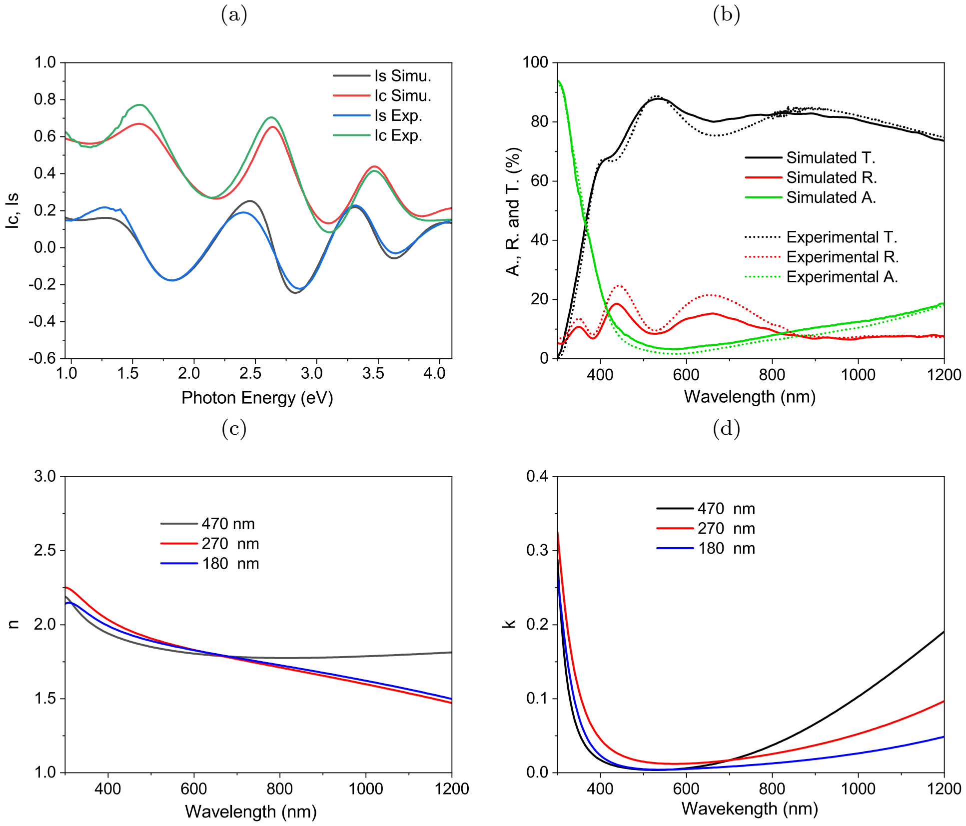
(a)

(b)

(c)

(d)

Figure 4.6: (a) Simulated and experimental ellipsometry measurements for ITO. (b) Simulated and experimental spectra of transmission, reflection and absorption of ITO. (c) Refractive index and (d) Extinction coefficient k of ITO layers with different thicknesses.

4.1.1.5 Perovskite and Spiro-OMeTAD

Spiro-OMeTAD and perovskite have been poorly characterized by ellipsometry in the literature, and their characteristics seem to change according to their compounds, preparation method and processing condition. In addition, different dispersion models and fitting methods can be used for these materials as their optical index show different peaks that cannot be fit with a single oscillator.

For this purpose, we choose the Tauc-Lorentz model [283] coupled to a Lorentz oscillator. Like the Forouhi-bloomer formulation, it describes the electronic transition parameters such as the optical band gap and the peak transition energy that can be found in the typical continuum of band absorption of these materials. For example, concerning the perovskite, the three peaks A, B and C observed at 400, 516 and 754 nm correspond to optical transition energies [284] and are attributed to direct semiconductor-type transitions at the X, M, and R points in the pseudo-cubic Brillouin zone, respectively [285, 286].

The formula for the indices n and k are obtained by the derivation of the complex electric permittivity for X oscillators:

$$\varepsilon_r(\omega) = \varepsilon(\infty) + \sum_{j=1}^{X} \frac{2P}{\pi} * \int_{\omega_g}^{\infty} \frac{\xi \varepsilon_i(\xi)}{\xi^2 - \omega^2} d\xi \tag{4.17}$$

$$\varepsilon_i(\omega) = \begin{cases} \sum_{j=1}^{X} \frac{1}{\omega} * \frac{A_j E_j C_j (\omega-\omega_g)^2}{(\omega^2-E_j^2)^2+C_j^2\omega^2} \; for\; \omega > \omega_g \\ 0 \; for\; \omega \leq \omega_g \end{cases} \tag{4.18}$$

with ε_r the real and ε_i the imaginary part of the electric permittivity, ε_∞ the high frequency dielectric constant, P the Cauchy principal value, A_j, C_j and E_j the parameters linked respectively to the amplitude, the width and the energy position of the absorption peak j, ω_j the photon energy when the k reaches a maximum for the oscillator j, and ω_g the energy band gap. The parameters used for our perovskite composition are detailed in Table. 4.5. With an $X^2 = 1.4$, the ellipsometric fit is very good as shown on Fig. 4.7a. All of the above transitions are correctly matched at 3.1, 2.4 and 1.64 eV and so are interferences generated. This allows to obtain a MAE lower than 2% for the TRA spectra, see Fig. 4.7b, even if the interference patterns observed in the IR do not seem to correspond completely to those observed in the experimental measurement.

(a) (b)

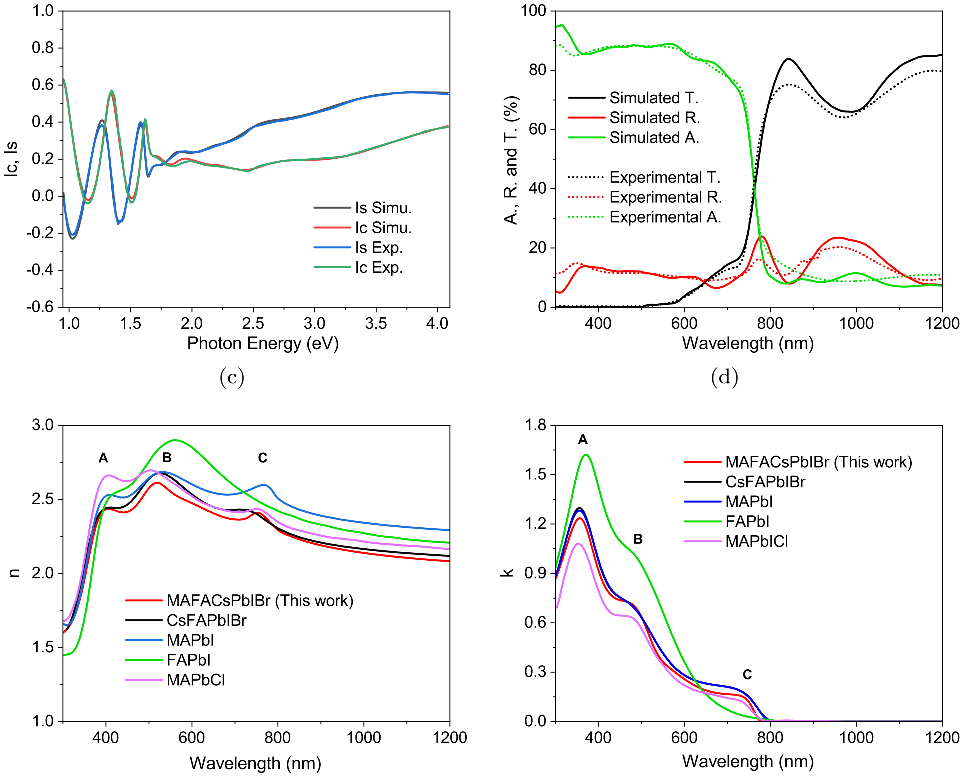

(c) (d)

Figure 4.7: (a) Simulated and experimental ellipsometry measurements for perovskite. (b) Simulated and experimental spectra of transmission, reflection and absorption of perovskite. (c) Refractive index and (d) Extinction coefficient k of perovskite layers k for different perovskite composition: MAFACsPbIBr synthesized at IPVf, CsFAPbIBr[196], MAPbI [197], FAPbI [287] and MAPbCl [210].

Materials	Tauc-Lorentz												
	ω_g	A_1	E_1	D_1	A_2	E_2	D_2	A_3	E_3	D_3	A_4	E_4	D_4
Perovskite	1.56	33.34	1.61	0.11	7.31	3.35	0.71	-64.08	2.24	0.63	29.48	4.47	7.78
Spiro	2.91	3.37	4.02	0.48	85.56	3.09	0.31	23.65	5.86	0.01	-22.16	3.12	3.03

Materials	Tauc-Lorentz			Lorentz Oscillator			
	A_5	E_5	D_5	$\varepsilon(\infty)$	ϵ_S	ω_t	Γ_0
Perovskite	85.53	2.25	0.75	1.17	2.62	11.73	0
Spiro	-	-	-	0.99	1.16	6.54	11.38

Table 4.5: Values of variables of Tauc-Lorentz and Lorentz Oscillator models used for the perovskite and the Spiro-OMeTAD.

Fig. 4.7c and b compare the indices n and k of our perovskite materials with indices from the literature. It confirms that there are differences for the same formula like simple cation perovskite MAPbI or double cation CsFaPbIBr. Moreover, the refractive index n of CsFaPbIBr seems higher than the CsMAFaPbIBr one by the substitution of FA by MA, whereas the extinction coefficient k is similar to double cation perovskite.

A dispersion model similar to that of the perovskite is used for the Spiro-OMeTAD, i.e. 4 Tauc-Lorentz and a Lorentz oscillator. The matching between the simulated and experimental data for the ellipsometry measurement is also very good with $X^2 = 1.7$, as shown in Fig. 4.8a. There is only a slight discrepancy around the gap at 2.91 eV. Fig. 4.8b represents the matching between the simulated and experimental TRA spectra, with a MAE inferior at 2.5%. It can be noticed that the reflection seems slightly underestimated between 500 and 1000 nm.

Nevertheless, Spiro-OMeTAD and perovskite layers deposited on glass are different from the layers in the complete stack. In particular, both the thickness and roughness of the spin-coated layers depend on the underlayer. In order to obtain reliable optical indices, the thickness and roughness of layers are first measured on glass, and then in the complete stack using the SEM cross-section.

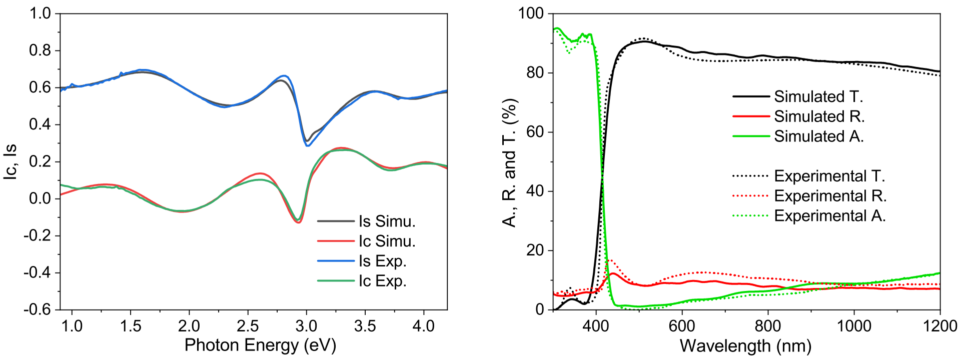
(a)

(b)

Figure 4.8: (a) Simulated and experimental ellipsometry measurements for Spiro-OMeTAD. (b) Simulated and experimental spectra of transmission, reflection and absorption of Spiro-OMeTAD.

4.1.1.6 Compact and mesoporous TiO_2

A single Lorentz oscillator is used for the refractive indices of the mesoporous and compact TiO_2 layers, as for the SnO_2 and SiO_2 layers. The parameter values used for both types of TiO_2 are detailed in Table 4.6.

The mesoporous layer is modeled by the following structure which allows to obtain after several iterations the lowest X^2 equal to 2.3: a layer made of 50% of TiO_2 and 50% of air (22 nm) is placed between two layers which contain 25% of TiO_2 and 75% of air (90 and 44 nm) to take into account the fact that the air and the mesoporous TiO_2 are mixed during this step of determination of the optical indices, see Fig. 4.9e for the corresponding ellipsometric fit. The final optical indices of this TiO_2 material are, however, combined with those of the perovskite and not of the air, since the mesoporous TiO_2 layer is filled by perovskite in the complete semi-transparent cell, as evidenced by scanning transmission electron microscopy analyses. This stack follows AFM observations (Fig. 4.9b) which shows thickness variations up to 107 nm while the layer is between 100 and 120 nm thick, see Fig. 4.9f.

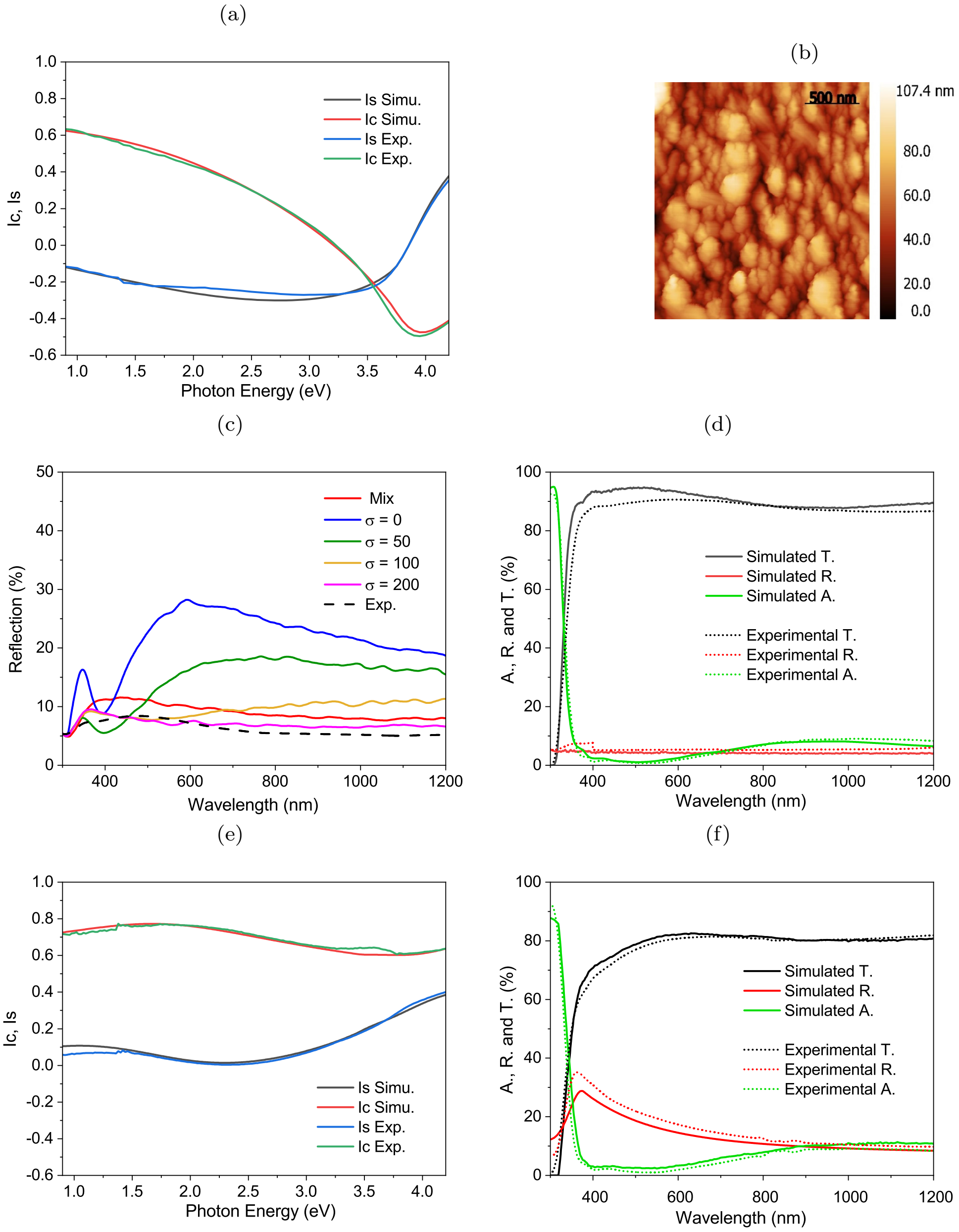
(a)

(b)

(c)

(d)

(e)

(f)

Figure 4.9: Simulated and experimental ellipsometry measurement for (a) compact and (e) mesoporous TiO_2. (b) AFM measurement of the mesoporous TiO_2 surface. (c) Experimental and simulated spectra of reflection with a “mixed” layer (TiO_2 /Air) or with roughness factor σ for mesoporous TiO_2 on glass. Simulated and experimental spectra of transmission, reflection and absorption of (d) compact and (f) mesoporous TiO_2.

Another solution has been tested to simulate the optical behavior of the mesoporous layer by modeling the roughness of its bottom and top interfaces, without modifying the optical indices established for this layer. A roughness factor is implemented on the refraction matrix I of a rough interface between two layers j and k as suggested by Szczyrbowski [288, 289], here between the mesoporous TiO_2 layer and the air:

$$I_{j\rightarrow k} = \begin{bmatrix} 1 & r'_{jk} \\ r'_{jk} & 1 \end{bmatrix} * \frac{1}{t'_{jk}} \tag{4.19}$$

$$r'_{jk} = \frac{\tilde{n}_j - \tilde{n}_k}{\tilde{n}_j + \tilde{n}_k} * e^{-2*(\frac{2\pi\tilde{n}_2\sigma}{\lambda})^2} \tag{4.20}$$

$$t'_{jk} = \frac{2\tilde{n}_j}{\tilde{n}_j + \tilde{n}_k} * e^{(\frac{2\pi\sigma}{\lambda})^2+\frac{(\tilde{n}_k-\tilde{n}_j)^2}{2}} \tag{4.21}$$

with $\tilde{n}_i$ and $\tilde{n}_j$ the complex refractive indices of the layers j and k, r'_{jk} and t'_{jk} the reflection and transmission Fresnel coefficients of the interface, and σ the roughness factor. The surface is flat when $\sigma = 0$. As show on Fig. 4.9c, the best fit of the experimental data is obtained with this second model and $\sigma = 200$, in particular between 300 and 600 nm. The fits of the transmission and absorption spectra are also correct as shown on Fig. 4.9f, with a MAE inferior at 2.8% .

In parallel, the compact TiO_2 is modeled as a single layer of 40 nm, leading to a least square error coefficient X^2 of 4.4. This X^2 is a bit high considering the simplicity of the layer and comes from an artefact of ellipsometric measurement. Fig. 4.9a shows a drop in the IR of the experimental curves Is and Ic, due to a failure of the ellipsometer. In the same way, the agreement between the simulated and experimental TRA spectra on Fig. 4.9d, leading to an MAE smaller than 2.5%. Again, the reflection seems slightly underestimated between 300 and 500 nm. The same optical indices cannot be used for compact and mesoporous TiO_2, because these two materials are not deposited by the same method (spin-coating vs. spray) and by the same solution and chemical differences are likely to exist (contamination or oxygen deficiency).

Materials	**Lorentz Oscillator**			
	ε_∞	ε_s	ω_t	Γ_0
Compact TiO_2	1	3.27	4.79	0.51
Mesoporous TiO_2	3.52	4.61	4.52	1.2

Table 4.6: Values of parameters of the single Lorentz oscillator used for compact and mesoporous TiO_2.

4.1.2 Modeling of the reference STPC

4.1.2.1 Optical model

The final indices n and k obtained for each layer after the iterative method are presented in Fig. 4.10a and b, respectively. The indices obtained without the iterative method are presented in Fig. 4.10c and d. Differences can be observed for all layers. In the case of perovskite, the intensities of the peaks of the optical transition energies for the indices n and k present strong variations. Another striking example is ITO, whose index n has a different behavior in the IR which will lead to different properties of reflection.

The second step B of the iterating process described in Fig. 4.1 is carried out to model the optical properties of the complete solar cell. The cell is in a superstrate configuration and modeled as illuminated through the glass first. Using the TMM, absorption, transmission, and reflection spectra of the semi-transparent perovskite solar cell without front contact grid are simulated and compared with experimental data in Fig. 4.11. A very good agreement is obtained, with MAE around 2% in each case (see Table 4.7). The bandgap of the perovskite absorber is Eg = 1.58 eV, corresponding to a wavelength of 785 nm. If the incident photons are fully absorbed for wavelengths below 500 nm, a slow increase of optical transmission is observed between 500 nm to 750 nm. This behavior that is usually described in the literature is related to the thickness of the perovskite layer (650 nm) that remains too thin to absorb all the incident light in this range. Beyond the perovskite bandgap wavelength, transmission reaches a maximum of 72% at 820 nm, and decreases until 1200 nm at 52%. The total reflection is constant and below 10% over the whole spectral range, except between 800 and 1000 nm where interference fringes appear and are responsible for a reflection maximum of about 17% at 900 nm. Additional interference fringes are observed in transmission spectra that are well described by the simulation. Finally, an unexpectedly high absorption is observed above 800 nm, rising from 20% to 40% at 1200 nm.

In order to better evidence the influence of the iterative method on MAE, the simulated spectra are compared with results obtained using optical indices published in the literature and determined using our experimental data without the iterative method. The stack and the thicknesses of each layer are similar for the 3 simulations and only the optical indices and the interface roughness change. The total absorption fits approximately the experimental data when the iterative method is not used (MAE = 2.69%), but

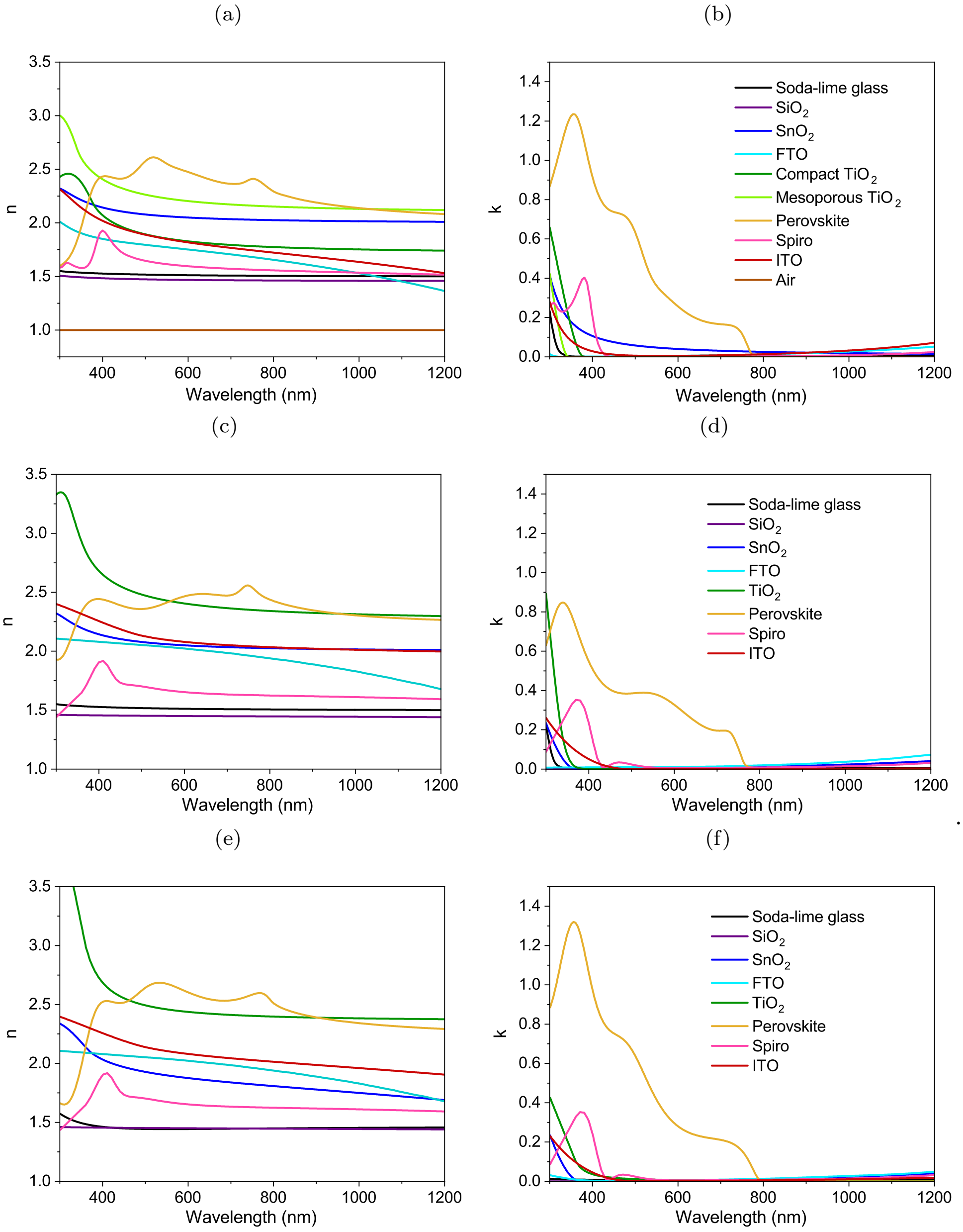
(a) (b) (c) (d) (e) (f)

Figure 4.10: Final optical indices (a) n and (b) k for each layer. Optical indices (c) n and (d) k for each layer when the iterative method is not used. Optical indices (e) n and (f) k for each layer from the literature: SnO_2 [197], SiO_2 [290], FTO [194], TiO_2, $MAPbI_3$ perovskite [197], Spiro-OMeTAD [291] and ITO [292].

the transmission spectra (Fig. 4.11b) show that only the simulation using the iterative method allows to correctly fit the interference figures in the range 800 nm – 1200 nm. This is reflected in the MAE values, which remain above 3% when the iterative method is not used, see Table 4.7.

Simulation allows to calculate absorption in each single layer of the structure separately, and to reveal the origin of the main losses. The simulation results for the absorption in each layer are plotted in Fig. 4.12a. They show that the main parasitic absorption occurring in the infrared region, and responsible for significant transmission losses, are located in transparent conductive oxide layers and may be attributed to free-carrier absorption. The FTO electrode is the most problematic because it absorbs 15% of incident light at 1000 nm. At this wavelength, the second electrode made by ITO also absorbs 7.3%, the soda-lime glass 5.2% and the Spiro-OMeTAD 2.5%. In the visible between 400 nm and 800 nm, the absorption in the perovskite layer is limited by the absorption of the FTO (5.2% at 600 nm). Similarly, Fig. 4.12b and c present the simulated absorption of each layer using indices published in the literature and fitted from experiments without the iterative method. Although the total absorption simulated with these two models presented in Fig. 4.11a seems accurate compared to the experimental spectrum, its decomposition in every layer shows marked differences between the 3 models. They exhibit

Sample	**T(%)**	**R(%)**	**A(%)**
Iterative method	1.19	1.21	1.12
No iterative method	2.57	4.20	2.69
Indices of literature	4.59	3.14	4.21

Table 4.7: MAE between experimental and simulated absorption, transmission and reflection spectra of the semi-transparent perovskite solar cell stack with indices from the literature, and from experiments fitted with or without the iterative method.

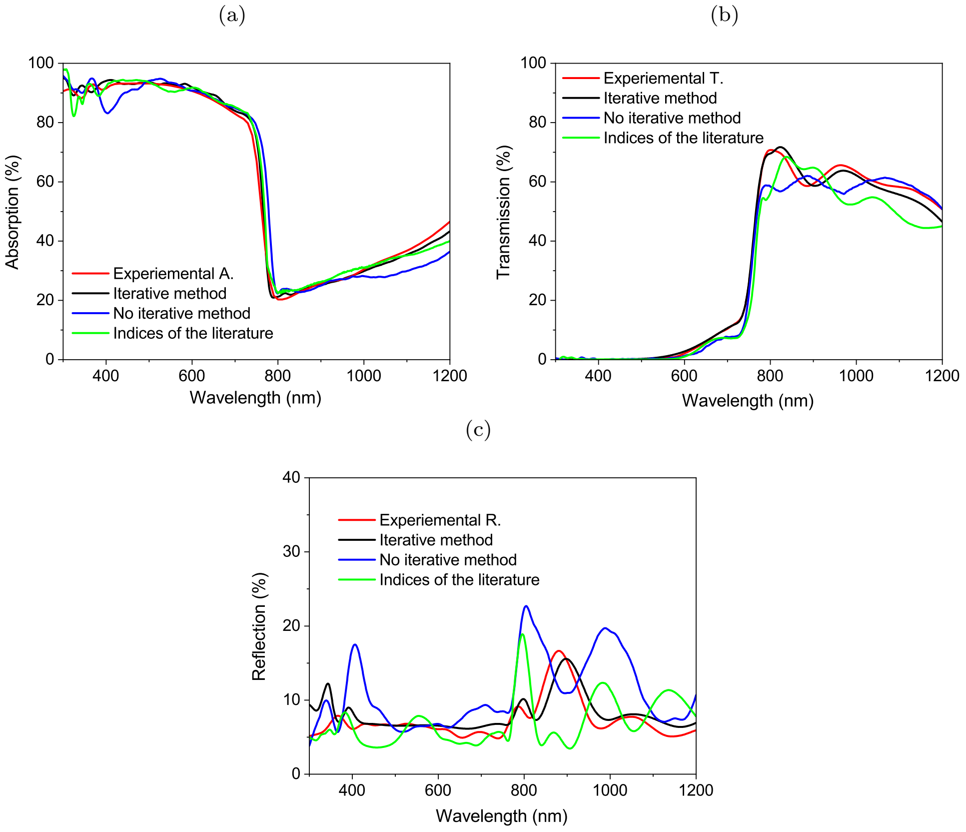

Figure 4.11: Experimental and simulated spectra for A) absorption, B) transmission and C) reflection of the semi-transparent perovskite solar cell stack using indices from the literature (as close as possible to our materials) and using fits of our experimental data with or without the iterative method.

striking differences in the parasitic absorption in TCO layers (FTO, ITO and TiO_2) at short (400 nm) and long (1100 nm) wavelengths. Overall, the iterative method leads to more balanced parasitic absorption between these TCO layers, and a significantly higher absorption efficiency in the perovskite layer. The accuracy of the model is of high importance to further improve semi-transparent perovskite solar cells for tandem devices.

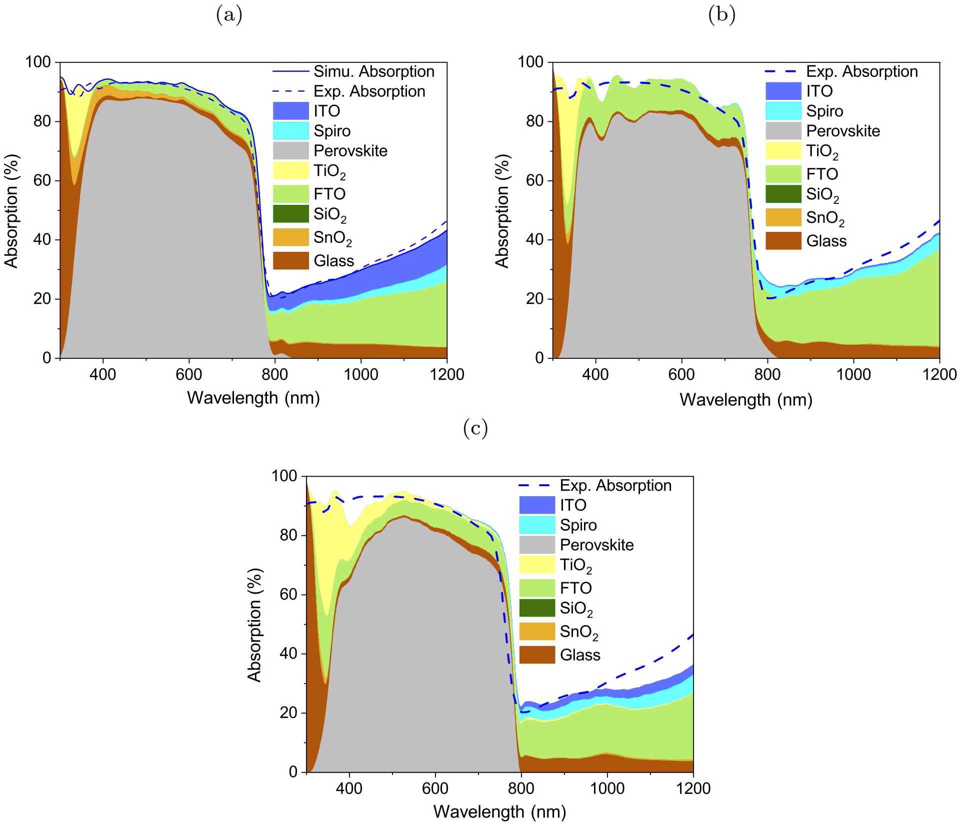
(a) (b) (c)

Figure 4.12: Simulated (blue curve) and experimental (blue dashed curve) total absorption of the perovskite cell and simulated absorption into each layer of the semi-transparent perovskite solar cell stack using our experimental data (a) with or (b) without the iterative method, and (c) using indices from the literature (as close as possible to our materials).

Reflection phenomena inside the STPC are also responsible for significant optical losses. They are analyzed by simulating gradually the reflection on parts of the whole stack starting from the first Air / Glass interface and adding each layer of the perovskite solar cell stack one after the other. Thus, the reflection at the ITO / Air interface considers the whole stack and the reflections due to other interfaces. Each reflection intensity is defined as the square module of the reflection coefficient r_j on the stack made of layers 1 to j-1, including the interface between layer j-1 and a semi-infinite layer j. It is derived from the TMM:

$$R_j = |(r_j)|^2 = \left|\left(\frac{S'_{j\,21}}{S'_{j\,11}}\right)\right|^2 \; and \; S'_j = \begin{bmatrix} S'_{j\,11} & S'_{j\,12} \\ S'_{j\,21} & S'_{j\,22} \end{bmatrix} = (\prod_{v=1}^{j-1} I_{(v-1)v} L_v).I_{(j-1)/j} \tag{4.22}$$

with I_n the refraction matrix, L_n the phase matrix and S'_j the partial transfer matrix of the system including the first layer until the layer j-1.

Fig. 4.13 shows that the main interference patterns visible in the total reflection spectrum at 780 nm and 880 nm are due to two interfaces: the Perovskite / Spiro-OMeTAD interface, which first generates two peaks with reflections up to 7.1% and 9.2%, respectively, and the ITO / Air interface, which further increases the reflection maxima up to 9.5% and 17.2%, respectively. This is caused by the difference between the refractive indices of the couples Perovskite / Spiro-OMeTAD, and ITO / Air at 900 nm (2.19 – 1.55 and 1.67 – 1, respectively). This is also the case for the SnO_2 - SiO_2 interface but due to the very small thickness of the SiO_2 film, a large part of the evanescent wave generated at the interface reaches the rear face and spreads into the stack without generating reflection. The first Air / Glass interface is also responsible for a no-negligible reflection of 4.4% over the entire spectrum. Finally, a small interference pattern is also visible at 360 nm (reflection maximum of 7.1%) and it is related to the FTO / Compact TiO_2 interface.

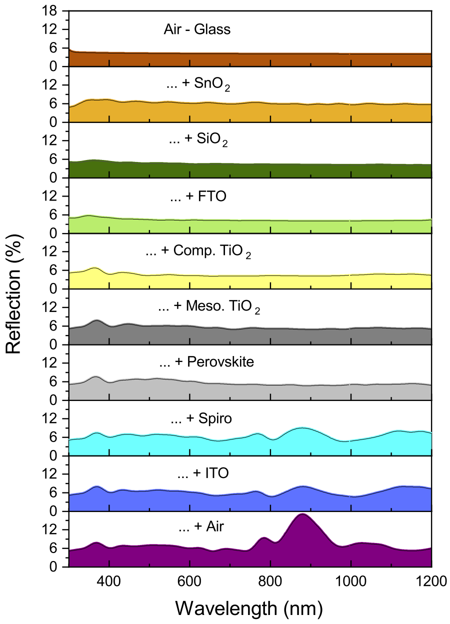

Figure 4.13: Reflection generated at each interface of the perovskite cell. The spectrum for the ITO / Air interface corresponds to the total reflection on Fig. 4.11.

4.1.2.2 Electrical model

4.1.2.2.1 Theoretical modelling details

The optical and electrical performances of the tandem solar cell are intrinsically linked because it is always a question of finding a compromise between transparency and conductivity. Indeed, the power generated in the silicon cell depends on the optical transmission through the perovskite stack, and particularly on the transparency of TCO layers. Then the optical and electrical properties of the TCO layers must be carefully balanced to optimize the whole tandem cell. In the following, we propose a simple electrical model to predict the performances of a 4T tandem device when the perovskite stack is tuned compared to the experimental reference structure presented here.

Firstly, the IQE of the perovskite cell (IQE_{pero}) is defined using the ration between the experimental EQE ($EQE_{exp-pero1}$) and the simulated absorption of the perovskite layer ($A_{simu-pero1}$) obtained with the optical model presented in the previous section:

$$IQE_{pero}(\lambda) = \frac{EQE_{exp-pero\,1}(\lambda)}{A_{simu-pero\,1}(\lambda)} \tag{4.23}$$

$$EQE_{exp-pero\,1}(\lambda) = EQE_{simu-pero\,1}(\lambda) \tag{4.24}$$

IQE_{pero} then is used to predict the EQE for the perovskite cell for optically different structures :

$$EQE_{simu-pero\,2}(\lambda) = IQE_{pero}(\lambda) * A_{simu-pero\,2}(\lambda) \tag{4.25}$$

with $A_{simu-pero2}$ is the simulated absorption of the perovskite layer in the new stack. For the silicon solar cell, we define the normalized EQE_{Norm} as:

$$EQE_{Norm}(\lambda) = \frac{EQE_{exp-Si}(\lambda)}{T_{exp\,1}(\lambda)} \tag{4.26}$$

with $T_{exp\,1}$ the measured transmission of the experimental perovskite cell and EQE_{exp-Si} the measured EQE of the silicon cell. EQE_{Norm} is close to 100%. The EQE predicted for a silicon cell filtered by the simulated transmission of the perovskite cell is given by:

$$EQE_{simu-Si}(\lambda) = EQE_{Norm}(\lambda) * T_{simu}(\lambda) \tag{4.27}$$

with T_{simu} the simulated transmission of the perovskite cell, obtained with the optical model presented in the previous section. If the perovskite solar cell architecture is modified with no change of the active layers (absorber and TiO_2/Spiro-OMeTAD selective contacts), IQE_{pero} and EQE_{Norm} can be considered as unchanged to evaluate the performances of the resulting tandem cell. The simulated electrical characteristics of both perovskite and silicon cells ($J_{sc-simu}$ and $V_{oc-simu}$) are derived as follows [227]:

$$J_{sc-simu} = -q \int_{\lambda_2}^{\lambda_1} EQE_{simu}(\lambda)\phi(\lambda)d\lambda \tag{4.28}$$

$$V_{oc-simu} = ln(\frac{J_{sc-simu}}{J_{sc-exp}}) * \frac{mk_bT}{q} + V_{oc-exp} \tag{4.29}$$

with EQE_{simu} the simulated EQE of the cells, m the ideality factor, J_{sc-exp} and V_{oc-exp} the experimental electrical characteristics of the reference cells.

In the semi-transparent perovskite solar cell, FF is strongly affected by the sheet resistance of TCO. Thus, FF can depend of two contributions: (1) losses due to the sheet resistance of the TCO and (2) the other contributions. In the case of our experimental devices, the contact design is asymmetrical. The two TCO are made of two different materials, do not have the same conductivity and geometrically, the current does not travel the same distance inside. This results in different equations for the front and back electrodes. The power loss P_{TCO} due to the sheet resistance of the rear (ITO) and the front (FTO) electrodes can be calculated as follows [293]:

$$P_{TCO-rear} = \int I^2\, dR = 2\int_0^{\frac{D}{2}} (JLy)^2 \frac{R_{sheet-rear}}{L}\, dy = \frac{J^2LD^3R_{sh-rear}}{12} \tag{4.30}$$

$$P_{TCO-front} = \int I^2\, dR = \int_0^{d} (JLy)^2 \frac{R_{sheet-front}}{L}\, dy = \frac{J^2Ld^3R_{sh-front}}{3} \tag{4.31}$$

with D the distance between two gold contacts for the rear electrode and d the distance to the gold contact for the front electrode, due to our asymmetrical geometry see Fig. 4.14c and d, L the finger length, R_{sheet} the sheet resistance of the TCO, y the distance between a gold contact and a point of the TCO surface, I the current and J the current density. Afterwards, P_{TCO} is normalized by the power estimated at MPP to find the FF losses X due to the sheet resistance of one TCO:

$$X_{TCO-rear} = \frac{P_{TCO-rear}}{P_{mpp}} = \frac{R_{sheet-rear}D^2}{12} * \frac{J_{mpp}}{V_{mpp}} \tag{4.32}$$

$$X_{TCO-front} = \frac{P_{TCO-front}}{P_{mpp}} = \frac{R_{sheet-front}d^2}{3} * \frac{J_{mpp}}{V_{mpp}} \tag{4.33}$$

with J_{mpp} and V_{mpp} the current and voltage at the maximum power point, respectively. Finally, the efficiency of the cell can be estimated by:

$$PCE_{simu} = \frac{1}{P_i} * J_{sc-simu} * V_{oc-simu} * FF \tag{4.34}$$

$$FF = FF_0 - X_{TCO-rear} - X_{TCO-front} \tag{4.35}$$

with P_i the incident light power and FF_0 the FF without electrical losses in the electrodes.

4.1.2.2.2 Experimental results

The experimental perovskite top cell used to develop this optical model reached 16.6% efficiency under 1 sun illumination and allowed to build a 4T tandem at 21.7% of efficiency by associating it to a filtered commercial silicon bottom cell at 5.1%, as shown at the end of the previous chapter. This device suffers from electrical and optical losses and constitutes an interesting starting point to validate our model. IQE_{pero} is close to 90% in the reduced range 450 - 700 nm as show on Fig. 4.14b. Limit values are reached beyond this range as the experimental EQE on which this calculation is based (eq. 4.23) approaches zero. IQE is limited by defects in the film such as pinholes and requires very good crystallization for eliminating recombination sites [294, 295].

The IV curve of the experimental perovskite cell is fitted with a diode model to obtain the value of the ideality factor m, i.e. m = 3.3. While the ideality factor is generally between 1 and 2, higher ideality factors can be observed in perovskite cell, and it is due to the presence of strong coupling between ions and electrons near the electrode interface. A presence of such interfacial defects are known to give an abnormally large ideality factor for organic photovoltaic cells [296, 297]. For the silicon cell, we consider m = 1. As visible on Fig. 4.14a, simulated EQE for the silicon cell has a slight discrepancy with the experimental measurement, with no impact on the J_{sc} because losses and gains cancel each other. EQE is mainly limited by the transmission through TCO at the front side and the rear side of the perovskite cell.

In the case of the perovskite device, the losses are also due to the sheet resistance of TCO. Losses due to sheet resistance can be obtained using d = 8 mm for the anode (FTO) and D = 3 mm for the cathode (ITO), see diagram in Fig. 4.14c and d. Consequently, $X_{TCO-rear}$ loss is equal to 4.58% and

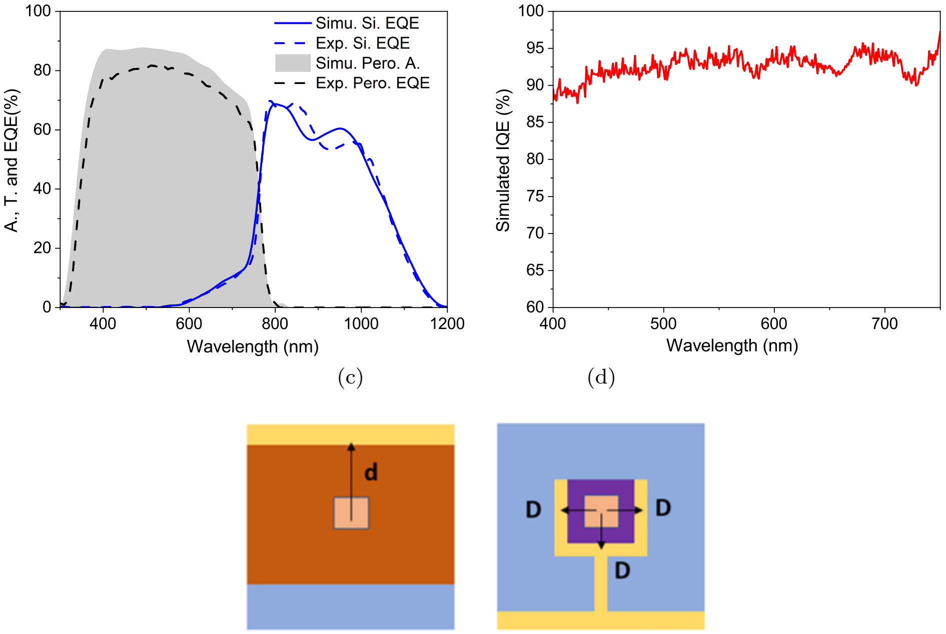

(a) (b)

(c) (d)

Figure 4.14: (a) Simulated (blue curve) and experimental (blue dash curve) EQE of the filtered silicon cell and simulated absorption (grey area) and experimental EQE (black dash curve) of the STPC. (b) Simulated IQE of the reference experimental STPC. Schematic representation of (c) the front side of the perovskite device (Glass/FTO) and (d) the back side (ITO/Air). The yellow bars represent the gold electrodes, the brown rectangle the FTO coated surface and the purple square the ITO electrode. The central orange square represents the illuminated area of the sample constituting the 0.09 cm^2 STPC.

$X_{TCO-front}$ loss is equal to 0.28% following the equations (4.31) and (4.32), respectively. Consequently, by using equation (4.33), FF_0 is equal to 78% to obtain the same fill factor and efficiency as experimentally measured (73%). It is interesting to note that, according to the Shockley-Queisser model, the upper limit of FF is close to 90% for perovskite solar cells with open circuit voltages of 1.2 V and an ideality factor m = 1. This first percentage of loss (10%) is due to radiative recombination which is an unavoidable loss mechanism. However, in many cases as here, the maximum reachable FF is about 83% [226]. In such devices, it is then mainly limited by non-radiative recombination losses. In addition, best practical devices have generally lower FF (around 70-75%). The presence of defects in the absorber material, inefficient charge extraction or current leakage through shunts can already limit the achievable FF below the maximum value, even in the absence of resistance effects in the electrodes or other layers [225, 226]. It shows the good quality of the perovskite solar cell used in this work regardless the electrodes.

In summary, we developed an optical model and an iterative methodology to simulate accurately an experimental perovskite cell, and a 4T perovskite/silicon tandem device. It is based on an iterative method: the determination of the optical indices of every layer of the structure, and the model of the complete structure. Optical losses in the perovskite cell have been analyzed. Parasitic infrared absorption is mainly caused by the electrodes (ITO and FTO), Spiro-OMeTAD and the glass substrate. Furthermore, the Air / Glass and ITO / Air interfaces are responsible of parasitic reflection. In addition, to predict the impact of changes in the initial structure, for instance new TCO layers, we developed a simple electrical model to simulate the full tandem cell. In our design, FTO is the main factor limiting the FF of the perovskite cell, even if its sheet resistance is lower than ITO. In the rest of this chapter, we will progressively modify our model in order to propose different improvements to increase the efficiency of our 4T tandem.

4.2 New tandem architecture with low parasitic absorption and reflection: modified STPC

The model developed previously can be used to further improve the efficiency of the 4T tandem solar cells. It provides a simple way to test many materials in order to optimize the complete device, for instance by replacing the soda-lime glass or by using IZO and IO:H for the electrodes. Parasitic reflection could be reduced by the use of additional anti-reflective coatings, and by adding an optical coupling layer between the cells.

4.2.1 Improved optical properties of the dielectric layers and interfaces

A first optimization consists in adding or replace materials which do not participate in the transport of charges and consequently, have no direct impact on the electrical properties. The modifications proposed here have only an optical influence on the whole structure, see Fig. 4.15. These improvements contribute to increase the amount of light which reaches the perovskite and the silicon absorbers.

4.2.1.1 replacement of the soda-lime glass substrate

Soda-lime glass can be easily replaced by borosilicate glass, quartz or fused silica, without compatibility problems with the full synthesis process. These substrates do not absorb in the IR and they absorb less in the UV range because their optical gaps are lower, as it shown on Table 4.8. The gap and absorption of these substrates has been obtained experimentally, and for the others in the literature. Methodology presented in Section 4.1.1.1 used on the reference stack is applied with these substrates. Borosilicate glass and quartz substrate can increase the efficiency of the tandem cell by +0.6% and +0.8%, respectively. However, quartz and UV Fused Silica substrates are expensive compared with a borosilicate glass substrate, thus it seems more interesting to consider the borosilicate glass as the best choice. Plastic substrates like Polyethylene terephthalate (PET) or Polyethylene naphthalate (PEN) could be interesting to make for perovskite cell and low cost although the annealing at 450 °C of TiO_2 is still an issue today. PET and PEN do not absorb in the IR too but they have a higher refractive index than soda-lime glass [298]. For this reason, they generate more reflection at the Air / Substrate interface and the total efficiency is similar for PET and soda-lime glass with 21.7%. However, the total efficiency is lower in the case of PEN (22.1%) because this polymer absorbs more in the UV region, due to its lower gap [299].

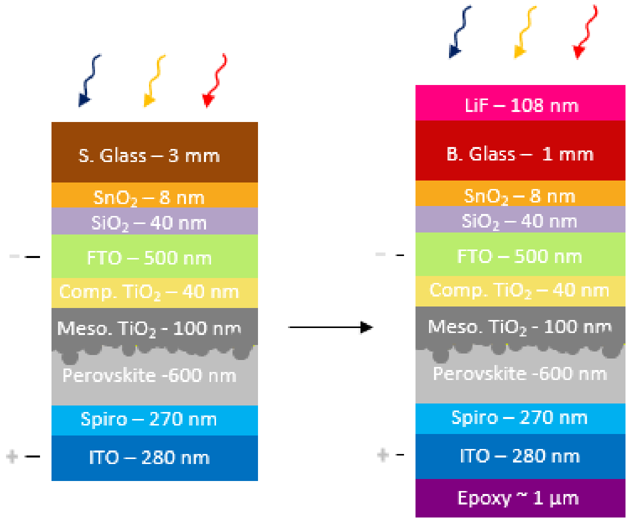

Figure 4.15: Evolution of the STPC structure between the reference and the modified architecture for the reduction of optical losses in the dielectric layers and at interfaces.

Substrate	**Gap (nm)**	**A. at 1000 nm (%)**	**Efficiency (%)**		
			Perov.	**Filtered Si.**	**Tandem**
Soda-lime glass (Solems)	325	10.7	-	-	-
Borosilicate glass (Solems)	295	0	+0.3	+0.3	+0.6
PET (ADDEVMaterials)	325	0	-0.1	+0.1	0
PEN (Dupond)	395	0	-0.8	+0.2	-0.6
Quartz (EscoOptics)	270	0	+0.5	+0.3	+0.8
UV Fused Silica (EscoOptics)	175	0	+0.5	+0.3	+0.8

Table 4.8: Optical characteristics of different substrates (optical gap and absorption at 1000 nm) and their influence on the efficiency of the perovskite, the silicon and the tandem cells.

4.2.1.2 Anti-reflection coating deposited on glass substrate

Many solutions already exist to decrease the reflection at the Air / Glass interface, such as an ARC or surface texturation [300–302]. To have the best effect possible, ARC needs to respect these two conditions:

$$n_1 n_3 = n_2^2 \tag{4.36}$$

$$e = (2N+1)\frac{\lambda}{4n_2} \tag{4.37}$$

with n_1, n_2 and n_3 the indices of refraction of air, ARC and glass, respectively, e the thickness of the ARC, λ the wavelength where the ARC is designed to be the most efficient and N an integer. From the first equation, the optimal value for n_2 is 1.22. In the literature, Lithium Fluoride (LiF, n = 1.40 at 500 nm [303]) is often used on glass substrate for perovskite solar cell, because it is transparent and easy to synthesize [43, 68, 199].

In order to know for which wavelength (or which thickness) LiF needs to be optimized, Fig. 4.16a shows the effect of LiF on the whole spectral range when it is placed on the 3 mm soda-lime glass substrate used in our reference STPC.

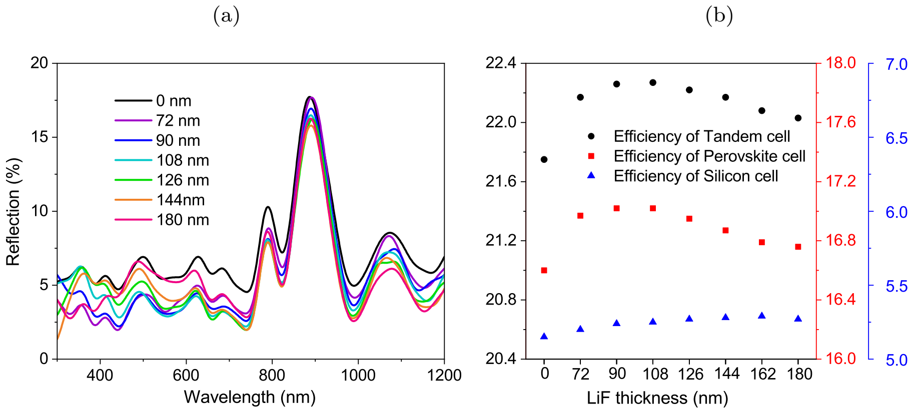

Figure 4.16: (a) Evolution of the reflection of the perovskite cell as function of the thickness of LiF ARC. (b) Evolution of the efficiency of perovskite, silicon and tandem solar cells as a function of the thickness of LiF ARC.

LiF allows to decrease reflection from 5% to 2% at 700 nm as a function of the thickness but its effect is more limited on the most important interference figure at 900 nm. Moreover, even the LiF optimized for this wavelength does not have a more significant effect, because this interference figure of reflection is not caused by this interface, but by the ITO / Air interface. Fig. 4.16b compares the efficiency of the perovskite, silicon and complete tandem solar cell as a function of the thickness of LiF compared to reference STPC. The results show that optimizing the LiF with a thickness of 108 nm is the best choice, and it corresponds to a minimum reflection for the wavelength range near to 600 nm. The choice of 108 nm of Lif on the glass can increase the efficiency of the tandem solar cell to 22.3% (+0.5% absolute). These improvements impact both the perovskite (+0.4%), and the silicon (+0.1%) cells.

4.2.1.3 Interlayer between the perovksite and silicon solar cells

Perovskite and silicon cell are mechanically stacked and thus an air gap is formed between the two cells. To limit the optical losses in the air gap due to the reflection at the ITO / Air interface, an interlayer could be added between the two cells. This layer needs to have a refractive index similar to the ones of ITO and the top layer of the silicon bottom cell (SiN) and has to be transparent and insulating. SiN layer is textured with a thickness of 70 nm and it is considered that the gap between SiN and ITO is 1 μm. The interlayer is considered as fully transparent between 300 and 1200 nm (k=0) and its refractive index n is constant in the same range. Fig. 4.17a shows the impact of the interlayer with different refractive indices n on the reflection spectrum. For wavelengths inferior to 650 nm, there is no modification but above this limit, the interlayer allows to decrease the large interference figure at 900 nm and to create a new one at 1150 nm. The interference figure has a very limited impact on the efficiency of the tandem cell because the bandgap of the silicon cell is at 1150 nm.

Fig. 4.17b shows the effect of the refractive index of the interlayer on the efficiency of the perovskite, silicon and complete tandem solar cell, compared to our reference STPC. The index n has an effect on the efficiency on the range 1.6 - 2.0. For this range of values, the efficiency of the silicon cell is improved by 0.4% (absolute). However, it is interesting to note that the efficiency of the perovskite cell slightly decreases with the presence of the interlayer. This is due to the decrease of reflection between 600 and 775 nm, because these wavelengths do not go back into the perovskite to be absorbed. Adding an interlayer with $n = 1.6$, the efficiency of the tandem solar cell increases to 22.1% (+0.4%). These improvements impact negatively the perovskite cell (-0.1%), and positively the silicon cell (+0.5%). In most works, the coupling between the two cells is obtained with liquids like ethanol ($n = 1.36$). However, a supplementary point to commercial cell could be to use a type of glue, silicon-based organic polymer like polydimethylsiloxane (PDMS) or resin like epoxy ($n = 1.57$) which at the same time has a refractive index close to 1.6 and would allow to solidify the two cells between them. [37, 85, 157, 167, 196, 208, 209, 304].

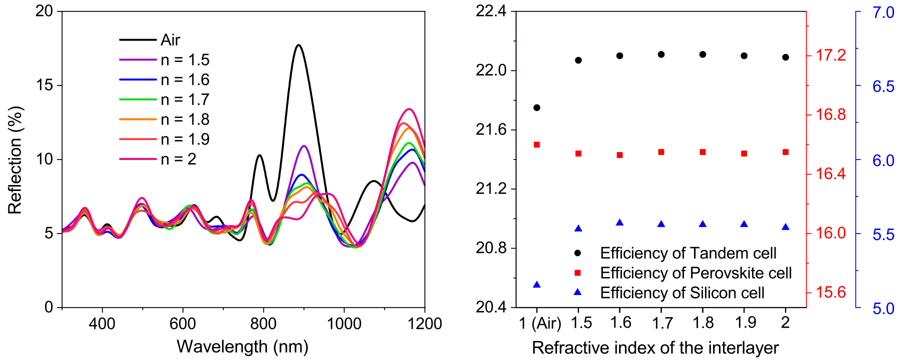
(a) (b)

Figure 4.17: (a) Evolution of the reflection of the perovskite cell as function of the refractive index n of the interlayer. (b) Evolution the efficiency of perovskite, silicon and tandem solar cells as a function of the refractive index n of the interlayer.

4.2.1.4 Effects on the Tandem

Fig. 4.18a represents the cumulative absorption of the different layers in a simulated STPC with an ARC, a coupling layer and a borosilicate glass substrate. Effects of these improvements are clearly visible on the reflection in the IR, with the absence of interference fringes, see Fig. 4.18b. The UV absorption of the perovskite absorber is improved too, because the borosilicate glass absorbs less in this region than the soda-lime glass. These two points lead to an increase in the Jsc of each cell: + 0.6% for the STPC and + 0.8% for the filtered silicon cell. The FF is kept constant because only the dielectric layers have been modified and the Voc evolves slightly because it is calculated with the relation 4.29. The combination of these three optimizations should allow to reach an efficiency of 23.2% (+1.4%), see Table 4.9.

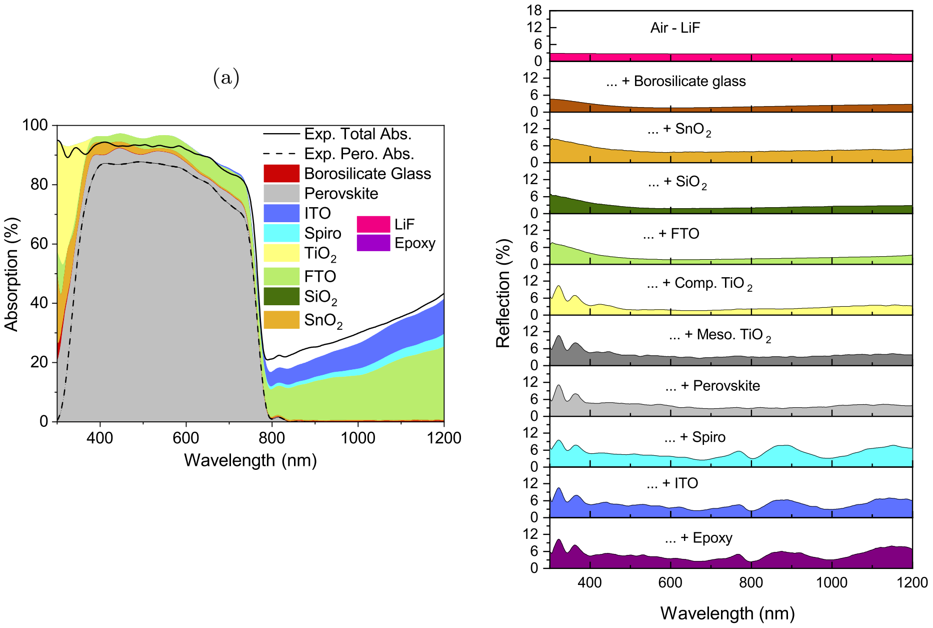
(a) (b)

Figure 4.18: (a) Simulated absorption distribution into the STPC between the different layers after the modifications of the glass substrate and the addition of the ARC and the coupling layer, compared to the total absorption before them (black line) and to the experimental EQE of the perovskite cell (dotted blue curve). (b) Reflection generated at each interface of the STPC after the modifications of the glass substrate and the addition of the ARC and the coupling layer.

Struc.	**Tandem**	**Perovskite cell**				**Silicon cell**			
	Eff. (%)	**Eff. (%)**	J_{sc} **(ma.cm^{-2})**	V_{oc} **(mV)**	**FF (%)**	**Eff. (%)**	J_{sc} **(ma.cm^{-2})**	V_{oc} **(mV)**	**FF (%)**
Reference	21.7	16.6	20.99	1080	73	5.1	11.54	590	77
Reference + LiF	22.3	17	21.49	1081	73	5.3	11.77	590	77
Reference + Epoxy	22.2	16.6	20.91	1080	73	5.6	12.43	592	77
Reference + B. Glass	22.4	16.9	21.39	1081	73	5.5	11.93	591	77
Reference + All	23.2	17.2	21.	1081	73	6.0	13.19	594	77

Table 4.9: Solutions for the dielectric layers and interfaces, and there influences on the efficiency of the tandem cell.

4.2.2 Improved electrical properties by introducing new electrodes

The second possible optimization consists in the replacement of electrodes which participate in the transport of charges and therefore have a direct impact on the electrical properties. These improvements have a direct influence on the performance of the tandem cell, by modifying the sheet resistance of the transparent conductive oxides and increasing the amount of light which reaches the perovskite and the silicon layers. This can be evaluated using the electrical model presented in Section 4.1.2.2.

4.2.2.1 TCO front electrode instead of FTO

FTO was chosen as rear contact of the perovskite cell for its good chemical resistance and because it can support the annealing of TiO_2 at 450 °C without degradation. However, even if it has a low resistivity of 10 Ω.sq, FTO absorbs in the IR, see Fig. 4.19a. Thus it appears necessary to use another material to improve the efficiency of the silicon bottom cell and consequently the tandem cell. The material chosen to replace the FTO needs to resist the annealing of TiO_2 and to the different solvents used during the process.

In order to replace the FTO and reach a similar resistivity (10 Ω.sq), a high temperature resistant ITO can be also a solution. The final structure would be symmetrical with ITO on each side. A commercial ITO - Glass substrate from Solems shows an absorption in the IR to 17% at 1000 nm, see Fig. 4.19a. The comparison of absorption spectra of FTO and ITO for identical sheet resistances should lead to an improvement of 10% at 1000 nm. However, it is necessary to use an ITO deposited at high temperature

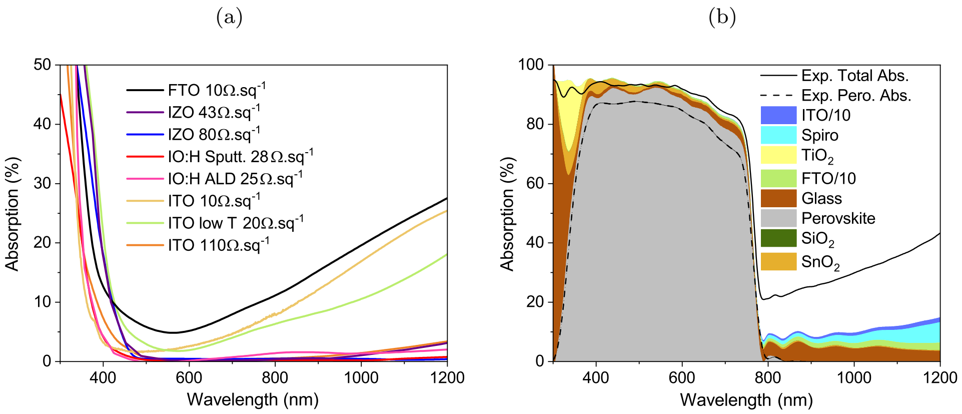
(a)

(b)

Figure 4.19: (a) (a) Absorption spectra of different TCO: FTO 10 Ω.sq (Solems), IZO 43 Ω.sq [163], IZO 80 Ω.sq [176], IO:H by sputtering 28 Ω.sq [176], IO:H by ALD 25 Ω.sq [305], ITO 10 Ω.sq (Solems), ITO 20 Ω.sq (homemade by sputtering) and ITO 110 Ω.sq [176]. (b) Absorption distribution into the STPC between the different layers after the replacement of ITO and FTO, compared to the total absorption before the optimization (dotted black line) and to the experimental EQE of the STPC (dotted blue curve).

which is able to resist to the annealing of TiO_2 without degradation of its opto-electronic properties. We have seen in the Appendix C that in our case this leads to an increase in the sheet resistance (17.3 Ω.sq before vs. 33.8 Ω.sq after). Thus, some tests are required to conclude if an ITO with a resistivity of 10 Ω.sq can be obtained with this process.

Another interesting solution could be to use IO:H to replace FTO, since it does not absorb infrared wavelengths (Fig. 4.19a). Synthesized by ALD and annealed at 180 °C, IO:H keeps a good conductivity (25 Ω.sq) without infrared significant absorption [163, 168, 176, 305]. Further tests are necessary to conclude if this material can support an annealing at 450°C and be a good candidate to replace the FTO.

4.2.2.2 TCO back electrode instead of ITO

ITO was also chosen as a front contact in this work because it offers one of the best conductivity/transparency ratio after deposition at room temperature. Moreover, it is compatible with the previous layers by limiting the exposition of the perovskite solar cell to high temperature and energetic process. ITO has a resistivity of 20 Ω.sq and absorbs 11% of incident light at 1000 nm, see Fig. 4.19a.

IO:H appears also as a good solution to replace ITO too but this time synthesized by sputtering without annealing to avoid damage of the perovskite and Spiro-OMeTAD layers [43, 176, 305, 306]. This type of layer has a resistivity of 28 Ω.sq with negligible light absorption in the infrared region as show on Fig. 4.19a.

IZO is also an interesting solution as transparent conductive oxide for the second electrode, it could be synthesized by sputtering and it does not require annealing to achieve optimal performance. Its absorption in the infrared region is lower than 3%. Its resistivity is higher, with 43 Ω.sq, thus it is necessary to test it experimentally to see if the impact on the electrical properties is not too important [163, 176, 307].

In order to simulate the results that could be obtained with more transparent TCO, we reduce the absorption of the FTO and ITO by a factor 10 after their gap, considering that these are the values that we would obtain by using IO:H on the front side and IZO on the back side. As expected, this optimization decreases the absorption of the electrodes in the IR as it is shown in Fig. 4.19b, where the absorption of the Spiro-OMeTAD layer appears significant now. The UV absorption of the perovskite absorber does not change but in the visible part, an increase of 4% is visible, due to the lower absorption in FTO. With these improvements, the efficiency of the tandem reaches 23.7% (+2%). However, we have seen that IZO tends to be more resistive than ITO and this would have an impact on FF and efficiency. One solution would be to rethink the design of our electrodes to reduce the distance between the contacts and thus allow the use of more resistive TCO.

4.2.2.3 Contact geometry

In the case of our experimental device, we have an asymmetrical structure (noted asy.) in which the current does not travel the same distance on the both sides, as detailed in the Section 4.1.2.2. For the anode (FTO), the distance is 8 mm and for the cathode (ITO), it is 3 mm. Fig. 4.20a shows the evolution of the perovskite cell efficiency as a function of the sheet resistance of the anode and the cathode in the case of our asymmetrical structure. Although the sheet resistance of FTO (9 Ω.sq) is lower than that of the ITO (16 Ω.sq), it is the most limiting parameter due to the 3 times longer distance between FTO and gold than between ITO and gold. Indeed, the sheet resistance of ITO has almost no influence in the 1-100 Ω.sq range, while it seems difficult to use a TCO with a higher resistivity than the current FTO electrode (9 Ω.sq). In order to offer a more general result without any restrictions related to our own device and to improve the design, D (the distance between two fingers) is now assumed equal to 3 mm for each electrode (symmetrical structure, noted Sy.). Consequently, the losses due to the sheet resistance of FTO decrease, as show in Fig. 4.20b. With a distance D of 3 mm for each electrode, the sheet resistance of the TCO can be higher without any impact on the efficiency. There is only a 0.8% difference in the efficiency of the STPC Sy. with electrodes of 1 or 100 Ω.sq.

With this design, the performance of the reference structure with ITO and FTO improves up to 22.7% efficiency (+0.9% previously), and the performance of the silicon cell remains unchanged at 5.1%, as reported in Table 4.10. The FF increases to 77% and is now identical to that of the silicon cell.

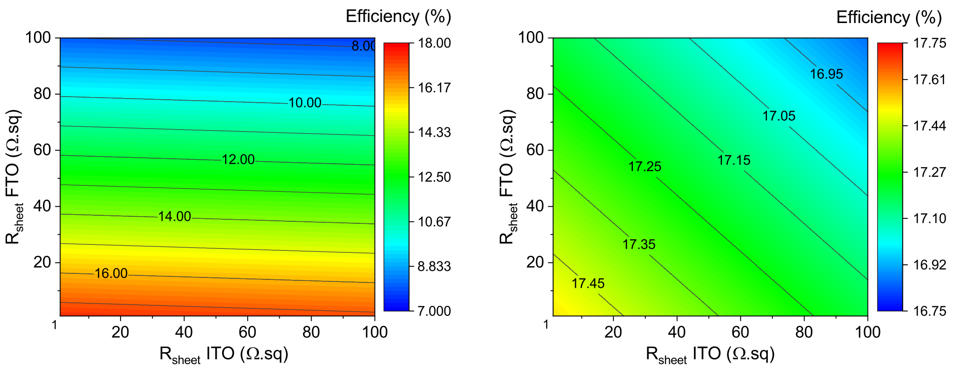
(a)

(b)

Figure 4.20: (a) Evolution of the efficiency of the reference STPC with an asymmetrical (a) and symmetrical (b) contact architecture as a function of the sheet resistance of ITO and FTO.

Struc.	Geo.	Tandem	Perovskite cell				Silicon cell			
		Eff. (%)	Eff. (%)	J_{sc} (mA.cm^{-2})	V_{oc} (mV)	FF (%)	Eff. (%)	J_{sc} (mA.cm^{-2})	V_{oc} (mV)	FF (%)
Reference	Asy.	21.7	16.6	20.99	1080	73	5.1	11.54	590	77
Reference	Sy.	22.7	17.5	21.00	1081	77	5.1	11.54	590	77
Modified	Sy.	26.3	18.9	22.82	1083	76	7.3	15.99	598	77

Table 4.10: Electrical characteristics of the reference and modified STPC with an Al-BSF Silicon cell.

4.2.3 Combined impacts on the tandem efficiency

Fig. 4.21a shows the influence of these modifications (solutions for the conductive and dielectric layers and interfaces) on the absorption distribution into the perovskite cell. This new STPC is called modified STPC. The transmission at 900 nm reaches now 85%, and the absorption of the perovskite layer is improved between 400 and 800 nm. The impact of the ARC and the interlayer on the reflection spectra is visible respectively in Fig. 4.21b, with a decrease of the reflection near 600 nm for the first interfaces and no longer influence of the ITO / Interlayer interface on the total reflection. With the modeling of electrical parameter shows in Section 4.2.2.3, the tandem cell could reach an efficiency of 26.3%, see Table 4.10. The design of the structure appears important because with the previous asymmetrical structure, the modified tandem cell reaches only 24.1% of efficiency with the same modifications.

4.2.4 Impact of other HTL and ETL

Replacing the extracting layers in our simulation no longer guarantees the validity of the previously presented electrical model. Nevertheless, if very good performances could be obtained by replacing either the ETL or the HTL on structures close to ours, we could first study the optical properties of a new stacking.

Thus, using PTAA as HTL instead of Spiro-OMeTAD, Jeong's team obtained a 22.1% opaque perovskite cell on a structure otherwise similar to ours [308]. As this layer is supposed to be completely transparent in the IR, it could further reduce the parasitic absorption in this area. On the other hand, TiO_2 and its annealing is currently a concern for the choice of front side electrodes as we have no guarantee that IO:H can withstand temperatures of 450°C without degrading its properties. In parallel, several teams are currently working on replacing it with a thin SnO_2 layer [309, 310], which has the advantage of being able to be deposited at room temperature without significant parasitic absorption. The results obtained are also very good on structures close to ours and even exceed 23% on opaque cells.

The Fig. 4.22 shows the simulated absorption distribution obtained using indices published in the literature (PTAA [311] and SnO_2 [197]), compared to the total absorption obtained on the reference structure. It can be seen that the use of SnO_2 instead of TiO_2 increases the absorption range of the

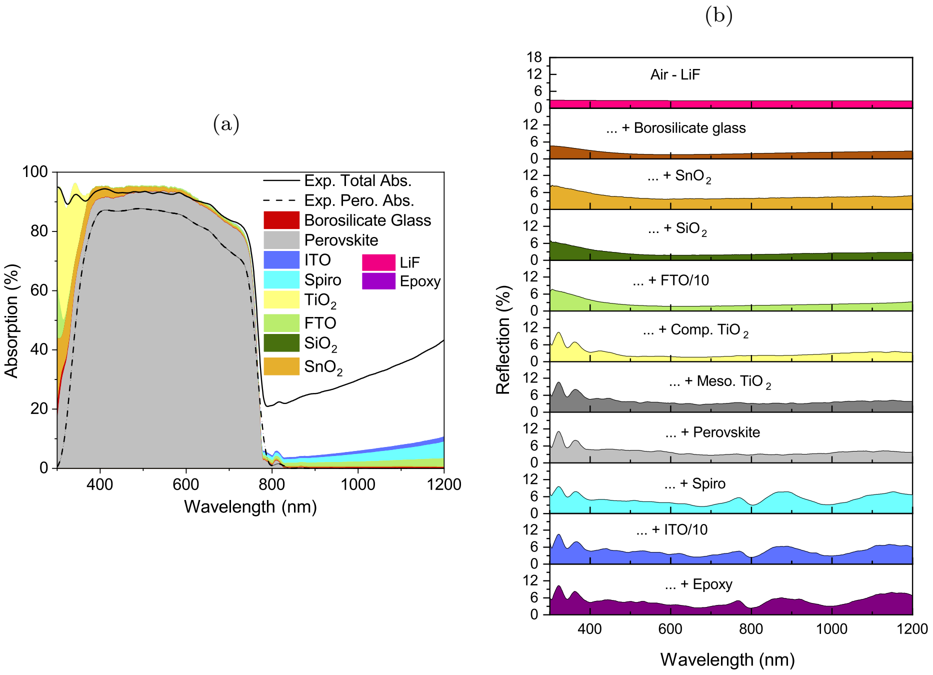

Figure 4.21: (a) Simulated absorption distribution into the STPC between the different layers after the modifications (modified STPC), compared to the total absorption before them (black line) and to the perovskite absorption before them (dotted black curve). (b) Reflection generated at each interface of the STPC after the modifications.

perovskite layer near the UV. Nevertheless, strong interference fringes appear between 300 and 600 nm, which could be due to a poor optical coupling of SnO_2 with the FTO electrode or the perovskite layer. Concerning the PTAA, it absorbs less than expected in the IR, which allows in this model to go below the 4% of total absorption at 1000 nm. There is therefore no strong optical contradiction to the use of these materials, but their effectiveness must nevertheless be demonstrated experimentally. For this reason, we will continue to discuss with the modified structure without taking these modifications into account for the rest of this chapter.

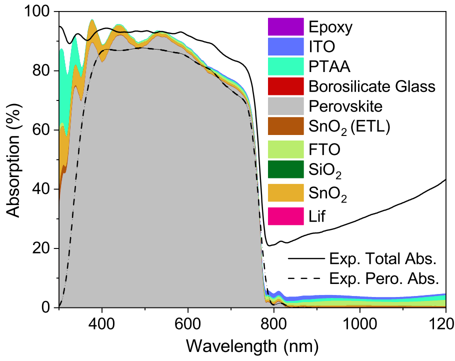

Figure 4.22: Simulated absorption distribution into the STPC between the different layers after the modifications (modified STPC + ETL/HTL), compared to the total absorption before them (black line) and to the perovskite absorption before them (dotted black curve).

4.2.5 Effect of the IQE and perovskite thickness on the efficiency

It is possible to further improve the modified STPC presented in the previous part. The changes proposed in this section affect the junction and are therefore more hypothetical than those presented so far. First of all, it may be considered IQE = 100% that means that the cell is able to dissociate the electron-hole pairs and extract them without loss by recombination. Jeong et al showed that this is possible, with a ternary halide perovskite $MAPbI_{2.9-x}Br_{0.1}Cl_x$ characterized by an IQE approaching 100% and 16% efficiency [312]. Simulated IQE of our experimental perovskite cell is close to 90%, see Fig. 4.14b. Thus, it is necessary to continue to improve the quality of our perovskite layer.

Secondly, in a STPC, replacing the gold anode with an ITO anode results in a decrease in reflection at the interface Spiro-OMeTAD / ITO. This causes a loss of absorption for the wavelengths near the gap, which reaches 10% at 720 nm, as shown in Fig. 4.23a. There are two solutions to increase the perovskite absorption in this region: the first one is to change the interface to have a higher reflection, but it is difficult without changing the electrical properties and still keep a good transparency by reflecting only the wavelength below 800 nm. This involves using a dichroic filter to split the light spectrum, reminiscent of the split spectrum 4T tandem. However, the additional cost of the filter limits the commercial potential of this architecture. The second solution is to increase the thickness of the perovskite layer. A layer that is too thick can have consequences on the opto-electronic device performances that are not visible in our optical simulations. The diffusion length of the photogenerated carriers inside a perovskite layer can usually vary between 100 and 1000 nm. Process modification [313, 314], replacement of solvents [315], introduction of a new additive such as chlorine [89], removal of impurities, improvement of extraction layers, or reduction of surface roughness [316] can reduce the defect density and increase the diffusion length. Such improvements have been demonstrated by Rehman who reported one of the longest diffusion lengths in a perovskite layer with a thick $FAPBI_3$ of 3.1 µm [317]. In parallel, Chen maintained 19% and 17% of efficiency with a perovskite layer thickness of 1150 nm, and 1600 nm, respectively [318]. Concerning our perovskite cell, in the case of a perovskite layer of 900 nm instead of 600 nm, the simulated EQE with an ITO electrode becomes similar to the EQE with a gold electrode, see Fig. 4.23a.

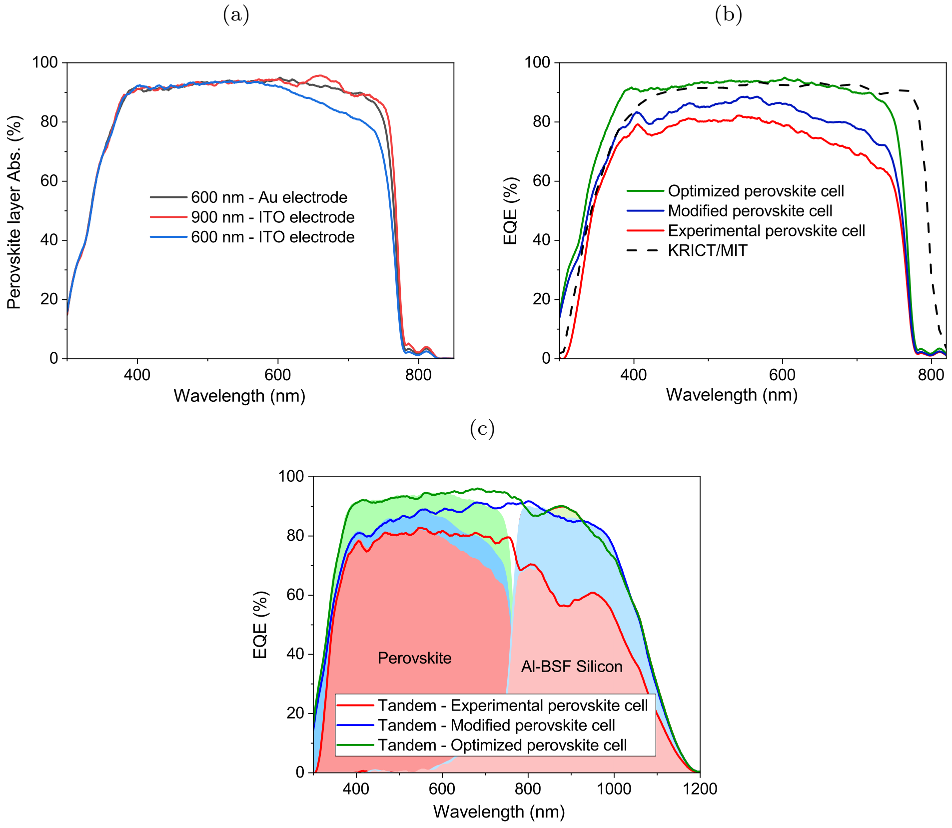
(a)
(b)
(c)

Figure 4.23: (a) Simulated absorption of a 600 nm thick perovskite layer with a gold anode and an ITO anode, compared to the simulated absorption of a 900 nm thick perovskite layer with an ITO anode. (b) Simulated EQE of the experimental perovskite cell (red), the modified (blue) and the modified with a thicker perovskite and an IQE near 100%, called optimized cell (green). Dashed black curve represents the experimental EQE for the perovskite cell. (c) Simulated EQE of the perovskite cell, the filtered Al-BSF silicon cell and tandem cell, with experimental (red), modified (blue) and optimized (green) perovskite cells.

In comparison, the EQE of the record perovskite cell manufactured by KRICT/MIT with 25.2% efficiency and a gold back electrode [126, 319] is shown in Fig. 4.23b. This perovskite cell has a smaller band gap than ours, resulting in a better EQE in the infrared region. However, for the range between 400 and 800 nm, the EQE is similar to the one simulated in green, corresponding to our modified simulated cell presented in Section 4.2.3 with in addition a 900 nm perovskite and assuming that the IQE is close to 100%. With such perovskite cell that we called "optimized" perovskite cell, the efficiency of the tandem cell reaches 28.2% with a conventional Al-BSF silicon cell, see Table 4.11.

Fig. 4.23c shows the simulated EQE with all the different optimizations. The effect of the improvements applied on the modified perovskite cell in blue is clearly visible on the Al-BSF silicon filtered EQE, with an infrared transmission through the perovskite cell greater than 80%, and with the reduction of the interference figures in the infrared region. As the EQE of unfiltered silicon reaches 100% in this region, the observed shortfall in filtered EQE is now mainly due to the reflection and absorption of the Spiro-OMeTAD layer. As expected, the optimized perovskite cell in green increases again slightly the absorption of the perovskite in the visible region.

To go further, if the optimized perovskite cell is modeled with the Fill Factor of the record perovskite cell of the KRICT/MIT (85%), the efficiency reaches this time 32.6% as show on Table 4.11. This result is obviously hypothetical, as there is no indication at this stage that it is possible to obtain a functional STPC by combining an IQE at 100%, an FF at 85% and a transmission at 90% in the IR. Nevertheless, it allows us to envisage the performance of such devices, which we will call Record STPC in the following.

Struc.	**Tandem**	**Perovskite cell**				**Silicon cell**			
	Eff. (%)	**Eff. (%)**	**J_{sc} (mA.cm^{-2})**	**V_{oc} (mV)**	**FF (%)**	**Eff. (%)**	**J_{sc} (mA.cm^{-2})**	**V_{oc} (mV)**	**FF (%)**
Reference (asy)	21.7	16.6	20.99	1080	73	5.1	11.54	590	77
Modified (sy)	26.3	18.9	22.82	1083	76	7.3	15.99	598	77
Optimized (sy)	28.2	21.2	25.68	1085	76	6.9	15.05	596	77
Record (sy)	32.6	25.7	25.68	1085	85	6.9	15.05	596	77

Table 4.11: Electric properties for different optimizations of the STPC for a perovskite/Al-BSF silicon 4T tandem solar cell.

4.3 Final optimized Tandem

4.3.1 Influence of silicon technologies

Considering the optimized perovskite/Al-BSF tandem cell as presented previously in this chapter, a 4T Tandem can also be model with different types of silicon solar cells. Four silicon cells of different technologies available in the laboratory (provided by different actors) are used and characterised: the classic Al-BSF, two different bifacial n-PERT, and a bifacial IBC. In addition, the data concerning the HJ-IBC silicon cell of Yoshikawa [320] with a very high efficiency have been also used.

The Al-BSF cell has the worst EQE at wavelengths larger than 900 nm (at least 10% lower at 1000 nm than for the other types of cells), see Fig. 4.24a. This is due to an important absorption in the infrared region by the full area aluminum rear contact of the cell. It therefore has the lowest Jsc (38.86 mA.cm^{-2}). Its efficiency is also the lowest among the 5 silicon cells (18.9%), and this is also due to FF of only 77%, see Table 4.12. However, it is also the cell that exhibits the lower efficiency loss after filtering by the perovskite cell (-12%): this allows to predict a tandem with 28.1% of efficiency as presented before. Fig. 4.24b shows the simulated EQEs once filtered by the optimized perovskite.

In PERT cells, a stack of dielectric layers is deposited on a large fraction of the rear side, which allows both to boost the passivation (lower electrical losses) and the back reflection (lower optical losses). These losses (infrared absorption and recombination) are mostly limited to the small local aluminum contacts and this is reflected in the filtered and unfiltered EQE of these cells. They are for example +15% higher at 1050 nm compared to the Al-BSF cell. The two PERT cells have an almost similar EQE but different electrical properties, the n-PERT silicon cell n°2 thus has slightly better properties than the n°1. A tandem with the first n-PERT silicon cell would lead to an efficiency of 29.1%, with the second n-PERT it increases up to 29.6%.

The IBC cell used is also bifacial, which is allowed by the fact that they do not rely on a full area rear metallization any more but only on local contacts (metallic grid). The absence of contacts on the front side reduces shading on the IBC cells and improves their efficiency up to 22.7%. Thus, its filtered EQE is slightly higher than previous cells and its use in tandem allows to reach 30% of efficiency. However, it is the silicon cell that loses the most in terms of efficiency when filtered (-13.9%).

To go further, the data concerning the SHJ-IBC silicon cell of Yoshikawa [320] are also used to present a very high performance theoretical tandem. These electrical properties are far superior to the IBC cell presented previously with an efficiency of 26.3%. The unfiltered EQE of this cell has a different behaviour from the others in the near UV range but this is not reflected in the EQE obtained once the radiation is filtered by the perovskite. With it, the tandem achieves a predicted efficiency of 31.8%.

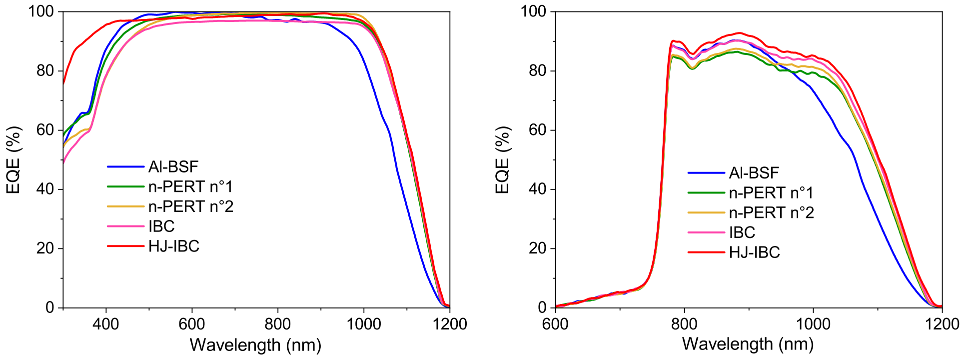
(a) (b)

Figure 4.24: (a) Experimental EQE for different silicon cells. (b) Simulated filtered EQE by the modified perovskite for the same silicon cells.

Silicon cell	**Tandem**	**No filtered - Experimental value**				**Filtered - Simulated values**			
	Eff. (%)	**Eff. (%)**	J_{sc} **(mA.cm^{-2})**	V_{oc} **(mV)**	**FF (%)**	**Eff. (%)**	J_{sc} **(mA.cm^{-2})**	V_{oc} **(mV)**	**FF (%)**
Al-BSF	28.1	18.9	38.86	619	77	6.9	15.14	596	77
n-PERT n°1	29.1	20.6	39.15	662	79	7.9	15.68	640	79
n-PERT n°2	29.6	21.4	39.33	678	80	8.4	15.89	656	80
IBC	30	22.7	40.91	684	81	8.8	16.46	662	81
SHJ-IBC	31.8	26.3	42.30	774	84	10.6	16.90	752	84

Table 4.12: Electrical characteristics of different filtered silicon cells with an optimized perovskite cell.

4.3.2 Which architecture to reach 30% and more?

Table 4.13 lists the performances of different devices presented in this chapter and new combinations between STPC and silicon cells. The reference + Al-BSF structure corresponds to the structure of the experimental tandem with an efficiency of 21.7%. Several combinations allow us to exceed the Shockley-Queisser limit of single-junction silicon cells with our perovskite cell (30%), which represents a gain of at least +8.3% on the final efficiency.

Firstly, structures with the modified perovskite already achieve more than 30% efficiency (18.9% + 11.2%) if Yoshikawa's record HJ-IBC silicon cell is used (30.1%). This STPC with a modified structure (ARC, interlayer and replacement of the substrate and electrodes) can be developed in the laboratory and will be the focus of the next chapters. Nevertheless, we do not have a silicon cell as efficient as the one used in this model.

Secondly, the optimised structure of the STPC (Modified + IQE 100% and thicker perovskite) makes it possible to achieve 30% efficiency (21.2% + 8.8%) by using the silicon IBC cell. Fig. 4.25 shows the evolution of the total EQE between the reference structure and this last one. However, more experimentation will be needed in relation with the modified structure in order to increase the thickness of the perovskite layer without losing performance, while still managing to improve IQE.

To go even further, it is possible to model a tandem with the HJ-IBC silicon cell and record STPC. This makes it possible to achieve an theoretical impressive efficiency of 36.2% (25.7% + 10.6%), which approaches the theoretical Shockley-Queisser limit for a double junction (42%), without even optimising the gap of the perovskite cell.

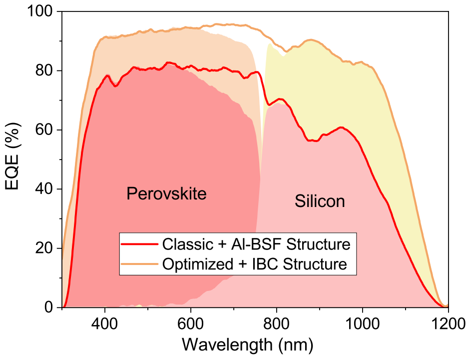

Figure 4.25: Simulated EQE of the perovskite cell, the silicon cell and tandem cell, with experimental structure for the STPC and a Al-BSF silicon cell (pink), and optimised STPC with a IBC silicon cell (yellow).

	T.	**Perovskite cell**				**Silicon cell**			
	Eff. (%)	**Eff. (%)**	J_{sc} **(mA.cm^{-2})**	V_{oc} **(mV)**	**FF (%)**	**Eff. (%)**	J_{sc} **(mA.cm^{-2})**	V_{oc} **(mV)**	**FF (%)**
Reference + Al-BSF	21.7	16.6	20.99	1080	73	5.1	11.54	590	77
Modified + Al-BSF	26.3	18.9	22.82	1083	76	7.3	15.99	598	77
Modified + IBC	28.2	18.9	22.82	1083	76	9.3	17.26	663	81
Modified + SHJ-IBC	30.1	18.9	22.82	1083	76	11.2	17.69	753	84
Optimized + Al-BSF	28.1	21.2	25.68	1085	76	6.9	15.14	596	77
Optimized + IBC	30.0	21.2	25.68	1085	76	8.8	16.46	662	81
Optimized + SHJ-IBC	31.8	21.2	25.68	1085	76	10.6	16.90	752	84
Record + Al-BSF	32.6	25.7	25.68	1085	85	6.9	15.05	596	77
Record + SHJ-IBC	36.2	25.7	25.68	1085	85	10.6	16.75	7531	84

Table 4.13: Electric properties for different optimizations of the 4T perovskite/silicon tandem solar cell.

Conclusion

In conclusion, we developed optical and electrical models based on an iterative method for the STPC, and 4T perovskite/silicon tandem device. As a first step, the optical indices of each layer of the structure were determined separately through ellipsometric measurements and the use of different dispersion models. The complete structure was then modelled and showed very good agreement with the experimental spectrophotometric measurements, much better than when this method is not used or when indices from the literature are used.

This modelling then made it possible, via an analysis of the optical losses, to highlight that same materials were poorly adapted to the tandem configuration. Infrared absorption losses are mainly caused by the electrodes (ITO and FTO), Spiro-OMeTAD and the glass substrate. Furthermore, the Air / Glass and ITO / Air interfaces are responsible for parasitic reflection. In addition, to predict the impact of changes in the initial structure, for instance new TCO layers, we developed in parallel a simple electrical model to simulate the full tandem cell. In our geometrical design, FTO electrode appear also as the main factor limiting the FF of the perovskite cell, even if its sheet resistance is lower than ITO.

In a second step, solutions were proposed to improve the opto-electronic performance of our reference STPC. On the one side, the use of an ARC, an interlayer between the cells and replacement of the glass substrate made it possible to reduce the near-infrared absorption and spurious reflection of this reference structure. On the other side, we studied the influence of ITO and FTO electrodes on performances. The interest of a symmetrical structure highlighted the importance of the structure design and alternative materials have been identified, such as IO:H and IZO, to strongly decrease the absorption in the IR. Finally, the interest of internal improvements of the perovskite cell has been shown, such as a greater thickness (900 nm) and the assumption that the average IQE value could still approach 100%. With these changes, the optimized tandem can reach 28.2% of efficiency with an Al-BSF silicon cell.

By combining the most interesting solutions and with a more efficient silicon cell (IBC), see Fig. 4.26, we have shown that it is possible for such a tandem to achieve 30% efficiency. The next step will be to implement all these solutions in the fabrication of an experimental device. We also took the opportunity to push the modelling further, this time taking the best developed silicon cell and associating it with a hypothetical STPC which would have an IQE at 100%, an FF at 85% and a transmission of 90% in the IR.

The resulting tandem shows that it is theoretically possible to achieve a total efficiency of 36.2%, which is well above the current experimental record. More generally, the methodology detailed here can be applied to other technologies of solar cells and allow building optical models based on experimental devices when the morphology, the optical, and electrical properties can be characterized. It can account for a wide variety of materials and stacks, and even oblique incidence angles. In addition to the analysis of optical losses, the ability to finely model interference patterns may be of particular interest in structures where their influence on transmission and reflection properties needs to be enhanced/suppressed for optical management.

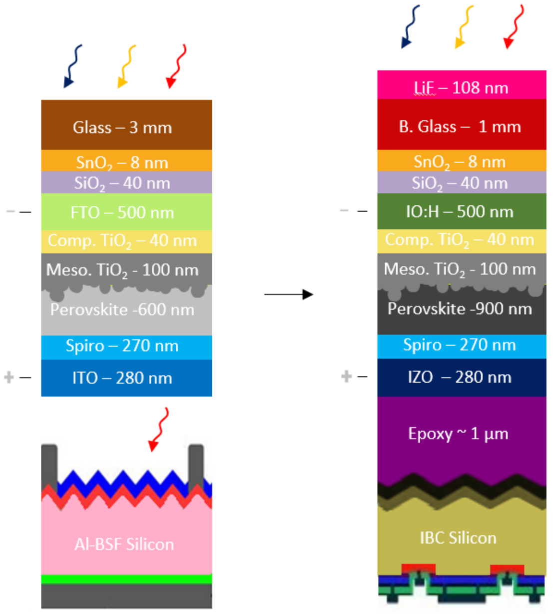

Figure 4.26: Evolution of the 4T tandem structure between the reference and the optimized architecture.

Chapter 5

Replacement of the hole and electron transport layers by PTAA and SnO_2

Introduction

Spiro-OMeTAD is the most widely used HTL in perovskite cells and it can leads to high efficiency [9]. However, its poor stability known in the literature and mentioned in Chapter 3 does not allow to consider mass production of STPC [321]. So far, numerous studies have been accomplished to enhance the efficiency of perovskite cells by engineering new HTL structures including small molecules [90–94], metal-phthalocyanines (metal complexes containing tetrapyrrolic cyclic organic ligands) [95–97], organic polymers (PEDOT:PSS, P3HT, PTAA ...) [98–100] and p-type inorganic semiconductors (CuO, MoO_3 and NiO_x) [101–103]. Specifically, polymeric HTL have broadly been applied due to their advantages including solution processing at low temperatures, mechanical flexibility, and the capability to form thinner films with a enhanced coverage. In this chapter, we present Polytriarylamine (PTAA) and it use as a HTL in perovskite solar cells.

In parallel, TiO_2 is the most common ETL in the n-i-p configurations [322]. However, TiO_2 only exhibits electrical conductivity when the material is annealed above 500°C [323]. In order to consider the replacement of the FTO by another more transparent TCO and the use of flexible plastic substrates like PET/PEN in the future, see Chapter 4 Section 4.2.1.1, it is necessary to look for other types of ETL. Currently, numerous n-type metal oxides such as SnO_2 [324], ZnO [104], WO_3 [105], $SrTiO_3$ [106], Nb_2O_5 [107] and $BaSnO_3$ [108] have been investigated as ETL. In particular, SnO_2 has several advantages including wide bandgap, deep conduction and valence band, excellent optical and chemical stability, high transparency, high mobility, and easy preparation at low temperature [325]. We will therefore detail in this chapter the properties of SnO_2-based opaque perovskite cells and STPC.

5.1 Polytriarylamine (PTAA) based perovskite solar cells

The Polytriarylamine (PTAA) is an amorphous polymer version of a small molecular triphenylamine (TPA) based material. The TPA-based polymers generally provide low hole mobility and hydrophilic surfaces. In addition, undoped, it has a relatively low carrier mobility [326]. However for enhancing hole mobility, it is most of the time conventionally p-doped with two co-dopants identical to Spiro-OMeTAD: LiTFSI and t-BP [327]. Doped PTAA was first applied as a HTL in perovskite cell in 2013 simultaneously by Heo et al. [328] and Noh et al. [84], outperforming Spiro-OMeTAD. By habit, Spiro-OMeTAD has nevertheless remained in use in many laboratories, and PTAA has its own disadvantages such as its thinness which prevents it from being deposited effectively on rough surfaces, its price and its suspected chemical incompatibility with some large gap perovskite [329, 330].

This HTL is known for its thermal stability up to 300°C under inert atmosphere and its ability to form very thin films [331, 332]. Indeed, compared to small and rigid HTL molecules like Spiro-OMeTAD, PTAA can be deposited in thinner layers (20 nm instead of 200 nm), which is advantageous for a better charge transport in an HTL [330]. This is due to the fact that the transit time of the holes through the HTL affects both the rate of extraction and recombination of the charges in the device. Thus in the case of the PTAA, non-radiative recombination losses, which account for half of the total FF losses, are almost eliminated [333]. Finally, the deposited films are generally covering without creating pinhole as opposed to the Spiro-OMeTAD. Pinholes can create shunts by the contact between the perovskite and the electrode material.

In this section we will first look at the optical properties of this layer, which we started to discuss in the previous chapter in Section 4.2.4. Then we will be interested in the dispersion of the electrical measurements within and between batches when PTAA is used as HTL instead of Spiro-OMeTAD, as well as in their evolution with time. The PTAA/ITO interface, suspected to host the mechanism responsible for the recovery of the S-shape on the IV curves will be analyzed with advanced characterization methods. Finally we will present the first results obtained on encapsulated cells.

5.1.1 Optical properties of PTAA deposited on glass

PTAA is deposited by spin-coating like Spiro-OMeTAD. It is diluted in toluene with 2 additives: LiTFSI and t-BP in order to increase its conductivity. LiTFSI normally functions as the p-dopant, which improves the hole conductivity, and t-BP performs a similar function in PTAA as it has been observed to have in Spiro-OMeTAD, where it forms complexes with LiTFSI to improve its distribution through the film and to avoid the negative effects of dopant aggregation on film morphology [330, 334–336]. The result is a very thin layer, between 15 and 20 nm. The optical properties of the layer are first evaluated on 1 mm thick borosilicate glass.

As shown in Fig. 5.1a the PTAA absorbs slightly between 300 and 450 nm but this is not a concern in n-i-p superstrate structure as in our case, because these rays are absorbed by the perovskite layer before reaching the HTL. This layer does not show any parasitic absorption in the infrared unlike the Spiro-OMeTAD.

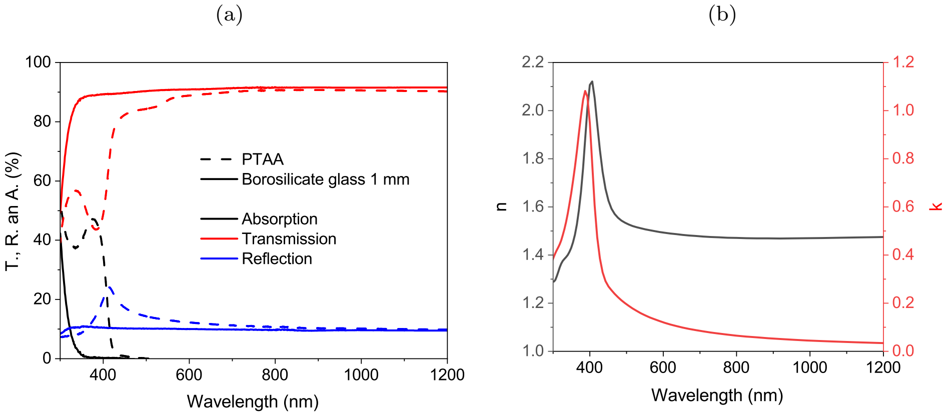
(a)

(b)

Figure 5.1: (a) Transmission, absorption and reflection spectra of PTAA on a 1 mm thick borosilicate glass, compared to the substrate alone. (a) Optical indices n and k of PTAA.

The refractive index n and extinction coefficient k have been measured by ellipsometry and are presented in Fig. 5.1b. This absorption peak at 400 nm observed above is directly related to the extinction coefficient k of this material at the same wavelength. In addition, k shows that this layer has a non-zero absorption in the infrared but which is not perceptible on the TRA spectra in Fig. 5.1a because of its very low thickness. This is consistent with the simulation performed in the previous chapter Section 4.2.4 with PTAA indices from the literature [311]. It refractive index n follows a similar trend to that of Spiro-OMeTAD, presented in Section 4.1.1.5, which indicates that its use should not generate more parasitic reflection at the interfaces with perovskite and ITO.

5.1.2 Differences between Spiro-OMeTAD and PTAA as HTL on STPC

5.1.2.1 Optical and morphological properties

Fig. 5.2d shows the absorption of two STPC with PTAA and Spiro-OMeTAD. The expected slight gain in the infrared due to the thickness of the PTAA layer compared to Spiro-OMeTAD is indeed visible on STPC (-8% at 1200 nm), which corresponds well to the simulated gain evaluated in Section 4.2.4 of the previous chapter. In terms of surface roughness, see Fig. 5.2a and b, the STPC with PTAA has an RMS of 13.9 nm and a valley trough amplitude of 85 nm. This is is twice the value as in the case with Spiro-OMeTAD, as discussed in Chapter 3 Section 3.1.1.

This can be explained by the small thickness of the PTAA compared to the Spiro-OMeTAD as shown in the cross-section seen at SEM, see Fig. 5.2c where PTAA is almost invisible. This does not allow to smooth and attenuate the variations of the perovskite layer.

Finally, a structure similar to the STPC stack but without electrical contact is realized on a surface of 16 cm^2, either with PTAA or with Spiro-OMeTAD. Each layer is deposited in exactly the same way, only the quantities are adapted for the spin coating steps. The ITO deposition is performed at the same time on the two samples, following the standard process for STPC mentioned earlier. The Spiro-OMeTAD stack shows a completely detached ITO electrode (see picture on Fig. 5.2f), similar to the one discussed in Section 3.2.2. On a larger surface, the constraints related to the deformation of the Spiro-OMeTAD

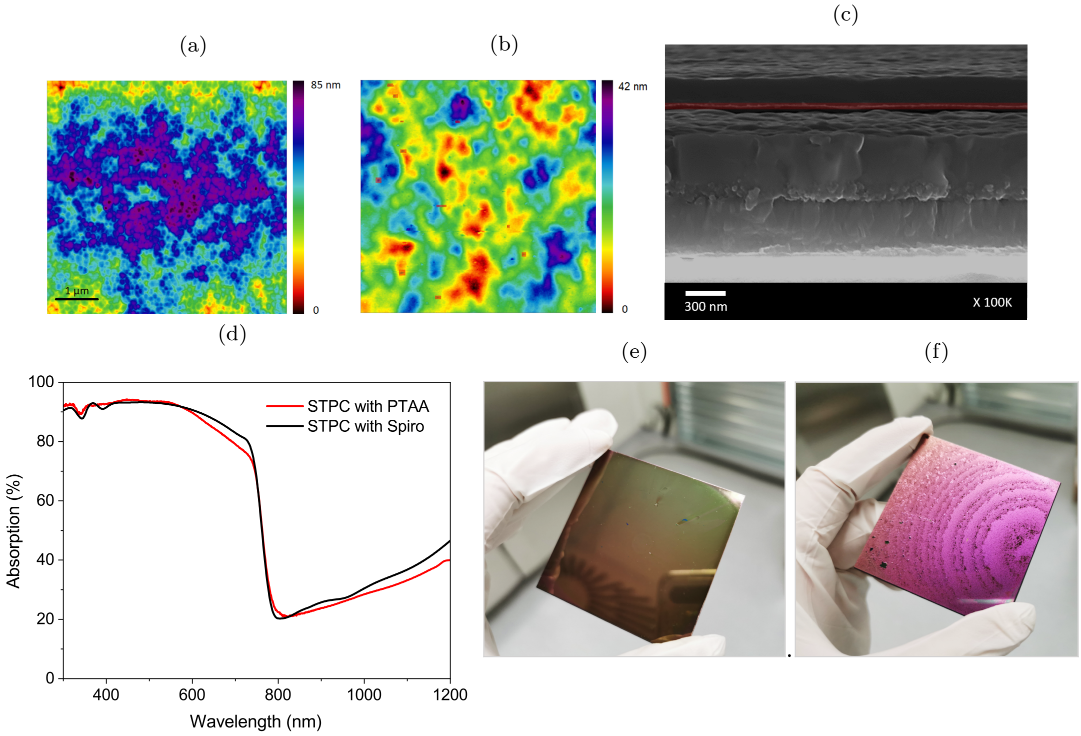
(a) (b) (c) (d) (e) (f)

Figure 5.2: AFM of the ITO surface of a STPC with (a) PTAA and (b) Spiro-OMeTAD as HTL. (c) SEM cross-section image of a STPC with PTAA as HTL (red area). (d) Absorption spectra of two STPC with PTAA or Spiro-OMeTAD as HTL. Pictures of complete STPC stacks on 16 cm^2 just after ITO deposition with (e) PTAA and (f) Spiro-OMeTAD as HTL.

with temperature are more important and limit the fabrication of large devices. On the other hand, we observe a smooth surface in the case of PTAA with an ITO electrode which seems to be well attached to the surface, see Fig. 5.2e. The PTAA has indeed a Coefficient of Linear Thermal Expansion of 50-150 10^6 K^{-1}, and a Young modulus E equal to 1 GPa, which are respectively twice and 15 times smaller than the Spiro-OMeTAD [337]. PTAA expands half as much as Spiro-OMeTAD with temperature and has a higher thermal stability. The low E value also indicates that it is a very elastic material that does not undergo permanent deformation easily. The ITO electrode is therefore subjected to much less stress and does not peel off.

5.1.2.2 Electrical properties

The AY45 batch is composed of 7 STPC with Spiro-OMeTAD and 7 with PTAA as HTL. ITO deposition is performed in the same way on STPC with PTAA as with Spiro-OMeTAD, i.e. 100 min at 50 W at 2 mtorr pressure and under the same temperature. Fig. 5.3a shows the dispersion of the electrical properties measured by IV after stabilization (here 9 days after the synthesis). These results are compared with those of 4 opaque reference perovskite cells using PTAA as HTL.

It clearly appears that the STPC with PTAA have a much lower dispersion than the one with Spiro-OMeTAD (σ = 2.19 vs. 5.95) but remains higher than the opaque reference cells (σ = 1.09). This is directly caused by a much lower dispersion of Voc and FF, while the Jsc are comparable. Three distinct populations can be distinguished. The first is made up of cells with an efficiency of less than 10% and is only present for STPC with Spiro-OMeTAD. This behaviour is reminiscent of the shunted STPC of Chapter 3, characterised by either a low FF and Voc. The second population, the most important one, groups the STPC that have performances close to 12.5% which is close to the average efficiency of PTAA STPC (12.7%). Finally, the last population gathers the two best STPC around 17% with Spiro-OMeTAD as with PTAA and which are thus close to the performances of the opaque reference cells. The best FF are reached by cells with Spiro-OMeTAD (73% vs. 68%). Thus, within the same batch, PTAA STPC have better reproducibility than Spiro-OMeTAD STPC and are able to achieve equally high performance.

Fig. 5.4a shows the IV of the best cells obtained with each condition from any batch. We can see here that the best STPC with PTAA and Spiro-OMeTAD have an almost identical behavior. The hysteresis is slightly more pronounced in the case of the PTAA STPC (1.2% difference in efficiency between RV and FW scan, vs. 0.3% for the Spiro-OMeTAD). The EQE obtained are presented in Fig. 5.4b and are comparable between the two types of HTL. In both cases, the integration of the EQE gives a smaller Jsc (18.39 and 18.34 mA.cm^{-2}) than that measured at the IV (21.84 and 21.46 mA.cm^{-2}). So it seems that we have a photogeneration dependent charge collection in both cases.

STPC with PTAA are therefore generally more resilient to temperature and sputtering than STPC with Spiro-OMeTAD, as evidenced by the electrode grip and the lower dispersion of electrical results. The best STPC are equivalent to the one obtained with Spiro-OMeTAD, so the use of PTAA seems to be a good solution to improve the process.

(a)

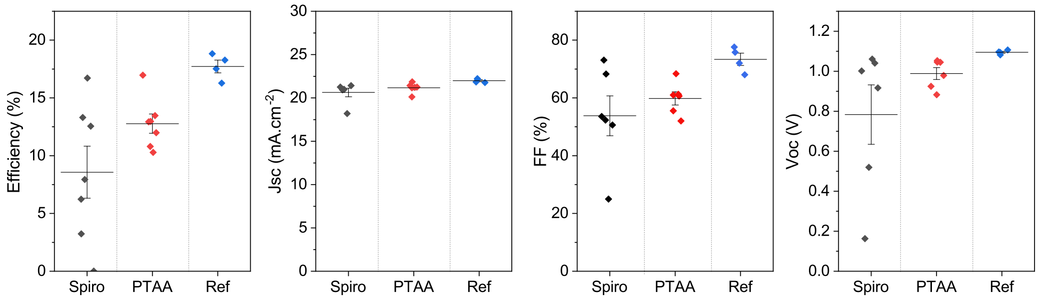

Figure 5.3: Dispersion of the electrical properties of AY45 STPC with Spiro-OMeTAD or PTAA as HTL, after stabilization time (9 days).

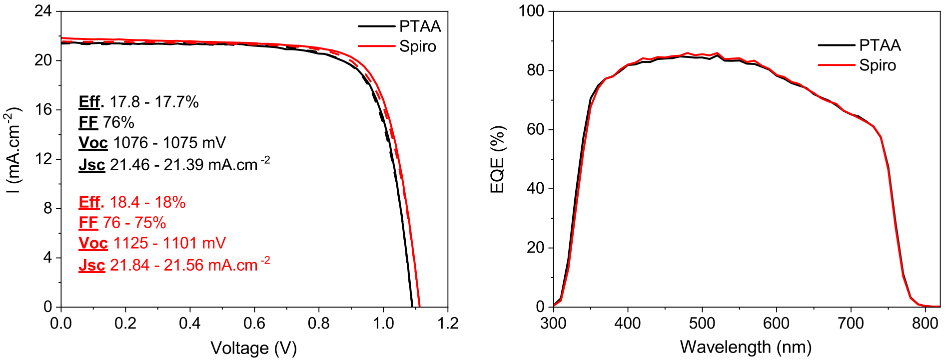

(a) (b)

Figure 5.4: (a) IV curves under illumination of the best STPC with both type (AY10-b-09 for Spiro-OMeTAD and MA17-08 for PTAA), after stabilization time. (b) EQE spectra of some AY45 STPC after stabilization time.

5.1.2.3 Reproductibility of PTAA based solar cells

Fig. 5.5a, b, c and d shows the dispersion of electrical properties measured by IV for STPC with PTAA as HTL after stabilization, grouped by batch and synthesized each time under the same conditions. The grey stars show the average values obtained for the opaque reference cells at each time. Similar scatter plots for the opaque cells can be found in Appendix B, as well as a summary of all the batches discussed in this section.

Concerning the opaque reference cells, some batches like MP16, MP39 and MA17 have a very low dispersion ($\sigma = 0.39$, 0.76 and 0.66) unlike MP22 and MP23 ($\sigma = 1.93$ and 2.36). Between the batches the average efficiency varies between 10.6 and 18.2% (9.7 and 18.3% with Spiro-OMeTAD) and σ reach 1.2 on average over all batches (1.71 with Spiro-OMeTAD). Thus, the dispersion observed between batches is comparable to that observed when Spiro-OMeTAD is used as HTL. This obstacle to batch-to-batch reproducibility is documented in the case of PTAA. This may be due to significant variations in the chain lengths of the polymers and the content of metal impurities in the different components of the final spin-coating solution. These variations between different batches when changing solutions can significantly affect their electronic and, to some extent, morphological properties [330, 338]. Variations in these parameters are not usually completely reported by the supplier and are costly to control precisely.

On the other hand, if we are interested in the dispersion of STPC for the same batches, the results are very different from those obtained with Spiro-OMeTAD presented in Chapter 3 Section 3.1.3.2 and confirms the phenomenon observed in the previous section on batch AY45. The dispersion within a batch of STPC is close to that observed on opaque cells ($\sigma = 1.36$ on average over all batches), compared to STPC with Spiro-OMeTAD ($\sigma = 3.15$). This dispersion is mostly caused by a dispersion of the FF and then by a slight variation of the Voc within the batches. In contrast to the Spiro-OMeTAD based batches presented in Chapter 3 Section 3.1.3.2, the Jsc never shows a significant dispersion and is constant between the batches presented here, except in the case of AY50 which had a synthesis issue.

The absence of cells with low performance compared to the whole batch is also noticeable, contrary to the Spiro-OMeTAD based STPC. Only the AY50 batch, which had a synthesis issue, has cells with an efficiency below 10%. Only two populations can be distinguished in the case of the PTAA-based STPC and they are not necessarily present in each batch. Batches AY43, AY45 and AY46 are composed of STPC with an efficiency around 12.5%, much below the opaque reference cells. In contrast, batches MP16, AY41 and AY48 have the work best cells with performance very close to the opaque reference cells. Finally, some batches (MP22 or MA17) include gold references in which the efficiencies are lower than STPC, which can be partly explained by too much humidity in the laboratory, which affects opaque cells more than STPC.

Moreover, the difference in efficiency between STPC and opaque reference cells is on average 1.6% in a batch, while it was 4.3% with Spiro-OMeTAD. The STPC have therefore a performance closer to the reference opaque cells with a similar dispersion when the PTAA is used in HTL.

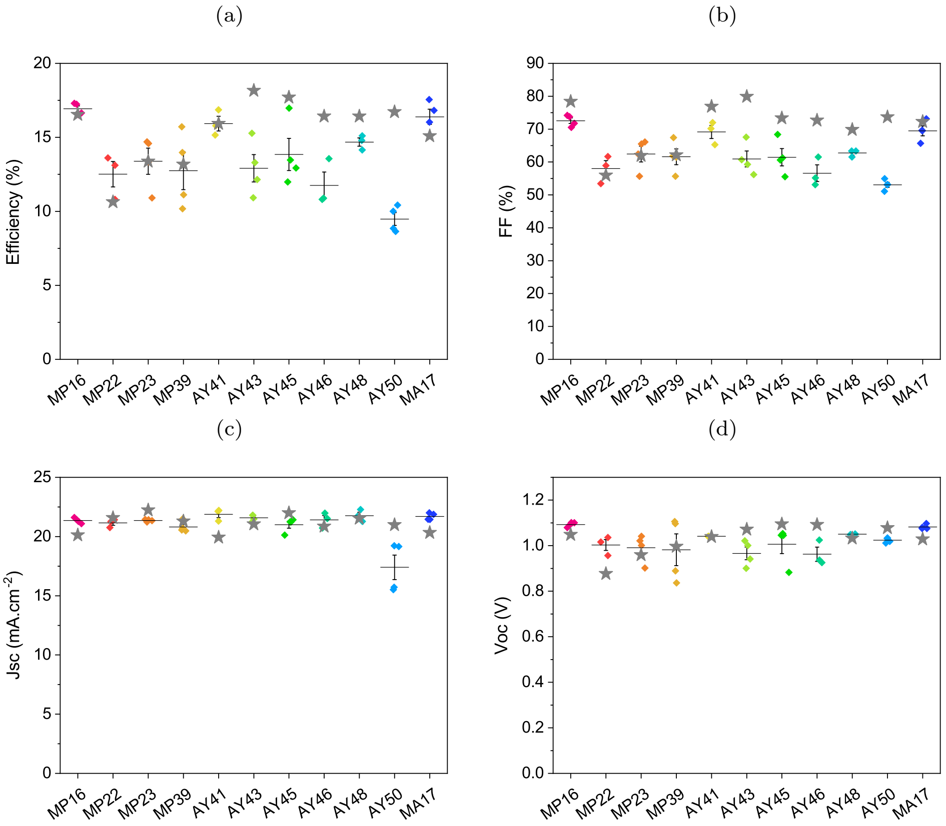

Figure 5.5: Dispersion of the electrical properties (a) efficiency, (b) FF, (c) Jsc and (d) Voc of STPC with PTAA as HTL from different batches. Grey stars represent the average of opaque perovskite cell values for the same batch.

5.1.3 Evolution in time as a function of the synthesis condition and storage

In order to study in more detail the PTAA/ITO interface and the evolution of the performance of STPC with PTAA as HTL, we look at the evolution of the kinetics on the usual structure mentioned above and when one of the two layers is modified (sputtering process or dopants) or when the storage conditions change.

5.1.3.1 S-shape on PTAA-based solar cells

Fig. 5.6a represents the dispersion of the electrical properties of the STPC of batch MP23 the first day after the synthesis and 30 days later. Between measurements, the cells are always stored under vacuum and in the dark. As for the STPC with Spiro-OMeTAD, the STPC with PTAA presents an important evolution of their electrical property in time and requires a time of stabilization. This evolution allows a gain of +5.8% on the average efficiency in RV, and +6.9% in FW, via the significant increase in FF (+17% and +24% respectively) and Voc (+109 mV in both cases). These improvements tend to reduce the hysteresis: 1.7% difference in average efficiency between RV and FW scans just after synthesis and only 0.5% after 30 days. Nevertheless, the dispersion does not evolve between these two periods ($\sigma = 1.9$). This phenomenon does not occur with opaque cells, which reach their maximum performance within a few days of synthesis.

As can be seen in Fig. 5.6b, the IV (MP23-17) shows a characteristic S-shape, synonymous of a non-ohmic contact where the interface effect is generally considered to be the main cause, just after the synthesis and which disappears with time [244, 245]. In response, the FF and Voc increase (+22% and +190 mV) and result in a significant increase in efficiency (16.1% vs. 8.9%). The hysteresis disappears in the course of time as expected.

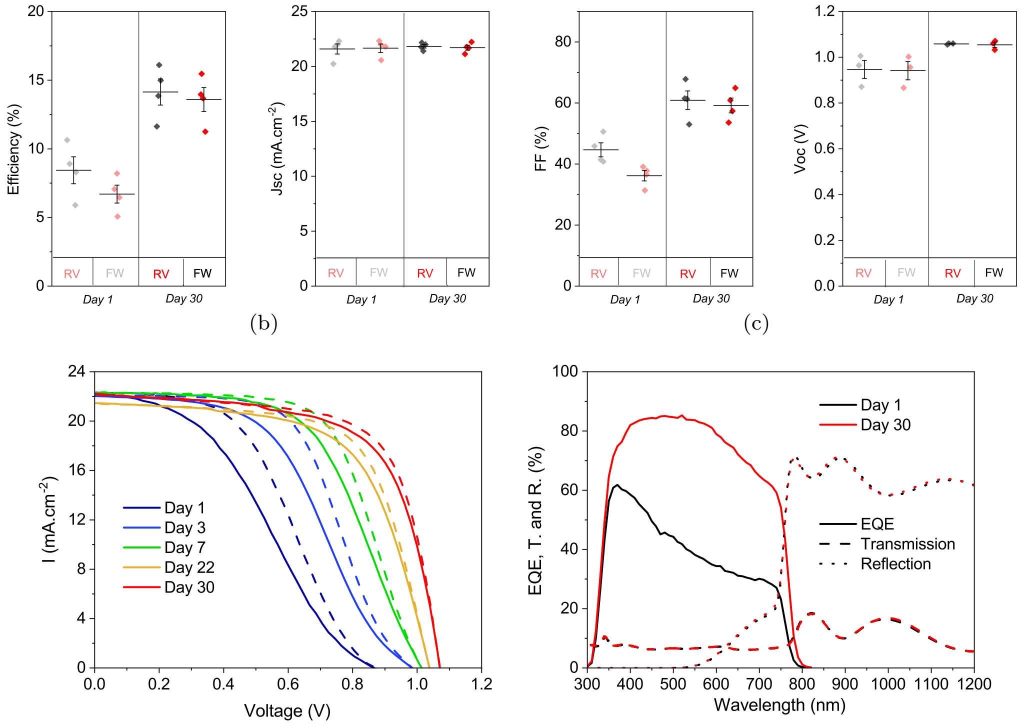
(a)

(b)

(c)

Figure 5.6: (a) Evolution of the dispersion of the electrical properties of MP23 STPC, first day after the synthesis and 30 days later. (b) IV curves under illumination and (c) EQE, transmission and reflection spectra of a MP23-17 STPC with PTAA as HTL, first day after the synthesis and 30 days later.

This evolution is also visible on the EQE spectrum as shown in Fig. 5.6c, while the Jsc on the IV does not evolve, which suggests a barrier for the photo current which is large under low light intensity or monochromatic illumination. As for Spiro-OMeTAD-based STPC in Chapter 3 Section 3.1.3.3, it can be due to a large number of micro shunts. This evolution is not perceptible on the spectrophotometric measurements. The transmission and the reflection do not evolve at all, either in terms of intensity or of shift of the interference patterns. No unusual evolution could be observed with XRD, confocal and SEM measurements.

The tests performed with Spiro-OMeTAD in Chapter 3 Section 3.3 allowed us in parallel to show that this effect is attenuated with the use of metallic buffer at the HTL-ITO interface, and that this phenomenon could not be directly related to a modification of the lateral resistivity of the ITO nor to an increase of the resistance of the Spiro-OMeTAD and its interface for electron transport. However, TLM tests were carried out on incomplete structures without perovskite, TiO$_2$ or TEC-7 substrate and an interaction with these layers in STPC cannot be excluded. Sputtering therefore seems to be a source of temporary degradation of STPC here too.

5.1.3.2 ITO bilayer and sputtering degradation

The PTAA has a higher resilience than the Spiro-OMeTAD to the heating caused by the sputtering. It is now possible to evaluate the effect of an ITO bilayer on the S-shape (this led to a detachment of the electrode on Spiro-OMeTAD, see Appendix E). The idea is to create an ITO buffer by performing a first ITO deposition at low power in order to degrade as little as possible the lower layers. Thus, we can check if the appearance of an S-shape on the STPC is linked to the power of sputtering during the first minutes of deposition. On 4 STPC of the AY41 batch, a first ITO layer is realized at low power (25 W) during 10 min before proceeding the standard ITO deposition, i.e 100 min at 40W.

In parallel, Spiro-OMeTAD and PTAA share the need to be oxygenated on the surface to allow an optimal contact with the top electrode. Our hypothesis is that ITO sputtering on STPC destroys the thin oxidized layer of HTL during the first minutes of deposition, which then regenerates via internal ionic migration or external input. Therefore, the S-shape can be impacted if oxygen is more present at the interface. For this purpose, 4 other STPC also receive an ITO buffer but this time with a higher oxygen content (added to the plasma at 0.16% compared to Ar, see Appendix F for the detailed properties of this layer). These 8 cells are compared to 4 STPC without buffer. Fig. 5.7a, b, c and d show the dispersion of electrical properties measured by IV for the STPC of this batch.

It is important to mention again that this batch has a higher dispersion than the others. It clearly appears that the use of an ITO buffer allows to improve significantly the efficiency from the second day after the synthesis (13.2% vs. 9.8% in average), thanks to the improvement of the Voc (+103 mV) and FF (+6%). So once again, these two parameters determine the efficiency while the Jsc does not evolve. 5 days after the synthesis, the STPC continue to evolve as usual, but in a less marked way, and reach an average efficiency of 15.1% (12.2% without buffer layer). Thus, the ITO buffer layer really allows to protect the interface with the PTAA and reduces the impact of the S-shape phenomenon without making it disappear (+1.9% of efficiency in 3 days). Unfortunately, these cells could not be measured electrically over time, so it is not certain that the stabilisation plateau has been reached.

Concerning the buffer with a higher oxygen content, it seems to degrade the electrical performances compared to the undoped buffer (10.9% vs. 13.2% in average) the first day after the synthesis, even if the performances remain higher than when the ITO is deposited as a in single layer. However, the evolution at day 5 seems on average more important with a very clear increase of the Voc (+177 mV) which was initially lower than the ones for the two other categories of STPC. Thus the presence of oxygen in the sputtering plasma does not result in better performing STPC at the end of the synthesis, but it does allow for greater recovery. It may be possible for oxygen to migrate from the ITO layer to the PTAA layer and this may be more important in the case of an oxygen-enriched ITO layer.

This study confirms the impact of the sputtering in the performance obtained on STPC and again the interest of using a buffer, here in ITO. On the other hand, the addition of oxygen at the PTAA/ITO interface does not improve the overall performances.

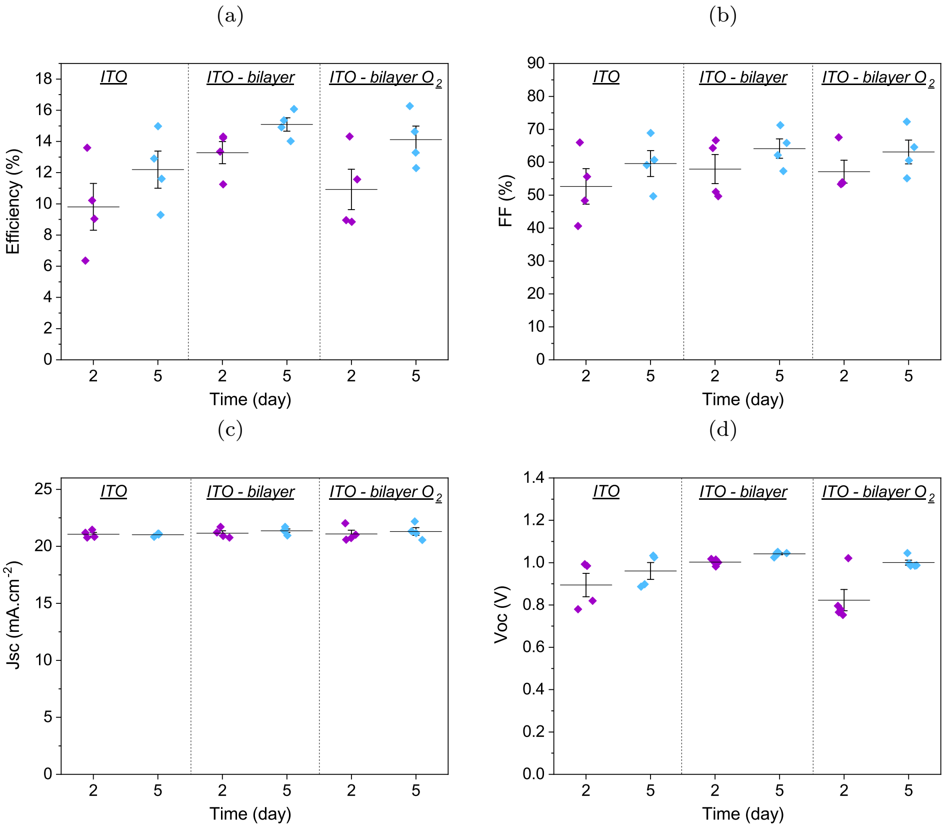
(a)
(b)
(c)
(d)

Figure 5.7: Dispersion of the electrical properties ((a) efficiency, (b) FF,(c) Jsc and (d) Voc) of AY41 STPC with PTAA as HTL, and a mono- or bilayer of ITO, with oxygen added to the plasma in certain cases, second day after the synthesis, and 5 days later.

5.1.3.3 Effect of other dopants (F4TCN, CuI and CuSCN) for PTAA synthesis

PTAA and Spiro-OMeTAD are synthesized with identical dopants: LiTFSI and t-BP. LiTFSI is especially used to allow the oxidation of these two HTL and to improve the hole mobility. This phenomenon of S-shape has not been observed with the use of CuSCN bulk as HTL (study not presented here as it was performed on module type samples). In parallel, Lee et al. have shown a similar S-shape phenomenon on their opaque perovskite cell (silver electrode with the Spiro-OMeTAD) which is resolved with time too. XPS and UPS analyses evidence the role of deoxygenation on the surface of the Spiro-OMeTAD just after the silver electrode deposition and which then disappears with time [339]. They point to a particular reaction of Ag to contact with Spiro-OMeTAD dopant normally responsible for the oxidation of HTL (LiTFSI).In order to verify if the same kind of phenomenon occurs in our structures, we replace in the MP22 batch the LiTFSI and t-BP dopants by 3 other dopants: F4TCNQ, CuI and CuSCN. F4TCNQ (2,3,5,6-tetrafluoro-7,7,8,8-tetracyanoquinodimethane) is regularly used as a dopant of PTAA in inverted p-i-n structures in the literature for enhancing conductivity [165, 340–342]. It was first introduced by Wang et al. into PTAA in an inverted perovskite cell and successfully reduced device series resistance by a threefold amount [342]. Its concentration (3%wt) was optimised on opaque perovskite in a study not presented here. On the other hand, copper salts such as CuSCN and CuI have already been demonstrated to be good HTL layers for perovskite cells due to their high conductivity, solution processability, and good stability[343, 344]. It has also been shown that they can be good dopants for Spiro-OMeTAD and PTAA, which can effectively improve the performance of standard and inverted perovskite cells [345]. The preparation and concentration of CuSCN and CuI (2 and 6%wt respectively) were based on the work of Liu et al [346].

Fig. 5.7a, b, c and d show the dispersion of the electrical properties measured by IV for each type of STPC of batch MP22. The performance for cells doped without LiTFSI/t-BP is much lower (3.4%, 5% and 6.4% of average efficiency for F4TCNQ, CuI and CuSCN doping respectively, compared to 10.6% for STPC LiTFSI/t-BP doped). This lower efficiency is mainly caused by a drop in FF, inferior to 40%.

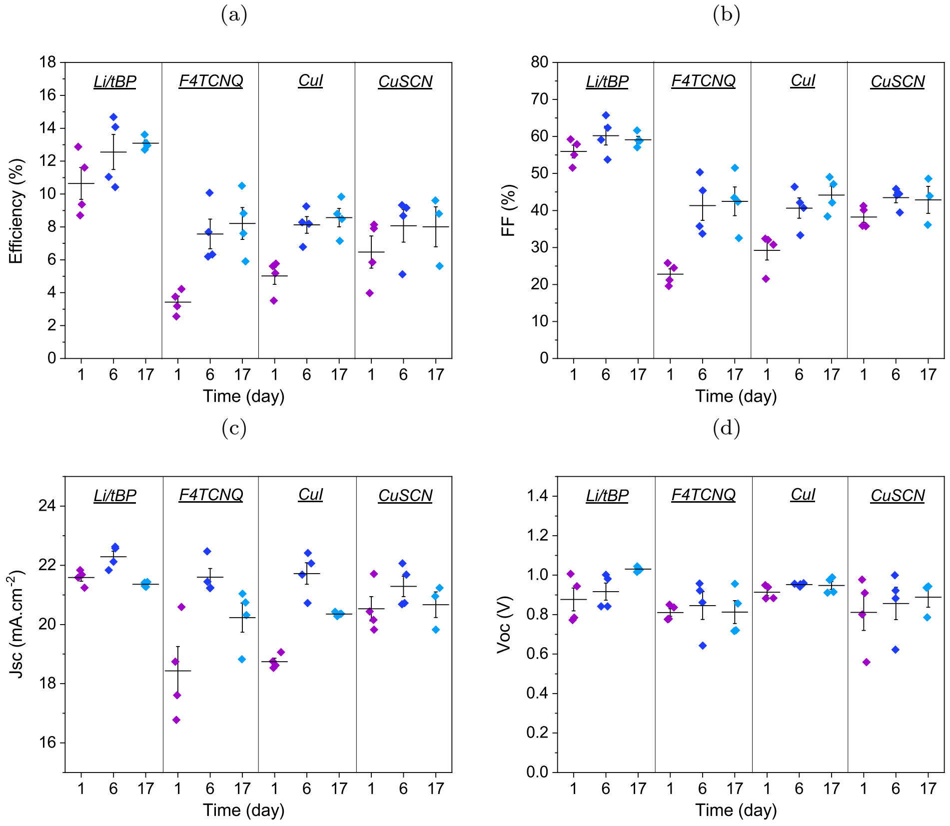
(a) (b)

(c) (d)

Figure 5.8: Dispersion of the electrical properties ((a) efficiency, (b) FF,(c) Jsc and (d) Voc) of MP22 STPC with PTAA doped with Li/t-BP (usual dopant), F4TCNQ, CuI or CuSCN, first day after the synthesis, 6 and 17 days later.

As observed so far, the Jsc evolves very little within the different categories except for the F4TCNQ-based STPC where it increases by more than 3% between the first and the sixth day. Nevertheless in Fig. 5.9a, b, c and d, the S-shape is present for all STPC just after the synthesis and only completely resolves 17 days later for the one doped with LiTFSI/t-BP and CuI. An improvement in efficiency is nevertheless visible for each group of cells, also directly caused by the attenuation of S-shape and the increase of FF. As there has been no optimisation of the concentration of these dopants prior to this batch, these results could be improved by slightly modifying the concentrations.

Unless each dopant used reacts chemically in the same way to the ITO electrode, it is more likely that the presence of the S-shape is not related to a direct interaction between the dopants and the ITO, as in the case of the silver electrode and the Spiro-OMeTAD of Lee et al [339]. We can again assume that this temporary degradation is more related to a local degradation of the interface between the HTL and the ITO.

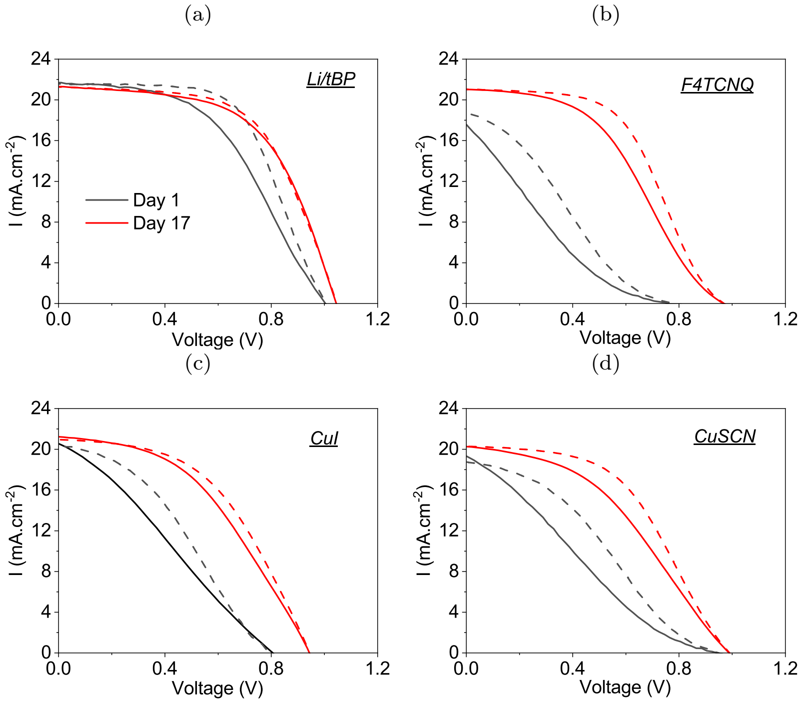
(a) (b) (c) (d)

Figure 5.9: IV curves under illumination of MP22 STPC with PTAA doped with (a) Li/t-BP (usual dopant), (b) F4TCNQ, (c) CuI or (d) CuSCN, first day after the synthesis and 17 days later.

5.1.3.4 Vacuum and dry air storage

If the presence of oxygen in the sputtering plasma does not result in better performing STPC at the end of the synthesis, it is possible to check if this oxygen contribution can come from an external source. In the AY45 batch, the STPC were separated into two groups of 4 cells each: half were aged in the usual way under vacuum and the other half was placed in an atmospheric pressure chamber with controlled humidity (5%) in order to degrade the perovskite layer as little as possible. Fig. 5.10a, b, c and d show the dispersion of electrical properties measured by IV for the STPC for this batch.

Until 2 days after the synthesis, STPC are all stored under vacuum and have a similar average efficiency (7.1% and 6.8% respectively). The STPC stored under dry air have an evolution of their efficiency faster than the others from the 5th day after the synthesis (12.8% vs. 8.9%). Finally, the dry air allows the STPC to reach their maximum efficiency more quickly (15.3%), here 9 days after the synthesis, while those stored in vacuum continue to evolve 4 days later (13.8%). The maximum efficiency of the vacuum cells is slightly lower than that of the dry air cells due to one cell at 11.2% which brings down the overall average. The other STPC have values comparable to the other category. We note however that the Jsc of STPC stored under dry air does not reach that of the cells under vacuum (21.3 vs. 21.7 mA.cm^{-2}), it is possible that the low ambient humidity degrades nevertheless slightly the perovskite layer. Fig. 5.10e shows the IV RV scan of the different STPC from batch to day 5. The cells under dry air do not have any more S-shape even if their FF has not yet reached their maximum while STPC under vacuum still have this atypical behavior.

In conclusion of this section on the evolution of the S-shape, we could show that only the storage under dry air allowed to accelerate its disappearance. We also showed that by using a first ITO deposit by very soft sputtering as a buffer, we limited the impact of the S-shape and the recovering was consequently less marked. This is in line with the hypothesis that sputtering would degrade the PTAA very locally on the surface, where it is supposed to be oxidized. The observed recovering would then come from an external source (ambient air) and infiltrate through the surface or sides of the cell. Further characterization must now focus on the PTAA/ITO interface to try to reveal this mechanism.

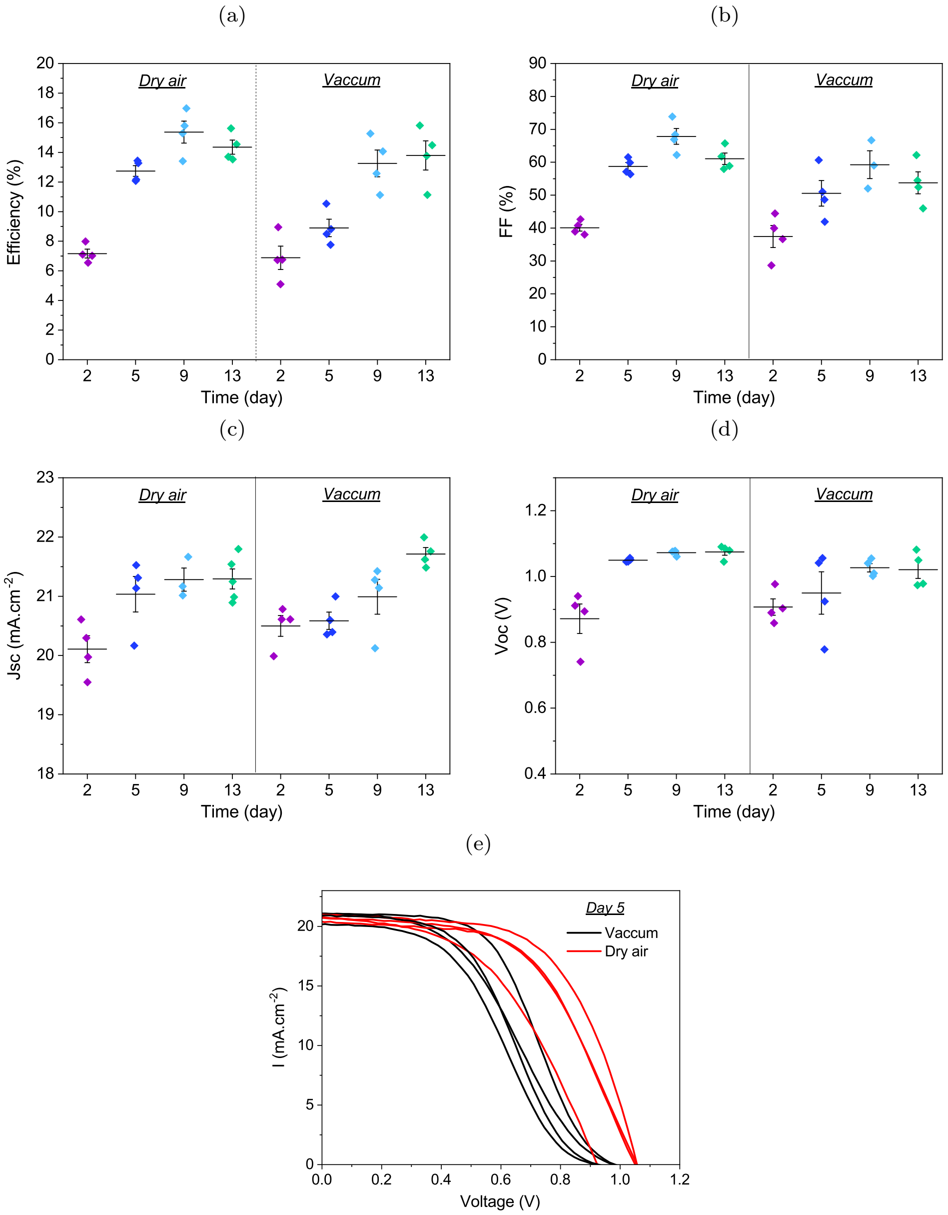

Figure 5.10: Dispersion of the electrical properties ((a) efficiency, (b) FF,(c) Jsc and (d) Voc) of AY45 STPC with PTAA as HTL, stored under vacuum or in dry air after ITO deposition, second day after the synthesis, 5, 9 and 13 days later. (e) IV RV curves of AY45 STPC with PTAA as HTL, stored under vacuum or in dry air after ITO deposition, 5 days after the synthesis.

5.1.4 PTAA / ITO interface characterization

In order to better understand what happens locally at the PTAA/ITO interface, we have performed XPS measurements in depth and in time, as well as hyperspectral PL measurements. The idea is to investigated the composition of the PTAA/ITO interface and an time evolution of the cell quality in time.

5.1.4.1 XPS measurements

In order to confirm or not a very local migration of oxygen at the PTAA / ITO interface over time, XPS measurements have been performed on a stack similar to an STPC but on 16 cm^2. The latter is composed of a PTAA doped with LiTFSI/t-BP and a single layer of ITO. The measurements presented here are made 1 day after the synthesis of the sample and one week later, with the sample stored under vacuum in between.

5.1.4.1.1 Methodology

As the ITO layer is too thick to be etched into the XPS setup itself, the electrode must first be locally etched via GDOES sputtering. Surface XPS measurements are then performed in the crater formed to obtain chemical information, as well as chemical environments of elements. Sputtering of Ar is again used but this time in the XPS equipment to progressively etch the already formed crater. This process is repeated twice: 1 day after the synthesis of the sample and 7 days later.

Concerning the abrasion by GDOES, preliminary tests were performed to stop the sputtering before reaching the interface to preserve the integrity of the measured chemical information. It is necessary to be able to detect the precise moment of the etching of the PTAA/ITO interface, but the difficulty in this method of abrasion is that the center of the crater is deeper than its edges and the different layers are not reached at the same time at each point. Too fast etching results in a very noisy signal where the compositions of the different layers are superimposed on each other. It is then impossible to distinguish the different interfaces of the multi-layer structure. The use of a low power and pressure (17 W and 250 Pa), and a plasma composed only of argon allowed to obtain a clear appearance of elements and interfaces ITO / PTAA / Perovskite in crater n°1, as shown in Fig. 5.11a.

The ITO / PTAA interface is reached after 45 seconds as shown by the drop in the amount of indium detected and the parallel increase in carbon. The perovskite signal can be seen a few seconds later via the evolution of Pb, Br and I. Thus, this process is used for 38 seconds to form the first XPS study (crater n°2) and to get as close as possible to the PTAA / ITO interface, as shown in Fig. 5.11b.

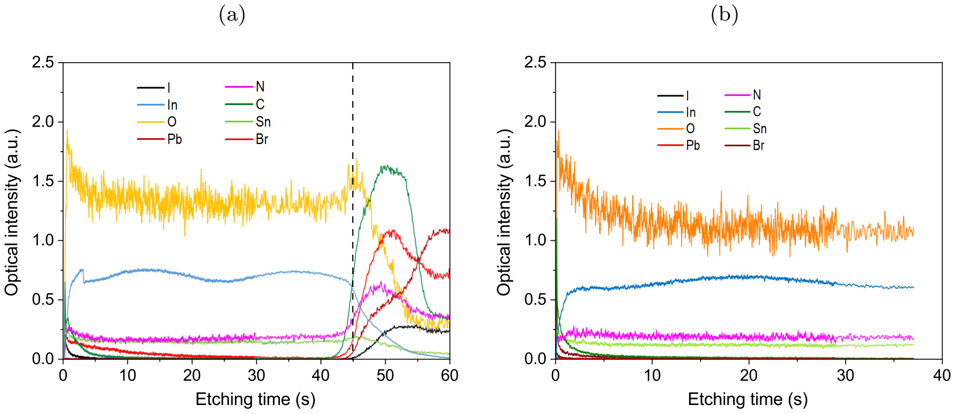

Figure 5.11: GDOES measurement during Ar sputtering and evolution of the optical intensity of different elements (a) until ITO / PTAA / Perovskite interfaces are reached at 45 seconds for preliminary tests and (b) before for the sample which is then characterized by XPS.

5.1.4.1.2 Analysis on the first day after the synthesis

A first surface XPS analysis is performed on the crater surface to study elemental compositions and chemical environments of elements in the ITO and then be able to detect finely the crossing of the ITO / PTAA interface with in-depth profiling measurements, see Table 5.1. The percentages are calculated from the survey spectra, which are wide range energy spectra that gather all the elements that can be present on the surface. Core levels in XPS use the nomenclature nl$_j$ where n is the principal quantum number, l is the angular momentum quantum number and j = l + s (where s is the spin angular momentum number and can be $\pm\frac{1}{2}$). In , O and Sn are expected, but C is also present due to contamination, as are I, Ar, Cl and Br.

Thanks to the high-resolution spectra, the decomposition of a peak allows us to obtain information on the presence of different chemical states in the sample volume. Table 5.2 shows the atomic percentage of the various contributions to I, In, Sn, C and O peaks. Cl and Ar are for example not taken into account because their percentage is low and does not interest us in the study. One can notice an oxidation of indium peak (InO), which is perhaps related to the formation of InO oxidized at ambient air or simply undoped areas with tin in the ITO bulk. The absence of any element of the PTAA layer confirms that the latter has not yet been reached.

XPS profiling is then performed in the crater n°2, the evolution of the atomic percentage of different elements can be followed on Fig. 5.12a as a function of the etching time. From 450 seconds of sputtering, the percentage of carbon and nitrogen increases while the oxygen and indium decreases, the interface with the PTAA is reached. At 600 seconds, iodine and lead start to be detected, indicating that the PTAA/perovskite interface has been reached. The peaks of carbon and nitrogen obtained after 600 s are presented in Fig. 5.13a and b, and the ratios corresponding for these two peaks only are presented in Table. 5.3. Ratio of C (PTAA) / C (C-NH$_3$) are equal to the theoretical ratio, no carbon or nitrogen oxide is detected at this level.

	Day 1 (%)	**Day 7 (%)**
I 3d$_{5/2}$	0.8	0.8
In 3d$_{5/2}$	28.8	29.3
O 1s	51.5	52.4
C 1s	14.7	13.9
Sn3d$_{5/2}$	2.0	1.9
Ar 2p	1.5	1.6
Cl 2p	0.8	-
Br 3d	-	0.1
Ratio O/In	1.79	1.79
Ratio In/Sn	14.4	15.42
Ratio O/(Sn+In)	1.67	1.68

Table 5.1: Atomic percentage decomposition of the different peaks of the element analyses from the survey spectra inside the ITO layer according to the XPS analysis the first day after the synthesis and one week after.

	Day 1 (%)	**Day 7 (%)**
I	0.7	1
In (ITO)	14.0	13.2
In (In$_2$O$_3$)	10.9	11.2
Sn (Sn-In)	0.7	1.1
Sn (Ox)	0.9	0.7
C (C-C)	12.2	7.6
C (RCOOH)	1.2	0.8
C (C-O)	2.8	2.6
C (C=O)	0.3	0.3
O (C-O)	5.3	8.3
O (O-H)	-	3.1
O (In-O)	35.7	24.5
O (In$_2$O$_3$)	15.4	23.4

Table 5.2: Atomic percentage after decomposition of the different analytical peaks of the elements I, In, Sn, C and O from the high-resolution spectra inside the ITO layer according to the XPS analysis the first day after the synthesis and one week after.

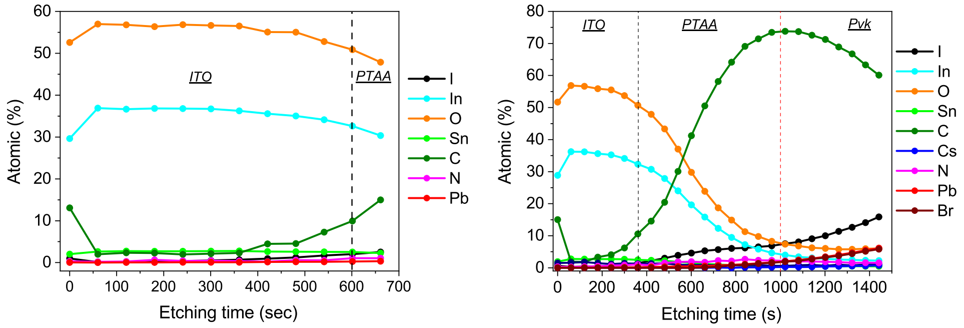
(a) (b)

Figure 5.12: XPS in-depth profiling etching and the evolution of the atomic percentage of different elements until the ITO / PTAA interface is reached at (a) one days after the synthesis and (b) one week later. ITO / PTAA and PTAA / Perovskite interfaces considered are marked by the black and red vertical dashed lines respectively.

	Day 1 (%)	**Day 7 (%)**	**Day 7 (%)**	**Theoretical ratio (%)**
	Interface	**Interface**	**PTAA layer**	**PTAA layer**
C (C-NH$_3$)	10.8	9.2	11	-
C (FA+)	1.4	-	2.5	-
C (C-O)	-	8	-	-
C (PTAA)	75.4	64.3	82.1	-
N (NH$_3$-C)	12.4	18.6	3.9	-
N (FA+)	-	-	0.6	-
C / N	7	4.4	21	21
C (PTAA) / (C-NH$_3$)	6.9	7	7.5	7

Table 5.3: Atomic percentage of specific element analyses (C and N) at the ITO / PTAA interface and inside the PTAA layer according to the XPS analysis the first day after the synthesis and one week after, and the theoretical corresponding ratio.

5.1.4.1.3 Analysis 7 days later

The same GDOES abrasion process is performed one week later on the same sample at another location (crater n°3). The analysis of the surface of the crater obtained by XPS shows a chemical environment very similar with the crater made one week earlier, see Table. 5.1. The composition in the bulk of the ITO layer has not changed.

XPS profiling is carried out in the crater n°3 and this time the interface with the PTAA is reached more quickly (360 seconds) due to a sputtering twice as powerful (1000 eV) in order to shorten the measurement time and to push the profiling into the perovskite layer, see Fig. 5.12b. The atomic ratios of indium (32%), oxygen (50%) and carbon (10%) are very close to those obtained during the first measurements with 600 seconds of abrasion, confirming a measurement at the same depth in the PTAA layer. The peaks of carbon and nitrogen obtained after 360 s are presented in Fig. 5.13c and d. The ratios are presented in Table. 5.3. The carbon profile clearly shows a new oxygen distribution compared to the profile observed one week before with a C - O contribution.

Fig. 5.13c and f show the peaks of carbon and nitrogen obtained by further abrading the crater (900 s) to enter the PTAA layer and thus moving away from the interface with the ITO. C - O contribution does not appear anymore at 900 s where the FA+ group signal attributed to the perovskite appears clearly in the nitrogen peak. The oxygen prevalence is therefore only at the interface and not in the whole PTAA layer.

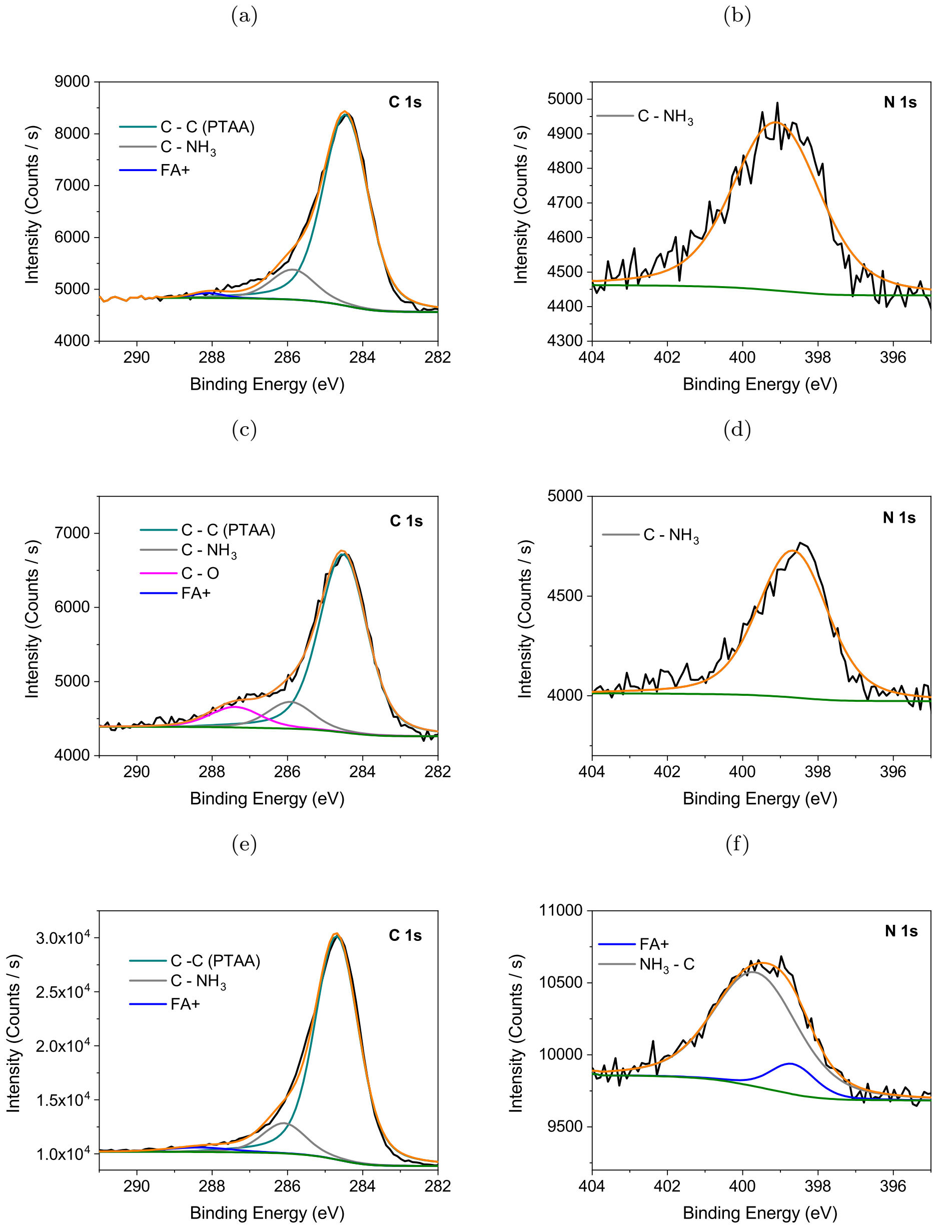
(a) (b) (c) (d) (e) (f)

Figure 5.13: De-convolution of XPS spectra of (a) C1s and (b) N1s at the ITO-PTAA interface (corresponding to 360 s in Fig. 5.12b), first day after the synthesis. De-convolution of XPS spectra of (c) C1s and (d) N1s at the ITO-PTAA interface and (e) C1s and (f) N1s in the PTAA layer (corresponding to 900 s in Fig. 5.12b), 6 days after the synthesis.

Another way to visualise this phenomenon is to superimpose the oxygen spectra. Fig. 5.14a shows the normalized spectra of oxygen obtained in the ITO bulk before and after aging, with no difference. However, in Fig. 5.14b, the normalized spectra of oxygen obtained at the interface with PTAA are compared and evidence an evolution of oxygen with time. The hypothesis of a non-immediate migration of oxygen at the ITO/PTAA interface in order to re-oxygenate the PTAA surface after sputtering is supported here. This migration appears only 7 days after the synthesis and it is visible only at the interface and not in the whole PTAA layer.

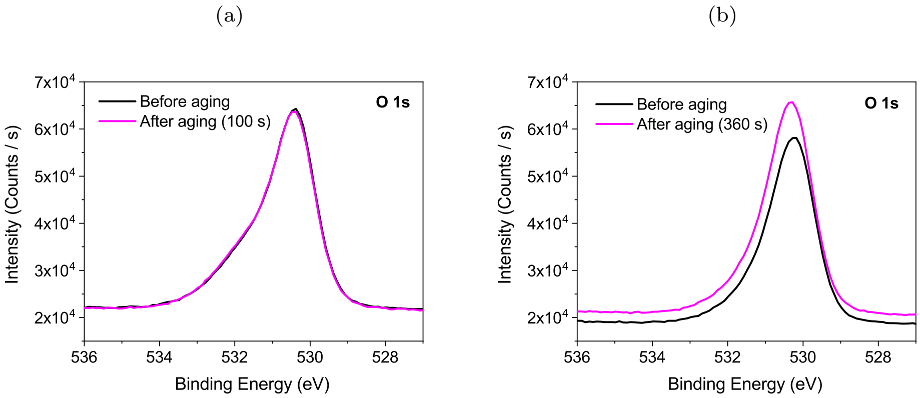

Figure 5.14: XPS spectra of O1s (a) in the ITO layer and (b) at the ITO-PTAA interface (corresponding to 360 s on Fig. 5.12b) first day after the synthesis and 6 days later.

5.1.4.2 Hyperspectral photoluminescence imaging

The objective of this study is to see if there is a visible spatial evolution of the quality of the cells over time via their photoluminescence. Hyperspectral photoluminescence imaging were performed on STPC type samples (similar to the one used for XPS) in 3 different sizes : 1, 2.25 and 4 cm^2 areas. There are kept in vacuum and in the dark between each measurement.

Fig. 5.15 represents the evolution of the position and intensity of the photoluminescence peak detected on the different samples 5, 7 and 13 days after the synthesis. We observe an increase in the intensity of the photoluminescence, which could be related to a gain of Voc. Over time, the PL evolves from the edge of the filters. In parallel, we also observe a red-shift of the gap of the perovskite, which starts also by the edge of the samples and propagates towards the center of the sample. This phenomenon seems to depend on the size of the samples and is more rapid for small samples. Thus in the center of the smallest sample, Eg increases on average from 761 to 765 nm between day 5 and day 13, while it increases from 756 to 760 for the largest sample.

In summary, XPS analyses showed oxygen migration over time at the PTAA/ITO interface. In parallel, hyperspectral measurements have shown a spatial evolution of the photoluminescence properties of the STPC in time. The hypothesis considered today is that the observed oxygen migration is possible via the contribution of this element from the external environment, as shown by the aging tests under vacuum and dry air in Section. ITO is a layer with recognized encapsulation properties, so oxygen may migrate from the edges of the electrode before propagating to the center of the sample.

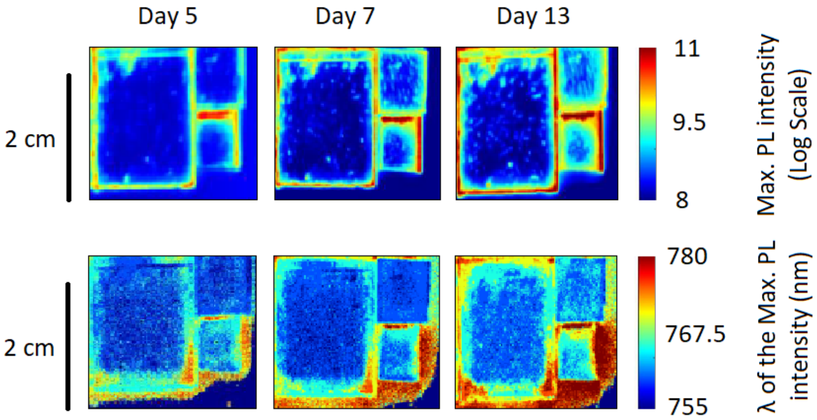

Figure 5.15: Hyperspectral photoluminescence imaging performed on STPC type samples of 1, 2.25 and 4 cm^2 areas as function of time after the synthesis. The upper images represent the evolution of the intensity of the detected photoluminescence peak and the lower ones, the position of the peak.

5.1.5 Encapsulation of PTAA-based STPC

After looking at the evolution of the electrical properties over time until the best performance is obtained on STPC with PTAA, we will focus in this section on their long term aging and the interest of encapsulating the cells.

We mentioned in Chapter 3 that the STPC have a stability in time largely superior to the opaque cells, which deteriorate via the migration of gold atoms in the perovskite layer. However, this behavior of STPC is only valid under vacuum or in a dry atmosphere. Fig. 5.16a and b show the aging of AY05b-15 with PTAA under illumination and in open air, its efficiency is monitored by MPP tracking. The efficiency definitely drops below 80% of its original value (13.1%) after 2 hours of continuous illumination. This decline is caused by both FF (-28%) and Jsc (-6.19 mA.cm^2). The photo in Fig. 5.16e, taken after 52h of tracking, shows that the orange perovskite layer has kept its absorbing properties by filtering the light. The degradation observed electrically is not visible to the naked eye. It can be assumed that the presence of water in the ambient air degraded the perovskite which is particularly sensitive to humidity.

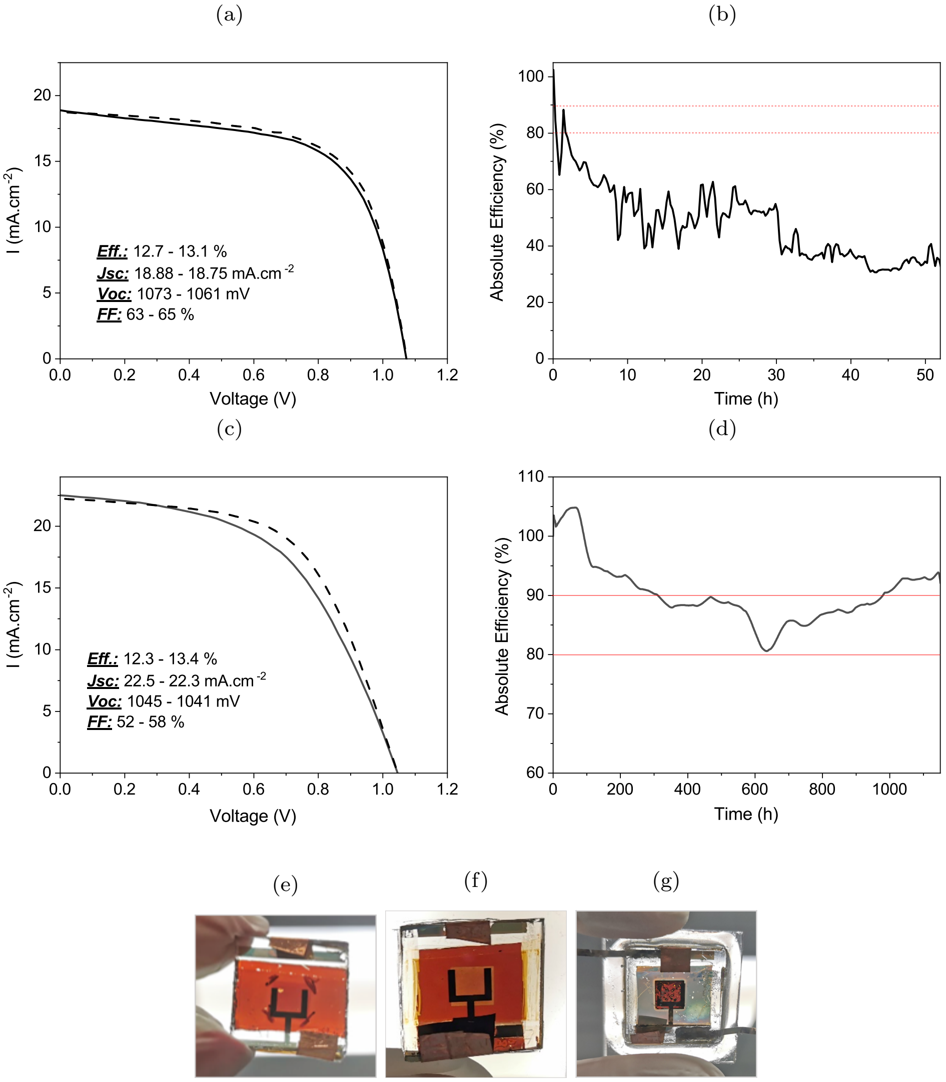
(a) (b) (c) (d) (e) (f) (g)

Figure 5.16: (a) IV curves of AY05b-15 STPC before MPP aging. (b) Evolution of absolute efficiency of AY05b-15 STPC after encapsulation process during 1150 hours, measured by MPP tracking under AM 1.5G illumination. (c) IV curves of MP23-13 STPC after encapsulation. (d) Evolution of absolute efficiency of MP23-13 STPC after encapsulation process during 1150 hours, measured by MPP tracking under illumination. (e) Pictures of back-illuminated AY05b-15 STPC after the 52 hours aging. Pictures of back-illuminated MP23-13 STPC (f) before and (g) after the 1150 hours aging.

Thus, the ability to effectively encapsulate the STPC cells is crucial for their aging over time and to protect them from moisture. A process of encapsulation was designed as follows. The electrical contacts are taken over with tin busbar, welded by ultrasonic welding. The cell is then encapsulated using a glass substrate with Surlyn contours (DuPont's ionomer resin-copolymer of ethylene and methacrylic acid). Surlyn has been used as an encapsulant in almost all organic electronic devices like OLEDs [347] and OPVs [348]. It has already been proven on small opaque perovskite cells [349, 350]. For example, Grancini et al. showed no loss of efficiency with a $MAPbI_3$ perovskite on small surface, even after one year when kept under sunlight (55 °C) [128]. This is one of the best stability found in the literature [350].

However, this process was not compatible with the use of Spiro-OMeTAD because it systematically caused the progressive detachment of the ITO electrode during heating, see Chapter 3 Section 3.2.2. On the other hand, this did not happen with PTAA and 4 STPC from the MP23 batch were therefore used to carry out a first encapsulation test and to observe the aging in ambient air and under illumination of the cells. As shown Fig. 5.16c and b, this process allowed to keep an efficiency at 93% of its maximum (13.4%) after 1150 h.

Fig. 5.16f and b show a photography before and after 1150 h of aging. The perovskite is completely degraded and became transparent except under the ITO electrode. The Surlyn-based encapsulation is therefore not sufficient to protect the perovskite layer but combined with the ITO which acts as a pre-encapsulating layer, the cell succeeds in maintaining its efficiency. Nevertheless, the success rate was low and the reproducibility poor, only few cells survive this process. A more efficient process developed for modules will be discussed in Chapter 7.

5.1.6 Conclusion on the use of PTAA as a replacement for Spiro-OMeTAD

In summary, PTAA is an easily synthesized thin film with no parasitic absorption in the infrared, making it completely compatible with tandem use. Furthermore, we have shown that the reproducibility of PTAA-based STPC is improved as compared to the use of Spiro-OMeTAD. The performance differences with the opaque reference cells are also reduced, and the STPC with PTAA have the potential to reach efficiency as high as the cells with Spiro-OMeTAD. The thermal resilience of PTAA also allows to consider encapsulation processes on STPC, and therefore to keep their performance in the open air and under constant illumination. On the other hand, the same phenomenon of S-shape appears on STPC with PTAA and Spiro-OMeTAD. Different tests and fine characterizations have shown that the disappearance of this phenomenon was linked to a local migration of oxygen from the ambient air to the HTL/ITO interface. Finally, we have demonstrated the ability to encapsulate our STPC when the PTAA is used as a HTL and to guarantee their durability over 1500 hours. In view of the results obtained with the PTAA, it was decided to use it as a reference instead of Spiro-OMeTAD for the rest of the results presented in this manuscript.

5.2 Replacement of the TiO_2 bilayer by SnO_2

The application of SnO_2 as an ETL was first demonstrated in dye-sensitized solar cells [351], but the initial studies on perovskite cells were almost concurrently carried out in many research teams such as Ke et al. [324] who reported an efficiency of 17.2%. The advantage of SnO_2 is its great diversity in terms of morphology (super planar to nanoparticle), crystallinity and deposition method (dry and wet routes), and there are many commercial solutions available today. However, a main issue with the use of SnO_2 as compact layers is that it suffers from degradation at high temperature, but this is also the case for perovskite layer [352]. Moreover, it is often deposited as a thin layer like compact TiO_2 and it is then necessary to ensure that it covers rough substrates like the FTO of TEC-7 substrate for example.

In this section, we will focus on SnO_2 in order to replace the TiO_2 bilayer as an ETL in perovskite cells. We will first detail its deposition method and its intrinsic properties on glass before looking at the replacement of the front electrode in FTO by other TCO on opaque structures. Finally, we will study the influence of SnO_2 on the optical and electrical properties of STPC.

5.2.1 Synthesis and optical properties of SnO_2 deposited on glass

SnO_2 is synthesized via Chemical Bath Deposition (CBD) which is a method that has already yielded particularly good perovskite cells (efficiencies superior to 20%) [353–355]. The CBD solution was prepared by mixing urea, HCl, thioglycolic acid, and $SnCl_2 - 2H_2O$ in 100 mL of de-ionized water. The CBD solution was loaded onto a glass reaction vessel and reacted at 90 °C until the desired pH is reached.

Freshly prepared chemical bath deposition solutions exhibit pH ≤ 1 and the pH increases as urea decomposes and releases OH–. The chemical bath deposition solution turns murky, owing to the formation of insoluble amorphous tin oxide species. Previously cleaned substrates are added to the vessel when the desired pH is reached. The pH of the reaction solution was monitored and the reaction was ended by removing the substrate at the target pH. After the reaction is completed, the substrates with SnO_2 were removed from the reaction vessel and cleaned via sonication with deionized water and IPA for 5 min each. The substrate were annealed in an ambient environment at 180°C for 60 min. The deposited layer has a thickness of about 40 nm.

The optical properties of the layer are first evaluated on 3 mm soda-lime glass. As shown in Fig. 5.17 the SnO_2 does not show any parasitic absorption even near to the UV region because of its optical gap at 3.9 eV, in contrast to TiO_2 (3.2-3.35 eV). On the other hand, its presence significantly amplifies the reflection and decreases the transmission, due to the refractive index contrast between SnO_2 and air. It is not a problem here as it is not representative of the final structure. In addition, this is consistent with the simulation performed in the previous chapter Section 4.2.4 with SnO_2 indices from the literature [197].

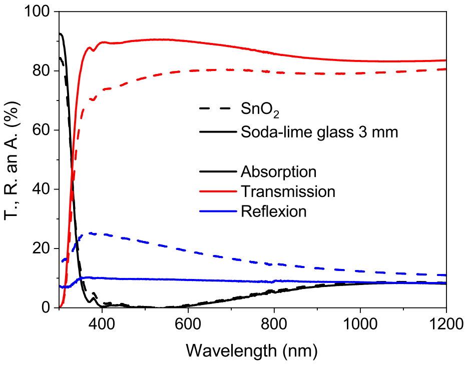

Figure 5.17: Transmission, absorption and reflection spectra of SnO_2 on 3 mm soda-lime glass, compared to the substrate alone.

5.2.2 SnO_2-based opaque perovskite cells

SnO_2 is a very thin layer and the roughness of the FTO on the TEC-7 substrate can be an obstacle to its use. In addition, the chemical sensitivity of other TCO to CBD acid should be investigated. For this reason, a batch of 32 cells was fabricated to compare the impact of different front side electrodes on the electrical performances of opaque perovskite cells. The synthesized cells are called MP45, -46 and -49.

5.2.2.1 Optical and electrical characteristics of different electrode: FTO, ITO and IZO

The TEC-7 substrate from Solems usually used with perovskite cells with the TiO_2 bilayer as HTL is used as a reference. It is composed of an FTO electrode deposited on a 3 mm soda-lime glass with a sheet resistance of 9 Ω.sq. A second commercial substrate called "ITO PGO" was used for comparison, it is composed of a 1 mm soda-lime glass and an ITO layer with a sheet resistance of 9 Ω.sq. We use in parallel our own substrates with an ITO electrode. The first one is called in this section "ITO std 100" and it is composed of a 1 mm soda-lime glass coated with an ITO layer deposited by sputtering at 45 W for 100 min and then annealed at 300°C for 1h. The optimisation and properties obtained through this annealing are detailed in Appendix C. We obtain a sheet resistance of 9 Ω.sq. The second one is called "ITO std 60" and differs from the previous one because the ITO deposition time was only 60 min instead of 100. The sheet resistance increases to 17 Ω.sq. Finally, we also make substrates with IZO as electrode on 1 mm soda-lime glass, the fabrication process is detailed in the next chapter, Section 6.1.3.1. It has a sheet resistance of 17 Ω.sq.

In the same way, all the depositions are also carried out or ordered on 3 mm soda-lime glass to compare its absorption to the TEC-7 substrate. ITO PGO and ITO std 100 have in the end an absorption almost similar to the TEC-7 in the infrared, see Fig. 5.18, while ITO is usually known to have a much better transparency than FTO in this region (-1.7% at 1100 nm). For the ITO std 60, it has a lower absorption in the IR (-9.3% at 1100 nm). Finally, the IZO substrate reveals a clear decrease of the parasitic absorption in the IR, as expected (-15.2% at 1100 nm).

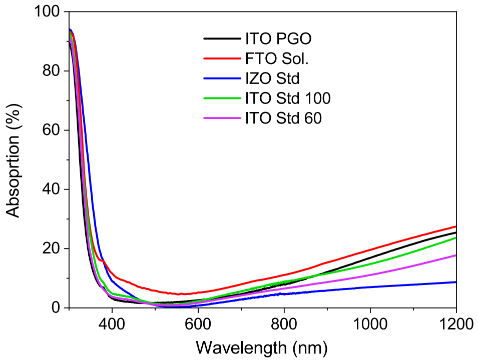

Figure 5.18: Absorption spectra of TEC-7 substrate (FTO) compared to ITO PGO, IZO, ITO Std 100 and 60 on 3 mm soda-lime glass.

5.2.2.2 Morphology of the opaque perovskite cells

SEM cross-section images are made after the complete perovskite solar cells have been deposited on the different electrodes FTO, ITO and IZO. Fig. 5.19d, b and c show that the SnO_2 was deposited correctly on the FTO, ITO PGO and ITO Std 100, and that the other layers also adhered correctly. Nevertheless, it is noted that TEC-7 has a much higher roughness than the other substrates and the SnO_2 layer is not flat on to of it. However, in the case of the IZO substrate, as shown in Fig. 5.19d, the electrode seems to have completely disappeared and the SnO_2 is directly on the glass. The CBD deposition seems to be too aggressive for the IZO which has dissolved completely because of its low chemical stability.

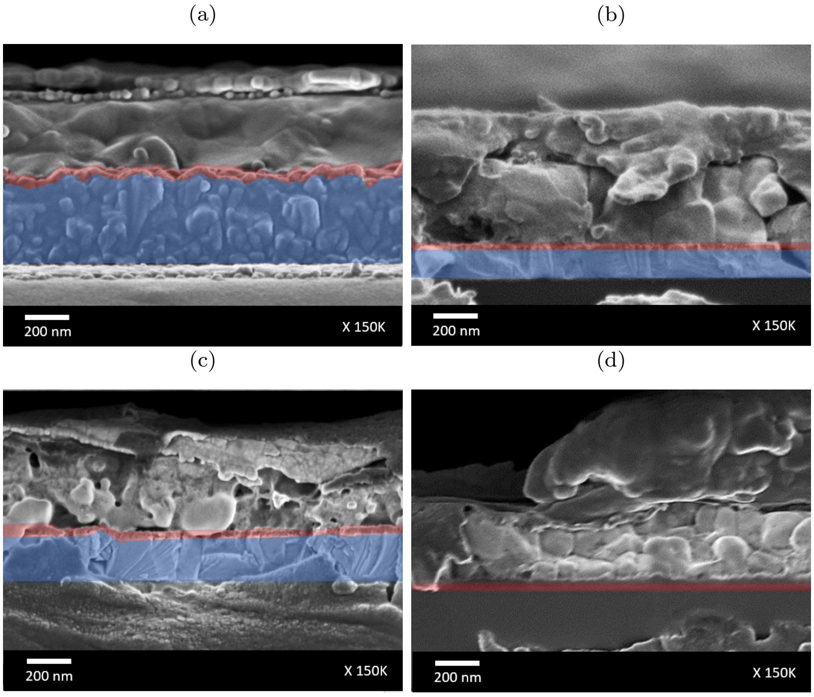

Figure 5.19: SEM cross-section image of STPC with (a) FTO TEC-7, (b) ITO PGO, (c) ITO Std 100 and (d) IZO substrates with SnO_2 as ETL. The red area is the SnO_2 layer and the blue area is the front electrode.

5.2.2.3 Electrical properties

Fig. 5.20a, b, c and d represent the dispersion of the electrical properties of the opaque perovskite cell of batch MP45-46-49. First of all, looking at the performances obtained on the reference cells with TiO_2 as the ETL, we observe that they are not very good with an average efficiency of 8.2% in FW scan, compared to the set of batches produced with PTAA, presented in Section 5.1.2.3 and Appendix B. This is caused by an unusually low Jsc (14.54 mA.cm^{-2} in FW scan), which may suggest a problem of synthesis of the perovskite layer. On the other hand, the higher quality of perovskite for the other cells suggests rather a specific concern of deposition of this layer on TiO_2 for the reference cells. The cells show a slight improvement over time (+1% for FW scan efficiency).

SnO_2 TEC-7 samples show a significant dispersion on the efficiency ($\sigma = 2.9$) caused by both FF and Voc, which are also on average lower than for the TiO_2 reference cells. Cells degrade rapidly over time and much like the references (-4.5% in FW scan). The roughness of the FTO and the thinness of the SnO_2 could be at the origin of an inhomogeneous coverage of the ETL on the electrode and generate additional resistance as well as a decrease in the reproducibility and diffusion of undesired elements.

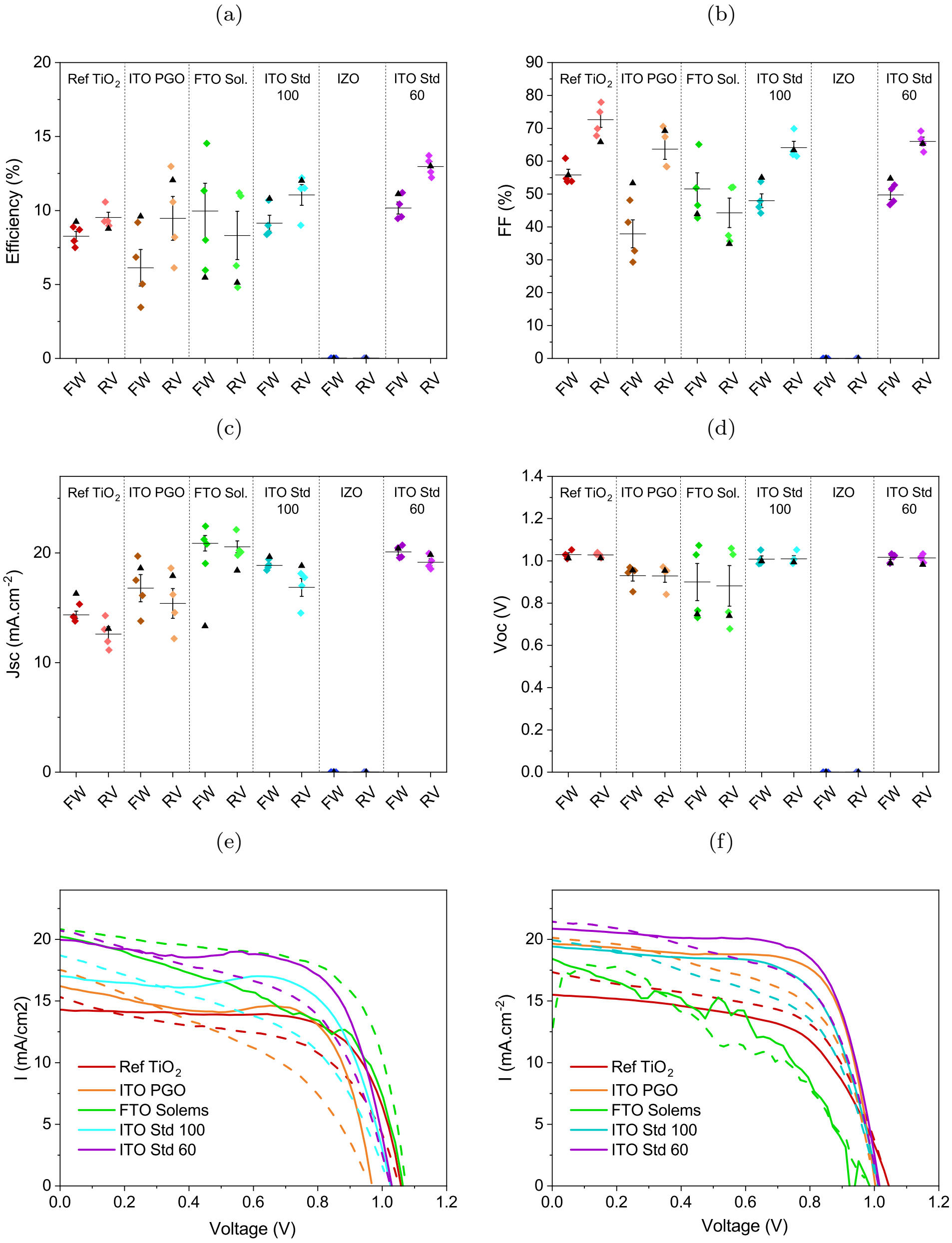
(a)

(b)

(c)

(d)

(e)

(f)

Figure 5.20: Dispersion of the electrical properties ((a) efficiency, (b) FF,(c) Jsc and (d) Voc) of MP45-46-19 opaques perovskite cells with TiO_2 or with SnO_2 as ETL, and different substrates : commercial ITO (PGO) and FTO (Solems), standard ITO and IZO deposited at IPVF, and a bilayer ITO+IZO. Black triangles represent the average values 7 days later. IV curves of some MP45-46-49 opaque perovskite cells (a) the first day after the synthesis, and (b) 7 days later.

Concerning the ITO PGO, efficiency is low on the first day after synthesis and particularly in FW scan (6.2%). It is primarily caused by a very degraded FF (37%). However, they have a fairly marked evolution in time (+3.5%) and are then more efficient than the SnO_2 and TiO_2 TEC-7 cells. The dispersion on the efficiency is even more important than for the TEC-7 ($\sigma = 3.7$) and an unusual morphology at the surface called cornflakes has been identified as responsible for the performance.

With ITO Std 100 and 60, we observe a good reproducibility and performances superior to the reference cells (9.1% and 10.2%). Their FF is lower but this is compensated by a better Jsc (18.86 and 20.02 mA.cm^{-2}). Thus, it seems that the morphology of our ITO is more suitable for SnO_2 deposition than the commercial ITO in this case. Moreover, the ITO std 60 min is sufficient to keep a correct FF and allows a better transparency in the IR because of its lower thickness. In the case of TCO deposited by sputtering, the absence of the IZO electrode observed in the SEM is confirmed here: none of the cells work.

Fig. 5.20e and f represent the IV of the best cells of each category, first day after the synthesis, and 6 days later. The cells do not show any S-shape as expected for opaque cells. Nevertheless, we notice some drops of the IV on the SnO_2 TEC-7 samples, which could correspond to the presence of a poor covering of the electrode by the SnO_2 and the presence of pinholes. The hysteresis remains important for all the cells 7 days later. Concerning all the cells using SnO_2 as ETL, except with IZO substrate, we can note that they have a higher average Jsc, but a lower FF and especially, a higher hysteresis. The use of SnO_2 seems to induce a higher series resistance, which may be related to a slightly too thick layer. Indeed, in the opaque devices presented in the literature, the structures reaching efficiencies above 20% have SnO_2 layers as ETLs with a thickness of 15-20 nm [76, 310, 356].

5.2.3 SnO_2-based STPC

5.2.3.1 Electrical properties

4 STPC using SnO_2 and ITO PGO (glass of 1 mm) as a substrate were fabricated on MP39 batch and compared to 4 standard STPC (TEC-7/TiO_2). Fig. 5.21a, b, c and d represent the evolution of the dispersion of the electrical properties of the STPC of batch MP39 over 20 days. Just after the synthesis and due to the use of ITO PGO, the dispersion of the STPC with SnO_2 is important ($\sigma = 5.1$ vs. 2.2) as we have underlined in the previous section. This dispersion is caused again by the Voc and FF. Nevertheless, one cell (MP39-07) have a better performance than the average of reference STPC with TiO_2 (11.8% vs. 10.1%).

This STPC has a slightly marked S-shape with hysteresis as shown in Fig. 5.21e. The time evolution of this cell is similar to the classical STPC with a progressive disappearance of S-shape associated with an increase of FF (+5%). Compared to the best reference STPC, the cell with SnO_2 has a lower Voc and a hysteresis still present after 20 days. Concerning the EQE of all the STPC in this batch, they are similar at 20 days as shown in Fig. 5.21f. Thus, STPC with SnO_2 as ETL have the potential to reach similar efficiency to conventional STPC with TiO_2. New tests will be necessary to stabilize the performances and see the efficiencies achievable with other types of substrates.

5.2.3.2 Optical properties and simulated tandem efficiency

TRA spectra of two STPC with TiO_2 or SnO_2 as ETL are shown in Fig. 5.22a and b. The STPC with SnO_2 uses the ITO PGO substrate of 1 mm. As in Section 5.2.2.1 during the deposition on glass, the presence of SnO_2 seems to be at the origin of strong reflection on the whole range studied. The latter even reaches 40% at 1200 nm. Thus, even if the ITO PGO substrate has an absorption similar to TEC-7 in the IR, the transmission of STPC is greatly degraded because of the interference patterns (49 vs. 70% at 900 nm).

In addition, a reflection twice as important is generated in front of the perovskite layer. This result, partially predicted by the simulation in Chapter 4, is potentially due to the absence of the SnO_2/SiO_2 bilayer between the glass substrate and electrode in the ITO PGO substrate. As show in Fig. 5.23, in addition to increasing the hardness of the glass and avoiding the diffusion of alkali oxides, the SnO_2/SiO_2 bilayer seems to play the role of an important anti-reflective coating in case of TEC-7. On STPC, it causes a decrease of 8% of total absorption at 550 nm. However, the Jsc of the STPC with SnO_2 is not

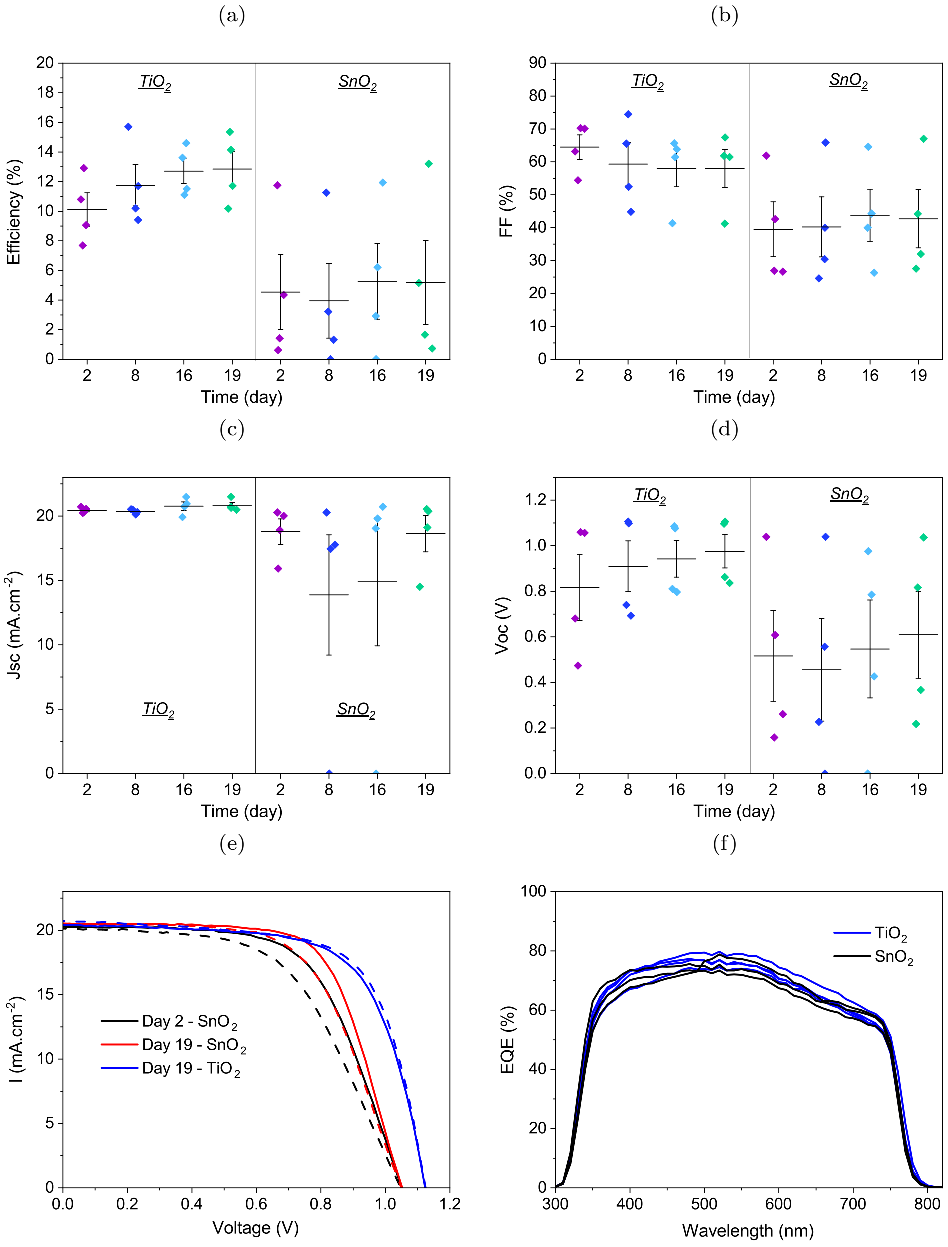
(a) (b) (c) (d) (e) (f)

Figure 5.21: Dispersion of the electrical properties ((a) efficiency, (b) FF,(c) Jsc and (d) Voc) of MP39 STPC with TiO_2 or with SnO_2 as ETL, second day after the synthesis, 8, 16 and 19 days later. (e) IV curves of MP39-12 STPC with SnO_2 as ETL, second day after the synthesis, and 19 days later, compared to MP39-08 STPC with TiO_2 as ETL. (f) EQE spectra of MP39 STPC with TiO_2 or with SnO_2 as ETL, made the second day after synthesis.

significantly lower than with TiO_2 as we saw in the previous section. Indeed, unlike TiO_2, SnO_2 does not show any spurious absorption over the whole spectrum and specially near to UV region. This certainly compensates for some of the losses due to reflection.

This lower transmission decreases the efficiency of the silicon cell placed at the back in tandem configuration. Based on the calculations presented in Chapter 4, this loss is estimated to 0.8% of efficiency in the case of an Al-BSF cell. Further tests must be conducted to see if this phenomenon is reproduced with our own ITO substrates that we would like to use in the future.

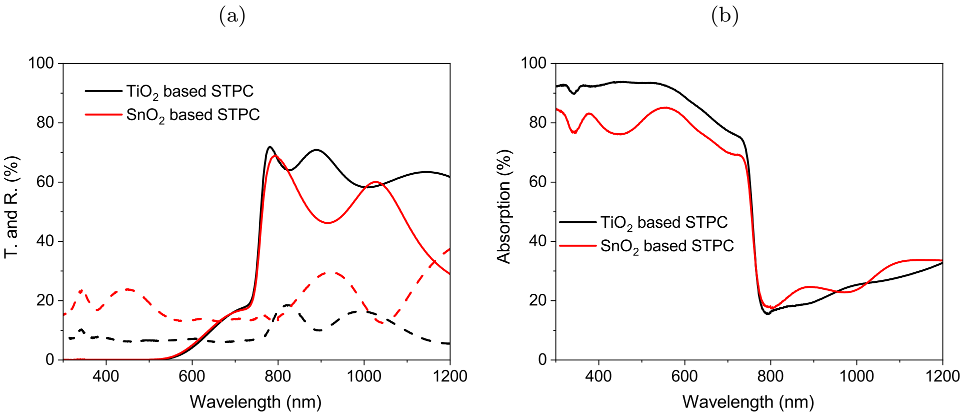

Figure 5.22: (a) Transmission, reflection and (b) absorption spectra of two STPC with TiO$_2$ or SnO$_2$ as ETL.

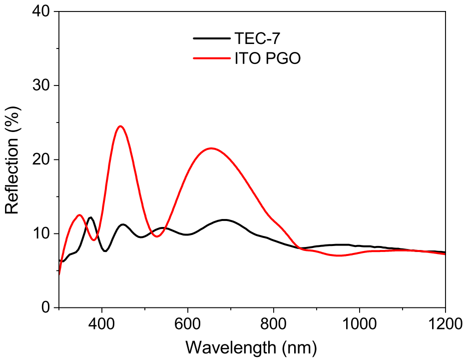

Figure 5.23: Reflection spectra of TEC-7 and ITO PGO substrate.

5.2.4 Conclusion on the use of SnO$_2$ as a replacement for TiO$_2$

SnO$_2$ showed interesting properties as an ETL. On opaque cells, it was found to be compatible with ITO substrate synthesized in our laboratory. However, its synthesis by CBD still shows some reproducibility problems which prevents today to consider the total replacement of TiO$_2$ in the baseline. Moreover, this type of deposition is very aggressive and destroys some TCO like IZO. Nevertheless, the first tests on STPC show that they have the potential to reach similar performances as cells with TiO$_2$ despite the use of substrates not adapted during these tests. The use of our own ITO seems to be the preferred way to guarantee a surface condition compatible with the SnO$_2$ layer.

Conclusion

In this chapter we have first investigated the replacement to replace Spiro-OMeTAD by PTAA in our STPC. These tests were successful and it allowed to reduce the dispersion of the performance of the STPC and at the same time, to get closer to the performance obtained with opaque cells. This was made possible by the intrinsic properties of PTAA which is a material more resistant to heat than Spiro-OMeTAD, and very elastic so it does not undergo permanent deformation easily. The ITO electrode is therefore subjected to much less stress and does not peel off as with Spiro-OMeTAD. Finally, PTAA has very interesting optical properties for use in tandem configuration. Thanks to its very low thickness, it has almost no parasitic absorption in the IR and therefore contributes to a better transparency of STPC. At this stage, we have chosen to replace Spiro-OMeTAD by PTAA in our perovskite cells.

An important part of our work was devoted to the understanding of the S-shape phenomenon which was already discussed in Chapter 3. By decreasing the sputtering power during the first minutes in order to avoid to damage the PTAA/ITO interface, we were able to mitigate this phenomenon, which highlights the direct responsibility of the energy power delivered by the sputtering. The aging under dry air also accelerates the disappearance of this phenomenon. On the other hand, the replacement of the PTAA dopants that caused its oxygenation on the surface did not result in the disappearance of the S-shape, neither the use of an oxygen-enriched plasma during the deposition of the ITO. These observations associated with XPS measurement allow to conclude to a local migration of oxygen to the PTAA / ITO interface after the sputtering in order to regenerate the upper oxide layer. The hyperspectral measurements have shown that this evolution is not spatially homogeneous and seems to come from the edges of the cell.

In a second step, we wanted to replace TiO$_2$ by SnO$_2$ in order to remove the technical barriers that prevented the future use of TCO more transparent in IR than FTO. SnO$_2$ is deposited as a very thin layer and does not show any particular parasitic absorption. Compatibility tests of this layer with different types of front electrodes showed that it was particularly sensitive to the morphology of the layers and their roughness, as in the case of TEC-7 and defective PGO substrates. Nevertheless, promising results have been obtained on opaque cells using a home-made ITO layer on the front panel. Finally, the tests on STPC did not show any electrical negative behavior and must now be reproduced using more suitable substrates in order to validate the performances obtained.

Chapter 6

Development of transparent conductive oxides for tandem applications

Introduction

In Chapter 4, we have shown that the TCO electrodes used in our STPC were responsible for the largest share of parasitic absorption in the infrared, which leads to a decrease in the performance of the silicon bottom cell. We identified two interesting materials to replace ITO and FTO in our STPC: IZO and IO:H.

First of all, the use of sputtering to synthesise IZO proved to be the best option because its deposition conditions are close to those of ITO. The optimization of the IZO was based on the work already done for the ITO, and the pressure, power, time and plasma parameters are first adjusted on glass substrate. The morphology, optical characteristics and temperature resistance are studied on the optimized IZO layer. Finally, the first cells with an IZO electrode are fabricated and their performances compared with reference cells. Adjustments to the deposition parameters are then made (low power bilayers and co-sputtering with ITO) to obtain the best possible performance on STPC. A new pattern for our electrodes, both front and back, is then be presented. It is based on the use of a non-metallic TCO grid to increase the conductivity while maintaining a high IR transparency.

Concerning the IO:H, the ALD deposition route has been chosen instead of sputtering and 2 different precursors, Trimethyindium (TMI) and Indium (III) acetylacetonate ($In(acac)_3$), have been tested. They have the advantage of being less expensive than the InCp precursor more used in the literature but they have also been less studied. The deposition of this material required a longer and more delicate optimization than IZO. For this reason, the optical and electrical properties and morphology of the different layers will be studied on glass substrates.

6.1 Indium Zinc Oxide (IZO)

Zinc Oxide (ZnO) is a wide band gap n-type semiconductor. It crystallizes in a wurtzite structure in which the zinc is in a tetrahedral environment, as is the oxygen. Undoped films of pure ZnO have a low electrical conductivity compared to most TCO electrodes. It is possible to dope ZnO with group III elements such as gallium or indium and group IV elements such as silicon, germanium, titanium or zirconium. In the context of transparent electrodes for solar cells, indium and aluminum doping are the most frequently mentioned [66, 163, 167, 307]. In the case of IZO, it is an amorphous TCO generally composed of 90% In_2O_3 and 10% ZnO, that can be deposited by sputtering using pure argon at a low deposition temperature [357, 358]. It has a better transmittance in the infrared and a higher work function than amorphous ITO (5.05 vs. 4.9 eV) [359–362]. Thus, the IZO is suitable to play the role of back contact in our STPC because it correctly aligned with the valence band of the PTAA (5.1 eV).

In the following, we will first detail the optical and electrical properties of the deposited layers by varying the deposition parameters in order to find our optimal recipe. Then, we will analyze more precisely the morphological and optical characteristics of the layer and we will proceed to the first tests on STPC.

6.1.1 Parameters of sputtering deposition

IZO is deposited by sputtering in the same frame as the one conventionally used for ITO at ambient temperature. The target is 3 inches long and consists of 90% In_2O_3 and 10% ZnO. Like ITO, the deposition process can be monitored with the mass spectrometer, see Fig. 6.1a. The rates observed for Ar, N, O and H_2O are similar to those observed during ITO deposition with the same parameters (50 W, a pressure of 2 mTorr, an Ar flow rate of 33 sccm and a residual vacuum of 7.10^{-7} mbar), see Chapter 2 Section 2.2.2.2.

However, the amount of Zn and ZnO detected is below the detection limit (10^{-8} counts.s^{-1}). On the other hand, the presence on the XRF spectrum of the characteristic Zn $K_{\alpha1}$ emission line is confirmed at 8.64 eV, see Fig. 6.1b. In $L_{\alpha1}$ and $L_{\beta1}$ emission lines can also be found at 3.29 and 3.49 eV, respectively. Finally, the XRF mapping reveals a homogeneity similar to ITO in Chapter 2 Section 2.2.2.2 .

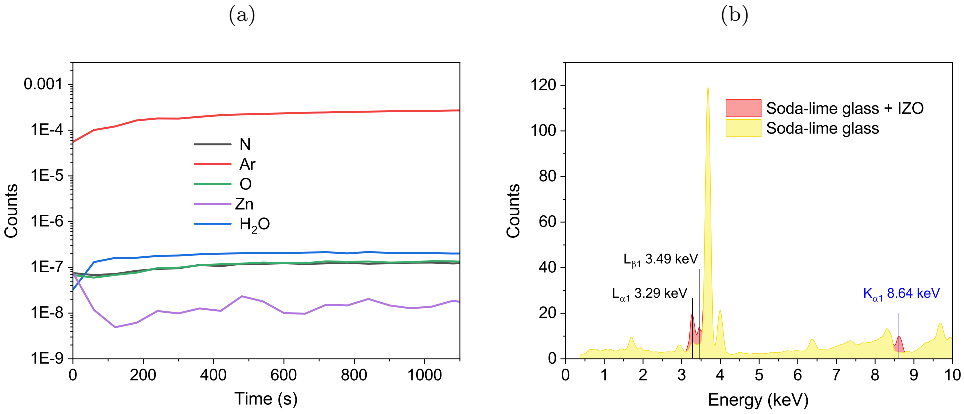

Figure 6.1: (a) Mass spectroscopy of N, Ar, O, Zn and H_2O in time during IZO sputtering. (b) XRF emission spectra of a 150 nm IZO sample on soda-lime glass and a soda-lime glass alone. The contribution of In emission lines are shown in black and the Zn one in blue.

6.1.2 IZO deposited on glass

6.1.2.0.1 Deposition time

This study will allow us to identify the optimal deposition parameters for our needs by adjusting the deposition time, pressure, power and Ar/O_2 ratio in the plasma. We start by IZO deposited using a process similar to ITO as described in Chapter 2: a power of 50 W, with a pressure of 2 mTorr in the chamber, an Ar flow rate of 33 sccm and a residual vacuum of 7.10^{-7} mbar.

Fig. 6.2a shows the electrical and optical properties of the IZO layers obtained with this process as a function of the deposition time. It can be seen that the sheet resistance decreases progressively with increasing thicknesses for a constant resistivity of 3.69 10^{-6} Ω.m, comparable to values in the literature [363, 364]. The sheet resistance remains a little higher than ITO for same deposition times while the latter has a similar resistivity of 4.28 10^{-6} Ω.m. This can be explained by the fact that the deposition rate of ITO is on average 1.69 times faster (2.1 vs. 3.6 nm.s^{-1}) and the ITO samples are therefore thicker. However, the sheet resistance reaches similar values (11 Ω.sq for 150 nm) for the 150 min deposition while the ITO deposition (506 nm) is much thicker than the IZO layer (315 nm). The carrier mobility for IZO is constant with the thickness at 27 $cm^2.V^{-1}$, it is higher than for ITO (15 $cm^2.V^{-1}$). On the other hand, the carrier concentration reaches 8.2 $10^{20}cm^3$ for ITO and 6.4 $10^{20}cm^3$ for IZO. Hall effect is used to measure the resistance, the doping, the mobility of thin films or bulks on samples of 2*2 cm^2.

Fig. 6.2b illustrates the absorption of these different samples on soda-lime glass. Between 20 min and 150 min of deposition time corresponding to a thickness of 42 nm and 315 nm, respectively, the absorption at 1100 nm only increases from 7.3% to 13.9%. This is still lower than the ITO absorption at 1100 nm for only 60 min of deposition with 14.1%. For an equivalent deposition time, i.e. 60 min here, we also note that the short wavelength absorption of these two materials is similar.

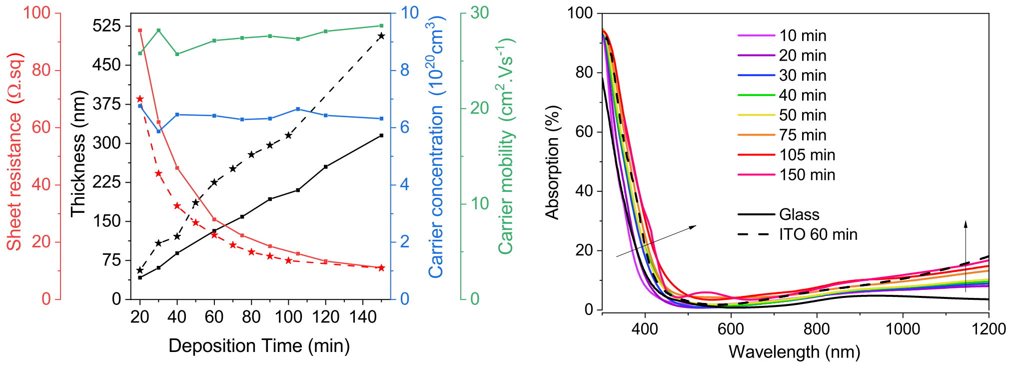
(a)

(b)

Figure 6.2: Evolution of (a) thickness (black), sheet resistance (red), carrier concentration (blue), carrier mobility (green) and (b) absorption of IZO layers as a function of sputtering deposition time, compared to a 60 nm ITO layer made with the conventional process described in chapter 2 (dash black and red lines).

6.1.2.0.2 Pressure

By fixing a deposition time of 60 min, Fig. 6.3a shows the effect of the pressure in the chamber during the deposition. The film thickness logically decreases with increasing pressure due to the reduction of the mean free path of atoms [365]. It can be seen that the carrier concentration also decreases with pressure, while the resistivity does not. Nevertheless, the highest carrier mobility is obtained at 2 mTorr (33 $cm^2.V^{-1}$). This evolution may result from the combined effects of increasing ionized scattering centers (0.5 to 2 Pa) and neutral scattering centers (above 2 mTorr) [366].

In terms of absorption, see Fig. 6.3b, the pressure has a visible impact just after the optical gap until the IR. At 1100 nm, the absorption is minimal at 2 and 4 mtorr (7.5%) but it is strongly increased between 450 and 625 nm in the case of a pressure of 4 mtorr. The choice to use a pressure of 2 mTorr seems therefore relevant.

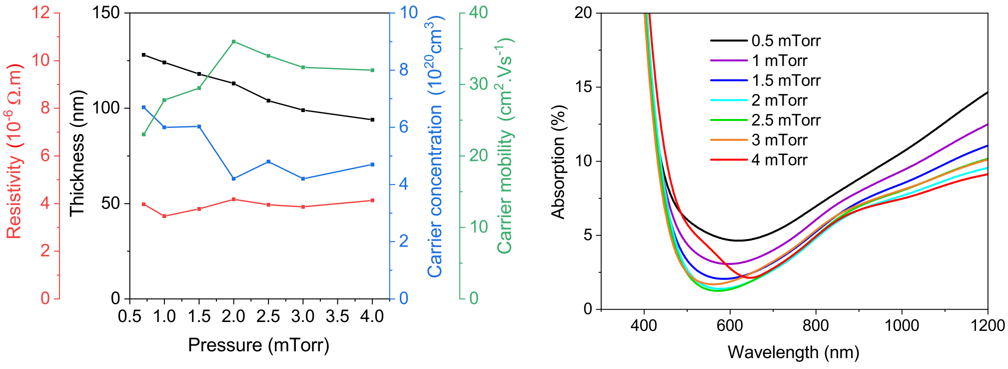
(a)

(b)

Figure 6.3: Evolution of (a) thickness (black), resistivity (red), carrier concentration (blue), carrier mobility (green) and (b) absorption of IZO layers as function of the pressure during the sputtering deposition.

6.1.2.0.3 Power

We then adapted the deposition time to obtain an identical final thickness of about 70 nm (± 5 nm) for different powers (the deposition rates increases linearly with the power). As can be seen in Fig. 6.4a, the power used on the target has no significant effect on the carrier concentration or resistivity, which remain close to the initial conditions. On the other hand, the carrier mobility decreases with the power, from 192 cm^2.V^{-1} at 20 W to less than 150 cm^2.V^{-1} at 60 W. Fig. 6.4b shows that the power has little influence on the absorption under 60 W and we only observe an increase of the IR absorption above 800 nm in the case of a power of 70 W. Thus the influence of the power appears limited on the intrinsic characteristics of the layer below 60 W. This parameter will be adjusted during the deposition on cells in order to find the best compromise between power and deposition time.

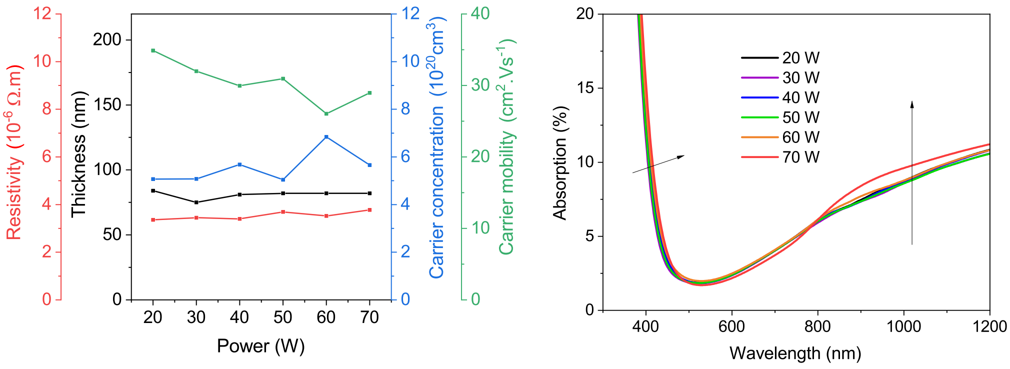
(a)

(b)

Figure 6.4: Evolution of (a) thickness (black), resistivity (red), carrier concentration (blue), carrier mobility (green) and (b) absorption of IZO layer as function of the power used on the IZO target.

6.1.2.0.4 Oxygen/Argon ratio and residual void

As for the ITO in Appendix F, the opto-electronic properties of IZO also evolve according to the quantity of O_2 present in the chamber compared to the quantity of Ar. We can see in Fig. 6.5a that the lowest IZO resistivity is found when no reactive oxygen is added to the sputter chamber. In parallel, the sheet resistance increase dramatically when the O_2/Ar ratio exceeds 0.45% (≥ 500 Ω.sq). A slight decrease of the thickness is observed (84 nm with 1% O_2 against 113 nm without). It can be attributed to an energy screen effect promoted by oxygen that makes the surface environment of the target less conductive [367]. A decrease in the density of oxygen vacancies thus leads to decrease in the carrier concentration (divided by 50, from 5.07 to 0.11 10^{20} cm^3) and an increase in the resistivity of the layer. We observed that the carrier mobility increased with O_2/Ar ratio between 0% and 0.33%, which is probably due to a decrease in the ionized scattering centers of carriers, such as electrically active oxygen vacancies [368, 369].

Regarding the absorption, see Fig. 6.5b, the impact of oxygen is mainly seen in the absorption after 600 nm. The variations are not linear, but we observe a maximum absorption at 1100 nm of 8.5% for a ratio of 0.22% and minimal for a ratio of 1% with 5.48% absorption, caused again by a decrease of O_2 vacancies. The impact on the absorption remains nevertheless minimal, with a gain of less than 2% between a ratio of 0 and 1%. Considering the important drop of the carrier concentration at the slightest addition of oxygen, it seems more interesting not to use oxygen during the deposition of the IZO.

Finally, argon flow and residual vacuum tests have been performed as for ITO in Appendix F. Contrary to ITO, they do not show any significant evolution of the opto-electronic properties. In view of these results, the deposition at less than 60 W for a pressure of 2 mTorr and a flow of Argon at 33 sccm without addition of oxygen, seems the most interesting and we will base on this process to detail the morphological and others properties of this layer. Thus, for 100 min of deposition, we obtain an IZO layer of 210 nm thickness for a sheet resistance of 14 Ω.sq.

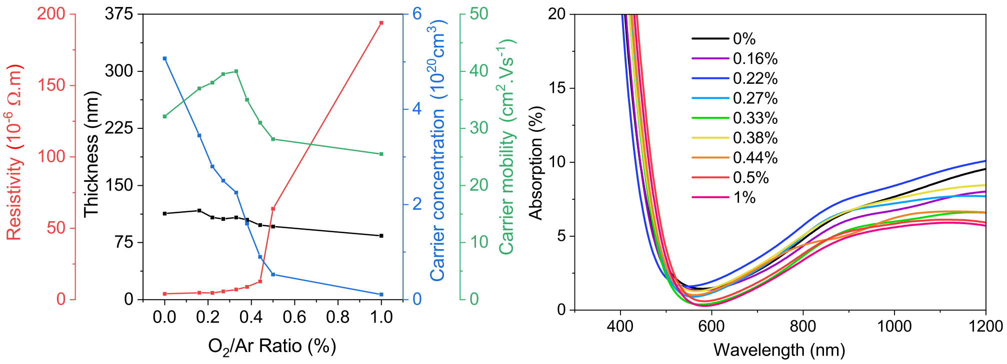
(a)

(b)

Figure 6.5: Evolution of (a) thickness (black), resistivity (red), carrier concentration (blue), carrier mobility (green) and (b) absorption of IZO layer as function of the ratio between oxygen and argon during sputtering deposition.

6.1.2.1 Morphology and optical properties

An IZO layer synthesized at 50W with a pressure of 2 mTorr and a flow of Argon of 33 sccm during 40 min is characterised by SEM (surface and cross-section). The layer is homogeneous and has a particularly smooth surface compared to ITO, except for some aggregates on the surface (see Fig. 6.6a and b).

No crystallite can be distinguished and the XRD spectra reveal a completely amorphous structure, see Fig. 6.6c. Most IZO thin films in the literature have an amorphous structure too. However, under specific conditions (sol–gel spin coating technique or annealing beyond 500 °C), it can exhibit a crystalline structure [362, 370–372].

From the optical point of view, the TRA spectra are compared with amorphous ITO for a similar thickness of 220 nm on soda-lime glass in Fig. 6.6d. We notice that the absorption in the infrared is less important for IZO than for ITO. The optical index of IZO is obtained thanks to the combination of the NAM and the Drude model as ITO and confirms this behavior in the infrared with a coefficient k inferior to the ITO beyond 800 nm, see Fig. 6.6e.

6.1.2.2 Annealing

Annealing tests similar to those performed with ITO are reproduced with IZO, see Fig. 6.7 and Table 6.1. They show the evolution of the absorption and sheet resistance of an ITO layer on glass as a function of temperature of the annealing during 1h. The sheet resistance starts to increase rapidly from

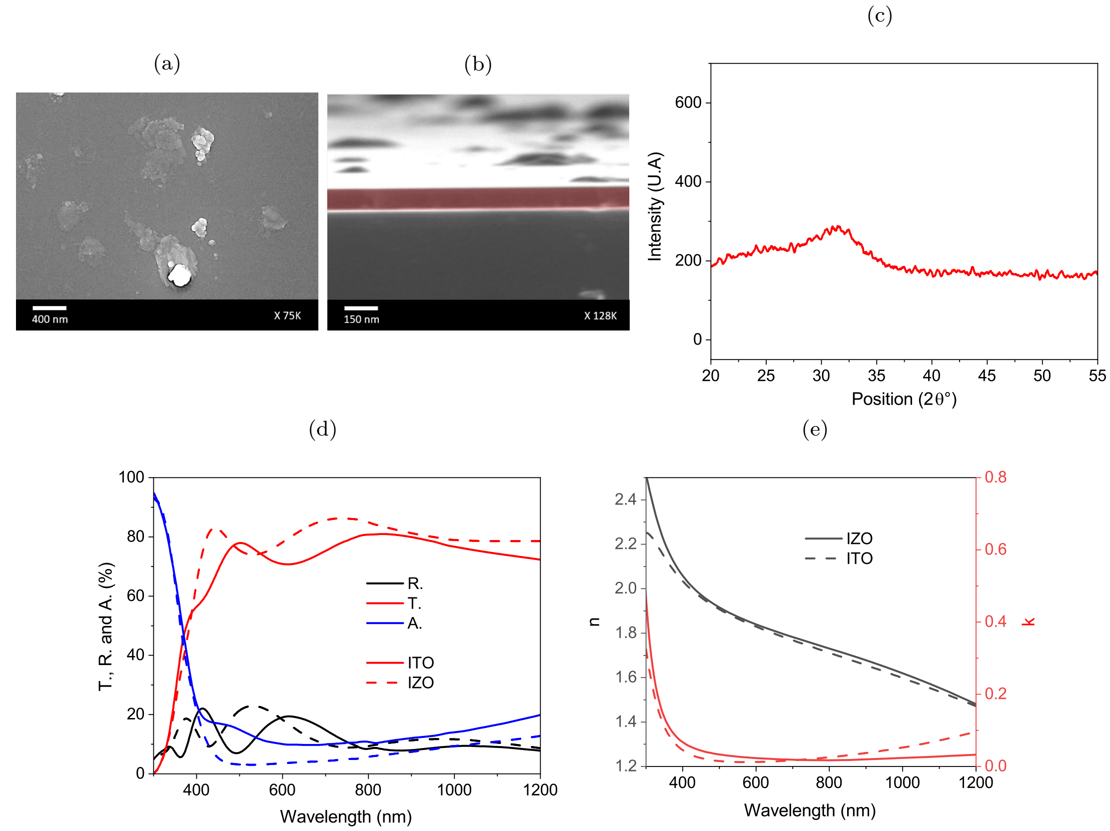
(a) (b) (c) (d) (e)

Figure 6.6: (a) SEM image of the surface and (b) cross-section of IZO layer on glass. (c) XRD spectra of 150 nm IZO on glass. (d) Transmission, absorption and reflection spectra of amorphous ITO and IZO layers of 220 nm on soda-lime glass. (e) Refractive index n and extinction coefficient k of IZO and amorphous ITO.

300°C. This behavior could be attributed to the incorporation of oxygen during annealing above 300°C. The incorporated oxygen reduces the number of vacancies in the layer and leads to a decrease in free carriers, since the electrical conduction of these oxides depends on the oxygen vacancies [373]. In parallel, the infrared absorption decreases dramatically and the optical gap shifts to higher wavelengths. This decrease of the band gap can also be explained by the decrease of the carrier concentration due to the creation of empty states near the conduction band edge [373, 374]. The decrease of the absorption in the infrared can also be explained by an incorporation of oxygen [373, 375]. However, unlike ITO, our IZO remains amorphous even after annealing at 500°C. IZO is therefore less heat resistant than ITO, but it is unlikely to reach such temperatures in our STPC.

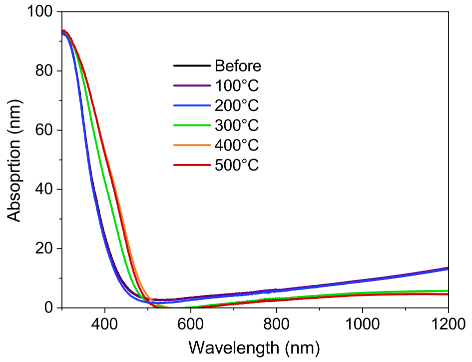

Figure 6.7: Absorption spectra of IZO on soda-lime glass for different annealing temperatures.

Temperature (°C)	**R$_{sheet}$ as deposited (Ω.sq)**	**R$_{sheet}$ after annealing (Ω.sq)**
100	17.2	16.8
200	17.2	15.6
300	17.2	49.9
400	17.3	320.2
500	17.4	863.2

Table 6.1: Sheet resistance of IZO layers on soda-lime glass before and after annealing at different temperatures.

6.1.3 Optimization on STPC

After optimizing the deposition of IZO on glass to obtain the desired opto-electronic properties, we wanted to replace the ITO electrode on our cells by an IZO electrode as designed with the model in Chapter 4. For this study, 2 batches of 16 samples (AY48 and MP16) and one batch of 8 samples (AY43) were studied. Referring to the process developed in Section 6.1.2, IZO is deposited on STPC using TiO_2 as the ETL and PTAA as the HTL.

6.1.3.1 STPC based on single and bilayer IZO

This study is performed in the batch MP16, which consists of 16 STPC, divided into 4 groups with different back electrodes: IZO, ITO, IZO bilayer and ITO bilayer. The IZO layer is deposited using the optimal deposition process identified in the previous section (50 W for a pressure of 2 mTorr and a flow of Argon at 33 sccm during 100 min). In parallel, we also deposited a bilayer of IZO following a process similar to that of ITO described in the Chapter 5, i.e. 10 min of deposition at low power (25 W) before proceeding with the classical deposition. As seen in Section 6.1.2.0.3, this first layer deposited at 25 W has a similar absorption, resistivity, carrier concentration and mobility to the layer deposited at 50 W for an equal thickness and only the deposit rate is lower. Cells with ITO and ITO bilayer electrodes are fabricated in the same way to serve as STPC reference.

6.1.3.1.1 Morphology and optical properties

SEM images of the surface (Fig. 6.8a and b) and AFM measurements of two cells (Fig. 6.8c and d) with ITO or IZO bilayer electrode reveal an almost identical surface morphology. The surface appears to form grains, probably due to the presence of perovskite grains below. The STPC has a RMS of 9.66 nm, lower than the cell with ITO at 13.99 nm.

Fig. 6.8e shows the transmission spectra obtained with ITO and IZO layers. Transmission spectra are compared with those deposited on glass. First of all, we notice that the use of bilayer does not degrade or modify the transmission of ITO and IZO layers compared to a single layer. The gain allowed in the infrared by the IZO is clearly visible at 1300 nm. However, due to an inadequate position of the interference figures in the spectra with IZO, this gain does not appear clearly between 900 and 1200 nm. It will therefore not be noticeable on the efficiency of a silicon cell placed in tandem. It will be necessary to slightly optimize the thickness of the IZO layer or to use a coupling liquid to see a significant difference.

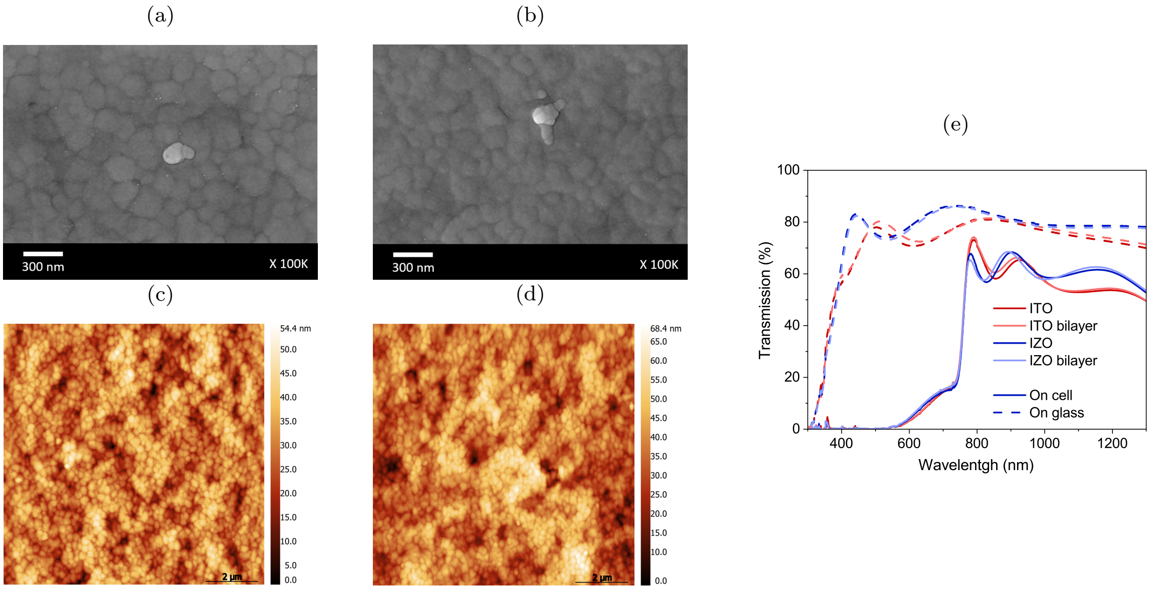

Figure 6.8: SEM images of the surface of a STPC from batch MP16 with a bilayer of (a) ITO and (b) IZO. AFM measurements of the surface of a STPC with a bilayer of (c) ITO and (d) IZO. (e) Transmission spectra of ITO and IZO, single or bilayer, deposited on glass or on cells from batch MP16.

6.1.3.1.2 Electrical properties

The electrical properties obtained over several days are shown in Fig. 6.9a, and the IV of the best cells obtained for each condition at days 2 and 15 are presented in Fig. 6.10. Cells with a single IZO layer have a lower efficiency than the ITO cells (11.4% vs. 12.8%) and this is directly caused by a lower FF (51% vs. 62%), see Fig. 6.9b. The reproducibility of IZO STPC appears correct but lower to the ITO one ($\sigma = 1.7$ vs. 0.11). This is caused by a specific STPC that has a very low Voc (300 mV on the first day after synthesis).

Similarly to ITO, cells with a bilayer of IZO reach higher efficiency (15.3% vs. 13.8% in average, 16.4% vs 16% for the best ones) and faster than cells with a single layer (day 15 instead of 22) as shown in Fig. 6.9a. The difference in efficiency between IZO and ITO bilayer cells at day 15 comes from the FF (66% vs 73%), see Fig. 6.9b and d. The reproducibility of bilayer IZO based STPC show a difference less marked with ITO bilayer one ($\sigma = 0.67$ vs. 1). Thus, the protective role of the first layer deposited at low power is again demonstrated and seems necessary also with IZO.

Cells with IZO, in single or bilayer, showed an S-shape IV curve with hysteresis similar to those obtained with ITO cells on day 2 after synthesis, see Fig. 6.10a for the best cells of each stack. They follow an evolution similar to the cells with ITO. The S-shape is gradually reduced. At day 15, it disappeared from the IV as shown in Fig. 6.10b. The hysteresis is low for all cells.

6.1.3.2 STPC based on IZO bilayer with lower power

We have seen previously that the FF was lower for the cells with IZO compared to the cells with ITO. Although the sputtering targets are the same size, and the power used is similar, the voltage measured on the targets appears higher on the IZO target (75 vs. 64 V). This is probably due to the fact that the IZO target is more recent and the deposition is therefore more energetic and more deleterious to the cells. We therefore choose to reduce our deposition power in the batch AY48. This batch consists of 8 STPC, divided into 2 groups with different back electrodes: IZO bilayer with lower power and classical ITO bilayer. Bilayers are done at 20 W and the second at 35 W (instead of 25/50 W used in the previous section). This allows us to obtain voltages on the target comparable with those of the ITO target.

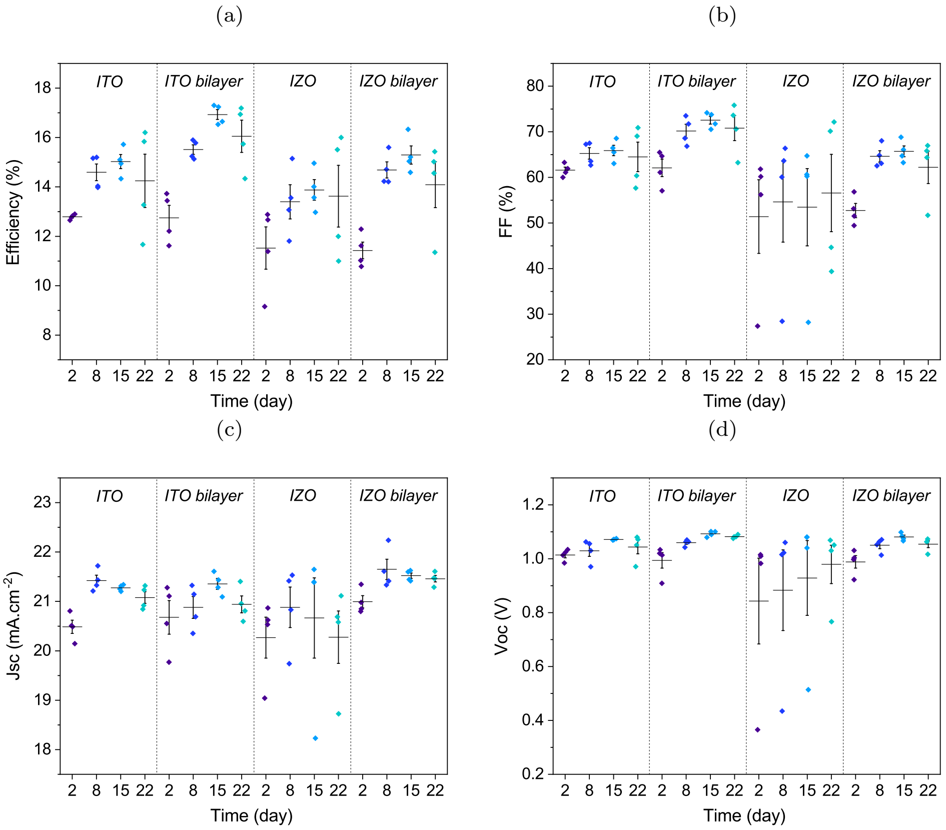

Figure 6.9: Dispersion of the electrical properties ((a) efficiency, (b) FF, (c) Jsc and (d) Voc) of MP16 STPC with ITO and IZO single and bilayer electrodes.

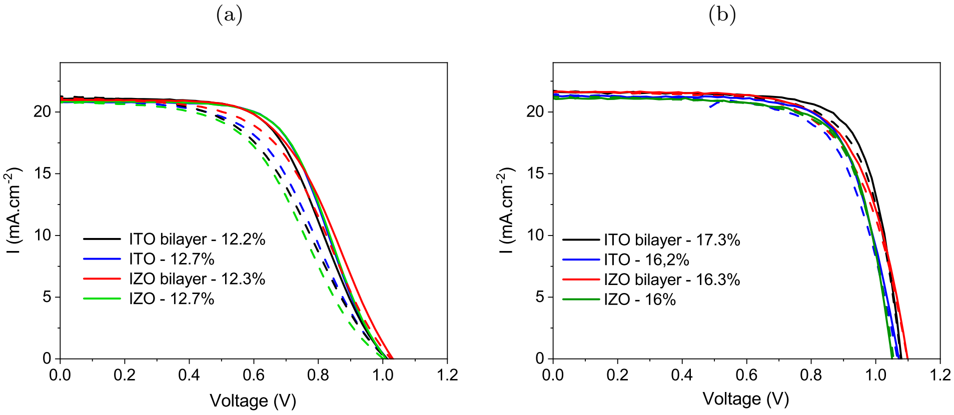

Figure 6.10: IV curves under illumination of the best cells of batch MP16 for each stack, (a) second day after the synthesis and (b) 15 days later.

The evolution of the electrical properties of this STPC over 11 days is presented in Fig. 6.11. The STPC with an IZO bilayer exhibit lower performances than those with an ITO bilayer on the first day after synthesis (see Fig.6.11a). However, the cell efficiencies are similar on day 11 (12.7% and 12.8%) and the best efficiency of the AY48 batch (15.6%) is achieved by an IZO STPC. It can be seen in Fig. 6.11b that the FF is similar for both sets of cells. We also notice that the dispersion is this time a little more important and the AY48 batch presents lower average efficiencies. This dispersion seems to come from synthesis concerns before the electrode depositions as shown by the results on opaque cells in the Appendix C, which are also more scattered and lower than average. In conclusion, the reduction of the power has led to similar performances for ITO and IZO electrodes, with the advantage of an improved transmission in the IR with IZO as shown in Chapter 4.

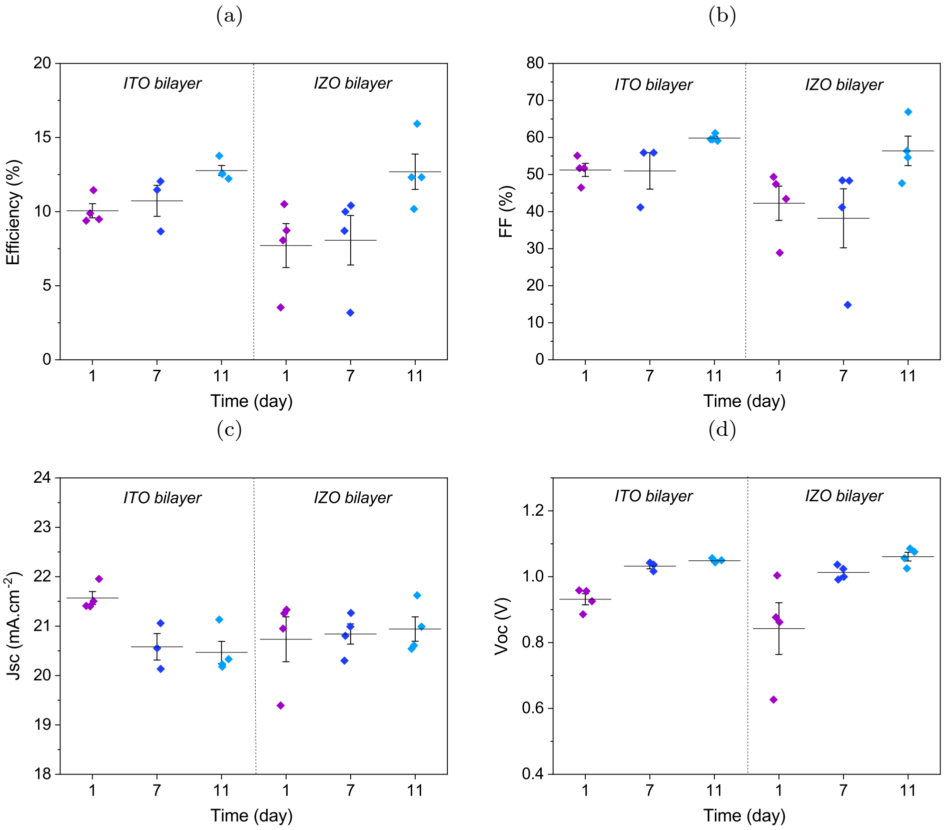

Figure 6.11: Dispersion of the electrical properties ((a) efficiency, (b) FF,(c) Jsc and (d) Voc) of AY48 STPC with ITO and IZO bilayer electrode.

6.1.3.3 Indium Zinc Tin Oxide (IZTO)

IZTO is a relatively new TCO that has some advantages. Like IZO, it is deposited at low or room temperature and does not require further thermal treatment after fabrication. It remains amorphous as long as it is not annealed above 300°C and does not form columnar structures like ITO after a certain thickness [376]. Furthermore, co-substitution of In_2O_3 by ZnO and SnO_2 raised the solubility due to isovalent substitution of a Sn4+ and Zn2+ cation for a pair of In3+ [377]. This material has been used especially in the synthesis of OLED due to it work function (4.6 to 5.2 eV), good conductivity, high transparency, in addition to its low deposition temperature [376, 378, 379].

Based on the promising results proposed by Noe et al. on perovskite cell [380], we performed a co-sputtering of ITO and IZO targets to form an IZTO layer. Both targets are used at 30 W, for a 100 min deposition after a first buffer layer of pure IZO at 30 W for 10 min. The deposition is performed at a pressure of 2 mTorr for a flow rate of 33 sccm of Ar.

Firstly deposited on glass, the optical absorption of this IZTO layer is similar to IZO, as shown in Fig. 6.12b, with a very low infrared absorption. The XRD reveals an amorphous structure and its surface on STPC appears similar to the two other TCO and to the morphology obtained by Noe et al., see Fig. 6.12c. Its sheet resistance is 16.5 Ω.sq for a thickness of 255 nm, which is close to the values obtained with ITO or IZO and twice lower than the IZTO of the same thickness of Noe et al. (35 Ω.sq). Its carrier concentration is evaluated to 5.8 10^{20}cm^3 and its carrier mobility at 28 cm^2.V^{-1}.

Then, this material was deposited on 4 STPC in batch AY43 and compared to 4 reference STPC with an ITO bilayer. The electrical properties measured are shown in Fig. 6.12a. The cells with IZTO work, but with a lower average efficiency than for the reference STPC (9.4% vs 11.9%). This is directly caused by the FF, which is 10% lower on average. We also observe a significant dispersion of the efficiency (σ = 2.8) on the first day after the synthesis, compared to the references (σ = 1.9). This dispersion is caused by both FF and Voc, similarly to IZO deposited at high power in the Section 6.1.3.1. 5 days after the synthesis, the evolution of the STPC with IZTO is negative, with a loss of 1.5% in efficiency, attributed this time to a decrease of all the electrical properties. The reference STPC, on the other hand, show the expected evolution, with an increase in efficiency (+0.8%) and all electrical parameters. Beyond a bad contact at the interface with the PTAA, the IZTO layer seems to deeply degrade the STPC and in a permanent way and more visible in time. Co-sputtering deposition may be too energetic for STPC and target power should be further reduced in the future.

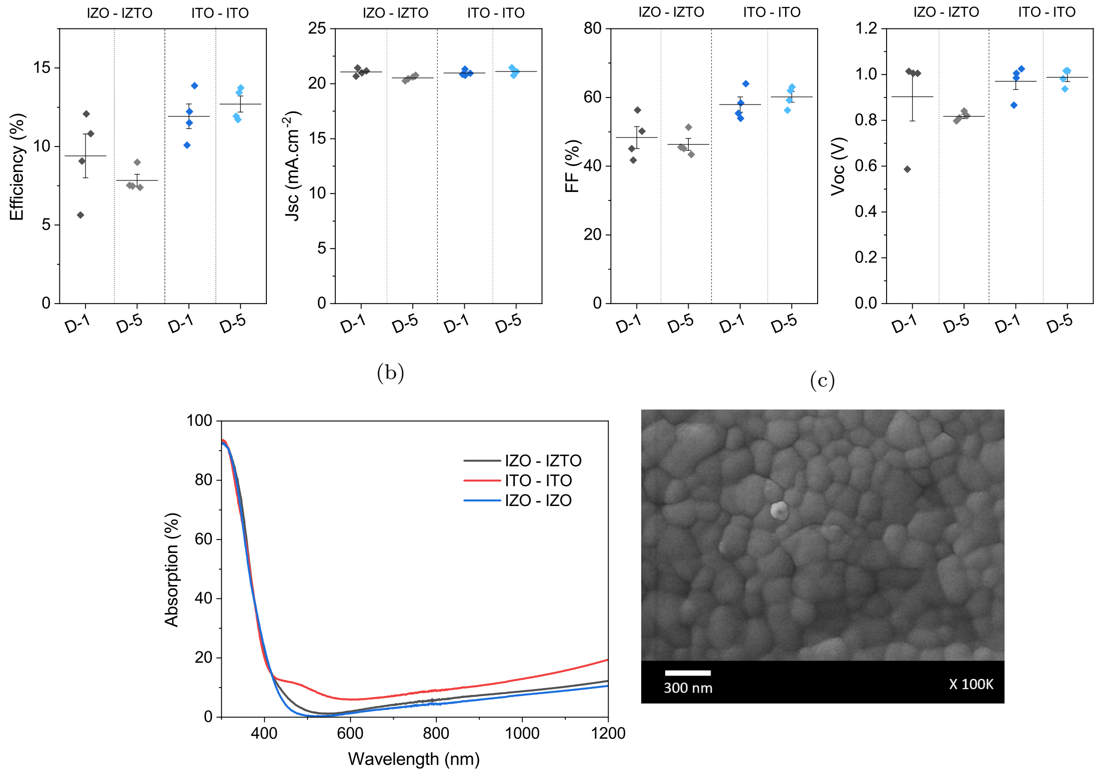
(a)

(b)

(c)

Figure 6.12: (a) Evolution of the dispersion of the electrical properties of the batch AY43, first day after the synthesis and 5 days later. (b) Absorption spectra of IZO-IZTO, ITO and IZO bilayers on soda-lime glass. (c) SEM image of the surface of a STPC from batch AY43 with a bilayer of IZO-IZTO.

6.1.3.4 IZO-based tandem efficiency

Proceeding in the same way as detailed in the Chapter 4, we calculate the reconstructed efficiency of a tandem made with the best IZO cell obtained so far namely MP16-18 (16.3% of efficiency), composed of a bilayer of IZO when the power was still too high. Using the different silicon cells, the efficiency of the reconstructed tandem varies between 21.7% and 23.1%, see Table 6.2. Compared to the results obtained with the best ITO/PTAA based STPC (MA16-05), it can be seen that the silicon cells perform slightly better with the use of IZO on the back side of the STPC (+0.1%). This increase is small because, as seen in the Section 6.1.3.1.1 on interference patterns in the transmission spectrum, they are not optimally placed and generate significant losses. In order to reduce this problem, it will be necessary in the future to use an optical coupling system between the cells, as mentioned in Chapter 4 Section 4.2.1.3, in order to better highlight the gain obtained with the IZO electrode.

In addition, we have seen in Section 6.1.3.2 that the electrical performances of IZO and ITO cells can be similar. This means that with a batch with very good intrinsic characteristics, it is seems possible to obtain in the future an IZO/PTAA based STPC with an efficiency similar to the ITO/PTAA record cell (17.8%).

Tandem cells	**Simulated filtered Silicon Eff. (%)**	**Simulated Tandem Eff. (%)**
IZO + Al-BSF	5.4%	21.7%
IZO + n-PERT 1	6.1%	22.4%
IZO + n-PERT 2	6.4%	22.7%
IZO + IBC	6.8%	23.1%
ITO + Al-BSF	5.3%	23.1%
ITO + n-PERT 1	6%	23.8%
ITO + n-PERT 2	6.3%	24.1%
ITO + IBC	6.7%	24.5%

Table 6.2: Electrical characteristics of the best IZO/PTAA based STPC (MP16-18) and ITO/PTAA based STPC (MA17-08), different unfiltered and filtered silicon cell and tandem cells associated.

6.2 Development of solar cells with TCO patterns

We have seen throughout this manuscript that the dilemma of TCO is the lateral conductivity of the electrodes which must be maximised while maintaining high transparency in the appropriate wavelength range. STPC are small devices (0.09 cm^2) and as we have shown in Chapter 4 Section 4.2.2.3, the sheet resistance of the top electrode can increase to nearly 100 Ω.sq without generating significant electrical losses. However, this situation is no longer viable it we consider a change of scale for our STPC, with larger surfaces. The conductivity of the TCO will be an increasingly critical parameter.

It is possible to artificially increase this conductivity by using a metal grid on the surface of the electrode, but it induces shadowing and therefore limits the current that can be collected. It is estimated that the losses linked to this shadowing are between 2 and 5% of the current generated by the cell [381–384]. It must be ensured that the gain in efficiency of the top cell due to the improved conductivity of such electrodes is greater than the loss on the bottom cell due to lower transmission.

However, if we consider a non-metallic grid deposited with TCO, the shading problems may become almost negligible. Increasing the doping rate or the thickness of the TCO locally will create a locally higher parasitic absorption, but incomparable to the parasitic absorption of a metal. The idea here is to locally modify the properties of the TCO layer, by increasing its doping rate or modifying its thickness in order to create a TCO grid. This solution has the advantage that it does not suffer from compatibility problems because the same material is used for the grid and the electrode.

The results exposed in this section are the subject of a patent application has been filled with the INPI on November 03, 2021 under the number FR2111650.

6.2.1 Electrical properties of TCO pattern

Initially, three samples were fabricated to perform TLM measurements in the same way as described in Chapter 3 Section 3.3.2. Structure A is composed of a glass substrate which has on its entire surface of a standard IZO layer deposited during 25 min (50W, 2 mTorr and 33 sccm of Ar), resulting in a thickness of 47 nm and a sheet resistance of 90 Ω.sq (4-probes measurements). Structure B has the same type of IZO but this time deposited during 205 min, which gives a thickness of 307 nm for a sheet resistance of 9.6 Ω.sq. Finally, structure C is shown in Fig. 6.13a and is covered over its whole surface with the IZO of 47 nm as the structure A, which is associated with a localized thickness of 307 nm. This localised deposition is achieved by means of a metal mask applied on the surface of the sample.

TLM measurements are performed on the 3 samples in order to determine the sheet resistance of structure C, as shown in Fig. 6.13b. Thus, sample C has an average sheet resistance of 51 Ω.sq, which is 44% lower than structure B, for an coverage rate of only 14.2% for the patterned IZO layer.

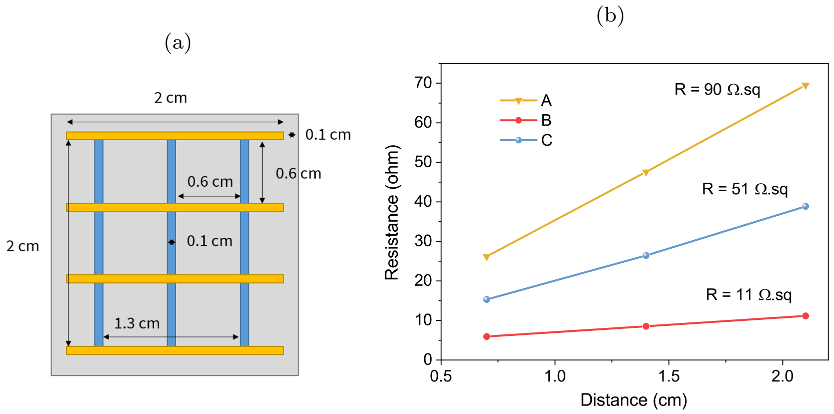

Figure 6.13: (a) Structure C for TLM measurement, with a localized excess thickness of 14.2% of the total surface. (b) TLM and sheet resistance measurements obtained on 3 TCO structures on glass (A, B and C).

6.2.2 Opto-electronic modeling of tandem cells

In a second step, we optically modeled 3 STPC with front and back electrodes similar to the structures A, B and C presented previously, see Fig. 6.14a. These models are based on the same principle as those carried out in Chapter 4 and thus make it possible to simulate the transmissions of such structures and the spectral response of an associated filtered silicon cell. However, it is difficult to simulate a geometrically textured layer with TMM and therefore to have a correct simulation of structure C. In terms of volume, a finger of localised thickness of 259 nm with a width of 0.1 cm and a thickness of 0.6 cm is equivalent to a full layer of 37 nm (14.2% of 259 nm) with a width of 0.7 cm and a length of 0.6 cm. By making approximations, we can model structure C as being composed of a full plate IZO layer of 84 nm (47 + 37), in order to compare its transmission to the structures A (47 nm) and B (307 nm). Fig. 6.14b shows that the structure C results in a transmission very close to a single layer of 47 nm thickness between 750 and 1200 nm, while structure A suffers from poor performance in this region. In addition, IZO was used here for ease of development.

Finally, these results are combined to realize an opto-electrical simulation of the structure according to the models realized in Chapter 4, see Table 6.3 for the efficiencies obtained for each structure. Each structure is simulated according to the asymmetric architecture of our STPC as discussed previously. The silicon cell used as the bottom cell in the tandem is an IBC. The decrease of the performances of the perovskite cell, from 14.1 to 13.3% according to the model, is due to the increase of the sheet resistance of the patterned IZO electrode compared to the thicker one. For the silicon cell, the gain in performance, from 7 to 8.1% with the structure C, is due to the increase in transparency of the top perovskite cell by the reduction in thickness of the two IZO electrodes. The performance obtained in tandem is therefore maximum with the integration of the patterned IZO (21.4%), which has both a higher conductivity than the thin IZO layer, while maintaining a much higher transparency over the entire range than the thick IZO layer. Thus, the use of TCO grids would allow to reach higher efficiencies in tandem configuration thanks to a very favourable opto-electrical balance. These simulated results must now be confirmed by experimental tests on STPC and larger surfaces.

Structure	**Tandem**	**Perovskite cell**				**Silicon cell**			
	Eff. (%)	**Eff. (%)**	**J_{sc} (mA.cm^{-2})**	**V_{oc} (mV)**	**FF (%)**	**Eff. (%)**	**J_{sc} (mA.cm^{-2})**	**V_{oc} (mV)**	**FF (%)**
A	14.8	6.8	21.34	1081	30	8	8	590	77
B	21.1	14.1	17.73	1076	74	7	13.07	656	77
C	21.4	13.3	20.63	1080	60	8.1	15.04	660	77

Table 6.3: Electric properties for the STPC, Silicon and 4T tandem simulated with the electrodes A, B and C on the front and back side of the STPC.

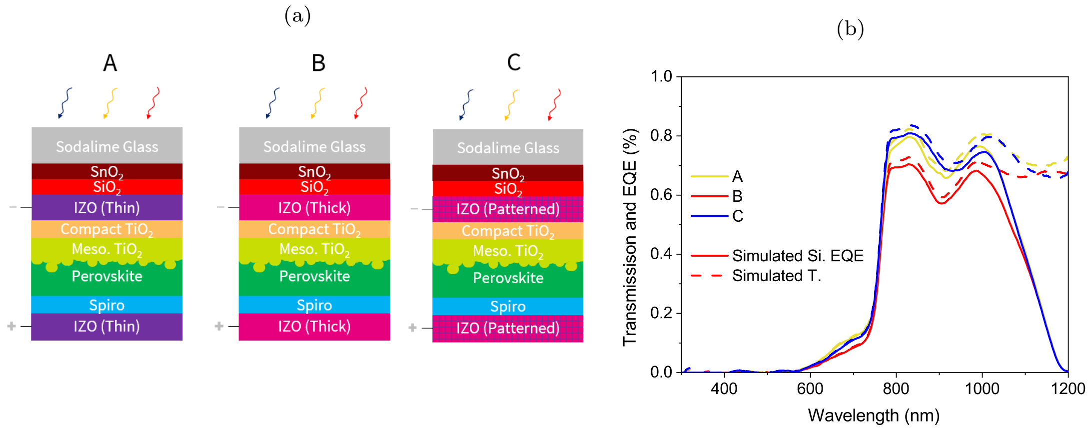

Figure 6.14: (a) 3 simulated STPC with front and back electrodes similar to the structures A, B and C. (b) Optical models of transmission and spectral response of a silicon cell for different thicknesses of IZO and the structure of the invention. In dotted line, transmission of the layers alone. Solid, spectral response of the silicon cell.

6.3 Indium Oxide doped by Hydrogen (IO:H)

Indium Oxide doped by Hydrogen ($In_2O_3 : H$), developed in 2007 by Koida et al. [385], is emerging as a TCO of interest because of its high mobility (>100 vs. 15 $cm^2.V^{-1}$ for ITO) at carrier density around 1–2 $10^{20}cm^3$ (8.2 $10^{20}cm^3$ for ITO) and high transparency. Compared to In_2O_3, hydrogen in IO:H is supposed to acts as an effective donor by occupying interstitial or substitutional sites in the lattice structure while maintaining excellent chemical stability [386, 387]. As seen in Chapter 4, this material appears to be a good candidate to replace the FTO on the front side.

IO:H was first developed by sputtering In_2O_3 in the presence of H_2O vapor which acts as the source of hydrogen [305, 385, 388, 389]. However, the need to add water during sputtering leads to a risk of too much contamination of other targets present in the chamber and is therefore not retained as a deposit method in this thesis. On the other hand, Macco et al. has paved the way for ALD of this material and was followed by different teams [305, 386, 389, 390]. Each reactant is sequentially pulsed into the reaction chamber with a purge of inert gas between the different reactant doses. In this way, all gas-phase reactions are eliminated and the growth is self limited to one monolayer per pulse. The method ensures consistent growth and pin-hole-free films over large areas with opto-electronic properties similar to sputtering deposits, see Chapter 2 Section 2.2.3 for more details about the experimental method [305].

Cyclopentadienyl Indium (InCp) has been used as a precursor to synthesize IO:H layer, in combination with H_2O, O_2, O_3 or hydrogen peroxide, of which a decent growth rate (0.13 nm/cycle). However, this precursor is relatively expensive (366 \$/g) and thus less of an economically viable option for commercial up-scaling. We tried to use less common precursors already used by some teams to synthesize In_2O_3 or IO:H, like Trimethylindium (TMI) [391–393] and Indium (III) acetylacetonate ($In(acac)_3$) [394, 395], with H_2O, O_3, O_2 plasma. As the quality of IO:H films depend strongly on the hydrogen and oxygen content during growth, the electrical, optical and structural properties of the thin films deposited using both precursors were studied.

6.3.1 Indium (III) acetylacetonate ($In(acac)_3$)

6.3.1.1 State of the art

ALD deposition of In_2O_3 has already been reported using $In(acac)_3$ and either H_2O and O_2 or O_3 as reactants, but the growth rates were very low. It seems caused by the low reactivity of H_2O towards β-diketonates like $In(acac)_3$ [396, 397]. This is also the case for O_2, which nevertheless remains much less used than water. Generally, to compensate for the lack of reactivity of metal precursors, O_3 is preferred. $In(acac)_3$ has the advantage of being 8 times cheaper than the InCp (44 \$/g).

Nielsen et al. succeeded in making films that completely cover the surfaces in a relatively uniform manner with an adapted sublimation temperature of $In(acac)_3$ at 146 °C. However, the electronic conductivity is not really interesting for solar applications (3.10^{-2} Ω.cm vs. 5.10^{-4} Ω.cm for ITO). In addition, it seems that the reaction rate of H_2O with the adsorbed In-complex is low and that saturation is not reached even after 7 s of pulsing. Thus, until now, the growth mechanisms did not show clear saturative reactions with the precursor pulsing [394]. They also show that it exists a possible ALD window in the ranges 165–200°C for In(acac)$_3$ and H_2O. Above these temperatures, an uncontrolled growth most probably involving decomposition of In(acac)$_3$ seems to prevail.

6.3.1.2 Growth of the IO:H layer on glass

Based on the Nielsen et al. deposition, we carry out several tests in order to obtain an IO:H deposition on soda-lime and borosilicate glass and silicon substrate with sufficient growth rates above all. Deposits are made in frame A, see Chapter 2 Section 2.2.3 for methodological details. It does not include QCM, so the thicknesses are measured by profilometer and ellipsometry. Depositions were performed each time on soda-lime and borosilicate glass of 3mm and silicon (100) wafer cut. For these depositions, the pressure in the chamber is around 3 hPA. The In(acac)$_3$ is heated continuously to 160°C and at the beginning of the cycle, it is sent into the chamber with a flow of 200 sccm. The O_2 plasma is then ignited, in a separate module of the chamber with a power of 2600 W, a pressure of 500 hPA, an oxygen flux of 20 sccm and an argon flux of 150 sccm. It is stabilized for 2 seconds with the shutter closed before being sent to the deposition chamber and finally switched off after the pulse. H_2O is sent into the chamber with a flux of 200 sccm too.

Initial tests based on the results of Bugot et al. [395] on the same frame did not yield a deposit. We have therefore varied pulse time of In(acac)$_3$ (0.1-7 s), H_2O (1-4 s) and Ar/O_2 plasma (2-9 s), as well as purge times (0-5 s), and the chamber temperature (160-200°C) until the material was deposited on the surface of the substrates, details not shown here. The process shown in Fig. 6.15 at 180°C is the one that allows us to obtain the highest growth rate (34 pm/cycle) after 1000 cycles.

It consists of a 7 s pulse of the In(acac)$_3$ precursor followed by 2 s of purging. The Ar/0_2 plasma is then turned on for 9 s and immediately followed by a 3 s pulse of H_2O. A final purge of 1 s concludes this ALD cycle. This rate is comparable to the highest growth rate achieved with only H_2O by Nielsen et al. (28 pm/cycle) [394]. Thus, the addition of plasma does not significantly increase the deposition rate.

To obtain a sufficient thickness, we reproduced the same deposit but this time with 2000 and 3800 cycles. Thickness is measured by a profilometer on the glass substrate. As shown in Table 6.4, the deposition rate decreases drastically with the increase of the number of cycles (34 vs. 11 pm/cycle between 1000 and 3800 cycles of deposition) and it seems difficult to grow a layer of more than 45 nm. The samples of 2000 and 3800 cycles are almost identical and we can therefore assume that the rate of 34 pm/cycle is not exact and is probably already affected by the saturation phenomenon in terms of growth.

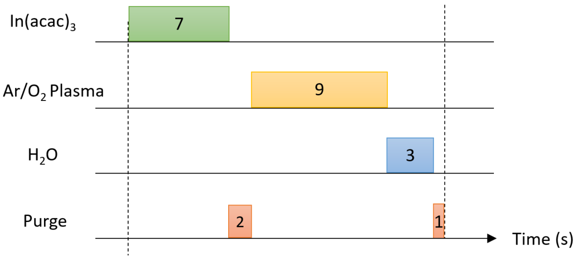

Figure 6.15: ALD cycle used to achieve 34 pm/cycle growth rate with In(acac)$_3$, H_2O and Ar/O_2 plasma.

Sample	Cycles	Thickness (nm)	Rate (pm.cycle)
1	1000	34	34
2	2000	41	20
3	3800	44	11

Table 6.4: Thickness and deposition rate of the layers deposited according to the process presented in Fig. 6.15 for 1000, 2000 and 3800 cycles.

Mane et al. discuss that the use of H_2O and O_2 (without plasma) as reactants can generate a surplus of O_2 [398]. The exposure of the surface to this excess leaves ligands on its surface which eventually passivate the surface and prevent further adsorption. A similar phenomenon can potentially occur in our case with the use of the H_2O and plasma O_2 duo.

6.3.1.3 Opto-electronic properties of the IO:H layer

Using the sample n°3 of 44 nm, various characterizations were nevertheless carried out. The XRF measurement on Fig. 6.16a confirms the presence of indium and hydrogen in the sample, with the identification of the characteristic emission lines at 3.29 and 3.49 eV.

GDOES measurement also allows to notice the presence of indium, see Fig. 6.16b. On the other hand, if we look at the evolution of the indium rate compared to the oxygen rate along with the layer, we see that it is richer in indium on the glass side than on the air side, while the oxygen rate does not evolve. This measurement highlights the inhomogeneous character of our layer and seems to show that the decrease of the In/O_2 ratio seems to be at the origin of the saturation phenomenon mentioned in the previous section. The layer appears amorphous in GXRD, contrary to the tendency of IO:H to crystallize above 150°C. The surface seen by SEM shows a set of small scattered structures of about 100 nm on average, see Fig. 6.16c.

Concerning the electrical properties, the sheet resistance of the sample appears extremely high (several millions of Ω.sq) even for such a thin sample and highlights an electrically insulating layer, which may be consistent with poorly crystalline material. Nielsen et al. show that they obtain a rather conductive layer (3.10^{-2} Ω.cm, i.e 3750 Ω.sq for a thickness of 80 nm) when the layer is crystallized and an insulating layer when the layer is an amorphous [394]. The samples of 2000 and 3800 cycles are almost identical from optics properties according to the ellipsometric measurements presented in Fig. 6.17a and b. This

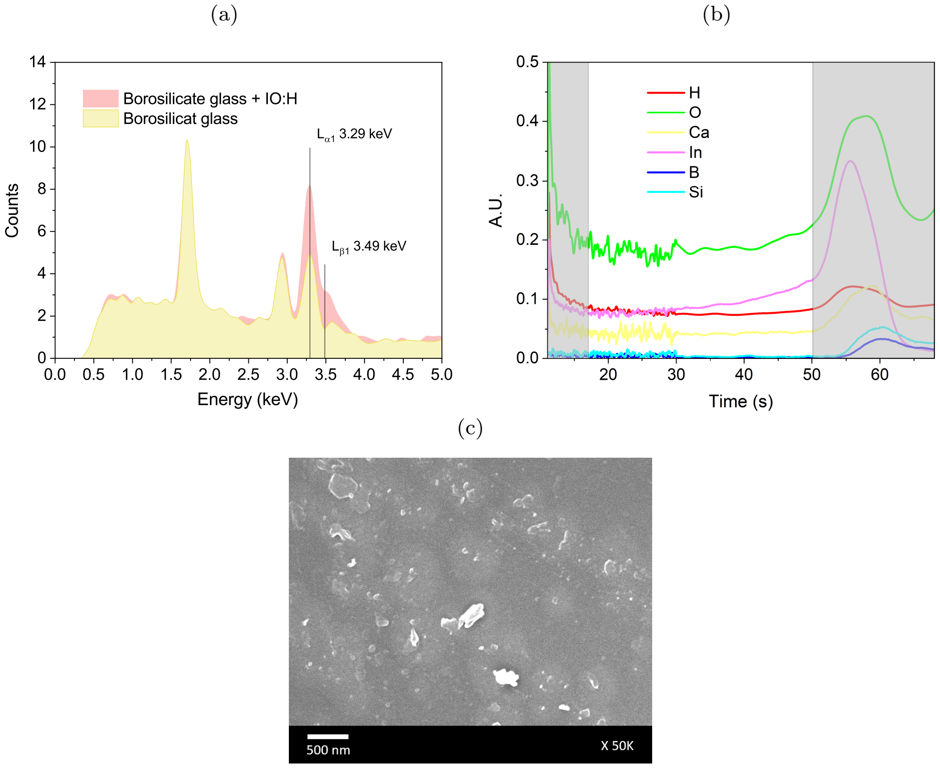
(a)

(b)

(c)

Figure 6.16: (a) XRF emission spectra of the sample with 3800 ALD cycles compared to a borosilicate glass alone. The contribution of indium emission lines is shown in black. (b) GDOES measurement of the sample with 3800 ALD cycles, the grey part on the left of the gas corresponds to the ignition of the plasma, made difficult by the low conductivity of the layer and the part on the right corresponds to the moment when the deposit has been crossed from one side to the other and the glass substrate is touched by the measurement. (c) SEM image of the surface of the sample with 3800 ALD cycles.

confirms that it is indeed a saturation phenomenon that completely stops the growth of films. We also determine the optical indices of these layers by the creation of an associated model (NAM, as for the IZO and ITO). Compared to existing indices of IO:H in the literature, we note a particular behavior of the index n, which is away from the expected values as the wavelength decreases as shown in Fig. 6.17c. Regarding the index k (Fig. 6.17d), we do not perceive any significant absorption in the IR.

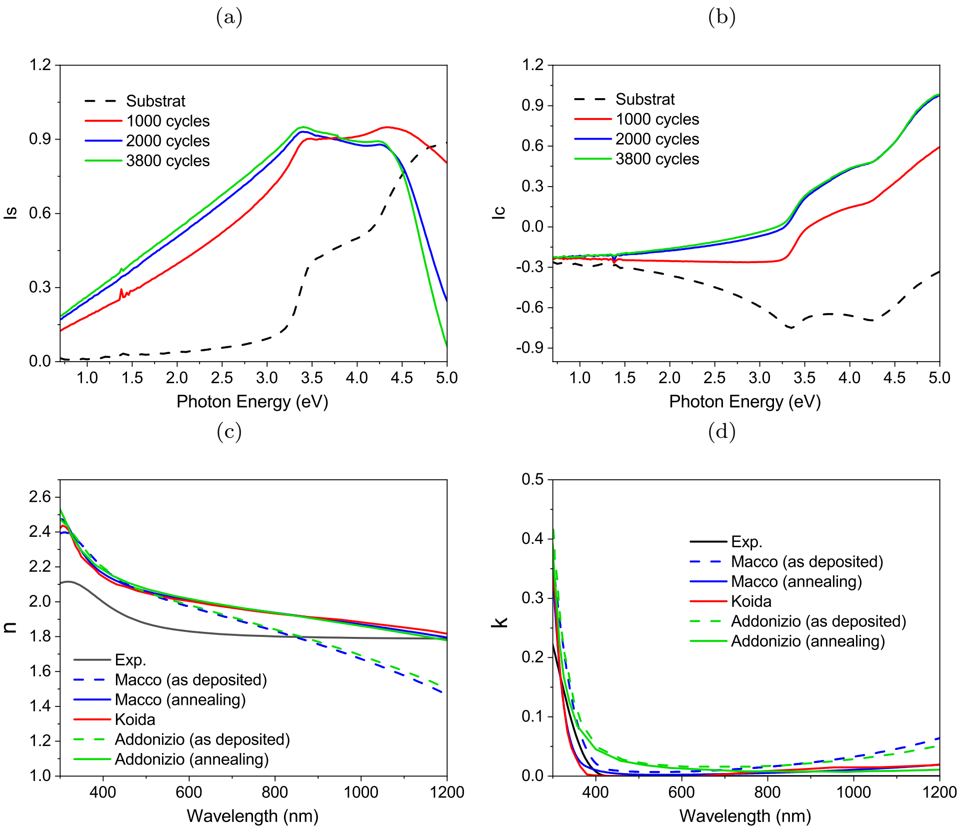
(a) (b) (c) (d)

Figure 6.17: (a) Is and (b) Ic values obtained during ellipsometric measurements on samples with 1000, 2000 or 3800 ALD cycles, compared to those obtained on a blank substrate. (c) Refractive index n and (d) extinction coefficient k of the sample with 3800 ALD cycles, compared to the existing values in the literature: Macco [399] and Addonizio [400] before and after annealing, and Koida [385].

Due to the very slow growth of our layers coupled with a saturation phenomenon at 40 nm, we did not continue testing with this precursor. Our results are in agreement with those of Nilsen et al. [394] and confirm the difficulty of growing indium oxide, doped or not, using In(acac)$_3$.

6.3.2 Trimethyindium (TMI)

Alkyls as TMI are very reactive compared to β-diketonates, in particular because of their metal-carbon bonds. However, they are limited by their decomposition at high temperatures and are only available for very few elements. They are also very often pyrophoric, as is the case with TMI. TMI has several advantages, including a simple chemical structure and high vapor pressure of 8 Torr at 45 °C [389, 401]. In addition, TMI is one of the most utilized commercial precursors for indium compounds and it remains 3 times cheaper than the Incp (114 $/g).

TMI has been used in combination with several oxygen sources such as O_3, O_2, and H_2O as a co-reactant. Ott et al. observed firstly an extremely high film growth rate (1 nm/cycle) at 252°C due to the pyrolysis of TMI [393]. Mane et al., on the other hand, showed that only O_3 was effective in forming In_2O_3 films (chemically pure smooth films with high optical transparency and electrical conductivity), using thermal ALD but a low growth rate (0.42-0.55 Å/cycle) [398]. They show that the TMI/H_2O system undergoes a typical binary reaction consisting of the adsorption of TMI onto the surface, and an extremely large exposure of H_2O (2 Torr.s^{-1}) was required to fully convert surface adsorbed $In-(CH_3)$ groups to In-(OH) groups. The film growth of the In_2O_3 at the deposition temperatures under 250°C was self-limiting as controlled by the surface-adsorption of TMI.

The reports so far, implying that the reaction between TMI and H_2O requires extra activation, in one form or another, for the continuous growth of the film because at temperatures below 250 C, H_2O is unable to completely break the $In-(CH_3)$ bonds. This surface reaction may be triggered by reactive species generated by plasma [389, 390]. Finally, Varanasi used a plasma enhancement to provide the necessary energy to boost this reaction [389]. Her plasma was composed of H_2 along with H_2O vapor, and succeeded to reach a growth rate of 0.8 Å/cycle at a temperature of 150°C, with a resistivity of $2.5.10^{-3}$ Ω.cm for a film with a thickness of 140 nm and high optical transparency (i.e. a sheet resistance of 178 Ω.sq).

6.3.2.1 Effect of Ar/O_2 plasma and water on the growth of IO:H

Due to the configuration of the chamber and the position of the QCM (under the sample holder), we suspect that the plasma does not reach the QCM. The QCM therefore perceives almost no deposition and the cycles are not identifiable. It is then impossible to observe the evolution of the growth in real time and to interpret it as a posteriori. In order to identify the parameters that would give the highest growth rate, a screening type Design Of Experiment (DOE) developed with the help of Minitab software was used.

6.3.2.1.1 Design of experiment

First tests based on the literature quickly showed the formation of deposits on the samples. Following the DOE established by Minitab software, 21 randomized trials were conducted to study the impact of 9 variables on the deposition rate, see Table 6.5 for the variables studied and Appendix G for the detailed list of runs. The tests have been carried out with only 200 cycles per condition to save the precursor, which results in fairly fine samples. Then, the thickness of each sample is measured by ellipsometry and the deposition rate is calculated. We have chosen here to talk about growth rate in Å/min and not in Å/cycle because the time per cycle varied between 17 and 41 s.

Variable	Min	Max
Precursor pulse	1 s	5 s
Precursor Purge	4 s	8 s
Precursor Temperature	35°C	55°C
Water Pulse	1 s	3 s
Water Purge	4 s	8 s
Plasma Pre-pulse	2 s	4 s
Plasma Pulse	2 s	8 s
Plasma Purge	1 s	5 s
Chamber Temperature	160°C	200°C

Table 6.5: 9 variables studied according to the DOE to optimize the growth rate, with their minimum and maximum bounds (1 intermediate value each time).

6.3.2.1.2 Interpretations of results

The Minitab software allows to analyze the results of the DOE and to propose a model describing the evolution of the deposition rate according to the variables. First of all, the S-value is calculated as the distance between the data values and the values fitted by the created model. The smaller S is, the better the model describes the response. In our case, S is equal to 0.0063. In the same way the value R^2 gives the percentage of agreement between the experimental values and those predicted by the model and we reach 97.97%. These results confirm that the model created by Minitab is reliable.

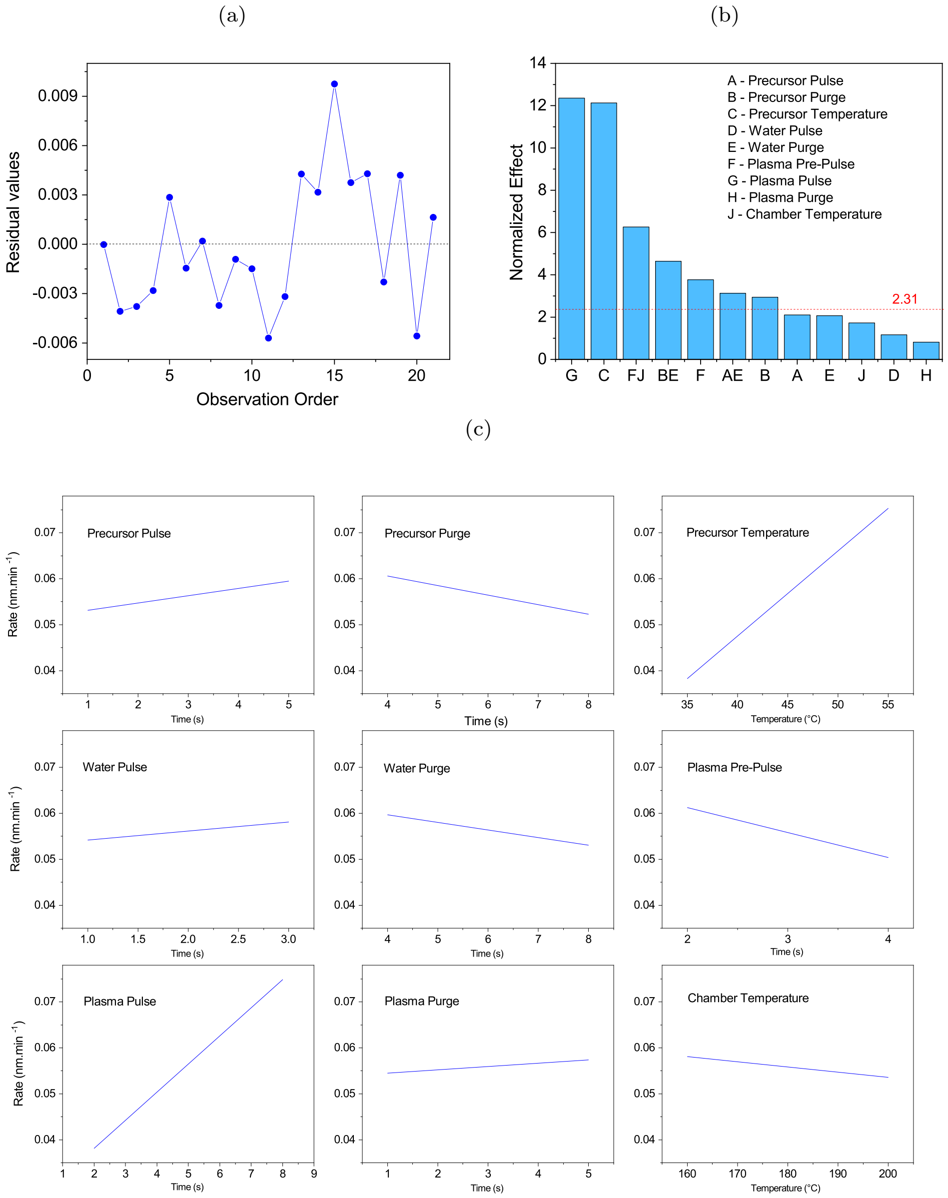

Figure 6.18: (a) Diagram of the residual values as a function of observation order. (b) Pareto chart of standardized effect, with the significance level α = 0.05. (c) Factorial plots of the deposition rate according to the 9 variables according to the created model.

Then, the diagram of the residual values presented in Fig. 6.18a shows the residual values (obtained by comparing model prediction and experimental values) in the order in which the data was collected. It allows verifying that the tests are well independent one from the other and they do not contain outliers. Independent trials do not generate any trend or pattern on the residual values diagram when they are displayed in chronological order, as observed here. Only trial n°15 really stands out from the others, and it has also been recognized by the software as an extreme value and excluded from the final model.

The Pareto chart of the standardized effects presented in Fig. 6.18b allows comparing the relative value and the statistical significance of the effects of each variable. The dotted line on the diagram delineates the threshold value for observing statistically significant effects. Four single variables (pre-pulse and pulse for plasma, temperature and purge for the precursor) as well as three interaction terms (plasma pre-pulse/chamber temperature, precursor purge/water purge and precursor pulse/water purge) are significant. These are the sets of parameters that will have a key role in the deposition rate.

The factorial diagrams presented in Fig. 6.18c show the evolution of the deposition rate according to the different variables. If we are only interested in the variable that has a significant influence on the deposition rate according to the Pareto chart, it is advisable to decrease the purge time of the TMI compared to the average values initially set. The temperature of the precursor should be at least 55°C. Finally, the plasma stabilization time has an unsuspected influence on the deposition time and must be limited in time, while the duration of the plasma pulse must then be increased.

The contour plots presented in Fig. 6.19 show the evolution of the deposition rate as a function of the interactions between the three interaction terms identified previously. The other parameters are fixed and the values are indicated above each graph. Thus, a long precursor pulse must be associated with a short water purge, see Fig. 6.19a. The purge that follows the precursor pulse is also defined according to the purge time of the water: it must be short if the water pulse is long and vice versa, see Fig. 6.19b. Finally, in Fig. 6.19c , the ideal stabilization time of the plasma outside the chamber depends on the temperature of the chamber. It must be increased at the same time as the temperature.

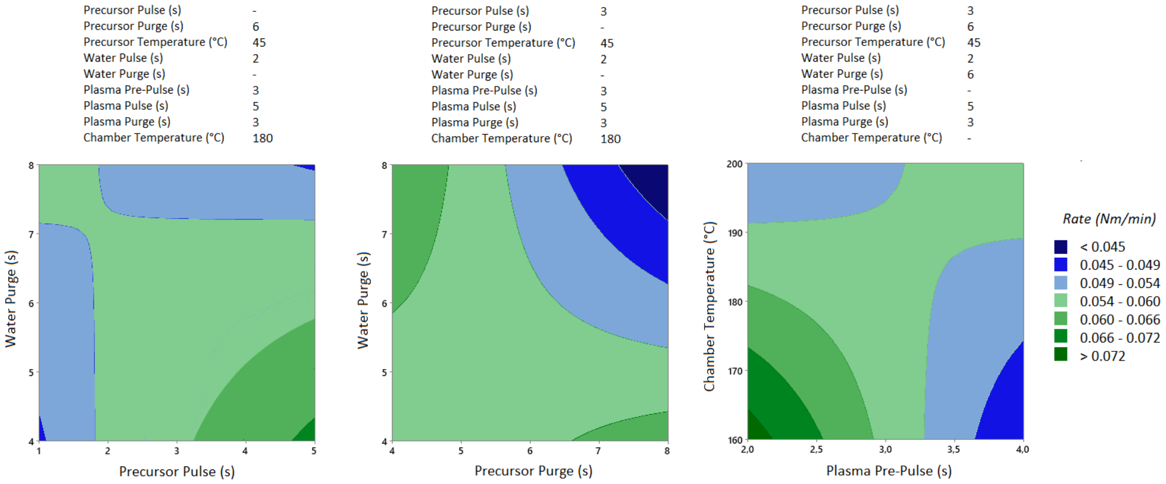

Figure 6.19: Contour plots of the deposition rate according to the interactions between the three interaction terms according to the created model: Precursor pulse/water purge, Precursor purge/water purge and Plasma pre-pulse/Chamber temperature. The hold values are indicated above each graph.

6.3.2.1.3 Optimal deposition and properties

Thus, thanks to the generated model, 3 optimal deposits in terms of speed are proposed, see Table. 6.6. These three deposits seem to allow particularly fast growth rates (>1.2 Å/min). A deposit of 1500 cycles is then realized using the proposed solution n°3 because it has the shortest TMI pulse time and thus allows to save some material. A layer of 88 nm is thus obtained on soda-lime glass and borosilicate, as well as on silicon.

The surface of the layer on glass seen by SEM shows a grainy appearance that differs from those on ITO and IZO, see Fig. 6.20a. Seen from the side, the layer seems nevertheless homogeneous and regular,as shown in Fig. 6.20b. As for the deposits made with $In(acac)_3$ as a precursor, the XRF measurement presented in Fig. 6.20c shows well the presence of indium in the sample on soda-lime glass, with the identification of the characteristic emission lines at 3.29 and 3.49 eV. However, this time the XRD reveals a crystalline sample whose peaks correspond to the preferential orientations of the (222), (400) and (440) In_2O_3 crystals that are the same as those of the IO:H, see Fig. 6.20d [176, 394, 399, 402].

The optical indices obtained by ellipsometry are close to those found in the literature as shown in Fig. 6.21a and b, which was not the case with the deposits with the $In(acac)_3$ precursor in the previous section. Thus optically, very good transparency is obtained as shown in Fig. 6.21c, the absorption after 900 nm is better than for an IZO layer of the same thickness (itself better than ITO), as is the optical gap. The 4-point measurements performed on the glass samples show a very high sheet resistance, 9k

Variable	**Solution 1**	**Solution 2**	**Solution 3**
Precursor pulse	5 s	5 s	1 s
Precursor Purge	8 s	4 s	4 s
Precursor Temperature	55°C	55°C	55°C
Water Pulse	3 s	3 s	3 s
Water Purge	4 s	8 s	8 s
Plasma Pre-pulse	2 s	2 s	2 s
Plasma Pulse	8 s	8 s	8 s
Plasma Purge	5 s	5 s	5 s
Chamber Temperature	160°C	160°C	160°C
Deposition Speed	1.29 Å/min	1.22 Å/min	1.26 Å/min
Deposition rate	0.75 Å/cycle	0.71 Å/cycle	0.65 Å/cycle

Table 6.6: 3 solution obtained and the values of the variables associated with the output of the DOE by the Minitab software in order to achieve deposition rates higher than 1.2 Å/min.

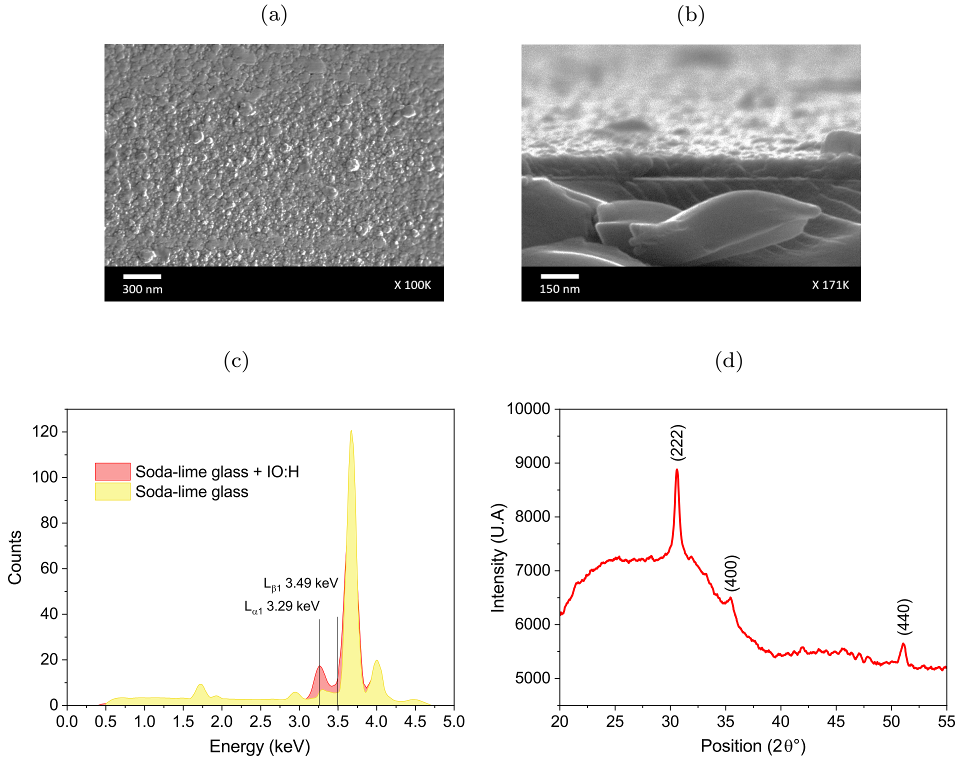
(a)

(b)

(c)

(d)

Figure 6.20: SEM image of (a) the surface of the solution n°3 on borosilicate glass, and (b) cross-section. (c) XRF emission spectra of the solution 3 compared to a borosilicate glass alone. The contribution of indium emission lines is shown in black. (d) XRD of the solution n°3, deposited on soda-lime glass (ICDD: 00-001-0929).

Ω.sq on borosilicate glass and 14k Ω.sq on soda-lime glass, which corresponds to 792 and 1320 mΩ.cm respectively. In comparison, Mane et al. obtain a resistivity of 19 mΩ.cm. before annealing with TMI by ALD, and Macco et al. synthesize a layer with a resistivity of 0.3 mΩ.cm by sputtering [398, 399].

As proposed by Mane et al. [398], we annealed the samples on glass at 400°C in free air to improve their conductivity. This proved beneficial as the resistivity decreased to 2k Ω.sq for both samples. However, after further SEM and spectrophotometric measurements, this annealing does not seem to have had any influence on the optical and morphological properties of our layers.

In conclusion, we have successfully deposited In_2O_3 by ALD using TMI as a precursor with H_2O and O_2/Ar plasma. The growth rate is comparable to that obtained in the literature, the optical properties and morphology seem to be correct but the resistivity is very high. It can potentially come from too much oxygen in the layer due to O_2/Ar plasma, which is known to be a dopant that makes TCO more transparent but resistive. The presence of hydrogen or not in the layer cannot be raised for the moment but future analyses by thermal desorption spectroscopy should allow us to conclude on this point.

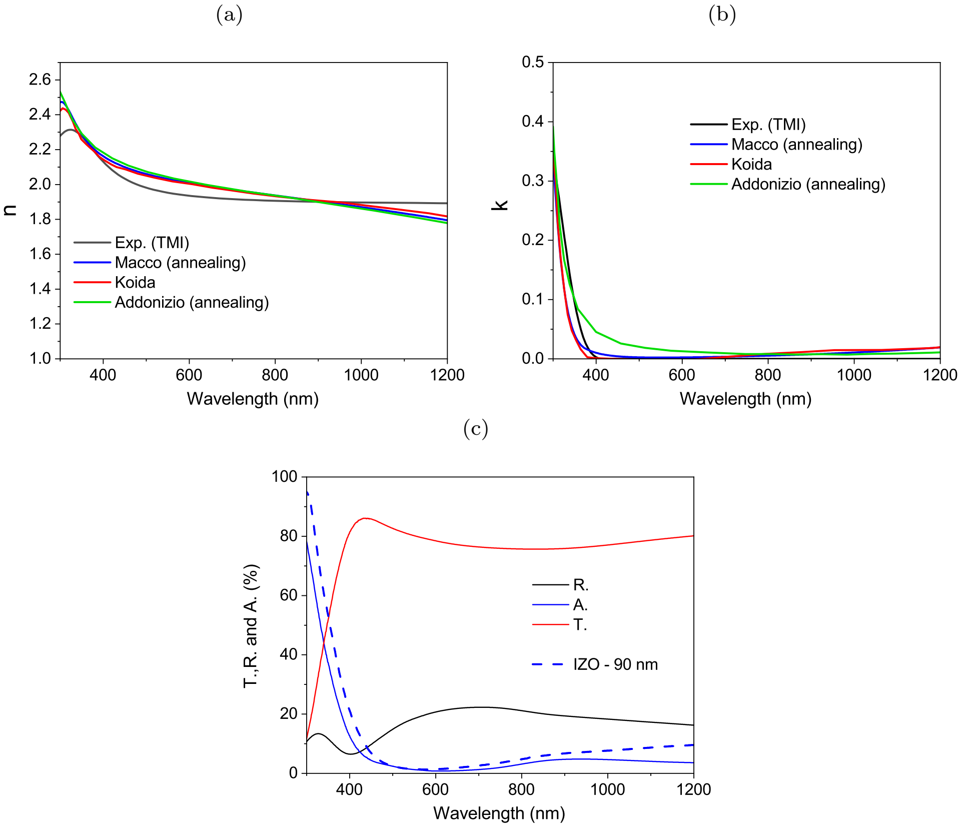
(a)

(b)

(c)

Figure 6.21: (a) Refractive index n and (b) extinction coefficient k of the solution n°3, compared to the existing values in the literature: Macco [399] and Addonizio [400] after annealing, and Koida [385]. (c) TRA spectra of the solution n°3 deposited on soda-lime glass.

6.3.2.2 Effect of ozone reactant on the growth of IO:H

We then tried to replace the use of the O_2/Ar plasma + H_2O duo by O_3 to see if it was possible to obtain a better conductivity, comparable to the one mentioned in the literature, or if this particular behavior came from elsewhere, see Chapter 2 Section 2.2.3.3 for details on the O_3 generation. As the plasma is no longer used, it is now possible to observe the growth of the layer in real time via the QCM, after calibrated it with a first deposit not shown here.

A dozen cycles with the following parameters are realized to check the functioning of O_3: 0.2 s of pulse for TMI and O_3, each time separated by a 4 s purge. The evolution of the thickness over 10 cycles is presented in Fig. 6.22a and shows a regular growth. By averaging the signal obtained by the QCM over the 10 cycles, Fig. 6.22b is obtained and the average evolution of the thickness is in red and the standard deviations is shown in black. We can see that the growth rate is very important, about 1 Å/cycle, i.e. 6.25 Å/min, higher than that observed in the previous section and than those found in the literature with the TMI.

Mane et al. show that the combination of H_2O and O_3 as an oxygen source for In_2O_3 generates layers virtually identical to that of O_3 alone [398]. In the idea of synthesizing the IO:H instead of In_2O_3, we add on our side a very fast water pulse (0.1 s) followed by a relatively long purge of 4.2 s. Compared to the use of O_3, continuous growth is kept as shown in Fig. 6.23a (1000 cycles) but the growth rate is reduced.

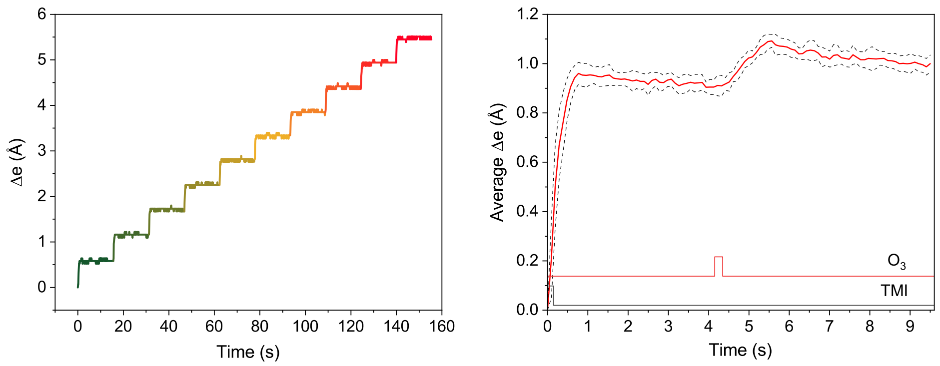
(a) (b)

Figure 6.22: (a) Thickness determining by QCM, of ALD In_2O_3 films deposited with O_3 as a reactant during 10 cycles. (b) Average on 10 cycles of the evolution of the thickness in red, dashed black plot represent the standard deviation.

It is now only 0.76 Å/cycle, or 3.35 Å/min. We notice that the thickness does not change between the end of the O_3 purge and the end of the cycle. The presence of H_2O seems in our case to slow down the deposit.

Finally, a thickness of 98 nm is obtained after 1500 cycles. The obtained layer has a resistivity of 1k Ω.sq, which is comparably obtained with plasma but after annealing. The SEM, spectrophotometric and XRD characterizations do not reveal any difference with the previous samples. Annealing similar to the one done in the previous section was done and did not affect the conductivity.

Thus, whether using H_2O and O_2/Ar plasma as reactant followed by annealing or H_2O and O_3, we obtain almost identical layers, still too resistive to imagine a use on solar cells. However, the growth rates obtained are correct without showing any saturation effect as with $In(acac)_3$. It is now possible to carry out another DOE, this time to find the ideal parameters to improve the conductivity of the layer. More annealing tests (temperature, duration, atmosphere...) can also be conducted with the same objective. In addition, the optical properties of the synthesized IO:H layer are also very encouraging, showing a higher transmission than IZO.

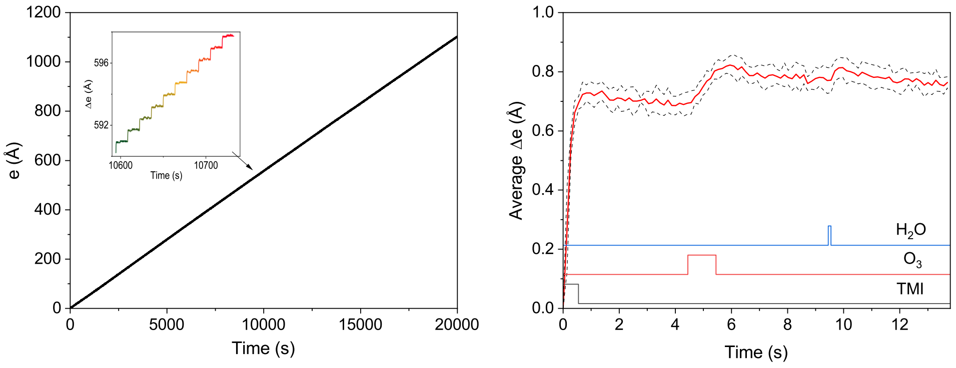
(a) (b)

Figure 6.23: (a) Thickness determined by QCM, of ALD In_2O_3 films deposited with O_3 and H_2O as reactants during 1000 cycles. Zoom is made on 10 cycles in the middle of the deposit. (b) Average on the 10 cycles presented in (a) of the evolution of the thickness in red plot, dashed black plot represents the standard deviation.

Conclusion

In this chapter, we have been able to apply the improvement tracks of the electrodes investigated in Chapter 4. Simulation allows to calculate absorption in each single layer of the structure separately, and it reveals that the origin of the main parasitic absorption is in transparent conductive oxide layers FTO and ITO.

We have first developed IZO deposition by sputtering in order to replace the ITO top electrode. After the study of the deposition parameter on glass, a process at 50 W for a pressure of 2 mTorr and a flow of Argon at 33 sccm without the addition of oxygen has made it possible to obtain a thinner and more transparent IZO layer for a sheet resistance similar to ITO (16 Ω.sq). Then, IZO-based solar cells have been studied and as for ITO, the use of a low power bilayer for IZO proved to be more interesting than single layers by reducing the dispersion and increasing the FF. Despite poorly positioned interferences, the gain in transmission and tandem performance is already visible. A slight modification of the IZO layer thickness and the use of an anti-reflective coating and a coupling liquid should make it possible to take full advantage of the gain in transparency offered by IZO.

The co-sputtering test of IZO and ITO targets resulted in the formation of an IZTO electrode, which has electrical and optical properties close to those of IZO. The first test on STPC resulted in a high dispersion in contrast to conventional STPC but this may be due to an inadequate power of the two targets and further tests could easily be performed.

We have also shown that the use of TCO grids by taking IZO as an example, would allow reaching higher efficiencies in tandem configuration thanks to a very favorable opto-electrical balance. Via experimental TLM measurements and optical simulations, the simulated performance obtained in tandem configuration is maximum with the integration of a structured thick IZO (21.4%), as this layer has both a higher conductivity than the thin IZO layer, while maintaining much higher transparency over the whole range than the thick planar IZO layer. These simulated results must now be confirmed by experimental tests on STPC and larger surfaces.

Concerning the FTO electrode at the rear side, we haven chosen IO:H as an ideal replacement material. In order not to contaminate the sputtering equipment by injecting water into them, we chose to use ALD as the deposition method. Different indium precursors can be used to synthesize In_2O_3 and consequently IO:H, and we chose to focus on $In(acac)_3$ and TMI because of their lower cost than others. Deposition with $In(acac)_3$ showed a saturation phenomenon above 45 nm thickness. These results are in agreement with the literature and confirm the difficulty of growing indium oxide, doped or not, using this precursor. On the other hand, with TMI, we used an experimental design to precisely identify the parameters influencing the deposition rate. This allowed us to succeed in growing layers of more than 80 nm with crystallographic, optical and morphological characteristics expected in IO:H, whether using H_2O and O_2/Ar plasma as reactants followed by annealing or H_2O and O_3. Further optimizations are now needed to reduce the resistivity of the layers before using them in the STPC structure.

Chapter 7

Toward a highly efficient large surface 4T perovskite/silicon tandem modules

Introduction

In the previous chapters, we have focused on developing and improving our STPC. In particular, we have improved their reproducibility and opened ways to manufacture devices that are always more transparent while remaining efficient.

Nevertheless, our STPC have an active surface of only 0.09 cm^2, which does not allow today to consider an industrial application. It will be necessary to increase the size of these devices and this must be done through two approaches conducted in parallel. In the medium term, the increase in size up to 25 cm^2 will require new the deposition techniques to replace spin coating, more suitable for industry and homogeneous over larger surfaces like slot die coating [403]. A first step has consisted of transferring the deposition process of perovskite layer from spin coating to slot die coating, actually developed at IPVF, and open the path toward the fabrication large size semi-transparent perovskite device.

In parallel, on surfaces larger than 1 cm^2, it is necessary to propose module-like devices connecting the cells together in order to avoid detrimental series resistance. The efficiency record of perovskite solar mini-modules (< 200 cm^2) is 20.1% with a designated illumination area of 63.98 cm^2 with 12 serial cells, manufactured by Utmolight [17]. Clearly, the efficiencies of this type of devices are still substantially lower than other kinds of commercialized solar modules, as well as small size perovskite record cells. Demonstrations of Semi-Transparent Perovskite Mini-module (STPM) and their improvements in efficiency are therefore at the heart of our strategies towards highly efficient large surface 4T tandem.

7.1 Slot-Die coating for large-area perovskite solar cells

As an alternative to spin coating, several compatible large-scale fabrication techniques have been investigated as blade-coating [129], spray-coating [130], screen-printing [131], or slot-die coating [132, 133]. Among these techniques, slot die coating remains one of the most studied techniques and probably the most preferred deposition route. However, depending on the drying techniques chosen, the solution chemistry and processing conditions developed for spin-coating coating cannot be directly applied from slot die and requires a new development phase. The incorporation of additives into the perovskite precursor solution may be necessary to promote nucleation and slow the growth rate. Finally, the final film morphology is highly dependent on the solvent extraction method. Indeed, a fast solvent extraction from the perovskite precursor solution is crucial to reach the supersaturation state faster, thus promoting a higher number of nuclei. The objective of this section is the transfer of this technology from opaque cells, realized in another thesis, to the case of semi-transparent cells.

The studies presented in this chapter only concern 0.09 cm^2 cell size samples in order to validate the process, but should eventually allow in the future the synthesis of modules and large devices. The detailed synthesis process of slot die based STPC can be found in Chapter 2 Section 2.1. In summary, the substrate (TEC-7) and all layers (mesoporous and compact TiO_2, PTAA and ITO) except the perovskite are deposited using the baseline process. The perovskite layer alone is deposited by slot die coating. Thus, we will start by investigating at the optical and morphological properties of the perovskite layer, which differs from the usual triple cation perovskite. We will then study how to integrate sputtering deposition on complete cells, their performance and their evolution in time.

7.1.1 Optical and morphological characteristic of the double cation perovskite

The double cation perovskite deposited by slot die ($Cs_{0.17}FA_{0.83}Pb(I_{0.83}Br_{0.17})_3$) has a different composition than the tripe cation perovskite used in the baseline process. Therefore, its optical properties are modified and in particular its bandgap due to the absence of MA as a cation [41, 81]. The Fig. 7.1a shows the ellipsometric fit obtained, according to the modelling detailed in Chapter 4, with a particularly complex stacking (TEC-7/Compact TiO_2/Perovskite). This is due to the impossibility to deposit perovskite by slot die directly on glass. As a consequence, the X^2 obtained is good (8.5) but still higher than for the triple cation perovskite of the baseline (1.7) seen in Chapter 4 Section 4.1.1.5. The MAE are below 3% for the TRA spectra which validates the accuracy of these indices. As it is shown in Fig. 7.1b, the optical indices show a slight variation of energetic levels due to the different bandgaps: 1.58 eV for the baseline and 1.64 eV for the slot-die coated perovskite films. The higher gap of the double cation perovskite is an advantage for its use in tandems. Indeed, as mentioned in Chapter 1 Section 1.2.3, the ideal gap of a perovskite cell is 1.7 eV when coupled to a silicon cell in 4T tandem configuration. Using a perovskite with a gap of 1.64 eV instead of 1.58 eV represents a gain of almost 5% on the maximum theoretical efficiency achievable in 4T tandem with a silicon cell.

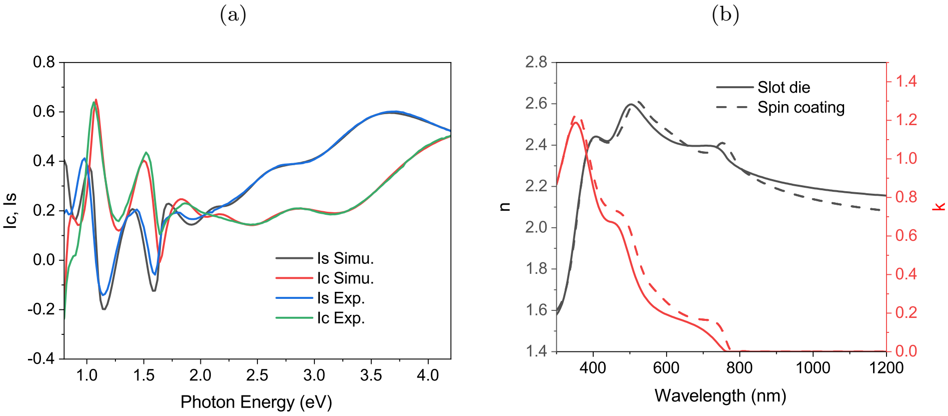

Figure 7.1: (a) Simulated and experimental ellipsometry measurement and (b) refractive index and extinction coefficient of double cation perovskite deposited by slot-die coating.

7.1.2 Synthesized STPC with slot die coating

This process should eventually replace the baseline in order to realize large-area perovskite solar cells with a higher gap. It is therefore important to evaluate the compatibility of this structure with ITO sputtering, both in electrical and optical properties. For this purpose, 12 STPC and 12 opaque cells were fabricated in batch SB32, half with Spiro-OMeTAD as HTL and the other half with PTAA.

7.1.2.1 Morphology of STPC

Fig. 7.2a and d show the confocal images of the ITO layer morphology deposited on slot die STPC with Spiro-OMeTAD and PTAA, respectively. The ITO layer grown on Spiro-OMeTAD layer presents a smooth surface (Sa = 22 nm). However, a rougher surface is observed when the ITO layer is deposited on PTAA (Sa = 42 nm). It is characterized by the presence of local dots of 250 nm thickness, and less than 1 µm in diameter. The SEM image in Fig. 7.2e shows that perovskite layer is not totally covered by the PTAA. As the double cation perovskite is rougher than the triple cation perovskite (Sa = 36 vs. 15 nm), the thinness of the PTAA (20 nm) may create a poor coverage of the perovskite layer while the Spiro-OMeTAD is much thicker (300 nm). We also notice that the morphology of the ITO on the surface is different between the deposition on Spiro-OMeTAD and PTAA, which is not the case on cells with triple cation. It forms much larger grains in the case of PTAA (200-500 vs. 30 nm diameter). Finally, we see on the cross-section in Fig. 7.2c and f that the ITO adheres perfectly to the Spiro-OMeTAD and PTAA surface.

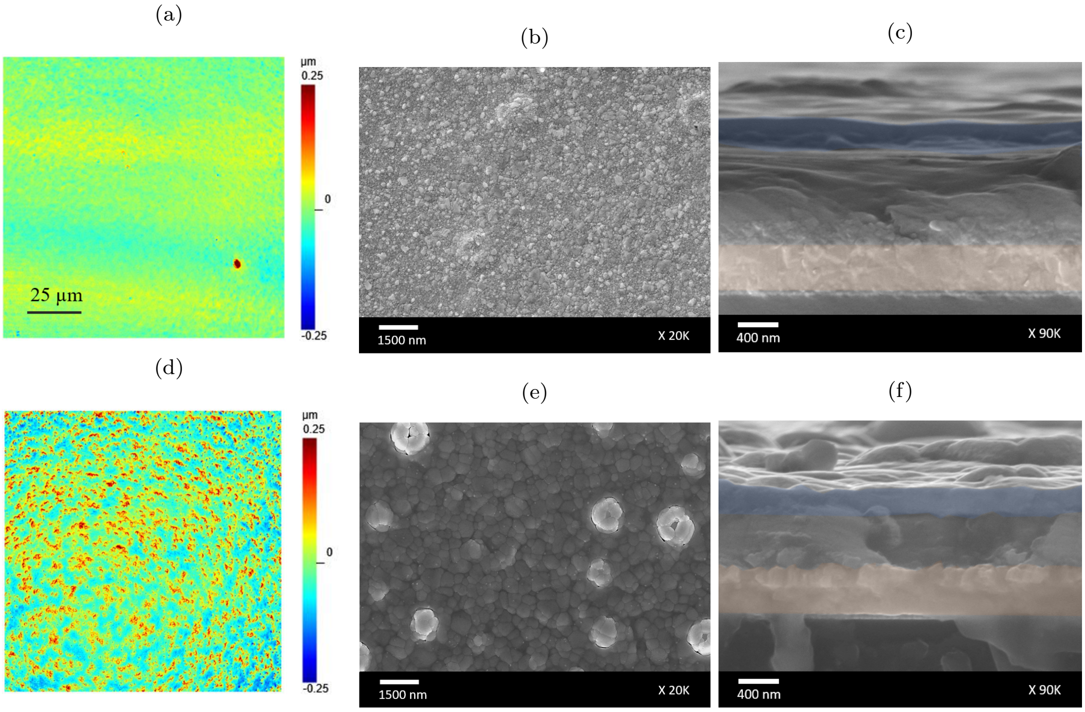
(a) (b) (c) (d) (e) (f)

Figure 7.2: (a) and (d) Confocal microscopy image of the surface, (b) and (e) SEM image of the surface and (c) and (f) cross-section of slot-die STPC with Spiro-OMeTAD and PTAA as HTL, respectively. The blue area corresponds to the ITO layer and the orange area to the FTO layer.

7.1.2.2 Electrical and optical properties of STPC

7.1.2.2.1 Effect of the perovskite deposition process on the dispersion of the electrical properties

Concerning the opaque cells manufactured with the slot die process, similar performances are observed whatever the HTL is employed (16.8% for the PTAA and 17.5% with the Spiro-OMeTAD), see orange line in Fig. 7.3a and b for the average values. Nevertheless, slightly higher hysteresis was observed in the case of the PTAA compared to Spiro-OMeTAD, which is the opposite with triple cation perovskite. On strictly identical structures except for the composition of the perovskite, these performances are the highest found in the literature [404]. On similar structures, the teams of Kim [405] and Whitaker [132] each showed efficiencies of 17.3% and 18% respectively when replacing TiO_2 with SnO_2 and retaining Spiro-OMeTAD as HTL.

Concerning the STPC on the first day after synthesis as shown in Fig. 7.3, cells with Spiro-OMeTAD already have a relatively high average efficiency of 14.1%. The difference with the performance of the opaque cells of the same batch is -3.5% and this is directly caused by lower average Jsc and FF, which is expected behaviour for STPC. These STPC have also a low dispersion ($\sigma = 1.11$) and this can be compared with the AY45 batch, which was produced by spin-coating, see Chapter 5 Section 5.1.2.2. The dispersion was much higher in batch AY45 for STPC with Spiro-OMeTAD ($\sigma = 5.95$). This is directly caused by a much higher dispersion of Voc and FF, while the Jsc is larger (20.3 versus 18.22 mA.cm^{-2}). It seems that Spiro-OMeTAD Slot die based STPC have better resistance to ITO sputtering.

On the contrary, SB32 STPC with PTAA have a very high dispersion ($\sigma = 4.99$) and only 2 of the 6 cells reach similar performances to the STPC with Spiro-OMeTAD (13 and 13.6%), whereas the opposite is observed with spin-coating based STPC such as the AY45 batch. The difference with the performance of the opaque cells is -8.3% for the PTAA cells (only -3.1% if we consider only the two best performing cells). This dispersion, due to both Voc and FF, can be caused by the poor covering of the perovskite layer by PTAA. Indeed, even if this phenomenon is not observed with opaque reference cells (similar dispersion whatever the HTL), the perovskite is here directly exposed to sputtering without any protection. Considering the effect of sputtering on organic layers like Spiro-OMeTAD observed in Chapter 3, a deleterious effect on the perovskite layer is highly probable.

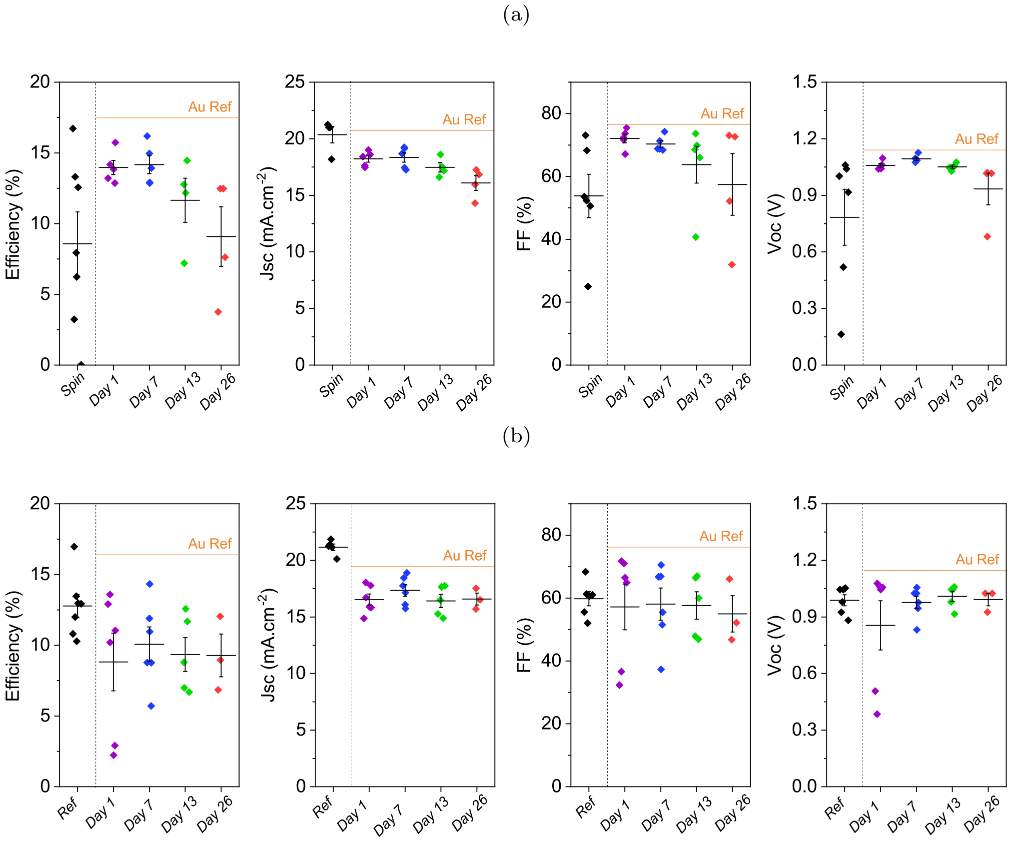

Figure 7.3: Dispersion of the electrical properties of SB32 slot die based STPC with (a) Spiro-OMeTAD and (b) PTAA as HTL, first day after the synthesis, and 7, 13 and 26 days later. Orange line represent the average value obtain for reference opaque cells in each case, fist days after the synthesis. These results are compared with those obtained in the AY45 batch (spin coating based perovskite), already presented in Chapter 5 Section 5.1.2.2.

The IV of the best STPC of each category are presented in Fig. 7.4a and b. We notice that the STPC with Spiro-OMeTAD have a less marked hysteresis than those with PTAA (-0.7 vs -3.8% on efficiency). This phenomenon is similar to spin-coating based STPC, although it is less pronounced. The latter has a particular behavior in forward scan on the low voltage side. Finally, the S-shape described and studied in Chapter 5 is not observed here. A reaction specific to the triple cation perovskite with HTL and indium-based TCO may be at the origin.

Finally, EQE highlights a conversion loss for longer wavelengths than 500 nm, see Fig. 7.4c. This tendency, common to both Spiro-OMeTAD and PTAA devices, results of an insufficient thickness of the absorber layer. This phenomenon is also visible on the STPC with triple cation perovskite between 500 and 700 nm, but in a less marked way, as shown in the absorption curves in Fig. 7.4d, where the slot-die STPC absorb 4.6% less than the baseline STPC at 710 nm. Moreover the total absorption reaches 74% at 710 nm, which does not seem to be in line with an EQE of only 53% on average at this wavelength. A greater extraction problem under low illumination could be the cause of this difference. In addition, the gap seems to vary between 750 nm and 770 nm. In the IR, we can also note again the interest to use PTAA, which results in a decrease of the total absorption of -7% at 1000nm compared to devices with Spiro-OMeTAD.

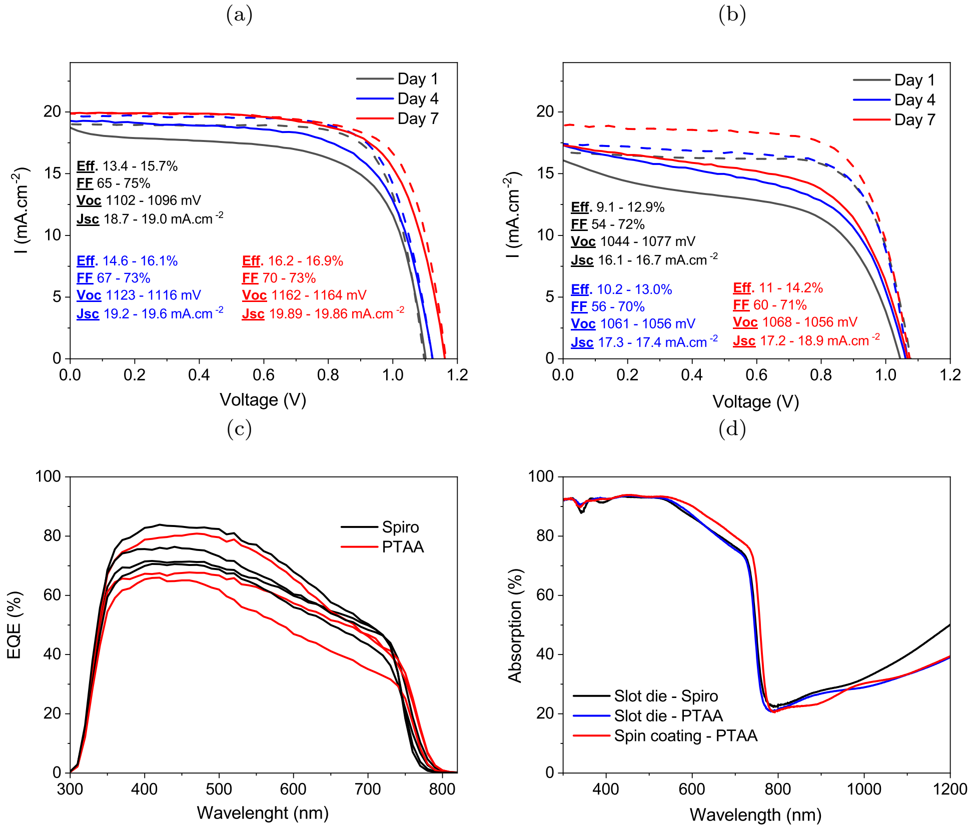
(a) (b) (c) (d)

Figure 7.4: (a) IV curves of the best slot die based STPC with (a) Spiro-OMeTAD (SB32-77) and (b) PTAA (SB32-97), 1, 4 and 7 days after the synthesis. (c) EQE spectra of slot die based STPC from batch SB32, with Spiro-OMeTAD or PTAA as HTL. (d) Absorption spectra of slot die based STPC with Spiro-OMeTAD or PTAA as HTL, and a spin-coating based STPC with PTAA.

7.1.2.2.2 Aging and stability of STPC

The performance of the Spiro-OMeTAD STPC increases slightly during the first seven days until it reaches an average efficiency of 14.1% (+0.1%). This increase is much smaller than in the case of spin-coating based STPC. Moreover, the performance then deteriorates rapidly. The average efficiency is only 9.1% 26 days after synthesis, see Fig. 7.3. This is due to the generation of pinholes on the surface of the STPC and the delamination of the ITO electrode even without special heating. This has an impact on all electrical parameters and leads to a decrease in Jsc, Voc and FF.

In contrast, the PTAA devices show only small variations over time. Two populations can be distinguished: the better performing cells stabilise and the worse performing ones improve, resulting in a significant reduction in dispersion over time. This behaviour is more similar to the triple cation based STPC. Thus, 26 days after synthesis, PTAA cells are on average more efficient than Spiro-OMeTAD based cells (9.3% vs. 9.1%).

Thus, slot die cells using Spiro-OMeTAD as HTL show higher efficiencies and lower dispersion than those using PTAA, but with less stability over time.

7.1.3 Conclusion

In summary, we have shown that ITO deposition by sputtering is compatible with the double cation perovskite deposition process by slot-die coating. The results obtained with Spiro-OMeTAD as HTL are close to those obtained with STPC fabricated by spin-coating but they have a negative time evolution. Coupled with the fact that it is not possible to encapsulate the STPC with Spiro-OMeTAD, this solution is not viable in the long term. The results with PTAA are promising but still have a lack of reproducibility due to the roughness of the perovskite compared to the thinness of the PTAA layer. This could be improved by using other surfactants for example. In the future, the use of this technique will make it possible to make semi-transparent devices exceeding 25 cm^2, with a band gap suitable for a 4T coupling with a silicon cell.

Nevertheless, in the remainder of this chapter, we will use the spin-coating process to study the size increase, due to the know-how of the laboratory and the best results currently obtained with this technique.

7.2 0.09 cm^2 optical pseudo-tandem devices

In high efficiency semi-transparent solar cells based on different perovskites (double or triple cation), different TCO (ITO or IZO) or different HTL (Spiro-OMeTAD or PTAA) have been synthesized on a small area. In parallel, at the end of Chapter 3, we presented our first 4T tandem of 0.09 cm^2, which consisted in mechanically stacking an STPC on a 1 cm^2 Al-BSF Silicon cell. In this section, we test a new process transferable to a larger surface, in order to obtain a real measurable 4T tandem and validate its compatibility with our different STPC structures. We start by using 25 cm^2 semi-transparent filters which reproduce the structure of different STPC. These filters are each associated with a 20.25 cm^2 silicon cell. The surface area of there optical pseudo-tandem devices is therefore 20.25 cm^2 but as the electrical measurements of the STPC were obtained on 0.09 cm^2, the measured tandem efficiencies will be considered as valid only at this size.

7.2.1 Opto-electrical properties of perovskite filters and associated STPC

5 stacks representing 5 types of STPC studied along this manuscript are fabricated (A,B,C,D and E), see Fig. 7.5a. They are the classical structure with Spiro-OMeTAD from Chapter 3, the structure with PTAA from Chapter 5, the structure with IZO from Chapter 6 and the two structures with a perovskite deposited by slot die presented earlier in this chapter. The different layers are deposited using the same process as STPC but without electrical contacts, and on a surface area of 25 cm^2 to created optical filter. The optical characteristics of these filters are similar to those of the associated STPC, as shown in Fig. 7.6 with filter B and the STPC MP16-25 composed of a triple cation perovskite, PTAA and IZO. The only exception is filter A with triple cation perovskite and Spiro-OMeTAD. We have seen in Chapter 5 Section 5.1.2 that it was not possible to deposit ITO on such a large surface with this kind of stacking because of the systematic detachment of the electrode. The solution found was to proceed to some thin etchings with laser on the sample in order to release the various constraints during the ITO sputtering, see Fig. 7.5a.

In addition, in Chapter 4 Section 4.2.3, we proposed an ideal structure allowing to reach realistically a high efficiency for STPC with a transmission of 90% in the IR. We are not able for the moment to synthesize such a structure because the development still in progress for IO:H layer, so we realize the filter F according to the close structure presented in Fig. 7.5a. It is composed of a borosilicate glass on which an anti-reflective coating of MgF_2 is deposited on one side, and on the other side, a thin layer of ITO replaces the IO:H. The SnO_2 used in Chapter 5 is used here as ETL. The triple cation perovskite and the PTAA are similar to those of structure B. Finally, 100 nm of IZO is deposited as a back electrode according to the process detailed in Chapter 6. The whole structure does not show any particular delamination and has a homogeneous surface.

The IV of the best STPC corresponding to each of the stacks, already presented in this manuscript, are recalled in Fig. 7.5b and Table 7.1. The two STPC A and B are composed of a triple cation perovskite deposited by spin coating, and Spiro-OMeTAD and PTAA as HTL respectively. Cell A reaches 18.4% of efficiency with a very low hysteresis and a fill factor at 76%. However, with this type of stacking, the reproducibility was not good. By replacing the Spiro-OMeTAD by PTAA, a significant gain in reproducibility was obtained. The best cell using PTAA achieved an efficiency of 17.8%. The differences between the efficiencies is due to a lower Voc for cell B (1076 vs. 1125 mV) than cell A. The C cell also has PTAA as HTL but the ITO electrode has been replaced by IZO. It reaches 16.3% efficiency, due to a lower FF than cell B (-8%) while it has a better Jsc and Voc.

Cells D and E differs from the others by the composition of the perovskite used and the deposition process of this layer (slot die coating instead of spin coating). Concerning the cell D with Spiro-OMeTAD HTL, its efficiency reaches 16.9%. The differences between the electrical parameters with cell A and B, a lower current together with a higher Voc, are related to the larger gap of the double cation perovskite that contains a higher ratio of cesium. However, results are significantly lower for cell E with PTAA and double cation perovskite (14.2% of efficiency) than for cell B (17.8%). This is caused mainly by a lower current (18.9 vs. 21.7 mA.cm^{-2}) and a similar Voc at 1056 mV not coherent with the larger gap of the double cation. In addition, cell E has a hysteresis larger than all other cells.

(a)

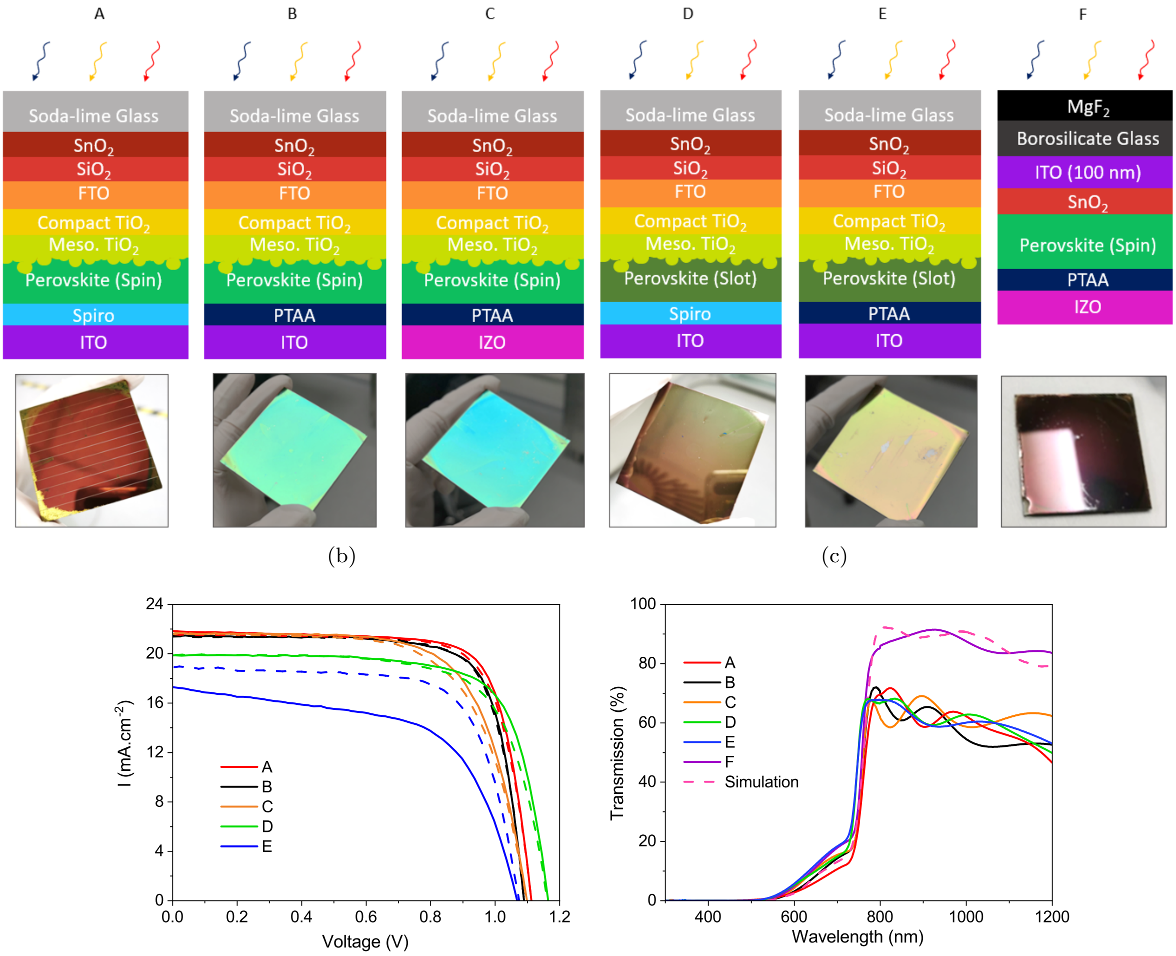

(b)

(c)

Figure 7.5: (a) Stack and picture of 6 different filter. (b) IV curves of the best STPC of each category, corresponding to the structures presented on (a). (c) Transmission spectra of STPC stack presented in (a).

STPC	**Scan**	**Jsc (mA.cm^{-2})**	**Voc (mV)**	**FF (%)**	**Efficiency (%)**
A) AY10-b-09	RV	21.84	1125	76	18.4
	FW	21.56	1101	75	18
B) MA17-08	RV	21.46	1076	76	17.8
	FW	21.39	1075	76	17.7
C) MP16-18	RV	21.60	1099	69	16.3
	FW	21.61	1098	66	15.7
D) SB32-97	RV	19.86	1164	73	16.9
	FW	19.89	1164	70	16.2
E) SB32-77	RV	18.9	1056	71	14.2
	FW	17.2	1068	60	11

Table 7.1: Electrical characteristics of best STPC of each category, corresponding to the structures presented in Fig. 7.5a.

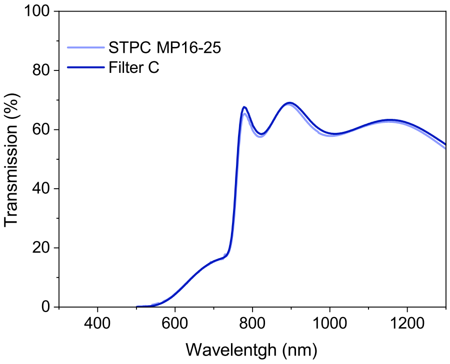

Figure 7.6: Transmission spectra of filter C and the associated STPC MP16-25.

Finally, the transmissions of each filter are shown in Fig. 7.5c. All the filters except the optimized one F have a similar behavior in the IR with a shift of the interference patterns between them. The slight difference in gap between the A/B/C (triple cation perovskite) and D/E (double cation perovskite) filters can be observed around 750 nm. Finally, we also observe that the C filter, which is the only one with an IZO electrode, has an improved transmission at 1200 nm despite the interference patterns. Concerning the transmission of the optimized structure F, it is indeed much better than the other (90% transmission at 900 nm) and matches with the simulation presented in Chapter 4 Section 4.2.4.

7.2.2 Choice of silicon bottom cells

The silicon cells used here are the same as those presented in Chapter 4 Section 4.3.1: IBC, n-PERT n°1 and n°2. We saw that the IBC Silicon cell had superior performance to both types of n-PERT cells. However, these IV measurements were performed on cells of various sizes and not encapsulated. In order to be able to use them in a 4T tandem of 16 cm^2, they have been cut and now have a stringed active surface area of 20.25 cm^2. In addition, as for the STPM, it is necessary to guarantee the durability of the Silicon cell in time and prevent any type of electrical interference with the top cell once in tandem configuration. Thus it was chosen to realize an encapsulation with a polyolefin film (PO) to protect them from moisture, see Fig. 7.7a which shows a cell of type n-PERT n°2 once encapsulated. These steps were not carried out at the IPVF but by the supplier.

Table 7.2 shows the electrical properties before and after encapsulation of the best silicon cells of each category. We can see that the properties of the IBC cell are more degraded after the encapsulation process (-5.9% of efficiency) and that it is the n-PERT n°2 cells that now have the best efficiency (19.3%). During size reduction, the metallization was adapted on the two types of n-PERT so that the laser cut would not pass over it and was optimized for the desired size. However, for the IBC cell, the metallization was not adapted before cutting. It is possible that the laser heats or melts the metallization, which can promote recombinations, in addition to those already created because of the edges generated during cutting. We observe in particular a deformation of the IBC cells once encapsulated, the cells are slightly bent because of the bus bar underneath. Therefore we will use the encapsulated n-PERT n°2 cells afterwards for the manufacture of our 4T tandem.

Silicon cell	**Encapsulation**	**Jsc (mA.cm^{-2})**	**Voc (mV)**	**FF (%)**	**Efficiency (%)**
n-PERT n°1	No	39.15	662	79	20.6
	Yes	37.88	640	74	18.1
n-PERT n°2	No	39.33	678	80	21.4
	Yes	39.33	684	74	19.9
IBC	No	40.91	684	81	22.7
	Yes	35.4	670	71	16.8

Table 7.2: Electrical characteristics of the different Silicon cell technologies, before and after encapsulation.

6 silicon n-PERT n°2 cells (a, b, c, d, e and f) with similar performance are chosen to be associated to each of the semi-transparent perovskite filters and form the pairs A-a, B-b, C-c, D-d, E-e and F-f. The IV measurements are made on a 16 cm^2 surface delimited by a mask. They show some variations in their electrical properties as shown in Fig. 7.7b and Table 7.3. The e Silicon cell presents higher FF (75%) than the others (72-74%). However, the a Silicon cell has the best efficiency (19.9%) with the highest Jsc (39.33 mA.cm^{-2}). The b and c cells shows the lower electrical properties, with efficiency of 19.1%.

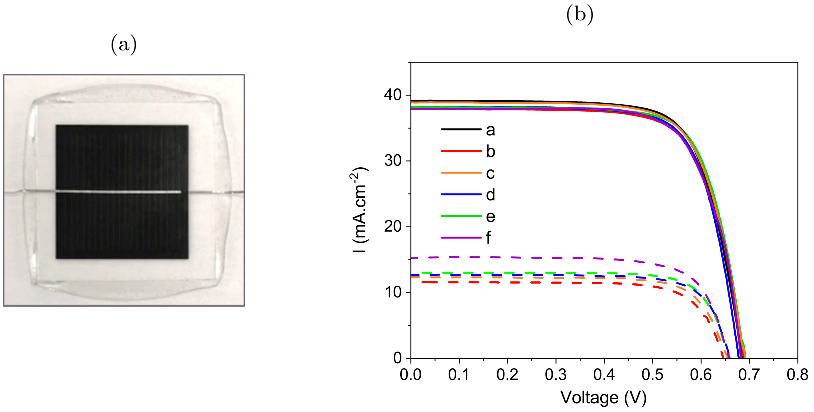
(a)

(b)

Figure 7.7: (a) Photo of a n-PERT n°2 Silicon cell once encapsulated. (b) IV curves of the different n-PERT n°2 Silicon cells (a-f) unfiltered and filtered by the associated filters after mechanical stacking.

n-PERT n°2 Si. cells	**Jsc (mA.cm^{-2})**	**Voc (mV)**	**FF (%)**	**Efficiency (%)**
a	39.33	684	74	19.9
b	37.83	688	73	19.1
c	38.79	689	72	19.1
d	38.21	679	74	19.3
e	37.98	690	75	19.7
f	37.94	684	74	19.1

Table 7.3: Electrical characteristics of the 6 unfiltered n-PERT n°2 Silicon cell associated to each filter.

7.2.3 Tandem association

7.2.3.1 Mechanical stacking of perovskite filters and silicon cells

First, each perovskite filter is mechanically stacked on the masked Silicon cell associated. This allows to assess the performance of filtered silicon bottom cells in tandem configuration, and to obtain a reconstructed tandem efficiency correct on 0.09 cm^2 using the properties of the STPC associated to each filter. The performances obtained for each tandem are presented in the Table 7.4.

For example, the rebuilt efficiencies for the A-a (Triple Cation/Spiro-OMeTAD/ITO) tandem is 24.8% (18.4% + 6.4%), making it the most efficient tandem we have ever made. However, this type of stacking creates an air gap between the bottom cell and the filter, which generates additional reflections. This is deleterious to the final tandem efficiency as we have shown in Chapter 4 Section 4.2.1.3.

When Spiro-OMeTAD is replaced by PTAA, as for tandem B-b, the final efficiency remains high with 23% efficiency. As the silicon b-cell is less efficient than the a-cell, this structure is able to reach the performance of the A-a tandem. However, when the ITO electrode is also replaced by IZO, the performance drops to 21.9%, while the silicon b and c cells are similar. Furthermore, when filtered, the c cell performs better than the b cell (5.6% vs. 5.2%). The worse performance in tandem is caused by the C-c structure. We have indeed seen in Chapter 6 that better electrical results with this STPC structure could be expected in the absence of synthesis concerns in the lower layers. The use of a double cation perovskite deposited by slot die with Spiro-OMeTAD or PTAA as HTL with ITO electrode results in tandem efficiencies of 22 and 20.2% respectively.

Finally, the silicon cell f filtered by the optimised perovskite filter F achieves 7.5%, which outperforms all others by more than 1.1% absolute, whereas the silicon cell was among the worst performers along with the b and c cells (19.1%).

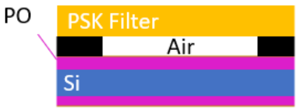

Figure 7.8: Scheme of perovskite filter mechanically stacked on the masked Silicon cell associated.

Filterd Si. cell	PDMS	Jsc (mA.cm^{-2})	Voc (mV)	FF (%)	Efficiency (%)	Tandem (%)
a	No	13.03	637	74	6.4	24.8
	Yes	11.17	657	77	5.7	24.1
b	No	10.79	647	74	5.2	23
	Yes	11.58	648	75	5.6	23.4
c	No	11.39	652	75	5.6	21.9
	Yes	12.29	658	75	6.1	22.4
d	No	11.60	657	76	5.8	22
	Yes	12.69	664	76	6.4	22.6
e	No	11.90	657	77	6	20.2
	Yes	13.08	659	77	6.6	20.8
f	No	15.23	653	75	7.5	-
	Yes	15.63	672	77	8.2	-

Table 7.4: Electrical characteristics of the filtered n-PERT n°2 Silicon cell by each of their associated filters, and tandem final efficiency with or without PDMS at the interface.

7.2.3.2 PLA case and PDMS for a compact and solid prototype

A second architecture is proposed to reduce the parasitic reflections between the two cells. For this purpose, a Polylactic Acid (PLA) case and an aperture mask have been 3D printed. The Silicon cell with its mask is centered inside the PLA case, see step 1 in Fig. 7.9. Then, PDMS is poured inside the case in order to cover the silicon cell and to hold it in its position. Simultaneously, a thin layer of PDMS is deposited on the perovskite filter, to protect the fragile ITO layer on the surface before making the tandem. The filter is then added in the PLA case, above the Silicon cell covered with PDMS, and correctly centered, see step 2 in Fig. 7.9. PDMS is again poured up to the filter height to hold it and link it to the rest of the structure, and a mask is added to obtain the final result shown in step 3 Fig. 7.9.

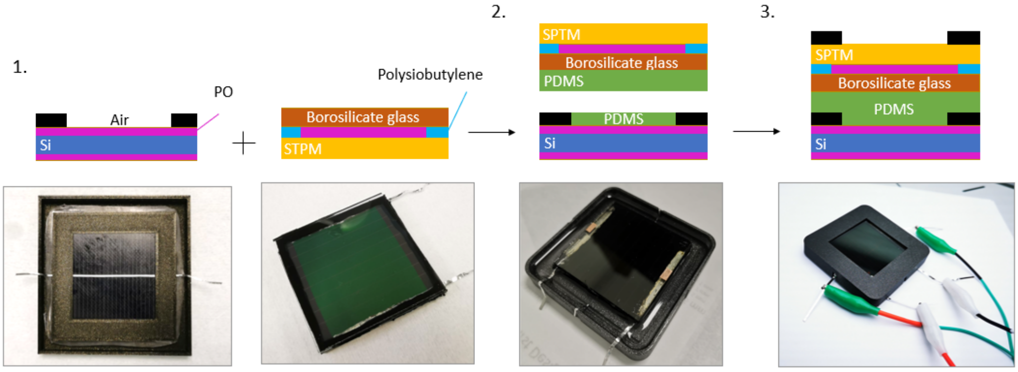

Figure 7.9: Manufacturing stage of the pseudo optical tandem: 1. Silicon cell with its mask is centered inside the PLA case and fixed with PDMS, 2. Optical perovskite filter covered by PDMS is added in the PLA case, above the c-Silicon cell, and correctly centered and 3. PDMS is poured up to the filter height to link it to the rest of the structure and a 16 cm^2 mask is placed on the surface.

The efficiency is improved by +0.4% and +0.5%, reaching 23.4% and 22.4% for B-b and C-c tandems respectively (PTAA and triple cation, with ITO or IZO electrode). This improvement originates from an increase of the short circuit current Jsc, thanks to the reduction of reflection at the electrode/air interface. It confirms the quality of optical interface obtained with PDMS. However, the tandem A-a with Spiro-OMeTAD as HTL instead of PTAA has an efficiency of 24.1%, which corresponds to a loss of -0.7%. Upon investigation, this is caused by a total delamination of the ITO from the rest of the filter A after optical coupling by PDMS, which generates a multitude of optical interfaces with air.

Concerning device D-d with the double cation perovskite and Spiro-OMeTAD as HTL, the rebuilt tandem with PDMS reaches a higher efficiency of 23.3%. Finally, the tandem E-e (double cation and PTAA) is close to 21% efficiency. Devices with double cation perovskite have a greater increase in efficiency (+0.6%) compared to the devices B-b and C-c (+0.4%). The simulation presented in Chapter 4 Section 4.2.1.3 predicted an increase in the efficiency of the filtered silicon cell of +0.4% with the use of an epoxy optical coupling. These experimental results are therefore consistent with the simulation. In Fig. 7.10, we can see that the total reflection is further reduced close to 880 nm with PDMS for the perovskite filter D (double cation, PTAA and ITO) compared to B one (triple cation, PTAA and ITO), which allows a better transmission.

Finally, the optimized filter F results in a filtered silicon efficiency of 8.2% with the use of PDMS. The main reason for this improvement compared to the other structures is still the increase the current density due to the optical optimizations of the full stack, i.e. the choice of the materials, the deposition process and their thickness. Assuming similar performances as for STPC A and B, the tandem could reach respectively 26.6% and 26% efficiency.

7.2.4 Conclusion

In this section, we have succeeded in fabricating 5 pseudo optical 4T tandem of 0.09 cm^2, based on the best STPC obtained with the different architectures presented in this manuscript. In the case of the Spiro-OMeTAD with mechanical stacking, the total efficiency reaches nearly 25%, which is a gain of +5% compared to the silicon cell alone. We have also shown that the simulation performed in Chapter 4 is correct and allows to obtain stacks with a transmission higher than 90% in the IR. Functional STPC with

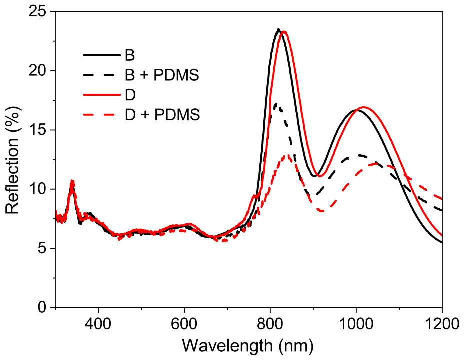

Figure 7.10: Reflection spectra of optical perovskite filter B and C before and after PDMS coating, according to the different configurations presented in Fig. 7.5a.

such properties could be used to synthesize 0.09 cm^2 tandem at more than 26% of efficiency. Nevertheless, we have also developed an external architecture with PDMS, which allows to optically couple the two cells and to propose a finished and compact object. It is now possible to transfer this process to the fabrication of real 4T 16 cm^2 tandem with the use of STPM. The next step is therefore to synthesise 16 cm^2 semi-transparent perovskite devices with electrical characteristics close to those of 0.09 cm^2 STPC.

7.3 Semi-transparent perovskite mini-module (STPM)

Today, all record-breaking perovskite devices have been achieved using substrates with active areas as small as 0.1 cm^2. However, to consider commercialization, large-scale modules ($>$ 800 cm^2) that achieve such high efficiency are required. To date, most modules have smaller surface areas and are often referred to as sub-modules (200-800 cm^2) or mini-modules ($<$ 200 cm^2), but do not match the performance of cell devices [17]. For example, 804 cm^2 perovskite solar module has been reported with an efficiency of 17.9% [406], which is significantly lower than the champion perovskite solar cell efficiency of 25.5% for an aperture area of 0.09 cm^2 [407]. Indeed, commercial production of these devices still faces serious challenges in terms of preserving module-scale cell efficiency, production throughput, process reliability, cost and stability. To move towards large-scale production, innovative technological solutions are needed in the manufacturing process.

In this section, we will present the P1P2P3 architecture which allows the realisation of perovskite mini-modules thanks to the series connection of several sub-cells. Based on the optimisations performed on the opaque structures, we will resize the sub-cells for the STPM first by means of modelling and then experimentally. We also compare the results obtained with PTAA or Spiro-OMeTAD, as well as the size effects between 4 and 16 cm^2. Appendix I present another application than tandem with these devices by tunning the color of the ITO electrode on the back side.

7.3.1 Process and P1P2P3 architecture

In order to limit photo-current and reduce resistive losses in thin films, the modular device must be divided into smaller cells interconnected in series. As shown in Fig. 7.11a, the interconnections between the individual sub-cells that make up the module were fabricated using a standard three-point interconnection scheme (P1, P2, and P3) used for conventional thin film PV modules [408]. This step is necessary for the spacing/isolation of the electrodes of adjacent subcells and to isolate the contact areas. Etching P1 models the backside FTO contact in a strip form; etching P2 is used for the formation of the series interconnection between adjacent cells after the deposition of the HTL; etching P3 is used for the isolation of neighboring cells after the deposition of the top ITO contact. These interconnections are made by laser patterning which reduces the Dead Area (DA), defined as the space between the P1 and P3 etchings that does not generate a photovoltaic effect.

Etchings were performed using an Innolas ILS LT laser. P1 scribing was performed using the UV laser at maximum power. In opaque reference modules, P2 and P3 were done using a green laser with powers of 12.7 W and 0.5 W, respectively. The P2 process is the most difficult because it must be able to completely etch all layers of the structure except the FTO. However, in the case of STPM, P3 is also a complex etch due to laser-induced thermal effects and ITO layer fragility, it was made by a mechanical scriber when the spiro-OMeTAD was used as HTL. In general, the width of P1, P2 and P3 by laser are about to 40, 50 and 25 µm, respectively. Finally, the areas between the P1/P2 and P2/P3 etchings are called the security area and are necessary to ensure that the etchings do not touch each other.

The different layers up to the HTL (compact and mesoporous TiO_2 triple cation perovskite and Spiro-OMeTAD or PTAA) are deposited according to the baseline spin-coating process of STPC detailed in Chapter 2 Section 2.1. Only quantities are adapted to obtain large surfaces up to 25 cm^2, which is the limit to have homogeneous deposition by spin-coating. Picture of a reference perovskite opaque module composed of 8 cells of 4*0.5 cm^2 is shown in Fig. 7.11b. It therefore has an module surface of 16 cm^2 for a substrate surface of 25 cm^2. As it can be seen, the top Au electrode is deposited over the entire surface except for two 0.5 cm strips perpendicular to the etchings. The contacts are taken back by copper tape after chemical etchings with DMF of the module edges.

At the module level, we have to distinguish between the efficiency of the aperture area and the efficiency of the module. The aperture area, also called active area, is defined as the area of the active photovoltaic part only (width W_a). A sub-cell area (width W_p) is given by the aperture area plus the dead area (width W_d) consisting of the interconnections and edges of the module. To obtain the efficiency of the module, it is then necessary to multiply by the number of sub-cells. It is clear that the aperture area efficiency of the module is higher than that of the total module. In the rest of the manuscript, we will refer to the total module efficiency by default when it is not specified. Jsc will be presented as the value of sub-cell area, unlike Voc which is presented as the value for the total module.

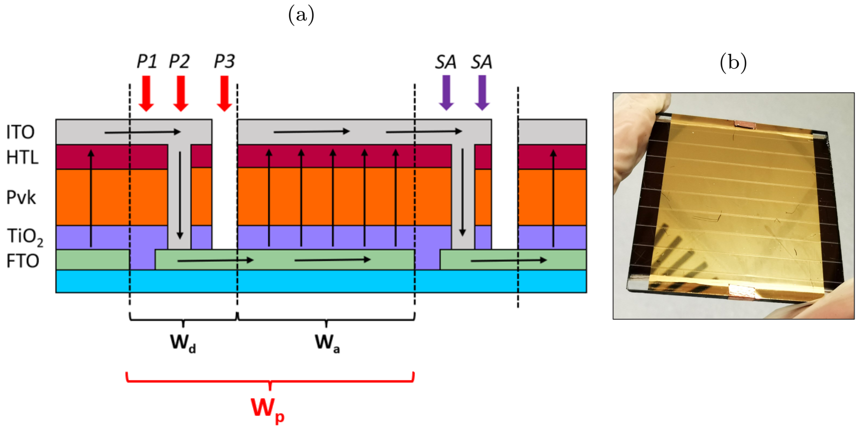
(a)

(b)

Figure 7.11: (a) Structure of a perovskite module with the P1, P2 and P3 scribing as well as the two security area (SA) in the dead zone with a width W_d on one side and the active zone with a width W_a on the other side which forms a subcell with a width W_p. (b) Photo of a 16 cm^2 opaque mini-module, composed of 8 cells of 2 cm^2 each.

7.3.2 Effect of the width of the death area and sub-cell size

7.3.2.1 STPM and opaque mini-modules with Spiro-OMeTAD as HTL

5 opaque modules with Spiro-OMeTAD as HTL have been synthesized in MA12 batch: on 3*3 cm^2 substrate, a modules was composed of 4 cells of 2*0.5 cm^2 for a total surface of 4 cm^2. For these modules, the width of the security area between the P1 and P2 etchings is too large and generates DA of over 500 µm. Fig. 7.12a shows the dispersion of the MA12 opaque modules after stabilization. The results obtained in this batch of opaque modules are the best on this stack and this size and this is thanks to several optimisation studies on laser etching not presented in this thesis. The average efficiency is 16%, which corresponds to an aperture area efficiency of 17.7% and therefore comparable to small area efficiencies of 0.09 cm^2. The Jsc is 18.04 $mA.cm^2$, which amounts to 19.84 $mA.cm^2$ excluding DA and is therefore slightly lower than that observed on small opaque cells (about 21%). The dispersion is more important and is directly related to Voc. The IV curves presented in Fig. 7.12b show that the dispersion results from one defective sub-cell among the 4 sub-cells of the module in a cases (Voc = 3.5 instead of 4.6 V).

In parallel, 4 STPM (MA09) with a similar size of MA12 opaque modules are synthesized with ITO as a back electrode, see the photo in Fig. 7.12c. All the information concerning the STPM batches (particularities, layers used, sizes...) are gathered in the Table B.2 in Appendix B. The P3 engraving is

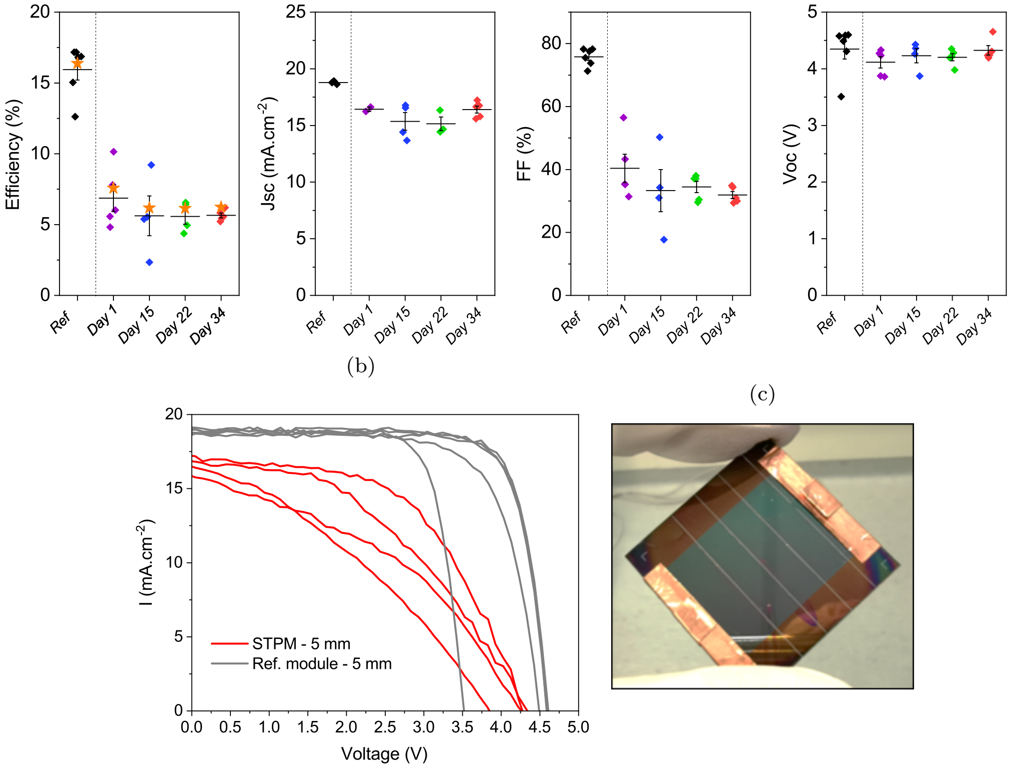
(a)
(b)
(c)

Figure 7.12: (a) Dispersion of the electrical properties of MA09 STPM with Spiro-OMeTAD as HTL, first day after the synthesis, and 15, 22 and 34 days later, compared to opaques modules form MA12 batch. (b) RV IV curves of MA09 STPM after 15 days and MA12 opaque reference modules. (c) Photo of a 4 cm^2 MA09 STPM, composed of 4 cells of 1 cm^2 each.

realized by mechanical scriber on the STPM and not by laser as on opaque modules. Indeed, the use of the laser once the ITO is deposited on the Spiro-OMeTAD causes an detachment of the electrode, similar to one observed during a heating, see Section 3.2.2. Mechanical etching allows to avoid this phenomenon but it is less precise, less clean and generates ITO splinters along the etching, see Fig. 7.13a. The P3 structuring is thus about 60-70 µm wide, which is 3 times wider than the P3 laser made on an opaque module. Nevertheless, as seen in the SEM images in Fig. 7.13b and c, the ITO grows well on the FTO in the P2 etching and form columns.

Concerning the electrical performances, the average efficiency of the STPM is much lower than that of the references the first day after the synthesis (6.9 vs. 16% respectively). This is directly caused by a very degraded FF (40 vs. 76% for opaque module), as well as a lower Jsc (16.40 vs. 18.40 mA.cm^2 for opaque module). The lower Jsc can be explained by the absence of the reflection generated at the

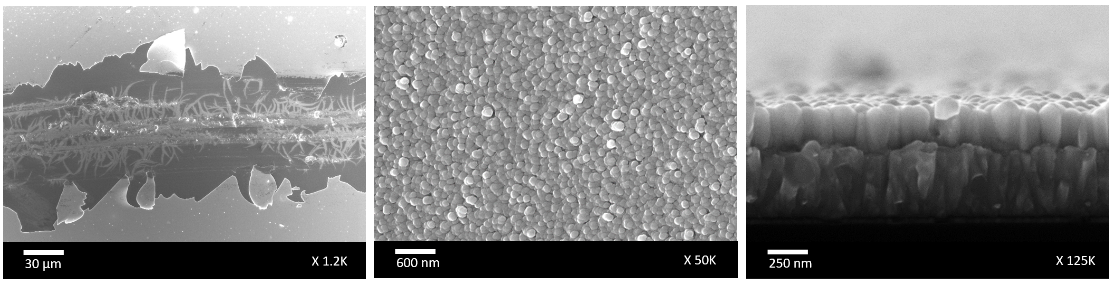
(a)
(b)
(c)

Figure 7.13: SEM surface image of (a) P3 engraving and (b) the inside of the P2 engraving of an STPM. c) SEM cross-section image of P2 engraving of an STPM.

Spiro-OMeTAD/gold interface on the opaque modules, as for the baseline cells. Concerning the low FF, far from the results obtained on comparable STPC in Chapter 3, its origin may come from a cell size too large (5 mm wide), not adapted to the 16 Ω.sq sheet resistance of the ITO electrode. Finally the dispersion is high the first days after the synthesis and seems to be reduced in time (σ = 2.13 vs. 0.37). This dispersion comes from the variation of the FF between the STPM.

7.3.2.2 Use of PTAA and improvement of P3 and DA

Because of the impossibility to encapsulate semi-transparent devices with Spiro-OMeTAD and with the very good results obtained on STPC with PTAA, PTAA has very quickly taken the place of Spiro-OMeTAD as HTL in STPM. Different types of P3 etching were then tested again (mechanical, handheld with scalpel and laser) as shown in the confocal images in Fig. 7.14. The use of the laser allows to obtain this time a clean etching which does not generate any particular detachment or splintering of the ITO electrode contrary to the mechanical and hand etching. In parallel, improvements have been made to the precision of the engravings. A new program now allows an optimized detection of the previous etchings on a sample and thus to obtain smaller DA, of the order of 250 µm.

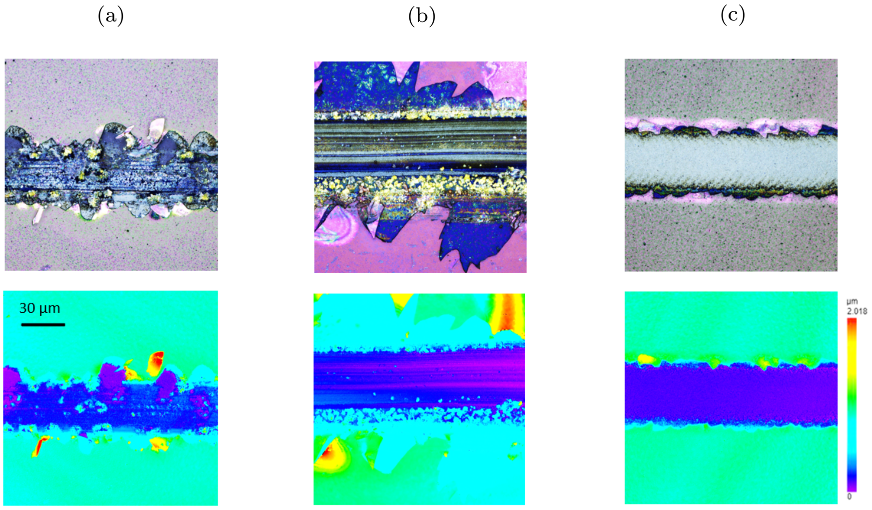

Figure 7.14: Confocal mircroscopy image of the surface of P3 engraving made with (a) mechanical (b) handheld with scalpel and (c) laser techniques.

Thus, these different improvements have been used for the STPM AY39 batch. These modules are still 2*2 cm^2 composed of 4 cells of 2*0.5 cm^2. The evolution and the dispersion of the electrical properties are presented Fig. 7.15a and again compared to the reference opaque modules MA12. The performances obtained the first day after the synthesis are very low (3.6%), and are due to the presence of an S-shape curve, see Fig. 7.15b. After 22 days, the average efficiency of the STPM reaches 11.3%, which is an improvement compared to the MA09 batch in the previous section even if it is still low. The Jsc reaches 18.72 mA.cm^2 on day 22, which corresponds to 19.65 mA.cm^2 without taking into account the DA. So there is still a slight difference with STPC (about 21 mA.cm^2). However, the reproductibility is better (σ = 1.28) which shows that the combination of PTAA and laser etching allows to decrease the dispersion. The S-curve has almost disappeared on the IV curves but the average FF is still low (54%) compared to the similar STPC in Chapter 5, probably again due to the size of the sub-cells (5 mm). Hyperspectral photoluminescence imaging study in aging was conducted as for the STPC in Chapter 5, see Appendix J. A similar trend was observed, namely a red shift of the perovskite gap.

7.3.2.3 Ideal sub-cell size for STPM

As we have just seen, STPM suffers from a low FF due to the too large size of the sub-cells compared to the resistivity of the ITO. The objective of the upcoming study is to propose a solution to size the cells on a STPM according to the resistivity of the electrodes. In addition, it would be interesting to evaluate the impact of the DA on the final efficiency of the tandem and to judge to what extent a gain

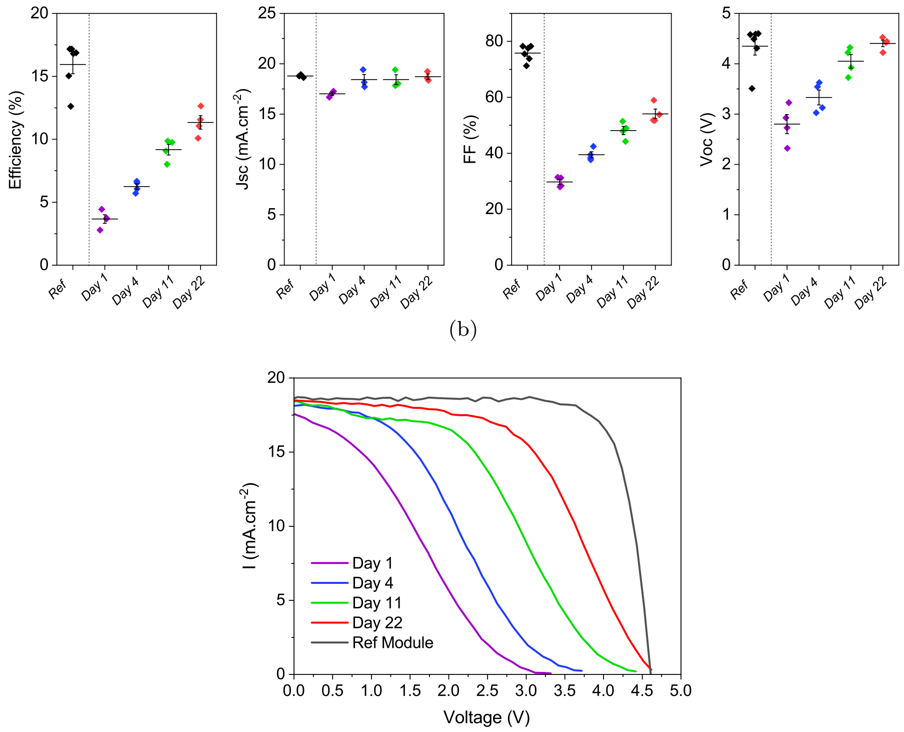
(a)

(b)

Figure 7.15: (a) Dispersion of the electrical properties of AY39 STPM with PTAA as HTL, first day after the synthesis, and 4, 11 and 22 days later, compared to opaques MA12 reference batch. (b) Evolution in time of RV IV curves of the best AY39 STPM, compared to MA12 opaque module.

in transparency is interesting. Fig. 7.16 show the evolution of the Geometrical Fill Factor (GFF - ratio of the active area to the total area) as a function of the size W_a of the active zone. The width of the DA W_d is set to 250 µm. Thus, if the perovskite sub-cells are 2.55 mm wide (W_p), the GFF is 90%, i.e. 10% of the surface is made up of dead zones, and this is considered as our limit.

7.3.2.3.1 Simulation

A simulation was developed to determine the ideal parameters to use experimentally on the STPM. In order to be as accurate as possible, we choose to consider that the transmission is not the same through the engravings as through the complete stack. From the TMM code presented in Chapter 4, the basic calculation is done for the transmission through the classical structure with PTAA as HTL, but also through engravings P1, P2 and P3, see Fig. 7.11a.

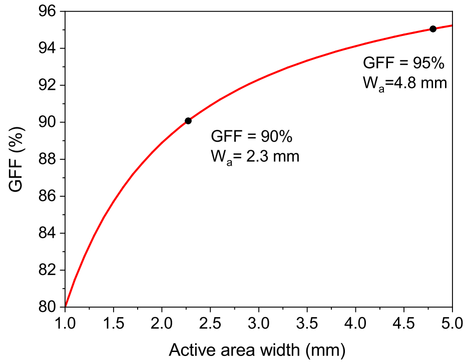

Figure 7.16: Evolution of GFF as a function of the active area width W_a.

Once the total, P1, P2 and P3 transmissions are obtained, they are implemented in a new code, allowing to determine the optimal size of perovskite sub-cells on a STPC. In order to evaluate the electrical losses F_{tot} and their impact on the final efficiency 4T tandem, the following calculation of losses is carried out [409]:

$$F_d = \frac{W_d}{W_d + W_a} \tag{7.1}$$

$$F_{TCO-X} = \frac{1}{3} R_{sheet-X} \left(\frac{J_{mpp}}{V_{mpp}} \right) \frac{W_a^3}{W_d + W_a} \tag{7.2}$$

$$F_{tot} = F_d + F_{TCO-1} + F_{TCO-2} \tag{7.3}$$

with F_d the relative power losses related to the size of the DA, F_{TCO-1} and F_{TCO-2} electrical losses related to the two TCO, $R_{sheet-X}$ the TCO sheet resistance, Jmpp and Vmpp the current and voltage associated to maximum power point Pmpp of a experimental STPC. In addition, laser ablation processes can lead to deterioration of electrical properties. Etching P1 and P3 can create shunts while etching P2 can create a non-negligible series resistance between the front and back contact due to the formation of a contact resistance at the interconnect interface [410]. An additional electrical loss F_{ctc} is provided in the original equations for this specific case [409]. However, TLM measurements of the ITO/FTO contact presented in Appendix H show that this resistance is minimal in our case and does not need to be taken into account in this model.

The experimental STPC used is the same as the one mentioned in Chapter 4. The calculation of the efficiency of the STPM is then expressed as :

$$Eff_{perovskite} = \frac{P_{mpp} * (1 - F_{tot})}{P_{inc}} \tag{7.4}$$

The calculation of the EQE of the silicon cell, related to the amount of light T_{tot} that passes through the structure and the different etchings, is expressed as :

$$T_{tot} = \frac{T_{W_a} * (W_a + W_{SA})}{W_d + W_a} + \frac{T_{P1} * W_{P1}}{W_d + W_a} + \frac{T_{P2} * W_{P2}}{W_d + W_a} + \frac{T_{P3} * W_{P3}}{W_d + W_a} \tag{7.5}$$

$$EQE_{Si-filtered} = T_{tot} * EQE_{Si-unfiltered} \tag{7.6}$$

with T_{W_a} the transmission through the active area and the two security areas, T_{P1}, T_{P2} and T_{P3} transmissions through each engraving, W_{P1}, W_{P2} and W_{P3} the widths of each engraving and W_{SA} the widths of the two security areas. Finally, the efficiency of the filtered silicon cell is derived as described in Chapter 4 Section 4.1.2.2, and allows to deduce the efficiency of the 4T tandem.

Concerning the inputs, we consider an STPM similar to the best STPC with PTAA experimentally obtained with an efficiency of 17.8%, see Chapter 5 Section 5.1.2. The R_{sheet} of the ITO is fixed at 16 Ω.sq and that of the FTO at 9 Ω.sq. The width of P1, P2 and P3 are respectively 45, 50 and 40 µm, based on measurements made on an STPM with PTAA.

Fig. 7.17a, b and c show the evolution of the efficiency of STPM, Al-BSF silicon cell and tandem respectively, as a function of the size of the active area. The maximum efficiency reached for the tandem is identified with a black triangle. Thus, the ideal perovskite sub-cell size is 2.85 mm (2.6 + 0.25 mm) which allow to obtain a tandem with an efficiency of 21% (15.6% and 5.4% of efficiency for STPM and silicon, respectively). The GFF is 91.2%. However the difference between 2.6 mm and 3.1 mm is small. Indeed, the size of the perovskite sub-cell can be extended to increase the GFF with limited loss of efficiency. For a range from 2.5 to 3.15 mm, the tandem efficiency does not vary by more than 0.1%, which leaves a relatively large margin for cell design. It can also be noted that the influence of the silicon cell is very limited, the gain in transmission allowed by the etchings is only felt on active area sizes smaller than 2 mm, see Fig. 7.17b. Finally, compared to the STPC presented previously, a perovskite sub-cell size of 5 mm instead of 3, results in an immediate 1% loss in efficiency.

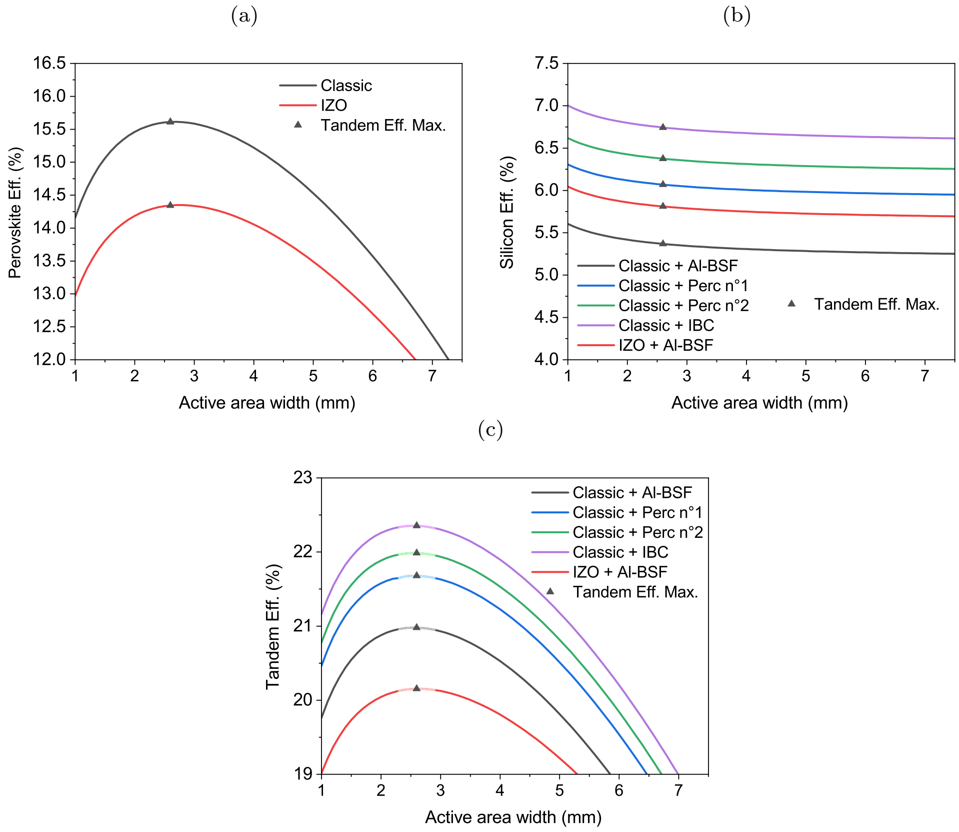
(a)
(b)
(c)

Figure 7.17: Evolution of (a) STPM, (b) Silicon cell and (c) Tandem efficiency as a function of the active area width W_a, the electrodes used (ITO or IZO) on STPM and the Silicon cell technology.

The same kind of simulation is performed by replacing the ITO by the IZO based on the best experimental STPC manufactured which reach an efficiency of 16.3% , see Chapter 6 Section 6.1.3.2. Due to the similar resistivity of the IZO compared to ITO, the ideal perovskite sub-cell size is the same as for the previous configuration. The maximum achievable efficiency is then of 20.2% (14.3% + 5.8%). Finally, taking up the different silicon cells proposed in the Chapter 4 Section 4.3.1, we will now focus on the evolution of the efficiency of the tandem with classic STPM according to the different silicon technologies. Results show that the ideal perovskite sub-cell size seems independent of the silicon technology used and remains at 2.85 mm. Only the maximum efficiency of the tandem evolves with the silicon cell used.

7.3.2.3.2 Experimental results

In order to test the validity of the developed model, we synthesize 8 STPM in the batch MA19 : half of 4 cm^2 composed of 5 cells of 0.8 cm^2 (4 mm width) and 4 others of 4.2 cm^2 composed of 7 cells of 0.6 cm^2 (3 mm width). The average dead area is 220 µm for this batch. The pictures in Fig. 7.18a, b and c show the different architectures of the STPM.

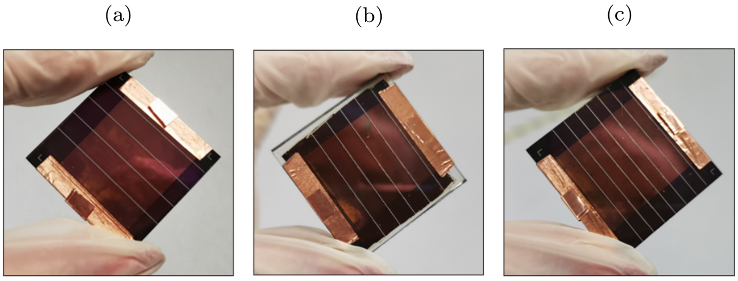
(a)
(b)
(c)

Figure 7.18: Photo of STPM with PTAA as HTL, composed of (a) 4 cells of 2*0.5 cm^2 each, (b) 5 cells of 2*0.4 cm^2 each and (c) 7 cells of 2*0.3 cm^2 each.

Fig. 7.19a shows the dispersion of the electrical properties over time for each group of STPM. We notice that the modules with 3 mm cells have a higher average efficiency (11.1 vs. 9.4%), which is directly due to their FF (+10%). These results confirm the model developed above and support the fact that the sub-cells of the STPM must measure between 2.55 to 3.15 mm to have an optimal operation. Nevertheless, the Jsc of these modules is lower than with 4 mm cells (17.19 vs. 18.74 mA.cm^{-2}). The Voc is obviously higher because these modules are composed of 7 cells instead of 5. The dispersion of the 3 mm is important ($\sigma = 2.64$) and this is due to a module where one of the cells does not work (Voc at 6.9 V instead of 8 V). This risk is indeed amplified with the number of cells and can be one of the drawbacks of this 3 mm architecture.

Finally, over time, we observe a usual evolution with a gain in efficiency, caused by the improvement of the FF (+9%). Fig. 7.19b shows the IV over time of the best 4.2 cm^2 STPM obtained (MA19-14). 12 days after synthesis, it reaches an efficiency of 14.8% with a GFF of 92%. This corresponds to an efficiency of 16.2% for the active area, a result very close to the usual efficiency obtained on STPC. Thus, thanks to the replacement of Spiro-OMeTAD by PTAA, the use of laser for P3 etching as well as the reduction of the size of the sub-cells, we have succeeded in transferring the process from opaque modules to STPM and we obtained performances close to those obtained on the best STPC with an identical structure on 4.2 cm^2 with a GFF above 90%. The size increase can be continued up to 16 cm^2 via spin-coating.

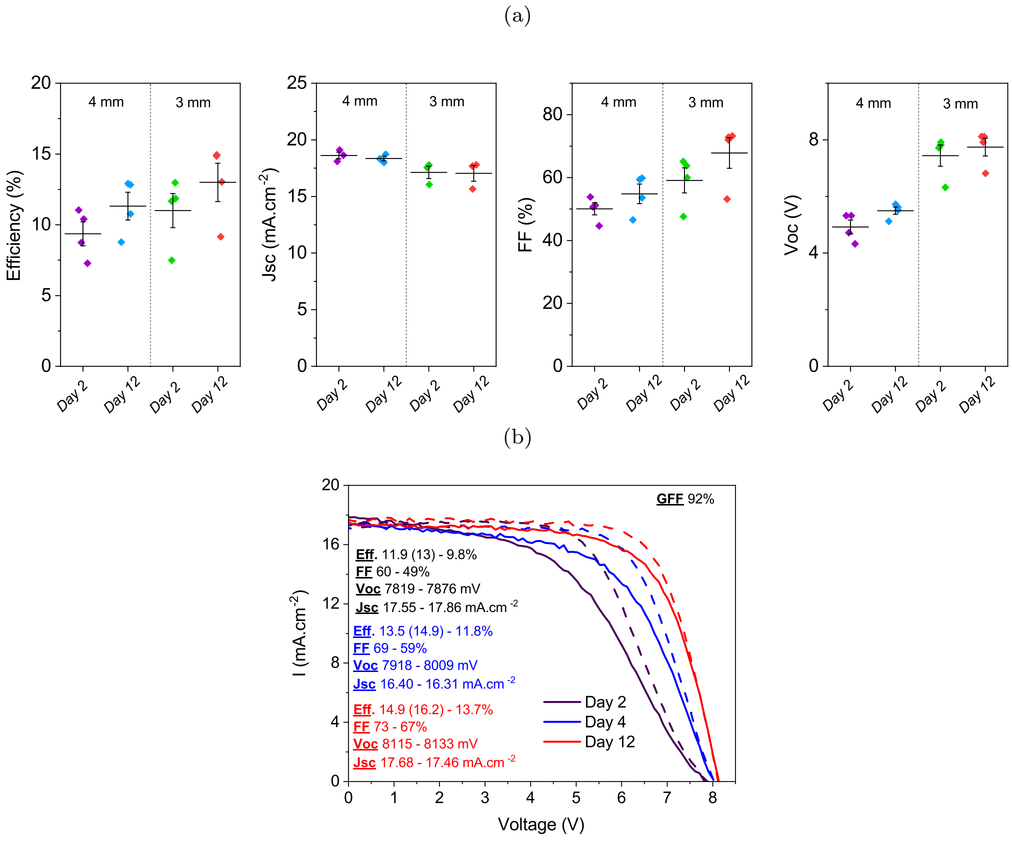
(a)

(b)

Figure 7.19: Dispersion of the electrical properties of MA19 STPM with sub-cell widths of 4 or 3 mm. (b) IV curves of the best 4.2 cm^2 STPM obtained (MA19-14), 2, 4 and 12 days after the synthesis.

7.3.2.4 Soldering

In order in the future to easily connect the STPM associated with the Silicon cell with PDMS, it is necessary to use other types of contacts than the copper tape used until now. Tests were conducted on the TG01 batch composed of 5 STPM with PTAA HTL of 4 cm^2 with 5 sub-cells of 2*0.4 cm^2. The first day after their synthesis, a first IV measurement is performed after the installation of the copper tape, see Fig. 7.20a for the electrical dispersion. A second measurement is then performed the same day, once the copper tape contacts have been carefully removed and replaced by two ultrasonically soldered busbars, see Fig. 7.20c. This allows to slightly increase the average efficiency (8.9 vs 8.3%) thanks to the increase of both FF (+ 4%) and Voc (+ 190 mV).

Furthermore, the follow-up over time reveals that this type of soldering does not have a negative effect on the electrical properties. 6 days after the synthesis, the average efficiency reached 13.1% thanks to the disappearance of the S-shape. In particular, there is an STPM whose IV curves are shown in Fig. 7.20b which reaches 14.9% efficiency (15.8% in active area), i.e. performances similar to the best STPM of this size presented in Section 7.3.2.3.2 although its cell size is not optimal (4 mm). The use of busbars is therefore beneficial for STPM and can be used routinely.

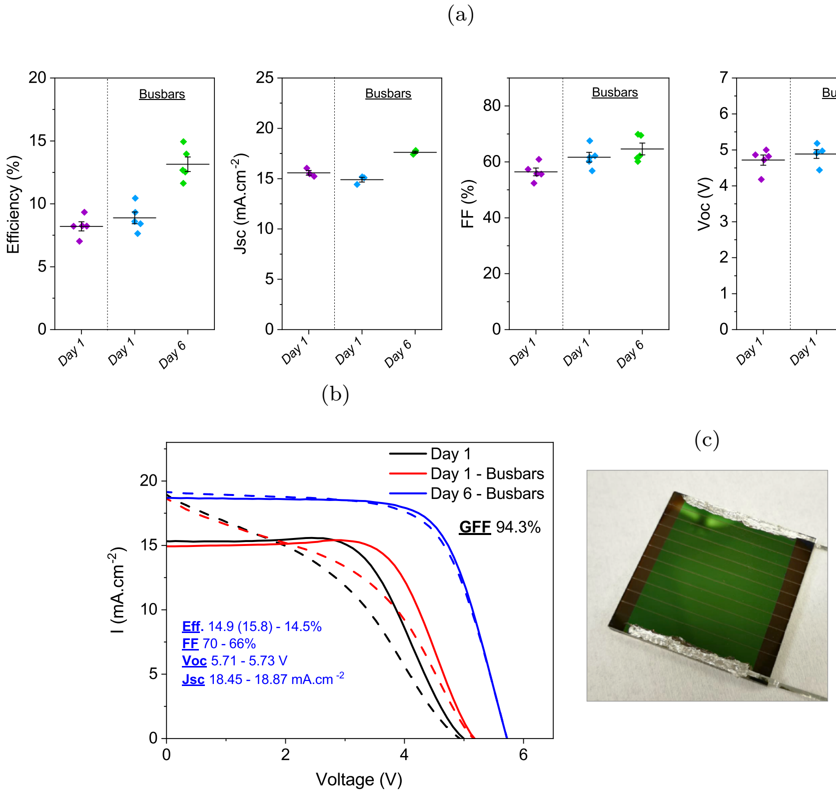
(a)

(b)

(c)

Figure 7.20: (a) Dispersion of the electrical properties of TG01 4 cm^2 STPM with sub-cell widths of 4 mm, before and after the installation of the busbars. (b) IV curves of the best STPM presented in (a). (c) Photo of a 16 cm^2 STPM, composed of 10 cells of 1.6 cm^2 each, after the installation of the busbars.

7.3.3 Up scaled STPM from 4 to 16 cm^2

At present, high efficiency semi-transparent devices are fabricated on a small surface area and there are few publications concerning these devices on large surface areas. Nevertheless, some research groups report a few STPC/STPM devices with an active area larger than 4 cm^2, see Appendix A. For example, Jaysankar et al. [411] demonstrated the operation of a 16 cm^2 semi-transparent mini-module at 11.2% and Know et al.[412] even reached 40.8 cm^2 of active surface for an efficiency of 9.04%.

Our process allows to manufacture STPM up to 16 cm^2 without changing the deposition techniques while waiting for the progress of slot die deposition. The different processes are similar to those used for the 4 cm^2, only the number and the surface of the sub-cells increase. In the MA05 batch, 15.6 et 16 cm^2 STPM have been synthesized. They have either 13 cells of 3 mm width (1.2 cm^2) or 10 sub-cells of 4 mm width (1.6 cm^2, see picture in Fig. 7.21c). The average DA obtained is 265 µm. Fig. 7.21a shows the evolution of their electrical properties. This batch is characterized by a low Jsc (14.42 mA.cm^{-2}), linked to a synthesis issue of the perovskite layer. The Voc increases, in accordance with the number of cells in series. Contrary to the previous section, the performances of the 3 mm STPM are slightly lower than those of the 4 mm (8.3 vs. 8.9%). Both samples have an identical FF (56%), which is in contradiction with the previous observations, while the Voc shows no dysfunctional cell. The STPM with sub-cells of 4 mm wide has the expected behavior with a FF similar to smaller STPM.

On the other hand, for the 3 mm STPM, the decrease of the FF can be due to the architecture of 13 cells in series without intermediate contact. Thus, the FF eventually decreases with the number of cells and the sample size. To keep a width of 3 mm while limiting electrical losses, solutions such as metal or TCO grids as mentioned in Chapter 7 could be considered.

New 4 mm STPM have been manufactured in the MA21 batch, which does not include this time any anomaly at the Jsc (18.30 mA.cm^{-2}). The average DA is 263 µm and the average efficiency obtained is 11.9%. Fig. 7.21b represents the IV of the best manufactured STPM of 16 cm^2 (MA21-02). It reached an efficiency of 13.2% with a GFF of 93%, that is 14.2% on the active area. This efficiency is lower than the STPC average performance due to a lower FF (61%).

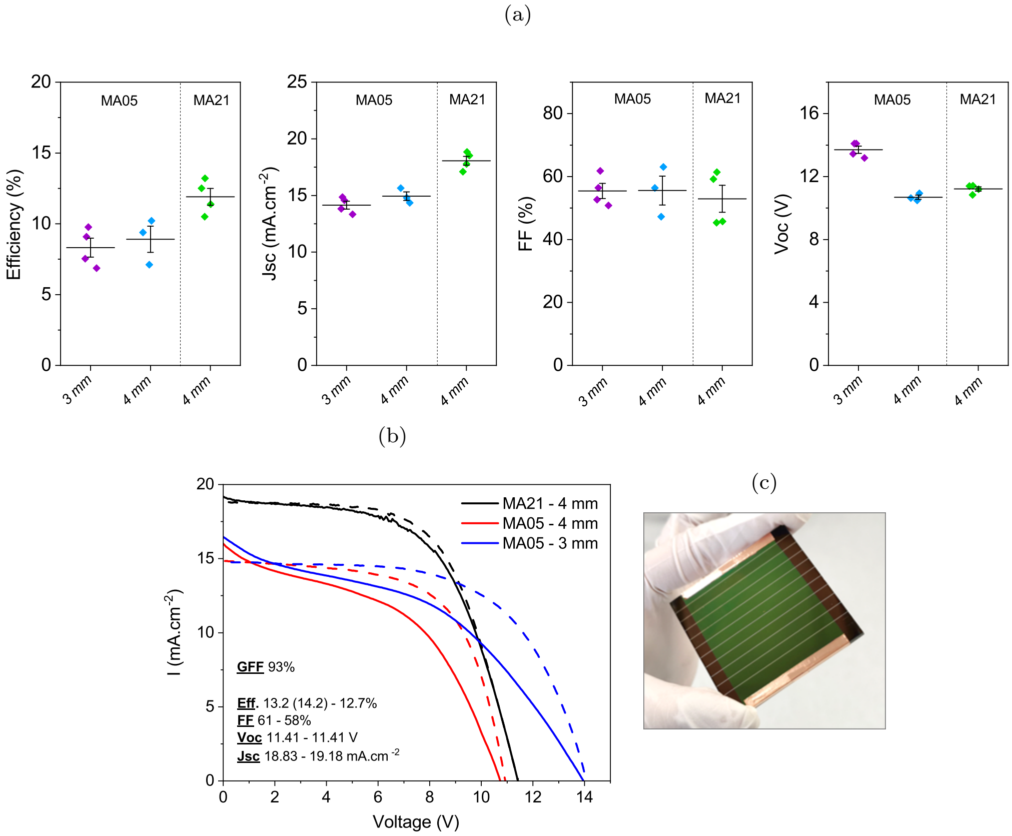
(a)

(b)

(c)

Figure 7.21: (a) Dispersion of the electrical properties of MA05 and MA21 16 cm^2 STPM with sub-cell widths of 4 or 3 mm. (b) IV curves of the best STPM of each category presented in (a). (c) Photo of a 16 cm^2 MA21 STPM, composed of 10 cells of 1.6 cm^2 each.

7.3.4 Conclusion

In this section dedicated to the development of STPM, we have shown how we have successfully transferred the process from opaque to semi-transparent modules. This was first done on 4-4.2 cm^2 samples, on which Spiro-OMeTAD was replaced by PTAA. Laser etching of the P3 resulted in improved reproducibility and the reduction of the cell width to 3 mm, predicted by simulation, resulted in a significant gain in FF. These devices have an active area efficiency comparable to that obtained on STPC and a similar evolution over time. However, when the size of the STPM was increased to 15.6-16 cm^2, the 3 mm width proved to be less efficient than expected while the STPM with 4 sub-cells performed identically. This point deserves to be studied in depth in order to present 16 cm^2 STPM with performances similar to smaller modules and STPC.

7.4 16 cm^2 4T perovskite/silicon tandem

Regarding the results obtained on more than 4 cm^2, we can nevertheless mention the tandem of Jaysankar et al. [411] with a surface of 16 cm^2 and an active area efficiency of 20.2%, as well as that of Werner one [167] with 23.9% on a smaller surface of 4 cm^2.

In this last section, we will present a 16 cm^2 4T tandem, in the form of a solid state compact object whose performances are measurable directly, without using filters or reconstruction via EQE. This is now possible thanks to the development of 16 cm^2 STPM on the one hand and the assembly process developed in the previous section on the other. At first, we will realize this device with a simple mechanical stacking, before addressing the issues of encapsulation and integrity over time.

7.4.1 Mechanical stacking

The first test of tandem using a STPM instead of a perovskite filter was performed by mechanical stacking. The best 16 cm^2 STPM presented in Section 7.3.3 was used (MA21-02). It is composed of 10 cells of 1.6 cm^2. This tandem of 16 cm^2 reaches a global efficiency of at 19.8% (13.2%+ 5.6%) and an active area efficiency of 20.8% (14.2%+ 5.6%), see Fig. 7.22 for IV curves. The Silicon cell (n-PERT n°2) has an efficiency of 19.3% when not filtered by the STPM, thus the tandem structure allows here a positive gain of +0.5% of total efficiency. These results are completely consistent with those obtained in the section on optical pseudo-tandem, the silicon cell reacts in a similar way between the STPM and the corresponding optical filter B.

Going from a size of 0.09 to 16 cm^2 for the same perovskite device structure and an identical silicon cell, the active area efficiency drops by 2.2%, which is still a relatively small loss compared to the increase in area by a factor of 177.

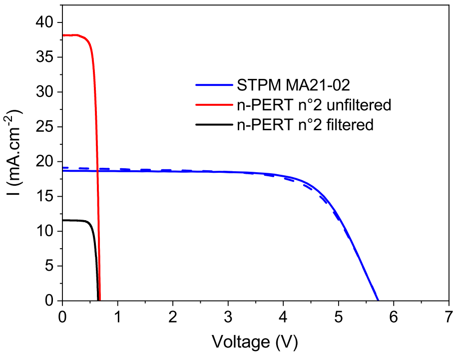

Figure 7.22: IV curves of the STPM MA21-02 and the silicon cell (n-PERT n°2) associated, unfiltered and filtered.

7.4.2 Improved stacking: case, PDMS optical coupling and PO encapsulation

This very encouraging result does not guarantee the durability of the device over time, due to the lack of encapsulation of the STPM. In order to also use the optical coupling presented in Section 7.2.3.2, it is important to ensure that the encapsulated method does not degrade the electrical properties of STPM. It is also necessary to ensure that the electrical connections of the STPM can be easily taken after the encapsulation, which is not possible today with the copper tapes. It is therefore necessary to work on these two points in order to propose a 16 cm^2 4T tandem sustainable over time.

The use of PDMS alone is not sufficient to effectively encapsulate STPM and ensure their performance over time, as shown in the study presented in Appendix K. A more robust encapsulation process, similar to the one used to age STPC over 1000 h in Chapter 5 Section 5.1.5 has been developed. The STPM has been encapsulated with Polyolefin film for the active area in order to maintain maximum transparency. The whole is sealed with 3 mm borosilicate glass and a polyisobutylene ribbon annealed at 140°C during 15 min into a laminator, see Fig. 7.23 for the final result. There is now a glass substrate on each side of the STPM. However, the measurements are still carried out in the superstrate configuration, i.e. the light first passes through the FTO electrode and then the TiO_2 etc.

The MA04-01 module is a 16 cm^2 STPM composed of 8 sub-cells of 2 cm^2 each. It is composed of a triple cation perovskite, PTAA and ITO, and is comparable to the record module MA21-02 presented in the previous section. Table 7.5 shows the performance and Fig. 7.24a shows the corresponding IV curves of this STPM before and after the installation of the busbars and after the encapsulation. This modulus reached 9.7% when stabilised, which is far from the 13.2% achieved by the identical record modulus MA25-02. Unfortunately, this encapsulation process still does not have full reproducibility (about 70% success rate), and the most efficient modules did not survive.

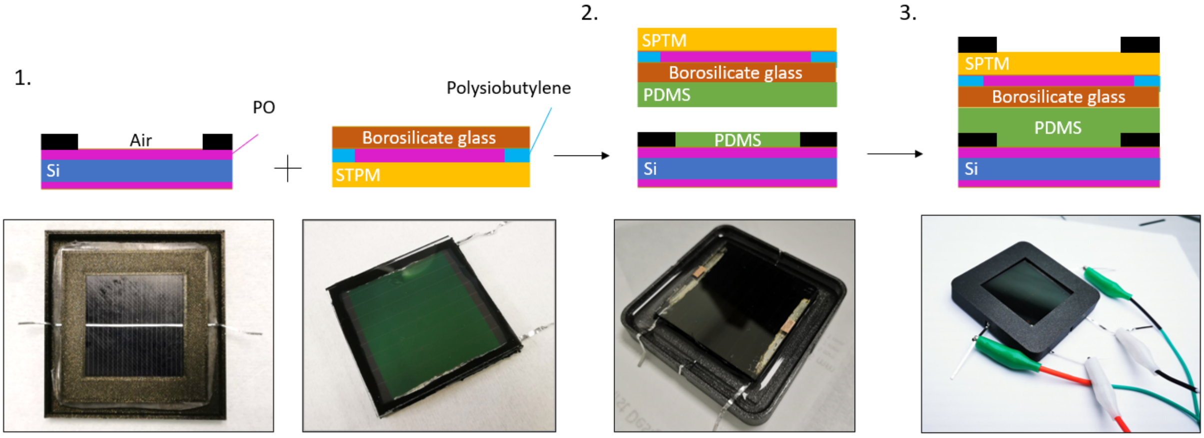

Figure 7.23: Manufacturing stages of the 16 cm^2 Perovskite Silicon 4T Tandem: 1. Silicon cell with its mask is centered inside the PLA case and the 16 cm^2 STPM is encapsulated. 2. The silicon cell and STPM are covered by PDMS. 3. PDMS is poured up to the filter height to link it to the rest of the structure and a 16 cm^2 mask is placed on the surface.

Steps	**Scan**	**Jsc (mA.cm^{-2})**	**Voc (V)**	**FF (%)**	**Efficiency (%)**	**Tandem (%)**
Standard	RV	16.42	8.92	53	9.7	-
	FW	16.49	9.06	51	9.4	-
Busbar	RV	16.68	8.80	58	10.7	-
	FW	16.45	9.02	55	10.2	-
Encapsulation Day 1	RV	16.54	9.05	59	11.1	17.5
	FW	16.73	9.05	55	10.3	16.7
Encapsulation Day 16	RV	16.51	9.10	57	10.8	17.2
	FW	16.63	9.14	56	10.6	17

Table 7.5: Electrical characteristics of the STPM MA04-01, and tandem final efficiency with or without busbars and encapsulation.

However, the replacement of copper tape by busbars resulted in a 1% efficiency gain through the improvement of the FF, as seen in the Section 7.3.2.4. Furthermore, the encapsulation had an additional beneficial effect on the performance of the module with a +0.4% gain in efficiency. This time, an improvement in Voc in RV scan (+250 mV) is observed.

The encapsulated MA04-01 is then associated to the Silicon cell according to the process detailed in Section 7.2.3.2 and described in Fig. 7.23. PDMS is poured between the two cells. The silicon cell is an n-PERT n°2 as for the optical pseudo tandem and reaches an efficiency of 19.1% under one sun illumination. The final tandem obtained is presented in Fig. 7.23. When filtered by STPM, the silicon cell reaches an efficiency of 6.4%, resulting in a 4T perovskite/silicon tandem of 16 cm^2 at 17.5%. In addition, it retains an efficiency 17.2% 16 days later. It therefore maintained more than 98% of its original efficiency in 15 days, without any particular atmospheric conditions.

These results show, although obtained on a STPM module without the best electrical properties, that we have succeeded in developing an efficient encapsulation process which preserves the STPM and allows a simple and efficient tandem fabrication. More tests are now needed to study the actual optical coupling of the two cells in tandem, as well as to increase the reproducibility rate.

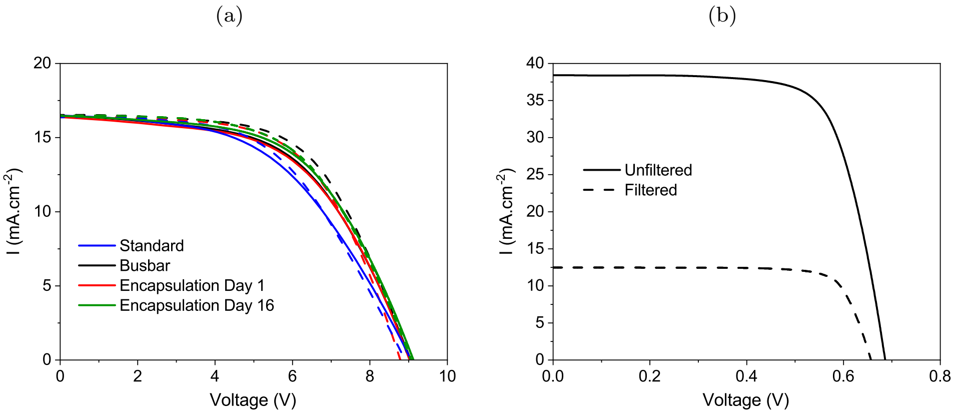

Figure 7.24: (a) IV curves of the STPM MA04-01 with or without busbars and after the encapsulation. (b) IV curves of the silicon cell associated to the STPM MA04-01, unfiltered and filtered.

Conclusion

In this last chapter, we studied the upscaling of our STPC. two ways have been studied in parallel: the development of mini-module up to 16 cm^2 and the replacement of the spin coating technique for the deposition of the perovskite by the slot die, in order to be able to propose mini-modules of larger sizes.

The results obtained via the slot die coating showed that ITO deposition by sputtering is compatible. In the case of Spiro-OMeTAD as HTL, the results are close to those obtained with the reference opaque cells with a low dispersion but the STPC havs a negative time evolution. The results with PTAA are moreover promising even if they still present a lack of reproducibility due to the roughness of the perovskite as compared to the thinness of the PTAA layer. Further investigations are planned such as testing other surfactants on opaque reference samples. In the future, the use of this technique will allow the realization of semi-transparent devices exceeding 25 cm^2, with a band gap more suitable for a 4T coupling with a silicon cell.

In parallel, we tested a new process to obtain a robust, measurable and compact 4T tandem, and validated its compatibility with our different STPC structures, using 25 cm^2 of semi-transparent filters that reproduce the structure of different STPC. These filters are each associated with a 20.25 cm^2 n-PERT silicon cell with the idea of manufacturing 0.09 cm^2 optical pseudo-tandem devices. In the case of the Spiro-OMeTAD with mechanical stacking, the total reconstructed efficiency on 0.09 cm^2 reaches nearly 25%, a gain of +5% compared to the silicon cell alone. Nevertheless, we have also developed an advanced architecture which, thanks to PDMS, allows to optically couple the two cells and to propose a finished and compact object. We have also validated experimentally the simulation performed in Chapter 4 to obtain stacks with a transmission higher than 90% in the IR. Functional STPC with such properties could be used to synthesize 4T tandem in the future with an efficiency higher than 26%.

Regarding the mini-modules, we have successfully transferred the spin-coating process from opaque to semi-transparent modules. This was possible by replacing Spiro-OMeTAD with PTAA, using laser etching of P3 and reducing the cell width to 3 mm. The latter was predicted by simulation and then experimentally tested, resulting in a significant gain in FF. These optimized devices have an active area efficiency of 16.2% comparable to those obtained on STPC when the module area is 4 cm^2. However, when the size of the STPM was increased to 15.6-16 cm^2, the 3 mm width proved to be less efficient than expected. This is because it requires more engravings on the surface of the sample compared to larger sub-cells. However, we were able to synthesise a 16 cm^2 STPM with 4mm wide sub-cells with an active area efficiency of 14.2%. It deserve to be further investigated in order to achieve 16 cm^2 STPM with performances similar to the smaller ones and to the STPC.

This process was then transferred to a real 16 cm^2 4T tandem with the use of STPM. By simple mechanical stacking, we obtained a tandem with an active area efficiency of 20.8% (14.2%+ 5.6%). By using an efficient encapsulation process with PO and a PDMS optical coupling, we showed that we could keep its global efficiency of 17.5% (11.1%+ 6.4%) over at least 16 days without any particular atmospheric aging conditions. We finally showed that we were able to fabricate a compact, robust 16 cm^2 4T tandem while addressing the issues of encapsulation and integrity over time.

General conclusion and perspectives

Perovskite cells are seen as a promising option for low-cost tandems because of the potentially low cost materials and their combination with a silicon cell, already suitable for commercial applications. The objective of the thesis was to synthesized a high performance, stable, and large size semi-transparent perovskite cell. This involves transferring the process from opaque cells to semi-transparent cells while maintaining optimal electrical properties, and the fabrication of 4T perovskite/silicon tandem.

As mentioned in the first chapter, several ways of research are currently considered. Among the different possible architectures, the four-terminal architecture was chosen in this work thanks to its numerous advantages as the electrical independence of both top and bottom cells, the insensitivity to spectral variations and the possibility to fabricate both cells separately. However, even though perovskites have received a lot of attention from the scientific community and have achieved a very high efficiency (25.7%) in ten years, many problems need to be solved before they can be used for an industrial scale application. First of all, perovskite cells have stability issues when in contact with the atmosphere and more particularly with humidity. Moreover, the most efficient cells are currently obtained on small areas (< 0.1 cm^2) and a significant drop in performance is observed when the size exceeds 10 cm^2. In addition, in the case of the semitransparent perovskite cells, a trade-off between transparency in the IR and efficiency has to be found for tandem applications. By replacing the usual metallic back electrode with a transparent one, additional electrical losses are occurring and a decrease in performance is observed compared to conventional cells. Consequently, it was important to focus not only on the electrical properties of the materials constituting the perovskite cell but also on the optical properties of the complete stack of the tandem cell.

The process used for both the opaque and semi-transparent perovskite cells of 0.09 cm^2 was detailed in Chapter 2. The different techniques such as spin-coating and slot die coating, as well as the etching schemes were described. An important point of the thesis was to move from an opaque to a semi-transparent cell and therefore it was necessary to develop an electrode recipe specific to STPC. In particular, we have focused on the synthesis techniques used for the ITO/IZO (sputtering) and IO:H (PEALD). The measurements of IV and EQE were crucial to understand our results and improve the performances of the devices. Complementary, the 4-point probe method and the Hall effect allowed to evaluate the resistivity of the different thin films. For the optical characterization of the STPC, the UV/Visible/IR spectrophotometer was used to determine the transmission, reflection and absorption properties of the different layers. Ellipsometry was used to determine the optical indices n and k of the layers. Other equipments, such as SEM, confocal microscopy and AFM measurements, allowed us to characterize the morphology of our different layers. The composition and structure of our materials were analyzed by XRF, XRD, XPS and GDOES.

In the third chapter, we replaced the Au metal back contact of the opaque perovskite cell with ITO. Firstly, it was observed that instability of STPC is more important than for opaque cells. Indeed, they required a variable time of 1 to 3 weeks to reach their full optimal performances following the disappearance of the S-shape characteristic. Performance was maintained during several months as long as they were kept under vacuum. Furthermore, wide dispersion of electrical performances was firstly observed in comparison to opaque cells. The origins of this dispersion appear multiple and as it is crucial to have a robust and reproducible reference cell for incrementing new materials, it was necessary to study different solutions. The study of non-functional cells allowed to evidence the important sensitivity of the Spiro-OMeTAD during the sputtering deposition of ITO. Moreover, studies with metallic buffers confirmed the interest of protecting the Spiro-OMeTAD layer. In particular, Ni buffer appeared to be promising, but the process is not yet well mastered and the layer is not reproducible. Thanks to the various improvements, semi-transparent cells with performances close to opaque cells were achieved and the efficiency was increased up to 18.4% on 0.09 cm^2, even if the dispersion remains relatively high. We finally fabricated a first tandem prototype at 22.3% on 0.09 cm^2 by combining an STPC and an Al-BSF silicon cell.

However, despite this good performance, the transmission and EQE spectra of STPC revealed the presence of absorption and reflection within the perovskite cell in the infrared, which is detrimental for the silicon bottom cell. The identification of the optical losses and the proposition of a new optically optimized structure was therefore the subject of the fourth chapter. As the optical indices of a thin film can strongly depend on the deposition and post-processing conditions, we chose to determine the optical indices of each film. Then, we developed a model using an iterative method based on the Transfer Matrix Method to obtain the most reliable results possible, based on the experimental characterization of each layer and of the full stack. This allowed to model the semi-transparent cell structure and it led to a very good agreement with the experimental results obtained by spectrophotometry. This modeling was used to highlight and quantify the optical absorption losses caused by some materials, and to determine the reflection losses at each interface. Furthermore, with the associated electrical model, it appeared that the FTO electrode was also the main factor limiting the FF of the perovskite cell. As the original model is fully tunable, we were able to make various modifications to improve the opto-electronic performance of our reference STPC. For example, alternative materials to ITO, FTO, TiO_2 and Spiro-OMeTAD were identified, such as IO:H, IZO, SnO_2 and PTAA, and integrated into the model. By combining the most interesting solutions with most efficient silicon cells (IBC instead of Al-BSF), we showed that such tandem can reach an efficiency of 30%.

In Chapter 5, we first investigated the replacement of Spiro-OMeTAD by PTAA. These tests were successful in reducing the performance dispersion of the STPC while maintaining performance close to those of opaque cells. The ITO electrode is subject to much less stress and does not delaminate as with Spiro-OMeTAD, while PTAA has a much higher temperature resistance. This has enabled previously impossible encapsulation tests, and we have managed to maintain a semi-transparent perovskite cell at over 90% of its original efficiency for 1500 hours under light with MPP tracking. We also showed that the time evolution of the STPC electrical properties was due to deoxygenation of this hole transport layer close to the surface after sputtering which led to an electrical barrier at the interface. Oxygen migration from the outside of the cell to the PTAA / ITO interface then allows the interface to regenerate in about 10 days, implying slow kinetics. In parallel, the use of TiO_2 as an electron transport layer was also problematic as its annealing at 450°C strongly limits the choice of the front side electrode. Compatibility tests of SnO_2 with different types of front electrodes have been conducted and promising results have been obtained on opaque cells using a home-made ITO layer on the front side.

We have worked on the replacement of the electrodes in Chapter 6. The sputtering of the IZO top electrode was optimized on glass before being applied to a semi-transparent cell. The use of IZO bilayers proved to be more attractive than single layers by reducing dispersion and increasing the Fill Factor. By taking IZO as an example and through TLM experimental measurements and optical simulations, we have also shown that TCO grids can achieve higher efficiencies in tandem configuration due to a very favorable opto-electrical balance. Finally, we used ALD for IO:H deposition. Between the two precursors used, the depositions with $In(acac)_3$ showed a saturation phenomenon above 45 nm thickness. These results are in agreement with the literature and confirm the difficulty of growing indium oxide, doped or not, with this precursor. On the other hand, with TMI and using an H_2O and O_2/Ar plasma as reagent or only H_2O and O_3, we succeeded in growing layers of more than 80 nm thickness with the crystallographic, optical and morphological characteristics expected for IO:H.

To conclude this Ph.D. work, in the seventh chapter, we have investigated the upscaling to increase the size of our cells to achieve 4T tandems of 16 cm^2. A first approach was explored by the replacement of the spin coating technique for the deposition of the perovskite by the slot die. The results obtained via the slot die process showed results close to those obtained with spin-coating when Spiro-OMeTAD is used as HTL. The results with PTAA are also promising even if they still present a lack of reproducibility due to the high roughness of the perovskite layer deposited by slot die. In a second step and keeping the baseline process, we have successfully transferred the spin-coating process from opaque to semi-transparent mini-modules with P1P2P3 structuring. This was made possible, among other developments, by reducing the width of the sub-cells to 3 mm, as predicted by the simulation and then tested experimentally. Thus, when the module area is 4 cm^2, we succeeded in reaching an active area efficiency of 16.2%, which is comparable to that obtained on 0.09 cm^2 cell. In addition, we also synthesized a 16 cm^2 semi-transparent mini-module with an active area efficiency of 14.2%. We obtain a total reconstructed efficiency on 0.09

cm^2 of nearly 25% in 4T tandem configuration. By simple mechanical stacking on n-PERT silicon cell, we obtained a 4T tandem of 16 cm^2 with an active area efficiency of 20.8%. We finally showed that we were able to fabricate a compact, robust 16 cm^2 4T tandem while addressing the issues of encapsulation and stability overtime during 16 days.

Perspectives

In order to further improve our semi-transparent perovskite cells, both electrically and optically, several avenues are now being explored.

First of all, the simulation chapter allowed us to design a theoretical cell that could achieve over 30% tandem efficiency. However, some of the solutions identified have not yet been implemented. The replacement of soda-lime glass by borosilicate glass is still dependent on the replacement of the FTO as a front electrode and therefore on the eventual replacement of TiO_2 by SnO_2. The development of SnO_2 is now underway at IPVF, the first tests carried out are encouraging and must now be reproduced using more suitable substrates (ITO/Borosilicate glass) to validate the performances obtained. The replacement of the FTO is also conditioned on the development of the IO:H layer by ALD. The use of the TMI precursor has enabled the synthesis of relatively thick layers, but they remain too resistive to be used as electrodes. A new experimental design based on the evolution of the conductivity could enable progress on this issue by fine tuning the deposition parameters such as pulse and purge times. Finally, to achieve the optimal optical structure predicted by the simulation, it will be necessary to implement in the baseline the systematic use of borosilicate glass with an anti-reflection coating and to increase the thickness of the perovskite layer.

Concerning the slot die coating, the results obtained are very promising but have only been tested for the moment on a small surface of 0.09 cm^2. Depositions on large surfaces would allow the rapid synthesis of modules larger than 16 cm^2 with a gap more suitable for tandem with a silicon cell. In parallel, slot die cells made of PTAA still have a lack of reproducibility due to the too high roughness of the perovskite compared to the thinness of the PTAA layer. This could be improved in the future by using other surfactants for example.

Finally, compared to the development of mini-modules and large tandem devices, there is still room for improvement in the 16 cm^2 devices by further reducing the resistive losses. This could be achieved, for example, by using a TCO grid to reduce the average surface sheet resistance of the sub-cells. In addition, we now have an encapsulation process capable of maintaining the efficiency of our various devices over a long period. However, this process currently has a high failure rate. To improve our chances of success, a more systematic study must be carried out in order to understand the origin of the degradation observed. In addition, aging tests under real conditions such as day/night cycling or weathering must now be carried out.

We are still in the early stages of understanding and solving the problems associated with the synthesis of semi-transparent perovskite devices. However, the rapid progress towards scaling up to a relevant performance level, coupled with the ability to fabricate perovskite solar cells at low cost, has already attracted substantial industrial interest worldwide. If the remaining efficiency and stability challenges can be overcome, the potential of perovskite/silicon tandem, compared to other PV technologies, could have an unparalleled impact on global energy production.

Appendix A

State of the art of perovskite cell, STPC and 4T perovskite/silicon tandem

Year	**Efficiency (%)**	**Composition**	**Institute**
2009	3.8	$MAPbI_3$	Toin U [9]
2011	6.5	$MAPbI_3$	SKKU [413]
2012	9.7	$MAPbI_3$	SKKU [414]
2012	10.9	$MAPbI_3$	Oxford U [415]
2013	12	$MAPbI_3$	KRICT [328]
2013	14.1	$MAPbI_3$	EPFL [10]
2014	16	$FAPbI_3$	SKKU [416]
2014	17	$MAPbI_3$	SKKU [417]
2014	17.9	$(FAPbI_3)_{0.85}(MAPbBr_3)_{0.15}$	KRICT [10]
2014	19.3	$MAPbI_3$	UCLA [418]
2014	20.1	$(FAPbI_3)_{0.95}(MAPbBr_3)_{0.05}$	KRICT [10]
2015	20.4	$MAPbI_3$	SKKU [419]
2016	22.1	$(FAPbI_3)_{0.95}(MAPbBr_3)_{0.05}$	KRICT [10]
2017	22.7	$(FAPbI_3)_{0.95}(MAPbBr_3)_{0.05}$	KRICT [10]
2018	23.7	$FA_{0.92}MA_{0.08}PbI_3$	ISCAS [10]
2019	24.2	-	KRICT/UNIST [10]
2019	25.2	-	KRICT/MIT [10]
2021	25.5	-	UNIST/EPFL [10]
2022	25.7	-	EPFL [10]

Table A.1: List of the best perovskite single junction cells.

Year	**Perovskite**	**Top electrode**	**Tandem eff. (%)**	**Perovskite eff. (%)**	**Silicon eff. (%)**	**Filtered Silicon eff. (%)**	**Ref.**
2014	$MAPbI_3$	ITO	13.4	6.2	?	7.2	[47]
2014	$MAPbI_3$	AgNW	17.0	12.7	11.4	4.3	[48]
2016	$MAPbI_3$	Cu/Au	23.0	16.5	21.2	6.5	[66]
2016	$FACsPbI_{3-x}Br_x$	ITO	25.2	16.4	22.1	8.8	[167]
2017	$RbFAMACsPbI_{3-x}Br_x$	ITO	26.4	15.9	23.9	10.4	[85]
2018	$FACsPbI_{3-x}Br_x$	ITO	25.3	16.7	23	8.6	[420]
2018	$FAMACsPbI_{3-x}Br_x$	ITO	25.7	15.7	23.8	10	[198]
2018	$MAPbI_3$	AgNW	26.7	17.1	22.4	9.6	[421]
2019	$MAPbI_3$	ITO	25.5	17.7	21.1	7.8	[422]
2019	$MAPbI_3$	ITO	26.2	15.6	21.4	10.6	[169]
2019	$FACsPbI_{3-x}Br_x$	ITO	27.1	13.8	23	13.3	[423]
2020	$FACsPbI_{3-x}Br_x$	ITO	25.7	17.5	23.2	8.2	[424]
2020	$FAMAPbI_{3-x}Br_x$	ITO	26.0	18.9	22.9	7.1	[172]
2020	$MAPbI_3$	Au	27	18.3	20.8	8.7	[64]
2020	$RbFAMACsPbI_{3-x}Br_x$	IZO	27.7	17.1	24.7	10.7	[425]
2020	$FAMACsPbI_{3-x}Br_x$	IZO	28.2	19.4	?	9.2	[426]
2020	$FACsPbI_3$	Cr/Au	28.3	19.8	?	8.5	[65]
2021	?	?	29.2	17.8	?	11.4	[10]

Table A.2: List of the best 4T perovskite/silicon tandems.

Year	**Active area (cm^2)**	**Pero. Eff. (%)**	**Institute**
2018	11.7	14.9	Chang Gun University [427]
2019	40.8	9	Yonsei University [428]
2019	4	14.8	IMEC [411]
2019	12	12	IMEC [411]
2020	16	11.2	NTU [429]

Table A.3: List of the STPC/STPM with an active area superior at 4 cm^2.

Appendix B

Dispersion of electrical performances of opaque reference cells and batch summaries

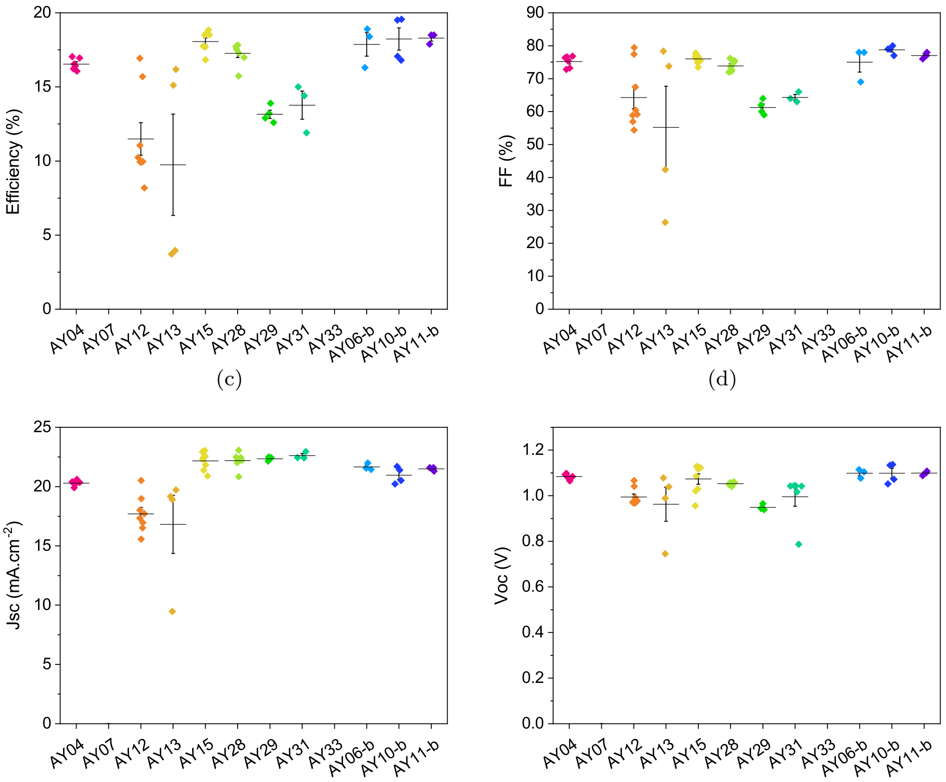
(a)
(b)
(c)
(d)

Figure B.1: Dispersion of the electrical properties (a) efficiency, (b) FF, (c) Jsc and (d) Voc of opaque perovskite cells from different batches with Spiro-OMeTAD as HTL.

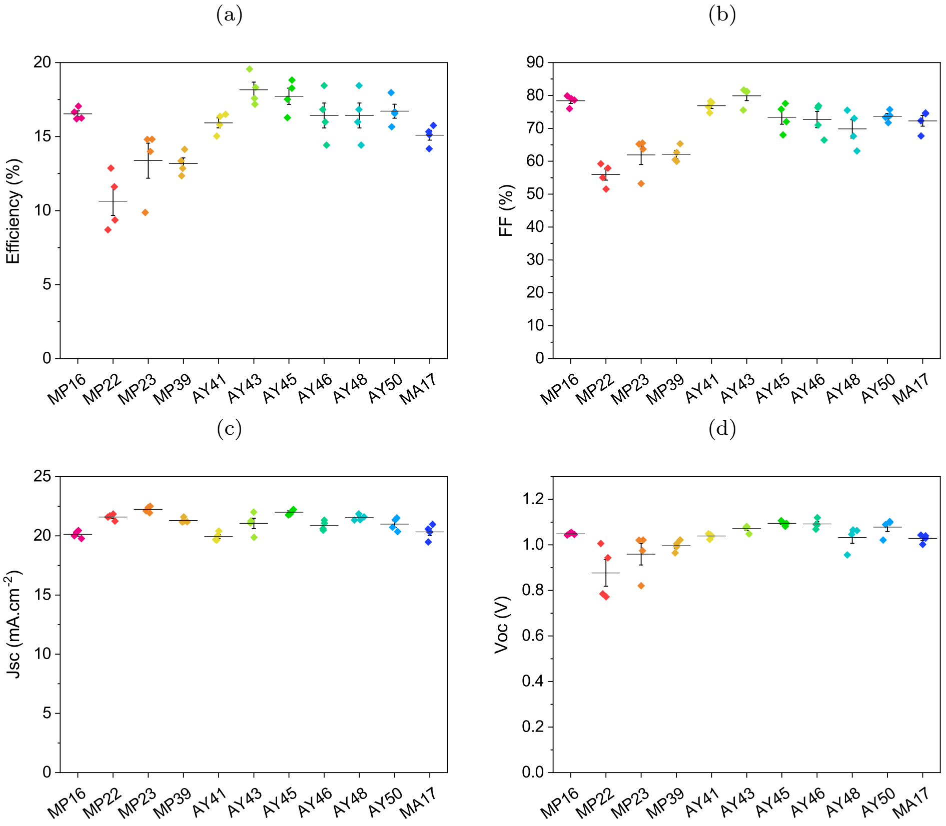

Figure B.2: Dispersion of the electrical properties (a) efficiency, (b) FF, (c) Jsc and (d) Voc of opaque perovskite cells from different batches with PTAA as HTL.

Batch	**HTL**	**ETL**	**TCO n°1**	**TCO n°2**	**Date**	**Comments**
AY04	Spiro	TiO_2	FTO	ITO	11.01.19	-
AY07	Spiro	TiO_2	FTO	ITO	19.03.19	Ti and Ag buffers
AY12	Spiro	TiO_2	FTO	ITO	27.05.19	-
AY13	Spiro	TiO_2	FTO	ITO	06.06.19	Au under ITO
AY15	Spiro	TiO_2	FTO	ITO	21.06.19	No Au anode
AY28	Spiro	TiO_2	FTO	ITO	26.11.19	Low dispersion
AY29	Spiro	TiO_2	FTO	ITO	12.12.19	Low dispersion
AY31	Spiro	TiO_2	FTO	ITO	29.01.20	Power too high
AY33	Spiro	TiO_2	FTO	ITO	20.02.20	Cooling system
AY06-b	Spiro	TiO_2	FTO	ITO	08.09.21	Ni buffer
AY10-b	Spiro	TiO_2	FTO	ITO	28.09.21	Record cell
AY11-b	Spiro	TiO_2	FTO	ITO	28.10.21	Au Buffer
MP16	PTAA	TiO_2	FTO	ITO IZO	29.09.20	Bilayer TCOs
MP22	PTAA	TiO_2	FTO	ITO	20.10.20	PTAA Dopants
MP23	PTAA	TiO_2	FTO	ITO	03.11.20	Encapsulation
MP39	PTAA	TiO_2-SnO_2	FTO ITO	ITO	04.02.21	SnO_2 STPC
MP45/46/49	PTAA	TiO_2-SnO_2	FTO ITO IZO	Au	12.02.21	Front electrode
AY41	PTAA	TiO_2	FTO	ITO	04.11.20	ITO buffer
AY43	PTAA	TiO_2	FTO	ITO IZO IZTO	01.12.20	IZTO
AY45	PTAA-Spiro	TiO_2	FTO	ITO	06.01.21	Vacuum/air aging
AY46	PTAA	TiO_2	FTO	ITO	02.02.21	-
AY48	PTAA	TiO_2	FTO	ITO IZO	10.03.21	Lower power
AY50	PTAA	TiO_2	FTO	ITO	14.04.21	Annealing
MA17	PTAA	TiO_2	FTO	ITO	24.01.21	-
SB32	Spiro-PTAA	TiO_2	FTO	ITO	11.12.20	Slot die

Table B.1: List of STPC batches discussed in this manuscript and their specificities.

Batch	**HTL**	W_a	**Area**	**TCO n°2**	**Date**	**Comments**
MA09	Spiro	5 mm	4 cm^2	ITO	15.06.20	First tests
MA12	PTAA	5 mm	4 cm^2	Au	08.07.20	Best opaques modules + PDMS
AY39	PTAA	5 mm	4 cm^2	ITO	05.07.21	Replaced Spiro by PTAA
MA19	PTAA	4-5 mm	4 cm^2	ITO	02.03.21	Reduction of $\mathrm{W_a}$
MA05	PTAA	3-4 mm	16 cm^2	ITO-Au	16.04.21	Reduction of $\mathrm{W_a}$
MA21	PTAA	4 mm	16 cm^2	ITO	05.03.21	16 cm^2 STPM
MA04	PTAA	5 mm	16 cm^2	ITO	16.04.21	16 cm^2 Tandem
TG01	PTAA	4 mm	4 cm^2	ITO	17.06.21	Welding
TG05	PTAA	4 mm	16 cm^2	ITO	05.07.21	Hyperspectral PL

Table B.2: List of STPM batches discussed in this manuscript and their specificities.

Appendix C

Annealing post-ITO deposition

C.1 Evolution of the opto-electrical properties on glass

It is well known in the literature that ITO requires a temperature increase to achieve ideal opto-electronic properties, either in situ by heating the substrate during deposition, or ex-situ by annealing. This is caused by two phenomena both activated by temperature :

- the evolution from an amorphous to a complete crystalline structure [249, 250, 430, 431]. This nucleation phenomenon and its growth are well described by the Avrami–Johnson– Mehl equation [432]
- the activation of tin as a dopant, which enters in substitution of the In3+ ions and largely increases the number of carriers n [249, 431, 433]

Fig. C.1a shows the evolution of the absorption of an ITO layer on glass as a function of the temperature of the annealing during 1 h. The ITO layer corresponds to the amorphous one presented in the previous section. At 100°C, the absorption of ITO does not change and appears constant. Indeed, annealing only becomes effective from 180°C when crystallization occurs. Below this temperature, as shown in Fig. C.1b, the material remains in its original state, here amorphous. At 200 and 300°C, a slight increase in absorption (+4.2 and 2.6% at 1000 nm respectively) is observed in the IR while its gap decreases from 365 to 328 nm. On the other hand, from 400°C, the absorption in the IR decreases by 8% at 1000 nm.

A crystallization is observed, which also reveals a preferential orientation along the (440) plane. These orientations are an imprint of the sputtering conditions. It is their deposition conditions that determine the orientations observed after annealing. A preferential orientation (400) is often reported in the literature on ITO, so much so that its diffraction peak sometimes appears almost alone on the

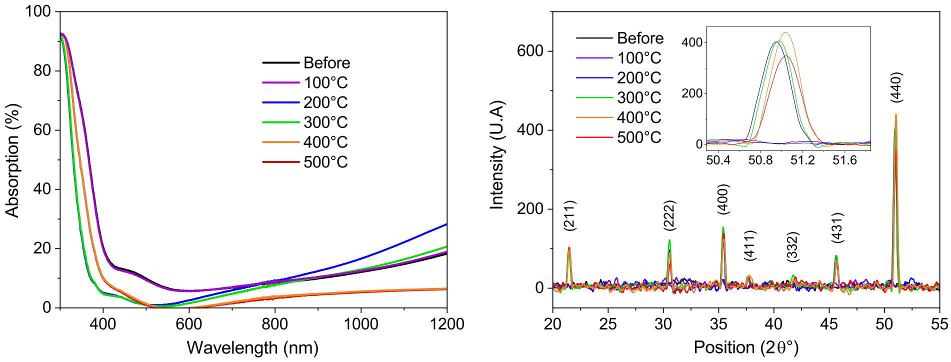
(a)

(b)

Figure C.1: (a) Absorption spectra and (b) XRD spectra of ITO on glass for different annealing temperatures.

diagrams presented [434–436]. However, the (400) orientation seems to be associated with energetic deposition conditions (high temperature [436, 437], high power and high deposition rate [438]), which is not our case with our 50W deposit. The lattice constant is deducted using the strongest peak, i.e. the (440) in the spectrum, the values are shown in Table C.1. The powder lattice constant of In_2O_3 is equal to 10.118 Å [439]. The lattice constant decreases with annealing temperature until 400°C but stay higher than the powder value, indicating that the samples are strained. This strain is probably due to a growth induced stress, which is reduced by annealing [373, 440].

In Table C.1, the sheet resistance of the pre- and post-annealed samples is also given. Thus, it appears minimal for annealing between 200°C and 300°C (9 vs 17 Ω.sq) before rising to 34 Ω.sq from 400°C. As the only annealing tolerable by the perovskite layer would be that of 100°C and that it brings only little improvement on sheet resistance (-0.8 Ω.sq) and does not cause any optical change, it does not seem relevant to anneal the ITO during or once deposited on the cell.

Temperature of annealing (°C)	**Rsh before (Ω.sq)**	**Rsh after (Ω.sq)**	**Position (2θ)**	**FWHM (2θ)**	**Lattice constant (Å)**
100	17.2	16.4	-	-	-
200	17.1	9.9	50.912	0.120	10.147
300	18.1	9.3	50.930	0.128	10.143
400	17.3	33.8	50.995	0.126	10.131
500	17.4	35.2	50.998	0.170	10.131

Table C.1: Sheet resistance of ITO on glass before and after annealing, and position of the peak (440), its width at half-height and the lattice constant after annealing.

C.2 Evolution of electrical performance of STPC on time

We have seen in Chapter 3 Section 3.2.2 that heating the STPC during ITO deposition leads to electrode delamination. However, it is possible to perform post-deposition annealing while respecting the temperature constraints of the perovskite. This annealing time must be short ($\leq$ 10 min) and at a maximum temperature of 110°C. Performed by a hot plate, this type of annealing protects the cell from too fast heating and the temperature increases progressively starting from the glass substrate. The same type of annealing carried out in an oven made take of the ITO electrode in the same way as a badly controlled sputtering.

Fig. C.2a, b and c show IV curves evolution of 3 cells that were annealed at 80°C for 10 min (AY15-01, -04 and -17). It carried out the first day of their synthesis for cells AY15-01 and AY15-04, and 15 days after the synthesis for the cell AY15-17. For samples AY15-01 and AY15-04, the S-shape resorbs immediately after annealing, increasing the FF, see Fig. C.2e. Thus, we observe an immediate increase in the efficiency measured at the IV (+ 1.66% on average), as shown in the Fig. C.2d and d. However, we can also already observe that the stabilized efficiency, measured in MPP tracking over 90 s, decreases after annealing in Fig. C.2d (- 1.19% on average).

The following days, the efficiency of the cells returns to its original level and the stabilized efficiency rises again. Nevertheless, the electrical performance was modified in Fig. C.2a: the S-shape did not reappear, the Voc did not evolve, but the Jsc started to decrease (-2.53 and 2.94 mA.cm^{-2}) and the FF too (- 6.5 and 6.7%). A drop in Jsc is an irreversible process, and is a direct indicator of cell degradation. Concerning the aged cell AY15-17 whose S-shape has already disappeared before annealing, we observe a similar evolution, except that the Jsc does not seem to move. Thus annealing after sputtering produces almost similar effects in the long run, except that the Voc does not move, and does not seem to be a solution to synthesize stable cells in time.

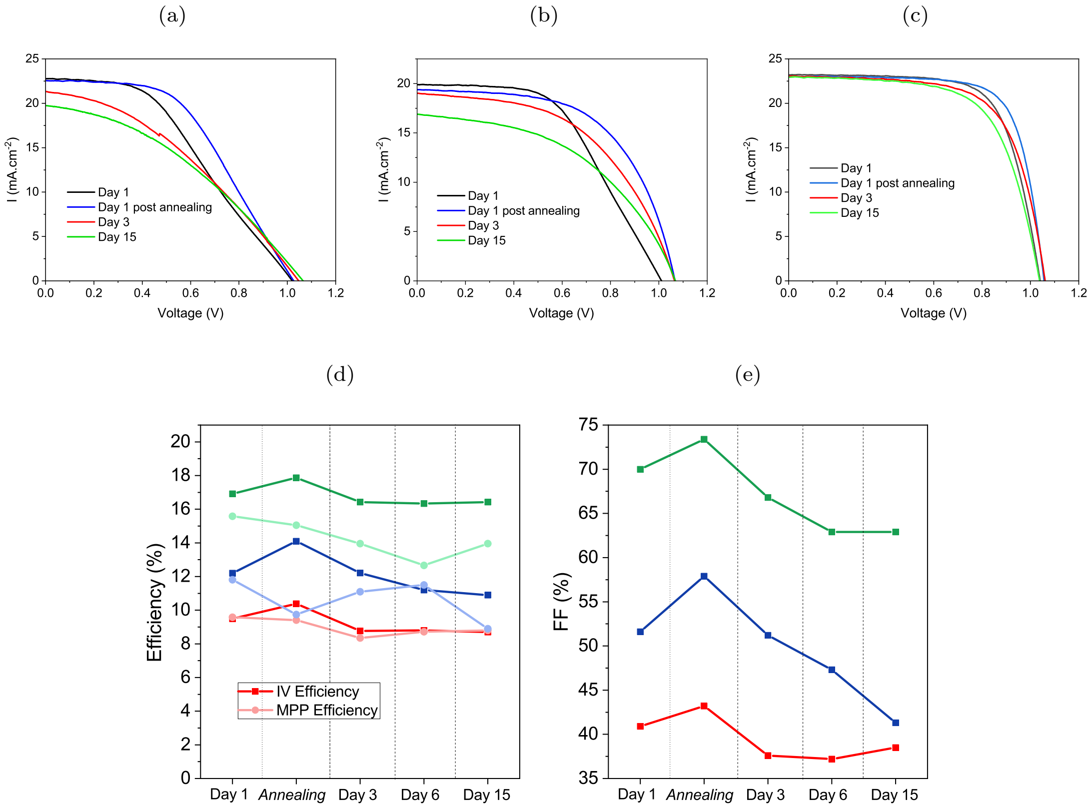

(a) (b) (c)

(d) (e)

Figure C.2: (a), (b) and (c) Evolution of IV curves in time of 3 STPC of the same batch (AY15-01, -04 and -17 respectively), before and after annealing. Evolution of (d) the IV and MPP efficiencies and (e) FF of the three STPC (red, blue and green curves correspond to STPC on Fig. C.2a, b and c respectively).

Appendix D

Transfert Matrix Method

The transfer Matrix Method allows to describe the behavior of light radiation, through its electric field, in a multilayer material such as a perovskite solar cell. In normal times, calculations become very quickly complex because one has to take into account the role of each interface, the reflected/transmitted part of the light within the structure, as well as the constructive/destructive interferences produced in each layer. The use of a transfer matrix simplifies this process. Multilayer structures composed of isotropic and homogeneous materials with flat and parallel interfaces between them can be described by two 2*2 matrices: the interface matrix and the phase matrix, which together allow the transfer matrix of the total system to be defined. This is because the equations governing the propagation of the electric field in such a structure are linear and the tangential component of the electric field is continuous.

D.1 Two layers

Let's start with an incident wave arriving from the left from a layer j on an interface with layer k. Each layer has a thickness $\mathrm{d_j}$ and its optical properties are described by its complex refractive index :

$$\tilde{n}_j = n_j + ik_j \tag{D.1}$$

When the electric field is perpendicular to the plane of incidence and the angle ϕ_0 of light incidence is equal to zero, the Fresnel coefficients of reflection and transmission $\mathrm{r_{jk}}$ and $\mathrm{t_{jk}}$ between a layer j and its neighbor k are defined by:

$$r_{jk} = \frac{\tilde{n}_j - \tilde{n}_k}{\tilde{n}_j + \tilde{n}_k} \quad and \quad t_{jk} = \frac{2\tilde{n}_j}{\tilde{n}_j + \tilde{n}_k} \tag{D.2}$$

The interface matrix, also known as the refraction matrix, is used to describe the interface in the structure at a given wavelength and is defined by the following equation:

$$I_{jk} = \begin{bmatrix} 1 & r_{jk} \\ r_{jk} & 1 \end{bmatrix} * \frac{1}{t_{jk}} \tag{D.3}$$

The phase matrix describing the propagation through layer j is described as follows:

$$L_j = \begin{bmatrix} e^{-i\xi_j d_j} & 0 \\ 0 & e^{i\xi_j d_j} \end{bmatrix} \quad with \quad \xi_j = \frac{2\pi}{\lambda}\tilde{n}_j \tag{D.4}$$

ξ_j is the phase difference corresponding to the phase change of the wave when it passes through the j-layer.

D.2 First interface

Let us now consider a multilayer structure having m layers whose first interface is with the outside air, as shown in Fig. D.1. Using the interface matrix (Eq. D.3) and the phase matrix (Eq. D.4), the transfer matrix of the total system S (also called the diffusion matrix), is written:

$$S = \begin{bmatrix} S_{11} & S_{12} \\ S_{21} & S_{22} \end{bmatrix} = (\prod_{v=1}^{m} I_{v(v-1)} L_v).I_{m(m+1)} \tag{D.5}$$

The electric optical field can be resolved at any point in the system using two components: one component propagating in the direction of the x increasing E_m^+(x) and one in the opposite direction E_m^-(x). In the special case of the first interface with air, the transfer matrix of the total system S connects the electric field on the ambient air side E_0 and the substrate side $\text{E}_{\text{m+1}}$ by:

$$\begin{bmatrix} E_0^+ \\ E_0^- \end{bmatrix} = S \begin{bmatrix} E_{m+1}^+ \\ E_{m+1}^- \end{bmatrix} \tag{D.6}$$

Incident light arrives from the ambient side in the direction of the positive x, no wave propagates in the opposite direction inside the first layer, which means that E_{m+1}^-=0. For the total structure, the reflection and transmission coefficients resulting from this first interface can be expressed using the elements of the transfer matrix of the total system S as:

$$r = \frac{E_0^-}{E_0^+} = \frac{S_{21}}{S_{11}} \quad and \quad t = \frac{E_{m+1}^-}{E_0^+} = \frac{1}{S_{11}} \tag{D.7}$$

D.3 Multilayer structure

In order to calculate the internal electric field in a j-layer within the structure, the structure can be divided into two subsets separated by the j-layer. The transfer matrix of the system can be written as follows:

$$S = S_j^{'} L_j S_j^{''} \tag{D.8}$$

Where $\text{S}_j^{'}$ is the transfer matrix of the partial system comprising the layers j= 0,...j-1 and $\text{S}_j^{''}$ is the transfer matrix of the partial system comprising the layers j= j+1,...,m. It is thus possible to link the electric field of layer j to that of layers j-1 and j+1:

$$\begin{bmatrix} E_0^+ \\ E_0^- \end{bmatrix} = S_j^{'} \begin{bmatrix} E_{j+1}^{'+} \\ E_{j+1}^{'-} \end{bmatrix} \quad with \quad S_j^{'} = \begin{bmatrix} S_{j11}^{'} & S_{j12}^{'} \\ S_{j21}^{'} & S_{j22}^{'} \end{bmatrix} = (\prod_{v=1}^{j-1} I_{v(v-1)} L_v).I_{(j-1)/j} \tag{D.9}$$

$$\begin{bmatrix} E_j^{''+} \\ E_j^{''-} \end{bmatrix} = S_j^{''} \begin{bmatrix} E_{m+1}^+ \\ E_{m+1}^- \end{bmatrix} \quad with \quad S_j^{''} = \begin{bmatrix} S_{j11}^{''} & S_{j12}^{''} \\ S_{j21}^{''} & S_{j22}^{''} \end{bmatrix} = (\prod_{v=j+1}^{m} I_{v(v-1)} L_v).I_{m/(m+1)} \tag{D.10}$$

where $\text{E}_j^{'+}$ and $\text{E}_j^{'-}$ are related to the left-hand interface (j-1)/j of layer j and $\text{E}_j^{''+}$ and $\text{E}_j^{''-}$ refer to the right-hand boundary j/(j+1) of layer j. It is possible to define complex reflection and transmission coefficients for layer j as a function of the matrix elements.

$$r_j^{'} = \frac{S_{j21}^{'}}{S_{j11}^{'}} \quad and \quad t_j^{'} = \frac{1}{S_{j11}^{'}} \tag{D.11}$$

$$r_j^{''} = \frac{S_{j21}^{''}}{S_{j11}^{''}} \quad and \quad t_j^{''} = \frac{1}{S_{j11}^{''}} \tag{D.12}$$

By combining equations (Eq. D.8) to (Eq. D.12), it is possible to express an internal transfer coefficient which relates the incident plane wave to the internal electric field propagating in the positive x direction from the (j-1)/j interface and another the internal electric field propagating in the negative x direction from the (j-1)/j interface:

$$t_j^+ = \frac{E_j^+}{E_0^+} = \frac{t_j^{'}}{1 - r_{j-}^{'} r_j^{''} e^{i2\xi_j d_j}} \quad with \quad r_{j-}^{'} = -\frac{S_{j21}^{'}}{S_{j11}^{'}} \tag{D.13}$$

$$t_j^- = \frac{E_j^-}{E_0^+} = \frac{t_j^{'} r_j^{''} e^{i2\xi_j d_j}}{1 - r_{j-}^{'} r_j^{''} e^{i2\xi_j d_j}} = t_j^+ r_j^{''} e^{i2\xi_j d_j} \tag{D.14}$$

The total electric field in an arbitrary plane in layer j at a distance x from the interface (j-1)/j in terms of the incident plane wave E_0^+ is given by:

$$E_j(x) = \frac{S_{j11}^{''} e^{-i\xi_j d_{j-x}} + S_{j21}^{''} e^{i\xi_j d_{j-x}}}{S_{j11}^{'} S_{j11}^{''} e^{-i\xi_j d_j} + S_{j12}^{'} S_{j21}^{''} e^{i\xi_j d_j}} E_0^+ \quad for \quad 0 < x < d \tag{D.15}$$

This calculation is thus repeated for each layer composing the studied structure, which makes it possible to know the E(x) field at any point of the structure to the nearest nanometre for each wavelength. The knowledge of E makes it possible to calculate the absorption of each layer as well as the total transmission via the knowledge of the previously calculated reflection and transfer coefficients.

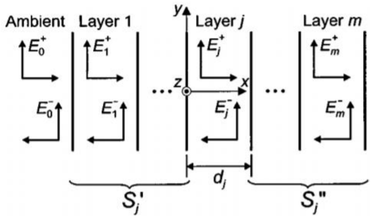

Figure D.1: Schematic diagram of a multilayer cell having m layers. Each layer j (j=1,2, ..., m) has a thickness d_j and its optical properties are described by its refractive and extinction indices. The electric field at any point on layer j is represented by two components: E_j^+ and E_j^- [441].

Appendix E

ITO bilayer on Spiro-OMeTAD

As shown in the literature, a buffer layer can be a solution to protect the STPC from the ITO sputtering. This leads to new questions about the compatibility between the different layers and can cause additional optical losses. This is why we have chosen to start by proposing an ITO buffer. It is deposited first at low power (25 instead of 40 W) during 10 min and has a thickness of about 9 nm. As shown in Fig. E.1a, these cells have a low average efficiency the first day after the synthesis (3.28 vs 7.39% for classic ITO electrode). It is mainly caused by an abnormal Jsc (7.88 vs. 16.02 mA.cm^{-2}) as expected. The IV obtained on these cells with this process have a shape comparable to the red IV curve on Fig. 3.4a. The EQE shows that the decrease of the Jsc is linked to a decrease of collection on the whole spectrum. It would seem that the problem is not only related to the Spiro-OMeTAD and its interface, but that here a general degradation of the absorber perovskite is taking place. However, Voc appears comparable to the other cells, contrary to the heated cells of Chapter 3 Section 3.2.2 and we notice the good homogeneity of the cells between them ($\sigma = 1.03$ vs. 7.91). These suggest that the buffer effect worked, prevents the fall of the Voc as seen in Chapter 3 Section 3.2.2 of heating in sputtering and is necessary to achieve good reproducibility.

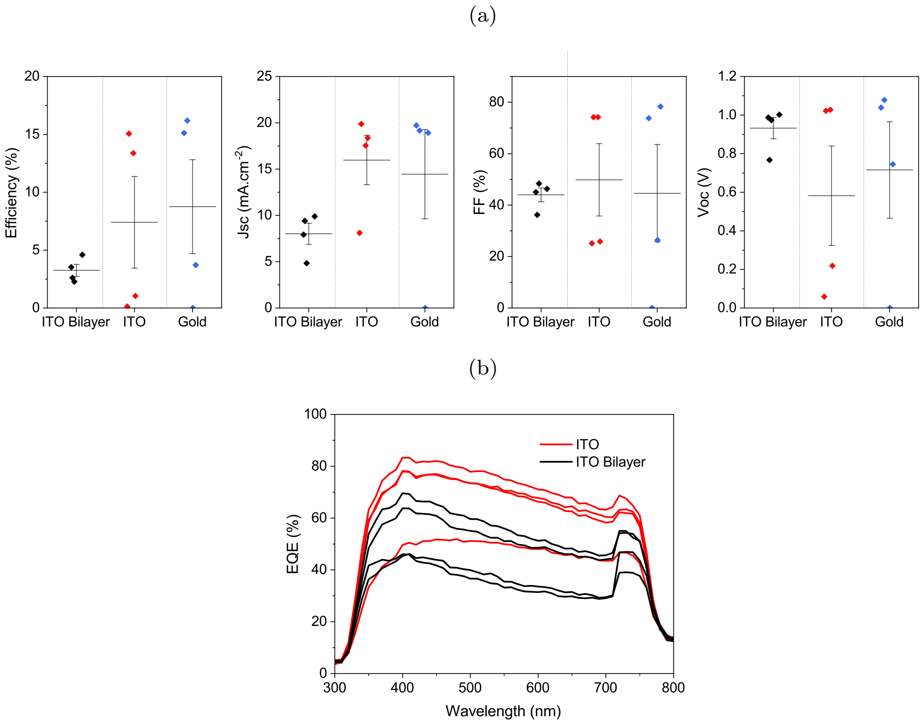
(a)

(b)

Figure E.1: (a) Dispersion of the electrical properties of 8 STPC (4 with a classical ITO and 4 with an additional ITO layer sputtered at low power on the Spiro-OMeTAD) and 4 opaque perovskite cells. (b) EQE spectra of the 8 STPC presented in Fig. E.1a.

Appendix F

Effect of oxygen on the opto-electronic properties

Legeay showed that adding oxygen flux in argon plasma allowed amorphous ITO to obtain better opto-electronic properties [431]. However, the optimum rate is 0.051% of O_2, which we cannot reach in our equipment. Indeed, first of all, by keeping a flow of argon at 33 sccm, we cannot go below 0.5% of O_2 because the flow meter does not allow to send less than 0.1 sccm of gas in the chamber. By increasing the argon flow rate to 90 sccm while keeping a pressure of 2 mTorr in the chamber, we obtained a more conductive and thinner ITO for similar transparency, see Fig. F.1 and Table F.1. It is then possible to obtain a ratio of 0.15% O_2. Despite an improvement of the transparency in the IR (+10%), the obtained resistivity of 38 Ω.sq seems to us too important to be used on STPC.

Zebaze Kana et al. showed in parallel that starting the ITO deposition at a lower vacuum could naturally boost the ITO due to the residual H_2O and O_2 present in the chamber. By starting the deposition at a higher residual pressure in the chamber of the order of 10^{-5} instead of 10^{-7} mbar, the IR absorption effectively decreases by 7% at 1200 nm without impacting the sheet resistance. On the other hand, the lack of control linked to this technique does not allow us to consider it in our optics to improve the reproducibility of our deposits.

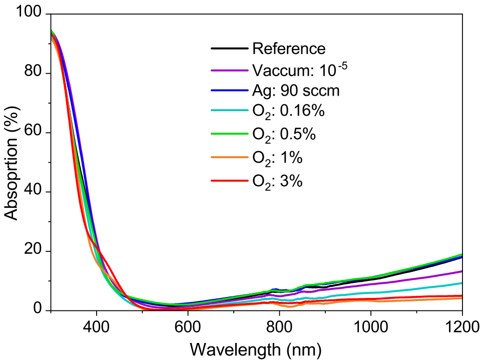

Figure F.1: Absorption spectra of ITO on glass for different ratios of O_2, an Ar flux at 90 sccm and a residual pressure of 10^{-5} mbar compared to the classic ITO deposition

Run	**Argon flow (sccm)**	**Oxygen flow (sccm)**	**Vaccum (mbar)**	**Rsh (Ω.sq)**	**Thickness (nm)**
1	33	0	7.10^{-7}	16	202
2	33	0	5.10^{-5}	20	206
3	90	0	5.10^{-5}	14	183
4	90	0.15	7.10^{-7}	38	200
5	33	1	7.10^{-7}	250	209
6	33	0.3	7.10^{-7}	861	127
7	33	0.15	7.10^{-7}	47k	160

Table F.1: Sheet resistance and thickness of ITO on glass for different ratios of O_2, an Ar flux at 90 sccm and a residual pressure of 10^{-5} mbar compared to the classic ITO deposition.

Appendix G

Design Of Experiment - List of runs

Run	TMI pulse (s)	TMI Purge (s)	TMI Temp. (°C)	Water Pulse (s)	Water Purge (s)	Plasma pre-p. (s)	Plasma Pulse (s)	Plasma Purge (s)	Reactor Temp. (°C)	Rate (Å/min)
1	3	8	55	3	8	4	8	5	200	0.77
2	3	4	35	1	4	2	2	1	160	0.35
3	5	6	35	1	8	4	2	5	200	0.26
4	1	6	55	3	4	2	8	1	160	1.11
5	5	4	45	1	8	4	8	1	160	0.59
6	1	8	45	3	4	2	2	5	200	0.31
7	5	4	35	2	4	2	8	5	200	0.55
8	1	8	55	2	8	4	2	1	160	0.30
9	5	8	55	1	6	2	2	1	200	0.42
10	1	4	35	3	6	4	8	5	160	0.51
11	5	4	55	3	4	4	5	1	200	0.87
12	1	8	35	1	8	2	5	5	160	0.39
13	5	8	35	3	4	4	2	3	160	0.20
14	1	4	55	1	8	2	8	3	200	0.98
15	5	8	55	1	4	3	8	5	160	1.14
16	1	4	35	3	8	3	2	1	200	0.27
17	5	8	35	3	8	2	8	1	180	0.48
18	1	4	55	1	4	4	2	5	180	0.38
19	5	4	55	3	8	2	2	5	160	0.81
20	1	8	35	1	4	4	8	1	200	0.50
21	3	6	45	2	6	3	5	3	180	0.55

Table G.1: 21 runs established by DOE regarding the development of IO:H via ALD using TMI as a precursor.

Appendix H

Evaluation of interface resistances between ITO and FTO

Proceeding in the same way as in Chapter 3 Section 3.3.2, we use the TLM to determine the interface resistance between the ITO and the FTO in an STPM. The TLM curves for samples A and B are similar despite the presence of the ITO layer on structure B. This suggests that the contact resistance between ITO and FTO is negligible compared to the rest (0.05 Ω), and lower than the resistance observed on other samples between Au and ITO (0.23 Ω).

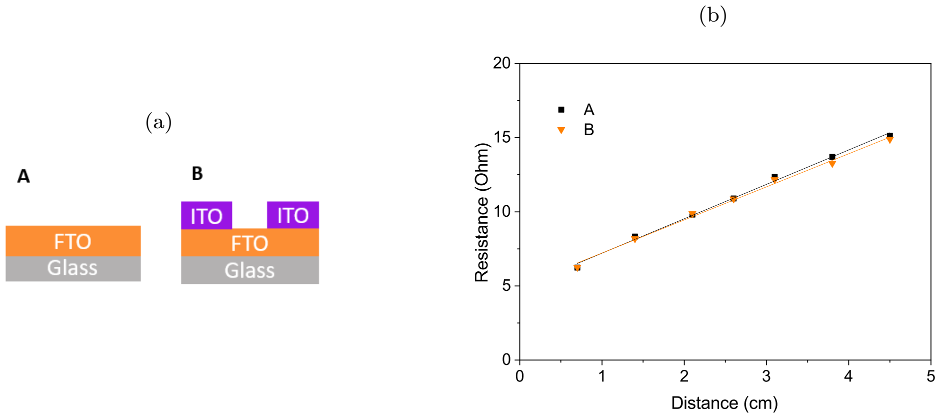
(a)

(b)

Figure H.1: (a) 2 structures measured with TLM. (b) TLM curves (resistance as a function of the distance) for the 2 structures presented on (a).

Structure	**A**	**B**
Intercept (Ω)	4.88	4.98
Slope (Ω.cm^{-1})	2.32	2.23

Table H.1: Slopes and intersections with y axis of the TLM curves presented in Fig. H.1b.

Appendix I

Colorful semi-transparent perovskite mini-module

The development of these STPM is done here to build a 4T perovskite/silicon tandem. Nevertheless, other possible applications support the interest in developing this kind of device. For example, semi-transparent colored bifacial solar cells are a way explored today to make the use of solar panels more attractive in terms of architecture while opening a whole new range of possibilities. The simultaneous harvesting of direct light and scattered/reflected light will allow to obtain higher efficiency than those of a mono-facial cell without the use of a tandem structure.

In this perspective, 16 cm² STPM with tunable color were fabricated by varying the thickness of the ITO semi-transparent electrode between 140 and 320 nm (Fig. I.1a and b), according to the work previously published by Nanyang Technological University [442]. These devices having been realized following a malfunction during the synthesis steps, these STPM do not have electrical performances. On the other hand, they allow to highlight that a large color tunability across the visible spectrum is possible by tuning the ITO electrode thickness and that the STPM can be a very promising candidate.

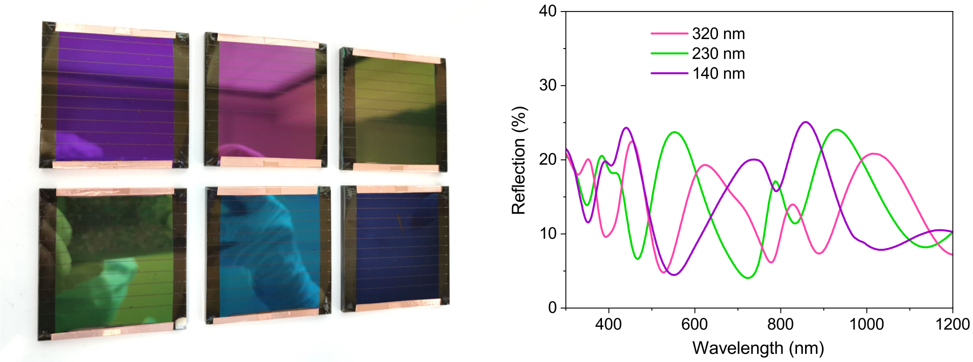
(a)

(b)

Figure I.1: (a) Photo of six 16 cm^2 STPM, composed of 10 cells of 1.6 cm^2 each, the color variations observed are due to the variation in the thickness of the ITO electrode. (b) Reflection spectra of the green, pink and purple STPM presented in (a).

Appendix J

Effect of laser graving on the opto-electronic properties

On some STPM (from 4 to 16 cm^2), we observe a change of color at the level of certain sub-cells, as shown in the photo in Fig. J.1. In order to understand the origin of this phenomenon and the impact of etching on the optical properties of perovskite, a PL study was carried out. The monitoring in time by hyperspectral was carried out on two 16 cm^2 STPM from batch TG05, composed of sub-cells of 4 mm wide.

These analyses, presented in Fig. J.2b, reveal a general increase in the intensity of the photoluminescence peak as a function of time. This result is expected and had already been observed in Chapter 5 Section 5.1.4.2 on filter type samples of different sizes. This evolution is relatively homogeneous on all the samples at 15 days after the synthesis, whereas we noted differences just after the synthesis.

Nevertheless, it is especially at the gap of the perovskite that the differences appear most marked. In reality, the PL peak is a convolution of the luminescence of the material and its gap. We observe in time a red-shift as expected but with a difference of 10 nm between the different sub-cells. As this phenomenon was not observed on the filter type samples in Chapter 5, we can assume that this phenomenon is caused by the etching. Moreover, an identical follow-up was done on a sample where only the P2 etching was carried out. It shows the same kind of behavior, see Fig. J.2a. The P2 etching would thus be at the origin of differentiation between the sub-cells. The laser reaches all the layers up to the FTO and potentially creates changes and degradation at the edges of some sub-cells.

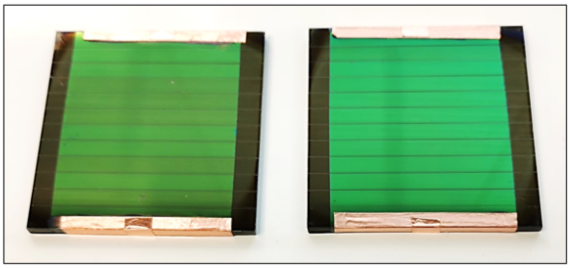

Figure J.1: Photo of two 16 cm^2 STPM, composed of 10 cells of 1.6 cm^2 each, one of which shows color variations between the sub-cells.

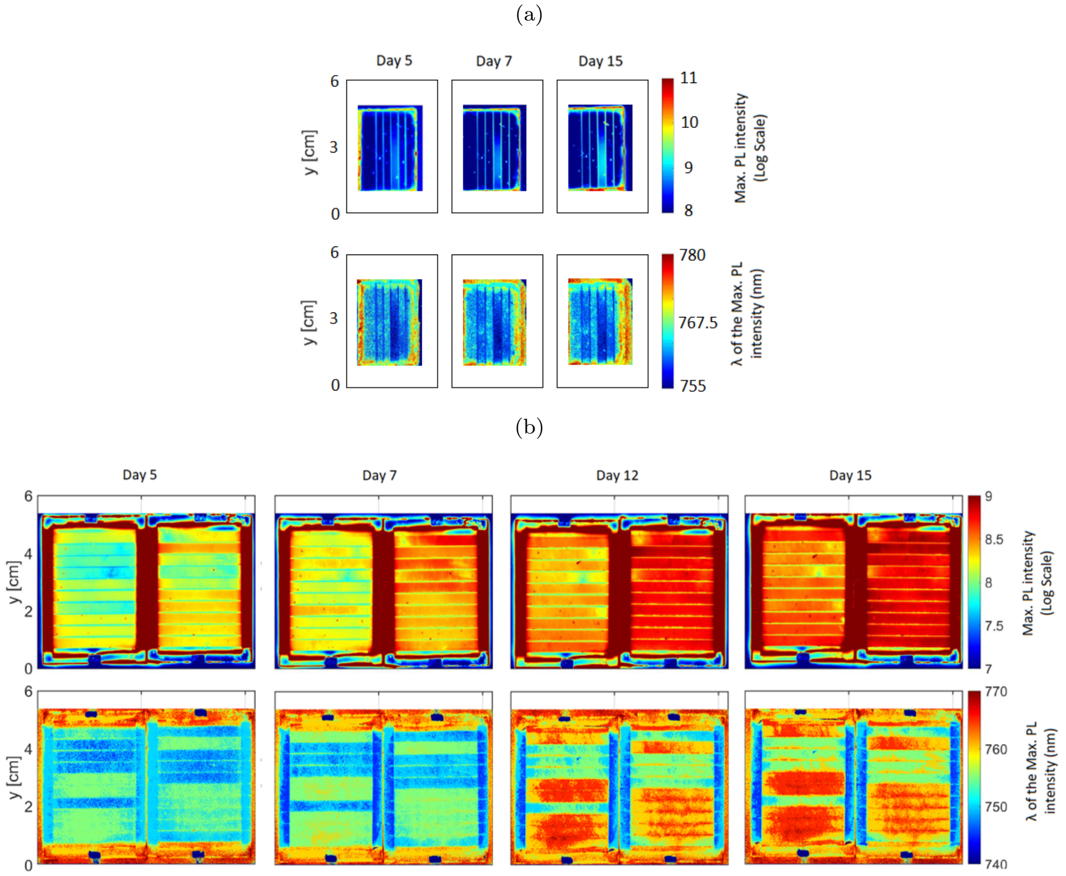

Figure J.2: (a) Hyperspectral photoluminescence imaging was performed on (a) semi-transparent filter with only P2 engraving of 12 cm^2 and (b) STPM type samples of 16 cm^2 areas as a function of time after the synthesis. The upper images represent the evolution of the intensity of the detected photoluminescence peak and the lower ones, the position of the peak.

Appendix K

PDMS covering

The first encapsulation attempt was made with PDMS. It was deposited on the surface of 4 STPM of batch AY39, 9 days after synthesis, according to the same process used in Chapter 7 Section 7.2.3.2 on the optical filters. These modules are still 3*3 cm^2 composed of 4 cells of 2*0.5 cm^2. The PDMS have a homogeneous and smooth aspect as on the filters, see Fig. K.1a. It also plays well the role of optical coupling by decreasing the reflections taking place at the ITO/Air interface, as shown in Fig. K.1b. The total reflection is decreased from 780 nm and the transmission increases between 780 and 1100 nm. Concerning the electrical properties, Fig. K.1c shows their evolution in time before and after PDMS deposition. No degradation of their electrical properties was observed, even 49 days later after being stored in a dry atmosphere. The average efficiency even increases slightly after 40 days of storage (+ 0.6%). Thus PDMS seems to play a correct role as an encapsulant, stabilizing the STPM without degrading its electrical performance while improving the optical coupling.

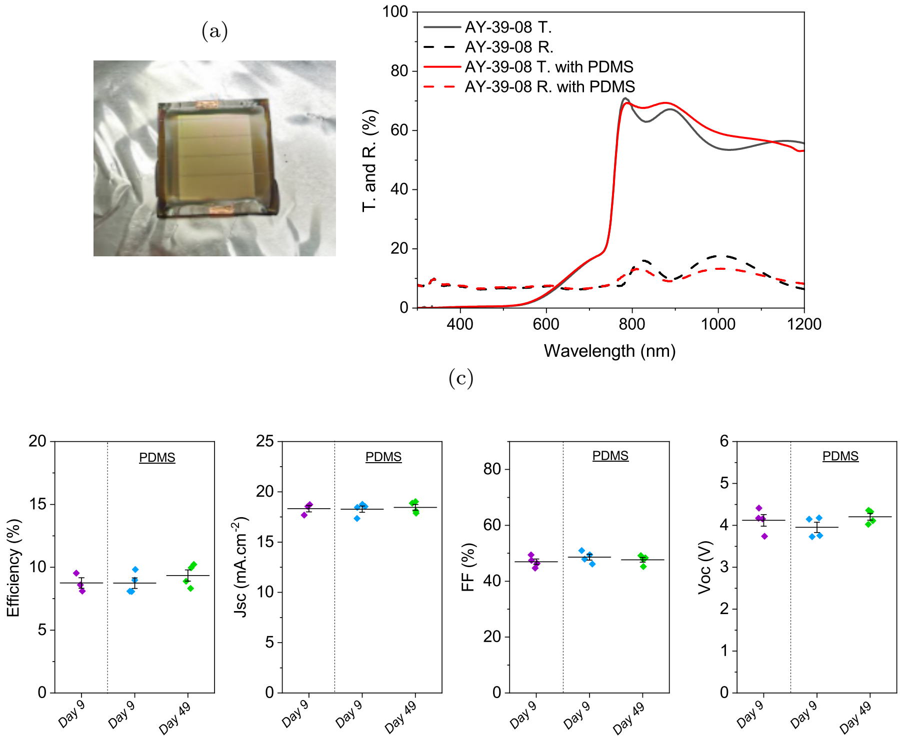
(b)

(a)

(c)

Figure K.1: (a) Photo of a 4 cm^2 AY39 STPM, covered by PDMS. (b) Transmission and reflection spectra of AY39-08 STPM before and after the PDMS covering. (c) Dispersion of the electrical properties of AY39 4 cm^2 STPM with 4 sub-cell with widths of 5 mm, before and after the covering of PDMS.

However, the aging did not happen as expected when STPM or filters are placed in a tandem configuration with silicon cells. After a few days, it peeled off due to stresses generated by the PDMS and the PLA case, tearing off part of the ITO electrode in the process (see Fig. K.2). This layer does not seem to be strong enough to allow the cells of the tandem to be completely fixed to each other, and allows tandem STPM measurements to be made only ephemerally. It is therefore necessary to find another encapsulation technique.

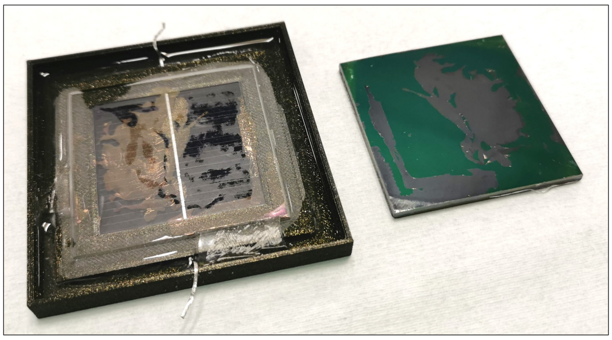

Figure K.2: Delamination of the ITO from the rest of the filter B after encapsulation by PDMS.

Bibliography

1. *World Population Prospects - Population Division - United Nations* ttps://population.un.org/wpp/Download/Standard/CSV/ (2022).
2. *World Energy Outlook 2021 – Analysis* https://www.iea.org/reports/world-energy-outlook-2021 (2022).
3. *CO2 emissions – Global Energy Review 2021* fr-FR. https://www.iea.org/reports/global-energy-review-2021/co2-emissions (2022).
4. *Paris Agreement;* 2015.
5. *Solar - Fuels & Technologies* fr-FR. https://www.iea.org/fuels-and-technologies/solar (2022).
6. *BP Statistical Review of World Energy;* tech. rep. (2019).
7. Simon, P. *Photovoltaics Report* tech. rep. (Fraunhofer ISE and Werner Warmuth, July 2021).
8. Hirst, L. C. & Ekins-Daukes, N. J. Fundamental losses in solar cells. en. *Progress in Photovoltaics: Research and Applications* **19,** 286–293. ISSN: 1099-159X. https://onlinelibrary.wiley.com/doi/abs/10.1002/pip.1024 (2018) (May 2011).
9. Kojima, A., Teshima, K., Shirai, Y. & Miyasaka, T. Organometal Halide Perovskites as Visible-Light Sensitizers for Photovoltaic Cells. en. *Journal of the American Chemical Society* **131,** 6050–6051. ISSN: 0002-7863, 1520-5126. http://pubs.acs.org/doi/abs/10.1021/ja809598r (2018) (May 2009).
10. *National Renewable Energy Laboratory (NREL)* https://www.nrel.gov/ (2018).
11. Almansouri, I., Ho-Baillie, A. & Green, M. A. Ultimate efficiency limit of single-junction perovskite and dual-junction perovskite/silicon two-terminal devices. en. *Japanese Journal of Applied Physics* **54,** 08KD04. ISSN: 1347-4065. http://iopscience.iop.org/article/10.7567/JJAP.54.08KD04/meta (2018) (July 2015).
12. Becquerel, A. E. Memoire sur les effects d´electriques produits sous l´influence des rayons solaire. *Annalen der Physick und Chemie* **54,** 35–42 (1841).
13. Fritts, C. On a New Form of Selenium Photocell. *American Journal of Science* **26,** 465 (1883).
14. *PVEducation* http://www.pveducation.org/ (2018).
15. *Energie+* https://www.energieplus-lesite.be/index.php?id=2 (2018).
16. Ehrler, B. *et al.* Photovoltaics Reaching for the Shockley–Queisser Limit. en. *ACS Energy Letters* **5,** 3029–3033. ISSN: 2380-8195, 2380-8195. https://pubs.acs.org/doi/10.1021/acsenergylett.0c01790 (2022) (Sept. 2020).
17. Green, M. A. *et al.* Solar cell efficiency tables (Version 58). en. *Progress in Photovoltaics: Research and Applications* **29,** 657–667. ISSN: 1062-7995, 1099-159X. https://onlinelibrary.wiley.com/doi/10.1002/pip.3444 (2021) (July 2021).
18. Semonin, O. E. *et al.* Peak External Photocurrent Quantum Efficiency Exceeding 100% via MEG in a Quantum Dot Solar Cell. en. *Science* **334,** 1530–1533. ISSN: 0036-8075, 1095-9203. https://www.science.org/doi/10.1126/science.1209845 (2022) (Dec. 2011).
19. Ehrler, B., Wilson, M. W. B., Rao, A., Friend, R. H. & Greenham, N. C. Singlet Exciton Fission-Sensitized Infrared Quantum Dot Solar Cells. en. *Nano Letters* **12,** 1053–1057. ISSN: 1530-6984, 1530-6992. https://pubs.acs.org/doi/10.1021/nl204297u (2022) (Feb. 2012).

20. Yu, Z. (, Leilaeioun, M. & Holman, Z. Selecting tandem partners for silicon solar cells. en. *Nature Energy* **1,** 16137. ISSN: 2058-7546. https://www.nature.com/articles/nenergy2016137 (2018) (Sept. 2016).

21. Ross, R. T. & Nozik, A. J. Efficiency of hot-carrier solar energy converters. en. *Journal of Applied Physics* **53,** 3813–3818. ISSN: 0021-8979, 1089-7550. http://aip.scitation.org/doi/10.1063/1.331124 (2022) (May 1982).

22. Dkhissi, Y. *et al.* Low temperature processing of flexible planar perovskite solar cells with efficiency over 10%. en. *Journal of Power Sources* **278,** 325–331. ISSN: 03787753. http://linkinghub.elsevier.com/retrieve/pii/S0378775314021326 (2018) (Mar. 2015).

23. Geisz, J. F. *et al.* Six-junction III–V solar cells with 47.1% conversion efficiency under 143 Suns concentration. en. *Nature Energy* **5,** 326–335. ISSN: 2058-7546. http://www.nature.com/articles/s41560-020-0598-5 (2022) (Apr. 2020).

24. Bläsi, B. *et al. Photonic structures for III-V//Si multijunction solar cells with efficiency ¿33%* in *Photonics for Solar Energy Systems VII* (eds Wehrspohn, R. B. & Sprafke, A. N.) (SPIE, Strasbourg, France, June 2018), 2. ISBN: 978-1-5106-1902-9 978-1-5106-1903-6. https://www.spiedigitallibrary.org/conference-proceedings-of-spie/10688/2307831/Photonic-structures-for-III-V--Si-multijunction-solar-cells/10.1117/12.2307831.full (2022).

25. Adhyaksa, G. W. P., Johlin, E. & Garnett, E. C. Nanoscale Back Contact Perovskite Solar Cell Design for Improved Tandem Efficiency. eng. *Nano Letters* **17,** 5206–5212. ISSN: 1530-6992 (Sept. 2017).

26. Lal, N. N. *et al.* Perovskite Tandem Solar Cells. en. *Advanced Energy Materials* **7.** ISSN: 1614-6840. https://onlinelibrary.wiley.com/doi/abs/10.1002/aenm.201602761 (2018) (Sept. 2017).

27. Anaya, M., Lozano, G., Calvo, M. E. & Míguez, H. ABX3 Perovskites for Tandem Solar Cells. *Joule* **1,** 769–793. ISSN: 2542-4351. http://www.sciencedirect.com/science/article/pii/S2542435117300910 (2018) (Dec. 2017).

28. Chen, B., Zheng, X., Bai, Y., Padture, N. P. & Huang, J. Progress in Tandem Solar Cells Based on Hybrid Organic–Inorganic Perovskites. en. *Advanced Energy Materials* **7.** ISSN: 1614-6840. https://onlinelibrary.wiley.com/doi/abs/10.1002/aenm.201602400 (2018) (July 2017).

29. Werner, J., Niesen, B. & Ballif, C. Perovskite/Silicon Tandem Solar Cells: Marriage of Convenience or True Love Story? – An Overview. en. *Advanced Materials Interfaces* **5.** ISSN: 2196-7350. https://onlinelibrary.wiley.com/doi/abs/10.1002/admi.201700731 (2018) (Jan. 2018).

30. Chung, H. *et al.* Modeling and designing multilayer 2D perovskite / silicon bifacial tandem photovoltaics for high efficiencies and long-term stability. EN. *Optics Express* **25,** A311–A322. ISSN: 1094-4087. https://www.osapublishing.org/oe/abstract.cfm?uri=oe-25-8-A311 (2018) (Apr. 2017).

31. Lal, N. N., Loo, Y. X. & Stocks, M. *Free the Bandgap! Series-Parallel Connection of Tandem Cells* en. in *32nd European Photovoltaic Solar Energy Conference and Exhibition* (July 2016), 223–227. http://www.eupvsec-proceedings.com/proceedings?paper=37635 (2018).

32. Uzu, H. *et al.* High efficiency solar cells combining a perovskite and a silicon heterojunction solar cells via an optical splitting system. en. *Applied Physics Letters* **106,** 013506. ISSN: 0003-6951. https://aip.scitation.org/doi/10.1063/1.4905177 (2018) (Jan. 2015).

33. Li, Y. *et al.* Reflective perovskite solar cells for efficient tandem applications. en. *Journal of Materials Chemistry C* **5,** 134–139. ISSN: 2050-7534. http://pubs.rsc.org/en/content/articlelanding/2017/tc/c6tc04510c (2018) (Dec. 2016).

34. Todorov, T. K., Bishop, D. M. & Lee, Y. S. Materials perspectives for next-generation low-cost tandem solar cells. *Solar Energy Materials and Solar Cells* **180,** 350–357. ISSN: 0927-0248. http://www.sciencedirect.com/science/article/pii/S0927024817304269 (2018) (June 2018).

35. Todorov, T., Gunawan, O. & Guha, S. A road towards 25% efficiency and beyond: perovskite tandem solar cells. en. *Molecular Systems Design & Engineering* **1,** 370–376. ISSN: 2058-9689. http://xlink.rsc.org/?DOI=C6ME00041J (2022) (2016).

36. Futscher, M. & Ehrler, B. Efficiency Limit of Perovskite/Si Tandem Solar Cells. *ACS Energy Letters* **1,** 863–868 (Oct. 2016).

37. Jaysankar, M. *et al.* Four-Terminal Perovskite/Silicon Multijunction Solar Modules. en. *Advanced Energy Materials* **7,** 1602807. ISSN: 16146832. http://doi.wiley.com/10.1002/aenm.201602807 (2018) (Aug. 2017).

38. Wang, Z., Song, Z., Yan, Y., Liu, S. (& Yang, D. Perovskite—a Perfect Top Cell for Tandem Devices to Break the S–Q Limit. en. *Advanced Science* **6,** 1801704. ISSN: 2198-3844, 2198-3844. https://onlinelibrary.wiley.com/doi/10.1002/advs.201801704 (2022) (Apr. 2019).

39. Cheng, Y. & Ding, L. Perovskite/Si tandem solar cells: Fundamentals, advances, challenges, and novel applications. en. *SusMat* **1,** 324–344. ISSN: 2692-4552, 2692-4552. https://onlinelibrary.wiley.com/doi/10.1002/sus2.25 (2022) (Sept. 2021).

40. Fang, Z. *et al.* Perovskite-based tandem solar cells. en. *Science Bulletin* **66,** 621–636. ISSN: 20959273. https://linkinghub.elsevier.com/retrieve/pii/S2095927320307015 (2022) (Mar. 2021).

41. Eperon, G. E. *et al.* Perovskite-perovskite tandem photovoltaics with optimized band gaps. fr. *Science,* aaf9717. ISSN: 0036-8075, 1095-9203. http://science.sciencemag.org/content/early/2016/10/19/science.aaf9717 (2018) (Oct. 2016).

42. Zhao, D. *et al.* Low-bandgap mixed tin–lead iodide perovskite absorbers with long carrier lifetimes for all-perovskite tandem solar cells. en. *Nature Energy* **2,** 17018. ISSN: 2058-7546. https://www.nature.com/articles/nenergy201718 (2018) (Apr. 2017).

43. Essig, S. *et al.* Raising the one-sun conversion efficiency of III–V/Si solar cells to 32.8% for two junctions and 35.9% for three junctions. en. *Nature Energy* **2,** 17144. ISSN: 2058-7546. http://www.nature.com/articles/nenergy2017144 (2018) (Aug. 2017).

44. Nguyen, P.-L. *et al. New Architecture and Bonding Process for III-V//Si Tandem Solar Cells* en. in *OSA Advanced Photonics Congress 2021* (OSA, Washington, DC, 2021), PvW1E.4. ISBN: 978-1-943580-94-1. https://opg.optica.org/abstract.cfm?URI=PVLED-2021-PvW1E.4 (2022).

45. Jung, S. I., Yoon, K. H., Ahn, S., Gwak, J. & Yun, J. H. Fabrication and characterization of wide band-gap CuGaSe2 thin films for tandem structure. en. *Current Applied Physics* **10,** S395–S398. ISSN: 15671739. http://linkinghub.elsevier.com/retrieve/pii/S1567173910000507 (2018) (May 2010).

46. Fuster, D. *et al.* System for manufacturing complete Cu(In,Ga)Se2 solar cells in situ under vacuum. en. *Solar Energy* **198,** 490–498. ISSN: 0038092X. https://linkinghub.elsevier.com/retrieve/pii/S0038092X20300803 (2022) (Mar. 2020).

47. Löper, P. *et al.* Organic–inorganic halide perovskite/crystalline silicon four-terminal tandem solar cells. en. *Physical Chemistry Chemical Physics* **17,** 1619–1629. ISSN: 1463-9076, 1463-9084. http://xlink.rsc.org/?DOI=C4CP03788J (2018) (2015).

48. Bailie, C. D. *et al.* Semi-transparent perovskite solar cells for tandems with silicon and CIGS. en. *Energy & Environmental Science* **8,** 956–963. ISSN: 1754-5706. http://pubs.rsc.org/en/content/articlelanding/2015/ee/c4ee03322a (2018) (Mar. 2015).

49. Li, H. & Zhang, W. Perovskite Tandem Solar Cells: From Fundamentals to Commercial Deployment. en. *Chemical Reviews* **120,** 9835–9950. ISSN: 0009-2665, 1520-6890. https://pubs.acs.org/doi/10.1021/acs.chemrev.9b00780 (2022) (Sept. 2020).

50. Kothandaraman, R. K., Jiang, Y., Feurer, T., Tiwari, A. N. & Fu, F. Near-Infrared-Transparent Perovskite Solar Cells and Perovskite-Based Tandem Photovoltaics. en. *Small Methods,* 2000395. ISSN: 2366-9608, 2366-9608. https://onlinelibrary.wiley.com/doi/abs/10.1002/smtd.202000395 (2020) (Sept. 2020).

51. Gilles, P. *Procédés laser pour la réalisation de cellules photovoltaïques en silicium à haut rendement* fr. PhD thesis (INSA de Lyon, Oct. 2012). https://tel.archives-ouvertes.fr/tel-00932583/document.

52. Desrues, T. *Développement de cellules photovoltaïques à hétérojonctions silicium et contacts en face arrière* fr. PhD thesis (Lyon, INSA, Jan. 2009). http://www.theses.fr/2009ISAL0084.

53. Reaux, D. *Cellules photovoltaïques à hétérojonctions de silicium (a-SiH/c-Si): modélisation des défauts et de la recombinaison à l'interface* fr. PhD thesis (Université Paris-Saclay, June 2017).

54. Kaminski, A. *et al.* Aluminium BSF in silicon solar cells. en. *Solar Energy Materials and Solar Cells* **72,** 373–379. ISSN: 09270248. https://linkinghub.elsevier.com/retrieve/pii/S0927024801001854 (2022) (Apr. 2002).

55. ITRPV. *International Technology Roadmap for Photovoltaic - 10th edition* tech. rep. (2019).
56. Fertig, F. *et al.* Mass production of p-type Cz silicon solar cells approaching average stable conversion efficiencies of 22 %. en. *Energy Procedia* **124,** 338–345. ISSN: 18766102. https://linkinghub.elsevier.com/retrieve/pii/S1876610217342790 (2022) (Sept. 2017).
57. Green, M., Blakers, A., Narayanan, S. & Taouk, M. Improvements in silicon solar cell efficiency. en. *Solar Cells* **17,** 75–83. ISSN: 03796787. https://linkinghub.elsevier.com/retrieve/pii/0379678786900608 (2022) (Mar. 1986).
58. Dullweber, T. & Schmidt, J. Industrial Silicon Solar Cells Applying the Passivated Emitter and Rear Cell (PERC) Concept—A Review. *IEEE Journal of Photovoltaics* **6,** 1366–1381. ISSN: 2156-3381, 2156-3403. http://ieeexplore.ieee.org/document/7493618/ (2022) (Sept. 2016).
59. Abramov, A. S., Andronikov, D. A., Abolmasov, S. N. & Terukov, E. I. en. in *High-Efficient Low-Cost Photovoltaics* (eds Petrova-Koch, V., Hezel, R. & Goetzberger, A.) Series Title: Springer Series in Optical Sciences, 113–132 (Springer International Publishing, Cham, 2020). ISBN: 978-3-030-22863-7 978-3-030-22864-4. http://link.springer.com/10.1007/978-3-030-22864-4_7 (2022).
60. Lu, M., Bowden, S., Das, U. & Birkmire, R. Interdigitated back contact silicon heterojunction solar cell and the effect of front surface passivation. en. *Applied Physics Letters* **91,** 063507. ISSN: 0003-6951, 1077-3118. http://aip.scitation.org/doi/10.1063/1.2768635 (2022) (Aug. 2007).
61. Gee, J., Schubert, W. & Basore, P. *Emitter wrap-through solar cell* in *Conference Record of the Twenty Third IEEE Photovoltaic Specialists Conference - 1993 (Cat. No.93CH3283-9)* (IEEE, Louisville, KY, USA, 1993), 265–270. ISBN: 978-0-7803-1220-3. http://ieeexplore.ieee.org/document/347173/ (2022).
62. Knauss, H., McCann, M. & Fath, P. *Large area metallization wrap through solar cells using electroless plating* in *Conference Record of the Thirty-first IEEE Photovoltaic Specialists Conference, 2005.* (IEEE, Lake buena Vista, FL, USA, 2005), 1201–1204. ISBN: 978-0-7803-8707-2. http://ieeexplore.ieee.org/document/1488354/ (2022).
63. Jooss, W. *et al. Back contact buried contact solar cells with metallization wrap around electrodes* in *Conference Record of the Twenty-Eighth IEEE Photovoltaic Specialists Conference - 2000 (Cat. No.00CH37036)* (IEEE, Anchorage, AK, USA, 2000), 176–179. ISBN: 978-0-7803-5772-3. http://ieeexplore.ieee.org/document/915783/ (2022).
64. Wang, Z. *et al.* 27%-Efficiency Four-Terminal Perovskite/Silicon Tandem Solar Cells by Sandwiched Gold Nanomesh. en. *Advanced Functional Materials* **30,** 1908298. ISSN: 1616-301X, 1616-3028. https://onlinelibrary.wiley.com/doi/10.1002/adfm.201908298 (2022) (Jan. 2020).
65. Yang, D. *et al.* 28.3%-efficiency perovskite/silicon tandem solar cell by optimal transparent electrode for high efficient semitransparent top cell. en. *Nano Energy* **84,** 105934. ISSN: 22112855. https://linkinghub.elsevier.com/retrieve/pii/S2211285521001920 (2022) (June 2021).
66. Chen, B. *et al.* Efficient Semitransparent Perovskite Solar Cells for 23.0%-Efficiency Perovskite/Silicon Four-Terminal Tandem Cells. en. *Advanced Energy Materials* **6.** ISSN: 1614-6840. https://onlinelibrary.wiley.com/doi/abs/10.1002/aenm.201601128 (2018) (Oct. 2016).
67. Mailoa, J. P. *et al.* A 2-terminal perovskite/silicon multijunction solar cell enabled by a silicon tunnel junction. en. *Applied Physics Letters* **106,** 121105. ISSN: 0003-6951. https://aip.scitation.org/doi/10.1063/1.4914179 (2018) (Mar. 2015).
68. Bush, K. A. *et al.* 23.6%-efficient monolithic perovskite/silicon tandem solar cells with improved stability. en. *Nature Energy* **2,** 17009. ISSN: 2058-7546. https://www.nature.com/articles/nenergy20179 (2018) (Apr. 2017).
69. Grant, D. T., Catchpole, K. R., Weber, K. J. & White, T. P. Design guidelines for perovskite/silicon 2-terminal tandem solar cells: an optical study. en. *Optics Express* **24,** A1454. ISSN: 1094-4087. https://opg.optica.org/abstract.cfm?URI=oe-24-22-A1454 (2022) (Oct. 2016).
70. Razzaq, A. *et al.* Infrared Absorption Enhancement Using Periodic Inverse Nanopyramids in Crystalline-Silicon Bottom Cells for Application in Tandem Devices. *IEEE Journal of Photovoltaics* **10,** 740–748. ISSN: 2156-3381, 2156-3403. (2022) (May 2020).
71. Wu, Y., Fell, A. & Weber, K. J. A Step-by-Step Optimization of the c-Si Bottom Cell in Monolithic Perovskite/c-Si Tandem Devices. en. *Solar RRL* **2,** 1800193. ISSN: 2367198X. https://onlinelibrary.wiley.com/doi/10.1002/solr.201800193 (2022) (Nov. 2018).

72. *Result of the search "solar cell' and "perovskite solar cell" in Google Scholar* https://scholar.google.com/ (2022).

73. J. Snaith, H. Perovskites: The Emergence of a New Era for Low-Cost, High-Efficiency Solar Cells. *The Journal of Physical Chemistry Letters* **4,** 3623–3630 (Oct. 2013).

74. Tan, Z.-K. *et al.* Bright light-emitting diodes based on organometal halide perovskite. eng. *Nature Nanotechnology* **9,** 687–692. ISSN: 1748-3395 (Sept. 2014).

75. Ball, J. M., Lee, M. M., Hey, A. & Snaith, H. J. Low-temperature processed meso-superstructured to thin-film perovskite solar cells. en. *Energy & Environmental Science* **6,** 1739. ISSN: 1754-5692, 1754-5706. http://xlink.rsc.org/?DOI=c3ee40810h (2022) (2013).

76. Wang, D.-L. *et al.* Highly efficient light management for perovskite solar cells. en. *Scientific Reports* **6.** ISSN: 2045-2322. http://www.nature.com/articles/srep18922 (2018) (May 2016).

77. Jeon, N. J. *et al.* Compositional engineering of perovskite materials for high-performance solar cells. en. *Nature* **517,** 476–480. ISSN: 0028-0836, 1476-4687. http://www.nature.com/articles/nature14133 (2022) (Jan. 2015).

78. Wang, R. *et al.* A Review of Perovskites Solar Cell Stability. en. *Advanced Functional Materials* **29,** 1808843. ISSN: 1616-301X, 1616-3028. https://onlinelibrary.wiley.com/doi/10.1002/adfm.201808843 (2022) (Nov. 2019).

79. Green, M. A., Ho-Baillie, A. & Snaith, H. J. The emergence of perovskite solar cells. en. *Nature Photonics* **8,** 506–514. ISSN: 1749-4893. https://www.nature.com/articles/nphoton.2014.134 (2018) (July 2014).

80. Gao, P., Grätzel, M. & Nazeeruddin, M. K. Organohalide lead perovskites for photovoltaic applications. en. *Energy & Environmental Science* **7,** 2448–2463. ISSN: 1754-5706. http://pubs.rsc.org/en/content/articlelanding/2014/ee/c4ee00942h (2018) (July 2014).

81. Pauporté, T. Cellules solaires à base de pérovskites hybrides. fr. *Ref : TIP958WEB - "Innovations technologiques".* https://www.techniques-ingenieur.fr/base-documentaire/innovation-th10/innovations-en-energie-et-environnement-42503210/cellules-solaires-a-base-de-perovskites-hybrides-re250/ (2018) (May 2016).

82. Saliba, M. *et al.* Incorporation of rubidium cations into perovskite solar cells improves photovoltaic performance. eng. *Science (New York, N.Y.)* **354,** 206–209. ISSN: 1095-9203 (2016).

83. Eperon, G. E. *et al.* Formamidinium lead trihalide: a broadly tunable perovskite for efficient planar heterojunction solar cells. en. *Energy & Environmental Science* **7,** 982–988. ISSN: 1754-5706. http://pubs.rsc.org/en/content/articlelanding/2014/ee/c3ee43822h (2018) (Feb. 2014).

84. Noh, J. H., Im, S. H., Heo, J. H., Mandal, T. N. & Seok, S. I. Chemical management for colorful, efficient, and stable inorganic-organic hybrid nanostructured solar cells. eng. *Nano Letters* **13,** 1764–1769. ISSN: 1530-6992 (Apr. 2013).

85. Duong, T. *et al.* Rubidium Multication Perovskite with Optimized Bandgap for Perovskite-Silicon Tandem with over 26% Efficiency. en. *Advanced Energy Materials* **7.** ISSN: 1614-6840. https://onlinelibrary.wiley.com/doi/abs/10.1002/aenm.201700228 (2018) (July 2017).

86. Ramos, F. J. *et al.* Highly efficient MoOx-free semitransparent perovskite cell for 4 T tandem application improving the efficiency of commercially-available Al-BSF silicon. en. *Scientific Reports* **8.** ISSN: 2045-2322. http://www.nature.com/articles/s41598-018-34432-5 (2019) (Dec. 2018).

87. Jacobsson, T. J. *et al.* An open-access database and analysis tool for perovskite solar cells based on the FAIR data principles. en. *Nature Energy.* ISSN: 2058-7546. https://www.nature.com/articles/s41560-021-00941-3 (2022) (Dec. 2021).

88. De Wolf, S. *et al.* Organometallic Halide Perovskites: Sharp Optical Absorption Edge and Its Relation to Photovoltaic Performance. eng. *The Journal of Physical Chemistry Letters* **5,** 1035–1039. ISSN: 1948-7185 (Mar. 2014).

89. Stranks, S. D. *et al.* Electron-Hole Diffusion Lengths Exceeding 1 Micrometer in an Organometal Trihalide Perovskite Absorber. en. *Science* **342,** 341–344. ISSN: 0036-8075, 1095-9203. http://science.sciencemag.org/content/342/6156/341 (2018) (Oct. 2013).

90. Milić, J. V. *et al.* Supramolecular Engineering for Formamidinium-Based Layered 2D Perovskite Solar Cells: Structural Complexity and Dynamics Revealed by Solid-State NMR Spectroscopy. en. *Advanced Energy Materials* **9,** 1900284. ISSN: 1614-6832, 1614-6840. `https://onlinelibrary.wiley.com/doi/10.1002/aenm.201900284` (2021) (May 2019).

91. Rodríguez-Seco, C., Cabau, L., Vidal-Ferran, A. & Palomares, E. Advances in the Synthesis of Small Molecules as Hole Transport Materials for Lead Halide Perovskite Solar Cells. en. *Accounts of Chemical Research* **51,** 869–880. ISSN: 0001-4842, 1520-4898. `https://pubs.acs.org/doi/10.1021/acs.accounts.7b00597` (2021) (Apr. 2018).

92. Wang, Y.-K., Jiang, Z.-Q. & Liao, L.-S. New advances in small molecule hole-transporting materials for perovskite solar cells. en. *Chinese Chemical Letters* **27,** 1293–1303. ISSN: 10018417. `https://linkinghub.elsevier.com/retrieve/pii/S1001841716302169` (2021) (Aug. 2016).

93. Azmi, R. *et al.* High-performance dopant-free conjugated small molecule-based hole-transport materials for perovskite solar cells. en. *Nano Energy* **44,** 191–198. ISSN: 22112855. `https://linkinghub.elsevier.com/retrieve/pii/S2211285517307693` (2021) (Feb. 2018).

94. Wan, L., Li, X., Song, C., He, Y. & Zhang, W. Benzobis(thiadiazole)-based small molecules as efficient electron transporting materials in perovskite solar cells. en. *Solar Energy Materials and Solar Cells* **191,** 437–443. ISSN: 09270248. `https://linkinghub.elsevier.com/retrieve/pii/S0927024818305531` (2021) (Mar. 2019).

95. Haider, M., Zhen, C., Wu, T., Liu, G. & Cheng, H.-M. Boosting efficiency and stability of perovskite solar cells with nickel phthalocyanine as a low-cost hole transporting layer material. en. *Journal of Materials Science & Technology* **34,** 1474–1480. ISSN: 10050302. `https://linkinghub.elsevier.com/retrieve/pii/S1005030218300628` (2021) (Sept. 2018).

96. Sfyri, G., Vamshikrishna, N., Kumar, C. V., Giribabu, L. & Lianos, P. Synthesis and characterization of tetratriphenylamine Zn phthalocyanine as hole transporting material for perovskite solar cells. en. *Solar Energy* **140,** 60–65. ISSN: 0038092X. `https://linkinghub.elsevier.com/retrieve/pii/S0038092X16305151` (2021) (Dec. 2016).

97. Cho, K. T. *et al.* Perovskite Solar Cells Employing Molecularly Engineered Zn(II) Phthalocyanines as Hole-transporting Materials. en. *Nano Energy* **30,** 853–857. ISSN: 22112855. `https://linkinghub.elsevier.com/retrieve/pii/S221128551630372X` (2021) (Dec. 2016).

98. Zhao, X. & Wang, M. Organic hole-transporting materials for efficient perovskite solar cells. en. *Materials Today Energy* **7,** 208–220. ISSN: 24686069. `https://linkinghub.elsevier.com/retrieve/pii/S246860691730028X` (2021) (Mar. 2018).

99. Jeong, I., Jo, J. W., Bae, S., Son, H. J. & Ko, M. J. A fluorinated polythiophene hole-transport material for efficient and stable perovskite solar cells. en. *Dyes and Pigments* **164,** 1–6. ISSN: 01437208. `https://linkinghub.elsevier.com/retrieve/pii/S0143720818325889` (2021) (May 2019).

100. Xie, Q. *et al.* Self-doped polymer with fluorinated phenylene as hole transport layer for efficient polymer solar cells. en. *Organic Electronics* **61,** 207–214. ISSN: 15661199. `https://linkinghub.elsevier.com/retrieve/pii/S1566119918302702` (2021) (Oct. 2018).

101. Miao, X. *et al.* Room-temperature electrochemical deposition of ultrathin CuOx film as hole transport layer for perovskite solar cells. en. *Scripta Materialia* **165,** 134–139. ISSN: 13596462. `https://linkinghub.elsevier.com/retrieve/pii/S1359646219301150` (2021) (May 2019).

102. Sun, Y. *et al.* Efficient, Air-Stable Bulk Heterojunction Polymer Solar Cells Using MoOx as the Anode Interfacial Layer. en. *Advanced Materials* **23,** 2226–2230. ISSN: 09359648. `https://onlinelibrary.wiley.com/doi/10.1002/adma.201100038` (2021) (May 2011).

103. Chen, W. *et al.* Cesium Doped NiO $_x$ as an Efficient Hole Extraction Layer for Inverted Planar Perovskite Solar Cells. en. *Advanced Energy Materials* **7,** 1700722. ISSN: 16146832. `https://onlinelibrary.wiley.com/doi/10.1002/aenm.201700722` (2021) (Oct. 2017).

104. Son, D.-Y., Im, J.-H., Kim, H.-S. & Park, N.-G. 11% Efficient Perovskite Solar Cell Based on ZnO Nanorods: An Effective Charge Collection System. en. *The Journal of Physical Chemistry C* **118,** 16567–16573. ISSN: 1932-7447, 1932-7455. `https://pubs.acs.org/doi/10.1021/jp412407j` (2021) (July 2014).

105. Wang, K. *et al.* Low-Temperature and Solution-Processed Amorphous WO $_X$ as Electron-Selective Layer for Perovskite Solar Cells. en. *The Journal of Physical Chemistry Letters* **6,** 755–759. ISSN: 1948-7185, 1948-7185. https://pubs.acs.org/doi/10.1021/acs.jpclett.5b00010 (2021) (Mar. 2015).
106. Bera, A. *et al.* Perovskite Oxide SrTiO $_3$ as an Efficient Electron Transporter for Hybrid Perovskite Solar Cells. en. *The Journal of Physical Chemistry C* **118,** 28494–28501. ISSN: 1932-7447, 1932-7455. https://pubs.acs.org/doi/10.1021/jp509753p (2021) (Dec. 2014).
107. Kogo, A., Ikegami, M. & Miyasaka, T. A SnO $_x$ –brookite TiO $_2$ bilayer electron collector for hysteresis-less high efficiency plastic perovskite solar cells fabricated at low process temperature. en. *Chemical Communications* **52,** 8119–8122. ISSN: 1359-7345, 1364-548X. http://xlink.rsc.org/?DOI=C6CC02589G (2021) (2016).
108. Shin, S. S. *et al.* Colloidally prepared La-doped BaSnO $_3$ electrodes for efficient, photostable perovskite solar cells. en. *Science* **356,** 167–171. ISSN: 0036-8075, 1095-9203. https://www.science.org/doi/10.1126/science.aam6620 (2021) (Apr. 2017).
109. Rahman, M. Z. & Edvinsson, T. How to Make a Most Stable Perovskite Solar Cell. en. *Matter* **1,** 562–564. ISSN: 25902385. https://linkinghub.elsevier.com/retrieve/pii/S2590238519301225 (2022) (Sept. 2019).
110. Li, M., Li, H., Fu, J., Liang, T. & Ma, W. Recent Progress on the Stability of Perovskite Solar Cells in a Humid Environment. en. *The Journal of Physical Chemistry C* **124,** 27251–27266. ISSN: 1932-7447, 1932-7455. https://pubs.acs.org/doi/10.1021/acs.jpcc.0c08019 (2022) (Dec. 2020).
111. Krishnan, U. Factors affecting the stability of perovskite solar cells: a comprehensive review. *Journal of Photonics for Energy* **9,** 1. ISSN: 1947-7988. https://www.spiedigitallibrary.org/journals/journal-of-photonics-for-energy/volume-9/issue-02/021001/Factors-affecting-the-stability-of-perovskite-solar-cells--a/10.1117/1.JPE.9.021001.full (2022) (Apr. 2019).
112. Wu, T. *et al.* The Main Progress of Perovskite Solar Cells in 2020–2021. en. *Nano-Micro Letters* **13,** 152. ISSN: 2311-6706, 2150-5551. https://link.springer.com/10.1007/s40820-021-00672-w (2022) (Jan. 2021).
113. Wang, K. *et al.* Defect Passivation in Perovskite Solar Cells by Cyano-Based π-Conjugated Molecules for Improved Performance and Stability. en. *Advanced Functional Materials* **30,** 2002861. ISSN: 1616-301X, 1616-3028. https://onlinelibrary.wiley.com/doi/10.1002/adfm.202002861 (2022) (Aug. 2020).
114. Xiong, S. *et al.* Defect-Passivation Using Organic Dyes for Enhanced Efficiency and Stability of Perovskite Solar Cells. en. *Solar RRL* **4,** 1900529. ISSN: 2367-198X, 2367-198X. https://onlinelibrary.wiley.com/doi/10.1002/solr.201900529 (2022) (May 2020).
115. Yang, Z. *et al.* Multifunctional Phosphorus-Containing Lewis Acid and Base Passivation Enabling Efficient and Moisture-Stable Perovskite Solar Cells. en. *Advanced Functional Materials* **30,** 1910710. ISSN: 1616-301X, 1616-3028. https://onlinelibrary.wiley.com/doi/10.1002/adfm.201910710 (2022) (Apr. 2020).
116. Chen, S. *et al.* Trapping lead in perovskite solar modules with abundant and low-cost cation-exchange resins. en. *Nature Energy* **5,** 1003–1011. ISSN: 2058-7546. http://www.nature.com/articles/s41560-020-00716-2 (2022) (Dec. 2020).
117. Jiang, Y. *et al.* Reduction of lead leakage from damaged lead halide perovskite solar modules using self-healing polymer-based encapsulation. en. *Nature Energy* **4,** 585–593. ISSN: 2058-7546. http://www.nature.com/articles/s41560-019-0406-2 (2022) (July 2019).
118. Ahmad, Z. *et al.* Degradation analysis in mixed (MAPbI3 and MAPbBr3) perovskite solar cells under thermal stress. en. *Journal of Materials Science: Materials in Electronics* **30,** 1354–1359. ISSN: 0957-4522, 1573-482X. http://link.springer.com/10.1007/s10854-018-0403-4 (2020) (Jan. 2019).
119. Burschka, J. *et al.* Sequential deposition as a route to high-performance perovskite-sensitized solar cells. en. *Nature* **499,** 316–319. ISSN: 0028-0836, 1476-4687. http://www.nature.com/articles/nature12340 (2022) (July 2013).

120. Shi, L. *et al.* Accelerated Lifetime Testing of Organic–Inorganic Perovskite Solar Cells Encapsulated by Polyisobutylene. en. *ACS Applied Materials & Interfaces* **9,** 25073–25081. ISSN: 1944-8244, 1944-8252. https://pubs.acs.org/doi/10.1021/acsami.7b07625 (2022) (Aug. 2017).

121. Matteocci, F. *et al.* Encapsulation for long-term stability enhancement of perovskite solar cells. en. *Nano Energy* **30,** 162–172. ISSN: 22112855. https://linkinghub.elsevier.com/retrieve/pii/S221128551630413X (2022) (Dec. 2016).

122. Ramasamy, E., Karthikeyan, V., Rameshkumar, K. & Veerappan, G. Glass-to-glass encapsulation with ultraviolet light curable epoxy edge sealing for stable perovskite solar cells. en. *Materials Letters* **250,** 51–54. ISSN: 0167577X. https://linkinghub.elsevier.com/retrieve/pii/S0167577X19306329 (2022) (Sept. 2019).

123. Cheacharoen, R. *et al.* Encapsulating perovskite solar cells to withstand damp heat and thermal cycling. en. *Sustainable Energy & Fuels* **2,** 2398–2406. ISSN: 2398-4902. http://xlink.rsc.org/?DOI=C8SE00250A (2022) (2018).

124. Wilderspin, T. J., De Rossi, F. & Watson, T. M. A simple method to evaluate the effectiveness of encapsulation materials for perovskite solar cells. en. *Solar Energy* **139,** 426–432. ISSN: 0038092X. https://linkinghub.elsevier.com/retrieve/pii/S0038092X16304443 (2022) (Dec. 2016).

125. McKenna, B., Troughton, J. R., Watson, T. M. & Evans, R. C. Enhancing the stability of organolead halide perovskite films through polymer encapsulation. en. *RSC Advances* **7,** 32942–32951. ISSN: 2046-2069. http://xlink.rsc.org/?DOI=C7RA06002E (2022) (2017).

126. Jung, E. H. *et al.* Efficient, stable and scalable perovskite solar cells using poly(3-hexylthiophene). en. *Nature* **567,** 511–515. ISSN: 0028-0836, 1476-4687. http://www.nature.com/articles/s41586-019-1036-3 (2019) (Mar. 2019).

127. Shi, L. *et al.* Gas chromatography–mass spectrometry analyses of encapsulated stable perovskite solar cells. en. *Science* **368,** eaba2412. ISSN: 0036-8075, 1095-9203. https://www.science.org/doi/10.1126/science.aba2412 (2022) (June 2020).

128. Grancini, G. *et al.* One-Year stable perovskite solar cells by 2D/3D interface engineering. en. *Nature Communications* **8,** 15684. ISSN: 2041-1723. http://www.nature.com/articles/ncomms15684 (2022) (Aug. 2017).

129. Deng, Y. *et al.* Scalable fabrication of efficient organolead trihalide perovskite solar cells with doctor-bladed active layers. en. *Energy & Environmental Science* **8,** 1544–1550. ISSN: 1754-5692, 1754-5706. http://xlink.rsc.org/?DOI=C4EE03907F (2021) (2015).

130. Jiang, Y. *et al.* All electrospray printed perovskite solar cells. en. *Nano Energy* **53,** 440–448. ISSN: 22112855. https://linkinghub.elsevier.com/retrieve/pii/S2211285518306244 (2021) (Nov. 2018).

131. Rong, Y. *et al.* Toward Industrial-Scale Production of Perovskite Solar Cells: Screen Printing, Slot-Die Coating, and Emerging Techniques. en. *The Journal of Physical Chemistry Letters* **9,** 2707–2713. ISSN: 1948-7185, 1948-7185. https://pubs.acs.org/doi/10.1021/acs.jpclett.8b00912 (2021) (May 2018).

132. Whitaker, J. B. *et al.* Scalable slot-die coating of high performance perovskite solar cells. en. *Sustainable Energy & Fuels* **2,** 2442–2449. ISSN: 2398-4902. http://xlink.rsc.org/?DOI=C8SE00368H (2021) (2018).

133. Bernard, S. *et al.* One-Step Slot-Die Coating Deposition of Wide-Bandgap Perovskite Absorber for Highly Efficient Solar Cells. en. *Solar RRL* **5,** 2100391. ISSN: 2367-198X, 2367-198X. https://onlinelibrary.wiley.com/doi/10.1002/solr.202100391 (2021) (Sept. 2021).

134. Xu, F. *et al.* Potassium Thiocyanate-Assisted Enhancement of Slot-Die-Coated Perovskite Films for High-Performance Solar Cells. en. *Small Science* **1,** 2000044. ISSN: 2688-4046, 2688-4046. https://onlinelibrary.wiley.com/doi/10.1002/smsc.202000044 (2022) (May 2021).

135. Wu, W.-Q. *et al.* Reducing Surface Halide Deficiency for Efficient and Stable Iodide-Based Perovskite Solar Cells. en. *Journal of the American Chemical Society* **142,** 3989–3996. ISSN: 0002-7863, 1520-5126. https://pubs.acs.org/doi/10.1021/jacs.9b13418 (2022) (Feb. 2020).

136. Li, Z. *et al.* Scalable fabrication of perovskite solar cells. en. *Nature Reviews Materials* **3,** 18017. ISSN: 2058-8437. http://www.nature.com/articles/natrevmats201817 (2022) (Apr. 2018).

137. Zheng, Z.-H. *et al.* Single Source Thermal Evaporation of Two-dimensional Perovskite Thin Films for Photovoltaic Applications. en. *Scientific Reports* **9,** 17422. ISSN: 2045-2322. http://www.nature.com/articles/s41598-019-53609-0 (2022) (Dec. 2019).

138. Zhao, J. *et al.* Is Cu a stable electrode material in hybrid perovskite solar cells for a 30-year lifetime? en. *Energy & Environmental Science* **9,** 3650–3656. ISSN: 1754-5706. http://pubs.rsc.org/en/content/articlelanding/2016/ee/c6ee02980a (2018) (Nov. 2016).

139. Xiang, Y. *et al.* Progress on growth of metal halide perovskites by vapor-phase synthesis and their applications. *Journal of Physics D: Applied Physics* **55,** 073001. ISSN: 0022-3727, 1361-6463. https://iopscience.iop.org/article/10.1088/1361-6463/ac2e32 (2022) (Feb. 2022).

140. Pérez-del-Rey, D., Boix, P. P., Sessolo, M., Hadipour, A. & Bolink, H. J. Interfacial Modification for High-Efficiency Vapor-Phase-Deposited Perovskite Solar Cells Based on a Metal Oxide Buffer Layer. en. *The Journal of Physical Chemistry Letters* **9,** 1041–1046. ISSN: 1948-7185, 1948-7185. https://pubs.acs.org/doi/10.1021/acs.jpclett.7b03361 (2022) (Mar. 2018).

141. Bishop, J. E., Read, C. D., Smith, J. A., Routledge, T. J. & Lidzey, D. G. Fully Spray-Coated Triple-Cation Perovskite Solar Cells. en. *Scientific Reports* **10,** 6610. ISSN: 2045-2322. http://www.nature.com/articles/s41598-020-63674-5 (2022) (Dec. 2020).

142. Fan, P. *et al.* High-performance perovskite CH3NH3PbI3 thin films for solar cells prepared by single-source physical vapour deposition. en. *Scientific Reports* **6,** 29910. ISSN: 2045-2322. http://www.nature.com/articles/srep29910 (2022) (Sept. 2016).

143. Du, M. *et al.* High-Pressure Nitrogen-Extraction and Effective Passivation to Attain Highest Large-Area Perovskite Solar Module Efficiency. en. *Advanced Materials* **32,** 2004979. ISSN: 0935-9648, 1521-4095. https://onlinelibrary.wiley.com/doi/10.1002/adma.202004979 (2022) (Nov. 2020).

144. *Microquanta achieves 14.24% efficiency with large-area perovskite solar module* fr. https://www.pv-magazine.com/2019/10/24/microquanta-achieves-14-24-efficiency-with-large-area-perovskite-solar-module/%20((2022).

145. *China's perovskite solar module efficiency exceeds 20%, setting a new world record* http://utmolight.com/news/117030.html (2022).

146. Green, M. *et al.* Solar cell efficiency tables (version 57). en. *Progress in Photovoltaics: Research and Applications* **29,** 3–15. ISSN: 1062-7995, 1099-159X. https://onlinelibrary.wiley.com/doi/10.1002/pip.3371 (2021) (Jan. 2021).

147. Celik, I. *et al.* Environmental analysis of perovskites and other relevant solar cell technologies in a tandem configuration. en. *Energy & Environmental Science* **10,** 1874–1884. ISSN: 1754-5706. http://pubs.rsc.org/en/content/articlelanding/2017/ee/c7ee01650f (2018) (Sept. 2017).

148. Makha, M. *Utilisation de diverses électrodes conductrices et transparentes comme anode des cellules photovoltaïques organiques, optimisation de l'interface à l'aide des couches tampons* fr. PhD thesis (Université d'Angers, Apr. 2014). https://tel.archives-ouvertes.fr/tel-01511059/document (2018).

149. Connell, A. *et al.* Low cost triazatruxene hole transporting material for ¿20% efficiency perovskite solar cells. en. *Journal of Materials Chemistry C* **7,** 5235–5243. ISSN: 2050-7526, 2050-7534. http://xlink.rsc.org/?DOI=C8TC04231D (2022) (2019).

150. Murray, A. T. *et al.* Modular design of SPIRO-OMeTAD analogues as hole transport materials in solar cells. en. *Chemical Communications* **51,** 8935–8938. ISSN: 1359-7345, 1364-548X. http://xlink.rsc.org/?DOI=C5CC02129D (2022) (2015).

151. Hajikhanmirzaei, L. *et al.* A cost-device efficiency balanced spiro based hole transport material for perovskite solar cells. en. *Journal of Materials Chemistry C* **8,** 6221–6227. ISSN: 2050-7526, 2050-7534. http://xlink.rsc.org/?DOI=D0TC00196A (2022) (2020).

152. Lyu, M., Yun, J.-H., Chen, P., Hao, M. & Wang, L. Addressing Toxicity of Lead: Progress and Applications of Low-Toxic Metal Halide Perovskites and Their Derivatives. en. *Advanced Energy Materials* **7,** 1602512. ISSN: 1614-6832, 1614-6840. https://onlinelibrary.wiley.com/doi/10.1002/aenm.201602512 (2022) (Aug. 2017).

153. Shao, S. *et al.* Highly Reproducible Sn-Based Hybrid Perovskite Solar Cells with 9% Efficiency. en. *Advanced Energy Materials* **8,** 1702019. ISSN: 16146832. https://onlinelibrary.wiley.com/doi/10.1002/aenm.201702019 (2022) (Feb. 2018).

154. Chen, M. *et al.* Highly stable and efficient all-inorganic lead-free perovskite solar cells with native-oxide passivation. en. *Nature Communications* **10,** 16. ISSN: 2041-1723. http://www.nature.com/articles/s41467-018-07951-y (2022) (Dec. 2019).

155. Yun, A. J., Kim, J., Hwang, T. & Park, B. Origins of Efficient Perovskite Solar Cells with Low-Temperature Processed SnO $_2$ Electron Transport Layer. en. *ACS Applied Energy Materials* **2,** 3554–3560. ISSN: 2574-0962, 2574-0962. https://pubs.acs.org/doi/10.1021/acsaem.9b00293 (2022) (May 2019).

156. Jung, K.-H., Seo, J.-Y., Lee, S., Shin, H. & Park, N.-G. Solution-processed SnO $_2$ thin film for a hysteresis-free planar perovskite solar cell with a power conversion efficiency of 19.2%. en. *Journal of Materials Chemistry A* **5,** 24790–24803. ISSN: 2050-7488, 2050-7496. http://xlink.rsc.org/?DOI=C7TA08040A (2022) (2017).

157. Peng, J. *et al.* Efficient Indium-Doped TiOx Electron Transport Layers for High-Performance Perovskite Solar Cells and Perovskite-Silicon Tandems. en. *Advanced Energy Materials* **7.** ISSN: 1614-6840. https://onlinelibrary.wiley.com/doi/abs/10.1002/aenm.201601768 (2018) (Feb. 2017).

158. Akhil, S. *et al.* Review on perovskite silicon tandem solar cells: Status and prospects 2T, 3T and 4T for real world conditions. en. *Materials & Design* **211,** 110138. ISSN: 02641275. https://linkinghub.elsevier.com/retrieve/pii/S0264127521006936 (2022) (Dec. 2021).

159. Kim, J., Lee, Y., Yun, A. J., Gil, B. & Park, B. Interfacial Modification and Defect Passivation by the Cross-Linking Interlayer for Efficient and Stable CuSCN-Based Perovskite Solar Cells. en. *ACS Applied Materials & Interfaces* **11,** 46818–46824. ISSN: 1944-8244, 1944-8252. https://pubs.acs.org/doi/10.1021/acsami.9b16194 (2022) (Dec. 2019).

160. Gil, B. *et al.* Recent Progress in Inorganic Hole Transport Materials for Efficient and Stable Perovskite Solar Cells. en. *Electronic Materials Letters* **15,** 505–524. ISSN: 1738-8090, 2093-6788. http://link.springer.com/10.1007/s13391-019-00163-6 (2022) (Sept. 2019).

161. Ellmer, K. Past achievements and future challenges in the development of optically transparent electrodes. en. *Nature Photonics* **6,** 809–817. ISSN: 1749-4885, 1749-4893. http://www.nature.com/articles/nphoton.2012.282 (2022) (Dec. 2012).

162. Brandt, R. E., Stevanović, V., Ginley, D. S. & Buonassisi, T. Identifying defect-tolerant semiconductors with high minority-carrier lifetimes: beyond hybrid lead halide perovskites. en. *MRS Communications* **5,** 265–275. ISSN: 2159-6859, 2159-6867. https://www.cambridge.org/core/journals/mrs-communications/article/identifying-defecttolerant-semiconductors-with-high-minoritycarrier-lifetimes-beyond-hybrid-lead-halide-perovskites/602E81969F657F9F9D8CE0CB69AB6693 (2018) (June 2015).

163. Werner, J. *et al.* Sputtered rear electrode with broadband transparency for perovskite solar cells. *Solar Energy Materials and Solar Cells* **141,** 407–413. ISSN: 0927-0248. http://www.sciencedirect.com/science/article/pii/S0927024815002937 (2018) (Oct. 2015).

164. Kranz, L. *et al.* High-Efficiency Polycrystalline Thin Film Tandem Solar Cells. eng. *The Journal of Physical Chemistry Letters* **6,** 2676–2681. ISSN: 1948-7185 (July 2015).

165. Fu, W. *et al.* Controlled crystallization of CH3NH3PbI3 films for perovskite solar cells by various PbI2(X) complexes. en. *Solar Energy Materials and Solar Cells* **155,** 331–340. ISSN: 09270248. https://linkinghub.elsevier.com/retrieve/pii/S0927024816302112 (2021) (Oct. 2016).

166. Hossain, I. M. *et al.* Nanostructured front electrodes for perovskite/c-Si tandem photovoltaics. en. *Optics Express* **28,** 8878. ISSN: 1094-4087. https://www.osapublishing.org/abstract.cfm?URI=oe-28-6-8878 (2022) (Mar. 2020).

167. Werner, J. *et al.* Efficient Monolithic Perovskite/Silicon Tandem Solar Cell with Cell Area ¿1 cm(2). eng. *The Journal of Physical Chemistry Letters* **7,** 161–166. ISSN: 1948-7185 (Jan. 2016).

168. Barraud, L. *et al.* Hydrogen-doped indium oxide/indium tin oxide bilayers for high-efficiency silicon heterojunction solar cells. en. *Solar Energy Materials and Solar Cells* **115,** 151–156. ISSN: 09270248. http://linkinghub.elsevier.com/retrieve/pii/S0927024813001372 (2018) (Aug. 2013).

169. Aydin, E. *et al.* Zr-Doped Indium Oxide (IZRO) Transparent Electrodes for Perovskite-Based Tandem Solar Cells. en. *Advanced Functional Materials* **29,** 1901741. ISSN: 1616-301X, 1616-3028. https://onlinelibrary.wiley.com/doi/10.1002/adfm.201901741 (2022) (June 2019).

170. Kanda, H. *et al.* Effect of Silicon Surface for Perovskite/Silicon Tandem Solar Cells: Flat or Textured? en. *ACS Applied Materials & Interfaces* **10,** 35016–35024. ISSN: 1944-8244, 1944-8252. `https://pubs.acs.org/doi/10.1021/acsami.8b08701` (2022) (Oct. 2018).
171. Jacobs, D. A. *et al.* Light Management: A Key Concept in High-Efficiency Perovskite/Silicon Tandem Photovoltaics. en. *The Journal of Physical Chemistry Letters* **10,** 3159–3170. ISSN: 1948-7185, 1948-7185. `https://pubs.acs.org/doi/10.1021/acs.jpclett.8b03721` (2022) (June 2019).
172. Park, H. H. *et al.* Transparent Electrodes Consisting of a Surface-Treated Buffer Layer Based on Tungsten Oxide for Semitransparent Perovskite Solar Cells and Four-Terminal Tandem Applications. en. *Small Methods* **4,** 2000074. ISSN: 2366-9608, 2366-9608. `https://onlinelibrary.wiley.com/doi/10.1002/smtd.202000074` (2022) (May 2020).
173. Della Gaspera, E. *et al.* Ultra-thin high efficiency semitransparent perovskite solar cells. en. *Nano Energy* **13,** 249–257. ISSN: 22112855. `http://linkinghub.elsevier.com/retrieve/pii/S2211285515000877` (2018) (Apr. 2015).
174. Roldán-Carmona, C. *et al.* High efficiency single-junction semitransparent perovskite solar cells. en. *Energy & Environmental Science* **7,** 2968–2973. ISSN: 1754-5706. `http://pubs.rsc.org/en/content/articlelanding/2014/ee/c4ee01389a` (2018) (Aug. 2014).
175. Lu, H. *et al.* Inkjet printed silver nanowire network as top electrode for semi-transparent organic photovoltaic devices. en. *Applied Physics Letters* **106,** 093302. ISSN: 0003-6951, 1077-3118. `http://aip.scitation.org/doi/10.1063/1.4913697` (2022) (Mar. 2015).
176. Tohsophon, T., Dabirian, A., Wolf, S. D., Morales-Masis, M. & Ballif, C. Environmental stability of high-mobility indium-oxide based transparent electrodes. en. *APL Materials* **3,** 116105. `https://aip.scitation.org/doi/10.1063/1.4935125` (2018) (Nov. 2015).
177. Park, H. *et al.* Front and Back TCO Research Review of a-Si/c-Si Heterojunction with Intrinsic Thin Layer (HIT) Solar Cell. en. *Transactions on Electrical and Electronic Materials* **19,** 165–172. ISSN: 1229-7607, 2092-7592. `http://link.springer.com/10.1007/s42341-018-0026-8` (2022) (June 2018).
178. Nian, Q. *et al.* Highly transparent conductive electrode with ultra-low HAZE by grain boundary modification of aqueous solution fabricated alumina-doped zinc oxide nanocrystals. en. *APL Materials* **3,** 062803. ISSN: 2166-532X. `http://aip.scitation.org/doi/10.1063/1.4915489` (2022) (June 2015).
179. Yang, Y. M. *et al.* Multilayer Transparent Top Electrode for Solution Processed Perovskite/Cu(In,Ga)(Se,S)2 Four Terminal Tandem Solar Cells. eng. *ACS nano* **9,** 7714–7721. ISSN: 1936-086X (July 2015).
180. Kim, H., Kim, H.-S., Ha, J., Park, N.-G. & Yoo, S. Empowering Semi-Transparent Solar Cells with Thermal-Mirror Functionality. en. *Advanced Energy Materials* **6.** ISSN: 1614-6840. `https://onlinelibrary.wiley.com/doi/abs/10.1002/aenm.201502466` (2018) (July 2016).
181. Zhao, J. *et al.* Self-Encapsulating Thermostable and Air-Resilient Semitransparent Perovskite Solar Cells. en. *Advanced Energy Materials* **7,** 1602599. ISSN: 16146832. `https://onlinelibrary.wiley.com/doi/10.1002/aenm.201602599` (2022) (July 2017).
182. Laurans, G. *Electrode transparente en nanofils d'argent : intégration dans les cellules et modules photovoltaïques organiques sur substrat souple* fr. PhD thesis (Université de Bordeaux, June 2016). `https://tel.archives-ouvertes.fr/tel-01370552/document` (2018).
183. Yang, K., Li, F., Zhang, J., Veeramalai, C. P. & Guo, T. All-solution processed semi-transparent perovskite solar cells with silver nanowires electrode. *Nanotechnology* **27,** 095202. ISSN: 0957-4484, 1361-6528. `https://iopscience.iop.org/article/10.1088/0957-4484/27/9/095202` (2022) (Mar. 2016).
184. Jeon, I. *et al.* High-Performance Solution-Processed Double-Walled Carbon Nanotube Transparent Electrode for Perovskite Solar Cells. en. *Advanced Energy Materials* **9,** 1901204. ISSN: 1614-6832, 1614-6840. `https://onlinelibrary.wiley.com/doi/10.1002/aenm.201901204` (2022) (July 2019).
185. Guo, F. *et al.* High-performance semitransparent perovskite solar cells with solution-processed silver nanowires as top electrodes. eng. *Nanoscale* **7,** 1642–1649. ISSN: 2040-3372 (Feb. 2015).

186. Kato, Y. *et al.* Perovskite Solar Cells: Silver Iodide Formation in Methyl Ammonium Lead Iodide Perovskite Solar Cells with Silver Top Electrodes (Adv. Mater. Interfaces 13/2015). en. *Advanced Materials Interfaces* **2.** ISSN: 2196-7350. https://onlinelibrary.wiley.com/doi/abs/10.1002/admi.201570065 (2018) (Sept. 2015).

187. Fang, Y. *et al.* High-Performance Hazy Silver Nanowire Transparent Electrodes through Diameter Tailoring for Semitransparent Photovoltaics. en. *Advanced Functional Materials* **28.** ISSN: 1616-3028. https://onlinelibrary.wiley.com/doi/abs/10.1002/adfm.201705409 (2018) (Feb. 2018).

188. Lee, E. *et al.* All-Solution-Processed Silver Nanowire Window Electrode-Based Flexible Perovskite Solar Cells Enabled with Amorphous Metal Oxide Protection. en. *Advanced Energy Materials* **8.** ISSN: 1614-6840. https://onlinelibrary.wiley.com/doi/abs/10.1002/aenm.201702182 (2018) (Mar. 2018).

189. Lang, F. *et al.* Perovskite Solar Cells with Large-Area CVD-Graphene for Tandem Solar Cells. eng. *The Journal of Physical Chemistry Letters* **6,** 2745–2750. ISSN: 1948-7185 (July 2015).

190. You, P., Liu, Z., Tai, Q., Liu, S. & Yan, F. Efficient Semitransparent Perovskite Solar Cells with Graphene Electrodes. eng. *Advanced Materials (Deerfield Beach, Fla.)* **27,** 3632–3638. ISSN: 1521-4095 (June 2015).

191. Zhai, C.-H. *et al.* Effects of Al Doping on the Properties of ZnO Thin Films Deposited by Atomic Layer Deposition. *Nanoscale Research Letters* **11,** 407. ISSN: 1556-276X. https://doi.org/10.1186/s11671-016-1625-0 (2018) (Sept. 2016).

192. Shen, H. *et al.* Metal halide perovskite: a game-changer for photovoltaics and solar devices via a tandem design. en. *Science and Technology of Advanced Materials* **19,** 53–75. ISSN: 1468-6996, 1878-5514. https://www.tandfonline.com/doi/full/10.1080/14686996.2017.1422365 (2018) (Jan. 2018).

193. Tran, V.-D. *et al.* Transfer-free graphene electrodes for super-flexible and semi-transparent perovskite solar cells fabricated under ambient air. en. *Nano Energy* **65,** 104018. ISSN: 22112855. https://linkinghub.elsevier.com/retrieve/pii/S2211285519307256 (2022) (Nov. 2019).

194. Ball, J. M. *et al.* Optical properties and limiting photocurrent of thin-film perovskite solar cells. en. *Energy & Environmental Science* **8,** 602–609. ISSN: 1754-5706. http://pubs.rsc.org/en/content/articlelanding/2015/ee/c4ee03224a (2018) (Feb. 2015).

195. Jiang, Y. *et al.* Optical analysis of perovskite/silicon tandem solar cells. en. *Journal of Materials Chemistry C* **4,** 5679–5689. ISSN: 2050-7526, 2050-7534. http://xlink.rsc.org/?DOI=C6TC01276K (2018) (2016).

196. Werner, J. *et al.* Complex Refractive Indices of Cesium–Formamidinium-Based Mixed-Halide Perovskites with Optical Band Gaps from 1.5 to 1.8 eV. en. *ACS Energy Letters* **3,** 742–747. ISSN: 2380-8195, 2380-8195. https://pubs.acs.org/doi/10.1021/acsenergylett.8b00089 (2019) (Mar. 2018).

197. Manzoor, S. *et al.* Optical modeling of wide-bandgap perovskite and perovskite/silicon tandem solar cells using complex refractive indices for arbitrary-bandgap perovskite absorbers. en. *Optics Express* **26,** 27441. ISSN: 1094-4087. https://www.osapublishing.org/abstract.cfm?URI=oe-26-21-27441 (2018) (Oct. 2018).

198. Zhang, D. *et al.* High efficiency 4-terminal perovskite/c-Si tandem cells. en. *Solar Energy Materials and Solar Cells* **188,** 1–5. ISSN: 09270248. https://linkinghub.elsevier.com/retrieve/pii/S0927024818304033 (2018) (Dec. 2018).

199. Albrecht, S. *et al.* Monolithic perovskite/silicon-heterojunction tandem solar cells processed at low temperature. en. *Energy & Environmental Science* **9,** 81–88. ISSN: 1754-5706. http://pubs.rsc.org/en/content/articlelanding/2016/ee/c5ee02965a (2018) (Jan. 2016).

200. Zhang, W. *et al.* Highly conductive and transparent silver grid/metal oxide hybrid electrodes for low-temperature planar perovskite solar cells. en. *Journal of Power Sources* **337,** 118–124. ISSN: 03787753. https://linkinghub.elsevier.com/retrieve/pii/S0378775316315105 (2021) (Jan. 2017).

201. Anaya, M. *et al.* Electron injection and scaffold effects in perovskite solar cells. en. *Journal of Materials Chemistry C* **5,** 634–644. ISSN: 2050-7526, 2050-7534. http://xlink.rsc.org/?DOI=C6TC04639H (2018) (2017).

202. Ramírez Quiroz, C. O. *et al.* Coloring Semitransparent Perovskite Solar Cells *via* Dielectric Mirrors. en. *ACS Nano* **10,** 5104–5112. ISSN: 1936-0851, 1936-086X. http://pubs.acs.org/doi/10.1021/acsnano.6b00225 (2018) (May 2016).

203. Lin, A. *et al. The external light trapping for perovskite solar cells using nanoimprinted polymer metamaterial patterns* en. in (IEEE, June 2016), 0334–0337. ISBN: 978-1-5090-2724-8. http://ieeexplore.ieee.org/document/7749605/ (2018).

204. Mao, J. *et al.* Novel Direct Nanopatterning Approach to Fabricate Periodically Nanostructured Perovskite for Optoelectronic Applications. en. *Advanced Functional Materials* **27,** 1606525. ISSN: 1616301X. http://doi.wiley.com/10.1002/adfm.201606525 (2018) (Mar. 2017).

205. Saliba, M. *et al.* Structured Organic-Inorganic Perovskite toward a Distributed Feedback Laser. en. *Advanced Materials* **28,** 923–929. ISSN: 09359648. http://doi.wiley.com/10.1002/adma.201502608 (2018) (Feb. 2016).

206. Yin, J. *et al.* Light absorption enhancement by embedding submicron scattering TiO $_2$ nanoparticles in perovskite solar cells. en. *RSC Advances* **6,** 24596–24602. ISSN: 2046-2069. http://xlink.rsc.org/?DOI=C6RA01894G (2018) (2016).

207. Carretero-Palacios, S., Jiménez-Solano, A. & Míguez, H. Plasmonic Nanoparticles as Light-Harvesting Enhancers in Perovskite Solar Cells: A User's Guide. en. *ACS Energy Letters* **1,** 323–331. ISSN: 2380-8195, 2380-8195. http://pubs.acs.org/doi/10.1021/acsenergylett.6b00138 (2018) (July 2016).

208. Bush, K. A. *et al.* Thermal and Environmental Stability of Semi-Transparent Perovskite Solar Cells for Tandems Enabled by a Solution-Processed Nanoparticle Buffer Layer and Sputtered ITO Electrode. eng. *Advanced Materials (Deerfield Beach, Fla.)* **28,** 3937–3943. ISSN: 1521-4095 (2016).

209. Guchhait, A. *et al.* Over 20% Efficient CIGS–Perovskite Tandem Solar Cells. en. *ACS Energy Letters* **2,** 807–812. ISSN: 2380-8195, 2380-8195. http://pubs.acs.org/doi/10.1021/acsenergylett.7b00187 (2018) (Apr. 2017).

210. Jiang, Y., Green, M. A., Sheng, R. & Ho-Baillie, A. Optical modelling data for room temperature optical properties of organic–inorganic lead halide perovskites. *Data in Brief* **3,** 201–208. ISSN: 2352-3409. http://www.sciencedirect.com/science/article/pii/S2352340915000384 (2018) (June 2015).

211. Profijt, H. B., Potts, S. E., van de Sanden, M. C. M. & Kessels, W. M. M. Plasma-Assisted Atomic Layer Deposition: Basics, Opportunities, and Challenges. en. *Journal of Vacuum Science & Technology A: Vacuum, Surfaces, and Films* **29,** 050801. ISSN: 0734-2101, 1520-8559. http://avs.scitation.org/doi/10.1116/1.3609974 (2021) (Sept. 2011).

212. *Handbook of thin film materials* (ed Nalwa, H. S.) ISBN: 978-0-12-512908-4 978-0-12-512909-1 978-0-12-512910-7 978-0-12-512911-4 978-0-12-512912-1 978-0-12-512913-8 (Academic Press, San Diego, 2002).

213. Park, J.-S., Lee, M.-J., Lee, C.-S. & Kang, S.-W. Plasma-Enhanced Atomic Layer Deposition of Tantalum Nitrides Using Hydrogen Radicals as a Reducing Agent. en. *Electrochemical and Solid-State Letters* **4,** C17. ISSN: 10990062. https://iopscience.iop.org/article/10.1149/1.1353160 (2021) (2001).

214. Dai, S.-M. *et al.* Pristine fullerenes mixed by vacuum-free solution process: Efficient electron transport layer for planar perovskite solar cells. en. *Journal of Power Sources* **339,** 27–32. ISSN: 03787753. https://linkinghub.elsevier.com/retrieve/pii/S0378775316315737 (2021) (Jan. 2017).

215. Runa, A. *et al.* Highly reproducible perovskite solar cells based on solution coating from mixed solvents. en. *Journal of Materials Science* **53,** 3590–3602. ISSN: 0022-2461, 1573-4803. http://link.springer.com/10.1007/s10853-017-1842-7 (2021) (Mar. 2018).

216. Gujar, T. P. *et al.* The role of PbI $_2$ in CH $_3$ NH $_3$ PbI $_3$ perovskite stability, solar cell parameters and device degradation. en. *Physical Chemistry Chemical Physics* **20,** 605–614. ISSN: 1463-9076, 1463-9084. http://xlink.rsc.org/?DOI=C7CP04749E (2021) (2018).

217. Hu, Z. *et al.* Enhancing the Efficiency and Stability of Triple-Cation Perovskite Solar Cells by Eliminating Excess PbI $_2$ from the Perovskite/Hole Transport Layer Interface. en. *ACS Applied Materials & Interfaces* **12,** 54824–54832. ISSN: 1944-8244, 1944-8252. https://pubs.acs.org/doi/10.1021/acsami.0c17258 (2021) (Dec. 2020).

218. Chen, Y. *et al.* Mechanism of PbI $_2$ in Situ Passivated Perovskite Films for Enhancing the Performance of Perovskite Solar Cells. en. *ACS Applied Materials & Interfaces* **11,** 44101–44108. ISSN: 1944-8244, 1944-8252. https://pubs.acs.org/doi/10.1021/acsami.9b13648 (2021) (Nov. 2019).

219. *Nanoelectronics and Materials Development* en (ed Kar, A.) ISBN: 978-953-51-2525-9 978-953-51-2526-6. http://www.intechopen.com/books/nanoelectronics-and-materials-development (2022) (InTech, July 2016).

220. Yong, H. *Modeling of Perovskite Solar Cells, III-V Optoelectronic Devices and Kelvin Probe Microscopy* PhD thesis (INSA de Rennes, Mar. 2018).

221. Pitchaiya, S. *et al.* A review on the classification of organic/inorganic/carbonaceous hole transporting materials for perovskite solar cell application. en. *Arabian Journal of Chemistry* **13,** 2526–2557. ISSN: 18785352. https://linkinghub.elsevier.com/retrieve/pii/S1878535218301333 (2022) (Jan. 2020).

222. Elumalai, N. K. & Uddin, A. Hysteresis in organic-inorganic hybrid perovskite solar cells. *Solar Energy Materials and Solar Cells* **157,** 476–509. ISSN: 0927-0248. http://www.sciencedirect.com/science/article/pii/S0927024816301933 (2018) (Dec. 2016).

223. Dharmadasa, I. M., Rahaq, Y. & Alam, A. E. Perovskite solar cells: short lifetime and hysteresis behaviour of current–voltage characteristics. en. *Journal of Materials Science: Materials in Electronics* **30,** 12851–12859. ISSN: 0957-4522, 1573-482X. http://link.springer.com/10.1007/s10854-019-01759-2 (2021) (July 2019).

224. Shockley, W. & Queisser, H. J. Detailed Balance Limit of Efficiency of *p-n* Junction Solar Cells. en. *Journal of Applied Physics* **32,** 510–519. ISSN: 0021-8979, 1089-7550. http://aip.scitation.org/doi/10.1063/1.1736034 (2021) (Mar. 1961).

225. Stolterfoht, M. *et al.* Approaching the fill factor Shockley–Queisser limit in stable, dopant-free triple cation perovskite solar cells. en. *Energy & Environmental Science* **10,** 1530–1539. ISSN: 1754-5692, 1754-5706. http://xlink.rsc.org/?DOI=C7EE00899F (2021) (2017).

226. Wu, N. *et al.* Identifying the Cause of Voltage and Fill Factor Losses in Perovskite Solar Cells by Using Luminescence Measurements. en. *Energy Technology* **5,** 1827–1835. ISSN: 21944288. http://doi.wiley.com/10.1002/ente.201700374 (2021) (Oct. 2017).

227. Jäger, K.-D., Isabella, O., Smets, A. H., Swaaij, R. A. v. & Zeman, M. *Solar energy: fundamentals, technology and systems* English. OCLC: 1013815023. ISBN: 978-1-906860-73-8 978-1-906860-75-2 (UIT Cambridge, Cambridge, 2016).

228. Christians, J. A., Miranda Herrera, P. A. & Kamat, P. V. Transformation of the Excited State and Photovoltaic Efficiency of CH $_3$ NH $_3$ PbI $_3$ Perovskite upon Controlled Exposure to Humidified Air. en. *Journal of the American Chemical Society* **137,** 1530–1538. ISSN: 0002-7863, 1520-5126. https://pubs.acs.org/doi/10.1021/ja511132a (2021) (Feb. 2015).

229. Nie, W. *et al.* Light-activated photocurrent degradation and self-healing in perovskite solar cells. en. *Nature Communications* **7,** 11574. ISSN: 2041-1723. http://www.nature.com/articles/ncomms11574 (2021) (Sept. 2016).

230. Berhe, T. A. *et al.* Organometal halide perovskite solar cells: degradation and stability. en. *Energy & Environmental Science* **9,** 323–356. ISSN: 1754-5692, 1754-5706. http://xlink.rsc.org/?DOI=C5EE02733K (2021) (2016).

231. Tiep, N. H., Ku, Z. & Fan, H. J. Recent Advances in Improving the Stability of Perovskite Solar Cells. en. *Advanced Energy Materials* **6,** 1501420. ISSN: 16146832. https://onlinelibrary.wiley.com/doi/10.1002/aenm.201501420 (2021) (Feb. 2016).

232. Saliba, M. *et al.* Cesium-containing triple cation perovskite solar cells: improved stability, reproducibility and high efficiency. en. *Energy & Environmental Science* **9,** 1989–1997. ISSN: 1754-5692, 1754-5706. http://xlink.rsc.org/?DOI=C5EE03874J (2021) (2016).

233. Wang, C. *et al.* Low-Temperature Processed, Efficient, and Highly Reproducible Cesium-Doped Triple Cation Perovskite Planar Heterojunction Solar Cells. en. *Solar RRL* **2,** 1700209. ISSN: 2367-198X, 2367-198X. https://onlinelibrary.wiley.com/doi/10.1002/solr.201700209 (2021) (Feb. 2018).

234. Li, X. *et al.* Improved performance and stability of perovskite solar cells by crystal crosslinking with alkylphosphonic acid ω-ammonium chlorides. en. *Nature Chemistry* **7,** 703–711. ISSN: 1755-4330, 1755-4349. http://www.nature.com/articles/nchem.2324 (2021) (Sept. 2015).

235. Li, W. *et al.* Enhanced UV-light stability of planar heterojunction perovskite solar cells with caesium bromide interface modification. en. *Energy & Environmental Science* **9,** 490–498. ISSN: 1754-5692, 1754-5706. http://xlink.rsc.org/?DOI=C5EE03522H (2021) (2016).

236. You, J. *et al.* Improved air stability of perovskite solar cells via solution-processed metal oxide transport layers. en. *Nature Nanotechnology* **11,** 75–81. ISSN: 1748-3387, 1748-3395. http://www.nature.com/articles/nnano.2015.230 (2021) (Jan. 2016).

237. Zhang, F., Yang, X., Cheng, M., Wang, W. & Sun, L. Boosting the efficiency and the stability of low cost perovskite solar cells by using CuPc nanorods as hole transport material and carbon as counter electrode. en. *Nano Energy* **20,** 108–116. ISSN: 22112855. https://linkinghub.elsevier.com/retrieve/pii/S221128551500470X (2021) (Feb. 2016).

238. Kato, Y. *et al.* Silver Iodide Formation in Methyl Ammonium Lead Iodide Perovskite Solar Cells with Silver Top Electrodes. en. *Advanced Materials Interfaces* **2,** 1500195. ISSN: 2196-7350, 2196-7350. https://onlinelibrary.wiley.com/doi/10.1002/admi.201500195 (2021) (Sept. 2015).

239. Guerrero, A. *et al.* Interfacial Degradation of Planar Lead Halide Perovskite Solar Cells. en. *ACS Nano* **10,** 218–224. ISSN: 1936-0851, 1936-086X. https://pubs.acs.org/doi/10.1021/acsnano.5b03687 (2021) (Jan. 2016).

240. Wei, D. *et al.* Photo-induced degradation of lead halide perovskite solar cells caused by the hole transport layer/metal electrode interface. en. *Journal of Materials Chemistry A* **4,** 1991–1998. ISSN: 2050-7488, 2050-7496. http://xlink.rsc.org/?DOI=C5TA08622A (2021) (2016).

241. Zhang, H. *et al.* Pinhole-Free and Surface-Nanostructured NiO $_x$ Film by Room-Temperature Solution Process for High-Performance Flexible Perovskite Solar Cells with Good Stability and Reproducibility. en. *ACS Nano* **10,** 1503–1511. ISSN: 1936-0851, 1936-086X. https://pubs.acs.org/doi/10.1021/acsnano.5b07043 (2021) (Jan. 2016).

242. Misra, R. K. *et al.* Temperature- and Component-Dependent Degradation of Perovskite Photovoltaic Materials under Concentrated Sunlight. en. *The Journal of Physical Chemistry Letters* **6,** 326–330. ISSN: 1948-7185. https://pubs.acs.org/doi/10.1021/jz502642b (2021) (Feb. 2015).

243. Niu, G. *et al.* Study on the stability of CH $_3$ NH $_3$ PbI $_3$ films and the effect of post-modification by aluminum oxide in all-solid-state hybrid solar cells. en. *J. Mater. Chem. A* **2,** 705–710. ISSN: 2050-7488, 2050-7496. http://xlink.rsc.org/?DOI=C3TA13606J (2021) (2014).

244. De Castro, F. A., Heier, J., Nüesch, F. & Hany, R. Origin of the Kink in Current-Density Versus Voltage Curves and Efficiency Enhancement of Polymer-C $\_{\bf 60}$ Heterojunction Solar Cells. *IEEE Journal of Selected Topics in Quantum Electronics* **16,** 1690–1699. ISSN: 1077-260X, 1558-4542. http://ieeexplore.ieee.org/document/5416307/ (2021) (Nov. 2010).

245. Wagenpfahl, A., Rauh, D., Binder, M., Deibel, C. & Dyakonov, V. S-shaped current-voltage characteristics of organic solar devices. en. *Physical Review B* **82,** 115306. ISSN: 1098-0121, 1550-235X. https://link.aps.org/doi/10.1103/PhysRevB.82.115306 (2021) (Sept. 2010).

246. Domanski, K. *et al.* Not All That Glitters Is Gold: Metal-Migration-Induced Degradation in Perovskite Solar Cells. en. *ACS Nano* **10,** 6306–6314. ISSN: 1936-0851, 1936-086X. https://pubs.acs.org/doi/10.1021/acsnano.6b02613 (2021) (June 2016).

247. Matteocci, F. *et al.* Interface and Composition Analysis on Perovskite Solar Cells. en. *ACS Applied Materials & Interfaces* **7,** 26176–26183. ISSN: 1944-8244, 1944-8252. https://pubs.acs.org/doi/10.1021/acsami.5b08038 (2021) (Dec. 2015).

248. Kim, S. Y. & Lee, J.-L. Highly Reflective and Low-Resistant Ni/Au/ITO/Ag Ohmic Contact on p-Type GaN. en. *Electrochemical and Solid-State Letters* **7,** G102. ISSN: 10990062. https://iopscience.iop.org/article/10.1149/1.1676115 (2021) (2004).

249. Paine, D. C. *et al.* A study of low temperature crystallization of amorphous thin film indium–tin–oxide. en. *Journal of Applied Physics* **85,** 8445–8450. ISSN: 0021-8979, 1089-7550. http://aip.scitation.org/doi/10.1063/1.370695 (2021) (June 1999).

250. Shigesato, Y. & Paine, D. C. Study of the effect of Sn doping on the electronic transport properties of thin film indium oxide. en. *Applied Physics Letters* **62,** 1268–1270. ISSN: 0003-6951, 1077-3118. http://aip.scitation.org/doi/10.1063/1.108703 (2021) (Mar. 1993).

251. Shigesato, Y., Koshi-ishi, R., Kawashima, T. & Ohsako, J. Early stages of ITO deposition on glass or polymer substrates. en. *Vacuum* **59,** 614–621. ISSN: 0042207X. https://linkinghub.elsevier.com/retrieve/pii/S0042207X00003249 (2021) (Nov. 2000).

252. Yeom, H.-Y., Popovich, N., Chason, E. & Paine, D. C. A study of the effect of process oxygen on stress evolution in d.c. magnetron-deposited tin-doped indium oxide. en. *Thin Solid Films* **411,** 17–22. ISSN: 00406090. https://linkinghub.elsevier.com/retrieve/pii/S0040609002001669 (2021) (May 2002).

253. Wong, F., Fung, M., Tong, S., Lee, C. & Lee, S. Flexible organic light-emitting device based on magnetron sputtered indium-tin-oxide on plastic substrate. en. *Thin Solid Films* **466,** 225–230. ISSN: 00406090. https://linkinghub.elsevier.com/retrieve/pii/S0040609004002160 (2021) (Nov. 2004).

254. Park, J. O., Lee, J. H., Kim, J. J. & Cho, S.-H. Observation of Crystallization Behavior in ITO Thin Films Prepared by RF-Magnetron Sputtering with and without External Heating. *Materials Science Forum* **449-452,** 481–484. ISSN: 1662-9752. https://www.scientific.net/MSF.449-452.481 (2020) (Mar. 2004).

255. Vink, T., Walrave, W., Daams, J., Baarslag, P. & van den Meerakker, J. On the homogeneity of sputter-deposited ITO films Part I. Stress and microstructure. en. *Thin Solid Films* **266,** 145–151. ISSN: 00406090. https://linkinghub.elsevier.com/retrieve/pii/004060909506818X (2020) (Oct. 1995).

256. Bhagwat, S. & Howson, R. Use of the magnetron-sputtering technique for the control of the properties of indium tin oxide thin films. en. *Surface and Coatings Technology* **111,** 163–171. ISSN: 02578972. https://linkinghub.elsevier.com/retrieve/pii/S0257897298007270 (2020) (Jan. 1999).

257. Raiford, J. A. *et al.* Atomic layer deposition of vanadium oxide to reduce parasitic absorption and improve stability in n–i–p perovskite solar cells for tandems. en. *Sustainable Energy & Fuels* **3,** 1517–1525. ISSN: 2398-4902. http://xlink.rsc.org/?DOI=C9SE00081J (2021) (2019).

258. Tepliakova, M. M. *et al.* Incorporation of Vanadium(V) Oxide in Hybrid Hole Transport Layer Enables Long-term Operational Stability of Perovskite Solar Cells. en. *The Journal of Physical Chemistry Letters* **11,** 5563–5568. ISSN: 1948-7185, 1948-7185. https://pubs.acs.org/doi/10.1021/acs.jpclett.0c01600 (2021) (July 2020).

259. Lee, M., Jo, Y., Kim, D. S., Jeong, H. Y. & Jun, Y. Efficient, durable and flexible perovskite photovoltaic devices with Ag-embedded ITO as the top electrode on a metal substrate. en. *Journal of Materials Chemistry A* **3,** 14592–14597. ISSN: 2050-7488, 2050-7496. http://xlink.rsc.org/?DOI=C5TA03240G (2019) (2015).

260. Liang, J.-J. *et al.* Detrimental effect of silver doping in spiro-MeOTAD on the device performance of perovskite solar cells. en. *Organic Electronics* **69,** 343–347. ISSN: 15661199. https://linkinghub.elsevier.com/retrieve/pii/S1566119919301454 (2021) (June 2019).

261. Seo, S. *et al.* Amorphous TiO_2 Coatings Stabilize Perovskite Solar Cells. en. *ACS Energy Letters* **6,** 3332–3341. ISSN: 2380-8195, 2380-8195. https://pubs.acs.org/doi/10.1021/acsenergylett.1c01446 (2021) (Sept. 2021).

262. Jiang, Q., Sheng, X., Shi, B., Feng, X. & Xu, T. Nickel-Cathoded Perovskite Solar Cells. en. *The Journal of Physical Chemistry C* **118,** 25878–25883. ISSN: 1932-7447, 1932-7455. https://pubs.acs.org/doi/10.1021/jp506991x (2021) (Nov. 2014).

263. Wang, K.-C. *et al.* Low-Temperature Sputtered Nickel Oxide Compact Thin Film as Effective Electron Blocking Layer for Mesoscopic NiO/$CH_3NH_3PbI_3$ Perovskite Heterojunction Solar Cells. en. *ACS Applied Materials & Interfaces* **6,** 11851–11858. ISSN: 1944-8244, 1944-8252. https://pubs.acs.org/doi/10.1021/am503610u (2021) (Aug. 2014).

264. Jeng, J.-Y. *et al.* Nickel Oxide Electrode Interlayer in $CH_3NH_3PbI_3$ Perovskite/PCBM Planar-Heterojunction Hybrid Solar Cells. en. *Advanced Materials* **26,** 4107–4113. ISSN: 09359648. https://onlinelibrary.wiley.com/doi/10.1002/adma.201306217 (2021) (June 2014).

265. Liu, Z. *et al.* Nickel oxide nanoparticles for efficient hole transport in p-i-n and n-i-p perovskite solar cells. en. *Journal of Materials Chemistry A* **5,** 6597–6605. ISSN: 2050-7488, 2050-7496. http://xlink.rsc.org/?DOI=C7TA01593C (2021) (2017).

266. Van Eerden, M. *et al.* Optical Analysis of Planar Multicrystalline Perovskite Solar Cells. en. *Advanced Optical Materials* **5,** 1700151. ISSN: 21951071. http://doi.wiley.com/10.1002/adom.201700151 (2018) (Sept. 2017).

267. Jiang, Y., Green, M. A., Sheng, R. & Ho-Baillie, A. Room temperature optical properties of organic–inorganic lead halide perovskites. *Solar Energy Materials and Solar Cells* **137,** 253–257. ISSN: 0927-0248. http://www.sciencedirect.com/science/article/pii/S0927024815000781 (2018) (June 2015).

268. Burkhard, G. F., Hoke, E. T. & McGehee, M. D. Accounting for Interference, Scattering, and Electrode Absorption to Make Accurate Internal Quantum Efficiency Measurements in Organic and Other Thin Solar Cells. *Advanced Materials* **22,** 3293–3297. ISSN: 1521-4095. https://onlinelibrary.wiley.com/doi/abs/10.1002/adma.201000883 (2018) (2010).

269. Cauchy, A.-L. Sur la réfraction et la réflexion de la lumière. *Bulletin de Férussac,* 9 (1830).

270. Atchison, D. A. & Smith, G. Chromatic dispersions of the ocular media of human eyes. en. *Journal of the Optical Society of America A* **22,** 29. ISSN: 1084-7529, 1520-8532. https://www.osapublishing.org/abstract.cfm?URI=josaa-22-1-29 (2021) (Jan. 2005).

271. Rubin, M. Optical properties of soda lime silica glasses. en. *Solar Energy Materials* **12,** 275–288. ISSN: 01651633. https://linkinghub.elsevier.com/retrieve/pii/0165163385900528 (2019) (Sept. 1985).

272. Herzberger, M. The Dispersion of Optical Glass*. en. *Journal of the Optical Society of America* **32,** 70. ISSN: 0030-3941. https://www.osapublishing.org/abstract.cfm?URI=josa-32-2-70 (2019) (Feb. 1942).

273. Troparevsky, M. C., Sabau, A. S., Lupini, A. R. & Zhang, Z. Transfer-matrix formalism for the calculation of optical response in multilayer systems: from coherent to incoherent interference. en. *Optics Express* **18,** 24715. ISSN: 1094-4087. https://www.osapublishing.org/oe/abstract.cfm?uri=oe-18-24-24715 (2019) (Nov. 2010).

274. Chung, K. H. & Sturm, J. C. Chlorine Etching for In-Situ Low-Temperature Silicon Surface Cleaning for Epitaxy Applications. *ECS Transactions* **6,** 401–407. ISSN: 1938-6737. https://iopscience.iop.org/article/10.1149/1.2727426 (2021) (Dec. 2019).

275. Diana, T., Nomita Devi, K. & Nandakumar Sarma, H. On the optical properties of SnO2 thin films prepared by sol-gel method. en. *Indian Journal of Physics* **84,** 687–691. ISSN: 0019-5480, 0974-9845. http://link.springer.com/10.1007/s12648-010-0072-5 (2019) (June 2010).

276. Synowicki, R. & Tiwald, T. E. Optical properties of bulk c-ZrO2, c-MgO and a-As2S3 determined by variable angle spectroscopic ellipsometry. en. *Thin Solid Films* **455-456,** 248–255. ISSN: 00406090. https://linkinghub.elsevier.com/retrieve/pii/S0040609004002366 (2021) (May 2004).

277. Nosidlak, N., Dulian, P., Mierzwiński, D. & Jaglarz, J. The Determination of the Electronic Parameters of Thin Amorphous Organic Films by Ellipsometric and Spectrophotometric Study. en. *Coatings* **10,** 980. ISSN: 2079-6412. https://www.mdpi.com/2079-6412/10/10/980 (2021) (Oct. 2020).

278. Forouhi, A. R. & Bloomer, I. Optical dispersion relations for amorphous semiconductors and amorphous dielectrics. en. *Physical Review B* **34,** 7018–7026. ISSN: 0163-1829. https://link.aps.org/doi/10.1103/PhysRevB.34.7018 (2019) (Nov. 1986).

279. Forouhi, A. R. & Bloomer, I. Optical properties of crystalline semiconductors and dielectrics. en. *Physical Review B* **38,** 1865–1874. ISSN: 0163-1829. https://link.aps.org/doi/10.1103/PhysRevB.38.1865 (2019) (July 1988).

280. Miranda, C., Antonelli, A., da Silva, A. & Fazzio, A. Vacancy-like defects in a-Si: a first principles study. en. *Journal of Non-Crystalline Solids* **338-340,** 400–402. ISSN: 00223093. https://linkinghub.elsevier.com/retrieve/pii/S0022309304001619 (2019) (June 2004).

281. Laidani, N., Bartali, R., Gottardi, G., Anderle, M. & Cheyssac, P. Optical absorption parameters of amorphous carbon films from Forouhi–Bloomer and Tauc–Lorentz models: a comparative study. *Journal of Physics: Condensed Matter* **20,** 015216. ISSN: 0953-8984, 1361-648X. http://stacks.iop.org/0953-8984/20/i=1/a=015216?key=crossref.f1b6acef7b4298d0fec8b70b05681745 (2019) (Jan. 2008).

282. Connell, G. A. N. in *Amorphous Semiconductors* (ed Brodsky, M. H.) 73–111 (Springer Berlin Heidelberg, Berlin, Heidelberg, 1979). ISBN: 978-3-540-16008-3 978-3-540-70751-6. http://link.springer.com/10.1007/3-540-16008-6_158 (2019).

283. Jellison, G. E. & Modine, F. A. Parameterization of the optical functions of amorphous materials in the interband region. en. *Applied Physics Letters* **69,** 371–373. ISSN: 0003-6951, 1077-3118. http://aip.scitation.org/doi/10.1063/1.118064 (2019) (July 1996).

284. Xing, G. *et al.* Long-Range Balanced Electron- and Hole-Transport Lengths in Organic-Inorganic CH3NH3PbI3. en. *Science* **342,** 344–347. ISSN: 0036-8075, 1095-9203. https://www.sciencemag.org/lookup/doi/10.1126/science.1243167 (2021) (Oct. 2013).

285. Li, H. *et al.* A review of characterization of perovskite film in solar cells by spectroscopic ellipsometry. en. *Solar Energy* **212,** 48–61. ISSN: 0038092X. https://linkinghub.elsevier.com/retrieve/pii/S0038092X20311257 (2021) (Dec. 2020).

286. Bailey, C. G., Piana, G. M. & Lagoudakis, P. G. High-Energy Optical Transitions and Optical Constants of CH $_3$ NH $_3$ PbI $_3$ Measured by Spectroscopic Ellipsometry and Spectrophotometry. en. *The Journal of Physical Chemistry C* **123,** 28795–28801. ISSN: 1932-7447, 1932-7455. https://pubs.acs.org/doi/10.1021/acs.jpcc.9b08903 (2021) (Nov. 2019).

287. Xie, Z. *et al.* Refractive index and extinction coefficient of NH $_2$ CH = NH $_2$ PbI $_3$ perovskite photovoltaic material. *Journal of Physics: Condensed Matter* **29,** 245702. ISSN: 0953-8984, 1361-648X. https://iopscience.iop.org/article/10.1088/1361-648X/aa6e6c (2021) (June 2017).

288. Szczyrbowski, J. Determination of optical constants of real thin films. *Journal of Physics D: Applied Physics* **11,** 583–593. ISSN: 00223727. https://iopscience.iop.org/article/10.1088/0022-3727/11/4/021 (2021) (Mar. 1978).

289. Yin, G., Merschjann, C. & Schmid, M. The effect of surface roughness on the determination of optical constants of CuInSe $_2$ and CuGaSe $_2$ thin films. en. *Journal of Applied Physics* **113,** 213510. ISSN: 0021-8979, 1089-7550. http://aip.scitation.org/doi/10.1063/1.4809550 (2019) (June 2013).

290. *Handbook of optical constants of solids II* (ed Palik, E. D.) ISBN: 978-0-12-544422-4 (Academic Press, Boston, 1991).

291. Filipič, M. *et al.* CH_3NH_3PbI_3 perovskite / silicon tandem solar cells: characterization based optical simulations. en. *Optics Express* **23,** A263. ISSN: 1094-4087. https://www.osapublishing.org/abstract.cfm?URI=oe-23-7-A263 (2018) (Apr. 2015).

292. Holman, Z. C. *et al.* Infrared light management in high-efficiency silicon heterojunction and rear-passivated solar cells. en. *Journal of Applied Physics* **113,** 013107. ISSN: 0021-8979, 1089-7550. http://aip.scitation.org/doi/10.1063/1.4772975 (2019) (Jan. 2013).

293. Flat, A. & Milnes, A. Optimization of multi-layer front-contact grid patterns for solar cells. en. *Solar Energy* **23,** 289–299. ISSN: 0038092X. https://linkinghub.elsevier.com/retrieve/pii/0038092X79901221 (2020) (1979).

294. Sargent, E. H. Colloidal quantum dot solar cells. en. *Nature Photonics* **6,** 133–135. ISSN: 1749-4885, 1749-4893. http://www.nature.com/articles/nphoton.2012.33 (2020) (Mar. 2012).

295. Graetzel, M., Janssen, R. A. J., Mitzi, D. B. & Sargent, E. H. Materials interface engineering for solution-processed photovoltaics. en. *Nature* **488,** 304–312. ISSN: 0028-0836, 1476-4687. http://www.nature.com/articles/nature11476 (2020) (Aug. 2012).

296. Kirchartz, T., Deledalle, F., Tuladhar, P. S., Durrant, J. R. & Nelson, J. On the Differences between Dark and Light Ideality Factor in Polymer:Fullerene Solar Cells. en. *The Journal of Physical Chemistry Letters* **4,** 2371–2376. ISSN: 1948-7185, 1948-7185. https://pubs.acs.org/doi/10.1021/jz4012146 (2021) (July 2013).

297. Kumar, R. *et al.* Unveiling the Morphology Effect on the Negative Capacitance and Large Ideality Factor in Perovskite Light-Emitting Diodes. en. *ACS Applied Materials & Interfaces* **12,** 34265–34273. ISSN: 1944-8244, 1944-8252. https://pubs.acs.org/doi/10.1021/acsami.0c04489 (2021) (July 2020).

298. Sattler, K. D. *Handbook of Nanophysics.* English. OCLC: 691080636. ISBN: 978-1-4200-7541-0. http://public.ebookcentral.proquest.com/choice/publicfullrecord.aspx?p=581721 (2020) (CRC Press, Hoboken, 2010).

299. Sowade, E. *et al.* Roll-to-roll infrared (IR) drying and sintering of an inkjet-printed silver nanoparticle ink within 1 second. en. *Journal of Materials Chemistry C* **3,** 11815–11826. ISSN: 2050-7526, 2050-7534. http://xlink.rsc.org/?DOI=C5TC02291F (2020) (2015).

300. Ren, Z. *et al.* Strategies for high performance perovskite/crystalline silicon four-terminal tandem solar cells. *Solar Energy Materials and Solar Cells* **179,** 36–44. ISSN: 0927-0248. http://www.sciencedirect.com/science/article/pii/S0927024818300047 (2018) (June 2018).

301. Wilken, K. *et al.* Nanoimprint texturing of transparent flexible substrates for improved light management in thin-film solar cells: Nanoimprint texturing of transparent flexible substrates for improved light management in thin-film solar cells. en. *physica status solidi (RRL) - Rapid Research Letters* **9,** 215–219. ISSN: 18626254. http://doi.wiley.com/10.1002/pssr.201510040 (2018) (Apr. 2015).

302. Ulbrich, C., Gerber, A., Hermans, K., Lambertz, A. & Rau, U. Strategies for high performance perovskite/crystalline silicon. en. *Progress in Photovoltaics: Research and Applications* **21,** 1672–1681. ISSN: 10627995. http://doi.wiley.com/10.1002/pip.2249 (2018) (Dec. 2013).

303. Li, H. H. Refractive index of alkali halides and its wavelength and temperature derivatives. en. *Journal of Physical and Chemical Reference Data* **5,** 329–528. ISSN: 0047-2689, 1529-7845. http://aip.scitation.org/doi/10.1063/1.555536 (2021) (Apr. 1976).

304. Essig, S. *et al.* Realization of GaInP/Si Dual-Junction Solar Cells With 29.8% 1-Sun Efficiency. en. *IEEE Journal of Photovoltaics* **6,** 1012–1019. ISSN: 2156-3381, 2156-3403. http://ieeexplore.ieee.org/document/7460224/ (2018) (July 2016).

305. Keller, J. *et al.* Direct comparison of atomic layer deposition and sputtering of In2O3:H used as transparent conductive oxide layer in CuIn1xGaxSe2 thin film solar cells. en. *Solar Energy Materials and Solar Cells* **157,** 757–764. ISSN: 09270248. https://linkinghub.elsevier.com/retrieve/pii/S0927024816302392 (2021) (Dec. 2016).

306. Fu, F. *et al.* Low-temperature-processed efficient semi-transparent planar perovskite solar cells for bifacial and tandem applications. en. *Nature Communications* **6.** ISSN: 2041-1723. http://www.nature.com/articles/ncomms9932 (2018) (Dec. 2015).

307. Wahl, T., Hanisch, J., Meier, S., Schultes, M. & Ahlswede, E. Sputtered indium zinc oxide rear electrodes for inverted semitransparent perovskite solar cells without using a protective buffer layer. en. *Organic Electronics* **54,** 48–53. ISSN: 15661199. http://linkinghub.elsevier.com/retrieve/pii/S156611991730616X (2018) (Mar. 2018).

308. Jeon, N. J. *et al.* o-Methoxy Substituents in Spiro-OMeTAD for Efficient Inorganic–Organic Hybrid Perovskite Solar Cells. en. *Journal of the American Chemical Society* **136,** 7837–7840. ISSN: 0002-7863, 1520-5126. https://pubs.acs.org/doi/10.1021/ja502824c (2021) (June 2014).

309. Ren, X. *et al.* Chlorine-modified SnO $_2$ electron transport layer for high-efficiency perovskite solar cells. en. *InfoMat* **2,** 401–408. ISSN: 2567-3165, 2567-3165. https://onlinelibrary.wiley.com/doi/10.1002/inf2.12059 (2021) (Mar. 2020).

310. Xiong, Z. *et al.* Multifunctional Polymer Framework Modified SnO $_2$ Enabling a Photostable α-FAPbI $_3$ Perovskite Solar Cell with Efficiency Exceeding 23%. en. *ACS Energy Letters* **6,** 3824–3830. ISSN: 2380-8195, 2380-8195. https://pubs.acs.org/doi/10.1021/acsenergylett.1c01763 (2021) (Nov. 2021).

311. Miandal, K., Tak, H. H., Mohamad, K. A., Chee, F. P. & Alias, A. The Structural and Optical Properties of Poly(Triarylamine) (PTAA) Thin Films Prepared at Different Spin Rate Using Spin Coating Method. en. *Advanced Science Letters* **23,** 1337–1339. ISSN: 1936-6612. http://www.ingentaconnect.com/content/10.1166/asl.2017.8363 (2021) (Feb. 2017).

312. Jeong, J. *et al.* Ternary Halide Perovskites for Highly Efficient Solution-Processed Hybrid Solar Cells. en. *ACS Energy Letters* **1,** 712–718. ISSN: 2380-8195, 2380-8195. https://pubs.acs.org/doi/10.1021/acsenergylett.6b00281 (2020) (Oct. 2016).

313. Xiao, Z. *et al.* Solvent Annealing of Perovskite-Induced Crystal Growth for Photovoltaic-Device Efficiency Enhancement. en. *Advanced Materials* **26,** 6503–6509. ISSN: 09359648. http://doi.wiley.com/10.1002/adma.201401685 (2020) (Oct. 2014).

314. Yuan, Z. *et al.* Approximately 800-nm-Thick Pinhole-Free Perovskite Films via Facile Solvent Retarding Process for Efficient Planar Solar Cells. en. *ACS Applied Materials & Interfaces* **8,** 34446–34454. ISSN: 1944-8244, 1944-8252. https://pubs.acs.org/doi/10.1021/acsami.6b12637 (2020) (Dec. 2016).

315. Adhyaksa, G. W. P. *et al.* Carrier Diffusion Lengths in Hybrid Perovskites: Processing, Composition, Aging, and Surface Passivation Effects. en. *Chemistry of Materials* **28,** 5259–5263. ISSN: 0897-4756, 1520-5002. https://pubs.acs.org/doi/10.1021/acs.chemmater.6b00466 (2020) (Aug. 2016).

316. Wang, K. *et al.* Efficiencies of perovskite hybrid solar cells influenced by film thickness and morphology of CH3NH3PbI3xClx layer. en. *Organic Electronics* **21,** 19–26. ISSN: 15661199. https://linkinghub.elsevier.com/retrieve/pii/S1566119915000804 (2020) (June 2015).

317. Rehman, W. *et al.* Charge-Carrier Dynamics and Mobilities in Formamidinium Lead Mixed-Halide Perovskites. en. *Advanced Materials* **27,** 7938–7944. ISSN: 09359648. http://doi.wiley.com/10.1002/adma.201502969 (2020) (Dec. 2015).

318. Chen, J. *et al.* High-Performance Thickness Insensitive Perovskite Solar Cells with Enhanced Moisture Stability. en. *Advanced Energy Materials* **8,** 1800438. ISSN: 16146832. http://doi.wiley.com/10.1002/aenm.201800438 (2020) (Aug. 2018).

319. Green, M. A. *et al.* Solar cell efficiency tables (Version 55). en. *Progress in Photovoltaics: Research and Applications* **28,** 3–15. ISSN: 1062-7995, 1099-159X. https://onlinelibrary.wiley.com/doi/abs/10.1002/pip.3228 (2020) (Jan. 2020).

320. Yoshikawa, K. *et al.* Silicon heterojunction solar cell with interdigitated back contacts for a photoconversion efficiency over 26%. en. *Nature Energy* **2.** ISSN: 2058-7546. http://www.nature.com/articles/nenergy201732 (2019) (May 2017).

321. Shariatinia, Z. Recent progress in development of diverse kinds of hole transport materials for the perovskite solar cells: A review. en. *Renewable and Sustainable Energy Reviews* **119,** 109608. ISSN: 13640321. https://linkinghub.elsevier.com/retrieve/pii/S1364032119308160 (2020) (Mar. 2020).

322. Yang, W. S. *et al.* High-performance photovoltaic perovskite layers fabricated through intramolecular exchange. en. *Science* **348,** 1234–1237. ISSN: 0036-8075, 1095-9203. https://www.science.org/doi/10.1126/science.aaa9272 (2021) (June 2015).

323. Wali, Q., Iqbal, Y., Pal, B., Lowe, A. & Jose, R. Tin oxide as an emerging electron transport medium in perovskite solar cells. en. *Solar Energy Materials and Solar Cells* **179,** 102–117. ISSN: 09270248. https://linkinghub.elsevier.com/retrieve/pii/S0927024818300588 (2021) (June 2018).

324. Ke, W. *et al.* Low-Temperature Solution-Processed Tin Oxide as an Alternative Electron Transporting Layer for Efficient Perovskite Solar Cells. en. *Journal of the American Chemical Society* **137,** 6730–6733. ISSN: 0002-7863, 1520-5126. https://pubs.acs.org/doi/10.1021/jacs.5b01994 (2021) (June 2015).

325. Xiong, L. *et al.* Review on the Application of SnO $_2$ in Perovskite Solar Cells. en. *Advanced Functional Materials* **28,** 1802757. ISSN: 1616301X. https://onlinelibrary.wiley.com/doi/10.1002/adfm.201802757 (2021) (Aug. 2018).

326. Kim, G.-W. *et al.* Hole Transport Materials in Conventional Structural (n–i–p) Perovskite Solar Cells: From Past to the Future. en. *Advanced Energy Materials* **10,** 1903403. ISSN: 1614-6832, 1614-6840. https://onlinelibrary.wiley.com/doi/10.1002/aenm.201903403 (2021) (Feb. 2020).

327. Zhao, Q. *et al.* Achieving efficient inverted planar perovskite solar cells with nondoped PTAA as a hole transport layer. en. *Organic Electronics* **71,** 106–112. ISSN: 15661199. https://linkinghub.elsevier.com/retrieve/pii/S1566119919302472 (2021) (Aug. 2019).

328. Heo, J. H. *et al.* Efficient inorganic–organic hybrid heterojunction solar cells containing perovskite compound and polymeric hole conductors. en. *Nature Photonics* **7,** 486–491. ISSN: 1749-4885, 1749-4893. http://www.nature.com/articles/nphoton.2013.80 (2021) (June 2013).

329. Spalla, M. *et al.* Effect of the Hole Transporting/Active Layer Interface on the Perovskite Solar Cell Stability. en. *ACS Applied Energy Materials* **3,** 3282–3292. ISSN: 2574-0962, 2574-0962. https://pubs.acs.org/doi/10.1021/acsaem.9b02281 (2022) (Apr. 2020).

330. Rombach, F. M., Haque, S. A. & Macdonald, T. J. Lessons learned from spiro-OMeTAD and PTAA in perovskite solar cells. en. *Energy & Environmental Science* **14,** 5161–5190. ISSN: 1754-5692, 1754-5706. http://xlink.rsc.org/?DOI=D1EE02095A (2021) (2021).

331. Ko, Y., Kim, Y., Lee, C., Kim, Y. & Jun, Y. Investigation of Hole-Transporting Poly(triarylamine) on Aggregation and Charge Transport for Hysteresisless Scalable Planar Perovskite Solar Cells. en. *ACS Applied Materials & Interfaces* **10,** 11633–11641. ISSN: 1944-8244, 1944-8252. https://pubs.acs.org/doi/10.1021/acsami.7b18745 (2021) (Apr. 2018).

332. Kim, J. *et al.* An effective method of predicting perovskite solar cell lifetime–Case study on planar CH 3 NH 3 PbI 3 and HC(NH 2) 2 PbI 3 perovskite solar cells and hole transfer materials of spiro-OMeTAD and PTAA. en. *Solar Energy Materials and Solar Cells* **162,** 41–46. ISSN: 09270248. https://linkinghub.elsevier.com/retrieve/pii/S0927024816305645 (2021) (Apr. 2017).

333. Sha, W. E. I., Ren, X., Chen, L. & Choy, W. C. H. The efficiency limit of CH $_3$ NH $_3$ PbI $_3$ perovskite solar cells. en. *Applied Physics Letters* **106,** 221104. ISSN: 0003-6951, 1077-3118. http://aip.scitation.org/doi/10.1063/1.4922150 (2021) (June 2015).

334. Wang, S. *et al.* Role of 4- *tert* -Butylpyridine as a Hole Transport Layer Morphological Controller in Perovskite Solar Cells. en. *Nano Letters* **16,** 5594–5600. ISSN: 1530-6984, 1530-6992. https://pubs.acs.org/doi/10.1021/acs.nanolett.6b02158 (2021) (Sept. 2016).

335. Juarez-Perez, E. J. *et al.* Role of the Dopants on the Morphological and Transport Properties of Spiro-MeOTAD Hole Transport Layer. en. *Chemistry of Materials* **28,** 5702–5709. ISSN: 0897-4756, 1520-5002. https://pubs.acs.org/doi/10.1021/acs.chemmater.6b01777 (2021) (Aug. 2016).

336. Bagheri, Z. *et al.* Light-induced improvement of dopant-free PTAA on performance of inverted perovskite solar cells. en. *Solar Energy Materials and Solar Cells* **215,** 110606. ISSN: 09270248. https://linkinghub.elsevier.com/retrieve/pii/S0927024820302099 (2021) (Sept. 2020).

337. Lee, I., Rolston, N., Brunner, P.-L. & Dauskardt, R. H. Hole-Transport Layer Molecular Weight and Doping Effects on Perovskite Solar Cell Efficiency and Mechanical Behavior. en. *ACS Applied Materials & Interfaces* **11,** 23757–23764. ISSN: 1944-8244, 1944-8252. https://pubs.acs.org/doi/10.1021/acsami.9b05567 (2021) (July 2019).

338. Lee, H. K. H. *et al.* Batch-to-Batch Variation of Polymeric Photovoltaic Materials: its Origin and Impacts on Charge Carrier Transport and Device Performances. en. *Advanced Energy Materials* **4,** 1400768. ISSN: 16146832. https://onlinelibrary.wiley.com/doi/10.1002/aenm.201400768 (2021) (Nov. 2014).

339. Lee, D. G. *et al.* Effect of Metal Electrodes on Aging-Induced Performance Recovery in Perovskite Solar Cells. en. *ACS Applied Materials & Interfaces* **11,** 48497–48504. ISSN: 1944-8244, 1944-8252. https://pubs.acs.org/doi/10.1021/acsami.9b14619 (2020) (Dec. 2019).

340. Luo, D. *et al.* Enhanced photovoltage for inverted planar heterojunction perovskite solar cells. en. *Science* **360,** 1442–1446. ISSN: 0036-8075, 1095-9203. https://www.science.org/doi/10.1126/science.aap9282 (2021) (June 2018).

341. Xu, G. *et al.* New Strategy for Two-Step Sequential Deposition: Incorporation of Hydrophilic Fullerene in Second Precursor for High-Performance p-i-n Planar Perovskite Solar Cells. en. *Advanced Energy Materials* **8,** 1703054. ISSN: 16146832. https://onlinelibrary.wiley.com/doi/10.1002/aenm.201703054 (2021) (Apr. 2018).

342. Wang, Q., Bi, C. & Huang, J. Doped hole transport layer for efficiency enhancement in planar heterojunction organolead trihalide perovskite solar cells. en. *Nano Energy* **15,** 275–280. ISSN: 22112855. https://linkinghub.elsevier.com/retrieve/pii/S2211285515001962 (2021) (July 2015).

343. Christians, J. A., Fung, R. C. M. & Kamat, P. V. An Inorganic Hole Conductor for Organo-Lead Halide Perovskite Solar Cells. Improved Hole Conductivity with Copper Iodide. en. *Journal of the American Chemical Society* **136,** 758–764. ISSN: 0002-7863, 1520-5126. https://pubs.acs.org/doi/10.1021/ja411014k (2021) (Jan. 2014).

344. Qin, P. *et al.* Inorganic hole conductor-based lead halide perovskite solar cells with 12.4% conversion efficiency. en. *Nature Communications* **5,** 3834. ISSN: 2041-1723. http://www.nature.com/articles/ncomms4834 (2021) (Sept. 2014).

345. Li, M. *et al.* Copper Salts Doped Spiro-OMeTAD for High-Performance Perovskite Solar Cells. en. *Advanced Energy Materials* **6,** 1601156. ISSN: 16146832. https://onlinelibrary.wiley.com/doi/10.1002/aenm.201601156 (2021) (Nov. 2016).

346. Liu, Y., Liu, Z. & Lee, E.-C. High-Performance Inverted Perovskite Solar Cells Using Doped Poly(triarylamine) as the Hole Transport Layer. en. *ACS Applied Energy Materials* **2,** 1932–1942. ISSN: 2574-0962, 2574-0962. https://pubs.acs.org/doi/10.1021/acsaem.8b02047 (2021) (Mar. 2019).

347. Jung, J. W., Chueh, C.-C. & Jen, A. K.-Y. High-Performance Semitransparent Perovskite Solar Cells with 10% Power Conversion Efficiency and 25% Average Visible Transmittance Based on Transparent CuSCN as the Hole-Transporting Material. en. *Advanced Energy Materials* **5.** ISSN: 1614-6840. https://onlinelibrary.wiley.com/doi/abs/10.1002/aenm.201500486 (2018) (Sept. 2015).

348. Seethamraju, S., Ramamurthy, P. C. & Madras, G. Organic passivation layer on flexible Surlyn substrate for encapsulating organic photovoltaics. en. *Applied Physics Letters* **105,** 104102. ISSN: 0003-6951, 1077-3118. http://aip.scitation.org/doi/10.1063/1.4895719 (2022) (Sept. 2014).

349. Kim, J. *et al.* Excitation Density Dependent Photoluminescence Quenching and Charge Transfer Efficiencies in Hybrid Perovskite/Organic Semiconductor Bilayers. en. *Advanced Energy Materials* **8,** 1802474. ISSN: 1614-6832, 1614-6840. https://onlinelibrary.wiley.com/doi/10.1002/aenm.201802474 (2022) (Dec. 2018).

350. Raman, R. K., Gurusamy Thangavelu, S. A., Venkataraj, S. & Krishnamoorthy, A. Materials, methods and strategies for encapsulation of perovskite solar cells: From past to present. en. *Renewable and Sustainable Energy Reviews* **151,** 111608. ISSN: 13640321. https://linkinghub.elsevier.com/retrieve/pii/S1364032121008844 (2022) (Nov. 2021).

351. Wang, Y.-F., Li, X.-F., Li, D.-J., Sun, Y.-W. & Zhang, X.-X. Controllable synthesis of hierarchical SnO2 microspheres for dye-sensitized solar cells. en. *Journal of Power Sources* **280,** 476–482. ISSN: 03787753. https://linkinghub.elsevier.com/retrieve/pii/S0378775315001317 (2021) (Apr. 2015).

352. Ke, W. *et al.* Effects of annealing temperature of tin oxide electron selective layers on the performance of perovskite solar cells. en. *Journal of Materials Chemistry A* **3,** 24163–24168. ISSN: 2050-7488, 2050-7496. http://xlink.rsc.org/?DOI=C5TA06574G (2021) (2015).

353. Zhang, J. *et al.* Batch chemical bath deposition of large-area SnO2 film with mercaptosuccinic acid decoration for homogenized and efficient perovskite solar cells. en. *Chemical Engineering Journal* **425,** 131444. ISSN: 13858947. https://linkinghub.elsevier.com/retrieve/pii/S1385894721030254 (2022) (Dec. 2021).

354. Jung, E. H. *et al.* Bifunctional Surface Engineering on SnO_2 Reduces Energy Loss in Perovskite Solar Cells. en. *ACS Energy Letters* **5,** 2796–2801. ISSN: 2380-8195, 2380-8195. https://pubs.acs.org/doi/10.1021/acsenergylett.0c01566 (2022) (Sept. 2020).

355. Halvani Anaraki, E. *et al.* Low-Temperature Nb-Doped SnO_2 Electron-Selective Contact Yields over 20% Efficiency in Planar Perovskite Solar Cells. en. *ACS Energy Letters* **3,** 773–778. ISSN: 2380-8195, 2380-8195. https://pubs.acs.org/doi/10.1021/acsenergylett.8b00055 (2022) (Apr. 2018).

356. Correa Baena, J. P. *et al.* Highly efficient planar perovskite solar cells through band alignment engineering. en. *Energy & Environmental Science* **8,** 2928–2934. ISSN: 1754-5692, 1754-5706. http://xlink.rsc.org/?DOI=C5EE02608C (2022) (2015).

357. Cheon, K.-E., Lee, D.-Y., Cho, Y.-R., Song, P.-K. & Lee, G.-H. Effect of Sputtering Conditions on the Mechanical Property and the Permeability of IZO Grown by DC Magnetron Sputtering for Application to Flexible OLEDs. en. *Journal of the Korean Physical Society* **53,** 396–401. ISSN: 0374-4884. http://www.jkps.or.kr/journal/DOIx.php?id=10.3938/jkps.53.396 (2021) (July 2008).

358. Wang, A. *et al.* Charge transport, optical transparency, microstructure, and processing relationships in transparent conductive indium–zinc oxide films grown by low-pressure metal-organic chemical vapor deposition. en. *Applied Physics Letters* **73,** 327–329. ISSN: 0003-6951, 1077-3118. http://aip.scitation.org/doi/10.1063/1.121823 (2021) (July 1998).

359. Park, Y., Choong, V., Gao, Y., Hsieh, B. R. & Tang, C. W. Work function of indium tin oxide transparent conductor measured by photoelectron spectroscopy. en. *Applied Physics Letters* **68,** 2699–2701. ISSN: 0003-6951, 1077-3118. http://aip.scitation.org/doi/10.1063/1.116313 (2021) (May 1996).

360. Balasubramanian, N. & Subrahmanyam, A. Studies on Evaporated Indium Tin Oxide (ITO)/Silicon Junctions and an Estimation of ITO Work Function. *Journal of The Electrochemical Society* **138,** 322–324. ISSN: 0013-4651, 1945-7111. https://iopscience.iop.org/article/10.1149/1.2085565 (2021) (Jan. 1991).

361. Parker, I. D., Cao, Y. & Yang, C. Y. Lifetime and degradation effects in polymer light-emitting diodes. en. *Journal of Applied Physics* **85,** 2441–2447. ISSN: 0021-8979, 1089-7550. http://aip.scitation.org/doi/10.1063/1.369564 (2021) (Feb. 1999).

362. Lee, J. J., Kim, J. S., Yoon, S. J., Cho, Y. S. & Choi, J. W. Electrical and Optical Properties of Indium Zinc Oxide (IZO) Thin Films by Continuous Composition Spread. en. *Journal of Nanoscience and Nanotechnology* **13,** 3317–3320. ISSN: 1533-4880. http://www.ingentaconnect.com/content/10.1166/jnn.2013.7274 (2021) (May 2013).

363. Kim, S. *et al.* The Electronic and Optical Properties of IZO Thin Films Prepared by Pulsed DC Magnetron Sputtering. en. *Journal of the Korean Physical Society* **50,** 662. ISSN: 0374-4884. http://www.kps.or.kr/jkps/abstract_view.asp?articleuid=7E2DDE62-3B93-428F-84E4-0F8432937D66 (2022) (Mar. 2007).

364. Jiang, H., Wang, S., Xu, Y. & Yang, S. Preparation of a-IZO thin films by RF magnetron sputtering for Cu (In, Ga) Se2 solar cells. *Journal of Physics: Conference Series* **1549,** 042036. ISSN: 1742-6588, 1742-6596. https://iopscience.iop.org/article/10.1088/1742-6596/1549/4/042036 (2022) (June 2020).

365. Kusaka, K., Taniguchi, D., Hanabusa, T. & Tominaga, K. Effect of sputtering gas pressure and nitrogen concentration on crystal orientation and residual stress in sputtered AlN films. en. *Vacuum* **66,** 441–446. ISSN: 0042207X. https://linkinghub.elsevier.com/retrieve/pii/S0042207X02001689 (2022) (Aug. 2002).

366. Shin, D.-H., Kim, Y.-H., Han, J.-W., Moon, K.-M. & Murakami, R.-I. Effect of process parameters on electrical, optical properties of IZO films produced by inclination opposite target type DC magnetron sputtering. en. *Transactions of Nonferrous Metals Society of China* **19,** 997–1000. ISSN: 10036326. https://linkinghub.elsevier.com/retrieve/pii/S1003632608603945 (2021) (Aug. 2009).

367. Fortunato, E., Pimentel, A., Gonçalves, A., Marques, A. & Martins, R. High mobility amorphous/nanocrystalline indium zinc oxide deposited at room temperature. en. *Thin Solid Films* **502,** 104–107. ISSN: 00406090. https://linkinghub.elsevier.com/retrieve/pii/S0040609005011181 (2021) (Apr. 2006).

368. Bender, M. *et al.* Dependence of oxygen flow on optical and electrical properties of DC-magnetron sputtered ITO films. en. *Thin Solid Films* **326,** 72–77. ISSN: 00406090. https://linkinghub.elsevier.com/retrieve/pii/S0040609098005215 (2021) (Aug. 1998).

369. Yonesu, A., Watashi, S., Kagawa, K. & Yamashiro, Y. Study on facing-target sputtering assisted by microwave plasma for enhanced ionization of sputtered atoms. en. *Vacuum* **74,** 521–524. ISSN: 0042207X. https://linkinghub.elsevier.com/retrieve/pii/S0042207X04000995 (2021) (June 2004).

370. Ghosh, K. & Pandey, R. K. Fractal and multifractal analysis of In-doped ZnO thin films deposited on glass, ITO, and silicon substrates. en. *Applied Physics A* **125,** 98. ISSN: 0947-8396, 1432-0630. http://link.springer.com/10.1007/s00339-019-2398-y (2021) (Feb. 2019).

371. Jeon, J.-W. *et al.* Effect of annealing temperature on optical band-gap of amorphous indium zinc oxide film. en. *Journal of Alloys and Compounds* **509,** 10062–10065. ISSN: 09258388. https://linkinghub.elsevier.com/retrieve/pii/S0925838811016719 (2021) (Oct. 2011).

372. Yaglioglu, B., Yeom, H.-Y. & Paine, D. C. Crystallization of amorphous In2O3–10 wt % ZnO thin films annealed in air. en. *Applied Physics Letters* **86,** 261908. ISSN: 0003-6951, 1077-3118. http://aip.scitation.org/doi/10.1063/1.1977209 (2021) (June 2005).

373. Gonçalves, G. *et al.* Influence of post-annealing temperature on the properties exhibited by ITO, IZO and GZO thin films. en. *Thin Solid Films* **515,** 8562–8566. ISSN: 00406090. https://linkinghub.elsevier.com/retrieve/pii/S0040609007004555 (2021) (Oct. 2007).

374. Kim, Y., Oh, J., Kim, T.-G. & Park, B. Effect of microstructures on the microwave dielectric properties of ZrTiO4 thin films. en. *Applied Physics Letters* **78,** 2363–2365. ISSN: 0003-6951, 1077-3118. http://aip.scitation.org/doi/10.1063/1.1366359 (2021) (Apr. 2001).

375. Özgür, Ü. *et al.* A comprehensive review of ZnO materials and devices. en. *Journal of Applied Physics* **98,** 041301. ISSN: 0021-8979, 1089-7550. http://aip.scitation.org/doi/10.1063/1.1992666 (2021) (Aug. 2005).

376. Park, H.-K., Jeong, J.-A., Park, Y.-S., Kim, H.-K. & Cho, W.-J. Electrical, optical, and structural properties of InZnSnO electrode films grown by unbalanced radio frequency magnetron sputtering. en. *Thin Solid Films* **517,** 5563–5568. ISSN: 00406090. https://linkinghub.elsevier.com/retrieve/pii/S0040609009004118 (2021) (July 2009).

377. Ambrosini, A. *et al.* Zinc Doping in Cosubstituted $In_{2-2x}Sn_{x}Zn_{x}O_{3-\delta}$. en. *Chemistry of Materials* **14,** 58–63. ISSN: 0897-4756, 1520-5002. https://pubs.acs.org/doi/10.1021/cm010073x (2021) (Jan. 2002).

378. Choi, K.-H., Jeong, J.-A. & Kim, H.-K. Dependence of electrical, optical, and structural properties on the thickness of IZTO thin films grown by linear facing target sputtering for organic solar cells. en. *Solar Energy Materials and Solar Cells* **94,** 1822–1830. ISSN: 09270248. https://linkinghub.elsevier.com/retrieve/pii/S0927024810003533 (2021) (Oct. 2010).

379. Marks, T. *et al.* Progress in high work function TCO OLED anode alternatives and OLED nanopixelation. en. *Synthetic Metals* **127,** 29–35. ISSN: 03796779. https://linkinghub.elsevier.com/retrieve/pii/S0379677901005938 (2021) (Mar. 2002).

380. Noh, Y.-J., Kim, J.-G., Kim, S.-S., Kim, H.-K. & Na, S.-I. Efficient semi-transparent perovskite solar cells with a novel indium zinc tin oxide top electrode grown by linear facing target sputtering. en. *Journal of Power Sources* **437,** 226894. ISSN: 03787753. https://linkinghub.elsevier.com/retrieve/pii/S0378775319308870 (2021) (Oct. 2019).

381. Bryant, D. *et al.* A Transparent Conductive Adhesive Laminate Electrode for High-Efficiency Organic-Inorganic Lead Halide Perovskite Solar Cells. en. *Advanced Materials* **26,** 7499–7504. ISSN: 1521-4095. https://onlinelibrary.wiley.com/doi/abs/10.1002/adma.201403939 (2018) (Nov. 2014).

382. Messmer, C. *et al.* Optimized front TCO and metal grid electrode for module-integrated perovskite–silicon tandem solar cells. en. *Progress in Photovoltaics: Research and Applications,* pip.3491. ISSN: 1062-7995, 1099-159X. https://onlinelibrary.wiley.com/doi/10.1002/pip.3491 (2021) (Oct. 2021).

383. Shi, B., Duan, L., Zhao, Y., Luo, J. & Zhang, X. Semitransparent Perovskite Solar Cells: From Materials and Devices to Applications. en. *Advanced Materials* **32,** 1806474. ISSN: 0935-9648, 1521-4095. https://onlinelibrary.wiley.com/doi/10.1002/adma.201806474 (2021) (Jan. 2020).

384. Zhang, D. *et al. Highly near-infrared-transparent perovskite solar cells and their application in high-efficiency 4-terminal perovskite/c-Si tandems* in *2018 IEEE 7th World Conference on Photovoltaic Energy Conversion (WCPEC) (A Joint Conference of 45th IEEE PVSC, 28th PVSEC & 34th EU PVSEC)* (IEEE, Waikoloa Village, HI, USA, June 2018), 3575–3577. ISBN: 978-1-5386-8529-7. https://ieeexplore.ieee.org/document/8547936/ (2018).

385. Koida, T., Fujiwara, H. & Kondo, M. Hydrogen-doped In_2O_3 as High-mobility Transparent Conductive Oxide. en. *Japanese Journal of Applied Physics* **46,** L685–L687. ISSN: 0021-4922. https://iopscience.iop.org/article/10.1143/JJAP.46.L685 (2021) (July 2007).

386. Macco, B., Knoops, H. C. M. & Kessels, W. M. M. Electron Scattering and Doping Mechanisms in Solid-Phase-Crystallized In_2O_3:H Prepared by Atomic Layer Deposition. en. *ACS Applied Materials & Interfaces* **7,** 16723–16729. ISSN: 1944-8244, 1944-8252. https://pubs.acs.org/doi/10.1021/acsami.5b04420 (2021) (Aug. 2015).

387. King, P. D. C. & Veal, T. D. Conductivity in transparent oxide semiconductors. *Journal of Physics: Condensed Matter* **23,** 334214. ISSN: 0953-8984, 1361-648X. https://iopscience.iop.org/article/10.1088/0953-8984/23/33/334214 (2021) (Aug. 2011).

388. Boccard, M., Rodkey, N. & Holman, Z. C. High-mobility Hydrogenated Indium Oxide without Introducing Water During Sputtering. en. *Energy Procedia* **92,** 297–303. ISSN: 18766102. https://linkinghub.elsevier.com/retrieve/pii/S1876610216305100 (2021) (Aug. 2016).
389. Varanasi, A. *Deposition of Hydrogen-Doped Indium Oxide Thin Films Using Atmospheric Pressure Plasma-Enhanced Spatial Atomic Layer Deposition* English. PhD thesis (Delft Univeristy of Technology, Delft, Sept. 2017).
390. Wu, Y., Kessels, W., Roozeboom, F. & Verheijen, M. *Growth, phase and doping control in ZnO and In2O3 thin films prepared by atomic layer deposition* English. ISBN: 9789038640891 OCLC: 989561662. PhD thesis (Technische Universiteit Eindhoven, Eindhoven, 2016).
391. Rit, M., Asikainen, T., Leskelä, M. & Skarp, J. Ale Growth of Transparent Conductors. en. *MRS Proceedings* **426,** 513. ISSN: 0272-9172, 1946-4274. http://link.springer.com/10.1557/PROC-426-513 (2021) (1996).
392. Ozasa, K., Ye, T. & Aoyagi, Y. Deposition of gallium oxide and indium oxide on GaAs for *in situ* process use by alternating supply of TEGa, TMIn, and H_2O_2 as surge pulses. en. *Journal of Vacuum Science & Technology A: Vacuum, Surfaces, and Films* **12,** 120–124. ISSN: 0734-2101, 1520-8559. http://avs.scitation.org/doi/10.1116/1.578905 (2021) (Jan. 1994).
393. Ott, A., Johnson, J., Klaus, J. & George, S. Surface chemistry of In2O3 deposition using In(CH3)3 and H2O in a binary reaction sequence. en. *Applied Surface Science* **112,** 205–215. ISSN: 01694332. https://linkinghub.elsevier.com/retrieve/pii/S0169433296009774 (2021) (Mar. 1997).
394. Nilsen, O. *et al.* Thin films of In2O3 by atomic layer deposition using In(acac)3. en. *Thin Solid Films* **517,** 6320–6322. ISSN: 00406090. https://linkinghub.elsevier.com/retrieve/pii/S0040609009003381 (2020) (Oct. 2009).
395. Bugot, C. *Elaboration d'oxydes et de sulfures à grande bande interdite pour les cellules photovoltaïques à base de Cu(In,Ga)Se2 par dépôt chimique en phase vapeur par flux alternés (ALD) activé par plasma* Français. PhD thesis (Université Pierre et Marie Curie - Paris VI, Paris, Oct. 2015).
396. Elam, J. W., Martinson, A. B. F., Pellin, M. J. & Hupp, J. T. Atomic Layer Deposition of In2O3 Using Cyclopentadienyl Indium: A New Synthetic Route to Transparent Conducting Oxide Films. en. *Chemistry of Materials* **18,** 3571–3578. ISSN: 0897-4756, 1520-5002. https://pubs.acs.org/doi/10.1021/cm060754y (2021) (July 2006).
397. Elam, J. W., Libera, J. A. & Hryn, J. N. Indium Oxide ALD Using Cyclopentadienyl Indium and Mixtures of H, 147–155. http://ecst.ecsdl.org/cgi/doi/10.1149/1.3633663 (2020) (2011).
398. Mane, A. U., Allen, A. J., Kanjolia, R. K. & Elam, J. W. Indium Oxide Thin Films by Atomic Layer Deposition Using Trimethylindium and Ozone. en. *The Journal of Physical Chemistry C* **120,** 9874–9883. ISSN: 1932-7447, 1932-7455. https://pubs.acs.org/doi/10.1021/acs.jpcc.6b02657 (2021) (May 2016).
399. Macco, B., Wu, Y., Vanhemel, D. & Kessels, W. M. M. High mobility In_2O_3:H transparent conductive oxides prepared by atomic layer deposition and solid phase crystallization: High mobility In_2O_3:H transparent conductive oxides prepared by atomic layer deposition and solid phase crystallization. en. *physica status solidi (RRL) - Rapid Research Letters* **8,** 987–990. ISSN: 18626254. https://onlinelibrary.wiley.com/doi/10.1002/pssr.201409426 (2021) (Dec. 2014).
400. Addonizio, M., Spadoni, A., Antonaia, A., Usatii, I. & Bobeico, E. Hydrogen-doped In2O3 for silicon heterojunction solar cells: Identification of a critical threshold for water content and rf sputtering power. en. *Solar Energy Materials and Solar Cells* **220,** 110844. ISSN: 09270248. https://linkinghub.elsevier.com/retrieve/pii/S0927024820304426 (2021) (Jan. 2021).
401. Shenai-Khatkhate, D. V., DiCarlo, R. L. & Ware, R. A. Accurate vapor pressure equation for trimethylindium in OMVPE. en. *Journal of Crystal Growth* **310,** 2395–2398. ISSN: 00220248. https://linkinghub.elsevier.com/retrieve/pii/S0022024807010998 (2021) (Apr. 2008).
402. Morales-Masis, M., Martin De Nicolas, S., Holovsky, J., De Wolf, S. & Ballif, C. Low-Temperature High-Mobility Amorphous IZO for Silicon Heterojunction Solar Cells. *IEEE Journal of Photovoltaics* **5,** 1340–1347. ISSN: 2156-3381, 2156-3403. http://ieeexplore.ieee.org/document/7155475/ (2021) (Sept. 2015).

403. Galagan, Y. Perovskite Solar Cells: Toward Industrial-Scale Methods. en. *The Journal of Physical Chemistry Letters* **9,** 4326–4335. ISSN: 1948-7185. https://pubs.acs.org/doi/10.1021/acs.jpclett.8b01356 (2021) (Aug. 2018).

404. Patidar, R., Burkitt, D., Hooper, K., Richards, D. & Watson, T. Slot-die coating of perovskite solar cells: An overview. en. *Materials Today Communications* **22,** 100808. ISSN: 23524928. https://linkinghub.elsevier.com/retrieve/pii/S2352492819308414 (2022) (Mar. 2020).

405. Kim, Y. Y. *et al.* Fast two-step deposition of perovskite *via* mediator extraction treatment for large-area, high-performance perovskite solar cells. en. *Journal of Materials Chemistry A* **6,** 12447–12454. ISSN: 2050-7488, 2050-7496. http://xlink.rsc.org/?DOI=C8TA02868K (2022) (2018).

406. Higuchi, H. & Negami, T. Largest highly efficient 203 × 203 mm ^{2} CH $_3$ NH $_3$ PbI $_3$ perovskite solar modules. *Japanese Journal of Applied Physics* **57,** 08RE11. ISSN: 0021-4922, 1347-4065. https://iopscience.iop.org/article/10.7567/JJAP.57.08RE11 (2021) (Aug. 2018).

407. Jeong, M. *et al.* Stable perovskite solar cells with efficiency exceeding 24.8% and 0.3-V voltage loss. en. *Science* **369,** 1615–1620. ISSN: 0036-8075, 1095-9203. https://science.sciencemag.org/content/369/6511/1615 (Aug. 2020).

408. Bovatsek, J., Tamhankar, A., Patel, R., Bulgakova, N. & Bonse, J. Thin film removal mechanisms in ns-laser processing of photovoltaic materials. en. *Thin Solid Films* **518,** 2897–2904. ISSN: 00406090. https://linkinghub.elsevier.com/retrieve/pii/S0040609009018094 (2021) (Mar. 2010).

409. Palma, A. L. *et al.* Laser-Patterning Engineering for Perovskite Solar Modules With 95% Aperture Ratio. *IEEE Journal of Photovoltaics* **7,** 1674–1680. ISSN: 2156-3381, 2156-3403. http://ieeexplore.ieee.org/document/8003288/ (2022) (Nov. 2017).

410. Turan, B. Scribe Width Optimization of Absorber Laser Ablation for Thin-film Silicon Solar Modules. *Journal of Laser Micro/Nanoengineering* **8,** 234–243. ISSN: 18800688. http://www.jlps.gr.jp/jlmn/assets/bb00a5955d2761f7de652881ba79ebcf.pdf (2022) (Dec. 2013).

411. Jaysankar, M. *et al.* Toward scalable perovskite-based multijunction solar modules. en. *Progress in Photovoltaics: Research and Applications,* pip.3153. ISSN: 1062-7995, 1099-159X. https://onlinelibrary.wiley.com/doi/10.1002/pip.3153 (2022) (June 2019).

412. Kwon, H.-C. *et al.* Parallelized Nanopillar Perovskites for Semitransparent Solar Cells Using an Anodized Aluminum Oxide Scaffold. en. *Advanced Energy Materials* **6.** ISSN: 1614-6840. https://onlinelibrary.wiley.com/doi/abs/10.1002/aenm.201601055 (2018) (Oct. 2016).

413. Im, J.-H., Lee, C.-R., Lee, J.-W., Park, S.-W. & Park, N.-G. 6.5% efficient perovskite quantum-dot-sensitized solar cell. en. *Nanoscale* **3,** 4088. ISSN: 2040-3364, 2040-3372. http://xlink.rsc.org/?DOI=c1nr10867k (2022) (2011).

414. Kim, H.-S. *et al.* Lead Iodide Perovskite Sensitized All-Solid-State Submicron Thin Film Mesoscopic Solar Cell with Efficiency Exceeding 9%. en. *Scientific Reports* **2,** 591. ISSN: 2045-2322. http://www.nature.com/articles/srep00591 (2022) (Dec. 2012).

415. Lee, M. M., Teuscher, J., Miyasaka, T., Murakami, T. N. & Snaith, H. J. Efficient Hybrid Solar Cells Based on Meso-Superstructured Organometal Halide Perovskites. en. *Science* **338,** 643–647. ISSN: 0036-8075, 1095-9203. https://www.science.org/doi/10.1126/science.1228604 (2022) (Nov. 2012).

416. Lee, J.-W., Seol, D.-J., Cho, A.-N. & Park, N.-G. High-Efficiency Perovskite Solar Cells Based on the Black Polymorph of HC(NH $_2$) $_2$ PbI $_3$. en. *Advanced Materials* **26,** 4991–4998. ISSN: 09359648. https://onlinelibrary.wiley.com/doi/10.1002/adma.201401137 (2022) (Aug. 2014).

417. Im, J.-H., Jang, I.-H., Pellet, N., Grätzel, M. & Park, N.-G. Growth of CH3NH3PbI3 cuboids with controlled size for high-efficiency perovskite solar cells. en. *Nature Nanotechnology* **9,** 927–932. ISSN: 1748-3387, 1748-3395. http://www.nature.com/articles/nnano.2014.181 (2022) (Nov. 2014).

418. Zhou, H. *et al.* Interface engineering of highly efficient perovskite solar cells. en. *Science* **345,** 542–546. ISSN: 0036-8075, 1095-9203. https://www.science.org/doi/10.1126/science.1254050 (2022) (Aug. 2014).

419. Son, D.-Y. *et al.* Self-formed grain boundary healing layer for highly efficient CH3NH3PbI3 perovskite solar cells. en. *Nature Energy* **1,** 16081. ISSN: 2058-7546. http://www.nature.com/articles/nenergy201681 (2022) (July 2016).

420. Jaysankar, M. *et al.* Perovskite–silicon tandem solar modules with optimised light harvesting. en. *Energy & Environmental Science* **11,** 1489–1498. ISSN: 1754-5692, 1754-5706. http://xlink.rsc.org/?DOI=C8EE00237A (2018) (2018).

421. Ramírez Quiroz, C. O. *et al.* Balancing electrical and optical losses for efficient 4-terminal Si–perovskite solar cells with solution processed percolation electrodes. en. *Journal of Materials Chemistry A* **6,** 3583–3592. ISSN: 2050-7488, 2050-7496. http://xlink.rsc.org/?DOI=C7TA10945H (2018) (2018).

422. Dewi, H. A. *et al.* Highly Efficient Semitransparent Perovskite Solar Cells for Four Terminal Perovskite-Silicon Tandems. en. *ACS Applied Materials & Interfaces* **11,** 34178–34187. ISSN: 1944-8244, 1944-8252. https://pubs.acs.org/doi/10.1021/acsami.9b13145 (2022) (Sept. 2019).

423. Jaysankar, M. *et al.* Minimizing Voltage Loss in Wide-Bandgap Perovskites for Tandem Solar Cells. en. *ACS Energy Letters* **4,** 259–264. ISSN: 2380-8195, 2380-8195. https://pubs.acs.org/doi/10.1021/acsenergylett.8b02179 (2020) (Jan. 2019).

424. Gharibzadeh, S. *et al.* 2D/3D Heterostructure for Semitransparent Perovskite Solar Cells with Engineered Bandgap Enables Efficiencies Exceeding 25% in Four-Terminal Tandems with Silicon and CIGS. en. *Advanced Functional Materials* **30,** 1909919. ISSN: 1616-301X, 1616-3028. https://onlinelibrary.wiley.com/doi/10.1002/adfm.201909919 (2022) (May 2020).

425. Duong, T. *et al.* High Efficiency Perovskite-Silicon Tandem Solar Cells: Effect of Surface Coating versus Bulk Incorporation of 2D Perovskite. en. *Advanced Energy Materials* **10,** 1903553. ISSN: 1614-6832, 1614-6840. https://onlinelibrary.wiley.com/doi/10.1002/aenm.201903553 (2022) (Mar. 2020).

426. Chen, B. *et al.* Enhanced optical path and electron diffusion length enable high-efficiency perovskite tandems. en. *Nature Communications* **11.** ISSN: 2041-1723. http://www.nature.com/articles/s41467-020-15077-3 (2020) (Dec. 2020).

427. Lee, K.-M. *et al.* Highly efficient and stable semi-transparent perovskite solar modules with a trilayer anode electrode. en. *Nanoscale* **10,** 17699–17704. ISSN: 2040-3364, 2040-3372. http://xlink.rsc.org/?DOI=C8NR06095A (2022) (2018).

428. Kwon, H.-C. *et al.* A nanopillar-structured perovskite-based efficient semitransparent solar module for power-generating window applications. en. *Journal of Materials Chemistry A* **8,** 1457–1468. ISSN: 2050-7488, 2050-7496. http://xlink.rsc.org/?DOI=C9TA11892F (2022) (2020).

429. Li, J. *et al.* Highly Efficient Thermally Co-evaporated Perovskite Solar Cells and Mini-modules. en. *Joule* **4,** 1035–1053. ISSN: 25424351. https://linkinghub.elsevier.com/retrieve/pii/S2542435120300970 (2022) (May 2020).

430. Wulff, H., Quaas, M., Steffen, H. & Hippler, R. In situ studies of diffusion and crystal growth in plasma deposited thin ITO films. en. *Thin Solid Films* **377-378,** 418–424. ISSN: 00406090. https://linkinghub.elsevier.com/retrieve/pii/S0040609000012682 (2021) (Dec. 2000).

431. Legeay, G. *Couches minces amorphes d'ITO : caractérisation, structure, évolution et fonctionnalisation sous rayonnements UV.* fr. PhD thesis (Université Rennes 1, Jan. 2011). https://tel.archives-ouvertes.fr/tel-00567155/document (2018).

432. Avrami, M. Kinetics of Phase Change. II Transformation-Time Relations for Random Distribution of Nuclei. en. *The Journal of Chemical Physics* **8,** 212–224. ISSN: 0021-9606, 1089-7690. http://aip.scitation.org/doi/10.1063/1.1750631 (2021) (Feb. 1940).

433. Marezio, M. Refinement of the crystal structure of In $_2$ O $_3$ at two wavelengths. *Acta Crystallographica* **20,** 723–728. ISSN: 0365-110X. http://scripts.iucr.org/cgi-bin/paper?S0365110X66001749 (2021) (Nov. 1966).

434. Meng, L.-j., Maçarico, A. & Martins, R. Study of annealed indium tin oxide films prepared by rf reactive magnetron sputtering. en. *Vacuum* **46,** 673–680. ISSN: 0042207X. http://linkinghub.elsevier.com/retrieve/pii/0042207X94001502 (2018) (July 1995).

435. Thilakan, P. & Kumar, J. Studies on the preferred orientation changes and its influenced properties on ITO thin films. en. *Vacuum* **48,** 463–466. ISSN: 0042207X. https://linkinghub.elsevier.com/retrieve/pii/S0042207X96003090 (2021) (May 1997).

436. Qiao, Z., Latz, R. & Mergel, D. Thickness dependence of In2O3:Sn film growth. en. *Thin Solid Films* **466,** 250–258. ISSN: 00406090. https://linkinghub.elsevier.com/retrieve/pii/S0040609004002597 (2021) (Nov. 2004).

437. Meng, L.-j. & dos Santos, M. Properties of indium tin oxide films prepared by rf reactive magnetron sputtering at different substrate temperature. en. *Thin Solid Films* **322,** 56–62. ISSN: 00406090. https://linkinghub.elsevier.com/retrieve/pii/S0040609097009395 (2021) (June 1998).

438. Terzini, E., Thilakan, P. & Minarini, C. Properties of ITO thin films deposited by RF magnetron sputtering at elevated substrate temperature. en. *Materials Science and Engineering: B* **77,** 110–114. ISSN: 09215107. https://linkinghub.elsevier.com/retrieve/pii/S0921510700004773 (2021) (Aug. 2000).

439. Joshi, R., Singh, V. & McClure, J. Characteristics of indium tin oxide films deposited by r.f. magnetron sputtering. en. *Thin Solid Films* **257,** 32–35. ISSN: 00406090. https://linkinghub.elsevier.com/retrieve/pii/0040609094063311 (2021) (Feb. 1995).

440. Sathiaraj, T. Effect of annealing on the structural, optical and electrical properties of ITO films by RF sputtering under low vacuum level. en. *Microelectronics Journal* **39,** 1444–1451. ISSN: 00262692. https://linkinghub.elsevier.com/retrieve/pii/S0026269208003224 (2021) (Dec. 2008).

441. Pettersson, L. A. A., Roman, L. S. & Inganäs, O. Modeling photocurrent action spectra of photovoltaic devices based on organic thin films. *Journal of Applied Physics* **86,** 487–496. ISSN: 0021-8979. https://aip.scitation.org/doi/10.1063/1.370757 (2018) (June 1999).

442. Wang, H. *et al.* Bifacial, Color-Tunable Semitransparent Perovskite Solar Cells for Building-Integrated Photovoltaics. en. *ACS Applied Materials & Interfaces* **12,** 484–493. ISSN: 1944-8244, 1944-8252. https://pubs.acs.org/doi/10.1021/acsami.9b15488 (2021) (Jan. 2020).

Résumé en français

Introduction

Nous vivons dans une société moderne où le secteur de l'énergie est au cœur de notre fonctionnement. La demande d'énergie est toujours de plus en plus forte en raison du développement rapide des économies émergentes et de l'augmentation de la population mondiale, qui devrait atteindre 9,7 milliards d'habitants en 2050 [1]. En particulier, la demande en combustibles fossiles a continué de croître de manière significative en 2021, malgré la pandémie mondiale de coronavirus qui avait fortement freiné la consommation mondiale en 2020 [2]. Aujourd'hui, 80% de la consommation mondiale d'énergie provient de ressources fossiles (gaz, charbon, pétrole), et cette dernière augmente chaque année avec une tendance de 5% par an au cours des dernières décennies [3]. Il s'agit d'un véritable problème aujourd'hui car la combustion de combustibles fossiles est responsable de la plupart des émissions de gaz à effet de serre et de la pollution atmosphérique dans le monde. De plus, ces ressources sont très inégalement réparties dans le monde, ce qui est source de pressions géopolitiques dans des zones critiques [2]. Enfin, des difficultés d'extraction sont de plus en plus fréquentes en raison de l'épuisement des réserves et augmentent ainsi le coût d'exploitation et les investissements nécessaires. En parallèle, la prise de conscience du réchauffement climatique est devenu un enjeu sociétal incontournable. La communauté scientifique exprime son inquiétude depuis les années 1950 et lors des récentes négociations internationales sur le climat, la plupart des acteurs se sont engagés à limiter le réchauffement climatique à 1,5°C en réduisant leur empreinte carbone [4]. Pour respecter cet engagement, un rééquilibrage des ressources énergétiques primaires par des ressources renouvelables est indispensable. Cela se traduit notamment par une demande plus importante en énergies renouvelables, qui notamment a augmentée de 3% en 2020 [5].

L'énergie solaire est par ailleurs aujourd'hui une alternative de plus en plus sérieuse aux combustibles fossiles. Au cours des 15 dernières années, le nombre d'installations photovoltaïques dans le monde a explosé, tandis que le coût des systèmes a considérablement baissé, comme le montre la Fig. 1a. Cette évolution est liée à l'introduction sur le marché de cellules solaires à base de silicium qui permettent une production d'énergie propre, durable et peu coûteuse. Entre 2010 et 2020, le prix des modules silicium cristallin a été divisé par 9,5 pour atteindre un prix moyen de 0,18 €/Wp. Cette baisse est due à différents facteurs tels que la délocalisation et une augmentation du nombre de modules photovoltaïques et de leur efficacité. Par conséquent, le coût de l'électricité produite par le solaire à l'échelle industrielle a diminué de 13% par an, pour atteindre près de 7 US cents par kWh en 2019. Parallèlement, la capacité photovoltaïque mondiale a augmenté en moyenne de 20% par an depuis 2000, voir la Fig.1b. Cette augmentation est la plus élevée parmi toutes les technologies d'énergie renouvelable au cours de la dernière décennie. En effet, la capacité totale installée a atteint 713 GWp fin de 2020, avec en tête la Chine, qui représente près de la moitié de cette capacité (soit 260 GWp), ou 3% du mix mondial de production d'électricité. [7].

Cependant, le rendement des cellules silicium se rapprochent de plus en plus de sa limite théorique, fixée par la loi de Shockley-Queisser, à 29,1% [8]. Dans ce contexte, les cellules tandem, qui peuvent être considérées comme un empilement de deux cellules simples, sont actuellement étudiées car leur limite d'efficacité est beaucoup plus élevée (jusqu'à 45%). Cela est possible car chaque cellule absorbe dans une gamme spectrale spécifique. L'avantage de la technologie tandem est que la cellule en silicium peut être utilisée comme cellule inférieure. En revanche, un autre type de cellule doit être utilisé pour la partie supérieure. Cette technologie est utilisée depuis longtemps dans les applications spatiales mais le coût des composants utilisés était jusqu'à présent incompatible avec une commercialisation à grande échelle.

Récemment, une nouvelle classe de matériaux appelée pérovskite est devenue populaire comme matériau absorbeur dans une cellule solaire supérieure en configuration tandem avec une cellule inférieure en silicium. Synthétisées pour la première fois en 2009 par Kojima et al [9], le développement de ces cellules

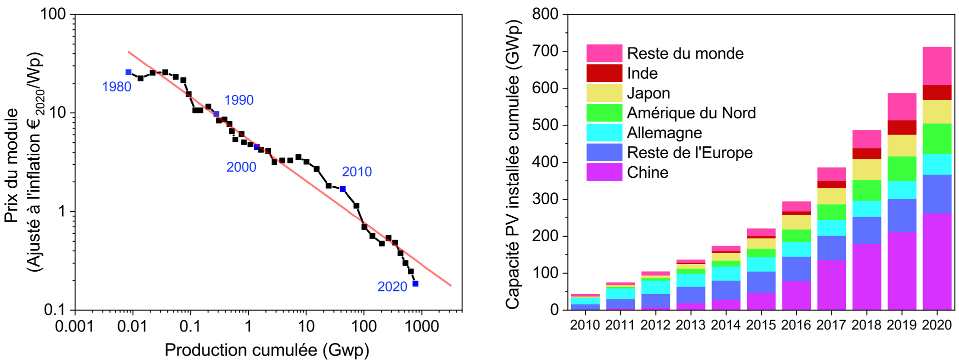
(a) (b)

Figure 1: (a) Courbe des prix incluant toutes les technologies photovoltaïques disponibles sur le marché [7]. (b) Installations photovoltaïques mondiales cumulées de 2010 à 2020 [7].

a été extrêmement rapide et elles ont maintenant atteint un rendement de 25,7% [10]. Les cellules pérovskites sont donc considérées comme une option prometteuse pour les tandems à faible coût, en raison des matériaux dont elles sont constituées et de leur association possible avec une cellule en silicium, déjà adaptée à un usage commercial. Aujourd'hui, les rendements de ces tandems à base de pérovskite ont dépassé la limite théorique des cellules en silicium seules (29,2%) mais restent bien en deçà de leur limite théorique à environ 40% [11]. En effet, dans une cellule idéale et parfaite, tous les photons dont l'énergie est supérieure au gap de la première et de la deuxième cellule seraient absorbés. En réalité, une partie de la lumière est perdue par absorption parasite dans les autres couches de la cellule et diverses résistances électriques réduisent le rendement final. Cela signifie qu'il y a encore beaucoup de travail à faire pour améliorer ces cellules.

Objectifs

L'objectif de cette thèse est de fabriquer une cellule pérovskite semi-transparente de haute performance, stable et de grande taille. Il s'agit de transférer le processus des cellules opaques aux cellules semi-transparentes tout en maintenant des propriétés électriques optimales, ainsi que de mettre en place la fabrication de tandem pérovskite/silicium jusqu'à 16 cm^2 dans le laboratoire de l'IPVF. Parmi les différentes architectures possibles, l'architecture tandem à quatre terminaux (4T) a été choisie dans ce travail en raison de ses nombreux avantages tels que la séparation totale de la synthèse des deux cellules, l'insensibilité aux variations spectrales et le large choix possible pour le type de chaque cellule utilisée. Cependant, malgré le fait que les pérovskites aient reçu beaucoup d'attention de la part de la communauté scientifique et qu'elles aient atteint un rendement très élevé en tout juste dix ans, de nombreux problèmes doivent être résolus avant qu'elles puissent être utilisées à l'échelle industrielle. Tout d'abord, les cellules pérovskites ont un problème de stabilité au contact de l'atmosphère et plus particulièrement de l'humidité. De plus, les cellules les plus efficaces sont actuellement de petite taille ($<$ 0,1 cm^2) et connaissent une baisse significative de leurs performances dès que leur taille dépasse 10 cm^2. Enfin, en remplaçant l'électrode arrière métallique habituelle par une électrode transparente, des pertes électriques supplémentaires apparaissent et une diminution des performances est observée par rapport aux cellules conventionnelles. Par conséquent, il était important de se concentrer non seulement sur la synthèse et la caractérisation électrique des matériaux constituant la cellule pérovskite mais aussi sur l'optique pour prendre en compte leur complémentarité dans l'empilement complet de la cellule tandem.

Développement d'un processus reproductible

Le premier axe de cette thèse consiste à améliorer la reproductibilité de la cellule pérovskite semi-transparente dont un schéma de l'architecture est présenté en Fig.2a. En raison du remplacement du contact arrière en métal Au de la cellule pérovskite opaque par de l'oxyde d'indium-étain (ITO), les cellules ont un comportement différent des références opaques et surtout une moins bonne reproductibilité. Les origines de cette dispersion semblent multiples et les courbes d'IVs nous permettent de classer les cellules dysfonctionnelles en plusieurs catégories : court-circuitées, soucis de synthèse ou interface dégradée. Comme il est crucial de disposer d'une cellule de référence robuste et reproductible pour incrémenter de nouveaux matériaux, il est nécessaire de tester différentes solutions.

Ceci est fait dans un premier temps par l'utiliation d'un nouveau design pour la cellule pérovskite semi-transparente ainsi que par une meilleure compréhension de la sensibilité de l'interface Spiro-OMeTAD / ITO à la chaleur. En parallèle, et après avoir éliminé l'hypothèse d'une résistance latérale trop importante de l'ITO ou à une resistance élevée de l'interface Spiro-OMeTAD / ITO, des tests avec des couches tampons métalliques ont montré l'intérêt de protéger la couche de Spiro-OMeTAD lors du dépot par pulvérisation de l'ITO. En particulier, une couche mince de nickel est apparu comme une technique intéressante pour limiter la dispersion, mais ce procédé n'est pas encore bien maîtrisé et n'est pas reproductible. Néanmoins, grâce aux différentes améliorations proposées, des cellules semi-transparentes avec des performances proches des cellules opaques ont pu être fabriquées, à l'image de l'échantillon AY10-b-09 dont les courbes IV sont présentées en Fig.2b et qui a atteint 18.48% d'efficacité.

De plus, les cellules semi-transparentes ont une évolution puis une stabilité dans le temps que les cellules opaques n'ont pas. Elles nécessitent une durée variable de 1 à 3 semaines pour atteindre leur plein potentiel suite à la disparition d'une forme en S sur les courbes IV. Elles peuvent ensuite se maintenir pendant plusieurs mois à cette performance tant qu'elles sont conservées sous vide. Nous avons finalement fabriqué un premier prototype tandem à 22.3% sur 0.09 cm^2 en combinant une cellule pérovskite semi-transparente (16.6%) et une cellule en silicium AL-BSF (5.7%).

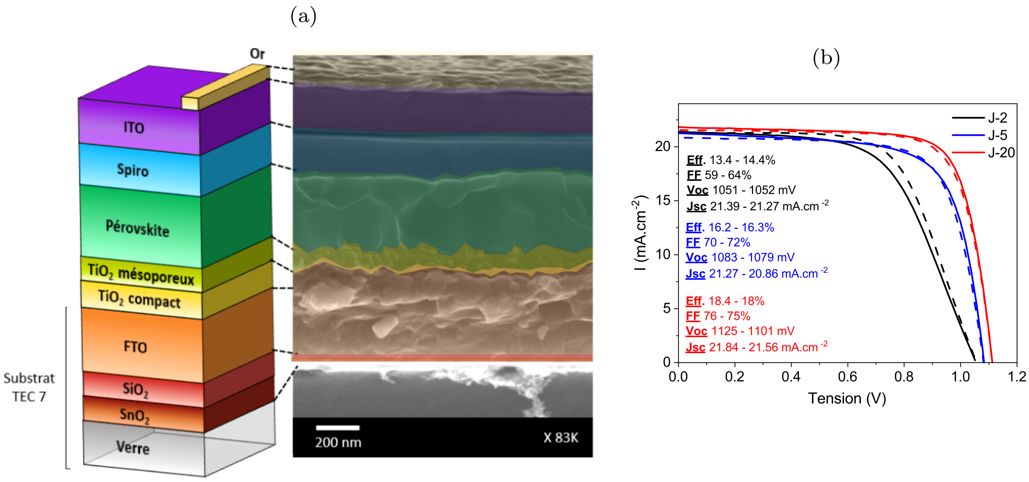

Figure 2: (a) Croquis et image en coupe vus au microscope électronique à balayage d'une cellule semi-transparente classique. (b) Évolution de l'IV sur 20 jours de la cellule semi-transparente AY10-b-09, qui atteint le rendement le plus élevé à 18,48% du laboratoire sur 0.09 cm^2.

Modélisation optique

Au-delà des attentes concernant la reproductibilité, qui concernent également la cellule pérovskite opaque, la cellule pérovskite semi-transparente doit présenter une qualité supplémentaire : une transparence dans l'infrarouge. Cette dernière doit être maximisée autant que possible pour permettre à la cellule en silicium située en dessous de fonctionner à son plein potentiel.

Malgré les bonnes performances électriques obtenues, les spectres de transmission des cellules semi-transparentes révèlent la présence d'absorption et de réflexion parasites au sein du dispositif. Afin d'identifier leur origine, des simulations numériques basées sur la propagation d'ondes optiques dans des couches minces ont été réalisées par plusieurs groupes [29, 138, 194, 195, 197, 266, 267]. Cependant, comme les indices optiques d'une couche mince pouvant fortement dépendre des conditions de dépôt et de post-traitement, à l'image des pérovskites à triple cations, nous avons choisi de déterminer nous-mêmes les indices optiques de chaque couche. Nous avons ensuite développé une méthode itérative pour obtenir les résultats les plus fiables possibles, basée sur la caractérisation expérimentale de chaque couche séparément à l'aide de différentes techniques spectroscopiques, et l'utilisation de la méthode des matrices de transfert. Ceci nous a permis de modéliser notre structure semi-transparente avec un très bon accord entre les résultats expérimentaux et simulés.

Cette modélisation nous a ensuite permis de mettre en évidence et de quantifier les pertes par absorption optique causées par certains matériaux, ainsi que d'évaluer les pertes par réflexion à chaque interface. La Fig.3a montre par exemple l'absorption simulée dans chaque couche de la cellule semi-transparente. Ainsi, les principales absorptions parasites dans l'infrarouge sont dues aux couches d'oxyde jouant le rôle d'électrodes transparentes (ITO et FTO). L'électrode en FTO est la plus problématique car elle absorbe 15% de la lumière incidente à 1000 nm. À cette longueur d'onde, l'électrode en ITO absorbe également 7,3%, le verre sodo-calcique 5,2% et le Spiro-OMeTAD 2,5%. Dans le visible entre 400 nm et 800 nm, l'absorption dans la couche de pérovskite est aussi limitée par l'absorption du FTO (5,2% à 600 nm). Grâce à l'utilisation d'un modèle électrique associé, il est apparu que l'électrode FTO était également le principal facteur limitant la FF de la cellule pérovskite.

La modélisation originale étant entièrement modulable, nous avons pu proposer diverses solutions pour améliorer les performances opto-électroniques de notre cellule semi-transparente de référence. Par exemple, des matériaux alternatifs à l'ITO, au FTO, au TiO_2 et au Spiro-OmMeTAD ont été identifiés : il s'agit de l'IO:H, l'IZO, le SnO_2 et le PTAA respectivement. En combinant les solutions les plus intéressantes et avec une cellule en silicium plus efficace (IBC au lieu de Al-BSF), nous avons montré qu'il est possible pour l'empilement proposé en Fig.3b d'atteindre un rendement de 30%.

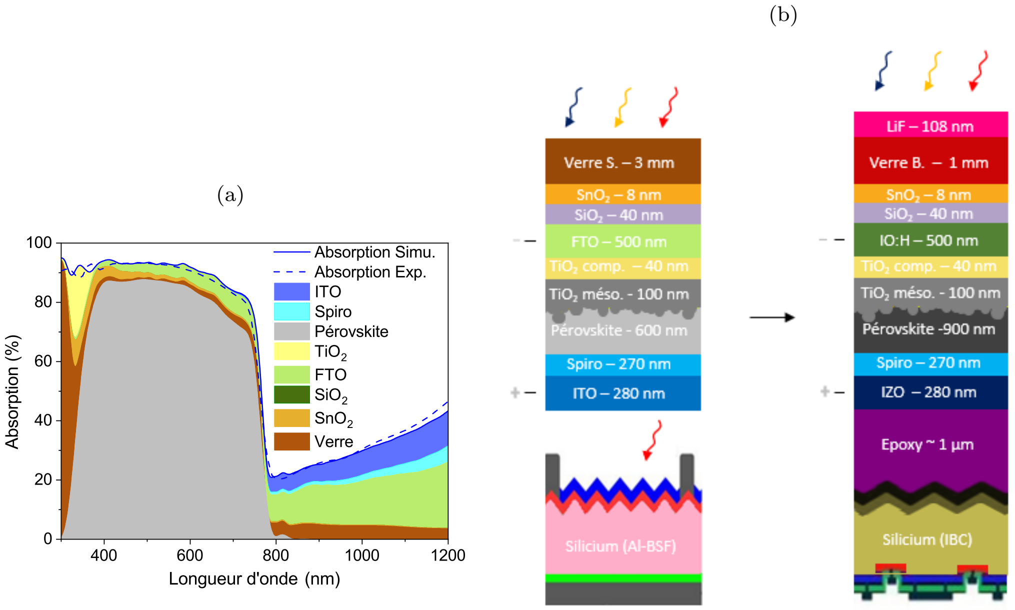
(a)

(b)

Figure 3: (a) Absorption totale simulée (courbe bleue) et expérimentale (courbe en pointillés bleus) de la cellule en pérovskite et absorption simulée dans chaque couche en utilisant la méthode itérative. (b) Evolution de la structure tandem 4T entre l'architecture de référence et l'architecture optimisée.

Remplacement des couches de transport de trous et d'électrons

Suite aux résultats obtenus en modélisation, nous avons cherché à remplacer le TiO_2 et du Spiro-OMeTAD dans l'empilement de référence. Ces composés présentent un alignement de bande optimal avec la couche pérovskite mais le Spiro-OMeTAD présente une sensibilité élevée et une absorption parasite dans l'infrarouge. D'autre part, le TiO_2 nécessite une température de synthèse supérieure à 500°C, ce qui limite le choix en termes d'électrode pour remplacer le FTO.

Les essais visant à remplacer le Spiro-OMeTAD par du PTAA ont permis de réduire encore davantage la dispersion des performances des cellules semi-transparentes tout en conservant un rendement proche de celui obtenu avec des cellules opaques. L'électrode en ITO est soumise à moins de contraintes en raison de la stabilité du PTAA et ne se délamine pas comme avec le Spiro-OMeTAD. Ceci a permis de réaliser des tests d'encapsulation auparavant impossibles, et nous avons réussi à maintenir une cellule pérovskite semi-transparente à plus de 90% de son efficacité pendant 1500 heures sous illumination, comme le montre la Fig.4. Nous avons également montré que l'évolution temporelle des propriétés électriques de ces dispostifs, similaires à ceux réalisés avec Spiro-OMeTAD, était due à une désoxygénation de la couche de transport de trous après la pulvérisation de l'ITO, ce qui conduit à la formation d'une barrière électrique à l'interface. La migration d'oxygène de l'extérieur de la cellule vers l'interface PTAA / ITO permet ensuite à l'interface de se régénérer en une dizaine de jours et la forme en S de se résorber sur les courbes IV.

En parallèle, des tests de compatibilité du SnO_2 avec différents types d'électrodes en face avant (ITO, IZO et FTO) en vue de remplacer TiO_2 ont été réalisés. Le SnO_2, comme le PTAA, est déposé sous forme de couche très fine et ne présente pas d'absorption parasite particulière. Les tests de compatibilité ont montré qu'elle était particulièrement sensible à la morphologie des couches et à leur rugosité. Néanmoins, des résultats prometteurs ont été obtenus sur des cellules pérovskites opaques en utilisant une couche ITO maison en face avant. Enfin, les premiers tests sur cellules semi-transparentes n'ont pas montré de comportement électrique négatif et doivent maintenant être reproduits en utilisant des substrats plus adaptés afin de valider les performances obtenues.

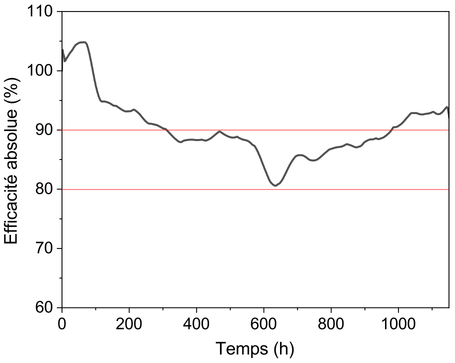

Figure 4: Évolution de l'efficacité absolue de l'échantillon MP23-13 après encapsulation pendant 1150 heures sous illumination.

Développement d'oxydes transparents conducteurs

Toujours dans l'idée d'améliorer optiquement nos cellules, le remplacement des électrodes avant et arrière est un point clé à étudier car l'ITO et le FTO actuellement utilisés présentent une absorption parasite non négligeable dans l'infrarouge. Le développement de deux nouveaux oxydes transparents conducteurs plus adaptés à nos applications a ainsi été réalisé : l'oxyde d'indium-zinc (IZO) et l'oxyde d'indium dopé à l'hydrogène (IO:H). Ces matériaux présentent une meilleure transparence dans l'infrarouge pour des propriétés électriques similaires.

La pulvérisation de l'électrode supérieure en IZO a tout d'abbord été optimisée sur verre avant d'être appliquée à une cellule semi-transparente. L'utilisation de bicouches d'IZO sur cellules s'est par la suite avérée plus intéressante que les couches simples en réduisant la dispersion et en augmentant le fill factor des cellules. En prenant l'IZO comme exemple et grâce à une simulation, nous avons également montré que des grilles d'oxydes transparents conducteurs peuvent permettent atteindre des efficacités plus élevées en configuration tandem en raison d'un équilibre électro-optique très favorable.

Enfin, nous avons utilisé l'ALD (ou dépôt de couches atomiques) pour déposer l'IO:H. Entre les deux précurseurs utilisés, les dépôts avec l'$In(acac)_3$ ont montré un phénomène de saturation à partir de 45 nm d'épaisseur. Ces résultats sont en accord avec la littérature et confirment la difficulté de faire croître l'oxyde d'indium, dopé ou non, avec ce précurseur. En revanche, avec le TMI et en utilisant un plasma d'H_2O et d'O_2/Ar comme réactif ou seulement d'H_2O et d'O_3, nous avons réussi à faire croître des couches de plus de 80 nm d'épaisseur avec les caractéristiques cristallographiques, optiques et morphologiques attendues de l'IO:H.

Un tandem 4T pérovskite/silicium de grande surface et efficace

Les diffférentes études menées jusqu'ici s'appuient sur l'utilisation de cellules semi-transparentes de 0,09 cm^2, ce qui est évidemment une taille insuffisante pour envisager une industrialisation.

Une première approche a consisté à s'interesser au remplacement de la technique de dépot par spin coating par le dépot par slot die, afin de pouvoir proposer un jour des dispositifs de tailles supérieures à 25 cm^2. Les résultats obtenus par le procédé slot die ont montré des résultats proches de ceux obtenus par spin-coating lorsque le Spiro-OMeTAD est utilisé comme couche de transport de trous. Les résultats avec le PTAA sont également prometteurs même s'ils présentent encore un manque de reproductibilité dû à la forte rugosité de la couche de pérovskite lorqu'elle est déposée par slot die.

Dans un deuxième temps et en conservant l'utilisation du procédé de base, nous avons transféré avec succès la fabrication de mini-modules opaques à des mini-modules semi-transparents avec un système de gravure P1P2P3. Ceci a été rendu possible, entre autres, en réduisant la largeur des sous-cellules à 3 mm, comme prédit par la simulation. Ainsi, pour un module de 4 cm^2, nous avons réussi à atteindre une efficacité de surface active de 16,2% comparable à celle obtenue sur des cellules de 0,09 cm^2. De plus, nous avons également synthétisé un mini-module semi-transparent de 16 cm^2 avec une efficacité de surface active de 14,2%, voir Fig.5a. Par simple empilement mécanique sur une cellule silicium de type n-PERT, nous avons ainsi obtenu un tandem 4T de 16 cm^2 avec une efficacité de surface active de 20,8%.

Enfin, nous avons améliorer notre dispositif tandem en couplant optiquement les cellules pérovskites et silicium comme prévu par la modélisation. Cela nous a pemris d'obtenir un tandem 4T de 0,09 cm^2 avec une efficacité proche de 25%. En utilisant de plus un contenant rigide et en procédant à un nouveau type d'encapsulation comme montré sur la Fig.5b, nous avons montré que nous étions capables de fabriquer un tandem 4T compact et robuste tout en répondant aux problèmes d'encapsulation et d'intégrité dans le temps pendant 16 jours.

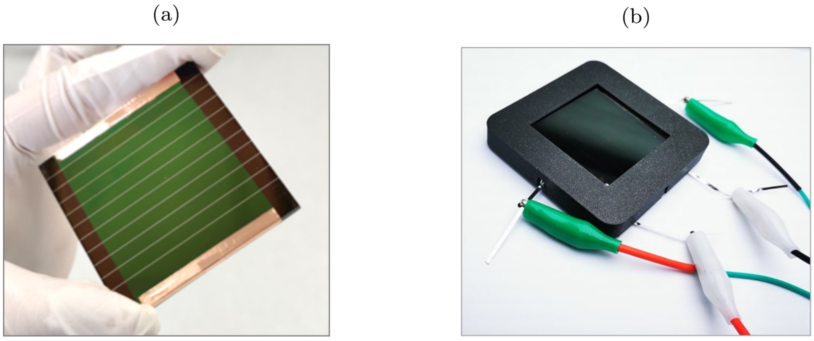
(a)

(b)

Figure 5: (a) Photo d'un module semi-transparent de 16 cm^2, composé de 10 sous-cellules de 1,6 cm^2 chacune.(b) Tandem 4T perovskie/silicium de 16 cm^2.

Perspectives

Afin d'améliorer davantages nos cellules semi-transparentes en pérovskite, tant sur le plan électrique qu'optique, plusieurs pistes sont actuellement explorées.

Tout d'abord, la modélisation réalisée nous a permis de concevoir un tandem théorique qui pourrait atteindre une efficacité de plus de 30%. Cependant, certaines des solutions identifiées n'ont pas encore été mises en œuvre. Le remplacement du FTO comme électrode frontale depend du remplacement éventuel du TiO_2 par le SnO_2. Le développement du SnO_2 est maintenant bien avancé à l'IPVF, les premiers tests réalisés sont encourageants et doivent maintenant être reproduits sur des substrats plus adaptés afin de valider les performances obtenues. Le remplacement du FTO est également conditionné par le développement de la couche d'IO:H par ALD. L'utilisation du précurseur TMI a permis la synthèse de couches relativement épaisses, mais elles restent trop résistives pour être utilisées comme électrodes. Un nouveau plan expérimental basé sur l'évolution de la conductivité pourrait permettre de progresser sur cette question en ajustant finement les paramètres de dépôt tels que les temps de pulse et de purge. Enfin, pour atteindre la structure optique optimale prédite par la simulation, il sera nécessaire de mettre en place l'utilisation systématique de verre borosilicate avec un revêtement anti-reflet et d'augmenter l'épaisseur de la couche de pérovskite.

En ce qui concerne le dépot par slot-die, les résultats obtenus sont très prometteurs mais n'ont été testés pour l'instant que sur petite surface de 0.09 cm^2. Des dépôts sur grandes surfaces de type mini-modules permettraient de synthétiser rapidement des dispositifs de plus de 16 cm^2. En parallèle, les cellules de type slot die avec PTAA présentent encore un manque de reproductibilité dû à la trop grande rugosité de la pérovskite par rapport à la finesse de la couche de PTAA. Ceci pourrait être amélioré à l'avenir en utilisant d'autres tensioactifs par exemple.

Toujours par rapport au développement des mini-modules, il est encore possible d'améliorer les dispositifs de 16 cm^2 en réduisant davantage les pertes résistives. Cela pourrait être réalisé, par exemple, en utilisant une grille TCO pour réduire la résistance de feuille des sous-cellules. Par ailleurs, nous disposons désormais d'un procédé d'encapsulation capable de maintenir l'efficacité de nos différents dispositifs sur une longue période. Cependant, ce procédé présente actuellement un taux d'échec élevé. Afin d'augmenter nos chances de succès, une étude plus systématique doit être menée afin de comprendre l'origine des dégradations observées. De plus, des tests de vieillissement dans des conditions réelles telles que la prise en compte du cycle jour/nuit ou des intempéries doivent désormais être réalisés.

Nous n'en sommes encore qu'aux premiers stades de la compréhension et de la résolution des problèmes liés à la synthèse des dispositifs semi-transparents pérovskites. Cependant, les progrès rapides réalisés associés à la possibilité de fabriquer ces dispositifs à faible coût, ont déjà suscité un intérêt industriel considérable dans le monde entier. Si les défis restants en matière d'efficacité et de stabilité peuvent être surmontés, le potentiel des tandems pérovskite/silicium comparé à d'autres technologies PV, pourrait avoir un impact inégalé sur la production d'énergie mondiale.

université PARIS-SACLAY

ÉCOLE DOCTORALE
Physique et ingénierie : Electrons, Photons, Sciences du vivant (EOBE)

Titre : Cellules solaires semi-transparentes en pérovskite pour des dispositifs tandem de grande surface à 4 terminaux à base de silicium

Mots clés : Cellule solaire en configuration tandem, Management optique, Pérovskite

Résumé : Le marché actuel du photovoltaïque est dominé par les cellules solaires à base de silicium, dont les performances de laboratoire se rapprochent de plus en plus de la limite théorique. Pour dépasser cette limite, l'approche la plus prometteuse est l'utilisation d'une architecture tandem associant une cellule solaire à grand gap à une cellule en silicium. L'objectif de la thèse est de fabriquer une cellule pérovskite semi-transparente à haut rendement, stable et de grande taille pour la réalisation d'une cellule tandem 4-terminaux à base de silicium. Les pertes optiques liées à l'absorption des matériaux et à la réflexion aux différentes interfaces ont été analysées en détail en couplant modélisation et caractérisation optique, afin de guider le développement de cellules semi-transparentes efficaces. Le travail a porté en particulier sur le remplacement du contact métallique arrière des cellules conventionnelles en pérovskite par une électrode transparente en ITO, IZO ou IO :H, et par l'introduction de contacts sélectif en PTAA et $\mathrm{SnO_2}$. Les empilements et les procédés ont été optimisés pour minimiser les pertes optiques et électriques, et améliorer la stabilité des dispositifs. Les études expérimentales réalisées sur des cellules pérovskite de petite surface et des cellules silicium filtrées, ont montré une efficacité potentielle de près de 25%. Elles ont également permis de mieux comprendre l'évolution temporelle des propriétés électriques, marquées par barrière électrique temporaire observé les premiers jours après la synthèse, puis s'estompant. Par ailleurs, le développement d'un procédé d'encapsulation a permis de maintenir une cellule pérovskite semi-transparente à plus de 90% de son efficacité initiale pendant plus de 2 mois. Enfin, une augmentation de la taille des dispositifs jusqu'à 16 cm^2 a été réalisée par la mise en série de plusieurs cellules pour former un mini-module avec une efficacité de surface active de 14,2%, et un tandem pérovskite sur silicium de même surface de 20,8%.

Title : Semi-transparent perovskite solar cells for large area 4-terminal silicon-based tandem devices

Keywords : Tandem solar cell, Light management, Perovskite

Abstract : The current photovoltaic market is dominated by silicon-based solar cells, whose laboratory performance is getting closer and closer to the theoretical limit. To overcome this limit, the most promising approach is the use of a tandem architecture combining a wide bandgap solar cell with a silicon cell. The objective of the thesis is to fabricate a high efficiency, stable and large-size semi-transparent perovskite cell for the realization of a 4-terminal silicon-based tandem cell. The optical losses due to material absorption and reflection at the various interfaces were analyzed in detail by coupling optical modelling and characterization, in order to guide the development of efficient semi-transparent solar cells. In particular, the work focused on replacing the metallic back contact of conventional perovskite cells with a transparent electrode made of ITO, IZO or IO :H, and introducing selective PTAA and $\mathrm{SnO_2}$ contacts. The stacks and processes were optimized to minimize optical and electrical losses, and improve the stability of the devices. Experimental studies on small area perovskite cells and filtered silicon cells have shown a potential efficiency of up to 25%. They also allowed a better understanding of the temporal evolution of the electrical properties, marked by a temporary electrical barrier observed in the first days after the synthesis, and then fading. In addition, the development of an encapsulation process has made it possible to maintain a semi-transparent perovskite cell at more than 90% of its initial efficiency for more than 2 months. Finally, an increase in the size of the devices up to 16 cm^2 was achieved by the series connection of several cells to form a mini-module with an active surface efficiency of 14.2%, and a perovskite-silicon tandem with the same surface area of 20.8%.